


SIDESWAY COLLAPSE OF DETERIORATING STRUCTURAL SYSTEMS
UNDER SEISMIC EXCITATIONS

A DISSERTATION
SUBMITTED TO THE DEPARTMENT OF CIVIL AND ENVIRONMENTAL
ENGINEERING
AND THE COMMITTEE ON GRADUATE STUDIES
OF STANFORD UNIVERSITY
IN PARTIAL FULFILLMENT OF THE REQUIREMENTS
FOR THE DEGREE OF
DOCTOR OF PHILOSOPHY

Dimitrios Lignos
September 2008

© Copyright 2008 by Dimitrios Lignos
All Rights Reserved

I certify that I have read this dissertation and that, in my opinion, it is fully adequate in scope and quality, as a dissertation for the degree of Doctor of Philosophy.



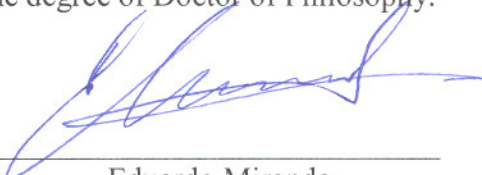
Helmut Krawinkler
(Principal Adviser)

I certify that I have read this dissertation and that, in my opinion, it is fully adequate in scope and quality, as a dissertation for the degree of Doctor of Philosophy.




Gregory G. Deierlein

I certify that I have read this dissertation and that, in my opinion, it is fully adequate in scope and quality, as a dissertation for the degree of Doctor of Philosophy.



Eduardo Miranda

I certify that I have read this dissertation and that, in my opinion, it is fully adequate in scope and quality, as a dissertation for the degree of Doctor of Philosophy.



Andrew S. Whittaker

Approved for the University Committee on Graduate Studies.

ACKNOWLEDGEMENTS

I would like to express my deep appreciation to my advisor, Professor Helmut Krawinkler, for his encouragement and support during all these years and for giving me the opportunity to work under his supervision. Working under your supervision was always an inspiration and honor. I must say that I am going to miss the long hour meetings that we had almost every week and of course the “bleeding” red pages during these meetings. Professor Krawinkler as simple as it sounds, since you taught me to keep things as simple as possible, “Thank you” for everything.

I would also like to express my appreciation to my reading and oral committee and advisors, Professors Anne Kiremidjian, Gregory G. Deierlein, Eduardo Miranda and Andrew Whittaker for providing me with their constructive comments. Special thanks to Professor Whittaker who made my stay at Buffalo during summer of 2007 very pleasant and of course for his friendship.

I would like to thank an “army” of graduate and undergraduate students who spent countless hours digitizing data and conscientiously inputting database information. Special thanks are due to the Stanford graduate students Yash Ahuja, Guillermo Soriano, and Richard Weiner, and to the University of Texas at Arlington REU student Yavor Yotov. Of course I cannot forget to thank Steven Patton for his help during the component tests that I conducted at Stanford during fall of 2005.

During my stay at the State University of New York at Buffalo in order to conduct the collapse test series of the model 4-frame, I had the opportunity to cooperate with three REU students. Many thanks to the Buffalo “collapse crew”; in particular the special thanks go to Matthew Alborn, Karhim Chiew and Melissa Norlund.

I have many appreciations for the researchers and students in John A. Blume Earthquake Engineering Center for their support in all levels. Since all of my officemates abandoned me I would like to thank my former office mates. Special thanks go to my good friend Professor Zareian (Farzin) for sharing a little bit of his wisdom in the office and of course for his friendship. I would like to thank the Blume Center Crew. Andy, Pablo, Marios and many others. Of course I could not forget Racquel who made my life easier in the Blume Center even if I was making hers hard sometimes.

My special appreciations go to my former advisor, Professor Charis Gantes from National Technical University of Athens since without your support and motivation I wouldn't be able to head this direction.

My study and also my research in this dissertation have been financially supported by the Network for Earthquake Engineering Simulation (NEES), a Blume Center fellowship during the first year of my PhD and also from Kajima Corporations as part of Phase VI of the Kajima-CUREE Joint Research Program. This support is gratefully appreciated and acknowledged.

During the time that I spent at Stanford I had the luxury to meet some really good friends that supported me during difficult times. My special thanks go to the Greek "gang" (Charis, Thanos, Yiannis, Gabriel and Euridiki) and of course Lambros...my Finite Element Instructor.

Finally, I would like to thank my family for all their support during my PhD and not only years. Their support was essential to the completion of my work and I truly thank you.

Dimitrios Lignos
September, 2008

*To my Parents,
Giorgos and Maria*

ABSTRACT

The primary objective of this research is to advance, through analytical and experimental research, knowledge on collapse assessment of structural systems. The focus is on sidesway collapse of frame structures, in which a specific story, or a series of stories, displaces sufficiently so that second order P-Delta effects fully offset the first order shear resistance and dynamic instability occurs. The effect of component deterioration that accelerates sidesway collapse of structural systems is of primary interest in this research.

Collapse assessment of structural systems is enhanced with the development of three extensive databases on steel and reinforced concrete beam elements. The three databases serve as the basis for validation and improvement of analytical models that explicitly model deterioration of structural components and are implemented in presently available dynamic analysis platforms. Through the calibration of several hundreds of experimental tests relationships are proposed that associate available deterioration modeling parameters with section properties and detailing criteria that control deterioration in structural components. The focus is on plastic hinge regions in steel components. These relationships and statistical measures accounting for modeling and material uncertainties serve as the basis for modeling recommendations of steel components.

Through the successful completion of earthquake-simulator collapse tests series of two scale model of a steel frame that serves as the lateral system of a 4-story office building, it is demonstrated that component deterioration has a significant effect on the collapse resistance of frame structures and that P- Δ effect can be quantified up to collapse. It is also demonstrated that it is possible to analytically predict sidesway collapse of frame structures, including the effects of component deterioration, fairly well using relatively simple models that can be incorporated in presently available dynamic analysis programs. Collapse assessment of deteriorating structural systems is enhanced with an array of case studies.

It is concluded that reliable prediction of collapse still has many hurdles to overcome, but the goal to improve the state of knowledge on how to predict the collapse capacity of deteriorating structural systems is achieved.

TABLE OF CONTENTS

Abstract.....	v
Acknowledgments.....	vi
List of Tables.....	xix
List of Illustrations.....	xxiii
1 Introduction.....	1
1.1 Objective and scope.....	1
1.2 State of Knowledge on Collapse Prediction of Structural Systems.....	2
1.3 “Point of Departure” for this Research.....	8
1.4 Outline.....	10
2 Hysteretic Models that Incorporate Component Deterioration.....	13
2.1 Purpose and Scope.....	13
2.2 Review of Basic Deterioration Models.....	14
2.2.1 Clough and Johnston Model.....	14
2.2.2 Takeda Model.....	15
2.2.3 Bouc – Wen Model and its Modifications.....	15
2.2.4 Ramberg-Osgood Model.....	17
2.2.5 Kunnath et al., Deterioration Models.....	18
2.2.6 Sivaselvan and Reinhorn Model.....	18
2.2.7 Yield – Line Plastic Hinge Models.....	19
2.2.8 FEMA 356 Component Model.....	20

2.2.9	Song and Pincheira Model	20
2.2.10	Ibarra-Medina-Krawinkler Deterioration Model	21
2.3	Modified Ibarra Krawinkler Deterioration Model Used in this Study.....	26
2.3.1	Modifications to Backbone Curve	26
2.3.2	Modifications to Cyclic Deterioration Modeling.....	29
2.4	Summary and Conclusions	33
3	Component Databases and Calibration	49
3.1	Purpose and Scope	49
3.2	Database Development	50
3.3	Calibration of Component Model Parameters	51
3.3.1	Calibrator Interactive Software.....	51
3.3.2	Calibrator Process Based on Engineering Judgment	53
3.4	Evaluation of Steel W-Section Database	56
3.4.1	Statistical Evaluation of Material Properties of US Structural Steel	57
3.4.2	Statistical Evaluation of Ratio of Effective to Predicted Bending Strength of Steel Beams	57
3.4.3	Post-Yield Hardening Stiffness.....	58
3.4.4	Trends for Deterioration Modeling Parameters	58
3.4.4.1.	Trends for Plastic Rotation Capacity θ_p	60
3.4.4.2.	Trends for Post Capping Rotation Capacity θ_{pc}	62
3.4.4.3.	Trends for Rate of Cyclic Deterioration A	63
3.4.5	Statistical Evaluation of Deterioration Modeling Parameters	64
3.4.6	Slab Effect.....	64
3.4.7	Residual Strength.....	66
3.4.8	Ductile Tearing	67
3.4.9	W-Columns	68
3.5	Evaluation of Steel Hollow Square Column Section Database	68
3.5.1.	Trends for Deterioration Modeling Parameters	70
3.5.1.1.	Plastic Rotation Capacity θ_p	70
3.5.1.2.	Post Capping Plastic Rotation Capacity θ_{pc}	71

3.5.1.3. Rate of Cyclic Deterioration λ	71
3.5.2. Residual Strength.....	71
3.5.3. Statistical Evaluation of Deterioration Modeling Parameters	71
3.6 Evaluation of Reinforced Concrete Database.....	72
3.6.1 Quantification of Modeling Parameters for Identical Specimens	73
3.6.2 Trends for Deterioration Modeling Parameters.....	74
3.6.3 Statistical Evaluation of Deterioration Modeling Parameters	77
3.7 Summary and Conclusions	77
4 Relationships for Modeling Deterioration Parameters of Plastic Hinge Regions	
.....	109
4.1 Objective and Scope	109
4.2 Multivariate Regression Analysis.....	110
4.3 W – Sections.....	112
4.3.1 Beams other than RBS.....	112
4.3.1.1. Plastic Rotation Capacity θ_p	112
4.3.1.2. Post Capping Rotation Capacity θ_{pc}	118
4.3.1.3. Cyclic Deterioration Parameter λ	121
4.3.2 Beams with RBS.....	124
4.3.2.1. Plastic Rotation Capacity θ_p	125
4.3.2.2. Post Capping Rotation Capacity θ_{pc}	127
4.3.2.3. Cyclic Deterioration Parameter λ	129
4.3.3 Hollow Square Tube Sections	131
4.3.3.1. Plastic Rotation Capacity θ_p	131
4.3.3.2. Post Capping Rotation Capacity θ_{pc}	134
4.3.3.3. Cyclic Deterioration Parameter λ	135
4.4 Summary and Conclusions	136
5 Design of Prototype Building and Test Frame for Shaking Table Collapse Tests	
.....	149
5.1 Objective and Scope	149

5.2	Design of Prototype 4 - story Steel Building	149
5.3	Design of Test Frame and Setup for Shaking Table Tests.....	153
5.3.1	Test Frame	154
5.3.2	Mass Simulator and Test Frame – Mass Simulator Links	156
5.3.3	Collapse Impact Prevention Blocks	157
5.3.4	Lateral Bracing Systems and Additional Safety Mechanisms.....	158
5.4	Summary	159
6	Component Tests.....	177
6.1	Objective and Scope	177
6.2	Target Deterioration Characteristics of Plastic Hinge Elements	178
6.3	Test Specimens – General Description	178
6.3.1	Experimental Setup.....	179
6.3.2	Support Frame.....	179
6.3.3	Specimen Type A.....	180
6.3.4	Specimen Type B.....	181
6.3.5	Instrumentation	183
6.3.6	Material Properties.....	185
6.4	Testing Program.....	186
6.4.1	Test Series of Type A Specimens	186
6.4.2	Test Series of Type B Specimens	187
6.5	Experimental Results	187
6.5.1	Definition of Deflection Components and Rotations.....	188
6.5.2	Definition of Yield Load and Yield Displacement	189
6.5.3	Specimens Type A – Results	190
6.5.3.1	Monotonic and Hysteresis Diagrams	190
6.5.4	Specimens Type B – Results.....	193
6.5.4.1	Monotonic and Hysteresis Diagrams	193
6.5.4.2	Strain Gage Results.....	195
6.6	Test Evaluation – Specimens Type B	196
6.6.1	Components of Deflection	198

6.6.2	Ductile Fracture	201
6.6.3	Ultimate Rotation Capacity	202
6.6.4	Calibration of Component Deterioration Parameters for Pre-Test Collapse Prediction.....	202
6.7	Post–Buffalo Component Tests.....	203
6.8	Summary and Observations.....	206
7	Shaking Table Collapse Test Series	239
7.1	Objective and Scope	239
7.2	Assembly of Test Frame and Installation on the Shaking Table.....	240
7.2.1	Assembly of Test Frame.....	240
7.2.2	Erection of Mass Simulator and Test Frame	240
7.3	Instrumentation.....	242
7.3.1	Load and Displacement Measurement Devices	242
7.3.2	Accelerometers	243
7.3.3	Strain and Deformation Measurements in Flange Plates	243
7.3.4	Krypton System.....	244
7.3.5	Cameras	244
7.4	Ground Motions and Testing Programs	245
7.4.1	Testing Program – Frame #1	245
7.4.2	Testing Program – Frame #2	246
7.5	Experimental Results.....	248
7.5.1	Test Frame #1	248
7.5.1.1	Modal Properties	248
7.5.1.2	Global Behavior.....	249
7.5.2	Test Frame #2	255
7.5.2.1	Modal Properties	255
7.5.2.2	Global Behavior.....	255
7.6	Test Evaluation.....	260
7.6.1	Friction Damping.....	260
7.6.2	Story Shear Distribution at Various Levels of Ground Motion	261

7.6.3	Base Shear – 1 st Story Drift and Quantification of P-Delta Effects.....	263
7.6.4	Moment Values During Plastification Based on Clip Gage Measurements	265
7.6.5	Post-Shaking Table Collapse Predictions	266
7.7	Summary and Conclusions	268
8	Case Studies.....	315
8.1	Objective and Scope	315
8.2	General Assumptions in 2-D Modeling of Frame Structures	316
8.3	4-Story Prototype Building Used in this Study.....	317
8.3.1.	Performance Evaluation-Nonlinear Static Analysis	318
8.3.2.	Dynamic Analysis.....	318
8.3.3.	Collapse Capacity of Prototype Frame Versus its 1:8 Scale Model	319
8.4	Kajima 15 Story Building Model A.....	321
8.4.1.	Deterioration Modeling.....	322
8.4.2.	Performance Evaluation.....	322
8.5	E-Defense 4-Story Steel Frame Structure.....	324
8.5.1.	Composite Action	325
8.5.2.	Deterioration Modeling.....	325
8.5.3.	Ground Motion and Testing Phases.....	326
8.5.4.	Static Pushover Analysis.....	327
8.5.5.	Dynamic Analysis Results-Comparison with Experimental Data	327
8.5.5.1.	Incipient Collapse Level (60% Takatori Record)	327
8.5.5.2.	Collapse Level (100% Takatori Motion).....	328
8.6	Collapse Assessment of Non-Ductile Building Structures	329
8.6.1.	Experimental Observations – Frames with Infill Walls.....	329
8.6.2.	Parameter Study Employing Deteriorating SDOF Systems	330
8.6.3.	Parameters of Structural Models.....	331
8.6.4.	Response - Examples	331
8.6.5.	Collapse Fragility Curves	332
8.6.6.	Evaluation of Median (and 10-percentile) Collapse Capacity.....	333

8.7	Collapse Assessment of Autoclaved Aerated Concrete Block Masonry Units.....	335
	
8.7.1.	Calibration of Moment Rotation Relationship for Specimens 15a and 15b (Case 1)	336
8.7.2.	Calibration of Moment Rotation Relationship for Assemblage Specimen (Case 2).....	337
8.7.3.	Ground Motions and its Scaling.....	337
8.7.4.	IDA Curves to Collapse.....	338
8.7.5.	Collapse Fragility Curves for Base Cases	338
8.8	Collapse Assessment of Reinforced Adobe Walls with Polymer Mesh.....	339
8.8.1.	Seismic Characteristics of a Representative Adobe Dwelling	340
8.8.2.	Collapse Fragility Curve for the Dwelling with Reinforced Walls.....	340
8.9	Summary and Conclusions	341
9	Summary and Conclusions	371
9.1	Development of Databases of Structural Elements	371
9.2	Improved Component Hysteresis/Deterioration Models	373
9.3	Development of Relationships for Modeling Deterioration of Plastic Hinge Regions 374	
9.4	Collapse Experiments and Predictions	375
9.5	Concluding Remarks	376
9.6	Suggestions for Future Work.....	377
A	Calibrated Values of Deterioration Model Parameters and Experimental Data	379
A.1	Beams Other than RBS.....	379
A.2	Beams with RBS.....	380
A.3	Tubular Hollow Square Column Sections.....	380
A.4	Tubular Hollow Square Column Sections.....	380

B	Design Drawings of Test Frame Used for Shaking Table Experimentation.....	397
C	Deduced Data from Component Tests.....	413
A.1	Equivalent Modulus for Deduction of Frame Plate Forces.....	413
D	Instrumentation Plan for Shaking Table Collapse Test Series.....	423
E	Summary of Results From Shaking Table Collapse Test Series.....	429
E.1	Test Frame #1.....	429
E.2	Test Frame #2.....	430
	References.....	443

LIST OF TABLES

Table 2.1.	Summary of capabilities of reviewed hysteresis models	35
Table 3.1.	Statistics of material yield strength from flange coupon tests	82
Table 3.2.	Statistics of material yield strength from web coupon tests	82
Table 3.3.	Statistics of ratios of effective to predicted component yield strength and capping strength to effective yield strength (steel data, W-sections)	82
Table 3.4.	Median and standard deviation of modeling parameters for all the data subsets of the W-section database	82
Table 3.5.	Correlation coefficients between modeling parameters (full data set, other-than-RBS)	83
Table 3.6.	Correlation coefficients between modeling parameters (full data set, RBS)	83
Table 3.7.	Correlation coefficients between modeling parameters (other-than-RBS, $d \geq 21"$)	83
Table 3.8.	Correlation coefficients between modeling parameters (RBS, $d \geq 21"$)	83
Table 3.9.	Correlation coefficients between modeling parameters (tubular columns)	84
Table 3.10.	Correlation coefficients between modeling parameters (tubular columns, monotonic data only)	84
Table 4.1.	Deterioration model parameters based on predictive Equations ((4.4), (4.8) and (4.12) for various beam sizes (beams other than RBS, assumed beam shear span $L=150"$, $L_b/r_y= 50$, expected yield strength $F_y=55$ ksi.)	139
Table 4.2.	Deterioration model parameters based on predictive Equations ((4.15), 4.17 and (4.19) for various beam sizes (beams with RBS, assumed beam shear span $L=150"$,	

	$L_b/r_y = 50$, expected yield strength $F_y = 55 \text{ksi}$)	139
Table 4.3.	Deterioration model parameters based on predictive equations for various tubular column sections and different N/N_y ratios (expected yield strength $F_y = 50 \text{ksi}$)	140
Table 5.1.	Dead loads of the prototype building	161
Table 5.2.	Estimation of seismically effective dead weight for typical floor	161
Table 5.3.	Calculated and design seismic weight per floor in the prototype	162
Table 5.4.	Parameters of reduced beam sections for final prototype design	162
Table 5.5.	Story drift under design lateral forces	162
Table 5.6.	Final sections for interior and exterior columns and beams of EW frame in prototype building, together with doubler plates for interior and exterior panel zones	163
Table 5.7.	Summary of similitude laws (after Moncarz, 1981)	163
Table 5.8.	Flange plate dimensions and bending strengths for Test Frame #1	164
Table 5.9.	Flange plate dimensions and bending strengths for Test Frame #2	164
Table 5.10.	Target and actual weight per floor of the test frame	165
Table 5.11.	Gap between collapse impact prevention blocks and mass plates together with maximum defined IDR	165
Table 6.1.	Target modeling parameters of components of the 4-story EW frame of the prototype structure	208
Table 6.2.	Material properties of steel material based on tensile coupon tests	208
Table 6.3.	Summary table of test results of type A specimens	208
Table 6.4.	Summary table of material properties obtained from tension tests of specimens of type B	208
Table 6.5.	Summary table of test results of specimens type B	209
Table 6.6.	Predicted stiffness for exterior test frame subassemblages	209

Table 6.7.	Experimental and analytical predictions of elastic stiffness for selected cantilever subassemblages	210
Table 6.8.	Modeling parameters for pre – Buffalo collapse prediction	210
Table 6.9.	Modeling parameters for post – Buffalo collapse prediction	210
Table 8.10.	Beam and column sections (Model A, units are in mm)	344
Table 8.11.	Weights per floor for Model A	344
Table 8.12.	Deterioration parameters for tubular sections of Model A including the effect of dynamic axial load in addition to gravity load	345
Table 8.13.	Deterioration parameters for steel beams of Model A	345
Table 8.14.	Section members for E-Defense 4-story structure (units in mm)	345
Table 8.15.	Seismic weight per floor for E-Defense 4-story moment resisting frames	346
Table 8.16.	Deterioration properties for beams of E-Defense 4-story frame	346
Table 8.17.	Deterioration properties for columns using 45 degrees configurations	346
Table 8.18.	Basic parameters for cases 1 and 2 (AAC)	346
Table A.1.	Beams other than RBS	381
Table A.2.	Connection Type	385
Table A.3.	Test configuration description for steel beams	
Table A.4.	Beams with RBS	386
Table A.5.	Tubular hollow square column sections	388
Table A.6.	Test configuration description for tubular hollow square column sections	390
Table A.7.	Reinforced concrete beams	391
Table A.8.	Test configuration description of reinforced concrete beams	395
Table C.1.	Equivalent modulus based on inner and outer strain of flange plates	415
Table D.1.	Instrumentation list notation	424

LIST OF FIGURES

Figure 2.1.	Peak – oriented (Clough) degrading stiffness model (after Clough and Johnston, (1965))	36
Figure 2.2.	Hysteretic model by Sucuoglu and Erberik (2004)	36
Figure 2.3.	Takeda hysteresis model (After Takeda et al. (1970))	37
Figure 2.4.	Bouc-Wen Model; separation of linear restoring force component from hysteretic restoring force component (Foliente, 1995)	37
Figure 2.5.	(a) Strength degradation, (b) Stiffness degradation (Foliente, 1995)	38
Figure 2.6.	Hysteresis pinching Baber and Nouri Model (Foliente, 1995)	38
Figure 2.7.	Simulations obtained with BWBN Model (Foliente, 1995)	39
Figure 2.8.	Ramberg-Osgood model (Carr, 2003)	40
Figure 2.9.	Example of calibrations of Sivaselvan and Reinhorn model (SAC Joint Venture 1996)	41
Figure 2.10.	Monotonic yield line plastic hinge model deformation (after Lee and Stojadinonic, 2004)	42
Figure 2.11.	General force-deformation behavior of structural components (FEMA 356, 2000)	42
Figure 2.12.	Song-Pincheira model; (a) backbone curve, (b) hysteresis rules for cycles of increasing def. amplitude, (c) hysteresis rules for small amplitude or internal cycles (after Song and Pincheira, 2000)	43
Figure 2.13.	Backbone curve of Ibarra-Krawinkler model, and associated definitions (after Ibarra et al., 2005)	33
Figure 2.14.	Individual deterioration modes for Ibarra-Krawinkler model, illustrated	

	on a peak-oriented model (after Ibarra et al., 2005)	44
Figure 2.15.	Backbone curve of modified Ibarra-Krawinkler model, and associated definitions	45
Figure 2.16.	Illustration of fracture incorporation in the modified Ibarra Krawinkler model; (a) fracture occurs after specimen reaches the residual strength path, (b) fracture occurs before the specimen reaches the residual path (b) for asymmetric backbone curve	46
Figure 2.17.	Illustration of different rates of cyclic deterioration based on the modified Ibarra-Krawinkler model	47
Figure 2.18.	Update strategy for the post capping strength deterioration modeling in the presence of residual strength.	48
Figure 2.19.	Stabilization of the hysteretic loop when the model reaches the residual strength value	48
Figure 3.1.	Use of Calibrator for matching experimental and predicted response	85
Figure 3.2.	Monotonic and cyclic responses of identical specimens, and skeleton curve fit to cyclic response (data from Tremblay et al. 1997)	86
Figure 3.3.	Calibration of monotonic test reported in Liddell et al. (2000)	86
Figure 3.4.	Yield to tensile strength histogram for A36 steel (a) taken from flange, (b) taken from web (W-sections database)	87
Figure 3.5.	Yield to tensile strength histogram for A572Gr.50 steel (a) taken from flange, (b) taken from web (W-sections database)	88

Figure 3.6.	Yield to tensile strength histogram for A992 Gr.50 steel (a) taken from flange, (b) taken from web (W-sections database)	89
Figure 3.7.	Dependence of θ_p on beam depth d for various data sets (W-sections database)	90
Figure 3.8.	Dependence of θ_p on beam span to depth ratio L/d of various data sets (W-sections database)	91
Figure 3.9.	Dependence of θ_p on L_b/r_y ratio for data sets with $d \geq 21$ " (W-sections database)	92
Figure 3.10.	Calibrated moment rotation diagrams for a beam with RBS; (a) no additional bracing provided, (b) additional bracing near the RBS region (data from Uang et al. 2000a)	92
Figure 3.11.	Dependence of θ_p on beam span to flange width to thickness ratio $b_f/2t_f$;	93
Figure 3.12.	Dependence of θ_p on ratio h/t_w ratio (W-sections database)	93
Figure 3.13.	Dependence of θ_{pc} of data sets (3) & (4) on various geometric parameters	94
Figure 3.14.	Dependence of λ of data sets (3) and (4) on various geometric parameters	95
Figure 3.15.	CDFs for θ_p ; left = full data sets (1) and (2); right = data sets (3) and (4)	96
Figure 3.16.	CDFs for θ_{pc} ; left = full data sets (1) and (2); right = data sets (3) and (4)	96
Figure 3.17.	CDFs for λ ; left = full data sets (1) and (2); right = data sets (3) and (4)	96
Figure 3.18.	Effect of slab on the deterioration characteristics of a composite beam with RBS; part of an exterior moment resisting frame (data from Ricles et al. 2004)	97

Figure 3.19.	Effect of slab on the deterioration characteristics of a beam; part of an interior moment resisting frame (data from E-Defense 2007)	97
Figure 3.20.	Effect of slab on the deterioration characteristics of a beam with RBS; subassembly of an exterior moment resisting frame (data from Tremblay et al. 1997)	98
Figure 3.21.	Effect of residual strength during loading history (a) residual strength is not attained (data from Lee et al. 2005); (b) stabilization, i.e residual strength (data from Krawinkler et al. 1983)	98
Figure 3.22.	Residual strength ratio κ versus beam depth for data sets (3) and (4) (W-sections database)	99
Figure 3.23.	Moment–rotation diagram of a heavy shallow column (test data from Newell and Uang, 2006)	99
Figure 3.24.	Dependence of θ_p on column tube depth to thickness ratio D/t and axial load ratio N/N_y (a) full data set (b) monotonic tests only	100
Figure 3.25.	Dependence of θ_{pc} on column tube depth to thickness ratio D/t and axial load ratio N/N_y (a) full data set (b) monotonic tests only (tubular column database)	101
Figure 3.26.	Calibration examples for monotonic tests of tubular section (data from Sugiyama & Igarashi, 1986)	101
Figure 3.27.	Dependence of A on column tube depth to thickness ratio D/t and axial load ratio N/N_y (tubular column database)	102
Figure 3.28.	Dependence of residual strength ratio κ on column tube depth to thickness ratio D/t and axial load ratio N/N_y (tubular column database)	102
Figure 3.29.	CDFs of deterioration model parameters	

	for tubular steel columns	103
Figure 3.30.	Calibrations of cyclic test “Berkeley loading history” from Liddell et al. (2000)	104
Figure 3.31.	Calibrations of cyclic test “EQA loading history” from Liddell et al. (2000)	104
Figure 3.32.	Dependence of θ_p & λ on f'_c	105
Figure 3.33.	Dependence of θ_p , & λ on $\rho_{sh,eff}$	105
Figure 3.34.	Dependence of θ_p , λ on s_n (left) and $s/d_{b,l}$ (right)	106
Figure 3.35.	Dependence of θ_p & λ on V_p/V_n	106
Figure 3.36.	CDFs of model parameters for RC beams (a) θ_p (b) λ	107
Figure 4.37.	Predicted versus calibrated values of θ_p (beams other than RBS, all data)	141
Figure 4.38.	Beams other than RBS with $d \geq 21$ "; (a) predicted versus calibrated θ_p ; (b) (b) interaction between d/t_w and $b_f/2t_f$ (beams other than RBS with $d \geq 21$ ")	141
Figure 4.39.	Predicted versus calibrated θ_{pc} values and dependence of θ_{pc} on yield strength for beams other than RBS for various data sets (W-section database)	142
Figure 4.40.	Predicted versus calibrated λ values for beams other than RBS and dependence of λ on yield strength for various data sets (W-section database)	143
Figure 4.41.	Predicted versus calibrated θ_p values for beams with RBS and dependence of θ_p of beams with RBS versus flange reduction c ($d \geq 21$ ")	144
Figure 4.42.	Predicted versus calibrated θ_{pc} values for beams with RBS and dependence of θ_{pc} on beam depth d ($d \geq 21$ ")	144

Figure 4.43.	Predicted versus calibrated λ values for beams with RBS ($d \geq 21"$)	145
Figure 4.44.	Predicted versus calibrated θ_p values for tubular steel columns; (a) all data, (b) monotonic data (HSS database)	145
Figure 4.45.	Predicted versus calibrated θ_{pc} values for tubular HSS steel columns; (a) all data, (b) monotonic data (HSS database)	146
Figure 4.46.	Predicted versus calibrated λ values for tubular HSS steel columns (HSS database)	146
Figure 4.47.	Effect of axial load ratio on cyclic deterioration of tubular HSS columns; (a) $N/N_y = 0.20$, $D/t = 28.5$, (b) data from Tsuji and Nakatsura (1986), $N/N_y = 0.40$, $D/t = 28.6$, data from Tsuji and Nakatsura (1986) (HSS database)	147
Figure 5.1.	Plan view of a typical story of the prototype office building	166
Figure 5.2.	Plan view of roof of the prototype office building. Penthouse is highlighted in grey	166
Figure 5.3.	Elevation views	167
Figure 5.4.	EW moment frame with leaning column	167
Figure 5.5.	Plan view and elevation of the scale model of the EW moment frame and mass simulator	168
Figure 5.6.	Dimensions of plastic hinge element	168
Figure 5.7.	Drawing and photo of an interior joint with four plastic hinge elements	169
Figure 5.8.	Drawing and photo of typical flange plates used in plastic hinge elements	170

Figure 5.9.	Plastic bending strength for beams and columns of the test frame	171
Figure 5.10.	Dimensions of elastic beam and column elements [Cad drawings in Solidworks (2004)]	172
Figure 5.11.	Exterior aluminum joint element of test frame [Cad drawing in Solidworks (2004)]	173
Figure 5.12.	Test frame for shaking table tests; (a) basic dimensions (b) after installation (b) on the shaking table	174
Figure 5.13.	Bracing systems for test frame and mass simulator	175
Figure 6.1.	Hysteretic behavior of basic structural components similar to ones used in the EW moment resisting frame of prototype structure (a) W27x94 beam (data from Partridge, 1997), (b) W21x62 beam (data from Tremblay et al. 1997) (c) W30x99 beam with RBS (data from Uang and Fan, 1999) and (d) W30x99 beam with RBS and additional lateral support near the RBS location (data from Uang and Fan, 1999)	211
Figure 6.2.	Exterior subassembly of test frame	212
Figure 6.3.	Test setup drawing	213
Figure 6.4.	Component test setup at Stanford 213	
Figure 6.5.	Cantilever subassemblage after installation (Specimen type A)	214
Figure 6.6.	Component end of cantilever subassemblage (plastic hinge region of specimen type A)	214
Figure 6.7.	Typical flange plate with $L/t = 8.0$ (specimen type A)	215

Figure 6.8.	Main parts of component end of specimen type B (plastic hinge region)	215
Figure 6.9.	Plastic hinge element of specimen type B; (a) dimensions (b) control parameters of flange plates attached to the plastic hinge element	216
Figure 6.10.	Relationship between bolt pretension force and applied torque	217
Figure 6.11.	Strain gage and clip gage instrumentation	217
Figure 6.12.	Experimental setup for component tests	218
Figure 6.13.	Material tests (a) general setup, (b) necking	219
Figure 6.14.	Engineering stress strain curve for A572 grade 50 steel plate used to machine flange plates	219
Figure 6.15.	Force equilibrium of free body during inelastic action of the component	220
Figure 6.16.	SAC loading protocol (Krawinkler et al. 2000), deformation parameter is interstory drift angle	220
Figure 6.17.	Deflection and rotation definitions for test specimens (specimen type B)	221
Figure 6.18.	Monotonic tests of single plate specimens with $L/t = 4$ (Type A)	222
Figure 6.19.	Tip load - tip displacement for specimen with two plates (specimen type A)	223
Figure 6.20.	$M - \theta_{1.5''}$ rotation diagram for specimen with two plates (specimen type A)	223
Figure 6.21.	Summary of observations from cyclic static test for specimen DB4-L/t=4.0-2 (specimen type A)	224
Figure 6.22.	Monotonic (compression and tension) tests of single plate specimens with $L/t=6,8,8$ (Type B specimens)	225

Figure 6.23.	Cyclic tests of single plate specimens with $L/t=6,8,8$ (Type B specimens)	226
Figure 6.24.	Tip load – tip displacement diagram of specimen “DB: 33,34- $L/t=6,8,8,2$ -Cyclic” (Type B specimens)	227
Figure 6.25.	$M_c - \theta_{Chord}$ diagram of specimen “DB: 33,34- $L/t=6,8,8,2$ -Cyclic” (Type B specimens)	227
Figure 6.26.	Summary of observations during the cyclic static test of specimen DB:33,34- $L/t=6,8,8,2$ -Cyclic (Type B specimens)	228
Figure 6.27.	Monotonic & cyclic flange plate force vs engineering strain relationships for outer & inner plate location of single plate specimens with $L/t=6,8,8$ (Type B specimens)	229
Figure 6.28.	Components of elastic tip deflection	230
Figure 6.29.	Detailed FEM model in ABAQUS	230
Figure 6.30.	Variations of stiffness and curvature along the cantilever beam	231
Figure 6.31.	Comparison between experimental data and data deduced from clip gage measurement plus elastic components of deflection of all parts based on curvature calculations (Type B)	232
Figure 6.32.	Exterior 1 st story prototype subassembly modeled in ABAQUS	232
Figure 6.33.	Simplified mathematical model used to simulate the behavior of model subassembly	233
Figure 6.34.	Comparison of FEM analytical predictions with ABAQUS versus experimental data of single plate specimens for monotonic and cyclic tests	234
Figure 6.35.	Monotonic and cyclic $M_c - \theta_{1.5}$ diagram for	

	typical plastic hinge location (Type B specimen)	235
Figure 6.36.	Calibrated $M_c - \theta_{1.5''}$ diagrams for typical plastic hinge locations	235
Figure 6.37.	Rotation history over 1.5" length for first floor beam at interior joint based on clip gage histories for all 5 testing phases (Frame #1)	236
Figure 6.38.	Contributions to elastic deflection of specimen subbaseembly for post-shaking table test evaluation	236
Figure 6.39.	Moment rotation($M_c - \theta_{1.5''}$) diagrams for plastic hinge locations at column base and 1 st floor beam obtained from component test using Buffalo rotation history as input (Frame # 1)	237
Figure 6.40.	Moment rotation ($M_c - \theta_{1.5''}$) diagram for plastic hinge location at top of third story column; Stanford component test withBuffalo rotation history followed by large displacement reversal	238
Figure 7.1.	Test frame after completion of assembly on the flat steel plate	272
Figure 7.2.	Mass simulator erection sequence; (a) installation of mass plates on the shaking table, (b) gravity links	272
Figure 7.3.	Installation of test Frame #1 on the shaking table	273
Figure 7.4.	Horizontal link connecting the test frame and mass simulator	273
Figure 7.5.	Test setup after completion of erection process on the shaking table (Frame #1)	274
Figure 7.6.	Krypton system	274

Figure 7.7.	First floor interior joint after installation of all the local instruments (Frame #1)	275
Figure 7.8.	Plan view and elevation of the test frame and mass simulator	275
Figure 7.9.	Various snap shots during erection and experimentation (Frame #1)	276
Figure 7.10.	Various snap shots during erection and experimentation (Frame #2)	277
Figure 7.11.	Northridge 1994 Canoga Park unscaled record	278
Figure 7.12.	Chile 1985 Lolleo unscaled record	279
Figure 7.13.	Transfer function at roof of Frame #1 based on a 0.1g WN test	280
Figure 7.14.	Roof drift ratio history for selected segments at various levels of intensity (Frame #1)	280
Figure 7.15.	Story drift history for selected segments at various levels of intensity (Frame #1)	281
Figure 7.16.	Flange plate local buckling at exterior column base after DBE and MCE tests (Frame #1)	282
Figure 7.17.	Flange plate local buckling at exterior column base after CLE and CLEF tests (Frame #1)	283
Figure 7.18.	Collapse mechanism of Frame #1 after completion of CLEF	284
Figure 7.19.	“Catching” mechanism of Frame #1 at the Incipient Collapse Level (ICL)	284
Figure 7.20.	Peak absolute floor acceleration of Frame #1 and mass simulator at various ground motion intensities	285
Figure 7.21.	Moment equilibrium at joints of Frame #1 at $t = 8.10\text{sec}$, SLE	286
Figure 7.22.	Story shear forces and distribution to story columns of Frame #1 ($t = 8.10\text{sec}$, SLE)	286

Figure 7.23.	Strain history of flange plates of exterior first floor beam of Frame #1, DLE test	287
Figure 7.24.	Peak interstory drift ratios at various ground motion intensities (Frame #1)	287
Figure 7.25.	Residual story drift ratios of Frame #1 at various ground motion intensities	288
Figure 7.26.	IDA curve for Frame #1 as obtained experimentally together with pre-test analytical prediction	288
Figure 7.27.	Residual $\theta_{1.5''}$ at plastic hinge locations of Frame #1; (a) DLE, (b) MCE	289
Figure 7.28.	Rotation $\theta_{1.5''}$ at plastic hinge locations of frame #1: (a) residual $\theta_{1.5''}$ after CLE, (c) $\theta_{1.5''}$ at ICL (positive direction is the same (d) as used for moment equilibrium)	289
Figure 7.29.	Transfer function at roof of Frame #2	290
Figure 7.30.	Mode shapes of Frame #2	290
Figure 7.31.	Roof drift history of Frame #2 for selected segments at various ground motion intensities	291
Figure 7.32.	story drift history of Frame #2 for selected segments at various ground motion intensities	292
Figure 7.33.	Comparison between input and achieved table motion of MCE test in model domain (Frame #2, $T_j=0.46\text{sec}$)	293
Figure 7.34.	Distorted fourth floor beam after MCE due to out-of-plane motion	293
Figure 7.35.	Collapse mechanism of Frame #2 after completion of CLEF	294
Figure 7.36.	“Catching” mechanism of	

	Frame #2 at the end of CLEF	294
Figure 7.37.	Peak absolute floor accelerations of Frame #2 and mass simulator at various ground motion intensities	295
Figure 7.38.	Correlation of strain history as measured from strain gages and clip gages over 1.5" length of flange plates of interior first floor beam of Frame #2	296
Figure 7.39.	Peak interstory drift ratios of Frame #2 at various ground motion intensities	296
Figure 7.40.	Residual interstory drift ratios of Frame #2	297
Figure 7.41.	IDA curve for Frame #2 as obtained experimentally together with pre-test analytical prediction	297
Figure 7.42.	Residual $\theta_{1.5''}$ at plastic hinge locations of Frame #2; (a) DLE, (b) MCE	298
Figure 7.43.	Residual $\theta_{1.5''}$ at plastic hinge locations of Frame #2; (a) CLE, (b) ICL	298
Figure 7.44.	Comparison of roof displacement history between Frames #1 and #2; (a) SLE, (b) DLE	299
Figure 7.45.	Friction element (a) mathematical model representetion; (b) simplified behavior of friction element	300
Figure 7.46.	Response comparison between analytical predictions using the calibrated friction element and experimental data at SLE level, Frame #1; (a) roof displacement,	300
Figure 7.47.	Response comparison between analytical predictions using the calibrated friction element	

	and experimental data at DLE level, Frame #1; (a) roof displacement,	301
Figure 7.48.	Response comparison between analytical predictions using the calibrated friction element and experimental data at DLE level, Frame #2; (a) roof displacement, (b) first story displacement	301
Figure 7.49.	Story shear forces and peak OTMs of Frame #1 at SLE	302
Figure 7.50.	Story shear forces and peak OTMs of Frame #1 at DLE	303
Figure 7.51.	Story shear forces and peak OTMs of Frame #1 at MCE	304
Figure 7.52.	Story shear forces and peak OTMs of Frame #1 at CLE	305
Figure 7.53.	Story shear forces and peak OTMs of Frame #1 at CLEF	306
Figure 7.54.	Inertia based and effective base shear force versus first story drift, Frame #1 (CLE, CLEF)	307
Figure 7.55.	Inertia based and effective base shear force versus first story drift, Frame #2 (CLEF)	307
Figure 7.56.	Effective base shear versus 1 st story drift of Frame #1, CLE	308
Figure 7.57.	1 st story drift history of Frame #1 during CLE (t=6.0sec to 8.5sec)	308
Figure 7.58.	Ground acceleration history of Frame #1 during CLE (t=6.4sec to 6.5sec)	309
Figure 7.59.	Story force histories of Frame #1 during CLE (t=6.4sec to 6.5sec)	309
Figure 7.60.	Ground acceleration history for Frame #1 during CLE (t=8.0sec to 8.5sec)	310
Figure 7.61.	Story force histories of Frame #1 during CLE (t=8.2sec to 8.5sec)	310
Figure 7.62.	Moment equilibrium during plastification at exterior first floor joint of	

	Frame #1 at four different “snap shots” at various ground motion intensities	311
Figure 7.63.	Experimental and post – test analytical 'IDA' curves; (a) Frame #1, (b) Frame #2	312
Figure 7.64.	Interstory drift ratios of Frames #1 and #2 during CLE	313
Figure 7.65.	Base shear – 1 st story IDR of Frame #1	314
Figure 7.66.	Base shear – 1 st story IDR of Frame #2	314
Figure 8.1.	Pushover curve for EW perimeter 4-story moment resisting frame	347
Figure 8.2.	Collapse mechanism for EW perimeter 4-story moment resisting frame based on static pushover analysis at 8% roof drift	347
Figure 8.3.	IDA plots for the EW 4-story moment resisting frame of the prototype building using a set of 40 ground motions	348
Figure 8.4.	Fragility curve for the EW 4-story moment resisting frame of the prototype building using the set of 40 ground motions	348
Figure 8.5.	Comparison between “IDA” curves of EW 4-story moment resisting frame of the prototype building and model Frame #1 using the Canoga Park record	349
Figure 8.6.	Kajima building Model A, basic dimensions	349
Figure 8.7.	Pushover curve for 15- story Japanese building Model A	350
Figure 8.8.	IDA plots for Model A for the set of 40 ground motions	350
Figure 8.9.	Collapse fragility function of Model A based on the set of 40 ground motions	351
Figure 8.10.	IDA plot for Model A using Canoga Park record	351
Figure 8.11.	Peak IDR for Model A for various levels of intensity using Canoga Park record up to incipient collapse	352

Figure 8.12.	Plan view of 4-story building tested in the E-Defense facility (information from https://www.blind-analysis.jp/index_e.html)	352
Figure 8.13.	North-South elevation view of the 4-story building tested in the E-Defense facility (information from https://www.blind-analysis.jp/index_e.html)	353
Figure 8.14.	East-West elevation view of the 4 story building tested in the E-Defense facility (information from https://www.blind-analysis.jp/index_e.html)	353
Figure 8.15.	E-Defense 4 story building after completion of construction on the shaking table (picture courtesy of Hyogo Earthquake Engineering Research Center)	354
Figure 8.16.	Calibration of moment rotation diagram for tubular column section at 45 degrees (data from E-Defense 2007, https://www.blind-analysis.jp/index_e.html)	354
Figure 8.17.	Spectral acceleration for 2% damping of Hyogoken – Nambu earthquake, Takatori NS component	355
Figure 8.18.	Pushover curve for E-Defense 4-story structure	355
Figure 8.19.	Displacement profiles of the E-Defense 4-story structure along the height based on pushover analysis	356
Figure 8.20.	Comparison of peak story drifts along the height of the 4-story structure during 60% Takatori motion (Incipient Collapse Level)	356
Figure 8.21.	Comparison of peak story shears of the 4-story structure during 60% Takatori motion	

	(Incipient Collapse Level)	357
Figure 8.22.	Comparison of peak overturning moments of the 4-story structure during 60% Takatori motion (Incipient Collapse Level)	357
Figure 8.23.	First story collapse mechanism of the 4-story structure	358
Figure 8.24.	Local buckling at the base exterior column after the end of the collapse test (100% Takatori motion)	358
Figure 8.25.	Analytical prediction of first story drift angle of the 4-story structure at 100% Takatori motion	359
Figure 8.26.	Analytical prediction of base shear – 1 st story drift angle of the 4-story structure during 100% Takatori motion	359
Figure 8.27.	Matching a cyclic response with the Ibarra-Krawinkler deterioration model (data from Mehrabi, 1996)	360
Figure 8.28.	“Low ductility” and “high ductility” central cases with parameter variations	360
Figure 8.29.	Generic backbone curve for infill wall systems, with parameter variations	361
Figure 8.30.	Effect of ultimate drift limit on collapse capacity, horizontal post-capping slope	361
Figure 8.31.	Collapse fragility curves for low and high ductility central cases with 50% residual strength; variation in base shear yield strength n_y	362
Figure 8.32.	Effect of various parameters on median collapse capacity for low ductility cases	363
Figure 8.33.	Effect of various parameters on median and 10-percentile collapse capacity for low and high ductility cases	363
Figure 8.34.	Test configurations for AAC case studies used for collapse assessment	364

Figure 8.35.	Comparison of measured and predicted responses, UTA Specimens 15a and 15b	365
Figure 8.36.	Comparison of measured and predicted responses, UTA Assemblage Specimen	366
Figure 8.37.	IDA curves to collapse, Case 1, (a) pessimist's model, (b) optimist's model	366
Figure 8.38.	IDA curves to collapse, Case 2, (a) pessimist's model, (b) optimist's model	366
Figure 8.39.	Collapse fragility curves, ATC-63 scaling of ground motions, optimist's and pessimist's model; (a) case study 1, (b) case study 2	367
Figure 8.40.	Collapse fragility curves, $S_a(0.2)$ scaling, optimist's and pessimist's	367
Figure 8.41.	Calibration of load-story - drift response using the PUCP reinforced wall test D1	368
Figure 8.42.	Isometric view of idealized adobe dwelling (figure by Hulburd, 2008)	368
Figure 8.43.	IDAs for the analytical model of the reinforced adobe dwelling	369
Figure 8.44.	Collapse fragility curve for reinforced adobe dwelling	369
Figure B.1.	Assembly drawing of test frame with material list	398
Figure B.2.	Exterior left joint of test frame	399
Figure B.3.	Exterior top left joint of test frame	400
Figure B.4.	Cross interior joint of test frame	401
Figure B.5.	Interior top joint of test frame	402
Figure B.6.	Exterior right joint of test frame	403
Figure B.7.	Exterior top right joint of test frame	404
Figure B.8.	Base link of test frame	405
Figure B.9.	Column of 1 st story of test frame	406
Figure B.10.	Column of 2 nd , 3 rd and 4 th story of test frame	407

Figure B.11.	Beam of 1 st and 2 nd floor of test frame	408
Figure B.12.	Beam of 3 rd and 4 th floor of test frame	409
Figure B.13.	Outside washer for beam and column plastic hinge elements of test frame	410
Figure B.14.	Washer for column plastic hinge elements of test frame	411
Figure B.15.	Washer for beam plastic hinge elements of test frame	412
Figure C.1.	Deduced data for specimen DB:38-L/t=6,8,8,1-C	416
Figure C.2.	Deduced data for specimen DB:39-L/t=6,8,8,1-T	417
Figure C.3.	Deduced data for specimen DB:41-L/t=6,8,8,1-C	418
Figure C.4.	Deduced data for specimen DB:42-L/t=6,8,8,1-Cyclic	419
Figure C.5.	Deduced data for specimen DB :C1S1B-L/t=6,8,8,2-BUF	420
Figure C.6.	Deduced data for specimen DB: B1F1R-L/t=6,8,8,2-BUF	421
Figure C.7.	Deduced data for specimen DB: C1S3T-L/t=6,8,8,2-BUF	422
Figure D.1.	Location of accelerometers and load cells installed in the test setup	425
Figure D.2.	Typical locations for clip and strain gages installed on plastic hinge elements	426
Figure D.3.	Typical locations of LEDs installed on selected plastic hinge elements of exterior left column of the test frame	427
Figure D.4.	Typical locations of LEDs installed on selected plastic hinge elements of interior joints of the test frame	428
Figure E.1.	Peak relative displacement profiles along the height of frame #1 normalized with respect to total height of the frame at various ground motion intensities	431
Figure E.2.	Story shear histories for frame #1 during SLE as measured from horizontal links	432
Figure E.3.	Overturning moment at the base of frame #1 based on horizontal link and acceleration measurements during SLE	432

Figure E.4.	Story shear histories for frame #1 during DLE as measured from horizontal links	433
Figure E.5.	Overturning moment at the base of frame #1 based on horizontal link and acceleration measurements during DLE	433
Figure E.6.	Story shear histories for frame #1 during MCE as measured from horizontal links	434
Figure E.7.	Overturning moment at the base of frame #1 based on horizontal link and acceleration measurements during MCE	434
Figure E.8.	Story shear histories for frame #1 during CLE as measured from horizontal links	435
Figure E.9.	Overturning moment at the base of frame #1 based on horizontal link and acceleration measurements during CLE	435
Figure E.10.	Story shear histories for frame #1 during CLEF as measured from horizontal links	436
Figure E.11.	Overturning moment at the base of frame #1 based on horizontal link and acceleration measurements during CLEF	436
Figure E.12.	Peak relative displacement profiles along the height of frame #1 normalized with respect to total height of the frame at various ground motion intensities	437
Figure E.13.	Story shear histories for frame #2 during SLE as measured from horizontal links	438
Figure E.14.	Overturning moment at the base of frame #2 based on horizontal link and acceleration measurements during SLE	438
Figure E.15.	Story shear histories for frame #2 during DLE	

	as measured from horizontal links	439
Figure E.16.	Overturning moment at the base of frame #2 based on horizontal link and acceleration measurements during DLE	439
Figure E.17.	Story shear histories for frame #2 during MCE as measured from horizontal links	440
Figure E.18.	Overturning moment at the base of frame #2 based on horizontal link and acceleration measurements during MCE	440
Figure E.19.	Story shear histories for frame #2 during CLE as measured from horizontal links	441
Figure E.20.	Overturning moment at the base of frame #2 based on horizontal link and acceleration measurements during CLE	441
Figure E.21.	Story shear histories for frame #2 during CLEF as measured from horizontal links	442
Figure E.22.	Overturning moment at the base of frame #2 based on horizontal link and acceleration measurements during CLE	442

CHAPTER 1

INTRODUCTION

1.1 Objective and Scope

Understanding, predicting, and preventing collapse has always been a major objective of earthquake engineering. From the perspective of financial losses, collapse constitutes a limit state associated with complete loss of the building, its content, and its function. This may not be a critical consideration because similar losses, which may require condemnation of the building, are likely to be encountered already at drifts significantly smaller than those associated with collapse. But collapse is the main source of injuries and loss of lives. Thus, it constitutes an engineering limit state that is needed to evaluate, in a probabilistic format, the life safety performance level, which is a primary societal concern. The step from collapse to casualties is not addressed in this research. This research is in support of a recently developed methodology for collapse assessment, with an emphasis on prediction and validation of collapse performance of frame structures. The focus is on a common collapse mode, namely that associated with sidesway (incremental) collapse in which an individual story (or a series of stories) displaces sufficiently laterally so that the second order P-Delta effects fully offset the first order story shear resistance and dynamic instability occurs, i.e., the structural system loses its gravity load resistance.

The capability for predicting collapse of structural systems is enhanced with the development of three extensive databases on steel and reinforced concrete beam elements. The three databases serve as the basis for validation and improvement of analytical models that explicitly incorporate deterioration of structural components and are implemented in

presently available dynamic analysis platforms. The intention is to provide relationships that associate deterioration parameters of component models with important geometric and material properties of the components. These relationships and associated statistical measures, which account for modeling and material uncertainties, serve as the basis for modeling recommendations for structural elements. Through the successful completion of earthquake-simulator collapse tests of two scale models of a steel frame it is demonstrated that it is possible to analytically predict sidesway collapse of frame structures, including the effects of component deterioration. Even if reliable prediction of collapse still has many hurdles to overcome, the goal of improving the state of knowledge on how to predict the collapse capacity of deteriorating structural systems is achieved.

1.2 State of Knowledge on Collapse Prediction of Structural Systems

Several collapse assessment approaches have been developed and proposed in the last several years. Researchers have worked independently in understanding and quantifying P- Δ effect and its influence on collapse capacity of non-deteriorating structural systems. Others have worked in developing deteriorating nonlinear component models that can reproduce experimental results. Recently, several efforts have been carried out to integrate all important factors that influence collapse in a unified methodology. The following is a summary of salient studies.

Collapse Studies on Non-Deteriorating Structural Systems: In the early studies on global collapse of structural systems hysteretic models were not capable to capture component deterioration. Global collapse of a structural system due to P- Δ effects is possible to occur only if the structure tangent stiffness becomes negative under large P- Δ effects, eventually leading to collapse of the system. For instance, using a one-story frame model with bilinear springs to account for material nonlinearity, Jennings and Husid (1968)

noted that structural collapse during earthquake motion can occur due to the effects of gravity loads.

Takizawa and Jennings (1980) evaluated the ultimate capacity of RC frame structures under earthquake excitations by utilizing an equivalent single – degree – of freedom (SDOF) model with trilinear non-degrading hysteretic behavior. They considered explicitly the P- Δ effect and concluded that structural collapse is strongly influenced by the duration of the ground motion.

The instability of buildings subjected to earthquake excitations was studied by Bernal (1987, 1992, 1998). He used two-dimensional moment resisting frames and concluded that dynamic instability cannot be prevented by simply limiting the maximum elastic story drifts under design lateral loads. Bernal also concluded that the minimum base shear capacity needed to withstand a given ground motion without collapse is strongly dependent on the shape of the controlling mechanism, validating earlier statements by Takizawa and Jennings (1980). More recently Bernal et al. (2006) also studied the instability inducing potential of near fault ground motions with the use of collapse spectra plots (strength versus period for constant values of a parameter that characterizes gravity) and tried to predict collapse after utilizing results from pushover analysis. McRae (1994) and Williamson (2003) extended Bernal's earlier studies to more complex hysteretic response while considering the P- Δ effect, and they both came to conclusions similar to those obtained in the studies by Bernal. Challa and Hall (1994) investigated the collapse capacity of a 20-story steel frame. They observed that the steel frame was likely to collapse under a severe ground motion excitation because of significant column plastic hinging in the structure.

Rahnama and Krawinkler (1993) investigated the effects of a negative post-yield stiffness (P- Δ) and strength deterioration on the demand imposed by ground motions on inelastic SDOF systems. They concluded that bilinear hysteresis systems with a negative post-yield stiffness drift significantly and their strength, compared to hardening systems, needs to be

increased considerably in order to limit the inelastic deformations to the same ductility ratio.

Miranda and Akkar (2003) used bilinear SDOF systems with negative post – yield stiffness and a set of 72 ground motions recorded in California and proposed a simplified equation that estimates the minimum lateral strength that is required to prevent collapse by dynamic instability due to P- Δ .

The assessment of destabilizing effects of gravity in highly inelastic non-deteriorating structures when subjected to seismic excitations was addressed by Adam et al. (2004). The proposed approach was based on equivalent SDOF systems of multi-story frame structures, which were subjected to a set of 40 ground motions developed by Medina (2002). They concluded that the application of the proposed equivalent SDOF system is appropriate to estimate P-Delta effects in non – deteriorating regular multi degree of freedom (MDOF) structures.

Martin and Villaverde (1996), based on a study with a steel cantilever beam and a 2-story three-dimensional steel moment-resisting frame tried to determine analytically if a structure will experience partial or total collapse when excited by a ground motion, based on the identification of the structural modes that correspond to zero or negative pivots of the triangularized effective stiffness matrix.

Collapse of composite structures consisting of RC columns and steel or composite beams was investigated by Mehanny and Deierlein (2000, 2001). They proposed a methodology to evaluate the likelihood of a structural collapse under earthquake effects using a component damage index. The damage index was used to degrade stiffness and strength of the damaged sections.

Medina (2002), in the context of Performance-Based Earthquake Engineering (PBEE) concepts developed within the Pacific Earthquake Engineering Research (PEER) Center, used one-bay generic frames to evaluate the performance of non-deteriorating structural systems. He utilized the incremental dynamic analysis (IDA) approach (Vamvatsikos and Cornell, 2002) and developed engineering demand parameter (EDP) hazard curves based on available seismic hazard information. Medina also proposed the use of global collapse fragility functions along with an intensity measure (IM) hazard curve to estimate the mean annual frequency of collapse.

Collapse Studies on Deteriorating Structural Systems: Experimental studies have shown that the hysteretic behavior of a structural component is dependent upon numerous structural parameters that greatly affect the deformation and energy dissipation characteristics, leading to the development of a wide range of more versatile deterioration models. Widely used deterioration models are discussed in detail in Chapter 2 in the context of this research.

Song and Pincheira (2000) studied the effect of stiffness and strength deterioration on the maximum inelastic displacement of SDOF systems without including geometric nonlinearities. They found that the displacement ratio between a deteriorating and non-deteriorating system could be as large as two (especially in the short period range) and that it varies significantly with the deterioration rate and type of ground motion.

A collapse assessment methodology for structural systems combining the $P-\Delta$ effect with component deterioration was proposed in Ibarra et al. (2002, 2005) and Ibarra and Krawinkler (2003). After incorporating the cyclic deterioration rules developed by Rahnama and Krawinkler (1993), Ibarra developed a component analytical model that is capable of capturing basic strength and cyclic deterioration. Ibarra computed collapse capacities for SDOF systems and MDOF frame structures. He identified the parameters that mostly influence collapse and assessed the sensitivity of collapse capacity to these

parameters. In the same study, collapse fragility curves for SDOF and MDOF systems were developed together with a methodology for computing the mean annual frequency of collapse [Ibarra et al. (2002), Ibarra, (2003), Ibarra and Krawinkler, (2005)].

Zareian (2006) introduced a Design Decision Support System (DDSS), which is supported by an extensive database of collapse capacities for a wide-range of combinations of structural parameters of frame and wall structural systems. Using this database Zareian and Krawinkler (2007) developed closed-form expressions for estimating the collapse potential of frame and wall structures.

Haselton and Deierlein (2006) calibrated the Ibarra-Krawinkler deterioration model (Ibarra et al., 2005) to data of 255 reinforced column tests provided by the Pacific Earthquake Engineering Research (PEER) center database (PEER) and performed analytical collapse studies in order to quantify seismic collapse risk of reinforced concrete (RC) frame structures in the United States. In the work by Haselton and Deierlein (2007) the collapse safety of modern code-conforming structures is assessed. These assessments were used to quantify the effectiveness of retrofitting techniques to reduce the collapse risk of older, non-ductile RC structures (Liel et al., 2008).

Experimental Collapse Investigations: Only few experimental studies have been conducted in which replicas of structures were tested all the way to collapse. Kato et al., (1973) tried to analytically predict collapse of relatively simple models that were tested on a shake table. In these analytical studies only the effect of $P-\Delta$ was included, but the effect of component deterioration was ignored.

Vian and Bruneau (2001, 2003), concluded that the stability coefficient has the most significant effect among structural parameters on the behavior of the SDOF systems. They based their conclusions on a series of shake table tests of 15 different SDOF steel frame

systems subjected to earthquake excitations of progressively increasing intensity up to collapse due to geometric nonlinearities (P- Δ effect).

The work by Vian and Bruneau (2001) was confirmed by Kanvinde (2003) after performing shake table tests up to collapse of similar SDOF structures. Using the Open System of Earthquake Engineering Simulation Platform (OpenSees 2007) Kanvinde confirmed that P- Δ collapse of SDOF systems can be accurately reproduced analytically.

A series of shaking table tests of two scale model reinforced concrete plane frames were conducted by Elwood (2002) to investigate the collapse mechanisms of RC frames with low-ductility columns. Based on this work and the work by Elwood and Moehle (2005), Moehle incorporated into nonlinear dynamic analysis software component models that incorporate component failure and progression to collapse.

Rodgers and Mahin (2006) investigated the consequences of beam-to-column connection fractures on the global behavior of the test frame through a series of shaking table experiments and numerical simulations that were carried out on a one-third scale, two-story, one-bay moment-resisting steel frame. Based on experimental and numerical investigations they demonstrated that severe strength loss due to the combination of numerous fractures, undesirable post-fracture hysteretic behavior, P-Delta, and large excitation can have severe consequences including collapse.

Nakashima et al. (2006) tested under pseudo dynamic loading a full scale three story steel moment frame up to collapse. Although not a shake table test, the objective was to assess the ability of numerical simulation to trace cyclic inelastic behavior of the test frame. The analytical model used to simulate component behavior of the test frame did not include any deterioration characteristics though.

In order to validate an experimental software framework for hybrid simulation of structures (OpenFresco, 2008) Schellenberg and Mahin (2006) performed a collapse test of a portal frame with the use of hybrid simulation approach. After incorporating geometric nonlinearities into the analytical portion of the hybrid model they demonstrated that hybrid simulation of structural systems up to collapse is possible. In this work it is pointed out that the lack of a shake table collapse test of the same frame did not permit the complete experimental validation of the hybrid model.

Kabeyasawa and Sanada (2002) conducted a shaking table test of a reinforced concrete frame-wall building with a soft first story at the NIED Large Scale Earthquake Simulator. They reported that the overall collapse mechanism of the test frame was formed with flexural yielding at the wall base and tensile yielding of columns. However, the mechanism changed into a sidesway mechanism with the progress of inelastic deformation in the 1st story due to the softening of the shear wall. In the same work a correlation between the test and simulation results was reported.

A challenging test series conducted on the E-Defense (2007) shaking table was the collapse test of a full scale steel 4-story building designed based on current Japanese seismic provisions in September of 2007 (Kasai et al. (2007), Tada et al. (2007), Suita et al. (2007, 2008)). The objective of the test was to enhance analytical methods for earthquake response simulation and provide information for new design guidelines for collapse assessment of steel structures. This work is discussed in more detail in Chapter 8.

1.3 “Point of Departure” for this Research

Taking stock of the present state of knowledge on collapse prediction of structural systems it is concluded that only recently significant progress has been made in our ability to predict collapse and to develop engineering measures that provide consistent collapse protection.

The main obstacles have been our inability to predict deterioration properties of structural components, to incorporate these properties into our analysis and design tools, and to account for all important sources of uncertainty (ranging from hazard to ground motion to structural modeling uncertainties) that may affect collapse prediction. Moreover, until recently there has not been a comprehensive physical experiment of a real structure that demonstrates that prediction of collapse is indeed feasible and reliable.

The primary objective of the work discussed in this report is to advance, through analytical and experimental research, knowledge on collapse assessment of structural systems. Collapse is multifaceted but in this context the focus is on sidesway collapse of frame structures. The approach used to obtain the collapse capacity of a structural system is reliability-based because of the uncertainties in the description of the seismic input. Uncertainties in modeling the deterioration properties of the structural components that make up the structural system are not considered but information on uncertainty measures and correlation coefficients between deterioration modeling parameters is provided based on experimental evidence. The main objectives of this research are summarized as follows:

- Develop an extensive database on deterioration parameters of structural steel and reinforced concrete components, including uncertainty measures accounting for modeling and material uncertainties
- Validate and improve analytical models that explicitly model component deterioration based on existing experimental data provided by the aforementioned component databases
- Develop relationships and statistical measures accounting for modeling and material uncertainties that will serve as the basis for modeling recommendations of structural elements

- Incorporate improved deteriorating component hysteresis models into analysis platforms
- Design, conduct and document two comprehensive collapse experiments of a 4-story steel frame
- Demonstrate that incremental collapse can be predicted, including the effects of component deterioration, with the use of relatively simple analytical models.
- Contribute to the Network for Earthquake Engineering Simulation (NEES) objective of coordinated analytical and experimental simulation.

1.4 Outline

Hysteresis models that incorporate component deterioration are discussed in Chapter 2. The same chapter addresses modifications to the Ibarra–Krawinkler deterioration model (Ibarra et al. 2005) to account for residual strength, composite action and ultimate deformation capacity. The deterioration model modifications are based on evaluation of experimental data from tests that have been conducted over the last 40 years on steel and concrete components. The improved deterioration models are implemented in an in-house single-degree-of-freedom (SDOF) program that carries out dynamic and quasi-static inelastic analysis, and in a dynamic nonlinear analysis program for multi-degree-of-freedom (MDOF) systems.

Chapter 3 focuses on the development of three databases of the monotonic and hysteretic behavior of structural steel and concrete components. The objective is to provide a comprehensive documentation of important experimental data and to quantify component deterioration parameters. The same chapter includes a general description of an interactive

computer software named “Calibrator” developed to calibrate deterioration parameters from data on several hundred experiments included in the component databases. The main calibration techniques used in this research are also discussed. Chapter 3 also provides qualitative and quantitative uncertainty measures to describe structural behavior parameters accounting for modeling and material uncertainties.

The development of relationships that associate deterioration model parameters, such as the ones proposed in Ibarra (2003), with criteria that control deterioration in actual structural components is discussed in Chapter 4. The relationships are developed based on multivariate regression analysis, after taking advantage of calibrated values of deterioration parameters from several hundreds of component tests. Since the primary focus in this research is the collapse assessment of steel structures, the proposed relationships are developed for steel members (W-sections and tubular hollow square column sections).

In Chapter 5 the design of a 4 – story steel moment frame office building is summarized. This building serves as the base case structural system in this research. The same chapter focuses on the design of a 1:8 scale model of the 4-story EW moment frame of the base case structural system, which was tested up to collapse at the NEES facility at the University at Buffalo.

The testing program conducted in the laboratory of the John A. Blume Earthquake Engineering Center at Stanford University in order to determine the deterioration characteristics of components of the 1:8 scale model test frame is discussed in Chapter 6 together with the subsequent data evaluation. The results of the component tests are utilized for analytical collapse simulations prior to the shaking table tests (pre-test predictions) In the same chapter a summary is presented of tests performed on important components of the model frames after completion of the shaking table tests, which provided additional data for post-test predictions.

Chapter 7 presents a discussion of the specimen fabrication, setup, instrumentation, and execution of shaking table tests performed on two nominally identical 1:8 scale models on the shaking table of the NEES facility at the State University of New York at Buffalo.. Quantification of P-Delta effects from elastic behavior up to collapse, and post–test analytical collapse simulations of the two test frames are discussed in the same chapter.

Chapter 8 summarizes case studies performed in order to evaluate the capability to predict collapse of structural systems based on the knowledge gained from the previous chapters of this research. In the same chapter analytical predictions and comparisons with experimental data of a full-scale 4-story building collapse test that was conducted on the world’s largest shaking table in the Hyogo Earthquake Engineering Research Center in Japan are presented.

Chapter 9 provides a summary of major findings and conclusions of this research in support of collapse assessment of deteriorating structural systems. Several appendices are included at the end of this dissertation that summarize auxiliary information generated in this research.

CHAPTER 2

HYSTERETIC MODELS THAT INCORPORATE COMPONENT DETERIORATION

2.1 Purpose and Scope

Collapse assessment of structural systems requires hysteretic models that are capable of capturing deterioration of structural components. The scope of this chapter is to review several widely used deterioration models and to describe a modified version of the Ibarra-Krawinkler deterioration model that is used extensively in this research. The modifications address asymmetric component hysteretic behavior including different rates of cyclic deterioration in the two loading directions and asymmetric backbone curve characteristics, residual strength, and incorporation of an ultimate deformation at which the strength of a component drops to zero. The modifications are based on observations from a large number of experimental data of steel and reinforced concrete components.

Component modeling in this research is based on the modified version of the Ibarra Krawinkler model presented in Section 2.3. The modified deterioration model was implemented in a single degree of freedom (SDOF) dynamic analysis program (SNAP) and a multi degree of freedom (MDOF) dynamic analysis platform (DRAIN – 2DX, 1993).

2.2 Review of Deterioration Models

2.2.1 Clough and Johnston Model

Bilinear elastic-plastic hysteresis models were the first to be used because of their simplicity. A model with softening of the reloading stiffness was proposed by Clough and Johnston in 1966. This model is a bilinear approximation of the trilinear model developed by Hisada et al. (1962) to represent the hysteretic behavior of a reinforced concrete structure (Hisada model). In the Clough and Johnston model the degradation of the reloading stiffness is based on the maximum displacement that has taken place in the direction of the loading path. Because of this characteristic this model is often referred to as the peak-oriented model. A deficiency of the Clough model was pointed out by Mahin and Bertero (1976). In Figure 2.1(a), after unloading from point A, consider a situation in which reloading takes place from point B.

The original Clough model assumes that reloading is directed towards the previous maximum response point C. The modification proposed by Bertero and Mahin is that reloading occurs elastically until the immediately preceding unloading point A is reached before the response is directed towards the previous peak point C (see Figure 2.1(b)). In the modified Clough model the amount of stiffness degradation is a function of the peak deformation. Others (Nielsen and Imbeault (1970), Anagnostopoulos (1972) and Iwan (1973)) have developed piece-wise linear hysteretic models that incorporate stiffness degradation.

Sucuoglu and Erberik (2004) developed a simple piece-wise linear hysteresis model that is based on the stiffness-degrading model by Clough and Johnston (1966) but incorporates an energy – based strength degradation rule. A total of 7 degradation rules for asymmetric behavior are incorporated in the deterioration model as seen in Figure 2.2.

2.2.2 Takeda Model

Based on experimental observations on the behavior of a number of medium-size reinforced concrete components tested under lateral load reversals with light to medium amount of axial load, a hysteresis model was developed by Takeda, Sozen and Nielsen (1970). The Takeda model includes (a) stiffness changes at flexural cracking and yielding, (b) hysteresis rules for inner hysteresis loops inside the outer loop, and (c) unloading stiffness degradation with deformation. The response point moves toward a peak of the one outer hysteresis loop. Figure 2.3 illustrates the Takeda model. It should be noted that the primary curve of the Takeda model can be made bilinear by simply choosing the cracking point to be the origin. Such a model is called the “bilinear Takeda” model, similar to the Clough model except that the bilinear Takeda model has more hysteresis rules for inner hysteresis loops (Otani and Sozen, 1972). Another degrading trilinear hysteresis model that simulates dominantly flexural stiffness characteristics of RC is the one proposed by Fukada (1969).

2.2.3 Bouc – Wen model and its modifications

The following short discussion is based on the paper by Foliente (1995), who presented an excellent summary of the widely known Bouc-Wen model and its modifications.

Bouc (1967) suggested a versatile, smoothly varying hysteresis model for a single-degree-of-freedom (SDOF) mechanical system under forced vibration. Wen (1980) generalized Bouc’s hysteretic constitutive law and developed an approximate solution procedure for random vibration analysis based on the method of equivalent (or statistical) linearization. Baber and Wen (1981) extended the model to admit stiffness and/or strength degradation as a function of hysteretic energy dissipation and applied it to a multiple- degree-of-freedom (MDOF) system. Baber and Noori (1985, 1986) further extended the modified Bouc model by incorporating pinching while maintaining it in a form compatible with Baber and Wen and Wen’s equivalent linearization solution. Response statistics obtained by the equivalent

linearization technique were shown to reasonably approximate those obtained by Monte Carlo simulation. The final model, with Baber and Noori's (1986) single-element pinching model, is known as the Bouc-Wen-Baber-Noori (BWBN) model.

Many researchers have used the early form of the modified Bouc (1967) model in random vibration investigations of hysteretic systems. With the features added by Baber and Wen (1981) and Baber and Noori (1986), it has more closely approximated the hysteretic behavior of structural elements and systems.

The model is based on a separation of a linear restoring force component, $F_k = aku$, and a hysteretic restoring force component, $F_h = (1-\alpha)kz$, see Figure 2.4, with u being the total relative displacement and z being the hysteretic displacement. Thus, the total restoring force is $F_T = aku + (1-\alpha)kz$. In the BWBN model the hysteretic displacement and the total displacement are related by the following first order differential equation:

$$\dot{z} = h(z) \cdot \left\{ \frac{A \cdot \dot{u} - \nu \cdot \left(\beta \cdot |\dot{u}| \cdot |z|^{n-1} \cdot z + \gamma \cdot \dot{u} \cdot |z|^n \right)}{\eta} \right\} \quad (2.1)$$

where A , β , γ , and n are hysteresis shape parameters (if $n = \infty$, the elasto-plastic hysteresis case is obtained); ν and η = strength- and stiffness-degradation parameters, respectively, (if $\nu = \eta = 1.0$, the model does not degrade); and $h(z)$ = pinching function introduced by Baber and Noori (1986) [if $h(z) = 1.0$, the model does not pinch]. Denoting the hysteretic energy dissipated at time t as ε , the strength and stiffness degradation parameters are defined as follows: $\nu(\varepsilon) = 1 + \delta_\nu \varepsilon$, and $\eta(\varepsilon) = 1 + \delta_\eta \varepsilon$. Illustrations of the effect of δ_ν and δ_η are provided in Figure 2.5. The pinching function $h(z)$ can take on different forms; it also depends on ε and on several other parameters. An example of its effect can be seen from the dz/du versus z/u plot illustrated in Figure 2.6.

There are 13 parameters in this model. Very few of them can be related to engineering quantities under control by the designer. Values for these parameters have been obtained for specific cases through system identification. The great advantage of this general model is its versatility, since almost any hysteresis behavior can be modeled somehow, as is illustrated in Figure 2.7. But its great disadvantage is its complexity and its lack of relations with engineering design parameters. Iwan (1990) showed that the model also violates basic principles since tends to exhibit a pronounced drift, particularly when post-yield stiffness is very small. For this reason this model is rarely used except for theoretical studies, for which it is an excellent choice.

It should be noted that Clarke (2005) developed a differential equation endochronic plasticity model as an alternative to the Bouc–Wen model. This model uses the hyperbolic sine function as the driving function as opposed to the F^n function used by Bouc and many researchers subsequently and is very stable and inexpensive in a nonlinear optimization process for system identification. Ten parameters need to be defined in order to fully characterize the model.

2.2.4 Ramberg-Osgood Model

The Ramberg-Osgood model (1943), Figure 2.8, has been used extensively in the 60-ies, and is still used if the “rounding” of hysteresis loops is deemed important. The model is a non-degrading smooth model and is a mathematical description of the loading and unloading/reloading curve, in which the value of the exponent r dictates the shape of the curve ($r = 1$ implies elastic behavior, and $r = \infty$ implies elastic-perfectly plastic behavior). A cyclic hardening factor can be applied to the unloading/reloading curve, but its value should be history dependent. Hardening parameters as well as strength and stiffness degradation parameters are implemented in the Ruaukoko analysis platform (Carr, 2003), which also includes a large list of other hysteretic models (see Carr, 2003). The general perception is

that this model is no longer widely used in the US, except for special conditions (Kukreti et al., 1999) or in the auto and air/space industry. Another smooth non-degrading hysteretic model is the Menegotto and Pinto, (1973), which is available in OpenSees analysis platform (OpenSees, 2007) the Bouc-Wen model (Bouc 1967; Wen, 1976).

2.2.5 Kunnath et al., deterioration Model

Since inelastic deformations in reinforced concrete members do not concentrate in critical sections but spread across a finite region known as the plastic hinge length, Kunnath et al. (1990) proposed a new deterioration model which was based on distributed plasticity concepts. This model is both an extension and a simplification of the Takizawa (1976) model. The Kunnath et al. (1990) model has been incorporated in recent versions of IDARC (Valles et al., 1996). The model in concept is both simple and versatile since it is based on integration of the curvature diagram that results in the basic incremental moment-rotation relationship. These integrals, which eventually result in the element stiffness matrix, can be obtained in closed form and directly used in a computer program. Kunnath et al., (1990) showed that shear deformations can be directly incorporated in the above model. Improved versions of such distributed models have also been investigated. A nonlinear distribution was developed for tapered elements (Kunnath et al., 1992) and a multilinear distribution with nonsymmetric properties was developed for the three dimensional model (Lobo et al., 1992, 1994).

2.2.6 Sivaselvan and Reinhorn Model

The model proposed by Bouc (1967) and modified by several others (Wen 1976; Baber and Noori 1985; Casciati 1989; Reinhorn et al. 1995) was modified by Sivaselvan and Reinhorn (2000) into a versatile smooth hysteretic model (SHM) with stiffness and strength degradation and pinching characteristics, derived from inelastic material behavior. It should

be noted that the Sivaselvan and Reinhorn (2000) model is conceptually based on general class of non-degrading and degrading models developed by Iwan (1966) but extended the model developed by Mostaghel (1999) to include smooth curvilinear segments. The model presents a holistic picture of the modeling of 1D inelastic material.

The derivation of the Sivaselvan and Reinhorn (2000) model is based on the theory of viscoplasticity and its resemblance to the endochronic constitutive theory. The model also permits the use of a curved or multi-linear backbone curve. As far as can be deduced from the reviewed literature, the model and its previous variations does not consider cyclic (isotropic) hardening, and it is not evident how strength cap and post-capping behavior are considered by the model.

In the review process we did not succeed in assessing the effects of the degradation parameters β_1 and β_2 (which relate to ductility and energy dissipation) on the hysteretic response and to review their effect individually. This may be more a shortcoming of the review process than of the models. Compared to the Bouc-Wen models the Sivaselvan and Reinhorn model seems to have a much closer relation to physical quantities that are under the control of the designers. Sample calibrations obtained from the Sivaselvan and Reinhorn model, obtained as part of the SAC study, are illustrated in Figure 2.9.

2.2.7 Yield – Line Plastic Hinge Models

Gioncu and Petcu (1997), Anastasiadis et al. (2000), and Möller et al. (1997) introduced the yield-line concept to model the buckled shapes observed in experiments. They constructed yield-line models and used this plastic mechanism to determine rotation capacity of European H-section beams. Lee and Stojadinovic (2004) developed a new cyclic yield-line plastic hinge model for estimating connection rotation capacity based on a similar concept (see Figure 2.10). The model considers post-peak connection strength degradation due to

local and lateral-torsional buckling. This limit state is used to establish a connection rotation limit similar to the limit used in FEMA-350 (SAC Joint Venture, 2000a). In order to predict crack initiation at the creases of the local buckles in the plastic hinge, the model also considers low-cycle fatigue crack initiation based on a cumulative local strain concept at the critical yield line. The primary purpose of the Lee and Stojadinovic model is to be used by designers to evaluate new connections before the required proof-tests.

2.2.8 FEMA 356 Component Model

In the ATC-33 project, which led to the publication of the FEMA 273 report and later to the FEMA 356 report, structural components with reliable ductility were modeled as shown in Figure 2.11. This model has a strength cap (point C) beyond which the strength drops rapidly (from C to D) to a much reduced residual value that is maintained until the deformation reaches a specified value (point E), where the strength drops to zero. This model was intended to be used for static pushover analysis but not for inelastic dynamic analysis. Thus the FEMA 356 (SAC Joint Venture 2000b) model does not include any hysteretic rules for cyclic deterioration. Even in the static analysis the steep “cliff” causes many problems of numerical stability and leads to pushover curves with strange looking saw-tooth behavior. Thus, the FEMA 356 deterioration model is of historical interest but not of practical value in the context of this study.

2.2.9 Song and Pincheira Model

This model incorporates a strength cap and post-capping behavior, but does not incorporate cyclic strength deterioration. The model deterioration rules are described in detail in Song and Pincheira (2000). The backbone curve of the model is shown in Figure 2.12(a). As seen, the model is capable to capture the strength “cap” after the system exceeds the deformation, Δ_u which corresponds to the ultimate strength F_u . A residual strength path is also incorporated in the model.

Figure 2.12(b) illustrates the hysteretic behavior for loading cycles of increasing displacement amplitude. Stiffness reductions upon unloading are considered after yielding and are controlled by a parameter α . Strength decay is introduced, however, only after reaching the peak strength, F_u . If the system unloads after the peak strength has been reached, reloading is directed toward the mirror image of the point at which unloading occurred, i.e., points A' and B' in Figure 2.12(c). However, additional strength decay may be considered by increasing the deformation of the reloading target point by a parameter β (points A'' and B''). Note that the reloading target points represent the maximum attainable resistance that the system can develop in subsequent cycles once the maximum strength, F_u , has been reached. Pinching of the hysteresis loops is considered in the model by modifying the reloading stiffness of the system and is controlled by a parameter γ as shown schematically in Figure 2.12(c). Strength degradation upon reloading is gradually reduced in subsequent cycles by a parameter ν at a rate of ν^{n-1} per cycle, where n is the number of internal cycles. The main disadvantage of the Song and Pincheira model is that it is not capable to capture basic strength and post-capping strength deterioration unless if an approximate procedure developed by Pincheira et al. (1999) is used to account for in-cycle degradation. The procedure consists on using very small time increments together with an arbitrary positive stiffness to compute a force unbalance which is applied in the subsequent time step.

2.2.10 Ibarra-Medina-Krawinkler Deterioration Model

This model has been reported first in Rahnama and Krawinkler (1993) and has been refined and utilized extensively over the last ten years. In its original form it has been described in several publications. A comprehensive description of the original model is provided in Ibarra et al. (2005) and Ibarra and Krawinkler (2005). The model is based on,

- a) a backbone curve that defines a reference skeleton behavior of an undeteriorated system, i.e., it defines strength and deformation bounds

- b) a set of rules that define the basic characteristics of the hysteretic behavior between the bounds defined by the backbone curve, and
- c) a set of rules that define four modes of deterioration with respect to the backbone curve

Backbone curve

The shape of the backbone curve with definitions is provided in Figure 2.13. The backbone curve defines the bounds within which the hysteretic response of the component is confined. It is close to the monotonic force-deformation response. It contains compromises that need to be made in order to simplify response description. For instance, it accounts for an average effect of cyclic hardening (which likely is small for RC components but may be significant for steel components).

The quantities F and δ are generic force and deformation quantities. For plastic hinge regions $F = M$ and $\delta = \theta$. In the unmodified model the emphasis is on the effective elastic stiffness K_e , the effective yield strength F_y , the effective strain hardening stiffness $K_s = \alpha_s K_e$, the capping point (point of maximum strength) defined by F_c and δ_c , the post-capping stiffness $K_c = \alpha_c K_e$, and the residual strength F_r . The ratio δ_c/δ_y is used as a reference value for the deformation capacity of the component.

Rules defining basic hysteretic characteristics

The model can be employed together with any of the three basic linearized hysteretic models, i.e., with the bilinear model, the peak-oriented model, or the pinching model.

Rules defining four modes of deterioration

The cyclic deterioration rates are controlled by the rules developed by Rahnama and Krawinkler (1993), which are based on the hysteretic energy dissipated when the component is subjected to cyclic loading. It is assumed that every component possesses a reference inherent hysteretic energy dissipation capacity, regardless of the loading history applied to the component. The cyclic deterioration in excursion i is defined by the parameter β_i , which is given by the following expression:

$$\beta_i = \left(\frac{E_i}{E_t - \sum_{j=1}^{i-1} E_j} \right)^c \quad (2.2)$$

where

β_i = parameter defining the deterioration in excursion i

E_i = hysteretic energy dissipated in excursion i

E_t = reference hysteretic energy dissipation capacity, expressed in the original model as a multiple of $F_y \delta_y$, i.e., $E_t = \gamma F_y \delta_y$. In the modified model (Section 2.3) the reference hysteretic energy dissipation capacity is expressed as a multiple of $F_y \delta_p$, i.e., $E_t = \lambda F_y \delta_p$, or $E_t = \Lambda F_y$, with $\Lambda = \lambda \delta_p$ denoting the reference cumulative deformation capacity

ΣE_j = hysteretic energy dissipated in all previous excursions

c = exponent defining the rate of cyclic deterioration

The β_i deterioration parameter can be applied to any of the following four deterioration modes (see Figure 2.14 for illustrations):

Basic strength deterioration, defined by translating the strain hardening branch towards the origin by an amount equivalent to reducing the yield strength to

$$F_i^+ = (1 - \beta_{s,i})F_{i-1}^+ \quad \& \quad F_i^- = (1 - \beta_{s,i})F_{i-1}^- \quad (2.3)$$

where

$F_i^{+/-}$ = deteriorated yield strength after excursion i .

$F_{i-1}^{+/-}$ = deteriorated yield strength before excursion i .

$\beta_{s,i}$ = based on an appropriate γ or λ (or A) value for basic strength deterioration

Post-cap strength deterioration, defined by translating the post-capping branch towards the origin by an amount equivalent to reducing the cap strength to

$$F_{ref,i}^{+/-} = (1 - \beta_{c,i})F_{ref,i-1}^{+/-} \quad (2.4)$$

with $\beta_{c,i}$ based on an appropriate γ or λ (or A) value for post-cap strength deterioration

Unloading stiffness deterioration, defined by reducing the unloading stiffness K_u in accordance with

$$K_{u,i} = (1 - \beta_{k,i})K_{u,i-1} \quad (2.5)$$

with $\beta_{k,i}$ based on an appropriate γ or λ (or A) value for unloading stiffness deterioration

Accelerated reloading stiffness deterioration, defined by moving the target deformation $\delta_{t,i}$ (which defines the point targeted in the reloading branch of the peak-oriented and pinching model) along the backbone curve to a value of

$$\delta_{t,i}^{+/-} = (1 + \beta_{a,i})\delta_{t,i-1}^{+/-} \quad (2.6)$$

with $\beta_{a,i}$ based on an appropriate γ or λ (or A) value for accelerated stiffness deterioration.

Application of these rules for the four modes of deterioration is illustrated in Figure 2.14 for a peak-oriented system.

Thus, the deterioration model has up to four deterioration parameters (appropriate γ or λ (or A) values for each deterioration mode [presuming that the exponent in Equation 3.2 is equal to 1.0, which is the only case considered so far]). It is found that the use of the same γ or λ (or A) value for all four deterioration modes usually provides adequate description of each deterioration mode.

The original version of the Ibarra-Krawinkler deterioration model was tested on hysteretic behavior data obtained from experiments on steel, reinforced concrete, and wood components. Adequate simulations were obtained in all cases by tuning the model parameters to the experimental data. Examples of calibrations are presented in Ibarra et al. (2005) for various types of specimens and hysteretic responses.

Table 2.1 summarizes the capabilities of the models reviewed in this section. The noted capabilities are those identified in the literature. It is quite possible that some of the models can be adapted for different capabilities (behavior modes) through minor modifications.

It should be pointed out that there are many other available hysteretic models (degrading and non-degrading) for evaluation of structural performance. A brief summary of a large number of models (non-degrading and degrading) categorized in piece-wise linear and smooth models is presented by Miranda (2008) as part of the ATC-62 project.

2.3 Modified Ibarra Krawinkler Deterioration Model Used in this Study

Over the last three years several modifications to the original Ibarra-Krawinkler model have been implemented. Some of these modifications are improvements of definitions, and some are improvements on the simulation of deterioration. The results presented later in this research are based on what will be referred to from now on as the modified Ibarra-Krawinkler Model. This model uses all the concepts and rules described in Section 2.2.10, with the modifications summarized below based on observations from experimental data from a database of several hundreds tests that have been conducted with steel and RC elements.

2.3.1 *Modifications to Backbone Curve*

The new terms used to define the backbone curve are illustrated in Figure 2.15. They are mostly refinements of the definitions presented in Figure 2.13. A new branch has been added to the original backbone curve that allows the simulation of complete loss of strength. This loss may occur at large inelastic deformations as is observed when ductile tearing takes place in steel components. The model can also simulate situations in which a complete loss of strength occurs before the system reaches the residual branch, i.e. in the post capping branch or even in the strain hardening branch. The latter may be the case of a brittle failure of a connection (see Figure 2.17) when the remaining post-fracture residual strength cannot be evaluated with confidence. The backbone curve has been also modified and can be asymmetric in positive and negative loading direction. There are good reasons for revising some of the definitions of the original Ibarra – Krawinkler deterioration model, as discussed below.

Plastic deformation capacity δ_p is used as reference value for deformation capacity rather than the ductility ratio δ_c/δ_y

Conventionally the ductility ratio, defined as the ratio of “maximum” deformation to yield deformation, has been used to assess component or structure performance. The term “maximum” may be associated with a limit on acceptable damage or with a limit on acceptable deterioration beyond which a component is considered to have “failed”. Acceptable performance is then defined as the ductility capacity exceeding the ductility demand predicted by an analytical model. The concept of ductility ratio is ingrained in many aspects of earthquake engineering, and researchers and engineers alike use this term to evaluate component, story, and structure behavior, mostly because it permits behavior description by means of a dimensionless quantity. But like any dimensionless quantity, its absolute value depends on the value that is used for normalization.

In the context of this research the emphasis is on simulating component and structure behavior close to collapse, utilizing the component load-deformation deterioration model discussed here. Thus, there is no specific component ductility capacity that is associated with this level of performance.

In the original Ibarra-Krawinkler model the ratio δ_c/δ_y had been used as a reference value for deformation capacity of a component and has been referred to as the backbone ductility capacity. Here it is argued to use the plastic deformation $\delta_p = \delta_c - \delta_y$ as a basic measure of component deformation capacity instead of δ_c/δ_y . From the perspective of component modeling the following arguments can be made for this change, particularly when considering that this research is concerned primarily with the effects of deteriorating plastic hinge regions on structural response.

For a given component (whether steel or reinforced concrete) both δ_y and δ_c (or $\delta_p = \delta_c - \delta_y$) depend on the moment gradient (the effective M/V ratio), which varies a great deal between structural configurations, and for a given configuration may vary significantly within a loading history (in beams because of gravity load effects, and in beams and particularly columns because of redistribution due to inelastic behavior). Thus, in concept, a given component has neither a well defined δ_y nor a well defined δ_p (or δ_c). It is then a matter of deciding which of the two parameters is more stable (less sensitive to the effective M/V ratio and to other assumptions made in defining reference values). Basic principles and an evaluation of experimental results indicate that δ_p is much more stable than δ_y (and therefore more stable than $\mu = \delta_p/\delta_y$). This holds true particularly for flexural plastic hinge regions in reinforced concrete components in which δ_y is not well defined even for a specific configuration.

The ratio F_c/F_y is used to define the hardening region rather than the strain hardening parameter α_s

The elastic portion of the backbone curve is followed by a branch with reduced stiffness, which is conventionally denoted as the “strain hardening” branch. This branch extends until maximum strength, F_c , is reached at δ_c . This portion of the backbone curve is conventionally defined by the ratio of the reduced stiffness of the component after yielding K_s to the elastic stiffness of the component K_e , and is denoted as the strain hardening ratio α_s . In this study we use the strength ratio F_c/F_y as the basic parameter to describe this branch of the backbone curve. In the following, supporting arguments for this change in definition are provided.

- Basic principles indicate that stiffness of the strain hardening branch is strongly dependent on the moment gradient and the hardening characteristics of the moment-curvature relationship of the cross section.

- As mentioned previously, due to the poor definition of elastic stiffness of reinforced concrete components, calibration of the strain hardening ratio α_s becomes subjective.
- Pilot studies with parts of the steel and RC databases presented in Chapter 3 have shown that the strength ratio F_c/F_y is a more stable parameter than the strain hardening ratio α_s .

The post capping deformation capacity δ_{pc} is used to define the softening region rather than the post-capping stiffness ratio α_c

As discussed previously, the value of the elastic stiffness of reinforced concrete components is ambiguous. Correlating the post capping stiffness and initial stiffness creates large variations in the post capping slope. Instead we propose to use the post capping deformation capacity to describe the range after the capping point.

2.3.2 Modifications to Cyclic Deterioration Modeling

The cyclic deterioration modeling rule contained in the original Ibarra-Krawinkler model (described in detail in Ibarra et al., (2005)) has been changed in order to be able to account for different rates of cyclic deterioration in both loading directions. As observed from experimental data included in W-sections database discussed in Chapter 3, in the case of a beam with slab, due to composite action, the component deteriorates much slower in the positive loading direction when the concrete is in compression compared to the negative loading direction when beam bottom flange is in compression and can easily buckle in a lateral torsional mode (see Section 3.4.8). In order to account for different deterioration rates in both loading directions we introduce the parameter D in the Equation 2.2.,

$$\beta_i^{+/-} = \left(\frac{E_i}{E_t - \sum_{j=1}^{i-1} E_j} \right)^c \cdot D^{+/-} \quad (2.7)$$

$D^{+/-}$ = parameter defining the decrease in rate of cyclic deterioration in the positive or negative loading direction (e.g. in the case of a composite beam the slab decelerates the deterioration in the positive direction). D can only be $D^{+/-} \leq 1$. When the rate of cyclic deterioration is the same in both loading directions then $D^{+/-} = 1$ and the cyclic deterioration rule is essentially the same as the one included in the original Ibarra-Krawinkler model. Figure 2.17 illustrates the deterioration model capabilities during cyclic response if we select to use asymmetric rates of deterioration. More examples are shown in Section 3.4.8, where the moment rotation diagrams of composite beams are calibrated.

Definition of reference energy dissipation capacity

In the original model the reference energy dissipation capacity E_t for each mode of deterioration was expressed as a multiple of $F_y \delta_y$, with the multiple denoted as γ_s , γ_c , γ_a and γ_k , respectively, for basic strength, post capping strength, accelerated reloading stiffness and unloading stiffness deterioration. Relating the energy dissipation capacity to the yielding deformation is not a very stable measure since δ_y is ill defined in many cases. For this reason it was decided to use the more stable parameter δ_p to normalize the reference energy dissipation capacity. Thus, in the modified model this reference value is expressed as

$$E_t = \lambda \cdot F_y \cdot \delta_p \quad (2.8)$$

where λ can take on different values for the four cyclic deterioration modes, i.e., λ_s , λ_c , λ_a and λ_k . For plastic hinge rotations it is convenient to introduce the parameter $\Lambda = \lambda \theta_p$, since

θ_p is dimensionless and Λ constitutes therefore a reference cumulative plastic rotation that can be visualized. For instance, if $\lambda = 20$ and $\theta_p = 0.05$ rad., then $\Lambda = 1.0$.

Post-capping deterioration modeling in the presence of residual strength

In moment rotation data for steel plastic hinge regions it is often observed that the post-capping strength does not drop to zero and that the hysteresis loops stabilize at a considerable value of residual strength (Ricles et al., (2004), Uang et al., (2000a), Cofie and Krawinkler, (1983)). Thus, residual strength needs to be simulated for many steel components. In such cases the need exists to modify the post capping deterioration model so that the post-capping tangent stiffness gradually changes from its initial (negative) value to a value of zero when the residual strength is attained. This gradual change in stiffness has been implemented in the modified version of the deterioration model as follows.

Assuming that the residual strength F_R is a fraction κ of the initial yield strength F_y , i.e.,

$$F_R^{+/-} = \kappa^{+/-} \cdot F_y^{+/-} \quad (2.9)$$

at increment i for positive excursion the updated post capping slope of the deterioration model is given by

$$a_{cap,i}^+ = a_{cap}^{initial,+} \cdot \left(1 - \frac{F_R^+}{F_{y,i}^+} \right) \quad (2.10)$$

in which

$a_{cap,i}^+$: positive post capping slope at positive excursion i

$a_{cap}^{initial,+}$: initial post capping slope for positive loading direction defined as,

$$a_{cap}^{initial,+} = \frac{F_c^+}{\theta_{pc}^+ \cdot K_e} \quad (2.11)$$

F_R^+ : residual strength for positive side (the yield strength for the deterioration model can be different of positive and negative side)

$F_{y,i}^+$: yield strength for positive excursion i

At increment i for negative excursion the updated post capping slope of the deterioration model is given by

$$a_{cap,i}^- = a_{cap}^{initial,-} \cdot \left(1 - \frac{F_R^-}{F_{y,i}^-} \right) \quad (2.12)$$

in which,

$a_{cap,i}^-$: negative post capping slope at negative excursion i

$a_{cap}^{initial,-}$: initial post capping slope for negative side defined as,

$$a_{cap}^{initial,-} = \frac{F_c^-}{\theta_{pc}^- \cdot K_e} \quad (2.13)$$

F_R^- : residual strength for negative side

$F_{y,i}^-$: yield strength for negative excursion i

Figure 2.18 illustrates the update strategy for the post capping deterioration modeling in the presence of residual strength using a bilinear model since stabilization of the hysteretic behavior is mostly observed in steel specimens. The same rules have been implemented in the peak-oriented and pinching model. Assuming that the residual strength in the positive

loading direction is F_R^+ as illustrated in the figure, the reference cap point for each excursion is defined based on the originally assumed post capping slope $\kappa_c^{L,+}$ after we consider post capping strength deterioration. The linear post capping branch is then defined by the new capping strength of the current excursion and the updated slope $\kappa_c^{2,+}$ using Equation (2.12) (see dashed lines in Figure 2.18). When the model reaches the residual strength (see Figure 2.19), it stabilizes and no longer deteriorates in strength. As observed in Figure 2.19, unloading stiffness deterioration continues even if the model reaches the residual strength. This modeling process is based on observations from experimental data (Ricles et al., 2004, Uang et al., 2000a).

The modified Ibarra-Krawinkler model is employed in all the case studies illustrated in the report. All the calibrations and regression results discussed in Chapters 3 and 4 are based on this model, and so are the collapse predictions discussed in Chapters 7, 8 and 9. Examples of calibrations after utilizing the modified Ibarra-Krawinkler deterioration model are shown in Chapter 3.

2.4 Summary and Observations

In this chapter we reviewed a number of deterioration models that have been used widely in research studies. After evaluating an extensive number of experimental data from the three databases on steel and RC components discussed in Chapter 3, we refined the original Ibarra-Krawinkler deterioration model. Some of the new terms (θ_p , θ_{pc} , λ or A) used to define the backbone curve and cyclic deterioration are refinements of the original model definitions and, in general, are considered to be more stable parameters compared to the original input parameters. In summary the modified Ibarra-Krawinkler deterioration model allows the simulation of:

1. A complete loss of strength as observed, for instance, as a consequence of ductile tearing in steel components.
2. Asymmetric hysteretic behavior of the components including different rates of cyclic deterioration in both loading directions. This is important for beams with a slab since due to composite action the component may deteriorate much slower in the loading direction in which the concrete is in compression compared to the loading direction in which the beam bottom flange is in compression. The backbone curve for the two loading directions can also be fully asymmetric.
3. Stabilization of strength at a residual value, as is observed often in steel beam specimens at relatively large inelastic deformations.

All these modifications of the Ibarra-Krawinkler model have been implemented for bilinear, peak-oriented and pinched hysteresis models.

Table 2.1. Summary of capabilities of reviewed hysteresis models

Model	Cyclic hardening	Bausch. effect	Strength capping	Residual strength	Cyclic deterioration			
					Basic Strength Det.	PostCap Strength Det.	Unloading Stiffness Det.	Accel. Stiffness Det.
Clough & Johnston & Modifications	X	X	X	X	X	X	O	O
Takeda Model	X	X	X	X	X	X	O	O
Bouc-Wen & modifications	O	O	X	X	O	X	O	O
Ramberg-Osgood	O	O	X	X	O	X	O	X
Kunath et al., Model	O	O	X	X	O	X	O	O
Syvaselvan & Reinhorn	O	O	X	X	O	X	O	X
FEMA -356	O	X	O	O	X	X	X	X
Yield – Line Plastic Hinge Models	O	O	O	O	O	O	O	O
Song-Pincheira	X	X	O	O	X	X	O	O
Ibarra - Krawinkler	X	X	O	O	O	O	O	O
Modified Ibarra Krawinkler	X	X	O	O	O	O	O	O

O = specified behavior mode incorporated in model

X = specified behavior mode not incorporated in model

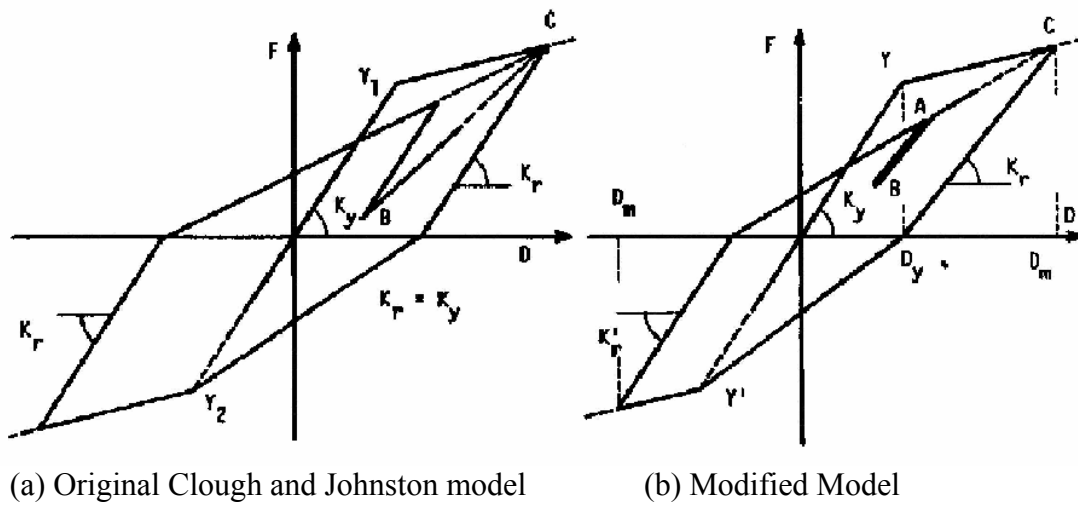


Figure 2.1. Peak – oriented (Clough) degrading stiffness model (after Clough and Johnston, (1965))

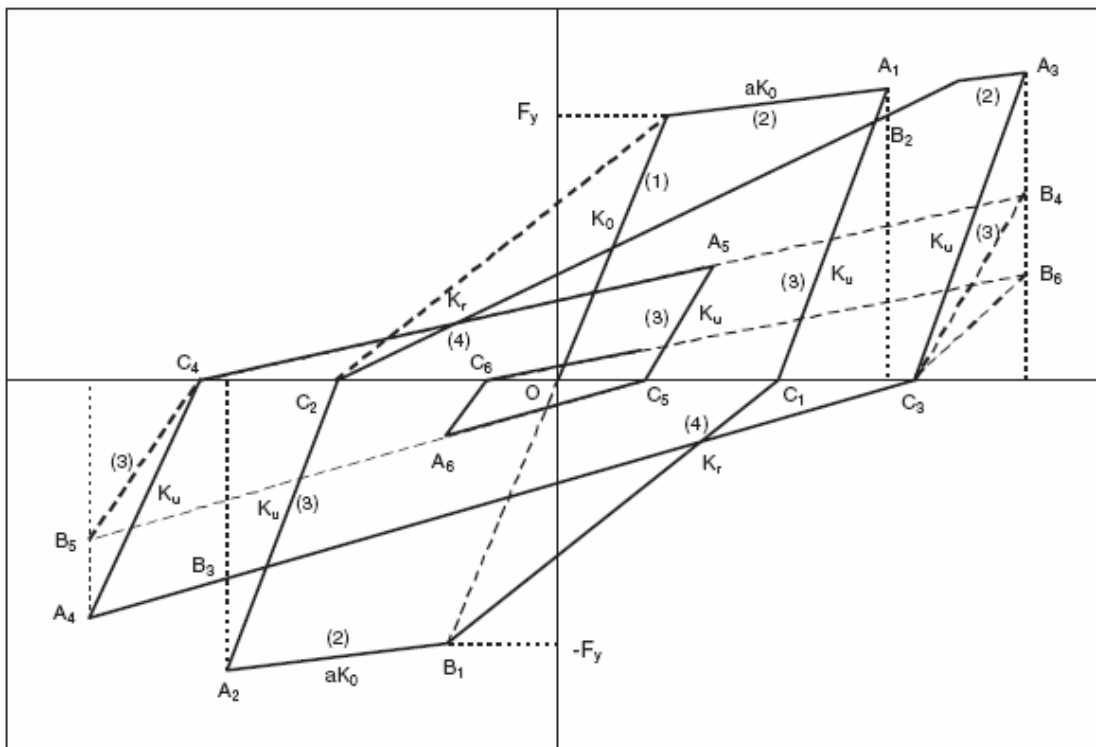


Figure 2.2. Hysteretic model by Sucuoglu and Erberik (2004)

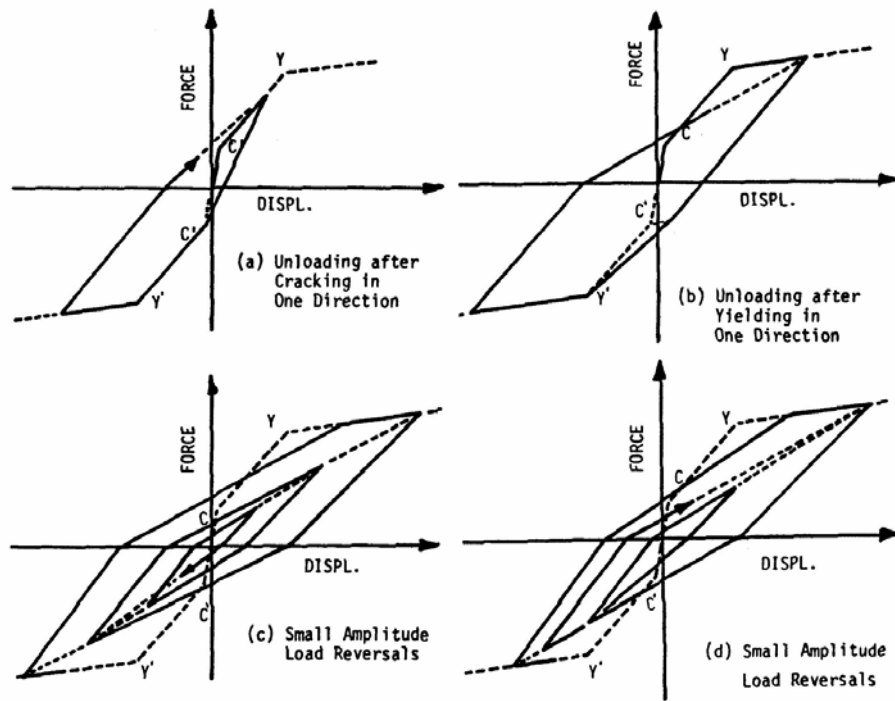


Figure 2.3. Takeda hysteresis model (After Takeda et al. (1970))

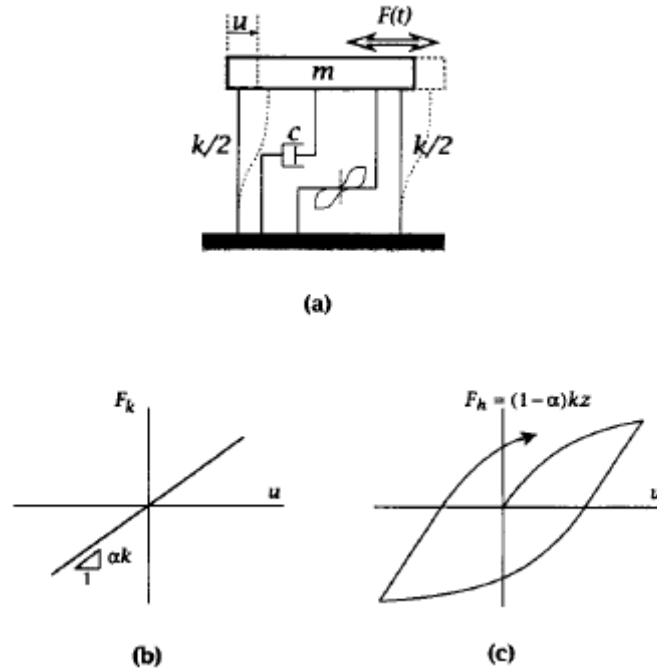


Figure 2.4. Bouc-Wen Model; separation of linear restoring force component from hysteretic restoring force component (Foliente, 1995)

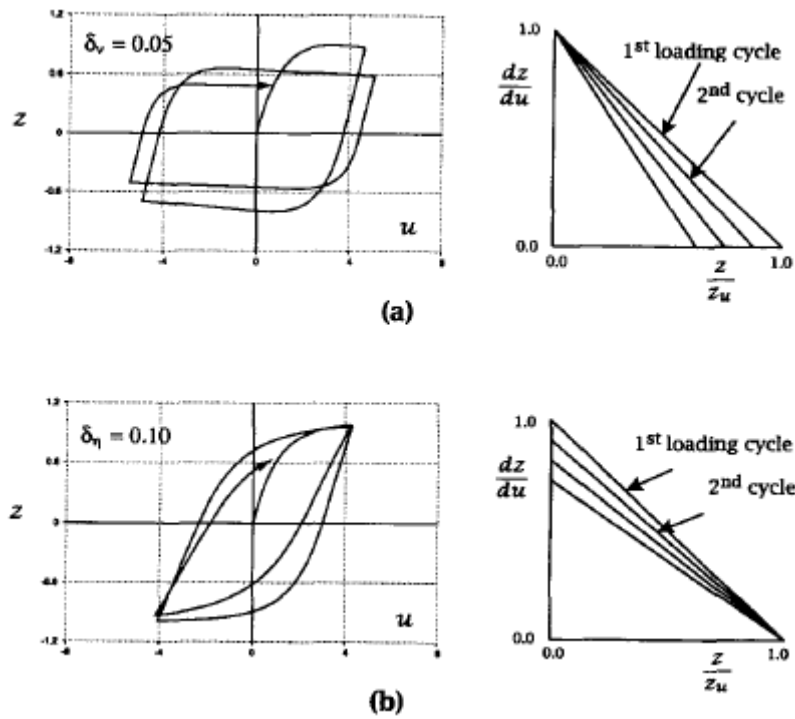


Figure 2.5. (a) Strength degradation, (b) Stiffness degradation (Foliente, 1995)

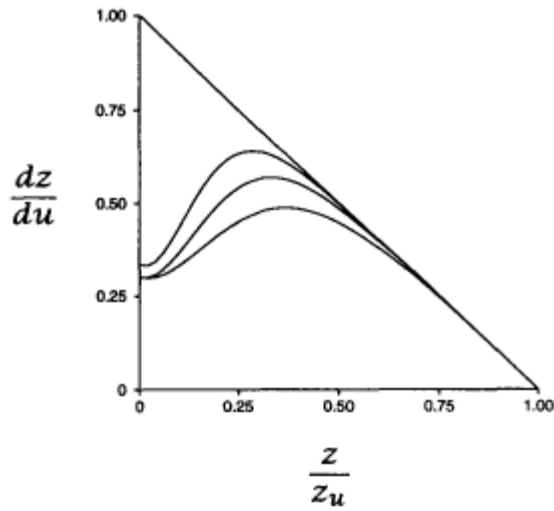
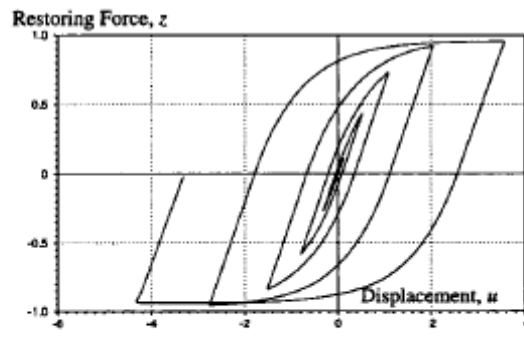
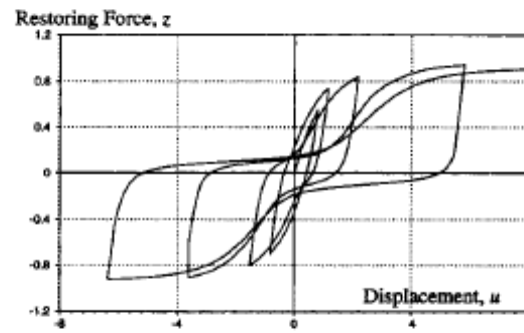


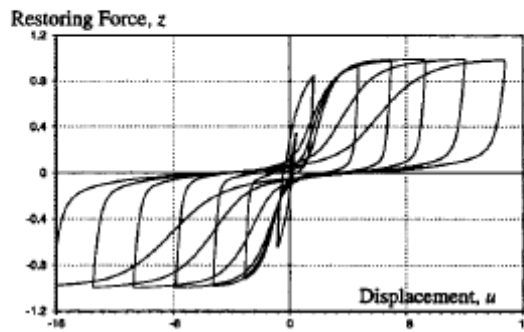
Figure 2.6. Hysteresis pinching – Baber and Nouri Model (Foliente, 1995)



(a)



(b)



(c)

Figure 2.7. Simulations obtained with BWBN Model (Foliente, 1995)

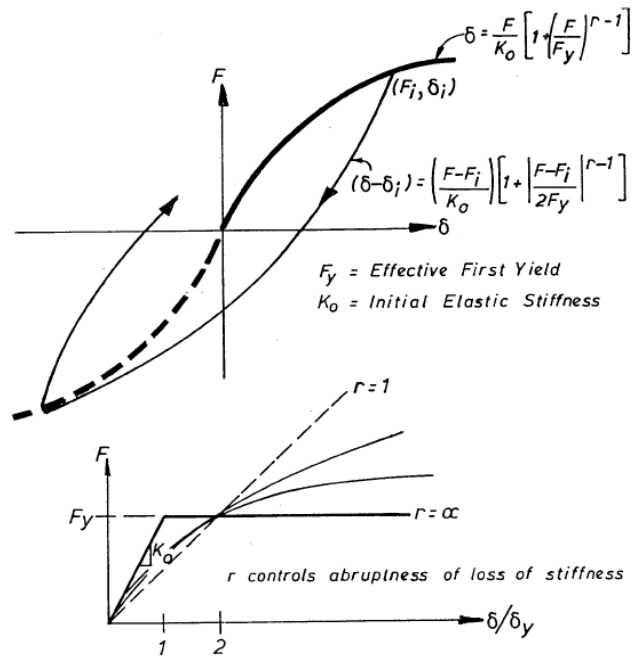
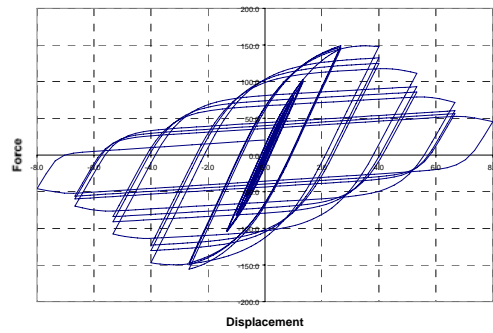
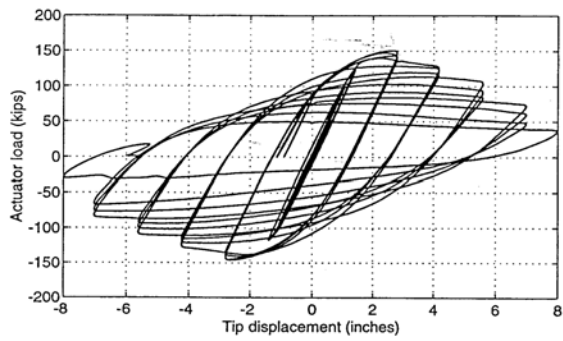
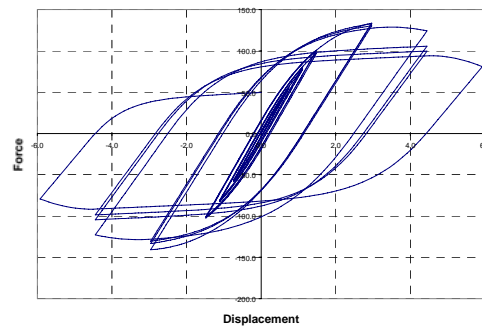
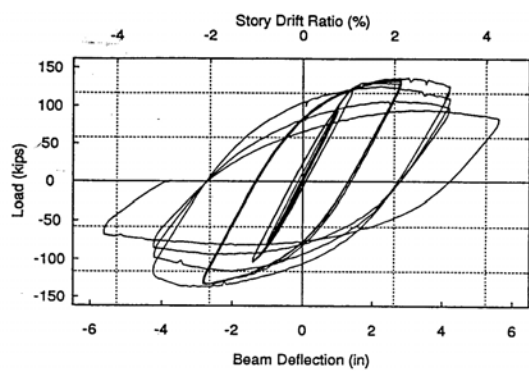


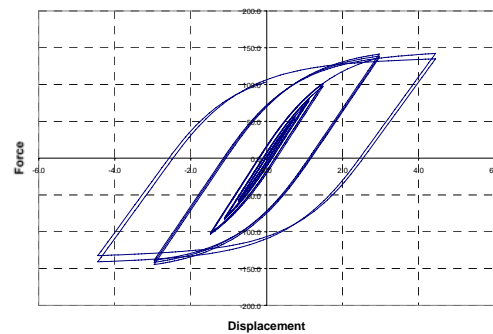
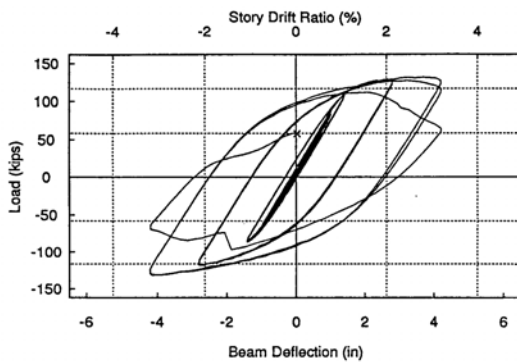
Figure 2.8. Ramberg-Osgood model (Carr, 2003)



(a) Test #16 of FEMA-289 (1996)



(b) Test # 17 of FEMA-289 (1996)



(c) Test # 18 of FEMA-289 (1996)

Figure 2.9. Example of calibrations of Sivaselvan and Reinhorn model (SAC Joint Venture 1996)

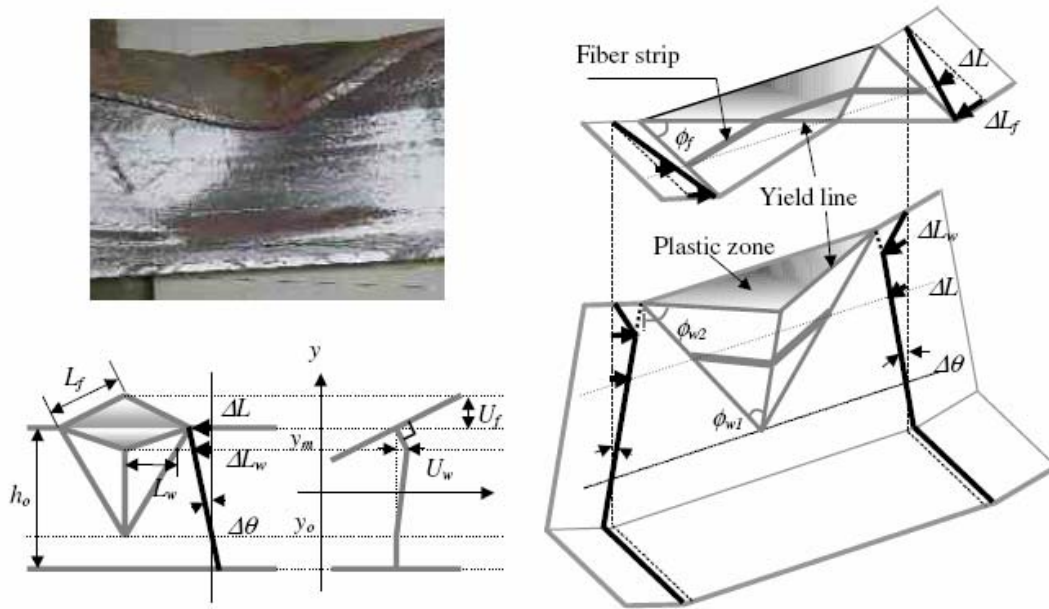


Figure 2.10. Monotonic yield line plastic hinge model deformation (after Lee and Stojadinonic, 2004)

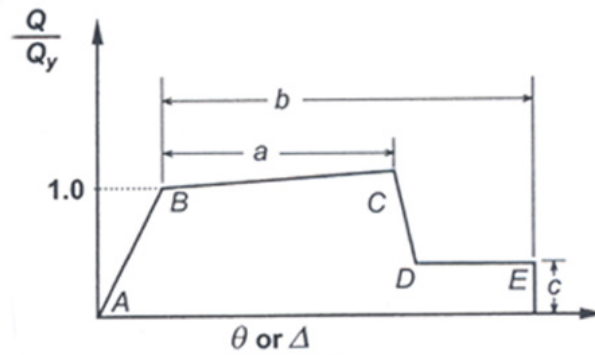


Figure 2.11. General force-deformation behavior of structural components (FEMA 356, 2000)

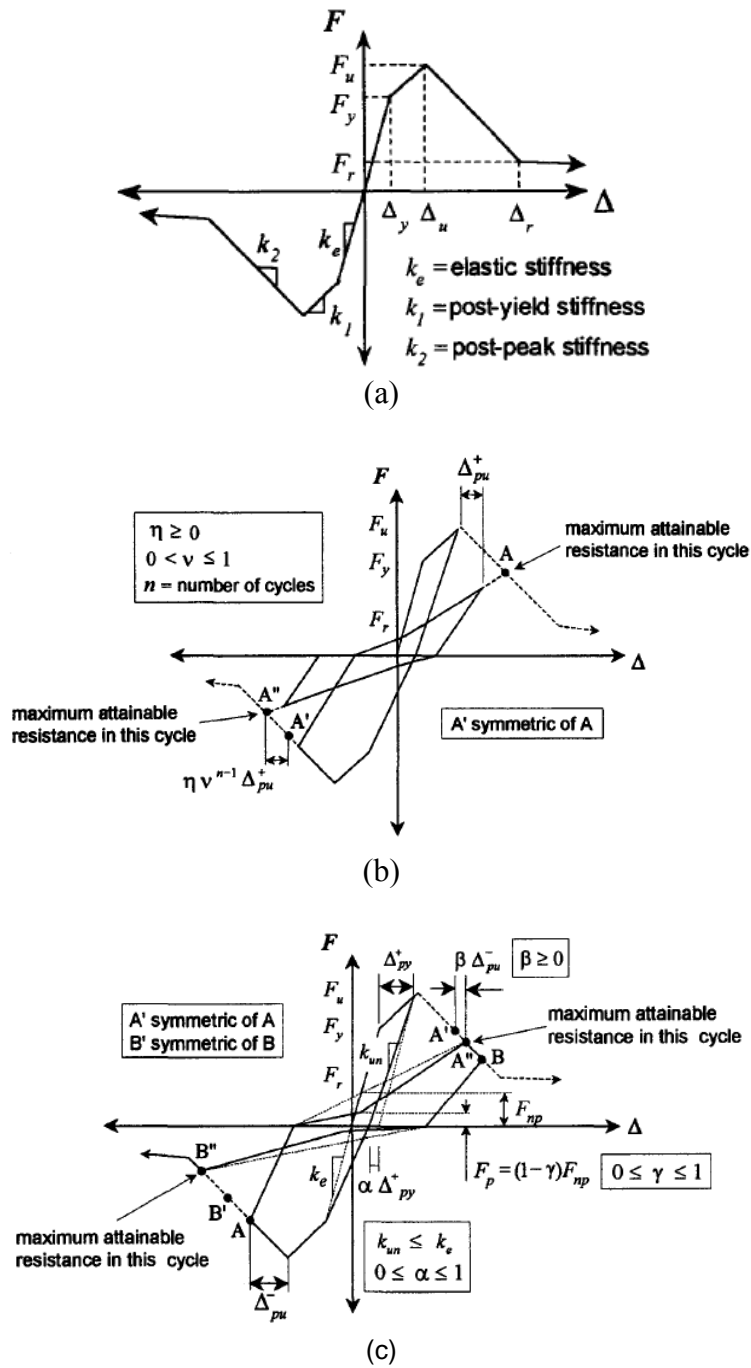


Figure 2.12. Song-Pincheira model; (a) backbone curve, (b) hysteresis rules for cycles of increasing def. amplitude, (c) hysteresis rules for small amplitude or internal cycles (after Song and Pincheira, 2000)

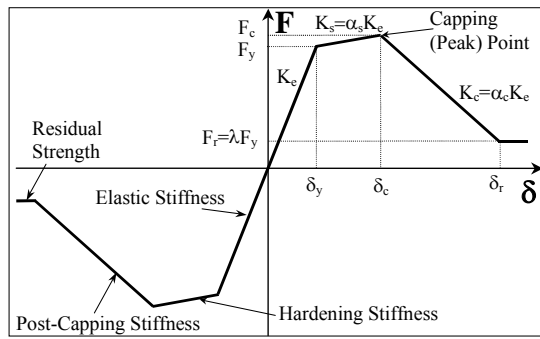


Figure 2.13. Backbone curve of Ibarra-Krawinkler model, and associated definitions (after Ibarra et al., 2005)

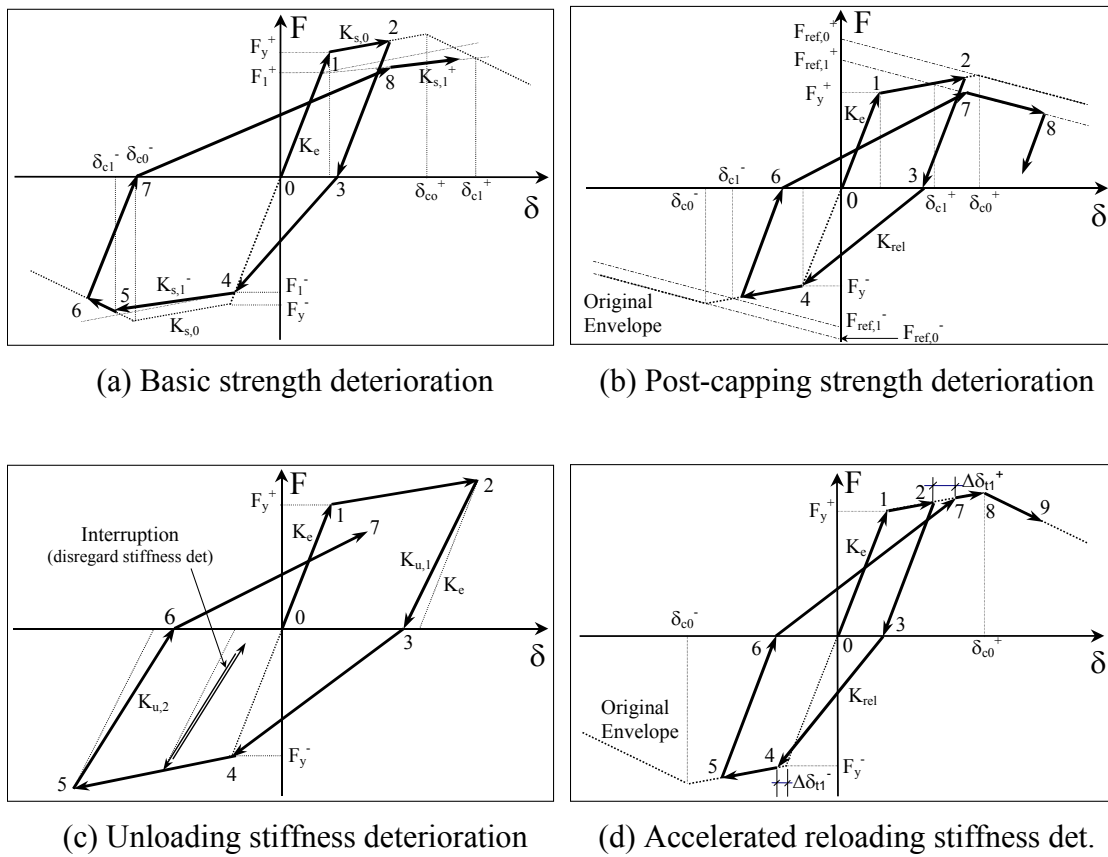
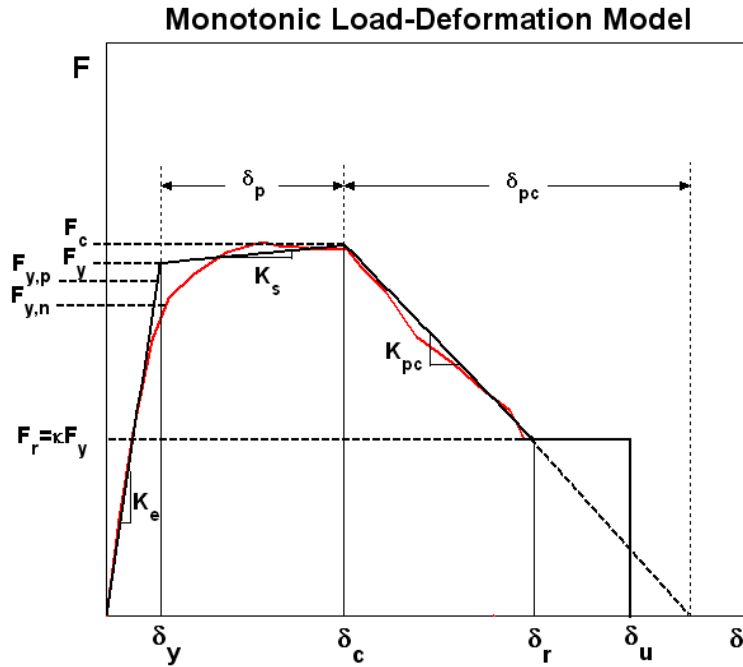


Figure 2.14. Individual deterioration modes for Ibarra-Krawinkler model, illustrated on a peak-oriented model (after Ibarra et al., 2005)



- δ_c = cap deformation (deformation associated with F_c for monotonic loading)
- F_y = effective yield strength, incorporating “average” strain hardening
- δ_y = effective yield deformation ($= F_y/K_e$)
- K_e = effective elastic stiffness
- F_r = residual strength capacity
- δ_r = deformation at residual strength
- δ_u = ultimate deformation capacity
- δ_p = plastic deformation capacity associated with monotonic loading
- δ_{pc} = post-capping deformation capacity associated with monotonic loading

- F_c/F_y = post-yield strength ratio
- F_{yp} = predicted effective yield strength (predicted from measured material properties)
- F_{yn} = nominal effective yield strength (predicted from nominal material properties)

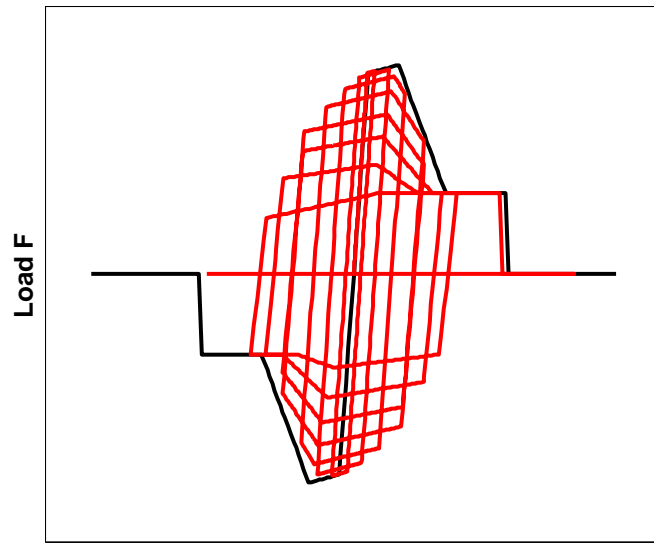
κ = residual strength ratio = F_r/F_y

Strain hardening ratio $\alpha_s = K_s/K_e = [(F_c/F_y)/\delta_p]/K_e$

Post-capping stiffness ratio $\alpha_c = K_{pc}/K_e = (F_c/\delta_{pc})/K_e$

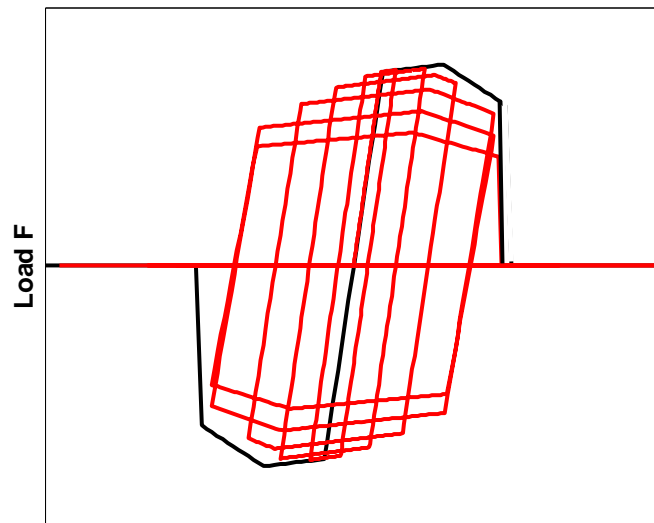
F_c = strength cap (maximum strength, incorporating “average” strain hardening)

Figure 2.15. Backbone curve of modified Ibarra-Krawinkler model, and associated definitions



Deformation δ

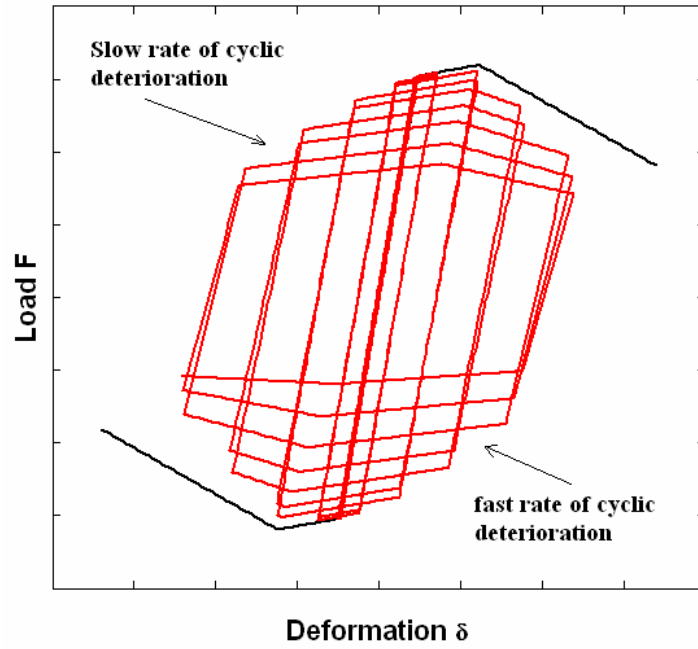
(a)



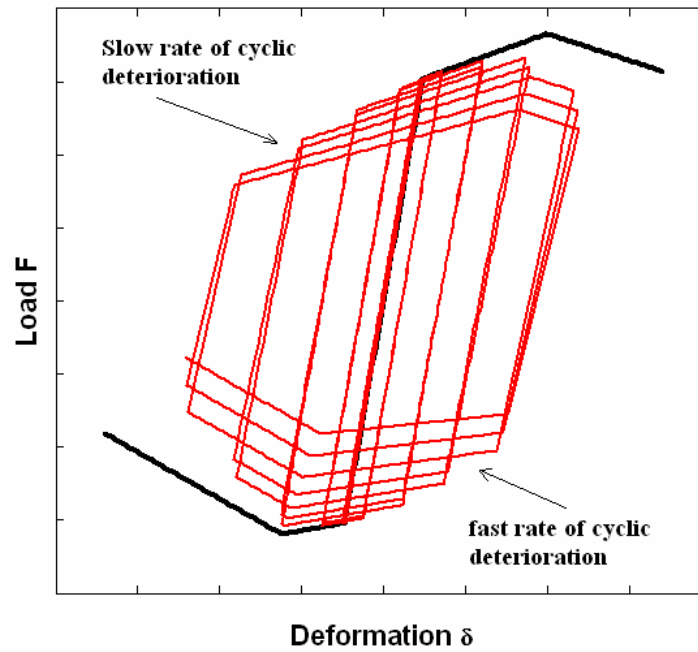
Deformation δ

(b)

Figure 2.16. Illustration of fracture incorporation in the modified Ibarra Krawinkler model; (a) fracture occurs after specimen reaches the residual strength path, (b) fracture occurs before the specimen reaches the residual path



(a) for symmetric backbone curve



(b) for asymmetric backbone curve

Figure 2.17. Illustration of different rates of cyclic deterioration based on the modified Ibarra-Krawinkler model

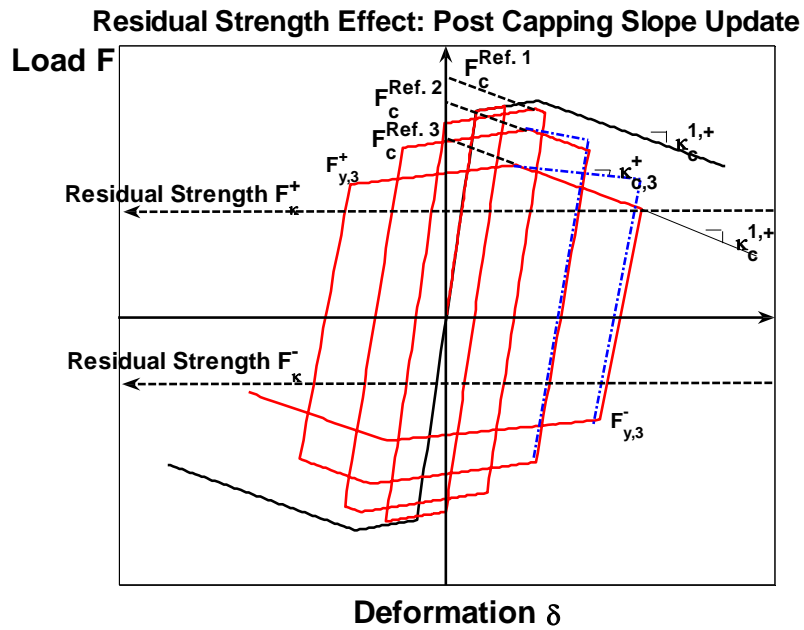


Figure 2.18. Update strategy for the post capping strength deterioration modeling in the presence of residual strength.

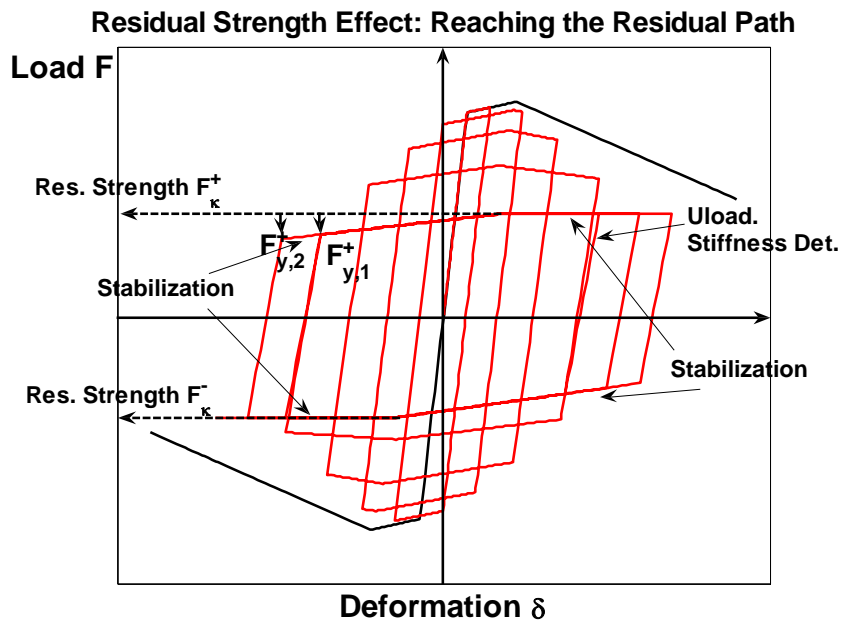


Figure 2.19. Stabilization of the hysteretic loop when the model reaches the residual strength value

CHAPTER 3

COMPONENT DATABASES AND CALIBRATION

3.1 Purpose and Scope

The missing aspect of comprehensive modeling of the deterioration characteristics of structural components is the availability of relationships that associate parameters of available deterioration models, such as the ones proposed in Ibarra et al. (2005) and summarized in Section 2.3, with geometric properties and detailing criteria that control deterioration in actual structural elements. In order to provide information for deterioration model parameters in support of collapse assessment of structural systems, a data collection of component tests is needed in a consistent format that permits validation and calibration of existing deterioration models. For this purpose, three databases have been developed for steel (wide flange beams and columns and a separate data collection for steel tubular sections) and concrete elements under cyclic bending moments (Lignos and Krawinkler, 2007).

At this time a small number of databases exist that provide partial information on component hysteresis of steel beams/connections (SAC, 1998) and reinforced concrete columns [e.g. PEER database (Berry et al., 2004), Panagiotakos and Fardis (2001), SAC database (<http://www.sacsteel.org/connections/>) Hoshikuma et al. (1997)]. In this chapter the main features of the database development and calibration process are discussed together with information related to statistical evaluation of material properties and deterioration modeling parameters. Trends of modeling parameters with respect to individual geometric or cross-sectional properties are also presented and discussed,

ignoring the effects of correlations between these properties. Trends with respect to combinations of these properties are addressed in Chapter 4 with the use of multivariate regression analysis.

3.2 Database Development

The database development effort was by far the most time consuming activity of this work, as it necessitated many attempts to solicit data from experimentalists and required manual input of metadata and in many cases of experimental results into the database. The information most needed for calibration of a deterioration model is a complete set of load-displacement and moment-rotation hysteretic response histories of a test specimen. In many cases these response histories are available only in graphical format and have to be hand-digitized for incorporation in the databases. To facilitate this effort a digitization software called Digitizer was developed (Lignos and Krawinkler, (2007)) in JAVA – programming language (Sun, 2007) that provides the aforementioned digitized data of interest.

The databases contain data in the following three categories: (1) metadata (configuration, geometry, properties); (2) reported results (measurements and observations as reported in test documentation); and (3) deduced data (information deduced from metadata and reported data for the purpose of calibration of deterioration models). A short description of the components of the databases is provided in Appendix A together with an abbreviated database notation and a table of only the specimens used for data evaluation included in this chapter and Chapter 4. The complete database notation together with the set of data can be downloaded through the NEESCentral repository (<https://central.nees.org/>).

Three databases have been developed, one for steel W-sections [mostly beams but also some columns, Newell and Uang (2006)], one for tubular sections that are primarily used in Japan for columns of low and mid-rise steel construction, and one for reinforced concrete

beams (including columns with a compression force less than 15% of the compressive strength, which is defined as the concrete compressive strength f'_c times the gross cross section area A_c). At this stage of database development the steel database of W-sections includes more than 300 specimens, the tubular database includes 113 specimens and the RC database includes 200 specimens.

3.3 Calibration of Component Model Parameters

The information stored in the databases is utilized to calibrate the cyclic moment-rotation behavior of plastic hinge regions in steel and reinforced concrete components. The calibration parameters are based on the modified Ibarra-Krawinkler model (Sections 2.3). The objective is to develop “complete” moment-rotation relationships (or for that matter any force-deformation relationship) that incorporate experimental evidence to quantify phenomena (such as cyclic deterioration) that are insufficiently described by presently available models of engineering mechanics. The emphasis is on modeling of component behavior at large inelastic deformations that will make it possible to trace the dynamic response of structures up to collapse.

3.3.1 Calibrator Interactive Software

An interactive software, named Calibrator, was developed to facilitate the calibration effort (Lignos and Krawinkler 2007). The Calibrator is a pre-processor, developed in MATLAB programming language (Mathworks, 2005) that provides an interface between hysteretic moment-rotation relationships stored in the database and a single-degree-of-freedom (SDOF) inelastic analysis program called SNAP that computes the hysteretic response based on modeling parameters input into the interface. The graphical interface is illustrated in Figure 3.1. The Calibrator’s actions are summarized as follows:

1. An experimental moment-rotation ($M-\theta$) relationship is imported from a database (frame 1 of Figure 3.1(a)) and displayed for visual inspection (Figure 3.1 (b)).
2. Based on the shape of the hysteresis loops of the experimental $M-\theta$ relationship a basic hysteresis model is selected (in the illustrated case the bilinear model is selected, see frame 1 of Figure 3.1(a)).
3. Based on a combination of visual observations and concepts of mechanics, backbone curve parameters are input in the interface module (frame 2 of Figure 3.1(a)). The backbone curve can be visually inspected to judge its match with the experimental result (see Figure 3.1(c)), and its parameters can be altered as deemed necessary to improve the match.
4. Cyclic deterioration parameters are input based on judgment and past experience (frame 3 of Figure 3.1(a)).
5. The Calibrator calls a tool that simulates the cyclic response, given the model parameters (backbone curve and cyclic deterioration parameters) and the history of deformation peaks of the experiment. In the present implementation the SDOF analysis program SNAP is used for this purpose since its hysteresis rules incorporate the modified Ibarra-Krawinkler model. With few modifications to the source code of the Calibrator it is possible to connect the software with other available analysis programs that include more hysteresis models for future evaluation.
6. The simulated hysteretic response is displayed together with the experimental results for visual inspection of the match. If the match is judged to be unsatisfactory (see left half of Figure 3.1(d)), improved backbone and deterioration parameters can be input and the process can be repeated until a satisfactory match is achieved (see right half of Figure 3.1 (d))

The results of several hundreds of experiments have been utilized in the calibration process. The general conclusion is that satisfactory simulations can be achieved in almost all cases, and that the parameters obtained from these calibrations show consistent patterns that follow established engineering principles. But it is also clear that these patterns exhibit large scatter, which demonstrates that there are large variations in model parameters due to various sources, some of which are based on material and construction uncertainties and on human errors during specimen fabrication, but others are inherent in the simplifications on which the presently employed model is based. Future research should lead to improvements and reduction in the variability of the model parameters.

Some of the challenges encountered in the calibration process are summarized in the following sections. It is believed that the quantitative values of deterioration parameters provided here are reasonable, but not necessarily accurate. But they fulfill the intended purpose, which is to serve as educated estimates of component properties needed to address the issue of collapse prediction of building structures.

3.3.2 Calibration Process Based on Engineering Judgment

This section discusses the process and judgment that was followed in order to select representative deterioration parameters for components using the modified Ibarra–Krawinkler deterioration model. The general process applies in all cases (steel and RC specimens). Additional considerations were taken into account though during the calibration of specimens of the three databases.

1. The effective elastic stiffness for K_e is based on the following considerations:
 - a. It should be close to the unloading stiffness at early post-yielding excursions. It is observed that this value is rather stable and easy to identify and quantify.

- b. The effective elastic stiffness, K_e for steel specimens (W and tubular sections) is obtained by analysis. If it differs significantly from the measured elastic stiffness, the sources for the differences are identified.
- c. For RC specimens the effective elastic stiffness should be close to the estimate based on connecting the origin with the close-to-monotonic deformation at 0.60 times the yield force.

It is emphasized that in this study the focus is on modeling behavior that affects collapse prediction. Specifically for RC specimens it is likely that the K_e estimate proposed here is not a good stiffness value for response prediction at a serviceability level.

- 2. For a steel specimen, the effective yield strength F_y used for the backbone curve should account for “average” cyclic (isotropic) hardening, which may be significant in steel components. This is illustrated in Figure 3.2, which shows the response from two tests in which the cyclic skeleton (dotted line) curve exceeds the monotonic loading curve because the cyclic hardening effect exceeds the deterioration effect. This can be accounted for by assigning an effective yield strength to the backbone curve that is somewhat larger than the monotonic yield strength. The amount of cyclic hardening depends on the material used (A36 versus A572 or A992) and on the cyclic loading history.

For an RC specimen the effective yield strength F_y is a compromise between the value of yield strength computed from mechanics principles (using measured properties) and the judgmental “kink” point of the experimental force-deformation result, see Figure 3.3. It usually is larger than the value predicted from mechanics. Assistance in identifying this parameter is provided by matching a hardening stiffness to the experimental results and intersecting the hardening line with the elastic stiffness line.

3. The capping strength F_c is equal to or larger than the maximum strength value obtained from a monotonic loading test. A conservative estimate is the maximum strength obtained from a cyclic test, but in many cases this may be too low an estimate because the cyclic loading protocol may prevent attainment of the maximum strength obtained under monotonic loading. In the calibrations the maximum strength from a cyclic test is used unless there are good arguments to use a larger value for F_c .
4. For monotonic tests the capping deformation δ_c is obtained directly from the force-deformation response curve (see Figure 3.3). For cyclic tests δ_c is estimated from an iteration process with the Calibrator, using a value that, together with cyclic deterioration parameters, results in the best match of the cyclic response (see Figure 3.1(d) right).
5. An estimate of the post-capping deformation capacity δ_{pc} is obtained by using the best estimate of the post-capping slope and extending this slope from the capping point to the point of zero resistance (see Figure 3.3 for the monotonic case). It is understood this is a simplified estimate of a quantity that is most difficult to evaluate.
6. Based on observations from many cyclic tests of steel specimens, the assumption of a residual strength F_r is usually justified for steel components whose primary deterioration mode is a combination of local and lateral torsional buckling. The magnitude of F_r is judged from the value of strength at which stabilization of the hysteresis loops is observed. It is understood that the residual strength will not stay constant at extremely large inelastic deformations, but faithful reproduction of the load-deformation response at extremely large deformations is not critical because it is found from collapse studies that a structure approaches collapse at a story drift between 6% and 10% (see Chapter 8).

For RC elements stabilization of inelastic hysteresis loops at large deformations is rarely observed from cyclic tests, i.e., deterioration continues until negligible strength is reached. The implication is that a residual strength value is difficult to justify for RC components. Hence in most cases the residual strength for RC elements is considered to be zero in the calibration process.

3.4 Evaluation of Steel W-Section Database

The steel W-section database documents data from experiments on beams or beam-to-column subassemblies in which inelastic deformations are primarily concentrated in flexural plastic hinge regions of W (or H) sections, and in which the primary deterioration mode is local and/or lateral torsional buckling. Several cases in which components fail in a brittle mode (e.g., fracture around weldments) are in the database but are not included in any regression analysis discussed in Chapter 4 unless the sudden failure mode occurs at a deformation that is clearly larger than that associated with the mode of behavior evaluated through regression (e.g., δ_u must be clearly larger than δ_c in order for this test to be included in the dataset from which capping point properties are determined). Various types of beam-to-column connections are employed in the test specimens, with the connection types clearly identified in the database. Many of the specimens have “reduced beam sections” (RBS) in which plastic hinges develop away from the beam-to-column connection. Since 1995 the use of RBS has become widespread in U.S. practice for special moment resisting frames.

In the data evaluation of modeling parameters presented in Chapters 3 and 4, the data of the W-section database are subdivided into RBS data and other-than-RBS data, with the latter including all other connection types for which the pertinent model parameters can be quantified with confidence. The types of connections incorporated in the other-than-RBS category are identified in the database notation section of Appendix A.

3.4.1 Statistical Evaluation of Material Properties of US Structural Steel

The steel database provides valuable information regarding material properties variation since all material properties obtained from coupon tests for both flange and web are stored in separate fields. A statistical study was performed using all the available wide flange specimens (beams and columns) of the steel database. Mean value and standard deviation of yield and ultimate strength are summarized in Tables 3.1 and 3.2 for both the flange and the web of the section, respectively. The values are very comparable with the study by Dexter et al., (2000) and Brockenbrough, (2001). The statistical evaluation was conducted for the three main types of structural steel in the United States, A36, A572 Grade 50 and A992 Grade 50. The tables include the linear correlation coefficient ρ between yield and ultimate strength (ρ_{F_y, F_u}), which is important for reliability based studies.

Figures 3.4 to 3.6 show the yield to tensile strength ratio histograms taken from flange and web for the three types of structural steel used in United States together with their empirical cumulative distribution function. The mean for each of the data sets is fairly close to values reported by Liu, (2003) and Liu et al. (2005). A reason for the small difference in the mean values is that the values reported by Liu are based on mill certificates.

3.4.2 Statistical Evaluation of Ratio of Effective to Predicted Bending Strength of Steel Beams

As stated in Section 2.3 the modified Ibarra-Krawinkler deterioration model does not account explicitly for cyclic hardening. But the effect of isotropic hardening is incorporated approximately by increasing the “yield” moment (bending strength) to an effective value M_y that accounts for isotropic hardening “in average”. The use of this effective yield strength will typically overestimate by a small amount the predicted bending strength (plastic section modulus times material yield strength based on measured material properties, $M_{y,p}$) for small cycles, and it might underestimate by a small amount the predicted bending

strength for large cycles— presuming that cyclic deterioration is not yet dominating the response.

Table 3.3 summarizes the mean and standard deviation of the ratio of effective to predicted component yield strength for W-section steel beams with RBS connections and other-than-RBS connections.

3.4.3 Post-Yield Hardening Stiffness

Post-yield hardening is described by the ratio of the maximum moment on the backbone curve (capping moment), M_c , to the effective yield bending strength, M_y , of the deterioration model used in this study. This ratio defines, together with the ratio δ_c/δ_y , the strain hardening stiffness of the backbone curve. This stiffness is important because of its effect on the P- Δ stability of the structural system (Medina and Krawinkler, 2003). Based on the evaluation of 297 specimens from the W-section database the mean value of the M_c/M_y ratio for RBS and other-than-RBS connections is 1.09 and 1.11, respectively. The standard deviation σ_{M_c/M_y} of the two subsets of data is 0.03 and 0.05 indicating that M_c/M_y is a more stable parameter than the “traditional” strain hardening ratio for describing the post-yield hardening stiffness of a structural component. Statistical values of M_c/M_y are summarized also in Table 3.3.

3.4.4 Trends for Deterioration Modeling Parameters

The following discussion, supported by representative plots, is intended to illustrate trends that show the dependence of modeling parameters on selected geometric properties. Since for most connection types the number of tests is small and the trends are not sufficiently clear to justify a distinction based on connection type, no distinction is made by connection type except that RBS connections are treated separately. For the same reason, only beams without a slab are considered in this evaluation. The slab effect is treated separately in

Section 3.4.6. It is emphasized that the trends alone do not provide sufficient information to quantify modeling parameters, because these depend on combinations of geometric and material parameters. The development of multivariate regression equations that account for these combinations in the quantification of modeling parameters is discussed in Chapter 4. Trends for the following four data sets are evaluated:

1. All experiments on beams with other-than-RBS connections (data set 1)
2. All experiments on beams with RBS connections (data set 2)
3. Experiments on beams with other-than-RBS connections with depth $d \geq 21''$ (data set 3)
4. Experiments on beams with RBS connections with depth $d \geq 21''$ (data set 4)

The full other-than-RBS data set (1) contains many experiments on small sections, which are useful to observe trends but conceivably de-emphasize trends for the sizes of sections that likely are part of the lateral system in moment resisting frame structures. This is why data sets (3) and (4) have been generated.

Trends are illustrated by plotting data points of a model parameter against a pertinent geometric parameter. The information presented in the plots is obtained from calibrations in which the parameters of the modified Ibarra-Krawinkler deterioration model, summarized in Section 2.3, are matched to the experimental moment-rotation relationships of the W-sections steel database. A typical match was shown on the right side of Figure 3.1(d). It should be noted that the data presented here are for deformations in the beams only, and that elastic and inelastic (when present) deformations from panel zone and column have been subtracted from the total deformations in the case of subassembly tests. A regression line is included in the individual plots only to illustrate the overall trends for the modeling parameter. In each plot we include also the coefficient of determination R^2 in order to get an

insight into the “goodness” of linear fit assuming that each one of the geometric parameters can be treated as an independent random variable (i.e., the correlation between various geometric parameters is ignored).

3.4.4.1 Trends for Plastic Rotation Capacity θ_p

Effect of Beam Depth d on θ_p : The dependence of the plastic rotation capacity θ_p on the beam depth d for the full data sets (1) and (2) is presented in Figure 3.7(a) and (b). For beams other than RBS the slope of the best fitted curve for data set (1) in the range of 21" to 36" is much flatter compared to the range of 4" to 21" indicating that the large dependence of the plastic rotation capacity on beam depth in the range of 4" to 21" is mostly driven by the incorporation of small sections in the database. As stated earlier data set (1) includes sections with a depth varying from 4" to 36". In typical steel buildings the range of beam sections used is larger than 21" [data set (3)]. For these beam sizes the dependence on d is illustrated in Figures 3.7(c). The observation for beams other than RBS is not confirmed for beams with RBS (see Figures 3.7(b, d)) since there is a clear dependence of θ_p on d .

Effect of span to depth ratio L/d on θ_p : Based on simple curvature analysis the plastic rotation capacity for a given beam section is expected to be proportional to the beam span L (distance from plastic hinge location to point of inflection). Figure 3.8 (a), which shows the dependence of θ_p on L/d for the full data set of beams with other-than-RBS connections, partially supports this perception. But the perception does not hold true when only beams of depth larger than 21" are considered (see Figures 3.8(c) and (d)). For the range W21 to W36 θ_p is only weakly dependent on L/d . The reason is that most deep beams are susceptible to a predominance of web buckling and lateral torsional buckling, and both of these susceptibilities increase with a decrease in the moment gradient (more uniform moment, as implied by an increase in the L/d ratio). This phenomenon offsets the curvature integration effect of a larger plastic hinge length. The consequence are the following observations for beams with depth ≥ 21 ”:

- The plastic rotation capacity is not very sensitive to the beam span (i.e., the length of the plastic hinge regions)
- A description of beam plastic deformation capacity in terms of a ductility ratio θ_p/θ_y is misleading because θ_y increases linearly with L (for a given beam section) but θ_p does not.

Effect of L_b/r_y on θ_p : Lateral torsional buckling of a beam is associated with the L_b/r_y ratio. L_b is defined here as the distance from the column face to the nearest lateral brace, and r_y is the radius of gyration about the weak axis of the beam. Figure 3.9 illustrates the effect of lateral torsional buckling ratio on the plastic rotation capacity for the two data sets with specimens that have $d > 21$ ". It is observed that a decrease in L_b/r_y is not very effective in improving the plastic rotation capacity θ_p , particularly for beams other than RBS. Based on Figure 3.9(b) for beams with RBS L_b/r_y has a small effect on θ_p compared to the negligible effect on θ_p of beams other than RBS (see Figure 3.10(a)) but the latter data set exhibits more scatter since the connection types included are not the same. The same observation regarding beams with RBS was made by Yu et al. (2000) and Uang et al. (2000a) in an experimental study on RBS connections, in which the insertion of additional lateral bracing close to the RBS portion of a beam had a small effect on θ_p . This is illustrated in Figure 3.10 in which we compare the cyclic behavior of "identical" beams with RBS. The only difference between the two test specimens is the addition of supplemental lateral bracing near the RBS region for the beam in Figure 3.10(b) ($L_b/r_y = 52.0$ versus $L_b/r_y = 36.3$). As seen from the calibrated moment rotation diagrams the effect of the additional brace on θ_p is not important.

Effect of Width to Thickness Ratio of the Beam Flange ($b_f/2t_f$) on θ_p : Figures 3.11(a) and 3.11(b) show the dependence of plastic rotation capacity of beams other-than-RBS and beams with RBS on the $b_f/2t_f$ ratio, which is an indicator for flange local buckling. Both data sets have a $d \geq 21$ ". The data indicate that θ_p is not very sensitive to the $b_f/2t_f$ ratio (for

the range of relatively low $b_f/2t_f$ values of the experiments contained in the database) and in particular for beams with RBS. - if $b_f/2t_f$ is treated as an independent random variable. On the other hand, a small $b_f/2t_f$ ratio often implies a narrow wide flange beam with small r_y and a large d/t_w , both of which have a detrimental effect on θ_p . This possibly conceals the importance of $b_f/2t_f$ on θ_p .

Effect of Depth to Thickness ratio of the Beam Web, h/t_w on θ_p : Figures 3.12(a) and 3.12(b) show the dependence of θ_p on h/t_w ratio, in which h is the clear web depth used for compactness checks based on AISC, 2005, and t_w is the web thickness of the beam section, for the full data sets (1) and (2) (beams with RBS and other-than-RBS). For both data sets h/t_w has a large effect on plastic rotation capacity. When specimens with $d \leq 21$ " are eliminated from both data sets the influence of h/t_w on θ_p becomes smaller compared to the full data sets based on Figures 3.12(c) and 3.12(d) but this may be due to the limited data since the h/t_w range for data sets (3) and (4) is between 30 to 55 compared to 5 to 55 for beams other than RBS and 20 to 55 for beams with RBS. Uang and Fan (1999) after conducting a statistical evaluation on beams with RBS came to the conclusion that h/t_w is the primary contributor to plastic rotation capacity of these beams. It should be pointed out that in the previous study by Uang and Fan the definition of plastic rotation capacity was different (plastic deformation from yield rotation to rotation that beam loses 20% of its maximum strength) compared to the one used in here in. The primary reasons for the large effect of h/t_w on θ_p are that a section with a large h/t_w ratio is subject to early web buckling and is more susceptible to lateral torsional buckling (smaller torsional constant and r_y).

3.4.4.2 Trends for Post Capping Rotation Capacity θ_{pc}

Figure 3.13 shows the dependence of post capping plastic rotation capacity θ_{pc} of data sets (3) and (4) (beams with $d \geq 21$ ") on various geometric parameters discussed earlier. Based on Figures 3.13(a) and 3.13(b) important parameters are h/t_w and $b_f/2t_f$ since local buckling triggers lateral torsional buckling, which happens during the late cycles of a loading history

of a beam. The effect of L_b/r_y on θ_{pc} is more significant for beams with RBS compared to beams other-than-RBS based on the R^2 values from Figures 3.13(c). A possible reason for this may be that the web at the RBS is not adequately restrained because of the flange width reduction at the RBS; hence the web buckles easier compared to a beam without RBS, and lateral torsional buckling, which is triggered by web buckling, occurs earlier for beams with RBS. Figures 3.10(a) and (b) in which calibrated moment rotation diagrams of two tests conducted by Uang and Fan (1999) are presented, show the effect of additional bracing on θ_{pc} . In general the values are in accordance with Figure 3.13(c).

3.4.4.3 Trends for Rate of Cyclic Deterioration \mathcal{A}

The effect of geometric parameters on the rate of cyclic deterioration, which is defined by the cumulative plastic rotation capacity \mathcal{A} as discussed in Section 2.3, is illustrated in Figure 3.14 for data sets (3) and (4). Both h/t_w and $b_f/2t_f$ have an important effect on \mathcal{A} , as seen from Figure 3.14(a) and (b). The effect of lateral bracing becomes somewhat important on the rate of cyclic deterioration for beams other-than-RBS but is clearly important for beams with RBS (see R^2 in Figure 3.14(c)) because lateral bracing delays deterioration due to lateral torsional buckling. Uang and Fan (1999) used the ratio of strength at 0.03rad plastic rotation over the strength at 0.02 rad plastic rotation to define the rate of cyclic deterioration of beams with RBS. They also concluded that additional bracing near the RBS delays the rate of cyclic deterioration. The same conclusion can be drawn from the calibrated moment-rotation diagrams in Figures 3.10.

Uang et al (2000b) conducted three tests with beams with RBS and deep columns. They concluded that the column flange connected to the beam is likely to experience severe out-of plane bending or column twisting since (1) beams with RBS tend to "kick-out" in the lateral direction, introducing torsion in the column, and (2) the torsional property of deep sections tends to produce higher warping stresses in the column.

3.4.5 Statistical Evaluation of Deterioration Modeling Parameters

A different way of representing the data discussed in the previous paragraphs is in the form of cumulative distribution functions, CDFs, which reveal statistical characteristics but do not display dependencies on individual parameters. The CDFs for θ_p , θ_{pc} , and λ are shown in Figures 3.15 to 3.17 for beams other-than-RBS and RBS sections. CDFs are presented for the full set of data [data sets (1) and (2)] and for the data sets with $d \geq 21$ " [data sets (3) and (4)]. The curves shown in each plot represent log-normal distributions fit to the data points. A Kolmogorov-Smirnov test (Benjamin and Cornell, 1970) was conducted to compare the values in each data set with the log-normal distribution. The CDFs for the four data sets are comparable, but in general the median value of the modeling parameters for beams with other-than-RBS connections is smaller than that for beams with RBS connections, and the dispersion is larger. One reason is that data sets (1) and (3) include specimens with different types of connections. Table 3.4 summarizes the median and standard deviation of deterioration modeling parameters for the four data sets. Tables 3.5 to 3.8 summarize the correlation coefficients between model parameters for the 4 data sets. Esteva and Ruiz (1989) reported similar values for correlation coefficients of deterioration parameters. Their values were based on analytical simulations but not on experimental evidence. The correlation coefficients between model parameters are valuable for studies related to quantification of modeling uncertainties on collapse capacity of structural systems.

3.4.6 Slab Effect

An important modeling issue is the effect of composite action in steel beams. Ricles et al. (2004) tested a series of deep beams to investigate the effect of a slab in a subassembly with RBS connections under symmetric loading histories (Figure 3.18). It is evident that the behavior of the subassembly is asymmetric in the two loading directions. Typically, due to composite action the component deteriorates much slower in the positive loading direction

when the concrete is in compression compared to the negative loading direction when beam bottom flange is in compression and can easily buckle in a lateral torsional mode. For the example illustrated in Figure 3.18 the plastic rotation capacity is about 3.5% versus 1.5% in the two loading directions.

The implication is that the backbone curve and cyclic deterioration rates in the two loading directions should be different if a composite slab is added to the beam. These differences are incorporated in the modified Ibarra-Krawinkler model to account for slab effect as discussed in Section 2.3.

For a composite beam of an exterior moment resisting frame (slab only on one side of the beam) the effect of slab on the rate of cyclic deterioration in the two loading directions may not be significant based on recent test series by Ricles et al. (2004). The same rate of cyclic deterioration is used for both directions in the example illustrated in Figure 3.18, which shows one of the calibrated Ricles et al. (2004) specimens included in the W-section database.

For composite beams part of an interior moment resisting frame, the effect of slab on the rate of cyclic deterioration becomes important as illustrated in Figure 3.19, which shows the results of two cyclic tests conducted recently in Japan as part of the E-Defense collapse testing program of a full scale 4 –story building. The calibrated moment-rotation diagrams presented in Figure 3.19 are for identical subassemblies, except that the specimen shown in Figure 3.19(b) has a composite beam.

For the tests in the W-section database the strength of a composite beam when the slab is in compression is typically 25% to 30% higher than the strength of the bare section as seen in Figure 3.19(b). For a composite beam with a gap between the slab and the column face the strength of the beam in the two loading directions is almost the same, as shown in a test series for beams with RBS conducted by Tremblay et al (1997). Figure 3.20 shows the

calibrated moment-rotation diagrams for two identical beams with RBS conducted by Tremblay et al. The test presented in Figure 3.20(b) includes a composite beam (same W-section with the one in Figure 3.20(a)), but with a gap between the slab and the column. The cyclic deterioration parameters in both loading directions are almost the same as seen from the figure. We should also mention that along the RBS region no shear studs have been provided in this specimen.

3.4.7 Residual Strength

Most steel elements whose hysteretic behavior deteriorates due to local instabilities, approach stabilization of the hysteretic response at large inelastic deformations. This stabilization occurs at a residual strength that is a fraction of the yield strength. In many of the test of the W-section database the loading program was terminated before the residual strength was attained, which means that relatively sparse data exists on residual strength. In some cases ductile fracture occurred before stabilization of hysteresis loops was observed or the test stopped before residual strength was attained (e.g., Figure 3.21(a)), and in most other cases the amount of residual strength was difficult to quantify (see Figure 3.21(b)). It is presumptuous to state that full stabilization occurs, but it is observed that the rate of deterioration becomes small enough to be neglected in analytical modeling. Based on an evaluation of the data sets of W-sections discussed in this chapter a residual strength ratio κ of about 40% for both sets (3) and (4) is suggested, but this value is considered only an estimate that is based on insufficient data. This value is based on data points plotted in Figure 3.22, in which κ is presented as a function of beam depth d for cases in which an estimate of residual strength could be made. Recall that κ is the ratio of residual strength (M_r) to effective yield strength (M_y). It should be noted that more experiments with very large deformation cycles are needed in order to assess residual strength with more confidence. Moreover, it is understood that residual strength cannot be maintained for extremely large deformation cycles. But for modeling purposes concerned with collapse of structures it is justified to assign some residual strength to steel beams, since the collapse

capacity of frame structures is attained when the plastic hinge rotations in beams are on the order of 6 to 10%.

3.4.8 Ductile Tearing

At very large inelastic rotations, cracks may develop in the steel base material at the apex of the most severe local buckle, and rapid crack propagation will then occur followed by ductile tearing and essentially complete loss of strength (see Ricles et al. 2004 for illustrations). The rotation associated with this rapid loss of strength is denoted as the ultimate rotation θ_u (experiments in which brittle fracture occurred are not part of this evaluation). This rotation depends on the loading history and may be extremely large for cases in which only a few very large cycles are executed (e.g., near-fault loading history). Estimates of θ_u are made here only for experiments with step-wise increasing cycles of the type required in the AISC seismic specifications (2005). For beams with RBS, an estimate of θ_u is 0.06 to 0.07 radians based on data from Ricles et al. (2004), Fry et al. (1997), and Engelhardt et al. (2000). For beams other-than-RBS an estimate of θ_u is 0.05 to 0.06 radians (Ricles et al. 2000, Kasai et al. 1996, Allen et al. 1996). Based on the case studies included in Chapter 8 and based on other analytical studies (Ibarra and Krawinkler, 2005, Zareian 2006) most structures collapse attain their collapse capacity around 6% to 10% maximum story drift ratio indicating that ductile tearing will not be critical in most of the cases.

For monotonic loading such as that experienced under near-fault ground motions or in case that a structure is drifting in one direction to collapse θ_u is significantly larger. In the component testing program for the scale model connections discussed in Chapter 6 for various loading histories we observed ductile tearing at 0.37 rad. based on component histories obtained from the Buffalo shaking table tests compared to 0.07 rad. under symmetric loading protocol.

3.4.9 *W-Columns*

Columns are susceptible to local and lateral torsional buckling of the type documented for beams, except that the susceptibility to lateral torsional buckling likely is higher than for beams because: (1) the column boundary conditions at the top of a story are often ambiguous and depend on local detailing; (2) the moment diagram in the inelastic range may be far from that indicated by elastic analysis and may cause single curvature bending between adjacent floors (Gupta and Krawinkler, 1999, Medina and Krawinkler, 2003); and (3) the presence of axial load effects. This may not be a major issue for heavy W14 columns, but deserves much consideration for deep column sections, particularly those with large r_x/r_y and d/t_w ratios (FEMA (2000-c)).

Newell and Uang (2006) tested a series of shallow and heavy W14 sections under the presence of axial loads showing that these types of columns have a large θ_p , given that d , L_b/r_y , $b_f/2t_f$, and d/t_w are relatively low. Figure 3.23 shows the deduced moment rotation diagram of one of the tests conducted by Newell and Uang (2006).

None of the tests found in the literature utilizes deep column sections in which plastic hinging occurs in the column. Based on tests of beams with RBS that are part of exterior subassemblies with deep columns (W27) (but without axial load and no variation of column moment gradient) Uang et al (2000b) concluded that for small column r_x/r_y and d/t_w ratios the RBS region may cause twisting of the column.

3.5 Evaluation of Steel Hollow Square Column Section Database

Most low and mid-rise buildings built in Japan have steel moment resisting frames with tubular columns. Examples are the 4-story building tested recently at E-Defense in Miki, Japan, and the 15-story frame designed by Kajima Corporations. Seismic performance of

both structures is discussed in Chapter 8 of this study. To support collapse assessment of steel moment frames with tubular columns, a separate database of steel hollow square sections (HSS) has been developed. A total of 113 monotonic and cyclic tests have been collected, based on experimental research that has been conducted by Japanese researchers [Tsuda and Matsui (1998), Tsuji and Nakatsura (1996), Kurata et al. (2005), Kawaguchi and Morino (2001), Yamanaka and Yamada (1984), and Sugiyama and Igarashi (1986)]. Hajjar et al. (1996), Hajjar (2000), and Tort and Hajjar (2004) developed a database of rectangular concrete – filled steel tubes (CFT) for performance – based design and evaluation of distributed and concentrated plasticity analytical models for cyclic analysis of CFT columns [Hajjar et al. (1997a, 1997b), Hajjar et al. (1998)].

Since tubular sections are used primarily for columns, the variation of the applied axial force (expressed by the ratio of applied axial force N over yield axial force N_y) becomes an important parameter. For instance, Kouchi and Yamada (1984) conducted a test series in which this ratio was varied from zero to 0.60. The tubular section database contains moment-rotation relationships in which the P-delta effect, which depends on the test configuration, is accounted for explicitly by taking into account a second order moment. Since there are a large number of monotonic tests in the steel tubular section database, the following two sets of data are considered in the calibrations utilizing the modified Ibarra-Krawinkler deterioration model:

1. All experimental data on tubes
2. All experimental data on tubes tested monotonically

Similarly to the W-sections database a straight line is included in the plots based on linear regression analysis in all the scatter plots showing dependences of deterioration modeling parameters on D/t (D , t are the depth and thickness of the hollow square section, respectively) and N/N_y . This line serves only to illustrate trends for deterioration modeling

parameters. The combined effect of D/t and N/N_y on model parameters is treated separately in Chapter 4 with the use of multivariate regression analysis.

3.5.1 Trends for Deterioration Modeling Parameters

3.5.1.1 Plastic Rotation Capacity θ_p

For both data sets both D/t and N/N_y have a strong effect on the plastic rotation capacity of a tubular column. Figure 3.24 shows the trends for plastic rotation capacity θ_p with respect to D/t and N/N_y for the full data set (Figure 3.24(a)) and the monotonic data set only (Figure 3.24(b)). In the range of $D/t=20$ to 33 θ_p the data set exhibits large scatter primarily due to variations or axial load.

After separating the monotonic tests from the full set of data (see Figure 3.24(b)) the sensitivity of θ_p to D/t and N/N_y is almost the same as for the full data set. The trends based straight line for both data sets are almost the same indicating (almost the same coefficient of determination R^2) that the predicted capping point of the backbone curve for all the cyclic tests included in the database may be close to the capping point of a monotonic test of the same specimens.

3.5.1.2 Post Capping Plastic Rotation Capacity θ_{pc}

Figure 3.25 illustrates the effect of D/t and N/N_y on the post capping plastic rotation capacity θ_{pc} for the full data set (Figure 3.25(a)) and the monotonic data set only (Figure 3.25(b)). From these figures it can be confirmed that column sections with relatively small D/t ratio ($D/t \geq 40$) or high axial load ratio ($N/N_y \geq 0.3$) degrade relatively fast (if N/N_y and D/t ratios are treated as independent random variables) As seen from Figures 3.25(a) and 3.25(b) the tendencies for θ_{pc} slightly differ when the monotonic tests are isolated from the total data points primarily due to the fact that for the cyclic tests the values of θ_{pc} are based

on judgment. For the monotonic data set most of the specimens are pushed far enough, i.e. θ_{pc} is reached, as seen from Figure 3.26 on two examples from monotonic tests conducted by Sugiyama and Igarashi, (1986).

3.5.1.3 Rate of Cyclic Deterioration A

Figure 3.27 shows the dependence of A on D/t and N/N_y ratios. The rate of cyclic deterioration may increase rapidly for a small increase of D/t ratio. With one exception the D/t ratio in these plots is less than 40 because cyclic tests with larger D/t values could not be found. Similar trends are observed from the same figure regarding the effect of N/N_y on A . No cyclic tests could be found in the data set with axial load ratios larger than 0.5.

3.5.2 Residual Strength

For a number of specimens included in the tubular section database the rate of deterioration becomes small enough at large cycles to be neglected in analytical modeling, i.e. a residual strength is reached. Figure 3.28 shows that the dependence of the residual strength ratio κ on D/t and N/N_y for the test specimens in which it was possible to observe residual strength. Based on the presented data an estimate for the residual strength ratio $\kappa = 0.25$ appears to be reasonable since there is not much data available that shows clearly that stabilization occurred.

3.5.3 Statistical Evaluation of Deterioration Modeling Parameters

Statistical information on deterioration model parameters for tubular column sections is presented with the use of cumulative distribution functions (CDFs). Figure 3.29 shows the CDFs for θ_p , θ_{pc} and A for the entire data set. A lognormal distribution was assumed to fit the calibrated values of modeling parameters. A K-S test was conducted and the hypothesis testing showed that the assumed distribution is representative. The standard deviation (β) of

the logarithmic data is also shown in the figures. The standard deviation is relatively large in all cases because of the strong dependence of the modeling parameters on D/t and N/N_y . Note that in Figures 3.29(a) and 3.29(b) the CDFs of θ_p and θ_{pc} based on monotonic tests only have been superimposed for comparison purposes. As seen from the figures the mean and β values of the monotonic data are very similar to the ones of the entire set of data indicating that the calibrated modeling parameters based on cyclic tests are not far from those of monotonic tests. In support of reliability studies Table 3.9 summarizes the correlation coefficients between modeling parameters for tubular steel columns based on the total data set available. Table 3.10 summarizes the correlation coefficients between θ_p and θ_{pc} based on monotonic tests only. As seen from the two tables the correlation coefficients between θ_p and θ_{pc} are approximately the same for all data and the monotonic data.

3.6 Evaluation of Reinforced Concrete Database

In support of collapse assessment of concrete structures a concrete database of beams and columns with relatively low axial load ratio ($P/P_y \leq 0.15$) was developed. As described earlier in this chapter the database contains 200 specimens. Only specimens in which the beams fail in flexure are included in the data set. Many of the specimens in the database were not tested to sufficiently large deformations to permit a clear determination of the capping point and of post-capping behavior. The same observation has been made by Haselton et al (2006), who calibrated RC plastic hinge deterioration models from a database of columns assembled by Berry et al. (2004). For the calibration of the moment-rotation diagrams of the RC components included in the database the peak-oriented model following the rules of the modified Ibarra-Krawinkler deterioration model is used. The exponent c , which controls the rate of cyclic deterioration for both loading cycles, was set to be 1.0. For the sake of simplicity all four modes of cyclic deterioration were assumed to have the same A value. Exceptions are cases in which the unloading stiffness deteriorated at a clearly

different rate, in which case a different rate of cyclic deterioration was used for this specific mode only.

3.6.1 Quantification of Modeling Parameters for Identical Specimens

One of the main problems for deterioration modeling is the lack of experimental data to uniquely identify the backbone curve from a monotonic test and then tune the cyclic deterioration parameters to cyclic test data. Most valuable in this regard are test series in which nominally identical specimens (it must be recognized that no two test specimens are identical) are subjected to different loading histories, including monotonic loading. Only two such test series have been found in the literature; one documented in the Kawashima database (six specimens by Kawashima et al. (2003)) and the other consisting of 12 “identical” specimens reported in Liddell et al. (2000).

Independent calibration was carried out for each of the Liddell tests, as if the results were obtained for different specimens. The modeling parameters obtained from the independent calibrations are comparable (with one exception) but far from identical. The coefficient of variation (COV) in effective stiffness is 0.26, and the COV in the cyclic deterioration parameter A (assuming that the same parameter applies to all deterioration modes) is 0.36. A second calibration was performed in order to evaluate the validity of the deterioration model, using the average of cyclic deterioration parameters obtained from all the tests and backbone curve values obtained from the monotonic loading test (see Figure 3.3).

Figure 3.30 and Figure 3.31 illustrate comparisons between the first and second calibration for two different loading histories. The observation that the results are comparable supports the concept of using a single set of model parameters for the same component regardless of loading history.

The independent calibration of one of the tests of the Liddell test series (Test #6) did result in modeling parameters that were very different from the others. This caused much concern

until it was discovered from careful reading of the Liddell report that there was a fabrication error during welding of steel studs to the longitudinal reinforcement, which strongly affected the material properties of the bar next to the instrumentation stud. Thus, the results of this test were discarded. The lesson to be learned is that no reliance can be placed into a single test results, and that human error have a clear effect on behavior, even in laboratory specimens. The fact that a single test cannot provide the information for generalization of test results to random loading histories was pointed out already in Krawinkler et al. (1983), after conducting an experimental study of steel component performance, considering deterioration and failure modes of local buckling in beam flanges and of crack propagation at weldments.

3.6.2 Trends for Deterioration Modeling Parameters

Previous work from Fardis and Biskinis (2003), Haselton and Deierlein (2006) on RC columns was used to identify the most important material, reinforcement, and detailing parameters on which deterioration modeling parameters for beams depend. Some of the parameters are listed below together with a series of plots emphasizing the trends for deterioration modeling parameters of RC beams. The number of specimens in the RC-database in which a clear post-capping slope is observed is small since in most of the tests the specimen was not pushed to large enough deformations for post-capping behavior to be clearly observed. This makes it difficult to accurately predict the post capping slope of an RC component. Haselton and Deierlein (2006) point out the same issue after evaluating a RC column database of 220 specimens. At this point information only on trends for θ_p and A of RC beams is included in this section.

A linear regression line is added in the plots together with the coefficient of determination R^2 to aid in the visualization of trends of the modeling parameters versus material and reinforcement/detailing parameters.

Bond-slip indicator variable (a_{sl}): Fardis and Biskinis (2003) showed that bond-slip is responsible for approximately one-third of the ultimate deformation. They used an indicator variable to distinguish between tests where slip is ($a_{sl} = 1$) or is not ($a_{sl} = 0$) possible. Haselton and Deierlein (2006) used the same term as Fardis and Biskinis to include bond-slip in their regression equations. In this research the same expression for a_{sl} is used as the previous studies. Bond-slip primarily depends on the longitudinal reinforcement anchorage and boundary conditions. Based on the concrete database notation six different cases have been identified given the longitudinal reinforcement anchorage. Zero bond slip is assumed only if the longitudinal reinforcement is anchored by welding the bars into a metal plate. A more systematic approach is needed though to evaluate the effect of bond slip on the model parameters, in which the deformation due to bond slip is quantified by subtracting the deformations due to flexure and shear from the total deformation of the RC component.

Concrete strength (f'_c): Fardis and Biskinis (2003) used a concrete strength term that causes the predicted deformation capacity to increase with an increase in concrete strength (Panagiotakos and Fardis, 2001). Haselton and Deierlein (2006), after their regression analysis using the PEER concrete database (Berry et al. 2004), revealed the opposite trend and proposed an equation that predicts a decrease in deformation capacity with an increase in concrete strength. Figures 3.32(a) and 3.32(b), in which θ_p , and Δ are plotted versus f'_c , indicate that the parameters of the modified Ibarra-Krawinkler model follow the trends pointed out in work by Haselton. But the trends are weak, and it is concluded that the modeling parameters are not very sensitive to the concrete compressive f'_c (the database does not include specimens made of high strength concrete).

Confinement effectiveness factor $\rho_{sh,eff}$: and Fardis and Biskinis (2003). used a term for confinement effectiveness, $\rho_{sh,eff} = \rho_{sh} f_{y,sh} / f'_c$ where $\rho_{sh} = A_{sh} / s.b$ is the area ratio of transverse reinforcement in the hinge region (A_{sh} is the bar area, s is the bar spacing, and b is the section width). Haselton and Deierlein found this term to be a statistically slightly more significant predictor than the transverse reinforcement ratio, but they decided to use

ρ_{sh} for lateral confinement in the interest of simplicity. Figure 3.33 illustrate the dependence of θ_p , and λ on $\rho_{sh,eff}$, which was found to be statistically more significant predictor than the transverse reinforcement ratio for all the deterioration parameters. The trends for θ_p and λ of $\rho_{sh,eff}$ are similar to the work by Haselton et al. for the same parameters and they indicate that in a better confined member shear deformations are of less importance, which is reflected in larger plastic rotation capacity and less strength deterioration.

Rebar buckling term: Dhakal and Maekawa (2002) investigated the post-yield buckling behavior of bare reinforcing bars using a term $s_n = (s / d_{b,l}) \sqrt{(F_y / 100)}$, in which s is the stirrup spacing, $d_{b,l}$ is the longitudinal rebar diameter and F_y is the reinforcing bar strength of the rebar in MPa units. In the work by Haselton and Deierlein it was pointed out that the s_n coefficient is a better predictor of element plastic rotation capacity θ_p than simple stirrup spacing. Figure 3.34(a) shows the dependence of θ_p of RC beams on s_n indicating that the larger the rebar buckling term the smaller the θ_p . Figure 3.34(b) shows the trends of λ with respect to s_n based on the available data set from the RC beams database. Based on the statistical evaluation of the data s_n is a slightly better indicator for θ_p than $s/d_{b,l}$ as seen from the R^2 values presented in Figures 3.34(a) and 3.34(c).

Normalized shear demand V_p/V_n : this parameter is defined as the ratio of the shear demand V_p , defined as bending strength divided by shear span, over the expected shear strength V_n of the member as defined in ACI-318-05 code requirements. Figure 3.35 illustrates the effect of V_p/V_n on various modeling parameters. The plots indicate that this ratio primarily affects the rate of cyclic deterioration λ . This observation agrees with the work by Haselton et al.

The axial load ratio ν , which is an important variable for column behavior and has been incorporated by Fardis et al. and Haselton and Deierlein (2006) is not considered in this work since in our RC database the emphasis is on experimental data for RC beams; hence

in most of the cases ν is zero. For the column specimens that are included in the RC database the axial load ratio was intentionally kept below 0.15.

The shear span ratio L_s/h is notably absent from any trend plots. The statistical evaluation of the data consistently showed L_s/h to be statistically insignificant. The relative unimportance of this predictor indicates that a rotation capacity concept based on curvature integration is not well-supported by this data set. Haselton et al. (2006) reached the same conclusion after evaluating 223 column specimens. This finding differs from the conclusions drawn by Panagiotakos and Fardis (2001), which are based on the evaluation of a database of more than 1000 specimens.

3.6.3 Statistical Evaluation of Deterioration Modeling Parameters

Similarly to W-section and steel tubular section databases it is valuable for reliability studies to present the deterioration modeling parameters by means of CDFs. Figure 3.36 shows the CDFs of θ_p and λ of the RC beams included in this data set, assuming a lognormal distribution for each of the deterioration parameters based on a K-S test. The dispersion for λ is very large, which in part is due to the variety of specimens contained in the database but in part is due also to the extensive use of judgment in quantifying these deterioration parameters.

3.7 Summary and Conclusions

In this chapter the development of 3 databases of the hysteretic behavior of steel components (W-sections and square tubular columns) and reinforced concrete beams is discussed. The three databases contain data in the following three categories: (1) metadata, (2) reported results and (3) deduced data, and serve as the basis for validation and improvement of analytical models that explicitly account for deterioration in strength and

stiffness. An interactive software named Calibrator was developed in order to facilitate the calibration process for force-deformation relationships of structural components included in the databases.. The Calibrator is a pre-processor that provides an interface between information stored in the database, i.e. moment rotation relationships, and an SDOF inelastic analysis program that computes hysteretic response based on the modified Ibarra-Krawinkler model.

Based on an evaluation of steel W-sections database we provide:

1. Statistical information (mean, standard deviation and correlation coefficients) for material properties of the main types of structural steel in United States, A36, A572 Grade 50 and A992 Grade 50.
2. Statistical information (mean and standard deviation) of the ratio of effective to nominal yield bending strength of steel beams, which is an “average” measure of cyclic hardening.
3. Statistical information on post yield hardening, defined by the ratio of capping strength over the effective yield strength of the component. From the evaluation it is concluded that the M_c/M_y ratio, together with the quantity $\theta_c - \theta_y$, is a more stable parameter to describe the post yield hardening stiffness than the “traditional” strain hardening ratio.
4. Trends for modeling parameters, after categorizing the connections into beams other-than-RBS and RBS sections. Based on the observed trends, and treating each geometric parameter of the component as an independent variable, it is concluded:
 - a. The apparent strong dependence of θ_p on the beam depth d is primarily driven by the incorporation of small sections for beams other than RBS in the database. For W21 sections and larger the dependence of θ_p on the beam depth d still exists but is not very strong for beams other than RBS. For beams with RBS the effect of d on θ_p is more significant compared to beams other than RBS possibly because of the flange reduction in the RBS region.

- b. Similarly, for the range W21 to W36, θ_p is only weakly dependent on the span to depth ratio L/d because most deep beams are susceptible to a predominance of web buckling and lateral torsional buckling, which occur earlier in regions of small moment gradient.
 - c. Decreasing the lateral torsional buckling slenderness ratio L_b/r_y is not as effective as expected in increasing θ_p , provided that seismic design criteria for compactness and lateral bracing are satisfied. The L_b/r_y ratio has a larger effect on the rate of cyclic deterioration Λ and θ_{pc} since lateral torsional buckling is a phenomenon that occurs later in the loading history and it is triggered by local instabilities.
 - d. For the four data sets used in this research the most important geometric parameter for deterioration modeling is the beam depth to web thickness ratio h/t_w . A large h/t_w ratio renders the beam section more susceptible to twisting. Particularly for data sets with $d \geq 21$ " the effect of h/t_w on θ_{pc} and Λ is of almost equal importance with the one of $b/2t_f$ ratio possibly due to the fact that flange local buckling triggers web local buckling, which in turn triggers lateral torsional buckling that occurs later in the loading history.
5. Cumulative distribution functions (CDFs) for θ_p , θ_{pc} and Λ have been developed. A lognormal distribution can be used to describe each of the modeling parameters as random variables. Given the distribution, correlation coefficients between model parameters are determined based on experimental evidence. The value of these correlation coefficients is important for studies related to quantification of modeling uncertainties and their effect on the collapse capacity of a structural system.
 6. Based on evaluation of composite beams with RBS it is shown that for beams that belong to an exterior moment resisting frame the slab does not really affect the rate of cyclic deterioration but greatly affects the plastic rotation capacity in the two loading directions. This observation does not hold true in the case of a composite beam of an interior moment resisting frame. The compression side (slab in compression) may have a strength about 30% larger compared to the bare steel

section and the rate of cyclic deterioration becomes much slower in the positive loading direction (slab in compression) compared to the negative one.

7. The residual strength ratio κ is in the order of 40% for beams with RBS and beams other-than-RBS. This value should be used with caution since there are not many tests available that have reached full stabilization.
8. For beams other-than-RBS an estimate of ultimate deformation capacity θ_u (rotation at which ductile tearing was observed) is between 0.05 to 0.06 rad. and for sections with RBS θ_u is 0.06 to 0.07 rad. These observations are based on symmetric cyclic loading. For monotonic loading such as that experienced under near-fault ground motions or in case a structure is drifting in one direction to collapse, θ_u is significantly larger.
9. Based on information on a few heavy W14 columns included in the W-section steel database it does not seem that susceptibility of these columns to lateral torsional buckling is large. Caution is needed when deep column sections are used since for widely used beam connection such as RBS with large r_x/r_y and h/t_w ratios twisting of the columns has been reported.

The following observations and conclusions are based on the evaluation of the steel column hollow square section database:

1. All deterioration modeling parameters strongly depend on the axial load ratio N/N_y and the depth to thickness D/t ratio of the column section.
2. After evaluating separately a large number of monotonic tests included in the database it is concluded that the estimated values of θ_{pc} from the cyclic tests are close to those obtained from monotonic tests since the dependence of θ_{pc} of the monotonic tests on N/N_y and D/t ratio is almost the same as the dependence of θ_{pc} from the total data set after comparing the coefficients of determination for the two data sets.

3. Based on the CDFs for modeling parameters for steel column square tubes the median θ_p is on the order of 0.01 rad. The logarithmic standard deviations of the CDFs are large because of the large sensitivity of modeling parameters to N/N_y and D/t ratios.
4. A residual strength ratio κ of 0.25 is a reasonable value for experiments for which stabilization was observed. But similarly to the W-sections database this value is only an estimate since full stabilization did not occur in most of the cases.

After evaluating the reinforced concrete database, which mostly consists of beams and few columns with relatively low axial load ratio ($P/P_y < 0.15$) that fail in flexure, the following observations are made:

1. Independent calibrations of two test series in which nominally identical specimens were subjected to different loading histories, including monotonic loading, and calibrations of cyclic tests using average values for the deterioration modeling parameters, indicate that the concept of using a unique set of model parameters for a component regardless of loading history is justified.
2. The shear span ratio L_s/h is notably absent from any trend plots. The relative unimportance of this predictor indicates that a rotation capacity concept based on curvature integration is not well-supported by this data set.
3. The rebar buckling coefficient s_n is an important parameter for θ_p and λ of RC beams
4. Based on a statistical evaluation of deterioration parameters of RC beams included in the RC database developed in this research the mean values of θ_p , and λ , using a lognormal distribution, are 0.05rad, and 1.0, respectively. Due to large scatter in the data set the values of standard deviations of the log of the same parameters are 0.42rad, and 0.77. In part the large scatter is related to the fact that most of the tests were not pushed to large enough deformations for capping and post-capping behavior to be clearly observed.

Table 3.1. Statistics of material yield strength from flange coupon tests

Material Specification	Mean F_y (ksi)	σ_{F_y} (ksi)	Mean F_u (ksi)	σ_{F_u} (ksi)	ρ_{F_y, F_u}
A36	45.0	5.2	66.1	4.3	0.851
A572 Gr.50	52.7	5.0	71.4	5.3	0.778
A992	55.1	5.6	74.5	4.6	0.784

Table 3.2. Statistics of material yield strength from web coupon tests

Material Specification	Mean F_y (ksi)	σ_{F_y} (ksi)	Mean F_u (ksi)	σ_{F_u} (ksi)	ρ_{F_y, F_u}
A36	50.3	6.4	68.3	4.6	0.735
A572 Gr.50	54.8	5.9	72.9	5.9	0.761
A992	54.7	3.3	74.9	4.2	0.902

Table 3.3. Statistics of ratios of effective to predicted component yield strength and capping strength to effective yield strength (steel data, W-sections)

Connection Type (no Slab)	Mean of M_c/M_y	σ_{M_c/M_y}	Mean of $M_y/M_{y,p}$	$\sigma_{M_y/M_{y,p}}$
RBS	1.09	0.03	1.06	0.12
Other than RBS	1.11	0.05	1.17	0.21

Table 3.4. Median and standard deviation of modeling parameters for all the data subsets of the W-section database

Connection Type (no Slab)	Median θ_p (rad)	σ_{θ_p} (rad)	Median θ_{pc} (rad)	$\sigma_{\theta_{pc}}$ (rad)	Median λ	σ_λ
Other than RBS	0.025	0.43	0.16	0.41	1.00	0.43
RBS	0.025	0.33	0.23	0.32	1.15	0.34
Other than RBS ($d \geq 21''$)	0.020	0.31	0.15	0.35	0.88	0.41
RBS ($d \geq 21''$)	0.025	0.29	0.21	0.30	1.00	0.34

Table 3.5. Correlation coefficients between modeling parameters (full data set, other-than-RBS)

	θ_p	θ_{pc}	\mathcal{A}
θ_p	1.00	0.69	0.44
θ_{pc}	0.69	1.00	0.67
\mathcal{A}	0.44	0.67	1.00

Table 3.6. Correlation coefficients between modeling parameters (full data set, RBS)

	θ_p	θ_{pc}	\mathcal{A}
θ_p	1.00	0.69	0.64
θ_{pc}	0.69	1.00	0.64
\mathcal{A}	0.64	0.64	1.00

Table 3.7. Correlation coefficients between modeling parameters (other-than-RBS, $d \geq 21''$)

	θ_p	θ_{pc}	\mathcal{A}
θ_p	1.00	0.60	0.56
θ_{pc}	0.60	1.00	0.58
\mathcal{A}	0.56	0.58	1.00

Table 3.8. Correlation coefficients between modeling parameters (RBS, $d \geq 21''$)

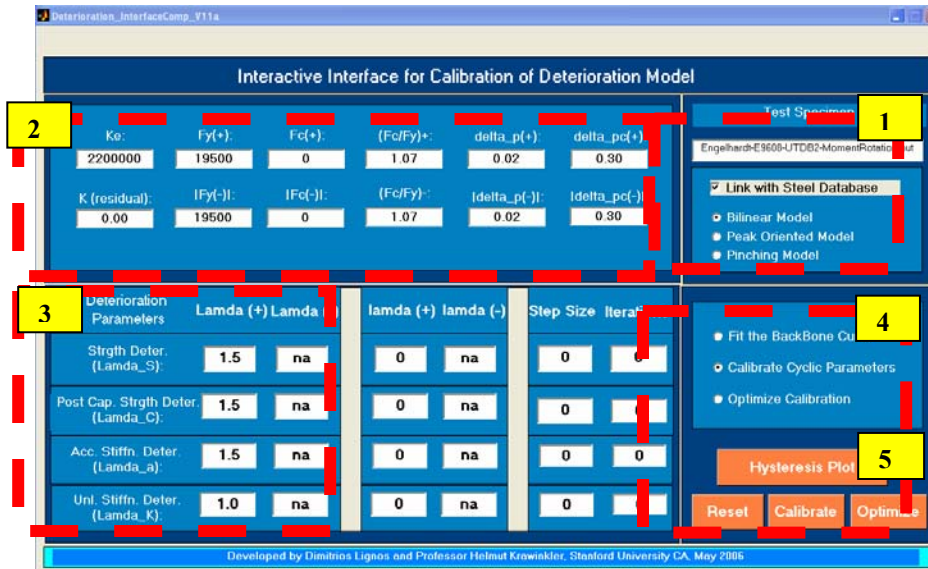
	θ_p	θ_{pc}	\mathcal{A}
θ_p	1.00	0.54	0.65
θ_{pc}	0.54	1.00	0.63
\mathcal{A}	0.65	0.63	1.00

Table 3.9. Correlation coefficients between modeling parameters (tubular columns)

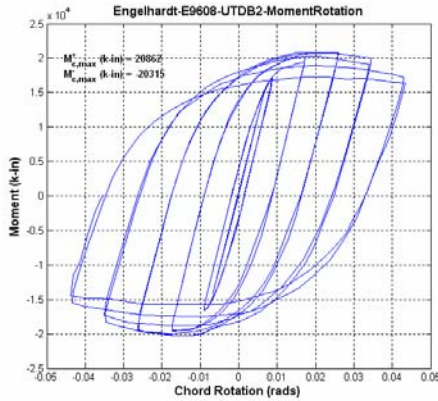
	θ_p	θ_{pc}	A
θ_p	1.00	0.74	0.80
θ_{pc}	0.74	1.00	0.85
A	0.80	0.85	1.00

Table 3.10. Correlation coefficients between modeling parameters (tubular columns, monotonic data only)

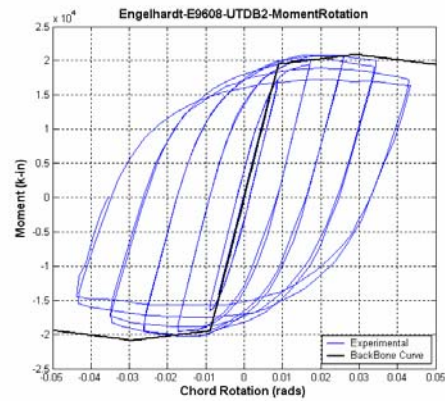
	θ_p	θ_{pc}
θ_p	1.00	0.71
θ_{pc}	0.71	1.00



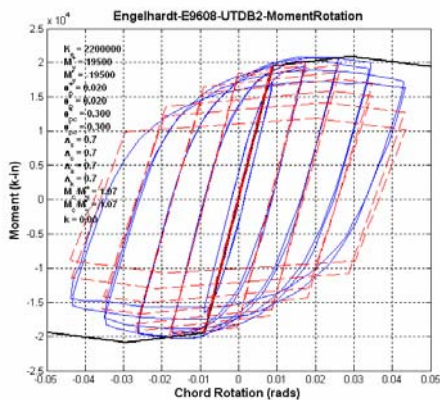
(a) Calibrator interface



(b) Experimental M-θ relationship from database



(c) Visualization of match of backbone curve



(d) Visualization of match of hysteretic response; left = inadequate match, right = adequate match

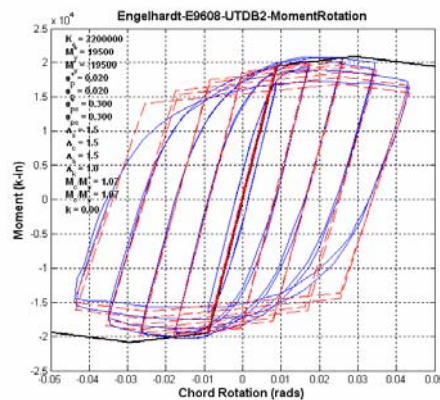


Figure 3.1. Use of Calibrator for matching experimental and predicted response

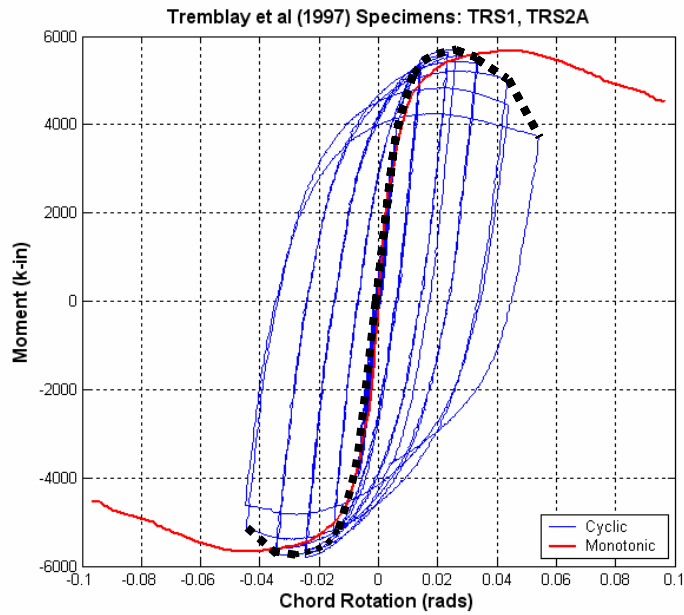


Figure 3.2. Monotonic and cyclic responses of identical specimens, and skeleton curve fit to cyclic response (data from Tremblay et al. 1997)

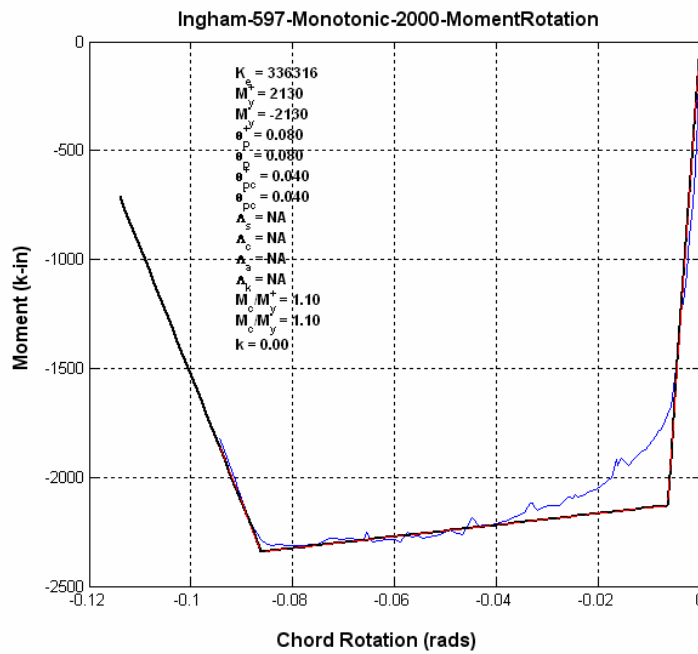
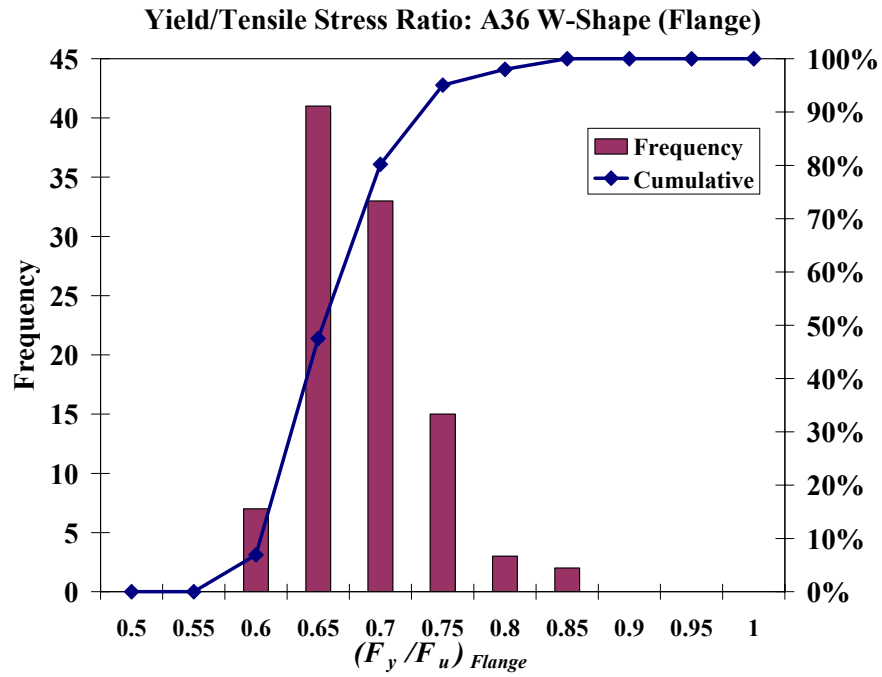
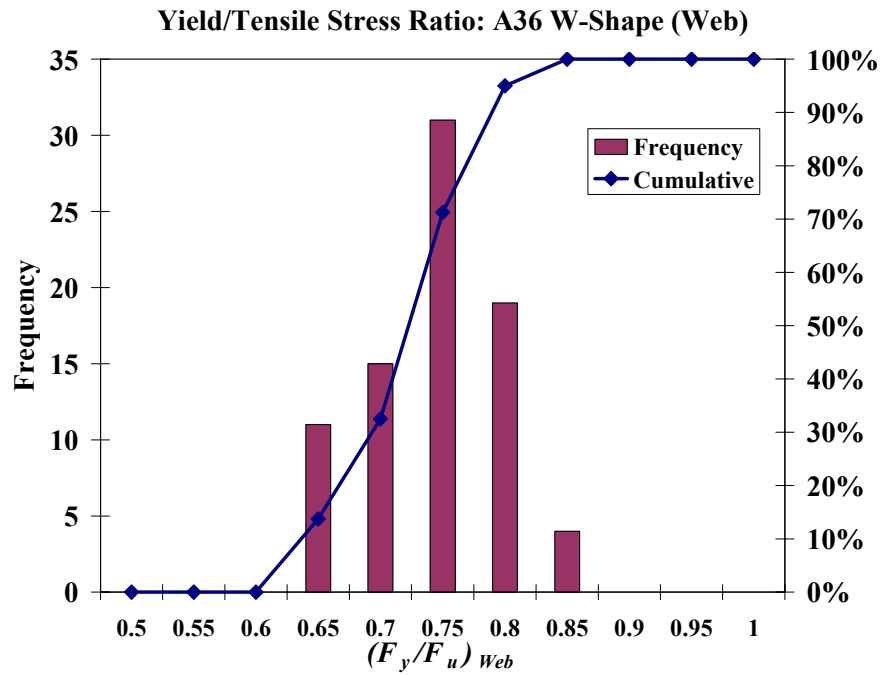


Figure 3.3. Calibration of monotonic test reported in Liddell et al. (2000)

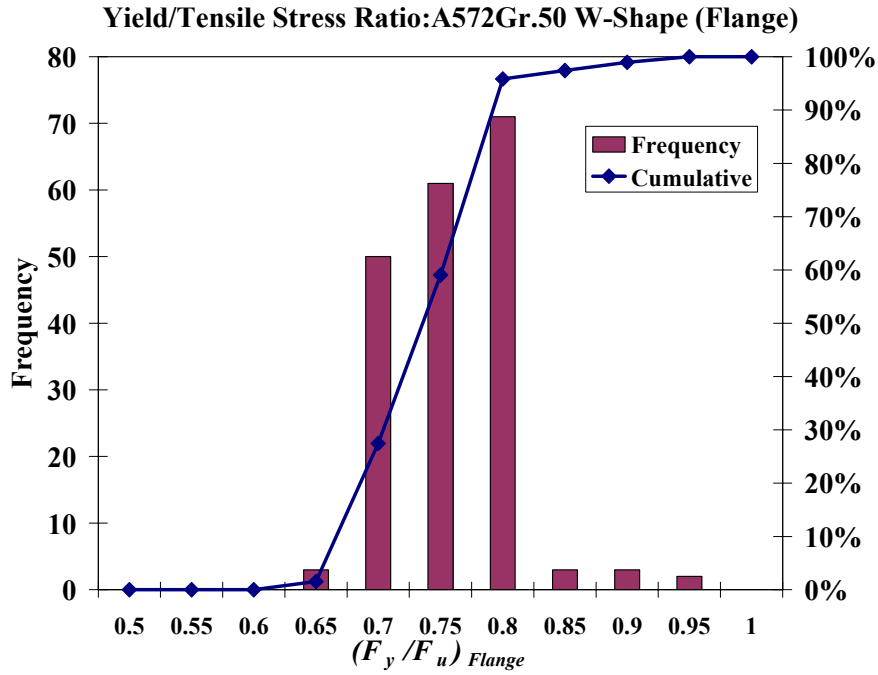


(a)

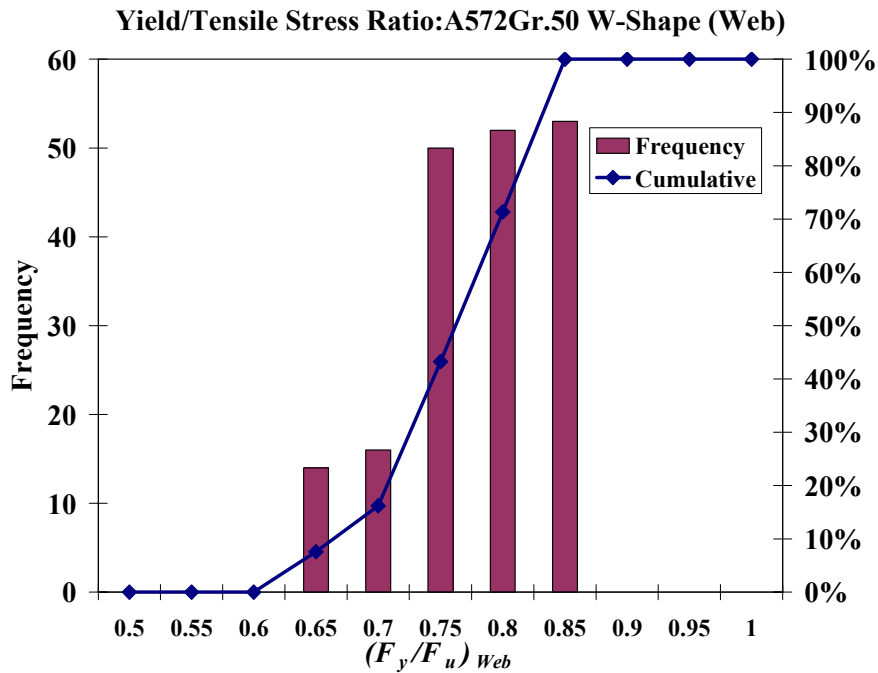


(b)

Figure 3.4. Yield to tensile strength histogram for A36 steel (a) taken from flange, (b) taken from web (W-sections database)

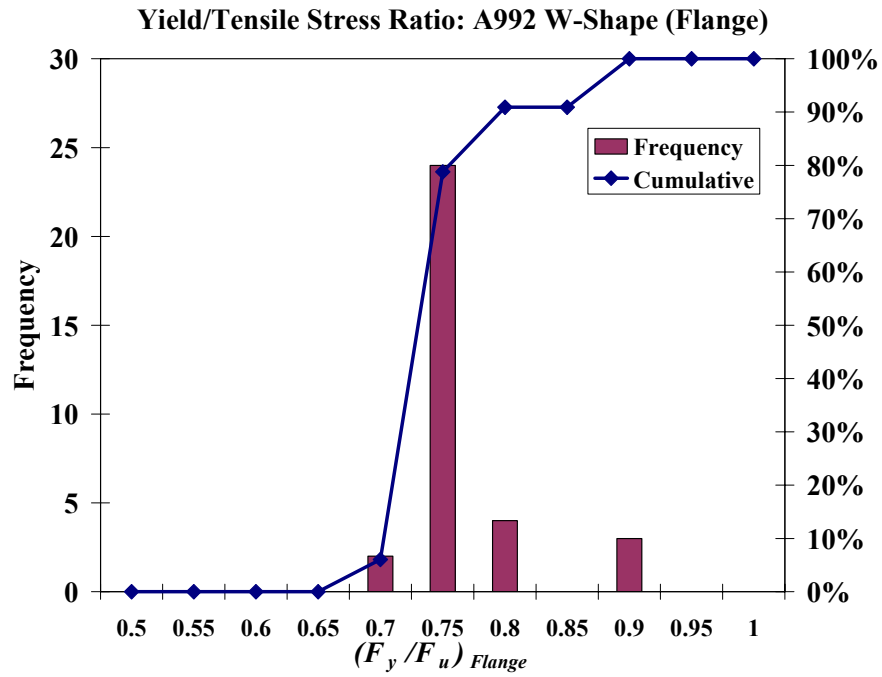


(a)

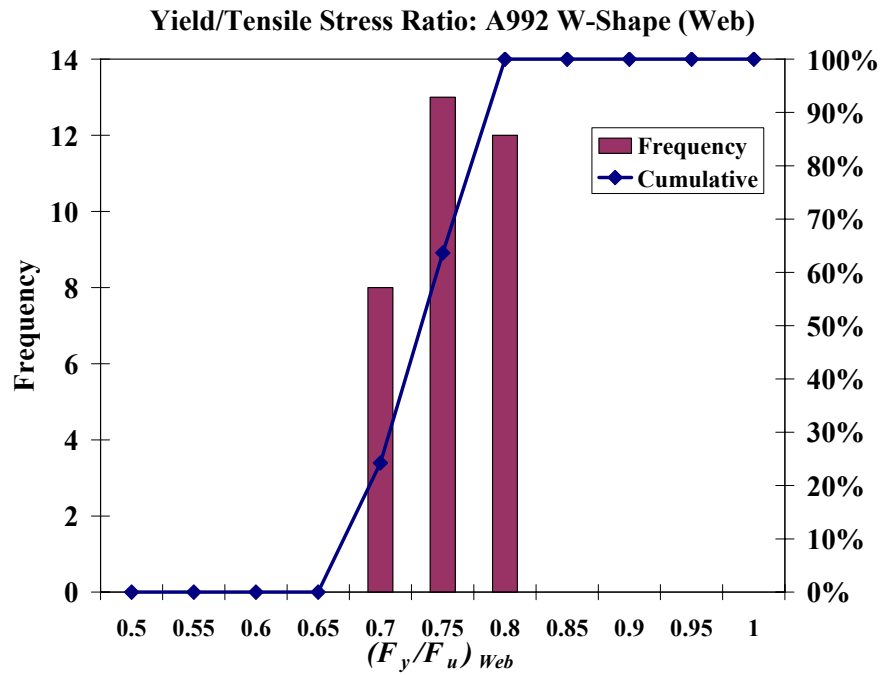


(b)

Figure 3.5. Yield to tensile strength histogram for A572Gr.50 steel (a) taken from flange, (b) taken from web (W-sections database)

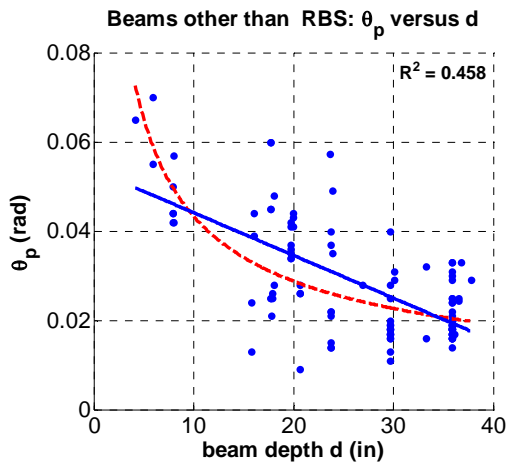


(a)

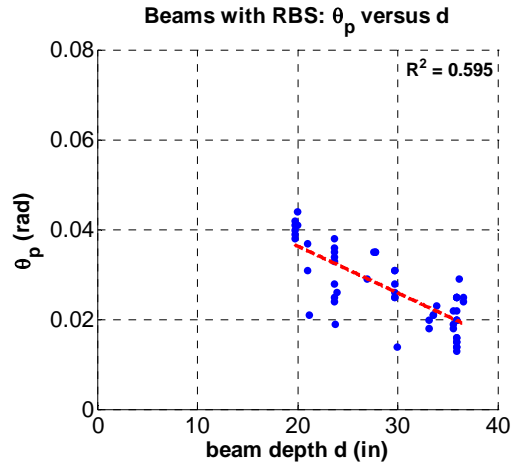


(b)

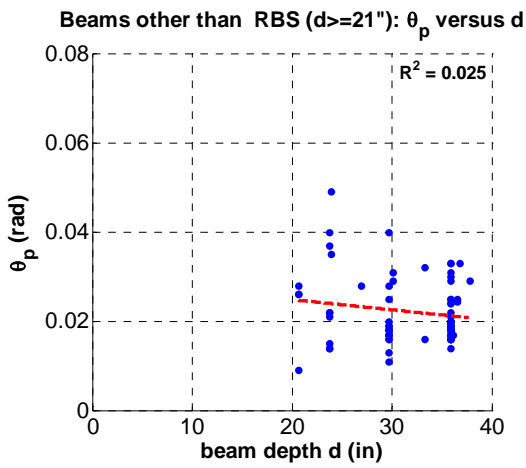
Figure 3.6. Yield to tensile strength histogram for A992 Gr.50 steel (a) taken from flange, (b) taken from web (W-sections database)



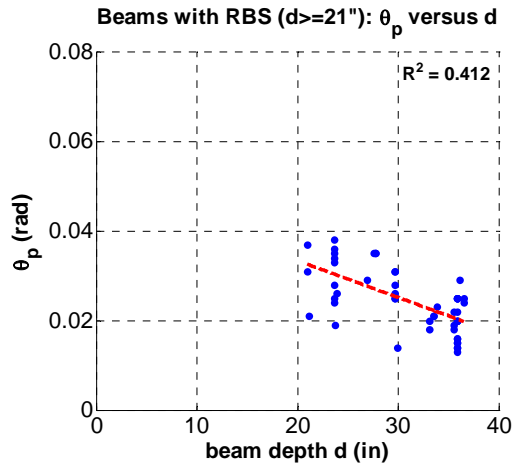
(a) full data set (1)



(b) full data set (2)



(c) data set (3)



(d) data set (4)

Figure 3.7. Dependence of θ_p on beam depth d for various data sets (W-sections database)

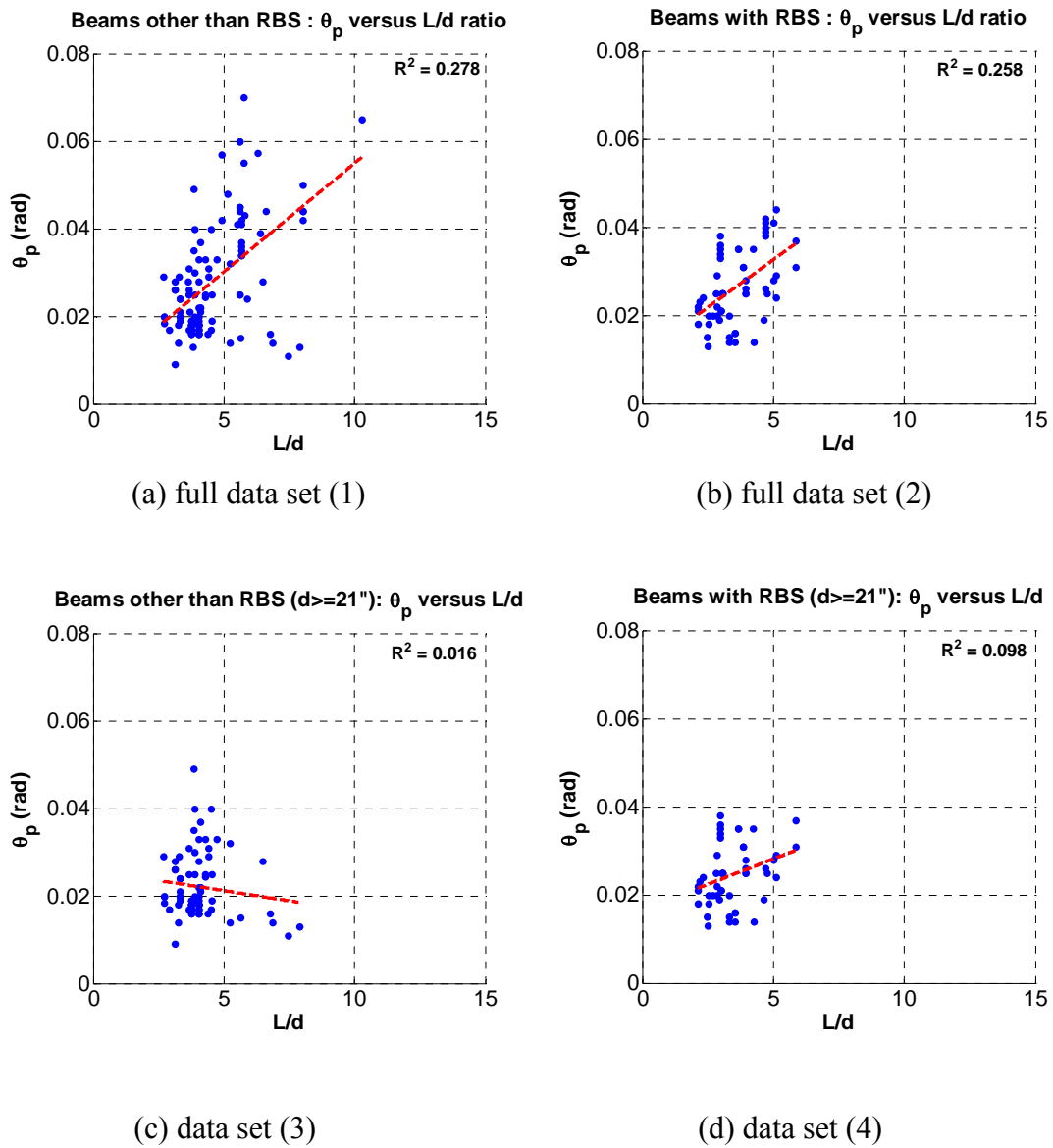


Figure 3.8. Dependence of θ_p on beam span to depth ratio L/d of various data sets (W-sections database)

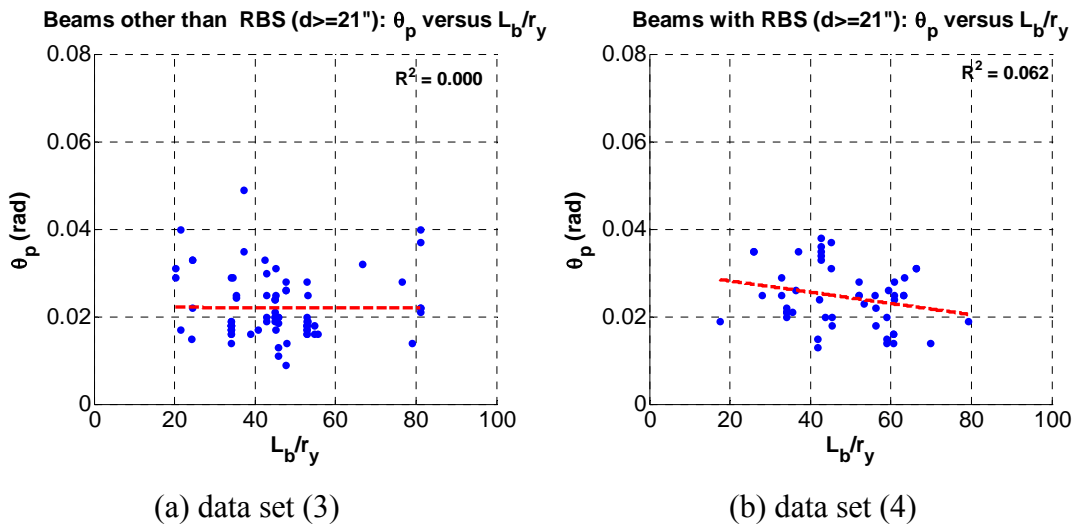


Figure 3.9. Dependence of θ_p on L_b/r_y ratio for data sets with $d \geq 21$ (W-sections database)

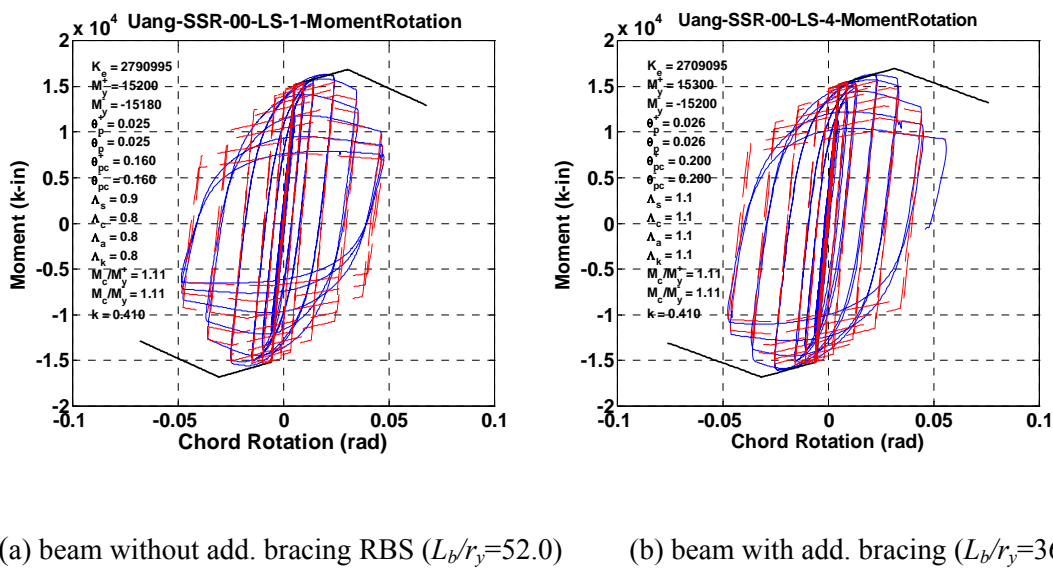


Figure 3.10. Calibrated moment rotation diagrams for a beam with RBS; (a) no additional bracing provided, (b) additional bracing near the RBS region (data from Uang et al. 2000a)

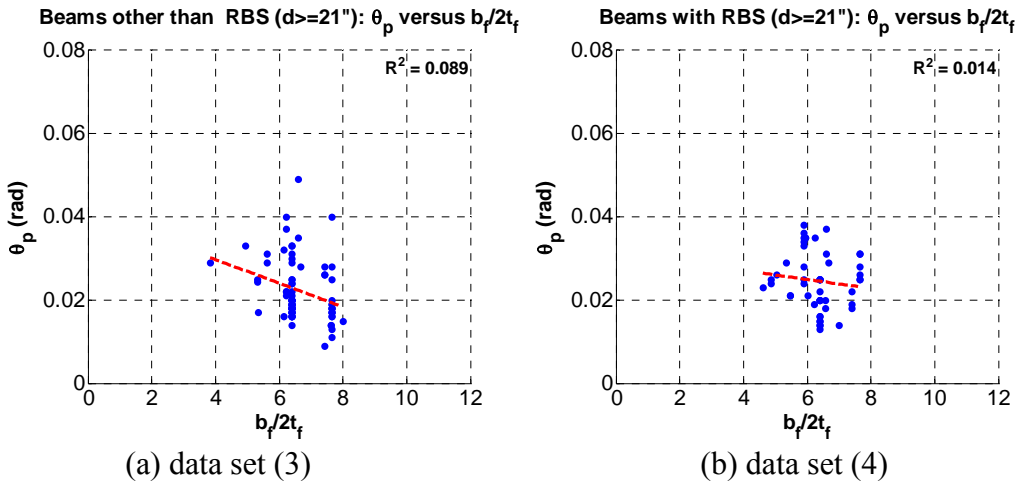


Figure 3.11. Dependence of θ_p on beam span to flange width to thickness ratio $b_f/2t_f$; (a) beams other-than-RBS ($d \geq 21''$), (b) beams with RBS ($d \geq 21''$)

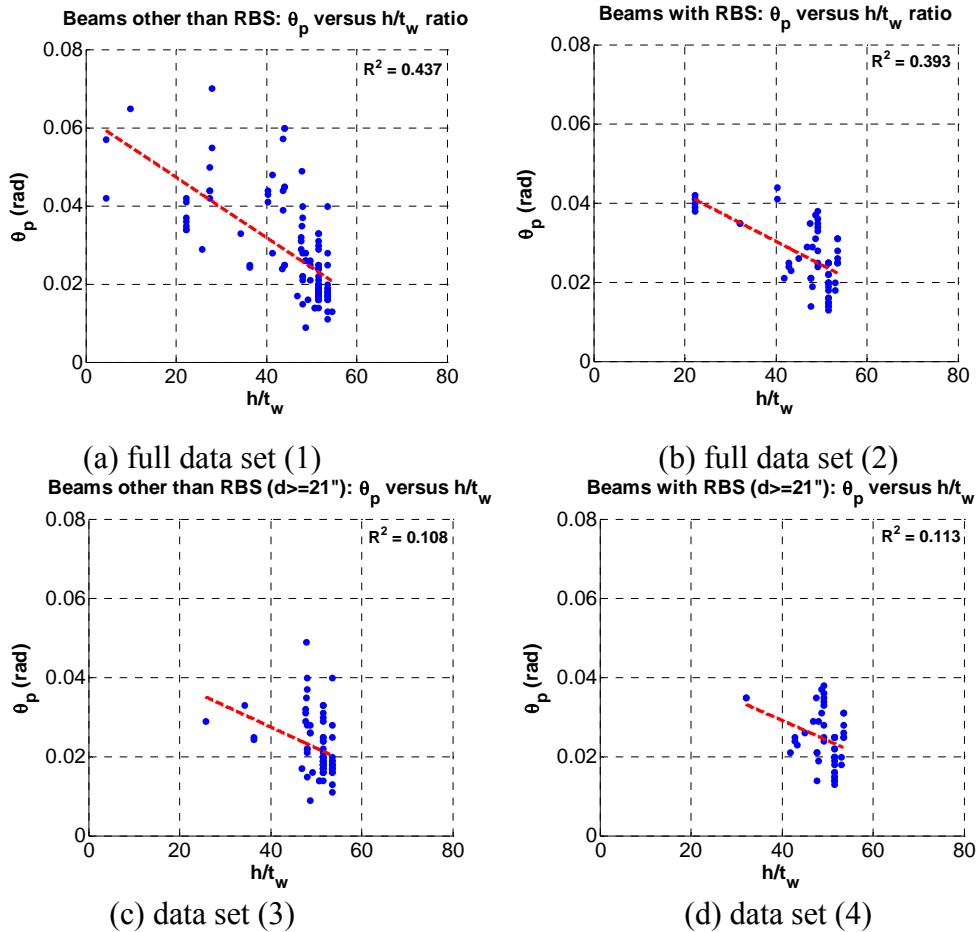
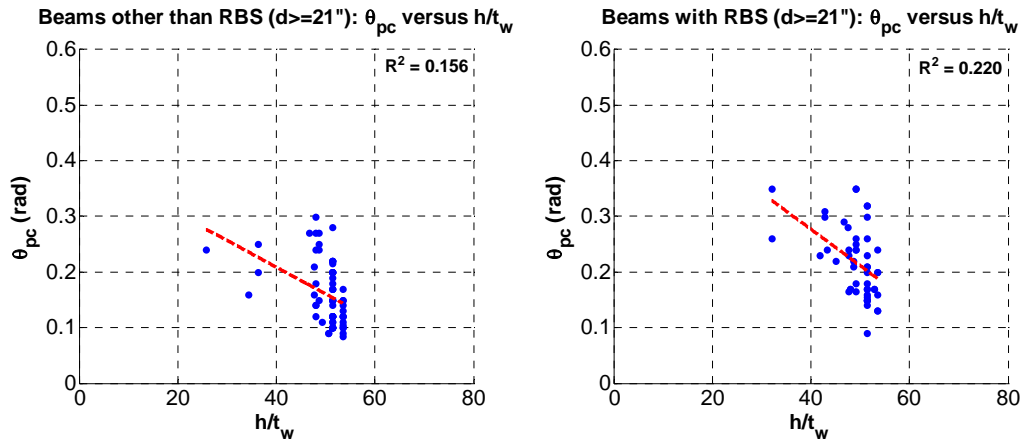
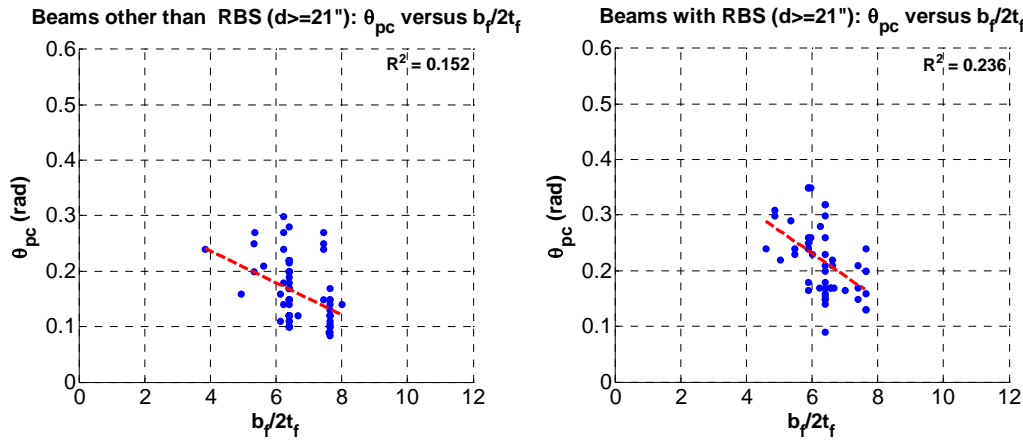


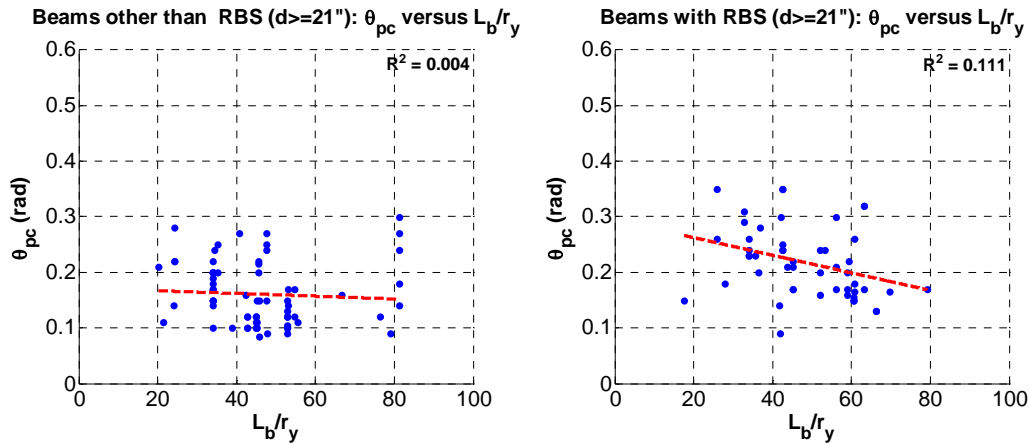
Figure 3.12. Dependence of θ_p on ratio h/t_w ratio (W-sections database)



(a) dependence of θ_{pc} on beam web depth to thickness ratio h/t_w (W-sections database)

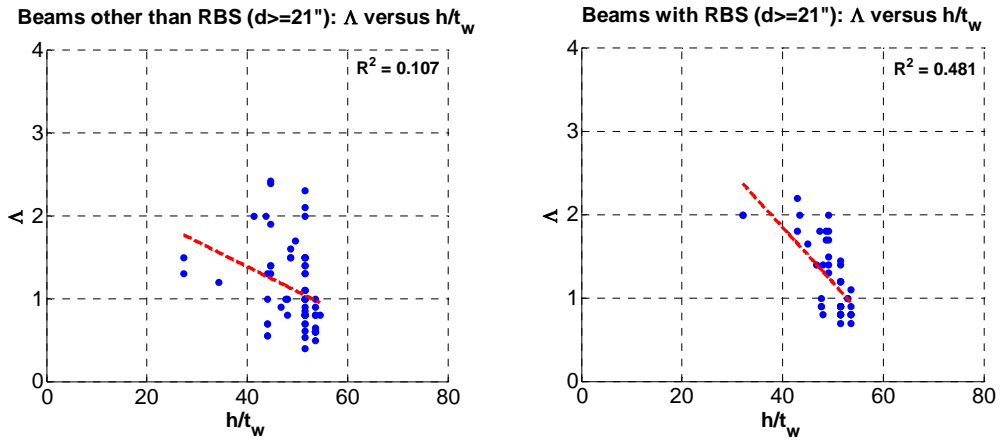


(b) dependence of θ_{pc} on beam flange width to thickness ratio $b_f/2t_f$ (W-sections database)

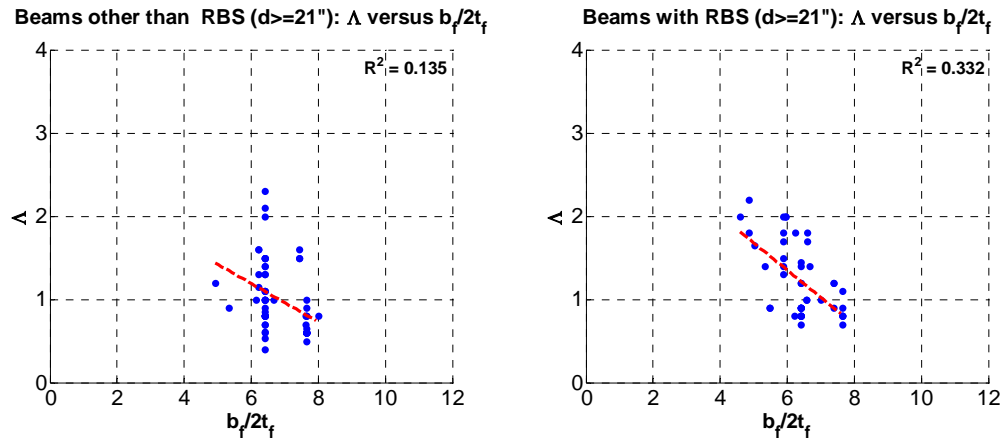


(c) dependence of θ_{pc} on L_b/r_y (W-sections database)

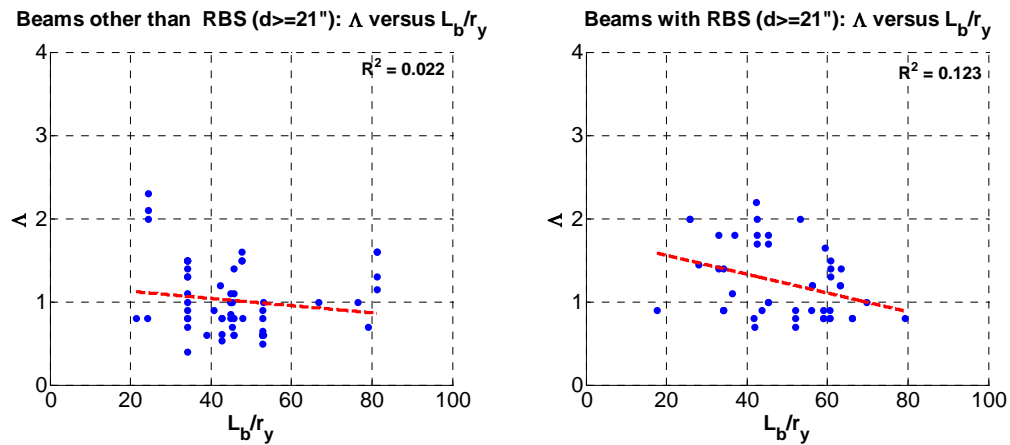
Figure 3.13. Dependence of θ_{pc} of data sets (3) & (4) on various geometric parameters



(a) dependence of Λ on beam web depth to thickness ratio h/t_w (W-sections database)



(b) dependence of Λ on beam flange width to thickness ratio $b_f/2t_f$ (W-sections database)



(c) dependence of Λ on L_b/r_y (W-sections database)

Figure 3.14. Dependence of Λ of data sets (3) and (4) on various geometric parameters

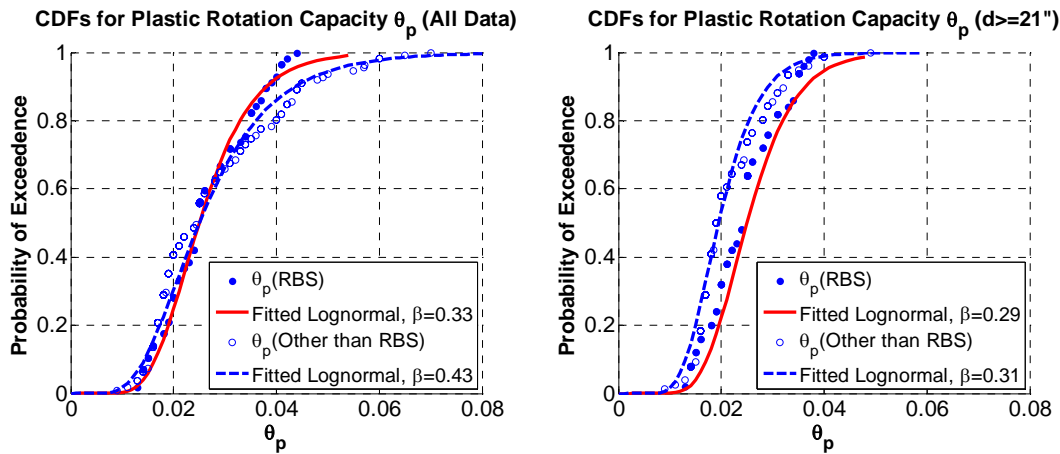


Figure 3.15. CDFs for θ_p ; left = full data sets (1) and (2); right = data sets (3) and (4)

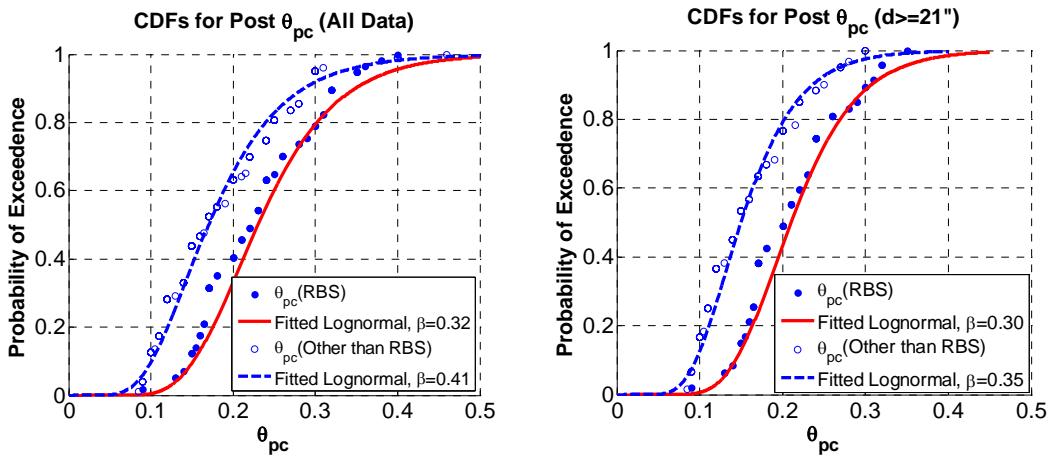


Figure 3.16. CDFs for θ_{pc} ; left = full data sets (1) and (2); right = data sets (3) and (4)

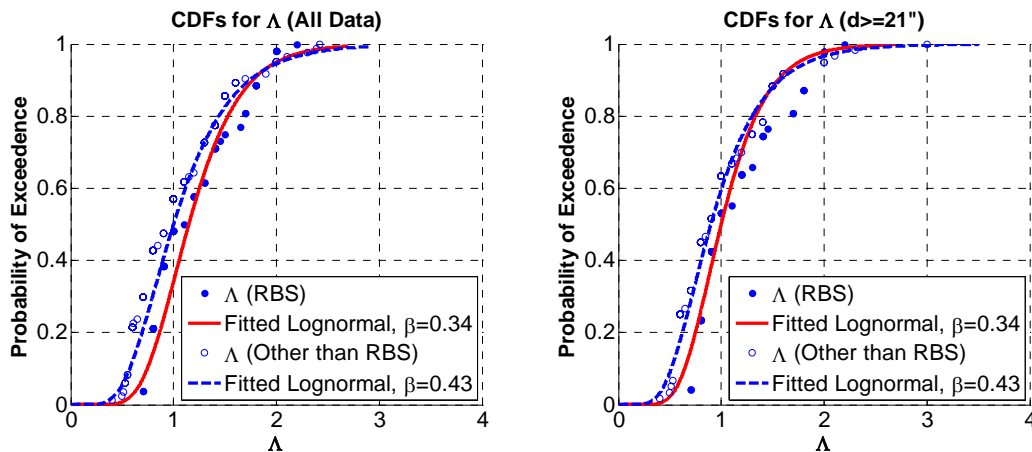


Figure 3.17. CDFs for Λ ; left = full data sets (1) and (2); right = data sets (3) and (4)

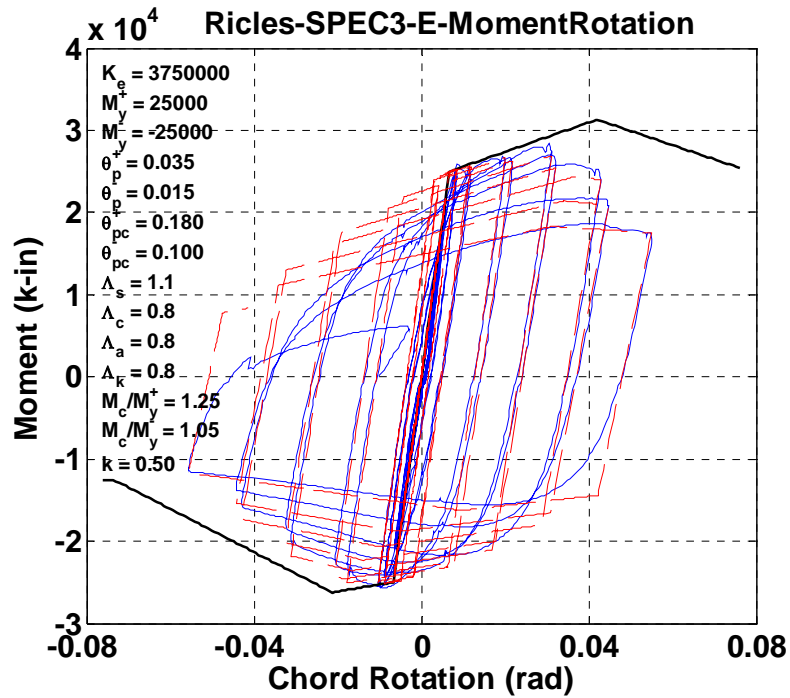


Figure 3.18. Effect of slab on the deterioration characteristics of a composite beam with RBS; part of an exterior moment resisting frame (data from Ricles et al. 2004)

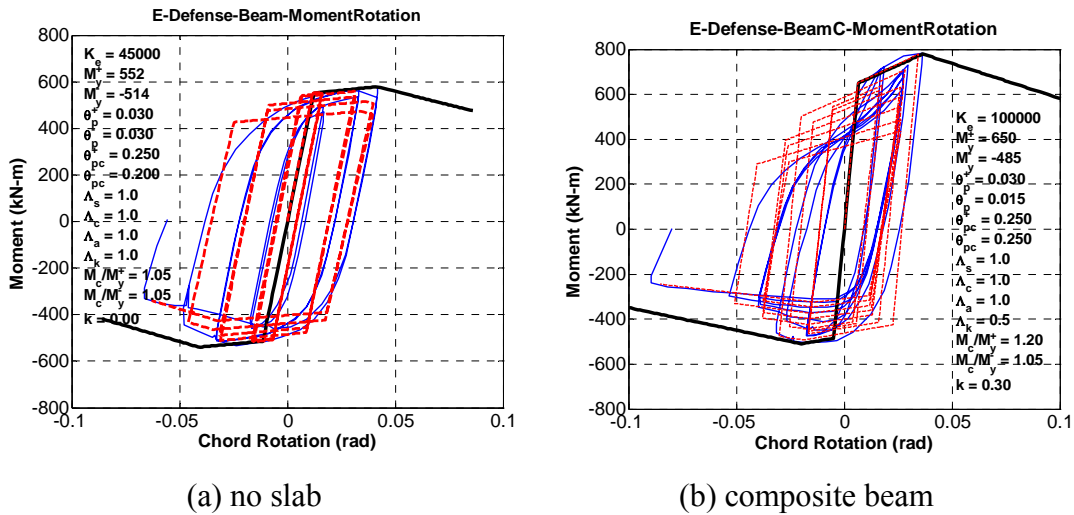
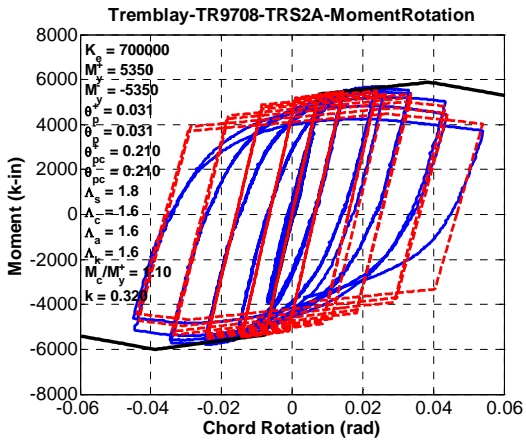
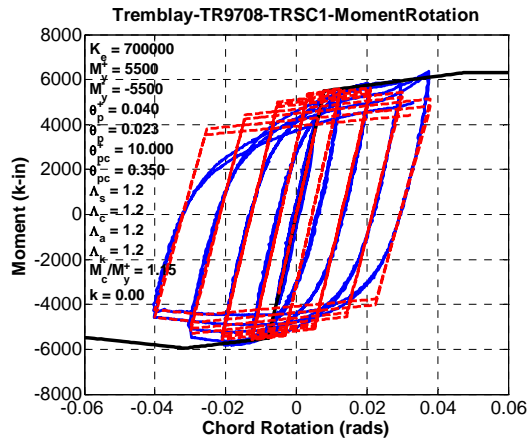


Figure 3.19. Effect of slab on the deterioration characteristics of a beam; part of an interior moment resisting frame (data from E-Defense 2007)

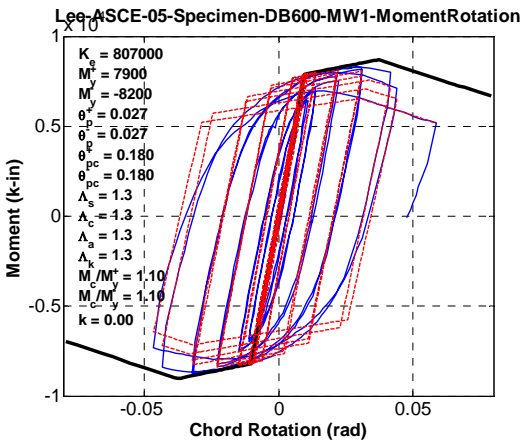


(a) no slab

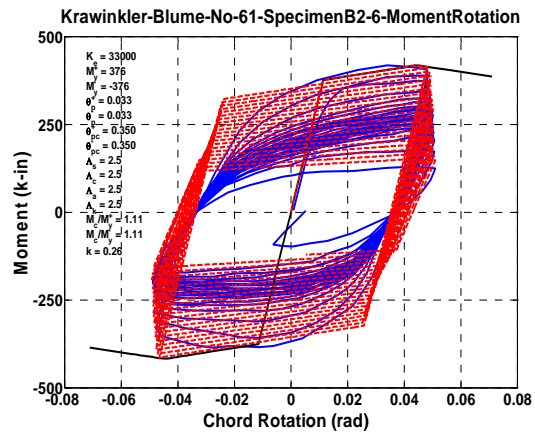


(b) composite beam

Figure 3.20. Effect of slab on the deterioration characteristics of a beam with RBS; subassembly of an exterior moment resisting frame (data from Tremblay et al. 1997)



(a) residual strength not attained



(b) stabilization at residual strength

Figure 3.21. Effect of residual strength during loading history (a) residual strength is not attained (data from Lee et al. 2005); (b) stabilization, i.e residual strength (data from Krawinkler et al. 1983)

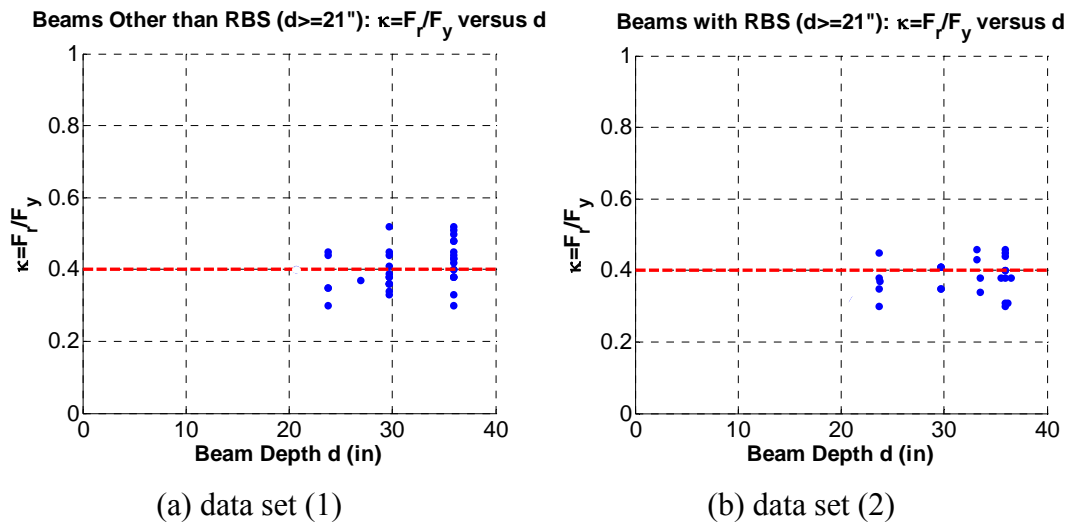


Figure 3.22. Residual strength ratio κ versus beam depth for data sets (3) and (4) (W-sections database)

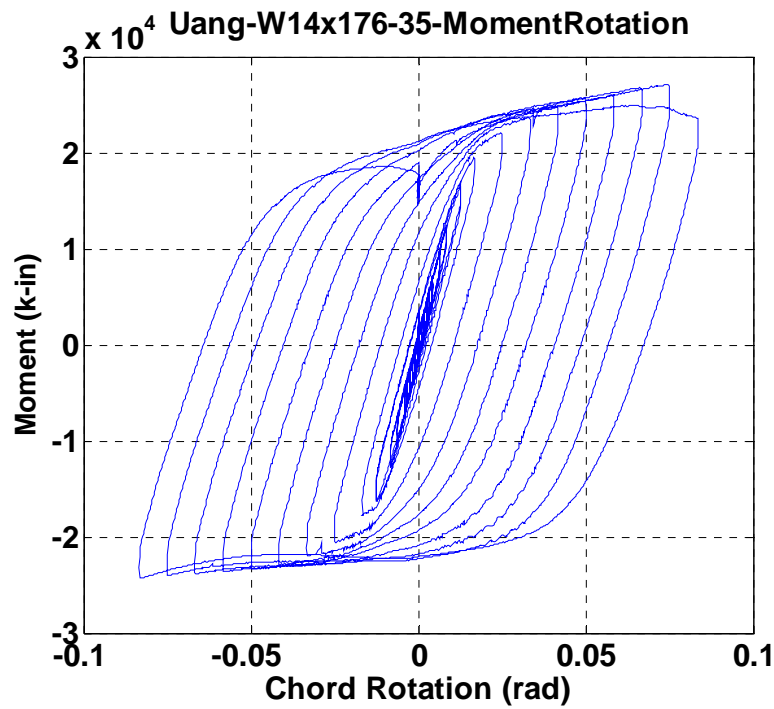
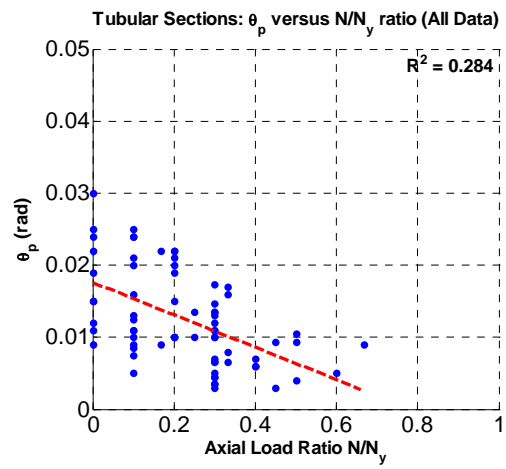
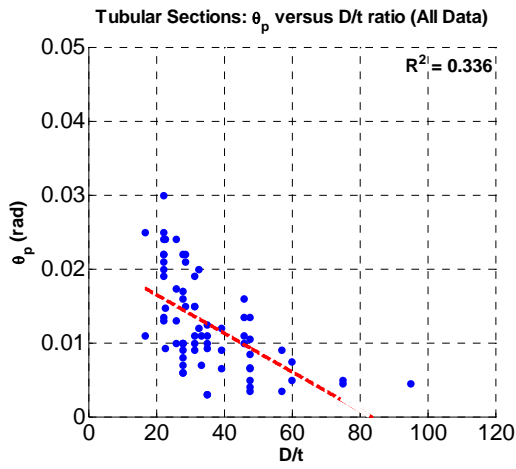
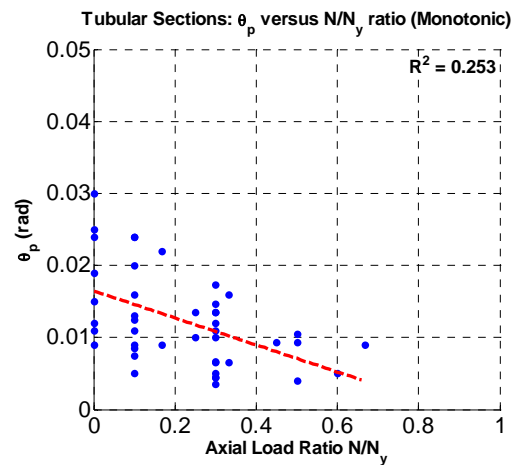
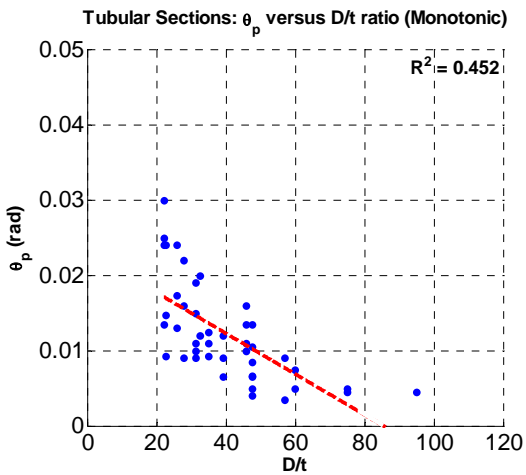


Figure 3.23. Moment-rotation diagram of a heavy shallow column (test data from Newell and Uang, 2006)

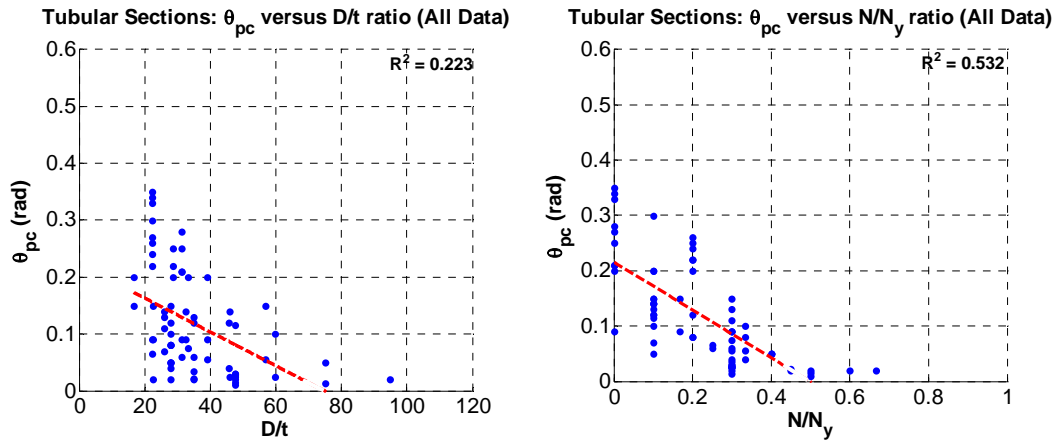


(a) all data columns (tubular column database)

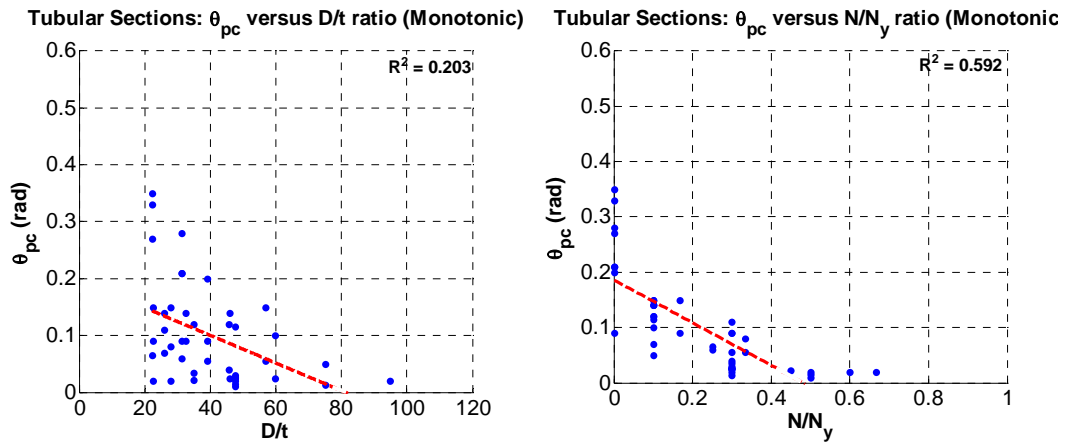


(b) monotonic data (tubular column database)

Figure 3.24. Dependence of θ_p on column tube depth to thickness ratio D/t and axial load ratio N/N_y (a) full data set (b) monotonic tests only



(a) all data (tubular column database)



(b) monotonic data (tubular column database)

Figure 3.25. Dependence of θ_{pc} on column tube depth to thickness ratio D/t and axial load ratio N/N_y , (a) full data set (b) monotonic tests only (tubular column database)

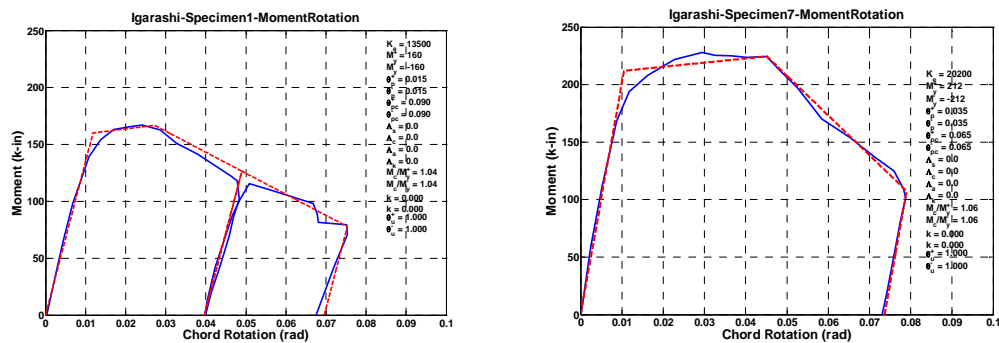


Figure 3.26. Calibration examples for monotonic tests of tubular section (data from Sugiyama & Igarashi, 1986)

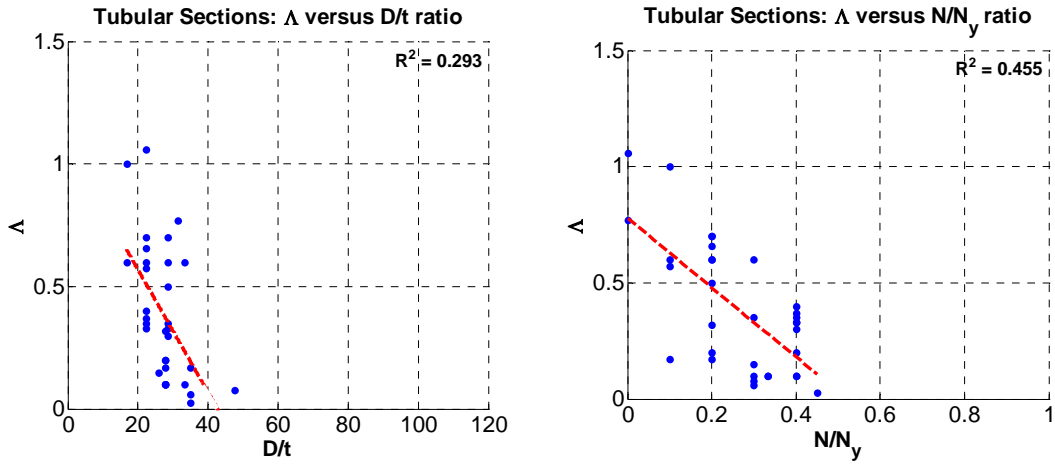


Figure 3.27. Dependence of Λ on column tube depth to thickness ratio D/t and axial load ratio N/N_y (tubular column database)

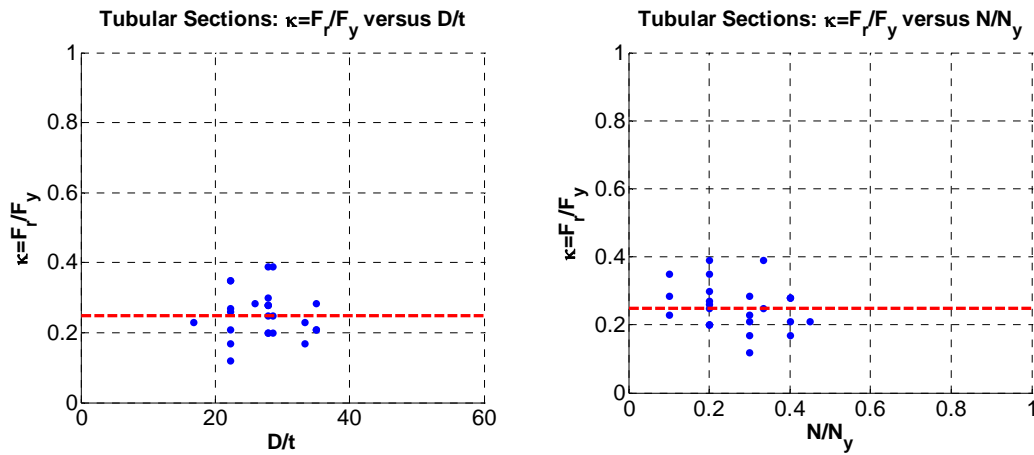


Figure 3.28. Dependence of residual strength ratio κ on column tube depth to thickness ratio D/t and axial load ratio N/N_y (tubular column database)

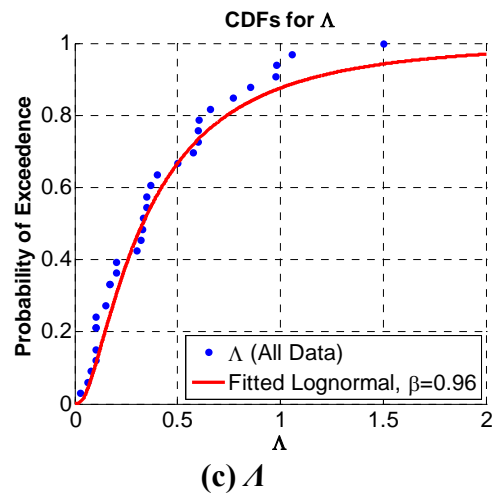
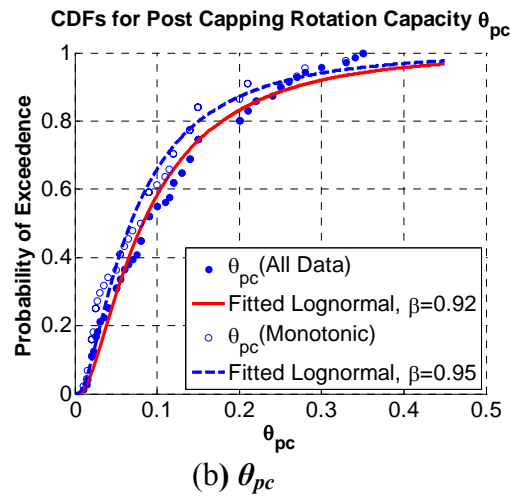
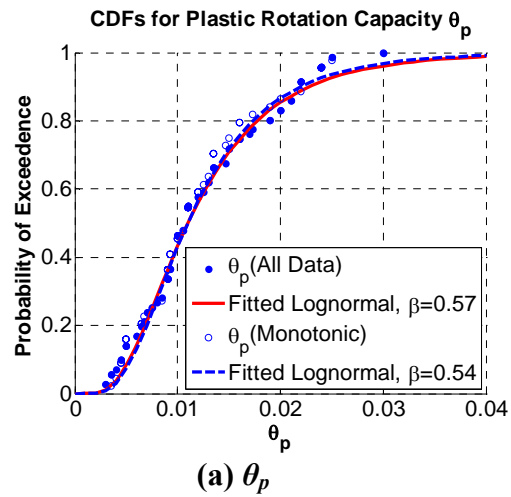
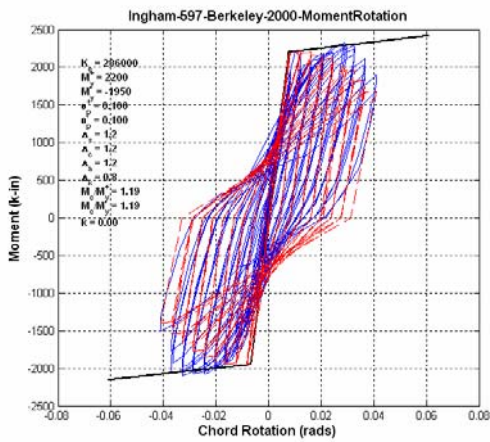
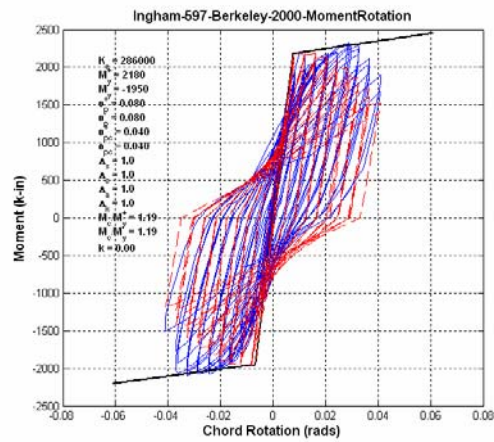


Figure 3.29. CDFs of deterioration model parameters for tubular steel columns



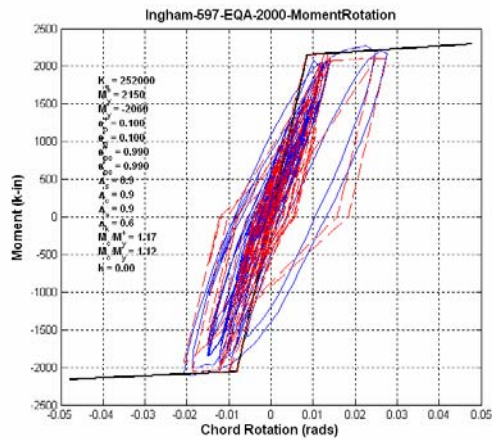
(a) Independent calibration



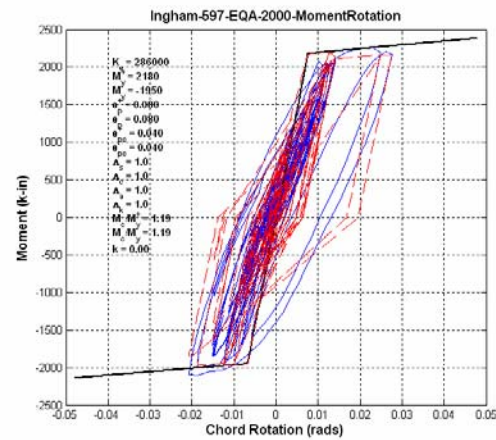
(b) Calibration based on average parameters

Figure 3.30. Calibrations of cyclic test “Berkeley loading history” from Liddell et al.

(2000)



(a) Independent calibration



(b) Calibration based on average parameters

Figure 3.31. Calibrations of cyclic test “EQA loading history” from Liddell et al. (2000)

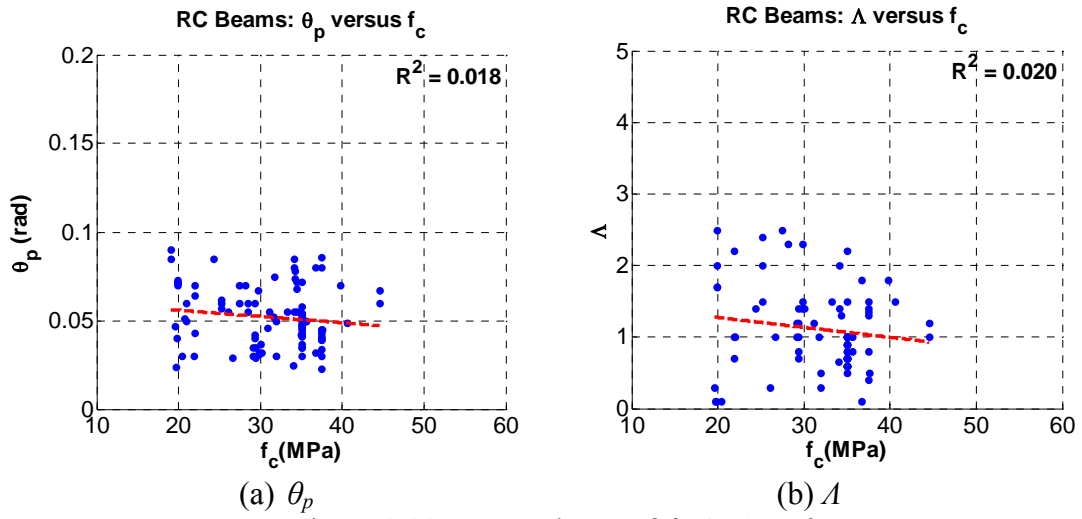


Figure 3.32. Dependence of θ_p & λ on f'_c

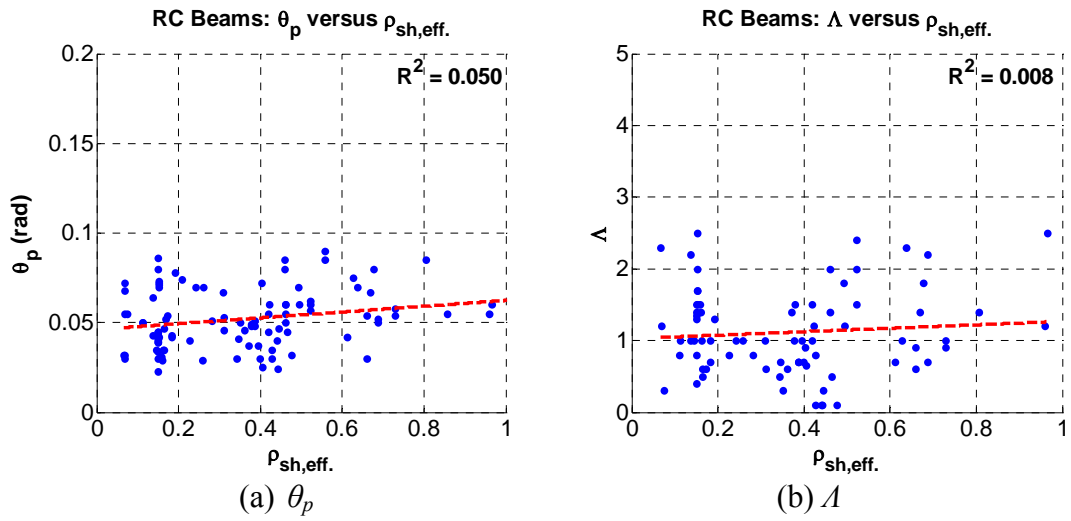
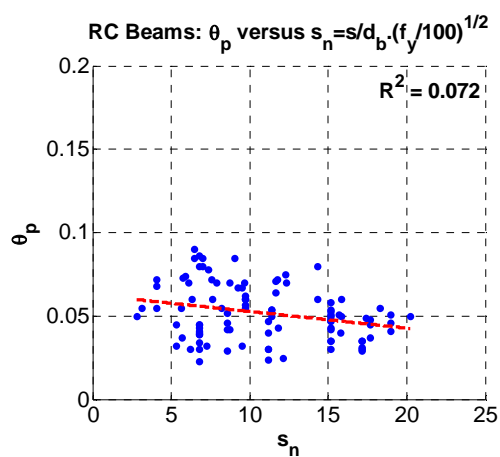
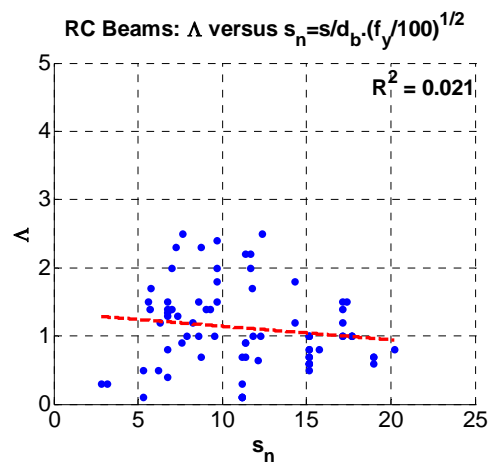


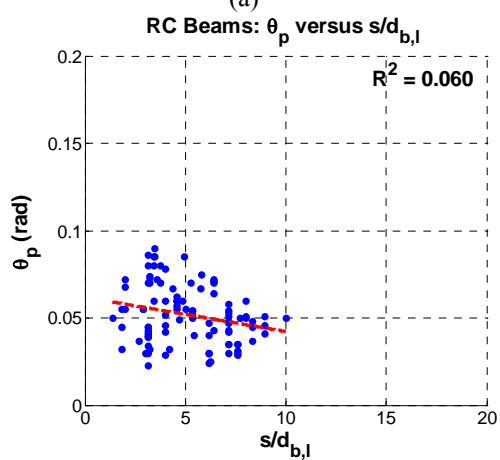
Figure 3.33. Dependence of θ_p , & λ on $\rho_{sh,eff}$



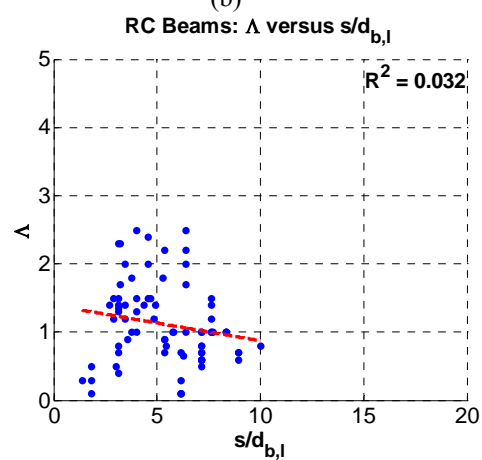
(a)



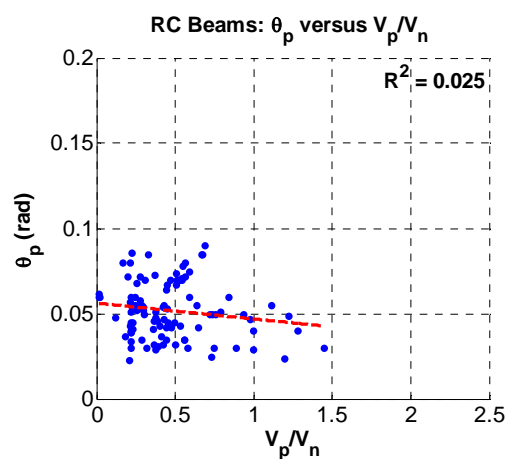
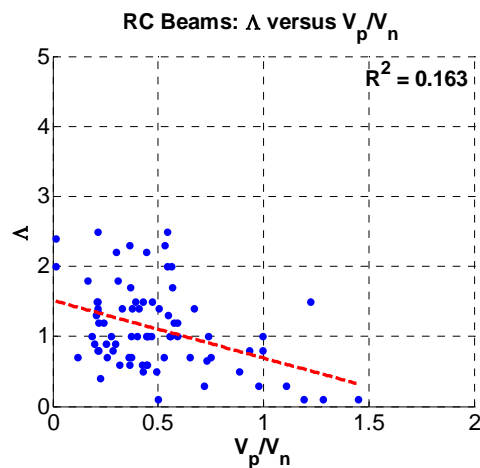
(b)



(c)



(d)

Figure 3.34. Dependence of θ_p, Λ on s_n (left) and $s/d_{b,l}$ (right)(a) θ_p (b) Λ Figure 3.35. Dependence of θ_p & Λ on V_p/V_n

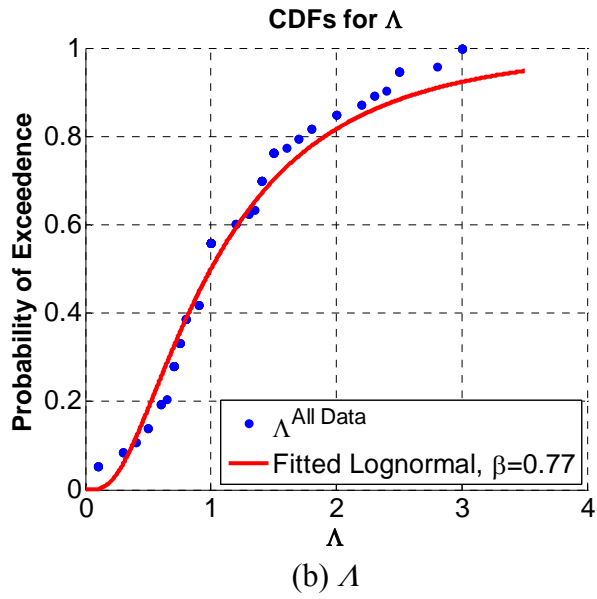
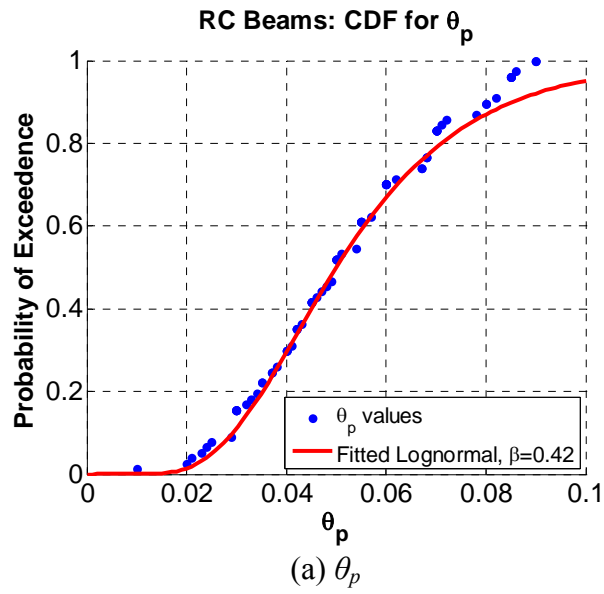


Figure 3.36. CDFs of model parameters for RC beams (a) θ_p (b) Λ

CHAPTER 4

RELATIONSHIPS FOR MODELING DETERIORATION PARAMETERS OF PLASTIC HINGE REGIONS

4.1 Objective and Scope

The missing aspect of comprehensive modeling of the deterioration characteristics of structural components is the availability of relationships that associate model parameters, such as the ones discussed in Chapter 2, with properties that control deterioration in structural components such as geometric and material properties and detailing criteria.

In support of collapse assessment of structural systems under seismic excitations relationships are proposed here for modeling of deterioration parameters [backbone curve parameters θ_p , θ_{pc} and rate of cyclic deterioration A] of plastic hinge regions in steel w-sections and hollow square tubular column sections, considering the interrelation of properties that significantly affect deterioration of structural components. At this point the focus is on steel components. The proposed relationships are empirical since they are developed with the use of stepwise multivariate regression analysis and utilizing the experimental data summarized in Chapter 3. As was seen already in Chapter 3, the trends are not always clear and the data exhibit large scatter. This affected also the regression analysis, and in some cases pure statistics had to be supplemented by engineering concepts and principles of mechanics. The predicted deterioration parameters are the ones of the modified Ibarra-Krawinkler model discussed in Section 2.3.

4.2 Multivariate Regression Analysis

Important aspects of creating an empirical equation are determining an appropriate functional form and selecting appropriate predictive variables. The functional form should reasonably represent the way in which the individual predictive variables affect the calibrated parameter and, additionally, how the various predictors interact with each other. To determine an appropriate functional form the following steps are performed: (1) inspect closely the data and isolate individual variables that significantly affect the parameter of interest based on the trend plots presented in Chapter 3, (b) take advantage of available knowledge based on principles of mechanics, and (c) use previous research when available. Using the stepwise multivariate regression analysis approach, only variables that are statistically significant (see Chatterjee et al. 2000) are included in the predictive equations.

After establishing the functional form, the data is transformed to fit the functional form (typically using various natural logarithmic transformations) and standard multivariable regression analysis is used to determine the coefficients in the equations. In Chapter 3 it was shown that all three model parameters, i.e., θ_p , θ_{pc} and A , follow a lognormal distribution based on a Kolmogorov-Smirnov test (Benjamin and Cornell 1973); hence the regression is always performed on the natural log of the model parameter (or the natural log of some transformed model parameter).

There is evidence from laboratory research on steel components that web local buckling is coupled with flange local buckling and lateral torsional buckling (Lay, 1965, Lay and Galambos, 1966, Uang and Fan, 1999). Hence a nonlinear regression model is used to evaluate the contribution of each important property identified in Chapter 3 to the selected response parameter (RP). The general nonlinear model used is

$$RP = a_1 \cdot (X_1)^{a_2} \cdot (X_2)^{a_3} \cdots (X_n)^{a_{n+1}} \quad (4.1)$$

in which:

$\alpha_1, \alpha_2, \dots, \alpha_{n+1}$ are constants known as regression coefficients and $X_1, X_2 \dots X_n$ are the predictor variables. Since the data is transformed to the natural log domain Equation (4.1) becomes

$$\log(RP) = \log(a_1) + a_2 \cdot \log(X_1) + a_3 \cdot \log(X_2) \cdots a_{n+1} \cdot \log(X_n) + \varepsilon \quad (4.2)$$

in which ε is the random variable representing the error in the regression estimates. The least square method is used in order to obtain the regression coefficients and sum of squares of estimation residuals SSE.

Regression equations are separated into three main categories based on the component type (W-sections, tubular steel columns). Depending on the component type, additional regression equations are proposed for representative data subsets. The choice of functional form for a model parameter is based on a process of developing an equation and then improving the equation based on the trends between the residuals (prediction errors) and the predicting parameters, i.e., using the functional form for which the coefficient of determination R^2 of the predictive equation is the largest one and residuals are distributed around zero error but it is mandatory that the proposed equation should follow basic principles of mechanics.

As mentioned previously the stepwise regression approach is used to develop the regression equations for the model parameters. In most of the cases discussed in the sections below only variables that are statistically significant at the 95% level using a standard t -test or F -test (see Chatterjee et al. 2000) are used in the regression equations.

4.3 W-Sections

The steel W-section database includes primarily specimens without slab. Most of the composite specimens that have been collected have W36 beams; hence the range of available sections is not adequate to propose regression equations for modeling parameters of composite sections, but quantitative information on composite action and its effect on deterioration parameters of composite steel beams is discussed in Section 3.4.6. None of specimens that failed in a brittle way (e.g. brittle fracture) before significant deterioration occurred are included in any of the regression equations since the focus is on gradual deterioration of components.

4.3.1 *Beams Other Than RBS*

Since for most connection types the number of tests is too small and the trends are not sufficiently clear to justify a distinction based on connection type, all connection types are lumped into one data set except for RBS connections, which are treated separately in Section 4.3.2. Relevant research on deterioration model parameters is summarized before addressing the empirical equation development.

4.3.1.1 **Plastic Rotation Capacity θ_p**

Previous research on predicting plastic rotation up to the maximum moment through engineering mechanics has been conducted by Lay and Galambos (1967) and McDermott (1969) considering the strain hardening range in the analytical expression. Kato (1989) and Mazzolani and Piluso (1992) used the same integration methodology of moment curvature as the study by Lay and Galambos but they considered the differences in stress levels for compression and tension flanges. Vayas and Psycharis (1995) used the method of effective width to obtain the moment-curvature diagram for a cross section and the rotation capacity for the beam in the descending branch. For reasons stated in Chapter 3 the curvature

integration method may lead to non-conservative prediction of deformation capacity; thus a more phenomenological approach is used in this research to predict plastic rotation capacity.

A summary on quantification of plastic rotation capacity of steel members based on yield line theory, which was first used to analyze the behavior of cylindrical shells near collapse (Kollar and Dulasca, (1984)), is provided in Gioncu and Mazzolani (2002). Even though this method has been validated with the use of experimental and numerical simulations it can be used only to determine the post-critical path of a moment rotation diagram. It is also important, after examining the experimental and numerical simulation of buckles shapes, to choose a proper pattern for the plastic mechanism; hence it is difficult to develop practical solutions that can be included in global analytical models of structural systems for collapse assessment.

Kuhlmann (1986) developed a software and used the finite element method (FEM) to calculate the plastic rotation up to the maximum moment. Greschik et al. (1990) tried to explain the effect of residual stresses and geometric imperfections on the difference between numerical prediction of deformation capacity and experimental data. Huang and Deierlein (1996) used the beams tested by Lukey and Adams (1969) and quantified the effect of out-of-plane rotation on the deformation capacity of steel beams. Others (Earls and Galambos, (1998), Ricles et al. (2004)) tried to predict plastic rotation capacity considering the effects of various parameters such as in plane and out of plane plastic buckling modes, moment gradients, lateral bracing and strain hardening. Even though the main experimental conclusions concerning rotation capacity are confirmed with FEM analysis a multi-scale environment is required to connect the FEM models to a global analysis model of a structure in order to evaluate its behavior up to collapse, which is computationally very expensive at this time. Thus the more practical solution to develop empirical rules for modeling of the deterioration parameters of components based on experimental data is used in this research.

Trends for plastic rotation capacity θ_p for beams other than RBS, as discussed in Section 3.4.4.1, showed that for the full data set (data set (1), see Section 3.4.4) the primary parameter that affects θ_p is the web depth over thickness ratio h/t_w and beam depth d . For this full data set the equation for θ_p obtained from multivariate regression analysis is

$$\theta_p = 0.07 \cdot \left(\frac{h}{t_w}\right)^{-0.35} \cdot \left(\frac{b_f}{2 \cdot t_f}\right)^{-0.10} \left(\frac{L_b}{r_y}\right)^{-0.01} \cdot \left(\frac{L}{d}\right)^{0.31} \cdot \left(\frac{d}{c_{unit}^1 \cdot 21''}\right)^{-0.281} \cdot \left(\frac{c_{unit}^2 \cdot F_y}{50}\right)^{-0.377} \quad (4.3)$$

$$R^2 = 0.46$$

Equation (4.3) can be further simplified to Equation (4.4) with slightly larger error, for reasons discussed in the next paragraph,

$$\theta_p = 0.07 \cdot \left(\frac{h}{t_w}\right)^{-0.35} \cdot \left(\frac{b_f}{2 \cdot t_f}\right)^{-0.09} \cdot \left(\frac{L}{d}\right)^{0.310} \cdot \left(\frac{d}{c_{unit}^1 \cdot 21''}\right)^{-0.281} \cdot \left(\frac{c_{unit}^2 \cdot F_y}{50}\right)^{-0.383} \quad (4.4)$$

$$R^2 = 0.45$$

Equations (4.3) and (4.4) are obtained using data for the following range of parameters:

- $20 \leq h/t_w \leq 55$
- $4 \leq b_f/2t_f \leq 8$
- $20 \leq L_b/r_y \leq 80$
- $2.5 \leq L/d \leq 7$
- $4'' \leq d \leq 36''$,
- $35 \leq F_y \leq 65$ ksi

in which

- h/t_w is the fillet to fillet web depth over web thickness ratio of the W-section (used for web compactness checks based on AISC-2005)

- L_b/r_y is the ratio between beam unbraced length L_b over radius of gyration about the weak axis of the cross section
- $b_f/2t_f$ is the flange width to thickness ratio used for compactness checks
- L/d is the shear span to depth ratio of the beam
- d is the beam depth of the cross section and,
- F_y is the expected yield strength of the flange of the beam in ksi units, which is normalized by 50ksi (typical nominal yield strength of structural US steel)
- c^1_{unit} and c^2_{unit} are coefficients for units conversion. They both are 1.0 if inches and ksi are used, and they are $c^1_{unit} = 0.0254$ and $c^2_{unit} = 0.145$ if d is in meters and F_y is in MPa.

Figure 4.1 illustrates the predicted θ_p values versus the calibrated θ_p values for all the data points of beams other than RBS.

In Section 3.4.4.1 it was pointed out that the effect of lateral restraint on θ_p is not significant. This is reflected in Equation (4.3) from the small regression coefficient for the L_b/r_y term. The R^2 value of the same equation without the L_b/r_y term becomes 0.45. Axhag (1995), White and Barth (1998), proposed a set of empirical equations based on evaluation of experimental data in order to predict plastic rotation capacity of steel beams, and they concluded the same regarding the effect of lateral restraint on plastic rotation capacity.

Kemp and Dekker (1991) after evaluating the behavior of 44 tests for assessment of the inelastic rotation capacity of structural components and their connections concluded that for L_b/r_y smaller than 60 local flange buckling occurs, which in turn induces web buckling as the critical failure mode. A large web depth to thickness ratio results in a section with a smaller warping constant, i.e., the section is more susceptible to torsion triggering lateral torsional buckling faster. Roeder, (2002) came to the same conclusion after evaluating a large number of experimental data.

For the full set of data the L/d ratio is included in Equation (4.3) since small sections are included in the data and the dependence on θ_p of L/d is driven by the small section sizes (see Figure 3.8 in Chapter 3). In this dataset there are specimens with different types of steel including A36, A572Gr.50 and A992Gr.50. The effect of F_y on R^2 though is not significant on θ_p (R^2 becomes 0.45 without the F_y term)

The effect of $b_f/2t_f$ on θ_p is of some importance due to the interaction with h/t_w . A small $b_f/2t_f$ ratio usually implies a narrow wide flange beam with small r_y and a large d/t_w ; hence there is an interaction between $b_f/2t_f$ and d/t_w .

The two terms that clearly affect θ_p the most are the h/t_w ratio and beam depth d . Based on the exponential coefficients and R^2 values if one of the two terms is excluded from the regression, the effect of these two predictors on θ_p for other-than -RBS beams is of equal importance. This is also confirmed from the trend plots for θ_p in Section 3.4.4.1 for the same data set.

For the set of data with depth $d \geq 21$ " (range of sections for a typical steel building construction identified as data set (3) in Chapter 3) θ_p may be predicted using the following equation,

$$\theta_p = 1.65 \cdot \left(\frac{h}{t_w}\right)^{-1.05} \cdot \left(\frac{b_f}{2 \cdot t_f}\right)^{-0.26} \cdot \left(\frac{L_b}{r_y}\right)^{-0.027} \cdot \left(\frac{L}{d}\right)^{0.09} \cdot \left(\frac{d}{c_{unit}^1 \cdot 21''}\right)^{-0.22} \cdot \left(\frac{c_{unit}^2 \cdot F_y}{50}\right)^{-0.15} \quad (4.5)$$

$$R^2 = 0.19$$

The small R^2 term ($R^2 = 0.19$) and a visual inspection of the relatively small range of parameters and the large scatter of the data indicate that not much confidence can be placed in this prediction equation. Also, the exponential coefficients are quite different from those

of Equations (4.3) and (4.4). But this is the best that can be done based on the available data.

As was pointed out in Section 3.4.4.1 the effect of L_b/r_y and L/d on θ_p is not significant for this data set, as indicated from the trends plots for these parameters. Excluding the L_b/r_y and L/d terms from Equation (4.5) the R^2 value becomes 0.18. The smaller exponential coefficient of the last term of Equation (4.5) compared to the one in Equation (4.3) is because the range of yield strength of data set (3) is between 35 to 55 ksi compared to 35 to 65ksi for data set (1). Redoing the regression analysis after eliminating the L_b/r_y and L/d terms results in the following simplified equation:

$$\theta_p = 1.74 \cdot \left(\frac{h}{t_w}\right)^{-1.05} \cdot \left(\frac{b_f}{2 \cdot t_f}\right)^{-0.21} \cdot \left(\frac{d}{c_{unit}^1 \cdot 21''}\right)^{-0.154} \cdot \left(\frac{c_{unit}^2 \cdot F_y}{50}\right)^{-0.151} \quad (4.6)$$

$$R^2 = 0.18$$

Figure 4.2(a) illustrates the predicted versus calibrated θ_p values based on Equation (4.6). Equation (4.6) indicates that the effect of the h/t_w dominates for θ_p and the effect of depth d on θ_p is negligible. As was pointed out earlier the effect of $b_f/2t_f$ on θ_p becomes somewhat more important due to the correlation between $b_f/2t_f$ and h/t_w . Figure 4.2(b) shows the interaction between $b_f/2t_f$ and d/t_w ratios and supports this statement. These observations confirm trend plots for θ_p with respect to h/t_w , $b_f/2t_f$ and d in Section 3.4.4.1 for specimens with $d \geq 21''$.

The small R^2 for both Equations (4.5) and (4.6) is due to the narrow range of h/t_w and $b_f/2t_f$ ratios of specimens included in this data set (see Figures 3.12(a) and 3.12(c)). Equations (4.5) and (4.6) are only valid for the following range of geometric and material parameters,

- $30 \leq h/t_w \leq 55$

- $5 \leq b_f/2t_f \leq 8$
- $20 \leq L_b/r_y \leq 65$
- $2.5 \leq L/d \leq 7$,
- $21" \leq d \leq 36"$,
- $33.5 \leq F_y \leq 58$ ksi

Effect of predictors on θ_p : In order to illustrate the usefulness of predictive equations a range of W-sections has been selected and the effect of various predictors on θ_p is summarized in Table 4.1 based on Equation (4.3). A common shear span of 150" and a $L_b/r_y = 50$ is used for all the sections. The expected yield strength of a A572Gr.50 steel is used ($1.1*50 = 55$ kips). From this table it is observed that when a shallow and stocky section (small h/t_w and $b_f/2t_f$) is used θ_p becomes large (more than 3%). Using Equation (4.4) to predict plastic rotation capacity for a W14x176 section θ_p becomes 0.05. Such high values have been confirmed in the experimental study by Newell and Uang (2006) (see Figure 3.23).

4.3.1.2 Post Capping Rotation Capacity θ_{pc}

Axhag (1995) and White and Barth (1998), using a backbone curve similar to the original Ibarra-Krawinkler model presented in Chapter 2, proposed an empirical equation for predicting the descending slope of the moment rotation curve of beams and concluded that flange and web local buckling are the primary contributors to the descending slope of the beams. It should be pointed out that in these studies all the beams considered were well supported laterally.

For the development of predictive equations for post capping rotation capacity θ_{pc} only specimens with clear indication of post-capping behavior were considered from the W-section database. The empirical equation for θ_{pc} , obtained from multivariate regression analysis of the full set of other-than-RBS beams is given by

$$\theta_{pc} = 5.931 \cdot \left(\frac{h}{t_w}\right)^{-0.450} \cdot \left(\frac{b_f}{2 \cdot t_f}\right)^{-0.826} \cdot \left(\frac{L_b}{r_y}\right)^{-0.069} \cdot \left(\frac{d}{c_{unit}^1 \cdot 21''}\right)^{-0.280} \cdot \left(\frac{c_{unit}^2 \cdot F_y}{50}\right)^{-1.100} \quad (4.7)$$

$$R^2 = 0.523$$

A slightly simpler expression for predicting θ_{pc} of beams other than RBS with almost the same error is given by

$$\theta_{pc} = 4.645 \cdot \left(\frac{h}{t_w}\right)^{-0.449} \cdot \left(\frac{b_f}{2 \cdot t_f}\right)^{-0.837} \cdot \left(\frac{d}{c_{unit}^1 \cdot 21''}\right)^{-0.265} \cdot \left(\frac{c_{unit}^2 \cdot F_y}{50}\right)^{-1.136} \quad (4.8)$$

$$R^2 = 0.515$$

These two equations have been derived using data for the following range of parameters:

- $20 \leq h/t_w \leq 55$
- $4 \leq b_f/2t_f \leq 8$
- $20 \leq L_b/r_y \leq 65$,
- $4'' \leq d \leq 36''$,
- $32.5 \leq F_y \leq 60$ ksi

Equation (4.7) indicates that the effect of unbraced length is not important for θ_{pc} (R^2 becomes 0.515 when L_b/r_y is not included in the regression equation), confirming conclusions from earlier studies by Axhag (1995) and White and Barth (1998). The effect of h/t_w is of almost equal importance as the effect of $b_f/2t_f$ and d since R^2 in Equations (4.7) and (4.8) becomes 0.45 when h/t_w or $b_f/2t_f$ or d is not included in the regression formula. One reason may be that web local buckling triggers lateral torsional buckling, which happens later in the loading history. In general the importance of the effect of each predictor on θ_p in Equations (4.7) and (4.8) agrees with the individual trends for θ_{pc} for this data set discussed in Chapter 3. Figure 4.3(a) shows the predicted post-capping rotation

capacities based on Equation (4.7) versus the calibrated θ_{pc} values. Equations (4.7) and (4.8) indicate that the effect of yield strength on θ_{pc} becomes important. The latter can be confirmed from Figure 4.3(b), which shows the dependence of θ_{pc} on F_y .

Due to lack of experimental data of beams other than RBS that are pushed to very large inelastic deformation, Equations (4.7) and (4.8) become questionable when their use results in very large post-capping plastic rotation capacities ($\theta_{pc} \geq 0.30\text{rad}$).

After eliminating specimens with $d < 21''$ (data set (3) in Chapter 3) the proposed empirical equation for predicting θ_{pc} is given by

$$\theta_{pc} = 7.744 \cdot \left(\frac{h}{t_w}\right)^{-0.550} \cdot \left(\frac{b_f}{2 \cdot t_f}\right)^{-0.691} \cdot \left(\frac{L_b}{r_y}\right)^{-0.100} \cdot \left(\frac{d}{c_{unit}^1 \cdot 21''}\right)^{-0.15} \cdot \left(\frac{c_{unit}^2 \cdot F_y}{50}\right)^{-1.282} \quad (4.9)$$

$$R^2 = 0.472$$

Figure 4.3(c) shows the predicted θ_{pc} values based on Equation (4.9) versus the calibrated θ_{pc} values. A simplified version of Equation (4.9) with slightly larger error is given by

$$\theta_{pc} = 4.802 \cdot \left(\frac{h}{t_w}\right)^{-0.551} \cdot \left(\frac{b_f}{2 \cdot t_f}\right)^{-0.469} \cdot \left(\frac{c_{unit}^2 \cdot F_y}{50}\right)^{-1.404} \quad (4.10)$$

$$R^2 = 0.453$$

These two equations have been derived using data for the following range of predictive parameters:

- $30 \leq h/t_w \leq 55$
- $5 \leq b_f/2t_f \leq 8$
- $20 \leq L_b/r_y \leq 65,$

- $21" \leq d \leq 36"$,
- $35 \leq F_y \leq 58$ ksi

Depth is notably absent from Equation (4.10) since its effect on θ_{pc} is negligible for this data set. The same observation is made from the individual trend for θ_{pc} . The effect of $b_f/2t_f$ and h/t_w is almost the same based on Equations (4.9) and (4.10) (R^2 becomes 0.38 if any of the two parameters is excluded from the regression equation). Similarly to data set (1) there is a clear trend between θ_{pc} and F_y for the specific data set as indicated from Figure 4.3(d), which shows the dependence of θ_{pc} on F_y . The effect of section geometry on θ_{pc} for a range of sections is summarized in Table 4.1 based on Equation (4.7). The values of θ_{pc} correlate well with the cumulative distribution function for θ_{pc} (see Figure 3.16 in Chapter 3) for the data set with $d \geq 21"$. Note that in all the predictive equations for θ_{pc} L/d is absent since it was found to be statistically insignificant for all the data sets.

4.3.1.3 Cyclic Deterioration Parameter λ

For the development of predictive equations for the cyclic deterioration parameter λ the specimens that have been selected from the steel database are the ones that fail in a ductile manner and for which cyclic deterioration is clearly observed. All the modes of cyclic deterioration are assumed to be defined by the same λ except for unloading stiffness deterioration. The exponent c of the hysteretic rule of the modified Ibarra-Krawinkler model that controls the rate of cyclic deterioration is kept equal to 1.0 for the sake of simplicity. It should be pointed out though that based on past experimental studies (Krawinkler and Zohrei (1983)) there are three main ranges of cyclic deterioration. During the first range the rate of cyclic deterioration is high with continuous growth of local buckles coupled with lateral torsional buckling. During the second range the rate of cyclic deterioration becomes slower, leading to stabilization of hysteretic response. During the third range, because of small cracks that have been formed during the first two ranges, rapid deterioration occurs due to crack propagation.

The proposed equation for cumulative rotation capacity Λ for the full set of otherthan-RBS beams is given by Equation (4.11) using the stepwise multivariate regression approach

$$\Lambda = \frac{E_t}{M_y} = 39.76 \cdot \left(\frac{h}{t_w}\right)^{-0.598} \cdot \left(\frac{b_f}{2 \cdot t_f}\right)^{-0.568} \cdot \left(\frac{L_b}{r_y}\right)^{-0.100} \cdot \left(\frac{c_{unit}^2 \cdot F_y}{50}\right)^{-1.378} \quad (4.11)$$

$$R^2 = 0.488$$

The main contributor in Equation (4.11) is the h/t_w ratio ($R^2=0.37$ excluding h/t_w from Equation (4.11)). The effect of flange local buckling and lateral bracing becomes more important for Λ compared to θ_p and θ_{pc} . The same was pointed out by Roeder (2002). Figure 4.4(a) shows the predicted Λ values based on Equation (4.11) versus the calibrated Λ values from the selected experimental data of beams other than RBS. Using only specimens that satisfy the AISC-2005 lateral bracing requirements, the L_b/r_y ratio becomes statistically insignificant and Equation (4.11) may be simplified to

$$\Lambda = \frac{E_t}{M_y} = 26.36 \left(\frac{h}{t_w}\right)^{-0.589} \cdot \left(\frac{b_f}{2 \cdot t_f}\right)^{-0.574} \cdot \left(\frac{c_{unit}^2 \cdot F_y}{50}\right)^{-1.454} \quad (4.12)$$

$$R^2 = 0.484$$

The R^2 value of Equation (4.12) indicates that the dominant contributor to cyclic deterioration is the h/t_w ratio for a beam well supported laterally. Equations (4.11) and (4.12) show that there is a dependence of Λ on yield strength of the beam. This is confirmed by Figure 4.4(b), which illustrates the trends for Λ with respect to yield strength.

These two equations have been derived using data for the following range of predictive parameters:

- $20 \leq h/t_w \leq 55$

- $5 \leq b_f/2t_f \leq 7.5$
- $20 \leq L_b/r_y \leq 65$,
- $7.5" \leq d \leq 36"$,
- $37 \leq F_y \leq 58$ ksi

For the data set of beams with nominal depth larger than 21" the following equation can be used to predict Λ ,

$$\Lambda = \frac{E_t}{M_y} = 190 \cdot \left(\frac{h}{t_w}\right)^{-1.254} \cdot \left(\frac{b_f}{2 \cdot t_f}\right)^{-0.296} \cdot \left(\frac{L_b}{r_y}\right)^{-0.100} \cdot \left(\frac{C_{unit}^2 \cdot F_y}{50}\right)^{-1.451} \quad (4.13)$$

$$R^2 = 0.413$$

Figure 4.4(c) shows the predicted Λ values based on Equation (4.13) versus the calibrated ones from the tests included in the regression process. The three specimens for which Λ is clearly underestimated compared to the calibrated values have bolted haunch bracket connections (Kasai and Hodgson, (1996)), which in general deteriorate very slowly compared to standard welded-flange-bolted-web or RBS connections. Roeder (2002) concluded the same after evaluating three main connection categories including the bolted haunch bracketed one. All the specimens included in the data set ($d \geq 21"$) satisfy the lateral bracing requirements based on AISC specifications; thus the effect of L_b/r_y on Λ in Equation (4.13) is not important. A slightly simpler equation for predicting Λ with almost the same R^2 is given by

$$\Lambda = \frac{E_t}{M_y} = 133.13 \left(\frac{h}{t_w}\right)^{-1.112} \cdot \left(\frac{b_f}{2 \cdot t_f}\right)^{-0.358} \cdot \left(\frac{C_{unit}^2 \cdot F_y}{50}\right)^{-1.517} \quad (4.14)$$

$$R^2 = 0.408$$

These two equations have been derived using data for the following range of predictive parameters:

- $35 \leq h/t_w \leq 55$
- $5 \leq b_f/2t_f \leq 7.5$
- $20 \leq L_b/r_y \leq 63$,
- $21" \leq d \leq 36"$,
- $37 \leq F_y \leq 58 \text{ ksi?}^*$

The effect of depth d and L/d on A was not found to be statistically significant in any of the data sets; thus these two predictors are absent in any of the regression equations for A . In general, trends for A versus various predictors presented in Chapter 3 agree with the influence of the same predictors using multivariate regression analysis.

Table 4.1 summarizes the effect of different section sizes on A . The shear span to beam depth ratio, L_b/r_y ratio, and expected yield strength are the same as used to illustrate the effect of section geometry on θ_p and θ_{pc} . The general conclusion that a shallow and stocky section, with small h/t_w and $b_f/2t_f$ ratios, deteriorates much slower than a slender section is validated.

4.3.2 Beams with RBS

Due to the large number of tests included in the W-sections database involving beams with RBS a separate set of regression equations is proposed for this type of connections that has become popular in steel construction in the US. The predictive equations proposed in this section are based on the set of tests with beams that have a $d \geq 21"$ (data set (4) in Chapter 3) since this range of sections is commonly used in practice. There are no beams with RBS with d smaller than 18" in the W-sections database, and a statistical evaluation with the use

of stepwise multivariate regression analysis indicated that predictive equations do not differ by much if we would make a distinction based on beam depth.

4.3.2.1 Plastic Rotation Capacity θ_p

Previous research on empirical equations for predicting deformation capacity of beams with RBS has been conducted by Uang and Fue (1999) after evaluating a dataset of 55 specimens. In this study the plastic rotation capacity is defined as the difference between the rotations at 80% of the ultimate strength and at yield strength. Uang and Fue used the envelope curve from the available moment-rotation diagrams to extract the values of plastic deformation for the 55 specimens used in their study. Roeder (2002) tried to quantify the rotation capacity of RBS connections as a function of the beam depth. Results from the Roeder (2002) study cannot be compared with findings of the earlier study by Uang and Fue (1999) and the research herein because Roeder combined beam inelastic rotations with panel zone shear deformations whereas the focus of the current research is on plastic hinge rotations at the location of the plastic hinge in the beam.

For the data set of beams with RBS with $d \geq 21$ " the proposed equation for plastic rotation capacity of θ_p is given by

$$\theta_p = 0.19 \cdot \left(\frac{h}{t_w}\right)^{-0.31} \cdot \left(\frac{b_f}{2 \cdot t_f}\right)^{-0.09} \cdot \left(\frac{L_b}{r_y}\right)^{-0.19} \cdot \left(\frac{L}{d}\right)^{0.11} \cdot \left(\frac{d}{c_{unit}^1 \cdot 21''}\right)^{-0.77} \cdot \left(\frac{c_{unit}^2 \cdot F_y}{50}\right)^{-0.05} \quad (4.15)$$

$$R^2 = 0.471$$

Equation (4.15) can be further simplified to Equation (4.16) with slightly larger error for reasons stated in the next paragraph,

$$\theta_p = 0.22 \cdot \left(\frac{h}{t_w}\right)^{-0.45} \cdot \left(\frac{b_f}{2 \cdot t_f}\right)^{-0.14} \cdot \left(\frac{d}{c_{unit}^1 \cdot 21''}\right)^{-0.854} \quad (4.16)$$

$$R^2 = 0.44$$

in which

- h/t_w is the fillet to fillet web depth over web thickness ratio of the W-section (used for web compactness checks based on AISC-2005)
- L_b/r_y is the ratio between beam unbraced length L_b over radius of gyration about the weak axis of the cross section
- $b_f/2t_f$ is the flange width to thickness ratio used for compactness checks
- L/d is the shear span to depth ratio of the beam
- d is the beam depth of the cross section and,
- F_y is the expected yield strength of the flange of the beam in ksi units, which is normalized by 50ksi (typical nominal yield strength of structural US steel)
- c_{unit}^1 and c_{unit}^2 are coefficients for units conversion. They both are 1.0 if inches and ksi are used, and they are $c_{unit}^1 = 0.0254$ and $c_{unit}^2 = 0.145$ if d is in meters and F_y is in MPa.

These two equations have been derived using data the following range of predictive parameters:

- $21 \leq h/t_w \leq 55$
- $4.5 \leq b_f/2t_f \leq 7.5$
- $20 \leq L_b/r_y \leq 65$,
- $21'' \leq d \leq 36''$,
- $38.5 \leq F_y \leq 63$ ksi

Figure 4.5 shows the predicted θ_p values based on Equation (4.15) plotted versus the calibrated θ_p values.

When the L/d term is excluded from the regression equation R^2 becomes 0.46 i.e., the dependence of θ_p on L/d is not significant. This observation agrees with the trends for θ_p versus L/d in Section 3.4.4.1 for beams with RBS and the observation that the curvature integration effect of a larger plastic hinge length is countered by the predominance of web buckling and lateral torsional buckling.

Experimental studies by Yu et al. (2000) and Uang et al (2000a) have shown that the effect of additional lateral bracing near the RBS region on θ_p is small. The same conclusion is drawn here since the R^2 value of Equation (4.15) changes only to 0.45 without the L_b/r_y term. Prior statistical studies by Uang and Fue (1999) and Roeder (2002) support this conclusion.

In Equations (4.15) and (4.16) the predominant effect of beam depth d on θ_p may be explained from the fact that in the RBS region the flange reduction by 40% in average (50% maximum reduction based on FEMA-2000) increases the effective length of the beam depth that can buckle compared to a beam other than RBS since the restraint from the flanges becomes negligible due to flange reduction. This observation is supported by Figure 4.5(b), which shows the dependence of θ_p on the flange reduction c of beams with RBS with $d \geq 21$ ". The level of influence of θ_p on d and h/t_w ratio in Equations (4.15) and (4.16) agrees with trends for θ_p versus the same parameters (see Figure 3.12 in Chapter 3).

4.3.2.2 Post Capping Rotation Capacity θ_{pc}

In Section 3.4.4.2 the trends for post capping rotation capacity θ_{pc} were discussed and the importance of h/t_w and $b_f/2t_f$ ratios on θ_{pc} for specimens with clear indication of post-

capping slope was pointed out. The same observation can be made from Equation (4.17), which predicts θ_{pc} for beams with RBS.

$$\theta_{pc} = 13.25 \cdot \left(\frac{h}{t_w}\right)^{-0.568} \cdot \left(\frac{b_f}{2 \cdot t_f}\right)^{-0.844} \cdot \left(\frac{L_b}{r_y}\right)^{-0.100} \cdot \left(\frac{c_{unit}^2 \cdot F_y}{50}\right)^{-0.389} \quad (4.17)$$

$$R^2 = 0.454$$

The primary parameter that affects θ_{pc} based on Equation (4.17) is the web local buckling term h/t_w , as validated statistically since the coefficient of determination becomes $R^2 = 0.285$ if h/t_w is excluded from Equation (4.17) (versus 0.377 if the $b_f/2t_f$ ratio is excluded from the same equation).

Similarly to the data set of beams without RBS with $d \geq 21$ " additional lateral bracing near the RBS region is not very important on θ_{pc} for specimens that are adequately supported laterally. If the L_b/r_y term is excluded from Equation (4.17) R^2 becomes 0.446. Based on Figure 4.6(a), which shows the predicted θ_{pc} versus calibrated θ_{pc} values for beams with RBS, Equation (4.17) provides adequate predictions. A simplified equation for predicting θ_{pc} for beams with RBS with $d \geq 21$ " is,

$$\theta_{pc} = 9.80 \cdot \left(\frac{h}{t_w}\right)^{-0.593} \cdot \left(\frac{b_f}{2 \cdot t_f}\right)^{-0.862} \cdot \left(\frac{c_{unit}^2 \cdot F_y}{50}\right)^{-0.403} \quad (4.18)$$

$$R^2 = 0.446$$

Beam depth is absent from Equations (4.17) and (4.18) since the dependence of θ_{pc} on d is not statistically significant for this range of data as shown in Figure 4.6(b). The same observation was made for beams other than RBS for $d \geq 21$ ". A possible reason is that the dependence of θ_{pc} on flange reduction in the RBS region is statistically insignificant. The

range of applicability of Equations (4.17) and (4.18) is the same with the one for θ_p for beams with RBS.

4.3.2.3 Cyclic Deterioration Parameter Λ

Only specimens that deteriorate gradually (no brittle fracture) have been used to develop an empirical expression for the cyclic deterioration parameter Λ for beams with RBS. Similarly to beams other than RBS, the parameter c that defines the rate of cyclic deterioration in the hysteretic rule of the modified Ibarra-Krawinkler deterioration model was set to 1.0 for the sake of simplicity. The Λ for all cyclic deterioration modes were constrained to be the same except for the unloading stiffness deterioration mode. The proposed equation for predicting the cumulative rotation capacity Λ for beams with RBS is

$$\Lambda = \frac{E_t}{M_y} = 630 \cdot \left(\frac{h}{t_w}\right)^{-1.153} \cdot \left(\frac{b_f}{2 \cdot t_f}\right)^{-0.646} \cdot \left(\frac{L_b}{r_y}\right)^{-0.170} \cdot \left(\frac{c_{unit}^2 \cdot F_y}{50}\right)^{-0.53} \quad (4.19)$$

$$R^2 = 0.482$$

This equation has been derived using data for the following range of predictive parameters:

- $40 \leq h/t_w \leq 55$
- $5 \leq b_f/2t_f \leq 7.5$
- $20 \leq L_b/r_y \leq 65$,
- $21" \leq d \leq 36"$,
- $38.5 \leq F_y \leq 63$ ksi

The coefficient of determination of Equation (4.19) becomes 0.39 if h/t_w is excluded from the regression and it becomes 0.44 if $b_f/2t_f$ is excluded from the equation, which indicates

that h/t_w ratio has the largest effect on A as was also pointed out in Section 3.4.4.3 in which the trends for A were discussed.

Uang et al. (2000a), and Yu et al. (2000) showed that beams with RBS are susceptible to twisting at the RBS region because of the reduced flanges, and additional lateral bracing reduces the rate of strength deterioration only at large deformation levels because it reduces the lateral buckling amplitude near the RBS location. Roeder (2002) came to the same conclusion. This is also confirmed by the coefficient of determination of Equation (4.19) since R^2 becomes 0.43 when L_b/r_y is excluded from the regression. Figure 4.7 presents the predicted versus calibrated values of A for beams with RBS based on Equation (4.19), indicating that the predicted A values correlate well with the experimental data.

Table 4.2 summarizes the variation of deterioration parameters of beams with RBS for a range of section sizes (W21 to W36) that satisfy seismic compactness criteria. The cases in which predictive parameters are outside the range of regression equation applicability are noted as “not applicable” (na) in this table. The range of deterioration parameter values obtained for the selected range of section sizes is also reflected in the cumulative distribution functions of the same parameters (see Figure 3.17 in Chapter 3).

In summary, similar to beams with other-than-RBS connections the effect of web local buckling on the deterioration parameters of beams with RBS is important as was also observed from the individual trends for deterioration parameters in Chapter 3. The effect of depth on θ_p of beams other than RBS becomes important when small sections are included in the data set but diminishes when the data set includes only specimens with $d \geq 21$ ". For beams with RBS the last observation does not hold true possibly due to the weak web restraint from the flange because of flange reduction in the RBS region. The effect of beam to span ratio L/d on all the deterioration parameters is not statistically significant for any of data sets with $d \geq 21$ ". Additional lateral restraint is not as effective in increasing θ_p and θ_{pc} , probably because most of the specimens included in the data sets are well supported

laterally. Based on multivariate regression analysis it was observed that the effect of L_b/r_y on A for beams with RBS is of some importance, which was also verified by past experimental studies and trend plots in Chapter 3.

4.3.3 Hollow Square Tube Sections

Many Japanese steel moment resisting frames are designed using square steel hollow structural sections (HSS) as columns. Using the database of 113 HSS columns described in Chapter 3 a set of equations to estimate deterioration model parameters of HSS columns is proposed in this section.

A primary difference between the steel W sections that were evaluated so far and the tubular sections is the effect of axial load on deterioration parameters. For HSS the axial load ratio has a dominant effect, especially on the post capping rotation capacity of the element as was already pointed out in Chapter 3 when the effect of individual predictors on deterioration parameters was evaluated ignoring the correlation between predictors.

Deterioration model parameters of tubular sections depend greatly on the axial load ratio N/N_y (N is the applied axial load and N_y is the yield load), which varies from zero to 0.70 for the set of data included in the HSS database, and the section depth D to thickness t ratio, which varies from 15 to 100 for the available set of data. The sample of the 113 data points consists of specimens of different steel types; thus the effect of the expected yield strength F_y on the empirical equations is also included. A value of 50ksi used to normalize the measured (expected) yield strength of the HSS elements.

4.3.3.1 Plastic Rotation Capacity θ_p

Kato and Akiyama (1981) and Ge and Usami (1995) proposed theoretical solutions to predict the total rotation capacity up to the maximum moment of square hollow section

beams with $N/N_y=0$. The derivation was based on the integration of the moment curvature diagram. For reasons stated in previous section, the emphasis in this research is to provide empirical equations based on experimental data to estimate the plastic rotation capacity. The proposed equation for plastic rotation capacity θ_p is given by

$$\theta_p = 0.572 \cdot \left(\frac{D}{t}\right)^{-1.000} \cdot \left(1 - \frac{N}{N_y}\right)^{1.210} \cdot \left(\frac{c_{unit}^2 \cdot F_y}{50}\right)^{-0.838} \quad (4.20)$$

with $R^2 = 0.627$

This equation has been derived using data for the following range of predictive parameters:

- $15 \leq D/t \leq 60$,
- $0 \leq N/N_y \leq 0.60$,
- $40 \leq F_y \leq 72.5\text{ksi}$ (F_y is the expected yield strength of the HSS column)

in which F_y is the yield strength of the HSS in ksi. In case F_y is in MPa a unit conversion factor $c_{unit}^2 = 0.145$ should be applied. The effect of D/t on θ_p is more important than the effect of N/N_y , since the coefficient of determination becomes 0.256 if D/t is excluded from Equation (4.20) versus 0.422 if N/N_y is excluded. Figure 4.8(a) shows the θ_p values based on Equation (4.20) versus the calibrated data from all experimental data. The same figure indicates that all the predicted data points are nicely distributed around 45° line, i.e. residuals of individual parameters are close to zero error.

The effect of D/t and N/N_y ratios on θ_p of three different HSS sections is summarized in Table 4.3, indicating that a column with $D/t = 33$ and a $N/N_y = 0.30$ (typical values for a 4-story building with HSS sections at the base columns) has a θ_p smaller than 0.01rad. Due to early local buckling of the column Kawaguchi and Morino (2001) came to the same

conclusion after evaluating the post buckling behavior of beams and columns under cyclic loading.

The HSS database includes 44 monotonic tests, which provided the opportunity to develop a prediction equation for θ_p from monotonic tests alone and compare this equation with the previously derived one. The regression equation based on monotonic tests, is

$$\theta_p = 0.700 \cdot \left(\frac{D}{t}\right)^{-1.079} \cdot \left(1 - \frac{N}{N_y}\right)^{0.828} \cdot \left(\frac{c_{unit}^2 \cdot F_y}{50}\right)^{-0.298} \quad (4.21)$$

$$R^2 = 0.726$$

This equation has been derived using data for the following range of parameters:

- $20 \leq D/t \leq 80$,
- $0 \leq N/N_y \leq 0.60$,
- $40 \leq F_y \leq 72.5\text{ksi}$ (F_y is the expected yield strength of the HSS column)

Equation (4.21) has a larger R^2 compared to Equation (4.20) because the calibration of θ_p is based on monotonic moment-rotation diagrams, which is a more reliable measure compared to the backbone θ_p obtained from cyclic tests. Figure 4.8(b) shows the predicted θ_p values based on Equation (4.21) versus the calibrated θ_p values from monotonic tests for the whole range of θ_p . Similarly to Equation (4.20) the effect of D/t on θ_p for the monotonic tests only is more important than the effect of N/N_y ratio (R^2 becomes 0.247 versus 0.601 when D/t and N/N_y is excluded from the regression equation). Equations (4.20) and (4.21) indicate that the calibrated θ_p values of the cyclic tests are close to the ones from the equivalent monotonic ones provided in the database.

4.3.3.2 Post Capping Rotation Capacity θ_{pc}

Previous research on prediction of the post capping slope of square hollow section beams ($N/N_y=0$) has been conducted by Kato and Akiyama (1981). They proposed a theoretical expression for the negative slope region which is based on moment curvature integration method. Others (Kecman, (1983), Gioncu and Petsu, (1995)) have employed the plastic collapse mechanism of yield line of plates for predicting the post-critical behavior of rectangular hollow sections.

Here an empirical formulation is proposed to predict the post-capping rotation capacity of tubular HSS columns. Only specimens with a clear indication of θ_{pc} in their monotonic or hysteretic response have been included in the statistical evaluation using a stepwise regression analysis approach. The post-capping rotation capacity θ_{pc} for the entire data set of tubular HSS columns is given by,

$$\theta_{pc} = 14.51 \cdot \left(\frac{D}{t}\right)^{-1.217} \cdot \left(1 - \frac{N}{N_y}\right)^{3.035} \cdot \left(\frac{c_{unit}^2 \cdot F_y}{50}\right)^{-0.498} \quad (4.22)$$

$$R^2 = 0.825$$

Based on monotonic data the following slightly different expression is obtained:

$$\theta_{pc} = 4.316 \cdot \left(\frac{D}{t}\right)^{-0.957} \cdot \left(1 - \frac{N}{N_y}\right)^{2.742} \cdot \left(\frac{c_{unit}^2 \cdot F_y}{50}\right)^{0.486} \quad (4.23)$$

$$R^2 = 0.842$$

These two equations have been derived using data for the following range of parameters:

- $20 \leq D/t \leq 60$,
- $0 \leq N/N_y \leq 0.50$,
- $40 \leq F_y \leq 72.5\text{ksi}$ (F_y is the expected yield strength of the HSS column)

The effect of axial load ratio N/N_y on θ_{pc} is more detrimental than the D/t ratio in both Equations (4.22, 4.23). This is also seen when the N/N_y term is excluded from the regression formulas. The R^2 value for Equations (4.22) and (4.23) becomes 0.26 and 0.37, respectively compared to 0.60 and 0.70 when the D/t ratio is excluded from the regression equations. The reason why N/N_y has a larger effect on θ_{pc} than D/t ratio is that once the tubular HSS column has buckled it is the axial force that controls how fast the component will deteriorate. The larger effect of N/N_y can be seen from Table 4.3, which summarizes the predicted values of θ_{pc} for three various HSS columns and for different axial load ratios.

Equations (4.22) and (4.23) are very similar, indicating that the calibrated post capping slope of the backbone curve of a cyclic test is not far from its equivalent monotonic curve. Figures 4.9(a) and 4.9(b) illustrate the predicted θ_{pc} values based on Equations (4.22) and (4.23), respectively, versus the calibrated θ_{pc} values.

4.3.3.3 Cyclic Deterioration Parameter A

In order to propose an empirical equation for predicting cumulative rotation capacity A for a tubular HSS steel column a subset of 40 data points of the steel HSS database is used, since only these specimens show slow strength deterioration under cyclic loading. Specimen that fail in a brittle manner (i.e., rapid deterioration due to brittle fracture) are not included for the equation development. The exponent c that defines the rate of cyclic deterioration was assumed to be 1.0. The proposed equation to predict A is given by

$$\Lambda = \frac{E_t}{M_y} = 3800 \cdot \left(\frac{D}{t}\right)^{-2.492} \cdot \left(1 - \frac{N}{N_y}\right)^{3.501} \cdot \left(\frac{c_{unit}^2 \cdot F_y}{50}\right)^{-2.391} \quad (4.24)$$

$$R^2 = 0.838$$

This equation has been derived using data for the following range of parameters:

- $20 \leq D/t \leq 40$,
- $0 \leq N/N_y \leq 0.40$,
- $40 \leq F_y \leq 66.5 \text{ksi}$ (F_y is the expected yield strength of the HSS column)

Figure 4.10 illustrates the predicted A values based on Equation (4.24) versus the calibrated A values. From this figure it is concluded that Equation (4.24) provides a good prediction for the full range of predictors in the database. HSS elements with D/t ratios larger than 30 and an average axial load ratio of 0.30 have severe strength deterioration mainly because of the early occurrence of local buckling. Kawaguchi and Morino (2001) reached the same conclusion based on an extensive experimental program they conducted. They suggested that one way to improve both post buckling behavior and energy dissipation capacity of HSS columns is to use concrete infill.

The effect of N/N_y on A based on Equation (4.22) is more detrimental than the effect of D/t . If the N/N_y term is excluded from the stepwise multivariate regression R^2 becomes 0.441 compared to 0.50 when D/t is excluded. Figure 4.11 presents individual examples of calibrated moment rotation diagrams of tubular HSS steel columns for different axial load ratios but constant D/t ratios illustrating the effect of axial load ratio on rate of cyclic deterioration. Table 4.3 summarizes the effect of design parameters of a HSS column on A for three different column sizes.

4.4 Summary and Conclusions

In this chapter the focus is on the two steel databases (W-sections and tubular HSS columns) that were developed in this research and presented in Chapter 3. Both databases are evaluated statistically in order to propose empirical equations that relate deterioration

modeling parameters of plastic hinge regions with geometric and material properties that control deterioration.

For other-than-RBS beams two sets of predictive equations are proposed after categorizing the data into two subsets based on beam depth. For beams with RBS one set of empirical equations is proposed for the range of data that includes specimens with a W21 or larger beams since this range of sections is commonly used in practice.

For tubular HSS columns two sets of predictive equations are proposed. The first set includes all the tests conducted and the second set predicts θ_p and θ_{pc} based monotonic tests only. Based on the coefficients of determination the two sets of predictive equations are very similar. The two parameters that greatly affect deterioration parameters are the axial load ratio N/N_y and the depth to thickness ratio D/t of the tubular hollow square column.

Based on a statistical evaluation of a representative range of sections and axial load ratios for both data sets after the development of predictive equations obtained from stepwise multivariate regression analysis it is concluded that:

1. in almost all the cases presented in this chapter regression equations reflect the trends and dependence of deterioration parameters on individual predictive parameters of W-Sections and tubular HSS columns presented in Chapter 3,
2. applicability of regression equations is restricted to the range of predictive variables included in the individual data sets since each one of the regression equations may give inconsistent results outside of that range,
3. reliability of the regression equations depends on the number of specimens used for each data set,
4. it was found that geometric parameters, such as h/t_w and $b_f/2t_f$ are correlated. In order to improve regression equations one should conduct an analysis of variance

and define equivalent predictive terms based on combinations of correlated predictive variables,

5. In order to reduce variability of deterioration parameters based on predictive equations a systematic approach of grouping the individual connections together similarly to beams with RBS is needed, i.e., more specimens of the same connection type are needed for a wide range of sections,
6. predictive equations for deterioration parameters of plastic hinge regions should always reflect engineering mechanics concepts. This does not necessarily mean that in all cases the proposed predictive equations represent the optimum solution for predicting θ_p , θ_{pc} and λ since mechanics principles may be violated based on the “optimum” mathematical manipulation.

Table 4.1. Deterioration model parameters based on predictive Equations ((4.4), (4.8) and (4.12) for various beam sizes (beams other than RBS, assumed beam shear span $L=150''$, $L_b/r_y= 50$, expected yield strength $F_y=55\text{ksi}$.)

Section Size	θ_p (rad)	θ_{pc} (rad)	A	h/t_w	$b_f/2t_f$	L/d	L_b/r_y	d (in)
W21x62	0.027	0.15	0.81	46.90	6.70	7.15	50.00	20.99
W21x147	0.033	0.23	1.67	26.10	5.40	6.80	50.00	22.06
W24x84	0.025	0.16	0.87	45.90	5.90	6.22	50.00	24.10
W24x207	0.030	0.26	1.43	26.60	4.40	5.89	50.00	25.47
W27x94	0.023	0.14	0.76	49.40	6.70	5.57	50.00	26.92
W27x217	0.027	0.23	1.55	29.20	4.70	5.28	50.00	28.43
W30x108	0.021	0.13	0.75	49.60	6.90	5.03	50.00	29.83
W30x235	0.025	0.20	1.18	32.50	5.00	4.79	50.00	31.30
W33x130	0.020	0.13	0.73	51.70	6.70	4.53	50.00	33.09
W33x241	0.022	0.17	1.03	36.10	5.70	4.39	50.00	34.18
W36x150	0.019	0.13	0.77	52.00	6.40	4.18	50.00	35.85
W36x210	0.021	0.20	1.12	39.10	4.50	4.09	50.00	36.69

Table 4.2. Deterioration model parameters based on predictive Equations ((4.15), 4.17 and (4.19) for various beam sizes (beams with RBS, assumed beam shear span $L=150''$, $L_b/r_y= 50$, expected yield strength $F_y=55\text{ksi}$)

Section Size	θ_p (rad)	θ_{pc} (rad)	A	h/t_w	$b_f/2t_f$	L/d	L_b/r_y	d (in)
W21x62	0.029	0.19	1.08	46.90	6.70	7.15	50.00	20.99
W21x147	0.034	0.32	na	26.10	5.40	6.80	50.00	22.06
W24x84	0.026	0.21	1.20	45.90	5.90	6.22	50.00	24.10
W24x207	na	na	na	26.60	4.40	5.89	50.00	25.47
W27x94	0.023	0.18	1.02	49.40	6.70	5.57	50.00	26.92
W27x217	na	0.34	na	29.20	4.70	5.28	50.00	28.43
W30x108	0.021	0.18	0.99	49.60	6.90	5.03	50.00	29.83
W30x235	0.023	0.30	1.99	32.50	5.00	4.79	50.00	31.30
W33x130	0.019	0.18	0.96	51.70	6.70	4.53	50.00	33.09
W33x241	0.021	0.25	1.62	36.10	5.70	4.39	50.00	34.18
W36x150	0.017	0.18	0.99	52.00	6.40	4.18	50.00	35.85
W36x210	na	0.29	na	39.10	4.50	4.09	50.00	36.69

Table 4.3. Deterioration model parameters based on predictive equations for various tubular column sections and different N/N_y ratios (expected yield strength $F_y=50$ ksi)

Section Size	θ_p (rad)	θ_{pc} (rad)	λ	N/N_y	D/t
HSS200x200x12	0.032	na	2.73	0	16.67
HSS300x300x9	0.016	0.19	0.49		33.33
HSS150x150x2.5	0.013	0.16	0.31		40.00
HSS200x200x12	0.022	na	1.00	0.25	16.67
HSS300x300x9	0.011	0.08	0.18		33.33
HSS150x150x2.5	0.009	0.06	0.11		40.00
HSS200x200x12	0.014	na	0.24	0.4	16.67
HSS300x300x9	0.007	0.02	0.04		33.33
HSS150x150x2.5	0.006	0.02	0.03		40.00

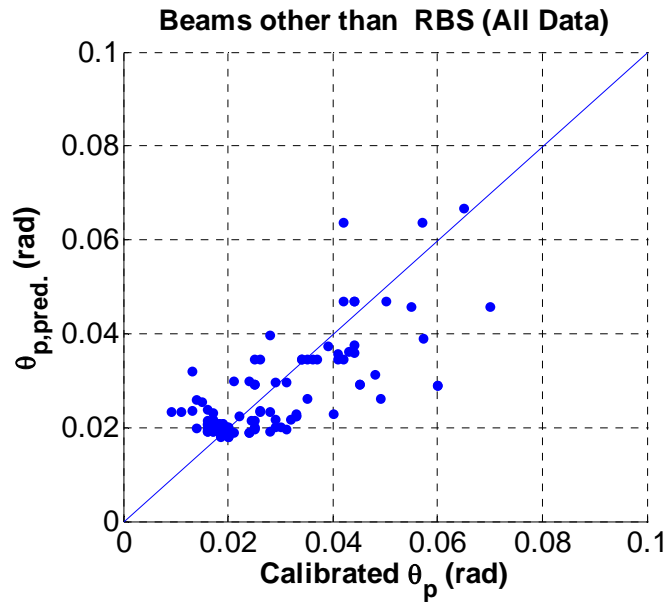
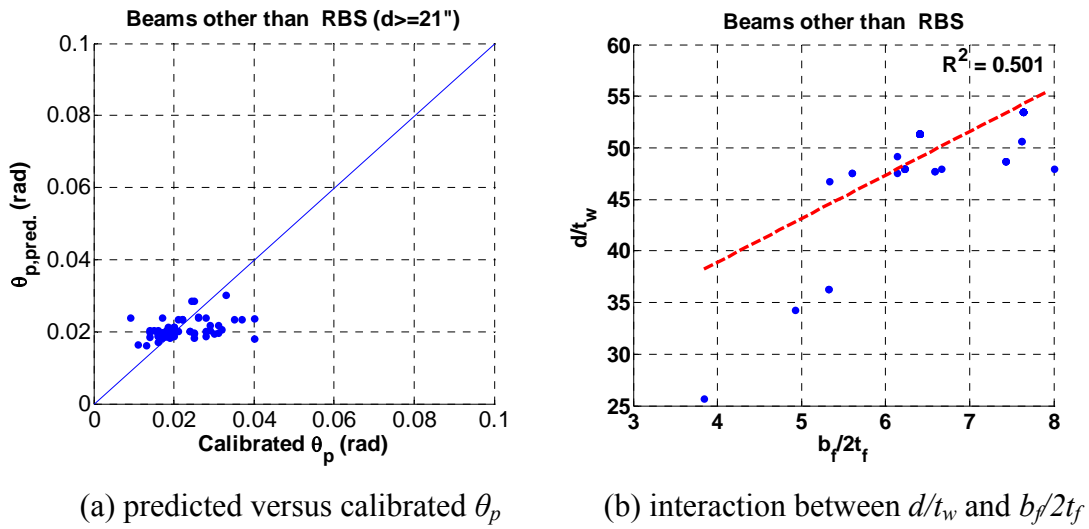


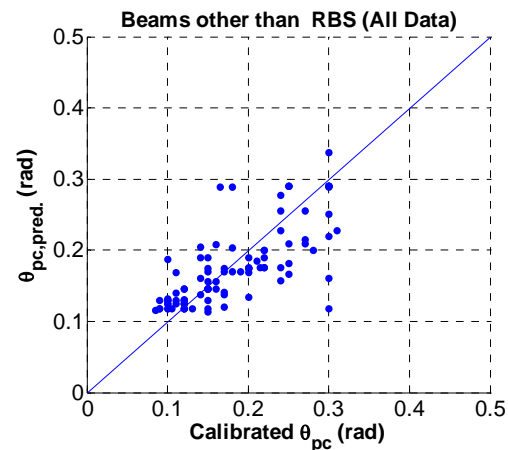
Figure 4.1. Predicted versus calibrated values of θ_p (beams other than RBS, all data)



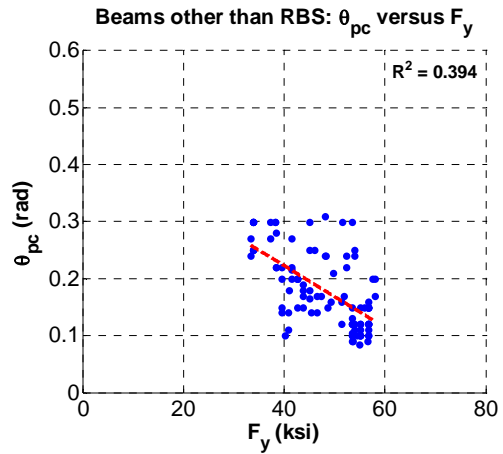
(a) predicted versus calibrated θ_p

(b) interaction between d/t_w and $b_f/2t_f$

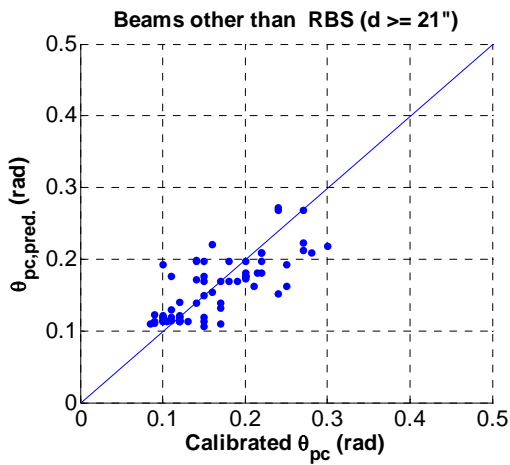
Figure 4.2. Beams other than RBS with $d \geq 21$ "; (a) predicted versus calibrated θ_p ; (b) interaction between d/t_w and $b_f/2t_f$ (beams other than RBS with $d \geq 21$)



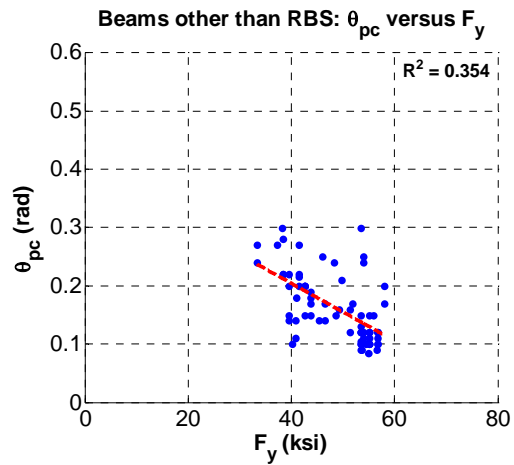
(a) Beams other than RBS (all data)



(b) dependence of θ_{pc} on F_y (all data)



(c) Beams other than RBS ($d \geq 21''$)



(d) dependence of θ_{pc} on F_y ($d \geq 21''$)

Figure 4.3. Predicted versus calibrated θ_{pc} values and dependence of θ_{pc} on yield strength for beams other than RBS for various data sets (W-section database)

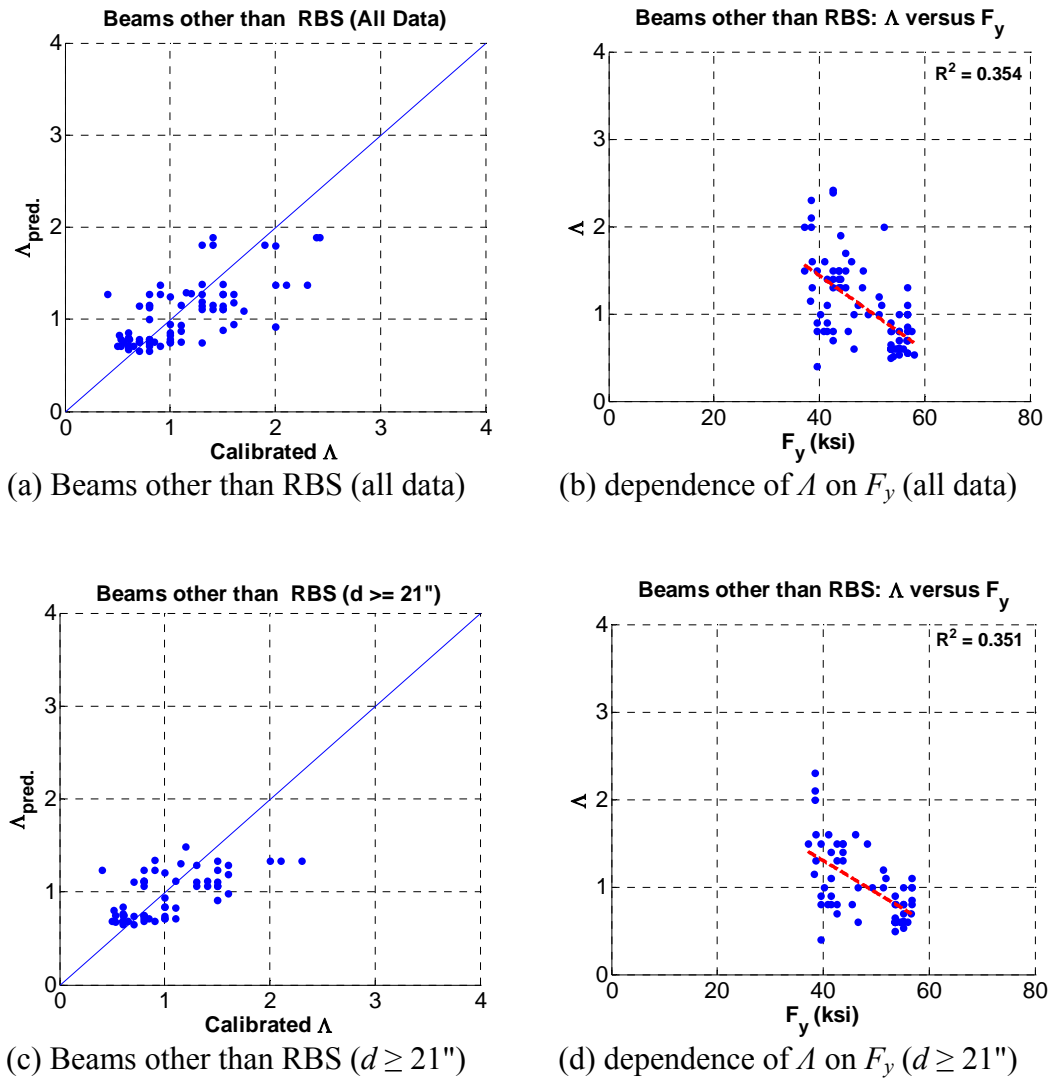
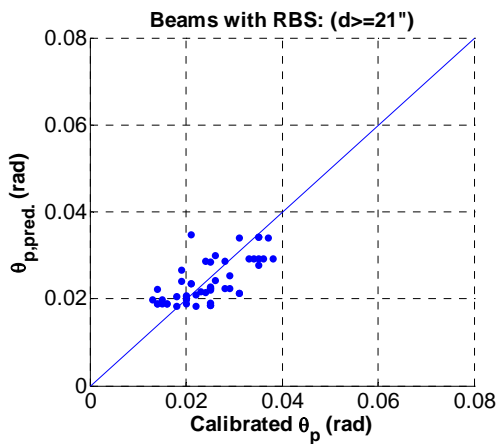
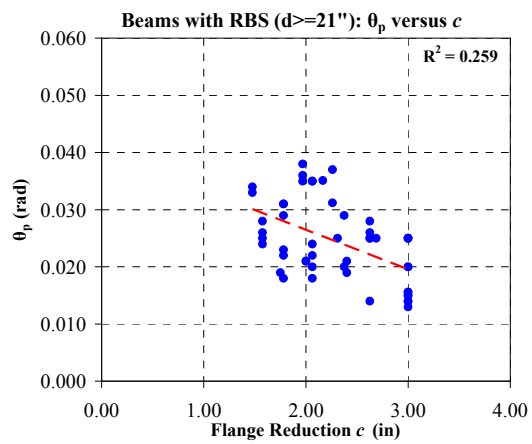


Figure 4.4. Predicted versus calibrated Λ values for beams other than RBS and dependence of Λ on yield strength for various data sets (W-section database)

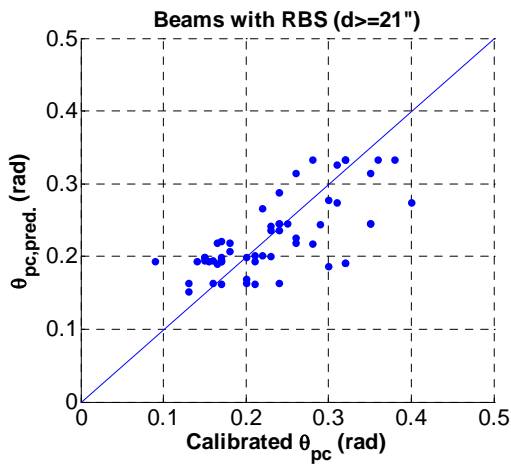


(a) Predicted versus calibrated θ_p

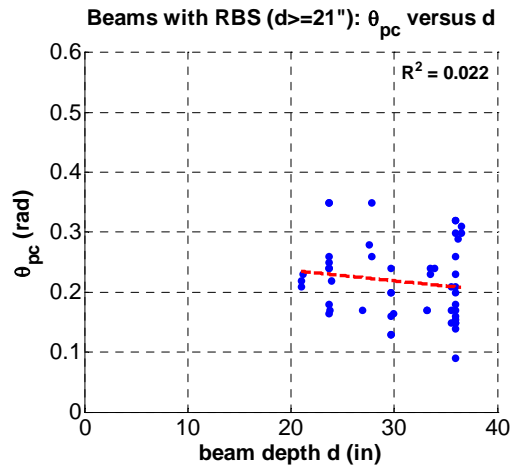


(b) dependence of θ_p on flange reduction c

Figure 4.5. Predicted versus calibrated θ_p values for beams with RBS and dependence of θ_p of beams with RBS versus flange reduction c ($d \geq 21$ ")



(a) Predicted versus calibrated θ_{pc}



(b) dependence of θ_{pc} on beam depth d

Figure 4.6. Predicted versus calibrated θ_{pc} values for beams with RBS and dependence of θ_{pc} on beam depth d ($d \geq 21$ ")

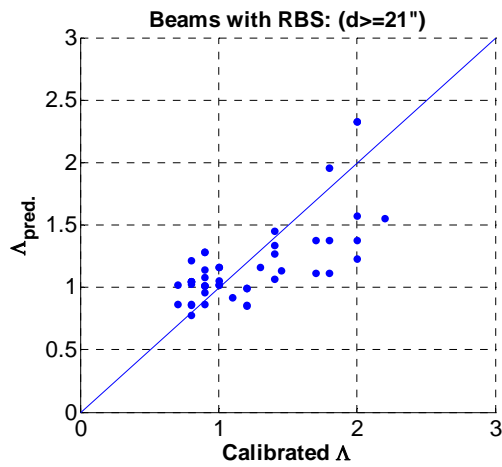


Figure 4.7. Predicted versus calibrated Δ values for beams with RBS ($d \geq 21''$)

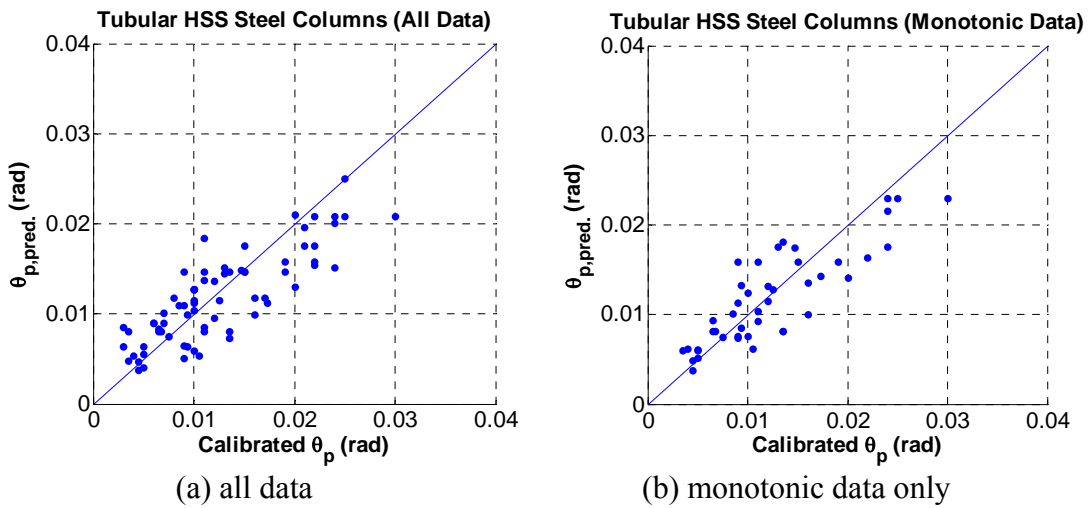


Figure 4.8. Predicted versus calibrated θ_p values for tubular steel columns; (a) all data, (b) monotonic data (HSS database)

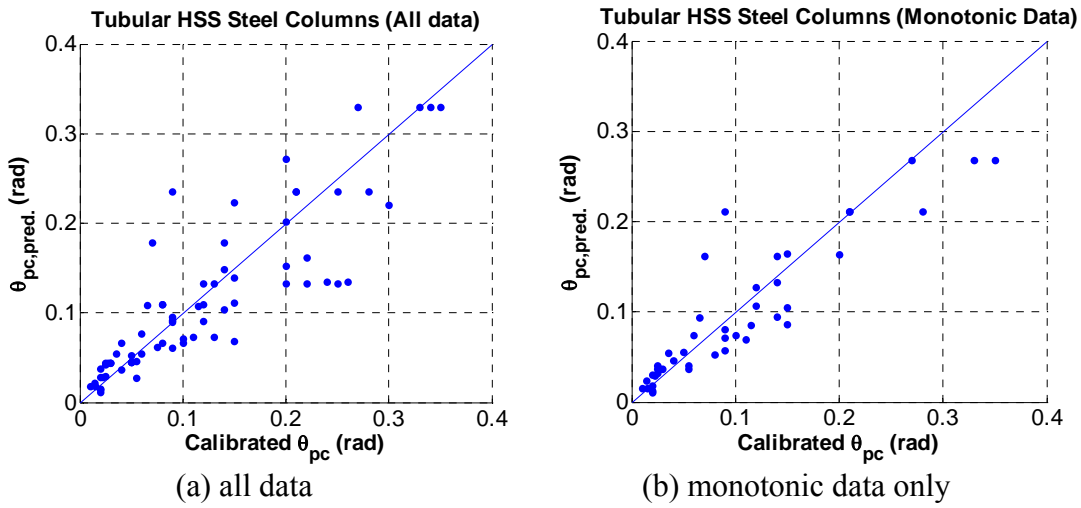


Figure 4.9. Predicted versus calibrated θ_{pc} values for tubular HSS steel columns; (a) all data, (b) monotonic data (HSS database)

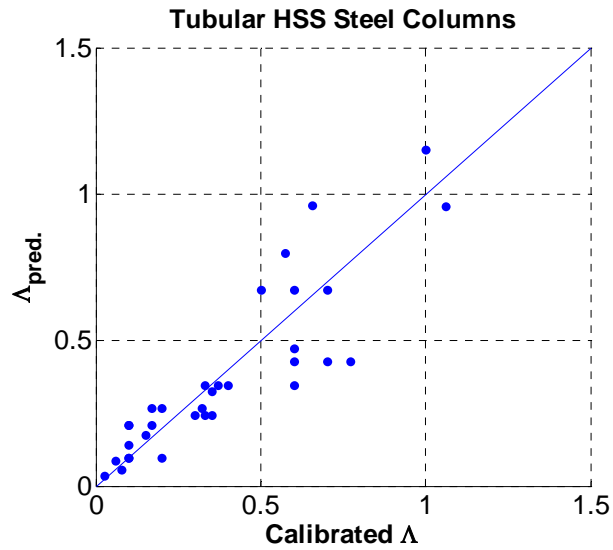
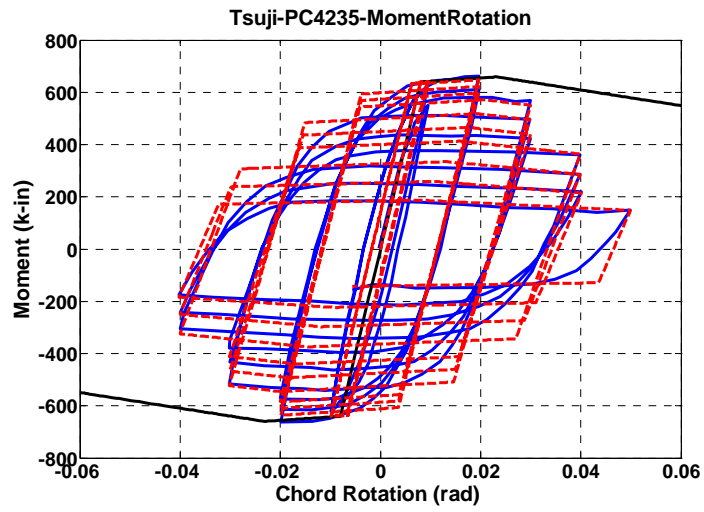
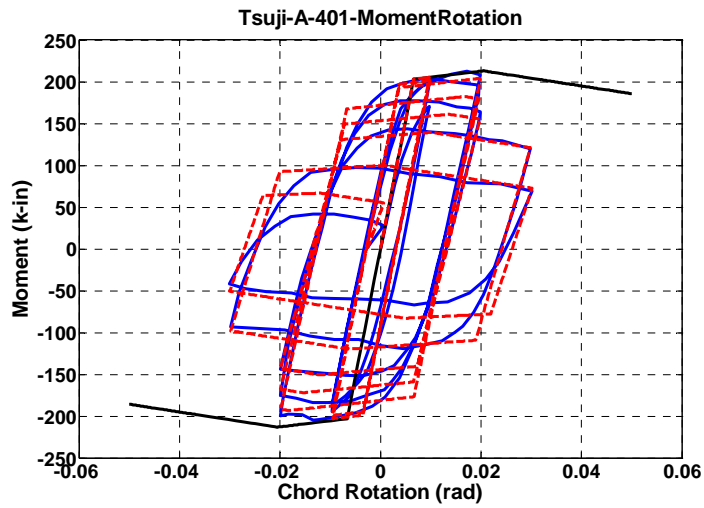


Figure 4.10. Predicted versus calibrated Λ values for tubular HSS steel columns (HSS database)



(a) $N/N_y = 0.20$, $D/t = 28.5$



(b) $N/N_y = 0.40$, $D/t = 28.6$

Figure 4.11. Effect of axial load ratio on cyclic deterioration of tubular HSS columns; (a) $N/N_y = 0.20$, $D/t = 28.5$, data from Tsuji and Nakatsura (1986), (b) $N/N_y = 0.40$, $D/t = 28.6$, data from Tsuji and Nakatsura (1986) (HSS database)

CHAPTER 5

DESIGN OF PROTOTYPE BUILDING AND TEST FRAME FOR SHAKING TABLE COLLAPSE TESTS

5.1 Objective and Scope

Collapse assessment of structural systems necessitates the use of a comprehensive collapse experiment to validate existing analytical modeling capabilities for collapse prediction of frame structures. For this reason a 4 – story steel structure was designed based on current seismic provisions (IBC–2003, AISC–2005), which serves as a prototype structure for this research. Two “identical” 1:8 scale models of the perimeter moment resisting frame of the 4-story steel structure were designed, fabricated and tested up to collapse on the shaking table at the NEES facility at the State University of New York at Buffalo (SUNY). This chapter describes the main design considerations for the 4-story building and summarizes the properties of the moment resisting frame that serves as the lateral load resisting system of this building. This description is followed by a discussion of the scale model used for shaking table experimentation, its structural components that were designed to simulate strength and deformation characteristics of the prototype frame, and the test setup used to simulate gravity and inertia forces on the Buffalo shaking table.

5.2 Design of Prototype 4 – Story Steel Building

The 4-story building shown in Figures 5.1 and 5.2 in plan view is designed for vertical and lateral loads in accordance with LRFD specifications, IBC (2003), SEI/ASCE-02 (2002)

and AISC (2005) design provisions. The building is assumed to be located in Los Angeles and is an office building with moveable partitions, a penthouse (shown in Figure 5.2 in plan view) and a floor system consisting of a metal deck with a 4 ¼" lightweight concrete slab. The structural system is a special moment resisting frame (MRF) with fully restrained reduced beam sections (RBS) designed based on FEMA–350 (2000) criteria. The first story of the building has 15 feet height and all the other stories have 12 feet height. A992 Grade 50 steel is specified for all structural steel components. The assumed dead loads of the building are presented in Table 5.1. Tables 5.2 and 5.3 summarize the seismically effective dead weight for a typical floor and the calculated and design seismic weight per floor, respectively. The focus is on the east west (EW) loading direction. The EW moment resisting frame is shown in Figure 5.3(a); the first three modal periods in this direction are 1.32sec, 0.39sec and 0.19sec. The NS direction moment resisting frame is shown in Figure 5.3(b); the first three modal periods in this direction are 1.22sec, 0.42sec and 0.26sec,.

The structure is classified as Category II; hence the seismic importance factor is equal to 1.0. The building is assumed to be located on Soil type D in Los Angeles. The maximum considered earthquake (MCE) spectral response acceleration at short periods (S_s) and at 1 second period (S_I) is assumed to be 1.5g and 0.9g, respectively, which is close to the values found from the United States Geological Survey (USGS) website (www.usgs.gov, 2004) for longitude 34.11° and latitude -118.55° (1.62g and 0.62g). The design spectral response acceleration parameters S_{DS} and S_{DI} are 1.0 and 0.6.

The upper limit for the predominant period of the structure based on ASCE 7-02 is 0.91sec in the EW loading direction of interest. This period is used to satisfy strength requirements for the building (see Section 9.5.5.3, ASCE 7-02 (2002)). Based on the 0.91sec period the seismic base shear of the structure is 360kips [the design base shear coefficient for the EW direction is $V/W = 0.082$].

Since the building represents a low hazard to human life in the event of collapse, the structure is assigned to seismic use group I in accordance with IBC (2003). For this seismic use group the IBC specifies an allowable story drift Δ_a of $0.025h_{sx}$, where h_{sx} is the story height below level x . The drift requirements of the building are satisfied based on the computer analysis period of the frame, which is 1.32sec in the EW loading direction, and factoring out the redundancy factor ρ ($\rho = 1.384$ for this structure), as permitted by current seismic provisions.

Columns are assumed to be fixed at the base. All columns are spliced at mid-height of the third story. Therefore, critical sections for design of the columns are at the base and the top of the third story. Moment resisting frame column sizes are constrained to W24 sections since such sections offer the potential for larger bending resistance for relatively small axial loads compared to W14 sections. All gravity columns are designed with W14 sections.

Reduced beam section (RBS) moment connections are used and are designed in accordance with FEMA-350 (2000) criteria. A summary of coefficients a , b and c , which specify the geometry of the “dogbone” beam section at each floor, together with the effective plastic section modulus of each girder are presented in Table 5.4.

In order to decrease the probability of having an undesirable mode of failure such as the formation of plastic hinges in columns and ultimately a story mechanism, the final sizes satisfy the strong column weak beam criterion (SCWB) of AISC seismic provisions given by

$$\frac{\sum M_{pc}^*}{\sum M_{pb}^*} > 1.0 \quad (5.1)$$

where $\sum M_{pc}^*$ is the sum of the moments in the column above and below the joint at the intersection of the beam and column centerlines. M_{pc}^* is determined by summing the projections of the nominal flexural strengths of the column above and below the joint to the beam centerline with a reduction to account for the axial force in the column. The final column sizes are also checked for excessive axial forces due to overstrength Ω , which may be critical especially for the exterior columns of the moment resisting frame.

Drift checks are performed based on a mathematical model that includes shear deformations of panel zones (see Sections 8.2.1 and 8.3). The EW moment resisting frame of the prototype structure is modeled in a modified version of the DRAIN-2DX analysis software [Prakash et al. (1993), Gupta (1999), Ibarra and Krawinkler (2005)]. In addition, a centerline mathematical model is used to verify results. The fundamental period of both models of the EW frame is 1.32sec. The applied lateral forces for story drift checks are determined based on this period. For final selection of structural sections, iterations are performed by changing section sizes in order to fulfill drift requirements. Table 5.5 summarizes the story drifts of the EW frame based on the design lateral forces for $T = 1.32$ sec. Forces and moments for strength requirements are based on 0.91sec period in the EW loading direction, as permitted by current seismic provisions. Final beam and interior and exterior column sizes are presented in Table 5.6 together with the expected yield bending strengths at the assumed plastic hinge locations. Table 5.6 includes also the doubler plate thickness of the panel zones designed in accordance with AISC (2005) specifications.

The performance of the SMRF of the 4-story prototype building in the EW loading direction from elastic behavior up to collapse was evaluated based on (1) the nonlinear static method (pushover analysis) [Krawinkler and Seneviratna, (1998)], assuming a lateral load pattern as determined by the equivalent lateral force procedure (Section 1617.4 of IBC (2003)) and (2) a nonlinear response history analysis with a set of 40 ground motions to account for record-to-record (RTR) variability. Section 8.3 includes a detailed evaluation

of seismic performance of the 4 – story EW moment resisting frame of the prototype structure.

5.3 Design of Test Frame and Setup for Shaking Table Tests

A major challenge of this research was the planning, design, specimen fabrication, erection and testing of two collapse test specimens using the shaking table of the Network for Earthquake Engineering Simulation (NEES) facility at the State University of New York at Buffalo (SUNY). The test specimen described in this section is a 1:8 scale model of the 4-story steel frame structure discussed in Section 5.2. The direction of interest is the EW direction in which the structure has two 2-bay perimeter SMRFs. Only one SMRF in the EW direction is represented. The main reasons for representing only half of the 4- story building are costs and the weight limitation of the Buffalo shaking table, since at the 1:8 model scale the total weight of the structure, which had to be simulated in accordance with model similitude laws (Moncarz and Krawinkler, 1982), would be close to 80 kips. A summary of similitude laws used on this research is presented in Table 5.7 based on Moncarz (1981).

The main challenge in the shaking table test was how to support masses and gravity loads of half of the structure, since the latter are required for simulating sidesway collapse. In an analysis model, gravity can be placed on a leaning P- Δ column as seen schematically in Figure 5.4. In the physical model tested on the Buffalo shaking table, two “sub-structures” are designed: (1) the scale model of the SMRF in the EW direction and (2) a mass simulator “frame”. Both frames are connected with “rigid” links at each floor level that carry the P- Δ effect from the mass simulator to the test frame. The “rigid” links have physical hinges at their ends. A detailed description of the main parts of the test setup on the shaking table follows in the subsequent sections. Figure 5.5 shows a schematic representation of the test frame and mass simulator (plan view and elevation) on the shaking table.

5.3.1 Test Frame

The test frame, which is shown in the left half of Figure 5.5, consists of elastic beam and column elements and elastic T or cruciform-shaped joint elements, joined together by plastic hinge elements. The configuration and details of the plastic hinge elements used in the shaking table test structure are the outcome of an extensive component testing program that is discussed in Chapter 6. The challenge was to develop a device that (1) is relatively easy to fabricate and assemble, (2) could be installed at all possible plastic hinge locations of the test frame, and (3) could simulate the deteriorating strength and stiffness properties of plastic hinge regions of beams and columns of the prototype structure at all levels of deformations up to incipient collapse. The mechanical properties of the plastic hinge elements are discussed in detail in Chapter 6. It should be stated up front that the effect of concrete slab (floor system composite action) on the strength and stiffness of the beams is not considered.

For all the case studies used in this research, beams and columns are modeled as elastic elements with plastic point hinges at the ends. The point hinges are represented by rotational springs whose properties are obtained from engineering mechanics principles supplemented by a backbone curve and deterioration rules obtained from the databases discussed in Chapter 3 and idealized by the modified Ibarra-Krawinkler model discussed in Chapter 2.

The use of point hinge models is a simplification of actual behavior. This must be acknowledged up front. It becomes a matter of realization that much more “refined” finite element modeling is quite feasible at this time, but that the reality of design, detailing, and construction uncertainties render refined modeling not necessarily more accurate than simplified point plastic hinge modeling. The plastic hinge elements of the test frame are based on the concentrated plasticity concept.

The plastic hinge element in the test frame, which is shown in Figures 5.6 consists of a spherical hinge whose function it is to transfer shear, two steel flange plates that are machined from bar stock so that plastic hinging (with appropriate deterioration) at the ends of beams and columns is realistically represented at model scales, spacer plates that permits adjustment of the distance between the flange plates and of the buckling length of the flange plates, and four bolts that are post-tensioned after all plastic hinge elements are installed and the test frame is carefully aligned. These plastic hinge elements are inserted at the ends of all beam and column elements of the model structure, acknowledging the possibility of inelastic behavior in each element. A typical interior joint of the test frame with four plastic hinge elements is shown in Figures 5.7(a) and 5.7(b). Figure 5.8 shows a photo and dimensions of a typical flange plate.

The distance from the center of the beam plastic hinge to the column face is set to be as close as possible to the scaled theoretical distance defined by the summation of the parameters a and $\frac{1}{2} b$ summarized in Table 5.4 for the prototype moment resisting frame. Because of geometric constraints it is not feasible to place the plastic hinge elements of the columns at their theoretically calculated locations. Thus, the width of the flange plates for each location needs to be adjusted so that the bending strength of the plastic hinge element is tuned based on the moment gradient of the components. The assumed moment gradients and the bending strength of the plastic hinge elements obtained from scaling laws are shown in Figure 5.9. Since two 1:8 scale models (noted as Frame #1 and Frame #2) are tested to collapse as described in Chapter 7 two sets of flange plates were designed and fabricated in order to match the target bending strengths of the plastic hinge elements. Tables 5.8 and 5.9 summarize the bending strengths and the flange plate dimensions of beams and columns for Frames #1 and #2. The two values of bending strengths for columns are for top and bottom locations in the story. Note that the flange plates for Frame #2 have smaller width because they are fabricated from different bar stock (larger yield strength), but the resulting bending yield strength at all plastic hinge locations is the same as the one of Frame #1.

The elastic beam (see Figure 5.10(a)), column (see Figure 5.10(b)), and joint elements (see Figure 5.11) of the model structure are machined from aluminum stock. All elements are of equal width (2.5"), and the depth of the beams is adjusted so that the lateral stiffness of each story is properly simulated (accounting for the differences in the effects of panel zone deformations on lateral stiffness between prototype and model). Figures 5.12(a) and 5.12(b) show a drawing and a photo of the test frame after completion of installation on the shaking table. A set of drawings of all the aluminum parts of the test frame can be found in Appendix B or can be downloaded from NEES central (<https://central.nees.org/>). Assembly and erection process of the test frame on the shaking table are summarized in Chapter 7.

5.3.2 Mass Simulator and Test Frame – Mass Simulator Links

A critical aspect of the shaking table tests is proper simulation of seismic masses and gravity load effects. Live load effects are ignored, i.e., seismic masses and gravity loads have the same origin. Based on similitude laws, and considering the small self-weight of the test frame, it is necessary to add almost 1/64 of half of the weight listed in Table 5.3 to the test frame. And the weight needs to be added in a manner that properly simulates P-Δ effects all the way to collapse, i.e., at all levels of lateral displacement. To solve this problem this weight is added by means of a mass simulator that is connected to the test frame with links that are axially very stiff but provide no rotational restraint.

Only half of the prototype structure is simulated; hence the total scaled weight that needs to be provided is approximately $4350/128 = 34$ kips. Four steel plates of almost ideal weight were available in the laboratory and are used to simulate gravity (one per floor). The plates, which are approximately 118x79x3.5 inches, are connected together with four vertical links per story. Each vertical link has physical hinges (rod ends) at both ends in order to permit free rotation. The mass simulator, which is illustrated in Figure 5.13(b), is in essence a mechanism that has no lateral resistance when disconnected from the test frame. Table 5.10

summarizes the weight per floor for the test structure together with the target scaled weight based on similitude rules. In Chapter 7 the installation of the mass simulator on the shaking table is discussed. The drawings of the mass simulator can be downloaded from NEESCentral (<https://central.nees.org/>).

The mass simulator is connected to the test frame with horizontal links installed at every floor level. In this manner the test frame and the mass simulator are forced to undergo equal horizontal displacements at every floor level, which is necessary for proper P- Δ effect simulation. The four links are instrumented and act as load cells that provide accurate measurement of story forces applied to the test frame, including P- Δ forces that are transferred from the mass simulator to the test frame. A detailed drawing of the links can be downloaded from NEESCentral (<https://central.nees.org/>).

5.3.3 Collapse Impact Prevention Blocks

Complete collapse of the mass simulator needs to be prevented in order to protect the shaking table facility. This is achieved by placing two carefully dimensioned wooden blocks in every story on the plates of the mass simulator. The height of each block is determined so that every story can rotate in average by 0.25 rad. before the steel plate makes contact with the block.

The gaps between the steel plates and the blocks are based on the collapse mechanism of the test frame, which is determined from pre-test analytical simulations discussed in Chapter 7. Table 5.11 summarizes the gap size per story and the corresponding maximum interstory drift ratio (IDR). The collapse impact prevention mechanism worked perfectly during the shaking table collapse tests, “catching” the mass plates at about the drifts listed in Table 5.11. Detailed drawings of the collapse impact prevention blocks can be downloaded from NEESCentral (<https://central.nees.org/>).

5.3.4 Lateral Bracing Systems and Additional Safety Mechanisms

The shaking table tests conducted at the NEES facility at the State University of New York at Buffalo are unidirectional tests. Both the test frame and mass simulator, described in Sections 5.3.1 and 5.3.2, respectively, have to be laterally supported in order to eliminate out of plane motion. Two separate bracing systems are used. Figures 5.13(a) and 5.13(b) illustrate the bracing systems for test frame and mass simulator, respectively. Each bracing system consists of two vertical braced frames and horizontal tubes that can be fine-adjusted so they act as sliders as the test frame and mass simulator displace horizontally (see Figures 5.13(a) and 5.13(b)). Only the north side (for orientation see Figure 5.5) of each bracing system is laterally braced to the shaking table with angle members because the south side is used for visual observations.

The bracing systems of both frames have multiple purposes, since apart from lateral support they also serve as backup safety mechanisms for the shaking table facility in case of an unexpected failure. Transverse angles are installed between the sliders [see Figure 5.13(a)] of the bracing system of the test frame. The angles are carefully placed to allow a maximum relative displacement at the top floor of the test frame of 20" (approximately 26% roof drift).

The bracing system of the mass simulator provides additional safety mechanisms for the mass plates at each floor. Transverse angles are installed between the top two sliders of the mass simulator (see Figure 5.13b) in order to “catch” the roof mass plate if its relative displacement exceeded 20”. Two sets of channel sections are used on top of the mass simulator bracing system to provide out of plane support for the two individual frames but also to prevent overturning of the mass plates in case that any of the gravity links fractured. An additional safety mechanism used is a 40-ton capacity crane. The top mass plate is connected with chains to the crane during the collapse testing phase. All the drawings of the lateral bracing systems are available through NEESCentral (<https://central.nees.org/>).

5.4 Summary

This chapter presents salient aspects of the design of the 4-story prototype structure and of the test setup used in the shaking table tests. The prototype structure fulfills all requirements of recent seismic provisions (IBC (2003), SEI/ASCE-02 (2002) and AISC (2005)). Strength checks are based on the “code” calculated period, and drift requirements are fulfilled based on the computer analysis period as the design code permits.

The test frame used in the shaking table studies is a 1:8 scale model of one of the two EW moment resisting frames of the prototype. Two nominally identical model frames are tested. The two frames are noted as Frame #1 and #2. Contributions of the gravity columns and beams to lateral strength and stiffness are not incorporated in the test structure. The single frame test configuration is dictated by cost considerations and pay load limitations of the Buffalo NEES shaking table facility.

Beam, column and joint elements of the test frame are machined from aluminum bar stock and are designed to behave elastic up to incipient collapse. Regions of inelastic deformations close to the ends of all beam and column elements of the test frame are represented by plastic hinge elements whose properties are tuned to replicate the moment-rotation characteristics of the prototype beams and columns, including deterioration characteristics. Tuning of these properties necessitated an extensive component testing program that is described in Chapter 6.

P- Δ effects are represented through the use of a mass simulator placed in parallel with the test frame and connected to the frame at all floor levels by very stiff horizontal links. Lateral resistance is provided only by the test frame. The links are instrumented in order to measure the story forces including the effect of P- Δ .

In order to eliminate the risk of damage to the shaking table facility due to gravity load impact after the model loses its lateral resistance, i.e., collapse occurs, a number of different safety mechanisms are designed. The primary collapse prevention mechanism is a set of wooden blocks placed between the mass plates. The wooden blocks are designed such that the gap between the blocks and the plates allows an average 0.25 rad interstory drift ratio.

Table 5.1. Dead loads of the prototype building

LOAD DESCRIPTION	LOAD
4 1/4" Lightweight Concrete Fill (110x5.25/12)	48 psf
Metal Deck	5 psf
Misc. (flooring, ceiling, MEP, fireproofing, etc.)	12 psf
Partition Loads	20 psf
Exterior Cladding	20 psf
Floor beams	50 plf
Girders (average)	100 plf
Columns (average)	200 plf

Table 5.2. Estimation of seismically effective dead weight for typical floor

FLOOR LOADING DESCRIPTION	FLOOR LOADING	TRIBUTARY AREA	WEIGHT IN kips
4 1/4" Concrete Slab	48 psf	10800 ft ²	518
18 ga. Steel Deck	5 psf	10800 ft ²	54
Interior Partitions ¹	10 psf	10800 ft ²	108
Girders (average)	100 plf	300 in.ft	30
Floor Beams	75 plf	840 in.ft	63
Columns (average)	200 plf	240 in.ft	48
Roofing Systems	15 psf	10800 ft ²	162
Misc (MEP, fire proofing, etc.)	12 psf	10800 ft ²	130
Exterior Cladding	20 psf	5040 ft ²	101

¹ for design dead load interior partitions are assumed to be 20psf

Table 5.3. Calculated and design seismic weight per floor in the prototype

Floor	Calculated	Units	Design	Units
Roof	1181	kips	1200	kips
4	1054	kips	1050	kips
3	1054	kips	1050	kips
2	1064	kips	1070	kips
total	4349	kips	4370	kips

Table 5.4. Parameters of reduced beam sections for final prototype design

Floor	<i>a</i> (in)	<i>b</i> (in)	<i>c</i> (in)	Z_{RBS} (in³)
Roof	6.28	18.17	1.88	144
4	6.28	18.17	1.88	144
3	7.50	22.50	2.25	199
2	7.50	22.50	2.25	199

Table 5.5. Story drift under design lateral forces

	Centerline model including structure P-Delta effects	Model with PZ deformations including structure P-Delta effects	Allowable
Story	δ_{xe}/h	δ_{xe}/h	Δ_{α}/ρ
4	0.0144	0.0144	0.0181
3	0.0179	0.0177	0.0181
2	0.0176	0.0174	0.0181
1	0.0128	0.0129	0.0181

Table 5.6. Final sections for interior and exterior columns and beams of EW frame in prototype building, together with doubler plates for interior and exterior panel zones

Floor	Interior & Exterior	$M_{y,p}$		$M_{y,p}$	Dbl. plates	Dbl plates
	Columns	(kips-in)	Beams	(kips-in)	for interior panel zone	for exterior panel zone
Roof	-	-	W21x93	7930	$\frac{3}{4}$ ''	$\frac{1}{4}$ ''
	W24x76	11000	-	-	-	-
4	-	-	W21x93	7930	$\frac{3}{4}$ ''	$\frac{1}{4}$ ''
	W24x76	11000	-	-	-	-
3	-	-	W27x102	10938	$\frac{1}{2}$ ''	-
	W24x131	20350	-	-	-	-
2	-	-	W27x102	10938	$\frac{1}{2}$ ''	-
	W24x131	20350	-	-	-	-

Table 5.7. Summary of similitude laws (after Moncarz, 1981)

Scaling Parameters	Model Type: Artificial Mass Simulation
Length l_r	l_r
Time t_r	$l_r^{1/2}$
Frequency ω_r	$l_r^{-1/2}$
Velocity v_r	$l_r^{1/2}$
Gravitational acceleration g_r	1
Acceleration a_r	1
Strain ϵ_r	1
Stress σ_r	E_r
Modulus of elasticity E_r	E_r
Specific stiffness $(E/\rho)_r$	**
Displacement δ_r	l_r
Force F_r	$E_r l_r^2$
Energy (EN) $_r$	$E_r l_r^3$

** scale ratio undefined is selected by the investigator

Table 5.8. Flange plate dimensions and bending strengths for Test Frame #1

Floor	Interior and exterior column flange plates	$M_{y,p}$ of columns* (kips-in)	Beam flange plates	$M_{y,p}$ of beams (kips-in)
Roof	-	-	0.15x0.58	13.5
-	0.15x0.58	13.5/13.5	-	-
4	-	-	0.15x0.58	13.5
-	0.15x0.58 0.15x1.10	13.5/27.0	-	-
3	-	-	0.15x0.83	19.0
-	0.15x1.10	27.0/27.0	-	-
2	-	-	0.15x0.83	19.0
-	0.15x1.10 0.15x1.34	27.0/33.0	-	-

*The two values for bending strengths are for top and bottom column location

Table 5.9. Flange plate dimensions and bending strengths for Test Frame #2

Floor	Interior and exterior column flange plates	$M_{y,p}$ of columns* (kips-in)	Beam flange plates	$M_{y,p}$ of beams (kips-in)
Roof	-	-	0.15x0.46	13.5
-	0.15x0.46	13.5/13.5	-	-
4	-	-	0.15x0.46	13.5
-	0.15x0.46 0.15x0.88	13.5/27.0	-	-
3	-	-	0.15x0.66	19.0
-	0.15x0.88	27.0/27.0	-	-
2	-	-	0.15x0.66	19.0
-	0.15x0.88 0.15x1.07	27.0/33.0	-	-

*The two values for bending strengths are for top and bottom column location

Table 5.10. Target and actual weight per floor of the test frame

Floor	Target Scaled Weight (kips)	Actual Weight (kips)
Roof	9.4	8.8
4	8.2	8.6
3	8.2	8.6
2	8.4	8.6

Table 5.11. Gap between collapse impact prevention blocks and mass plates together with maximum defined IDR

Story	Gap (in)	IDR (rad)
4	5/8	26%
3	5/8	26%
2	5/8	26%
1	3/4	23%

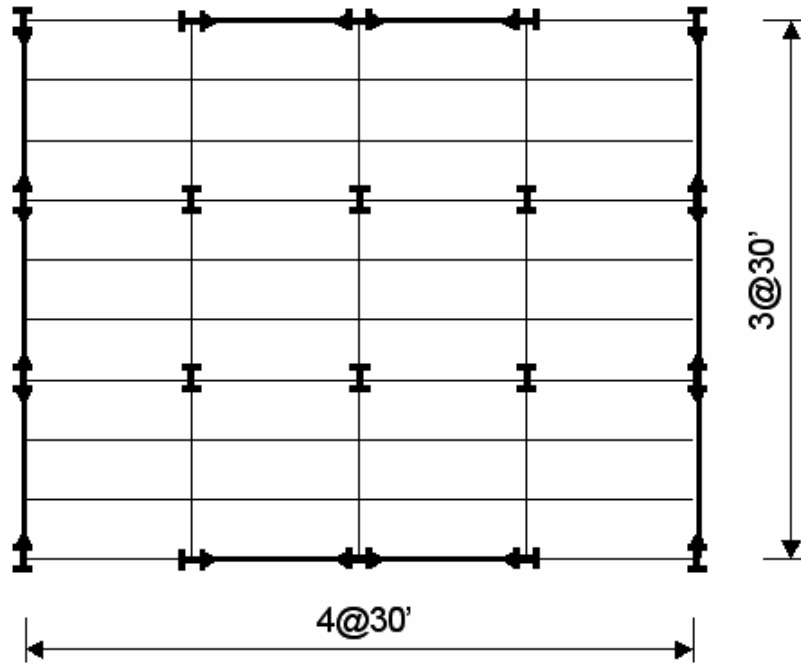


Figure 5.1. Plan view of a typical story of the prototype office building

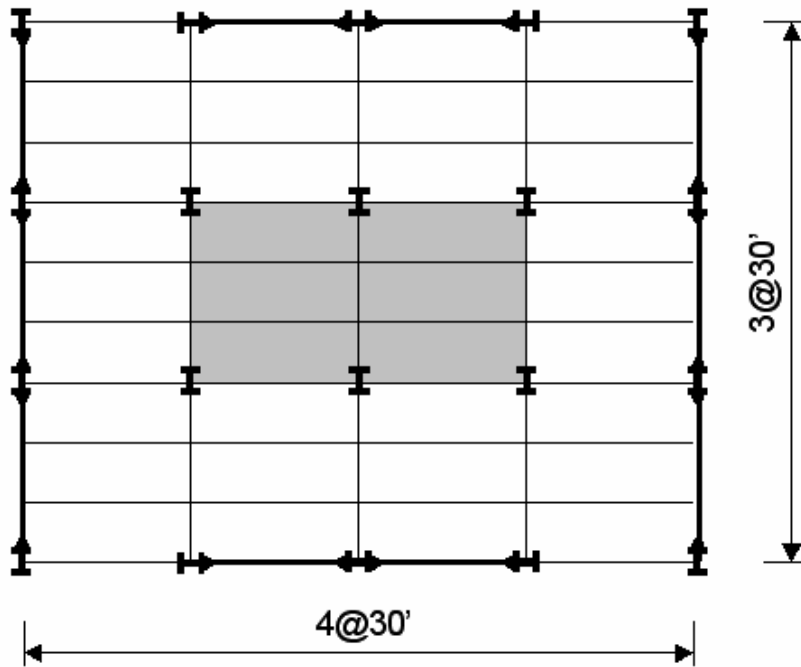
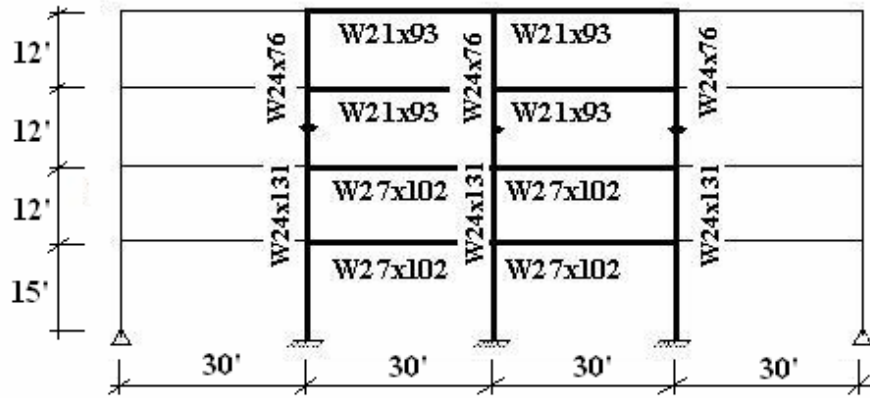
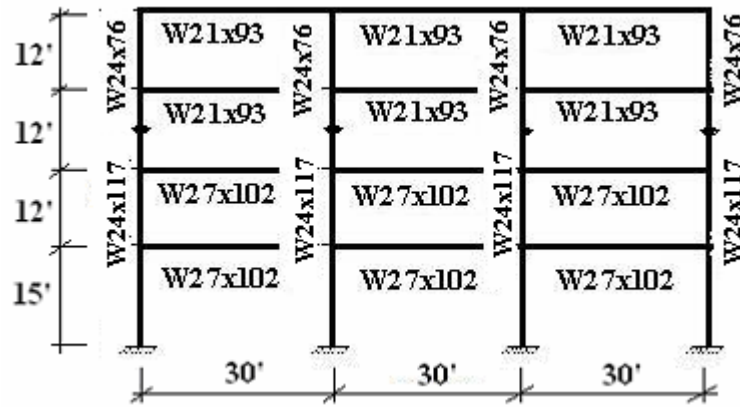


Figure 5.2. Plan view of roof of the prototype office building. Penthouse is highlighted in grey



(a) EW direction



(b) NS direction

Figure 5.3. Elevation views

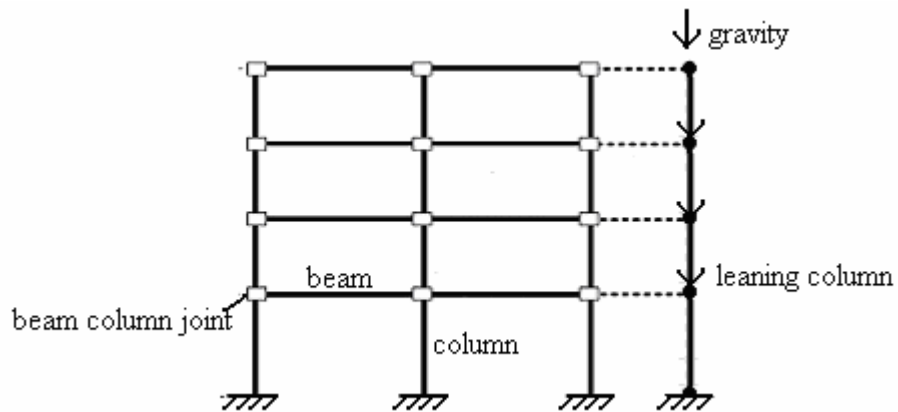


Figure 5.4. EW moment frame with leaning column

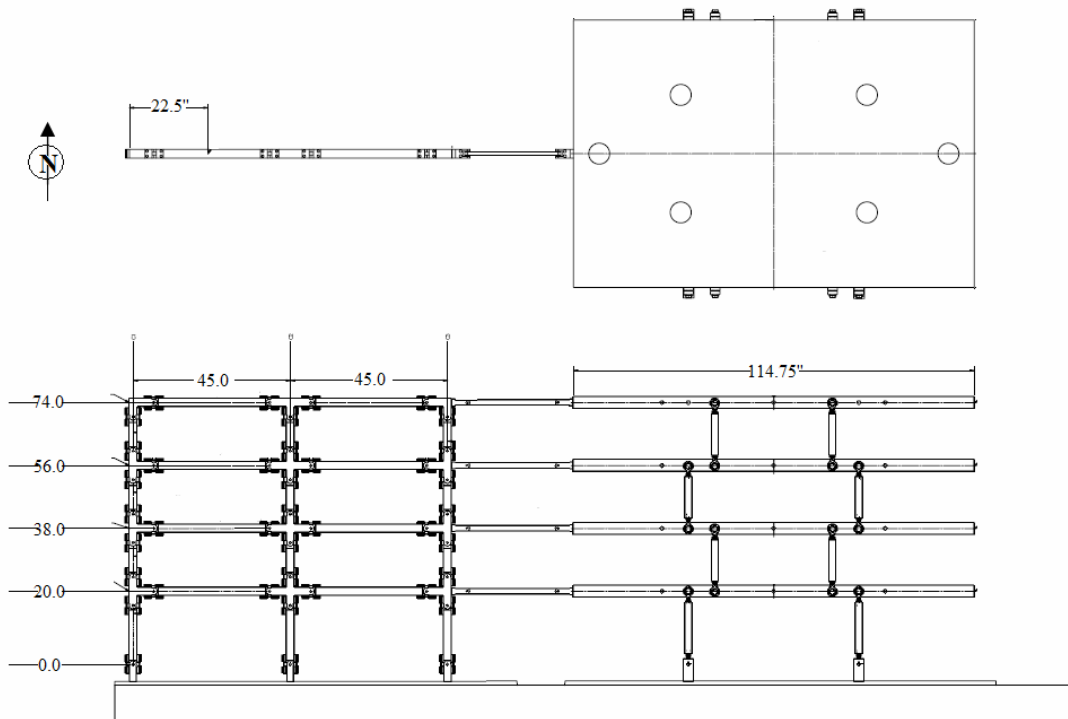


Figure 5.5. Plan view and elevation of the scale model of the EW moment frame and mass simulator

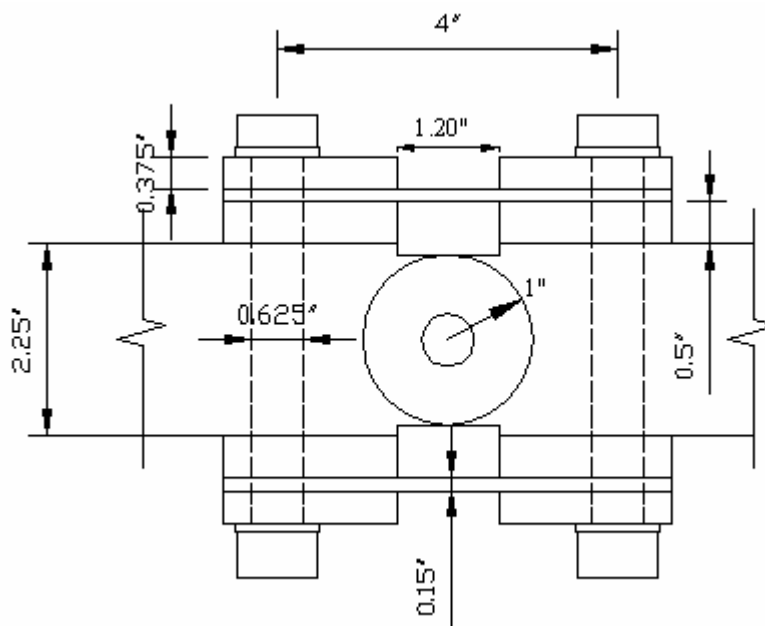
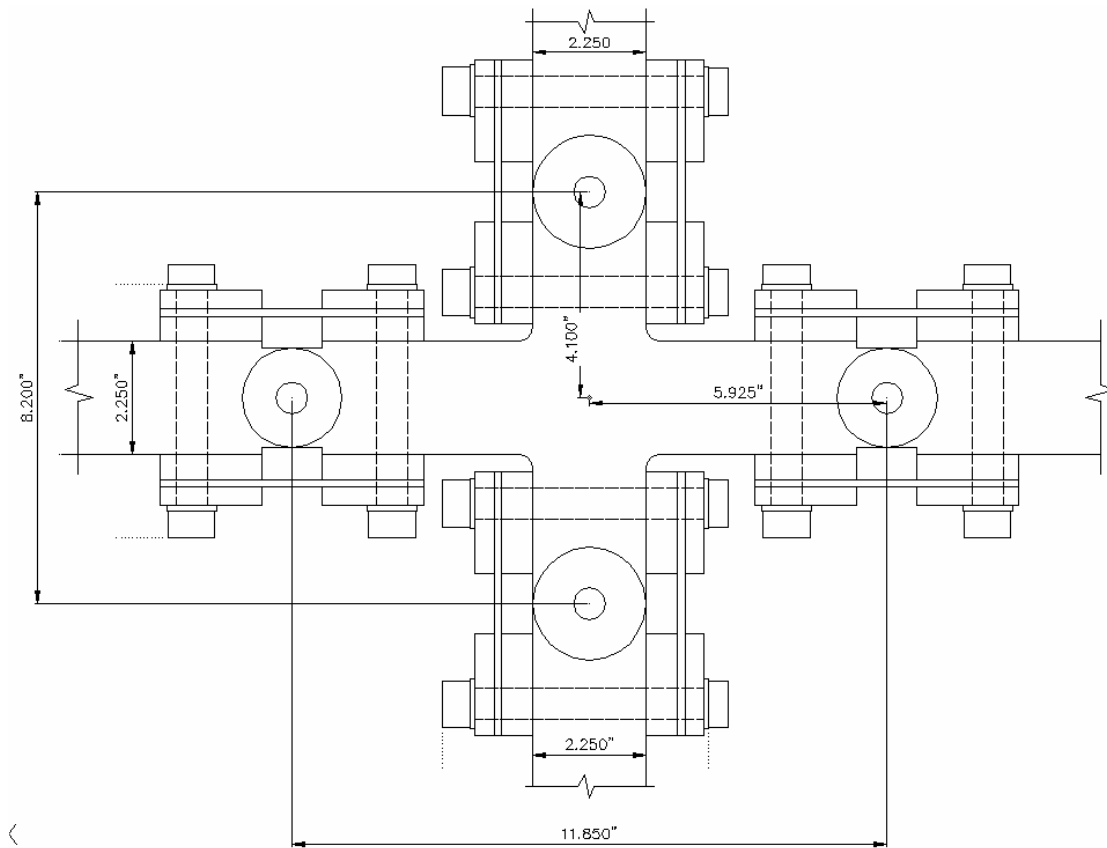
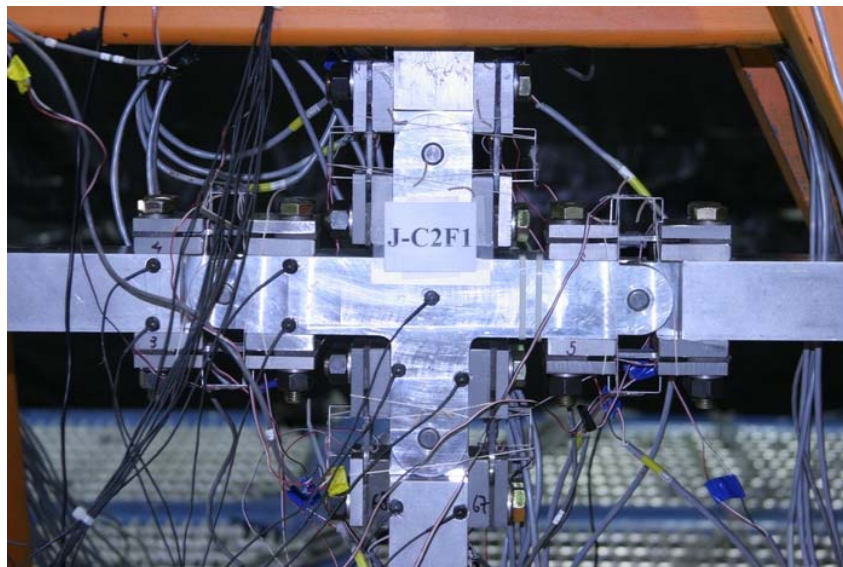


Figure 5.6. Dimensions of plastic hinge element

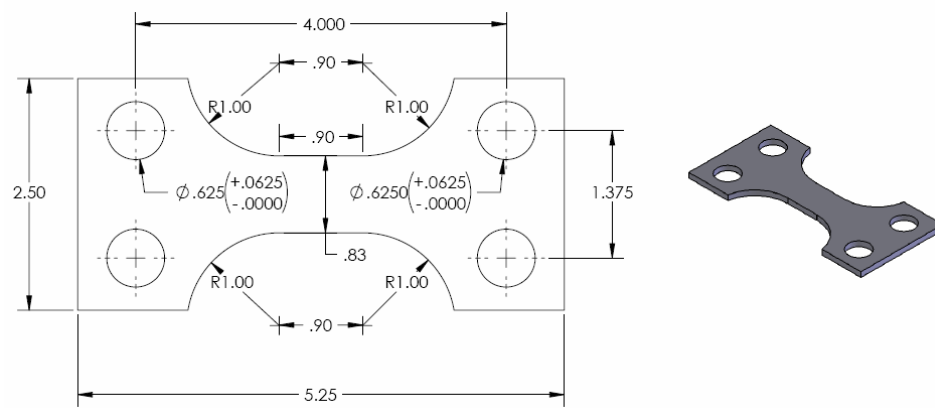


(a) Drawing of an interior joint of the test frame



(b) Photo of interior joint with four plastic hinge elements

Figure 5.7. Drawing and photo of an interior joint with four plastic hinge elements



(a) Typical flange plate



(b) Photo of typical flange plates

Figure 5.8. Drawing and photo of typical flange plates used in plastic hinge elements

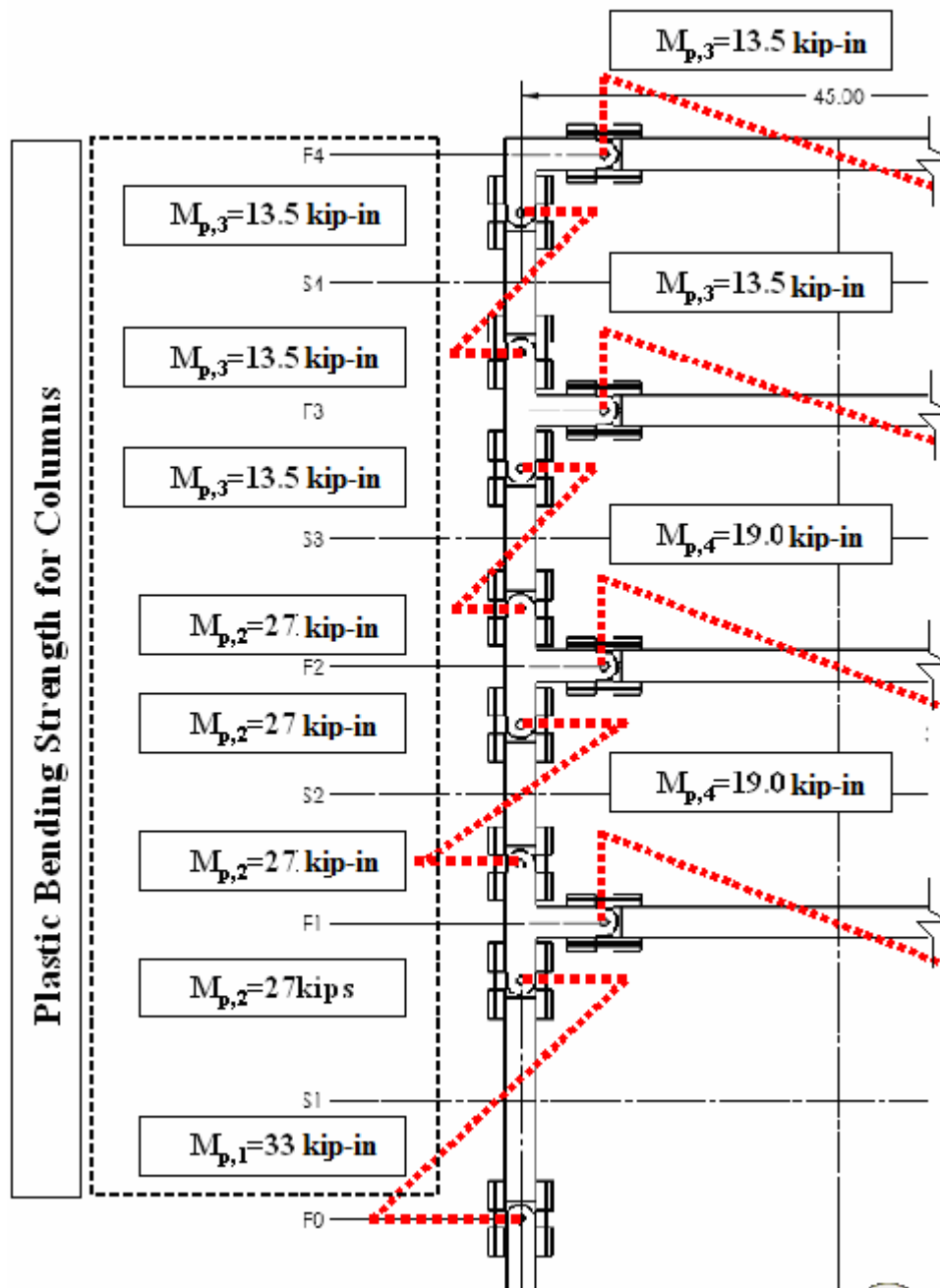
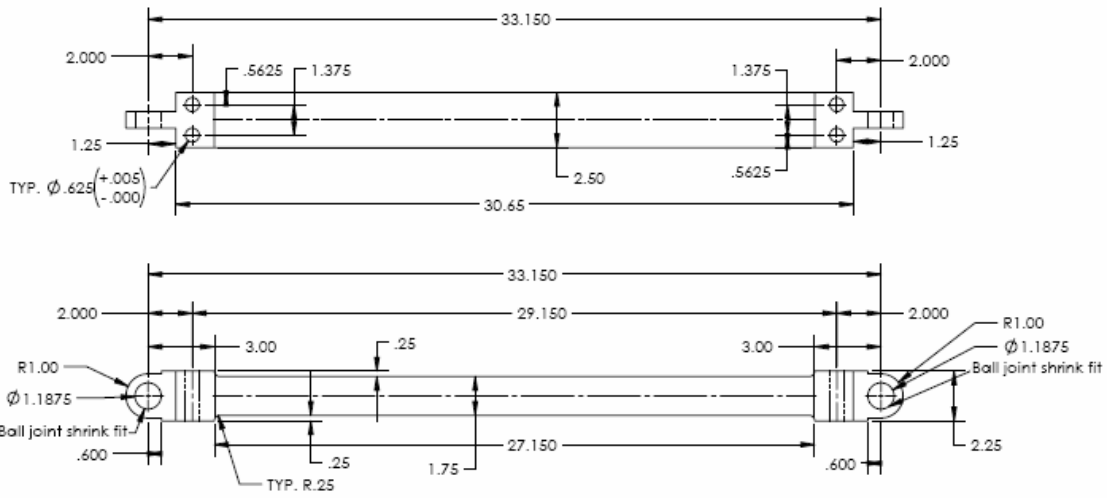
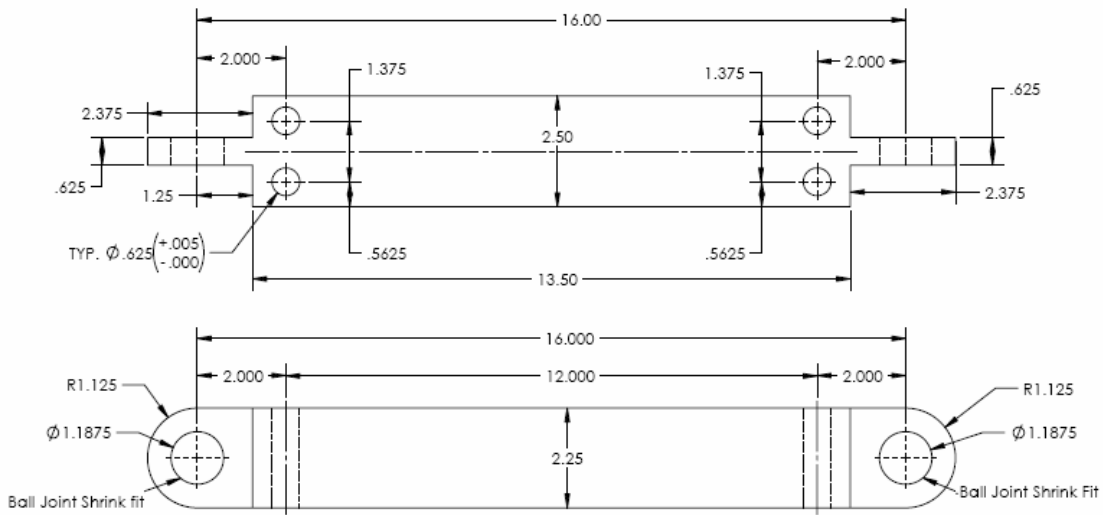


Figure 5.9. Plastic bending strength for beams and columns of the test frame



(a) aluminum beam at first floor



(b) aluminum column in the first story

Figure 5.10. Dimensions of elastic beam and column elements [Cad drawings in Solidworks (2004)]

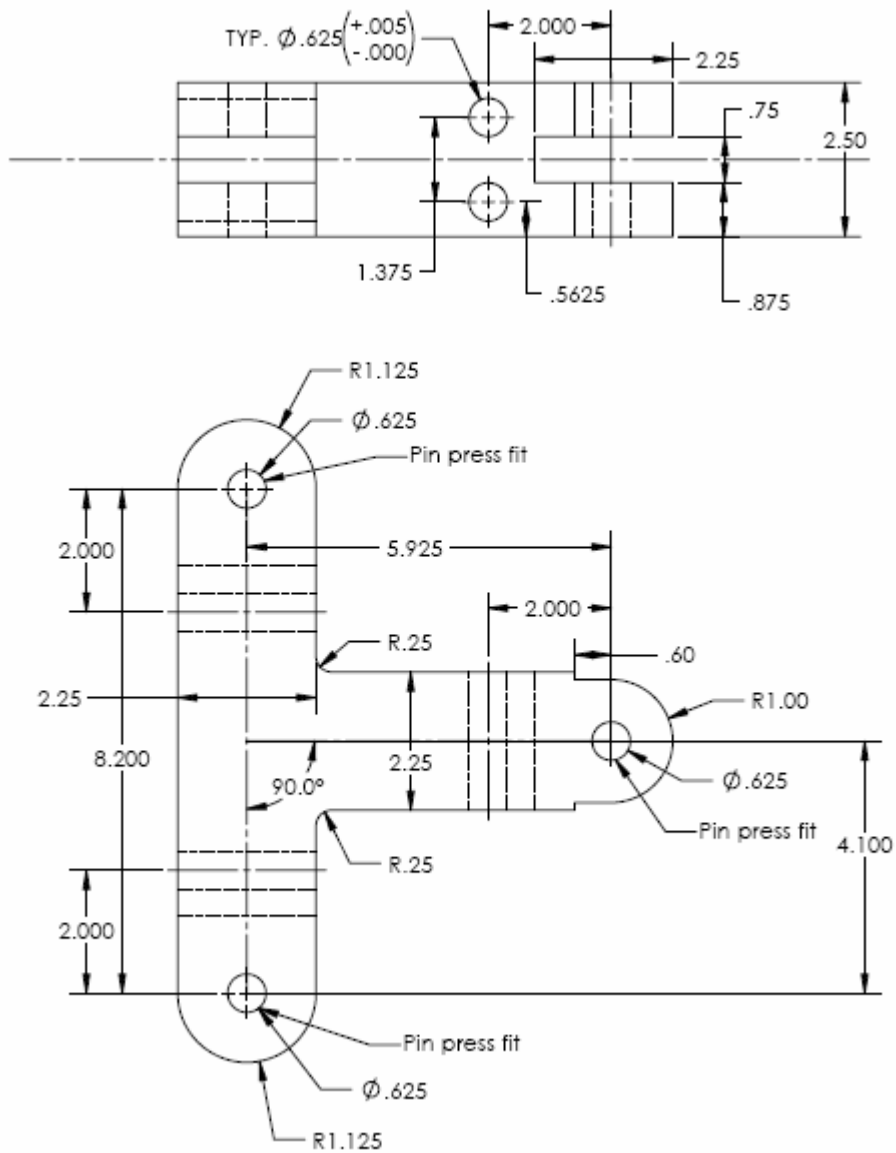
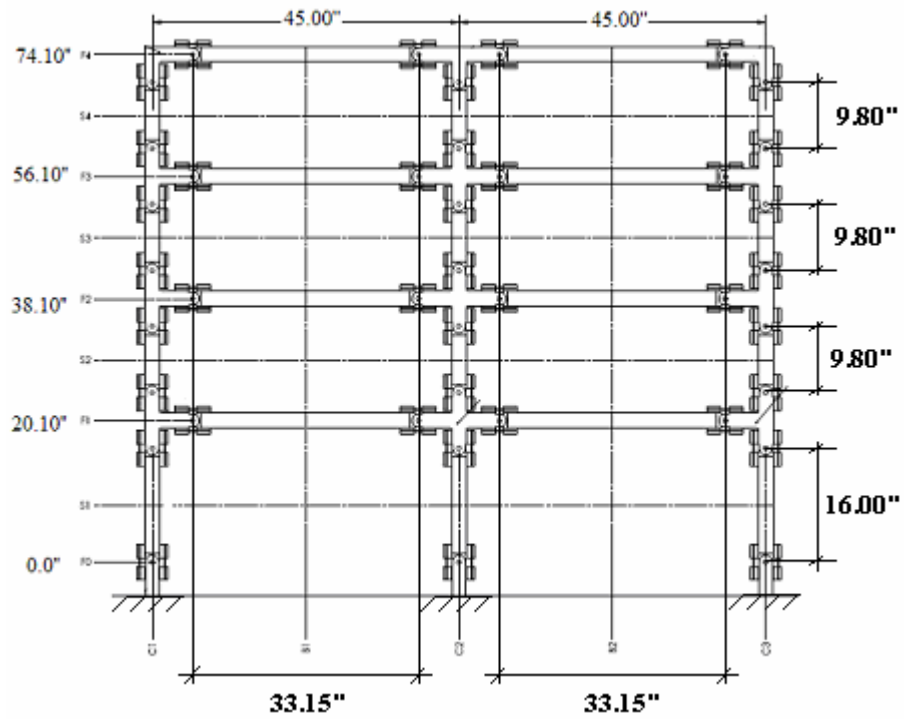


Figure 5.11. Exterior aluminum joint element of test frame [Cad drawing in Solidworks (2004)]

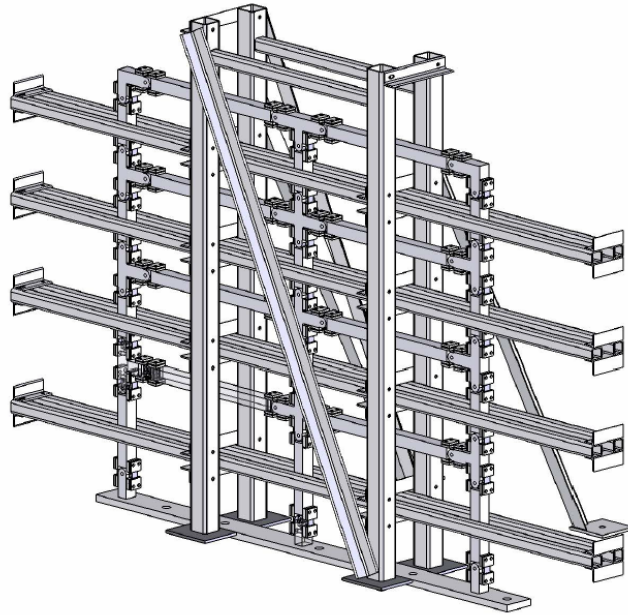


(a) drawing of test frame

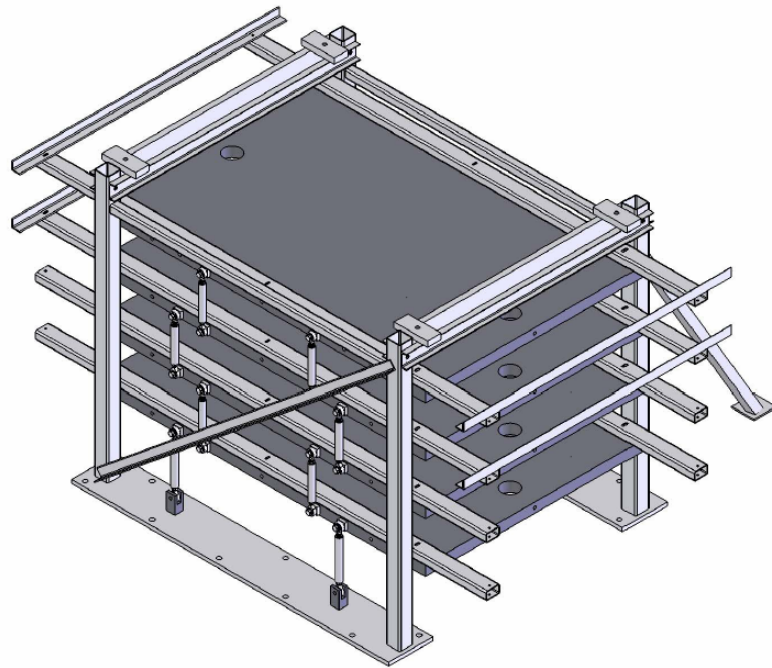


(b) test frame after installation on the shaking table

Figure 5.12. Test frame for shaking table tests; (a) basic dimensions (b) after installation on the shaking table



(a) lateral bracing system for test frame



(b) lateral bracing system for mass simulator

Figure 5.13. Bracing systems for test frame and mass simulator

CHAPTER 6

COMPONENT TESTS

6.1 Objective and Scope

Deterioration modeling and planning for the shaking table tests of the model frame discussed in Chapter 5 required a series of component tests. The objective is to simulate prototype east west (EW) moment resisting frame behavior. The component tests are aimed at (1) identifying the configuration of plastic hinge elements and the flange plates of each plastic hinge element of the test frame, (2) fine tuning the geometry and boundary conditions in order to replicate the hysteretic behavior of the prototype connections and (3) providing mechanical characterization of the deterioration characteristics of each component of the test frame. Additional objectives are the experimental validation of the scaled stiffness of the subassemblages of the test frame and fine tuning of aluminum beams per floor to achieve the target scaled stiffness. Thus a detailed program of component tests is carried out in which the basic dimensions of the flange plates together with their boundary conditions are varied systematically. Specimens with single and double flange plate arrangements are tested both monotonically and cyclically. This chapter focuses on the component test series performed prior to the shaking table collapse tests discussed in Chapter 7. All the component tests are conducted in the laboratory of the John A. Blume Earthquake Engineering Center at Stanford University.

Also discussed in this chapter are component tests of selected plastic hinge elements of the test frame carried out after completion of the shaking table tests at the State University of New York at Buffalo. The objective of these tests is to quantify the effect of deterioration

of critical components of the two test frames for post-shaking table collapse prediction for the two test frames.

6.2 Target Deterioration Characteristics of Plastic Hinge Elements

One of the primary objectives of the shaking table tests is to validate analytical models and their ability to predict sidesway collapse due to P- Δ effects and component deterioration. Since a scale model of the prototype frame is used to replicate “reality” the deterioration characteristics of the idealized plastic hinges need to “match” as close as possible the ones of the 4-story prototype structural components described in Section 5.2 of Chapter 5. The steel database described in Chapter 3 is used to identify the target component deterioration characteristics of the EW prototype frame.

Since it is not feasible to physically simulate the asymmetric behavior caused by composite action of reduced beam section (RBS) moment connections in the test frame, the effect of floor slab on the hysteretic behavior of the beams is also not considered in the component tests. Figure 6.1 illustrates the hysteretic behavior of steel components similar to the ones used in the design of the prototype frame described in Section 5.2. Table 6.1 summarizes the “target” deterioration parameters used for the collapse prediction of the prototype structure after calibrations with the modified Ibarra–Krawinkler deterioration model discussed in Section 2.3.

6.3 Test Specimens – General Description

In the design of the prototype structure in Section 5.2 four different section sizes are used as summarized in Table 6.1. The monotonic and hysteretic behavior of four different plastic hinge elements of the test frame is investigated. The four locations are circled in Figure

6.2(a). The highlighted exterior component subassembly shown in Figure 6.2(a) is used for all the component tests (see Figure 6.2(b)).

Two different options of plastic hinge elements are investigated (which herein will be referred to as specimens type A and type B). Both options include a plastic hinge element with two flange plates fabricated from bar stock. All the parts of the component subassembly that are designed to remain elastic (shown in Figures 5.10 and 5.11 of Chapter 5) are made of aluminum.

For reasons discussed later on in Section 6.4 Type B specimens are selected for final design of the test frame for shaking table experimentation. The subsequent sections include a description of the experimental setup and test specimens.

6.3.1 Experimental Setup

In order to carry out the component test program an experimental setup was built in the laboratory of the John A. Blume Earthquake Engineering Center at Stanford University. The experimental setup could accommodate a large variety of specimens including cantilever and exterior subassemblages. Figure 6.3 shows a specimen in the testing apparatus. The test setup consists of the support frame, loading devices and instrumentation. Figure 6.4 shows a photo taken during testing. The support frame is described in Section 6.3.2. Sections 6.3.3 and 6.3.4 describe specimens type A and B, respectively. Section 6.3.5 discusses loading devices and instrumentation.

6.3.2 Support Frame

The support frame consists of standard hollow square sections and two channel sections (see Figure 6.4). The purpose of the frame is to provide a sufficiently rigid support for the test specimen. A component specimen similar to the one shown in Figure 6.2(b) is attached

to the frame with a set of four bolts. The same frame with a set of two physical hinges can be used to test a beam to column subassembly. To prevent out of plane movement of the specimen, a lateral bracing system is provided. Lateral braces are attached to the support frame and are located on the sides of the two channel sections. Figure 6.4 shows a photo of the main parts of the test setup during a test.

6.3.3 Specimen Type A

Figure 6.5 shows a specimen type A during testing. The elastic parts of the specimen are made of aluminum as mentioned earlier. The exterior joint (see part 1 in Figure 6.6) is machined from a solid aluminum block and acts as a clevis. In the clevis a rod end and a pin are inserted, with the latter press-fitted to the clevis. The threaded rod is inserted in an aluminum block (see Part 2 in Figure 6.6) that is bolted to the aluminum beam made out of hollow square aluminum tube.

The type of component end, representing a plastic hinge element, is shown in Figure 6.6 after installation of all the parts. The two flange plates are machined from steel bar stock. Both flange plates are connected to the aluminum blocks with 1/2" high strength bolts, as shown in the same figure, providing a fixed end. The trapezoidal cut of the clevis (see Figure 6.6) allows to the steel plate to buckle freely.

The flange plates of the plastic hinge element are 1/4" thick at the unreduced region and have a length over thickness ratio (L/t) at the reduced region between 4 to 8. The L/t ratio characterizes the post - buckling behavior of the specimen. In order to achieve the selected L/t ratios each plate was water-cut using a computer numerical control (CNC) machine that reads G-code (Liu et al., 2004) instructions for selective removal of steel material. For ease of fabrication steel material was removed from only one side of the plate. A typical flange plate with L/t equal to 8 of specimens type A is shown in Figure 6.7.

The selected $L/t = 4$ to 8 ratios for exploratory testing are based on a literature review [ASTM E466, (1974) specifications, Morrow and Raske, (1969), Topper and Sandor, (1970)]. These studies suggest that in order to avoid local buckling in cylindrical specimens with tangentially blending fillets between the test section and the ends, the ratio of test section lengths to test section diameter should be less than 4. Zohrei and Krawinkler (1979) conducted monotonic and low cyclic fatigue tests of A36 cylindrical specimens with length-to diameter ratios (L/D) of 1.5 to 2.5 to avoid local buckling.

Each flange plate is sand-blasted near the bolt region in order to create a rough surface and increase the coefficient of friction. This was needed in order to prevent slippage between the flange plates and aluminum parts.

The flange plates are installed with the curved surface facing the inside of the plastic hinge element (see Figure 6.6), since the effect of the additional moment due to eccentricity of the flange plate in the reduced region was less compared to the opposite case.

The test matrix and a summary of results of selected tests of specimens type A is presented in Section 6.5.3.

6.3.4 Specimen Type B

The cyclic behavior of specimen type A is satisfactory except for the fact that early fracture occurs in the flange plates. As discussed later on in Section 6.5.4, the main problem of specimen type A is an undesirable slip; hence the target scaled stiffness of the subassembly was difficult to be predicted accurately.

An alternative to a specimen type A is what is referred to in this chapter as specimen type B. This is the configuration that is employed in the test frame for shaking table

experimentation. The concept is similar to specimens type A but the plastic hinge element and elastic parts are different compared to specimens type A.

The type of component end, representing a plastic hinge element of specimens type B, is shown in Figure 6.8. Drawing of the elastic parts (beams, columns and joint) were presented in Figures 5.10 to 5.11 of Chapter 5. Specimen type B shown in Figure 6.8 consists of two solid aluminum members and the plastic hinge element. A ball joint swivel bearing is shrink – fitted into the machined end of the beam element (Part 2, Figure 6.8). The aluminum beam is then pin-connected to the aluminum joint element whose end is machined into a clevis (Part 1, Figure 6.8). The pin is press – fitted into the clevis, which eliminated any “play” in the hinge. The advantage of specimen type B compared to type A is that any slippage between the aluminum parts is eliminated. A drawing of the plastic hinge element is shown in Figure 6.9(a).

The flange plates (“dogbones”) attached to specimens type B are machined from a steel plate (A572Gr.50). They are designed to be symmetric. Figure 6.9(b) shows the basic control parameters of these flange plates (w and L are the width and length of the reduced section). All flange plates have a constant thickness of 0.15". The width w in the reduced region is varied in order to satisfy the strength requirements of each plastic hinge location of the test frame. The reduced section is water-cut with a radius of 1". Using this radius, results in a stress concentration factor of 1.05 according to Peterson’s stress concentration factor tables for the given geometry (Pilkey et al., 1997).

The flange plates are placed between spacer and clamping plates (Parts 3 and 4 in Figure 6.8). The spacer plates have 1/2" and 5/8" thickness for beams and columns, respectively. The clamping plates are 3/8" thick. Flange plates, spacers and clamping plates are connected to the aluminum beam (Part 2 in Figure 6.8) and aluminum joint (Part 1 in Figure 6.8) with 5/8" high strength bolts, providing a fixed end. Since the aluminum parts of the

subassembly are designed to have a tolerance of 0.002" the holes of the flange and shim plates are oversized in order to have flexibility for final alignment adjustments.

The distance between the spacer plates and between the clamping plates, together with the L/t ratio of the flange plate in the reduced section, control the post-buckling behavior of the plastic hinge element. Thus these distances are considered as additional variables in the testing program of the component tests.

In order to avoid any slip between the surfaces of the aluminum parts and the steel plates the surfaces of the flange and clamping plates were sand-blasted. The pretension force in each bolt is calculated (Euler, 2002) to prevent slip at the maximum applied load on each flange plate. The required torque to pretension the bolts of the connection is determined based on a calibration diagram obtained by using a load cell and a calibrated torque wrench given the length of the bolt. The calibration diagram is shown in Figure 6.10. During installation of the flange plates, the plastic hinge element is first aligned and then clamped on a flat table. The strain gages installed on each flange plate at the outer and inner surfaces are connected to a data acquisition system. By keeping the strain recordings at a low level while pre-tensioning the bolts the stress level in the flange plates is kept low.

6.3.5 Instrumentation

Load and displacement measurements: The tip load applied to the specimens is measured with a load transducer. For all the specimens tested at Stanford University displacement control is used. The displacement is recorded with the displacement transducer of a universal testing machine (t-slot table) as illustrated in Figure 6.4. An additional displacement transducer (string pot) is used in order to measure tip displacement of the test specimens. In order to apply displacement/load to the beam tip a link with rod end bearings at both ends is used as shown in Figure 6.4.

Strain measurements: The instrumentation for the flange plates is designed to be capable of recording strains and deformations in the plastic hinge regions and the onset and propagation of local buckling. Electrical wire resistance gages in a quarter - bridge arrangement are installed at the top and bottom center locations of each flange plate (see Figure 6.11). Most of the strain gages operated satisfactory up to $15000\mu\text{in}/\text{in}$. The strain gages are used to

1. detect initiation and propagation of yielding and initiation of local buckling of the flange plates and
2. correlate strain measurements with forces in the flange plates. The plate force versus strain relationship for each plastic hinge served as a calibration for the shaking table test in order to deduce flange plate forces, plastic hinge moments and beam and column shear forces (see Table C.1 of Appendix C).

Plate deformation measurements: Clip gages are employed to measure the flange plate elongation during each test. These gages are home-made extensometers specially fabricated (thickness t and height h) to cover the entire range of behavior of a flange plate from elastic behavior up to fracture. The clip gages are made out of aluminum alloy. They measure the axial deformation of the flange plate over 1.5" length. The two "legs" of the clip gage have a knife edge that is inserted into a notch on the outside surface of the flange plate in order to make sure that the clip gage does not slip during testing. The clip gage is positioned on the outer surface of the flange plate and is held in place with a set of rubber bands as shown in Figure 6.11. Clip gages are used to

1. measure flange plate elongation/shortening during the experiment and
2. deduce the rotation of the plastic hinge region over 1.5" length

Recording equipment: Clip gage measurements, strain gage readings, tip displacement and load are continuously recorded through a DAQ, shown in Figure 6.12. A total of 9 channels are used for each test. All signals are recorded by a program written in G-language (Conway and Watts, 2003) using LabVIEW 6.1 software. The control unit for the experiment consists of a hydraulic pump and a computer unit that also records the applied load and displacement.

All recorded signals are initially filtered with an analog filter that is embedded into the DAQ and is set to 4Hz. The digital output from all signals is also filtered digitally using a low pass Butterworth filter, designed in MATLAB programming language (2006). The cut-off frequency for each signal is based on a Bode plot (log of magnitude of signal versus frequency), which shows the transfer function or frequency response of a linear, time-invariant system to the individual input signal [Oppenheim et al. (1999)].

6.3.6 Material Properties

Four sets of tensile tests are conducted (two sets each) in order to define the material properties of the A572 grade 50 steel plate used to fabricate the flange plates for all the plastic hinge elements of the model structure. Tensile specimens are fabricated based on ASTM (1974) specifications. The elongation over 1" of each tensile specimen is measured with an extensometer as shown in Figure 6.13(a). Figure 6.13(b) shows a tensile specimen after necking during a tensile test.

The first set of tensile test specimens was stress relieved but the second one was not, in order to quantify the effect of surface machining stresses on the tensile behavior of the flange plates. To remove the effects of prior cold work and machining and grain deformation the first set of specimens was heated to a temperature of 950°F (Totten, 2006), which is just below the eutectoid transformation temperature. The yield and ultimate strength for both materials is presented in Table 6.2 together with the exact dimensions of

the tensile specimens. Figure 6.14 shows the engineering stress strain curves for specimens cut from the A572 grade 50 steel plate with/without stress relief.

6.4 Testing Program

Since various flange plate sizes are needed for the test structure, and since different deterioration characteristics are targeted for the structural elements of the EW prototype four story moment resisting frame, a comprehensive specimen testing program is conducted. During the test series, the length/thickness ratio of the flange plates are varied systematically. The thickness and length of the flange plates need to be tuned such that their pre-and post-buckling axial behavior results in the desired moment rotation relationship of the plastic hinge at the end of the structural element.

For specimens with two flange plates, elastically the axial forces acting on both plates are equal. When one plate buckles, while the other plate is in tension, the force equilibrium in section AA of Figure 6.15 is satisfied with a force generated at the pin location..

6.4.1 Test Series of Specimens Type A

Five exploratory tests of specimens type A are conducted. Four of the specimens are loaded monotonically using a single plate arrangement and varying the L/t ratio. The fifth test is conducted with a specimen with two flange plates. This specimen is loaded cyclically with the SAC loading protocol (Krawinkler et al. 2000), as shown in Figure 6.16. Table 6.3 summarizes the test matrix including basic experimental results for three specimens. Results and subsequent test evaluation are discussed in Sections 6.5 and 6.6. The specimen identification distinguishes each specimen from the other based on (1) the type and number of flange plates used and (2) the test type (cyclic or monotonic tension or compression). For example, specimen “DB1-L/t=4-1-T” means that specimen #1 has a flange plate with L/t

ratio equals to 4, a single plate (1), the specimen is loaded monotonically such that the flange plate is in tension (T).

6.4.2 Test Series of Type B Specimens

For specimens Type B the distances between the spacer plates and between the clamp plates are considered as additional variables in the testing program. These distances control the boundary conditions of the flange plates. In total 38 specimens are tested, Four of them with two flange plates. Twenty eight tests have a single flange plate arrangement and are tested monotonically or cyclically using the SAC loading protocol (Krawinkler et al. 2000) discussed in Section 6.4.1. Table 6.4 summarizes the material properties of steel used for flange plate fabrication if the tensile specimens used are flange plates with $L/t = 3$ and 4 indicating that there is practically no variation of yield and ultimate stresses compared to material properties based on coupon tests discussed earlier. Table 6.5 summarizes the test matrix of specimens type B including basic experimental results for 9 selected specimens. The specimen identification used for specimens type B is slightly different from the one used for specimens type A. For example, a specimen with notation “DB:8- $L/t=4,12,4$ -1-T” means that specimen #8 has a flange plate with $L/t=4$ and an “effective” L/t ratio for clamping plates and spacers equals to 12 and 4, respectively, (here L is the edge-to-edge distance between clamping plates and between spacer plates, respectively), the specimen had a single flange plate (1) and is loaded monotonically such that the flange plate is in tension (T).

6.5 Experimental Results

In this section important experimental data obtained from selected tests conducted for specimens types A and B are presented in tables and graphs. The focus is on specimens of

type B since these specimens are used in the final design of the frames tested on the shaking table of the NEES facility in Buffalo.

6.5.1 Definition of Deflection Components and Rotations

Basic components of deflection are presented in Figures 6.17(a) and 6.17(b) for single and double flange plate specimens. In summary:

- δ_1 is the elastic tip deflection of the specimen due to bending of the aluminum joint (part 1-1)
- δ_2 is the tip deflection of the specimen due to bending of the flange plate(s) (part 2-3)
- δ_3 is the tip deflection of the specimen due to axial deformation of the pin region. This component of deflection is negligible for components with two flange plates and is not considered during test evaluation of specimens with double flange plate arrangement
- δ_4 is the tip deflection of the specimen due to bending of the aluminum beams (part 3-4)
- additional deflections due to panel zone distortion and bolt elongation are evaluated and are found to be negligible (see Section 6.6).

For all components of deflection, shear deformations are neglected.

The rotation over 1.5" length of the plastic hinge region, denoted as $\theta_{1.50''}$, is deduced based on the measured clip gage elongation/shortening. Assuming that the clip gages for top and bottom flange plates measure axial plate deformations of Δ_t and Δ_b , the deduced $\theta_{1.50''}$ is given by

$$\theta_{1.50''} = \frac{\Delta_t - \Delta_b}{h} \quad (6.1)$$

in which h is the centerline distance between the two flange plates. For single plate specimens Equation (6.1) becomes

$$\theta_{1.50''} = \frac{2 \cdot \Delta_{t(or\ b)}}{h} \quad (6.2)$$

Chord rotation θ_{Chord} is defined as the rotation with respect to the centerline of the pin (center of plastic hinge location). For single plate specimens θ_{Chord} is given by

$$\theta_{Chord} = \frac{\delta_2 + \delta_3 + \delta_4}{L} \quad (6.3)$$

in which L is the distance from the point of load application to the centerline of the pin, as shown in Figure 6.17. For a specimen with two flange plates the same equation is used but setting the δ_3 term equal to zero.

6.5.2 Definition of Yield Load and Yield Displacement

The tip load applied to the specimen is designated with P . The yield load for each specimen, P_y ($M_y = P_y \cdot L$), is obtained from the monotonic load-displacement curve and is considered to be the lower value of the plateau region before the specimen reaches the strain hardening slope. The yield displacement δ_y (rotation θ_y) is then defined as the ratio of the yield load over the elastic stiffness of the specimen (see discussion in Section 6.5.4.2).

Given the tip load P , the moment at the plastic hinge location is obtained as $M = P \cdot L$, and the force in the flange plate can be computed as $F = M/(h/2)$ if a single flange plate is used.

If two flange plates are used, the flange plate forces cannot be obtained directly from equilibrium (see Figure 6.15), but can be deduced from the force versus strain calibrations obtained from tests with a single flange plate.

6.5.3 Specimens Type A - Results

The principal experimental results are presented in Table 6.3 for selected tests of specimens type A. This table lists the specimen ID, the yield load, P_y , and associated tip displacement, δ_y , and plastic hinge moment, M_y , the load at which the plate buckles, P_b , and associated rotation over 1.5" length, $\theta_{1.5}^b$, and plastic hinge moment, M_b . The table also includes the ultimate rotation capacity over 1.5" length $\theta_{u,1.5}$ at which fracture of the flange plate occurs. The total elastic stiffness (K_e) of each specimen and the rotational stiffness over 1.5" length $K_{e,1.5}^R$ of the plastic hinge element are also included in Table 6.3. As observed from the experimental data, the K_e for specimens with a single plate is different for tension and compression loading because of the different axial deformation of the pin region for positive and negative loading.

6.5.3.1 Monotonic and Hysteresis Diagrams

Monotonic and hysteresis diagrams, characterizing the overall behavior of three selected specimens and the behavior of the plastic hinge element, are presented in Figures 6.18 to 6.20. The first specimen [Figures 6.18(a) to 6.18(c)] has a single plate with L/t ratio equal to 4 and is loaded monotonically such that the flange plate is in tension. The second single plate specimen (Figures 6.18d to 6.18f) has the same L/t ratio but the flange plate is loaded in compression. The third specimen has two plates (Figures 6.19 and 6.20) and is subjected to cyclic loading. The following plots are included:

1. Tip load – tip displacement ($P - \delta_{tip}$), describing the overall behavior of each specimen

2. Moment – rotation over 1.5" length ($M_c - \theta_{1.5''}$), describing the behavior of the plastic hinge region
3. Moment – chord rotation ($M_c - \theta_{Chord}$), describing the behavior of the beam including deformations due to bending in the plastic hinge element and elastic beam (parts 2-3 and 3-4 as defined in Figure 6.17). (Only for the monotonic tests)

An evaluation of these diagrams makes it possible to obtain a complete picture of the contribution of each component to the overall behavior of the subassembly.

As observed from the monotonic tests of single plate specimens [Figures 6.18(a) and 6.18(d)], the elastic stiffness is different for tension and compression loading directions as already mentioned earlier. The reason is the undesirable component of deflection δ_3 due to axial deformation of the pin (rod end), which is different in the two loading directions.

From the monotonic tension tests with single plate arrangement [see Figures 6.18(a) to 6.18(c)] it is observed that the specimen yields relatively early because of the combined axial and bending effect. The reason why no yield plateau is present is the eccentricity of the flange plate, which introduces an additional moment at the flange plate. Figure 6.18(b) shows that specimen DB1-L/t=4.0-1-T fractures at about $\theta_{1.5''} = 0.07\text{rad}$ under monotonic tension, which indicates that specimens Type A fracture relatively early.

Based on the compression test of an identical specimen with $L/t=4$ (see Figure 6.18(d)) the flange plate buckles at a load slightly smaller than the yield load in tension. Based on Figures 6.18(e) and 6.18(f), which show the moment at the centerline of the pin versus the rotation over 1.5" and chord rotation, respectively, it is difficult to estimate an elastic

rotational stiffness because of slip between parts 2 and 3 (see Figure 6.6 for description of parts 2 and 3) and because of clip gage sensitivity in the elastic range.

The bending effect due to eccentricity of the flange plates for specimens type A is also evident in the overall behavior of the specimen with two flange plates. As seen in the tip load -tip displacement diagram of Figure 6.19 and the $M-\theta_{1.5''}$ diagram of the same specimen in Figure 6.20 the hysteretic behavior is asymmetric.

The disadvantage of specimen type A, for final design of the test frame for shaking table testing, is an undesirable slip that is observed between parts 2 and 3 (see Figure 6.6 for definitions), which is reflected in the elastic loading and unloading stiffnesses of specimen DB5-L/t=4.0-2-Cyclic as shown in Figure 6.19. The prediction of a scaled stiffness of the subassembly becomes unreliable because of this slip. This would render a period calculation of the model structure tested at the NEES facility in Buffalo rather ambiguous.

As seen from Figure 6.18b, specimens of type A fracture monotonically at about $\theta_{1.5''} = 7\%$. Cyclically, as indicated in Figure 6.20, both flange plates fracture early during the loading history (during the 2nd cycle at 3% story drift). The reason is the combined axial and bending loading condition due to eccentricity of the flange plate. The ultimate rotation capacity $\theta_{u,1.5''}$ of specimens of type A under cyclic loading is very low (see Table 6.3) compared to the target values for beams with RBS. Ricles et al. (2004) reported that ductile tearing in an RBS region occurs at about 7 to 8% total rotation. Figure 6.21 shows a summary of photos at critical points of the loading history during a cyclic test. Figures 6.21(c) and 6.21(d) illustrate the fractured flange plates of specimen type A at 3% story drift.

For the reasons discussed in the last two paragraphs it was decided to explore a different plastic hinge element configuration. Hence, specimens of type B were designed and tested. Pertinent results are discussed in the following sections.

6.5.4 Specimens Type B - Results

The first five tests of specimens type B are uniaxial tensile tests performed in a tension test machine. These tests are used to: (1) confirm material properties from the coupon tests discussed in Section 6.3.6 (see Tables 6.2 and 6.3 for comparisons), and (2) assure that the radius cut is not causing early fracture.

Table 6.5 summarizes the principal experimental results of type B specimens, including the yield load, P_y , and associated tip displacement, δ_y , and plastic hinge moment, M_y , the load at which the plate buckles, P_b , and associated rotation over 1.5" length, $\theta_{1.5}^p$, and plastic hinge moment, M_b . The ultimate rotation capacity over 1.5" length at which flange plate fracture occurs, as well as the total elastic stiffness of the specimens and the rotational stiffness of the plastic hinge element over 1.5" are also reported in the table. The stiffness values are needed for fine-tuning the size of the elastic beams of the test frame to match the target scaled frame stiffness.

6.5.4.1 Monotonic and Hysteresis Diagrams

A summary of monotonic and hysteresis diagrams of five tests are presented herein, characterizing the overall behavior of selected specimens and the behavior of the plastic hinge element. Figure 6.22 summarizes results from monotonic compression and tension tests of specimens with a single plate with $L/t=6$ and width $w=0.92$ inches. The instant drops in strength at various locations of the monotonic diagrams of Figure 6.22 are attributed to the fact that at these points each test was paused for visual inspection. Appendix C includes a summary report of results for selected tests with single and double flange plate arrangement.

Comparing the compression and tension tests (see Figure 6.22) it is concluded that the compression specimen DB36 yields first, and then buckles at around 0.60kips (tip load) as

seen from Figure 6.22(d). For the definition of the yield moment based on the experimental data the lower bound of the plateau region of the monotonic tension curve is used (See Figure 6.22b).

The elastic stiffness of specimens with single plate arrangement in tension and compression is different (3.0 versus 2.74 kips/in) due to different axial deformation around the pin region in the two loading directions.

Typically, during a compression test and after loading the specimen to about 4" tip displacement (25% IDR) the specimen was unloaded and pushed all the way in the opposite direction (tension) till the flange plate fractured. As observed in Figure 6.22(a), during unloading the behavior of the specimen is pinched. The pinching is clearly noticeable in the execution of cyclic tests (see Figures 6.23 and 6.24 for specimens with single and double plate arrangements, respectively) with a symmetric loading protocol. This pinching effect is a weakness in the model simulation of prototype RBS behavior because pinching in actual RBS hysteretic diagrams is barely noticeable. Most of the pinching effect in the hysteretic response of the model connection is attributable to the absence of web bending resistance in the model plastic hinge element. In these elements flange plate buckling is not restrained by a web, and during subsequent load reversal the flange will straighten out at a much reduced axial stiffness before picking up full tensile resistance, which causes pinching behavior more characteristic for axially loaded steel members.

Figure 6.23 illustrates two cyclic tests of single plate specimens. The only difference between the two specimens is the width w of the flange plate (0.92" versus 0.58"). Apart from the noticeable difference in strength, the two specimens have very similar rates of strength deterioration.

Figure 6.24 shows the hysteretic behavior a specimen with two plates that have a width of 0.92" and an $L/t = 6$. The boundary conditions of the two flange plates are the same as for specimens DB35 and DB36.

Figure 6.25 shows the moment at the centerline of the plastic hinge element versus chord rotation of specimen "DB: 33,34-L/t=6,8,8,2-Cyclic" with respect to the pin. The ultimate rotation capacity of the connection is about 0.08 rad. Ricles et al. (2004) and Uang et al. (2000a) reported similar rotation capacities for beams with RBS before ductile tearing was observed within the RBS region. Figure 6.26 summarizes observations at important points during the cyclic loading history applied to the specimen with two flange plates from local buckling till fracture of both flange plates. Pinched behavior of the hysteresis loops again is evident for this test, which is performed with the symmetric step-wise increasing loading history prescribed by the loading protocol shown in Figure 6.6. As will be shown in Section 6.7, the pinching effect diminishes if a loading history deduced from the shaking table test results described in Chapter 7 is employed, in which the test frame is subjected to a series of ground motion of increasing intensity that cause drifting of the response to one side rather than the symmetric drift history applied to the specimens summarized in this section.

6.5.4.2 Strain Gage Results

Based on the experimental results obtained from strain gage readings of specimens Type B, strain values are reliable up to 15000μ in/in. Figure 6.27 shows the tip force versus strain (ϵ) at the outer and inner location of a flange plate for (1) a monotonic compression test (see Figure 6.27(a)), (2) a monotonic tension test (see Figure 6.27(b)) and (3) a cyclic test (see Figure 6.27(c)). All specimens have the same characteristics in terms of flange plate dimensions and boundary conditions. The yield strain ϵ_y ($1552 \mu\epsilon$) of the specimen is superimposed in all the figures as a reference value for tension and compression side. As observed from the experimental results, the outer surface of the flange plate always yielded

first because of local plate bending. But the average strain is close to the one obtained from the tension test.

In Appendix C a summary of calibrations for average strain versus flange plate force for all the critical plastic hinge elements is provided. The equivalent modulus defined as the ratio of the flange plate force over the average strain is used in Chapter 7 to validate story forces measured from horizontal links and to deduce plastic hinge moments and column shear forces at various locations of the test frame. These force calculations could be done only for elastic behavior because the strain measurements after yielding of the flange plates became too much history dependent.

6.6 Test Evaluation – Specimens Type B

In the following test evaluation of type B specimens mathematical modeling of component deterioration is discussed based on the results presented in Section 6.5. Evaluation of test results for specimens of type A is not included because only type B plastic hinge elements are employed in the Buffalo test frames for the reasons stated in Section 6.5.

Based on the experimental results obtained from the specimens all the components of total deflection of the specimens are analyzed using engineering mechanics and employing relatively simple analytical models that are used in Chapters 7 and 8 for collapse prediction of different structural systems, including the test frame that was tested at the NEES facility in Buffalo. Using these models and the modified Ibarra-Krawinkler deterioration model discussed in Chapter 2, the deterioration parameters of important components are calibrated using selected experimental data. These deterioration parameters are used for pre-test collapse prediction of the model test frame.

Finite element modeling and analysis of the plastic hinge elements using ABAQUS 6.5 (ABAQUS, 2005) is also presented. For finite element simulations of cyclic tests the hardening model used in the analysis includes combined isotropic and kinematic strain hardening. The engineering stress (σ_e) - strain (ε_e) curve (after stress relief) shown in Figure 6.14 is adjusted to establish the true stress (σ_{true}) – true plastic strain (ε_{true}^{pl}) relationship, where

$$\sigma_{true} = \sigma_e \cdot (1 + \varepsilon_e) \quad (6.4)$$

and

$$\varepsilon_{true}^{pl} = \ln(1 + \varepsilon_e) - \frac{\sigma_e}{E} \quad (6.5)$$

In order to calculate the potential for ductile fracture for selected specimens based on FEM simulation in ABAQUS the approach described in Kanvinde and Deierlein (2007, 2008) is used. For monotonic loading it is well established that ductile crack initiation results from void growth and coalescence, which occurs under the combined effects of plastic strains and hydrostatic tension stresses. Crack initiation is calculated to occur when the void ratio attains a critical size, i.e.,

$$\ln\left(\frac{R}{R_o}\right)_{monotonic}^{critical} = \int_0^{\varepsilon_p^{critical}} C \cdot \exp(1.5 \cdot T) d\varepsilon_p \quad (6.6)$$

The calculation is further simplified to express a crack initiation criterion through a Void Growth Index ($VGI_{monotonic}$), which is compared to its critical value ($VGI_{monotonic}^{critical}$) expressed as follows:

$$VGI_{monotonic} = \int_0^{\varepsilon_p^{critical}} C \cdot \exp(1.5 \cdot T) d\varepsilon_p > VGI_{monotonic}^{critical} = \ln\left(\frac{R}{R_o}\right)_{monotonic}^{critical} \quad (6.7)$$

Equation (6.7) forms the Void Growth Model (VGM) in which $VGI_{monotonic}^{critical}$ is treated as a material property that is relatively intensive to variations in stress and strain states.

To capture the void growth /shrinkage during cyclic loading at a continuum point, the preceding cycles are subdivided into tensile and compressive, and the VGI_{cyclic} during cyclic loading can be expressed by the following equation,

$$VGI_{cyclic} = C \cdot \left(\sum_{tensile-cycles} \int_0^{\varepsilon_p^{critical}} C \cdot \exp(|1.5 \cdot T|) d\varepsilon_p - \sum_{comp.-cycles} \int_0^{\varepsilon_p^{critical}} C \cdot \exp(|1.5 \cdot T|) d\varepsilon_p \right) \quad (6.8)$$

Similar to monotonic ductile fracture, ultra low cyclic fatigue (ULCF) fracture is calculated to occur when VGI_{cyclic} exceeds a critical value, i.e., $VGI_{cyclic} > VGI_{monotonic}^{critical}$. For all the FEM simulations of the plastic hinge regions we used standard hex three -dimensional stress elements with reduced integration. Material and geometric nonlinearities are considered. Only the flange plate(s) of the plastic hinge element of the specimen is modeled assuming that we have a rigid body motion with respect to the center of the pin of the plastic hinge element.

6.6.1 Components of Deflection

For the specimen of Figure 6.2(b) the components of deflection are coming from: (1) the panel zone; (2) the aluminum joint; (3) the plastic hinge region; and (4) the aluminum beam. The bolts used to tie back the subassembly on the test frame do not contribute to the tip deflection since they are pre-tensioned to 12kips. Figure 6.28 illustrates the

contribution to total elastic deflection of each component of the subassembly with two flange plates discussed in the previous section. As seen in this figure, the panel zone contribution is less than 2% of the total tip deflection. The aluminum joint (Clevis part) and the aluminum beam contribute about 40% each to the elastic tip deflection of the specimen.

In order to develop a simplified mathematical model, a study of the elastic curvature variation along the length of the beam is performed. Using the detailed FEM model shown in Figure 6.29 the equivalent stiffness $(EI)_{equiv.}$ of the region of the plastic hinge element outside the 1.5" length is calculated by assuming that all the other parts of the specimen are "infinitely" stiff. Based on the FEM model the $(EI)_{equiv.}$ for these regions is equal to 13200kips in². Using the experimental data from tests "DB33,34: 6,8,8,2-Cyclic" and "DB14,15: 5,5,10-2-Cyclic" and after "back" calculating the $(EI)_{equiv.}$ based on the principle of virtual work (PVW) the $(EI)_{equiv.} = 12925$ kips in² is obtained. The good match for $(EI)_{equiv.}$ between the experiment and the analytical model indicates that: (1) the detailed FEM model is capable to calculate the contributions to elastic deflection; and (2) the variations in $(EI)_{equiv.}$ along the beam is not significant. The latter can be confirmed also from Figure 6.30, which shows the variation of curvature along the length of the specimen.

Figure 6.31 shows the tip load – tip displacement diagram of specimen "DB: 14,15- 6,8,8,2-Cyclic" obtained from two different sources. The solid line shows the experimental data and the dashed line shows the same diagram as determined from elastic contribution of all the components of the subassembly based on simple curvature calculations plus the contribution to deflection of the plastic hinge region over 1.5" length measured with the clip gages (CG). Both curves are practically identical, indicating that the total deflection of the subassembly can be accurately predicted by using the rotation history as deduced from the clip gages over 1.5" length plus the contributions to deflection of the elastic parts with simple curvature calculations. Similar results are observed for all the tests conducted.

In order to calculate the stiffness of the interior and exterior subassemblages of the prototype EW frame we model beams, columns and panel zone contribution in ABAQUS with shell elements. Figure 6.32 illustrates the Von Mises stresses of the 1st story exterior subassemblage for a unit tip load. Based on the analytically predicted values of stiffness the scaled target stiffness $K_{el,target,FEM}$ is determined and is summarized in Table 6.6. The values match with the predicted values of stiffness based on simple curvature calculations of the same subassemblage. It should be noted that beam and column shear deformations are ignored in all calculations.

In order to predict model stiffness a simplified mathematical model is developed that is shown in Figure 6.33. This model consists of concentrated plasticity rotational springs and 6 elastic elements that have the properties of the aluminum regions 1 and 2 (see Figure 6.8). The rotational stiffness of the spring is equal to $K_{,1.5}^R$ of the plastic hinge element. The elastic aluminum elements have the same properties as the specimen tested in the laboratory in terms of strength and stiffness. Table 6.6 summarizes the predicted values of the stiffness ($K_{el,p}$) of the beam column subassemblies of the test frame based on the simplified mathematical model and based on final geometry of the test frame. In the same table the predicted values are compared with the target scaled stiffness based on the FEM analysis of the exterior prototype subassemblages (see Figure 6.32). As seen from the same table the predicted versus experimental values are fairly close.

If it is assumed that the subassemblage of Figure 6.33 has infinitely rigid columns then the simplified mathematical model of this figure represents the subassemblage that is tested in the laboratory. After determining the elastic stiffness $K_{el,p}$ of the same mathematical model it is found that $K_{el,p}$ is almost the same as the one obtained from the experimental data, $K_{el,exp}$, as shown in Table 6.7 for selected specimens.

6.6.2 Ductile Fracture

To predict analytically ULCF fracture in the connection type the approach presented in Section 6.6 and discussed in detail in Kanvinde and Deierlein (2008) is used. An FEM model is built in ABAQUS that simulates the inelastic behavior of the plastic hinge region of the specimens with single and double plate arrangement. The model includes only the flange plate(s) and a rigid body that rotates with respect to the pin. Figures 6.34(a) and 6.34(d) illustrate the Von Misses stresses of the plate for a monotonic and a cyclic test (Specimens “DB: 36-6,8,8,1-T” and “DB: 37-6,8,8,1-Cyclic”). Necking and local buckle are accurately represented in the FEM analytical model.

Figures 6.34(b) and (e) show the $M_c - \theta_{1.5}$ diagrams for the same monotonic and cyclic tests. The two specimens have the same boundary conditions. In the same figure the $M_c - \theta_{1.5}$ diagrams have been superimposed as predicted by ABAQUS simulation. It is judged that the FEM simulation is able to predict the monotonic and cyclic behavior of the plastic hinge region with satisfactory accuracy. Figure 6.34(c) and (f) show $VGI_{monotonic}$ and VGI_{cyclic} , normalized with respect to $VGI_{monotonic}^{critical}$ and $VGI_{cyclic}^{critical}$, respectively, versus $\theta_{1.5}$ and the number of cycles at selected points of the loading history for the two previous specimens. $VGI_{monotonic}^{critical}$ and $VGI_{cyclic}^{critical}$ are calculated based on a uniaxial monotonic tension and a cyclic test of a single plate specimen. As observed from the same figure, crack initiation in the flange plates starts when the predicted VGI becomes larger than the equivalent $VGI^{critical}$ for monotonic and cyclic loading, respectively. It seems that the Cyclic Void Growth Model (CVGM) proposed by Kanvinde and Deierlein (2007, 2008) works well. A more systematic approach needs to be established in the future in which one characterize $VGI_{monotonic}^{critical}$ and $VGI_{cyclic}^{critical}$ based on the approach developed by Myers et al. (2008).

6.6.3 *Ultimate Rotation Capacity*

After evaluating the test results from subassembly experimentation it is concluded that for the selected cyclic loading history the ultimate rotation θ_u at which ductile fracture occurs in flange plate is in the order of 7% regardless of the width w of the flange plate. This can be seen from Table 6.5, which summarizes the values of ultimate rotation capacity $\theta_{u,1.5''}$ for selected single and double flange plate cyclic tests. Ricles et al. (2004) and Engelhardt et al. (2000) reported similar values of θ_u after testing beams with RBS. Since ductile tearing is important for evaluating the performance of the model connection and the performance of full scale connections, θ_u is incorporated into the modified Ibarra–Krawinkler deterioration model as discussed in Section 2.3. The model fully deteriorates (strength drops to zero) when θ_u is exceeded.

6.6.4 *Calibration of Component Deterioration Parameters for Pre–Test Collapse Prediction*

The $M_c - \theta_{1.5''}$ diagram for the cyclic test discussed in Section 6.5 is presented in Figure 6.35. The backbone curve of the modified Ibarra-Krawinkler model is calibrated using the monotonic backbone curve of the same subassembly, which is superimposed on the cyclic response curve. The bilinear hysteretic response of the modified Ibarra-Krawinkler model is used to calibrate the cyclic deterioration parameters for each component, without considering the pinching effect that is evident in all symmetric cyclic loading tests. Figure 6.36 illustrates the calibrated $M_c - \theta_{1.5''}$ diagram for selected tests at the column base and first floor beam used for pre – shaking table test collapse prediction. Zero residual strength is assumed since there was no justification from monotonic and cyclic tests of a residual strength value. As seen later on in Section 6.7 the plastic hinge regions of the test frame did not reach a residual strength path during the shaking table collapse tests. Table 6.8 summarizes the calibrated deterioration parameters of the modified Ibarra–Krawinkler model used for the plastic hinge elements of the model structure for the pre-test prediction

of the shaking table collapse test series discussed in Chapter 7. The effect of the difference between scale model and prototype component deterioration parameters (see Table 6.1) on prototype collapse prediction is discussed in Section 8.3.

6.7 Post Buffalo Component Tests

Several component tests are performed after the execution of the shaking table tests at the Buffalo shaking table facility. The objectives of these tests are to (1) obtain realistic moment – rotation response histories for selected plastic hinge regions up to collapse, and (2) utilize these response histories to check the modeling parameters for collapse prediction as obtained from the pre-shaking table cyclic component tests discussed earlier in this chapter.

In the Buffalo shaking table tests only the rotation histories of all the plastic hinge elements of both test frames are recorded, but the associated moments are unknown or have to be deduced from strain measurements or analytical models. In the elastic response regime the strain – moment calibrations provide good data on moments (see Section 7.5.1.2), but in the inelastic regime the strain - moment calibrations become strongly history dependent.

After the completion of the shaking table tests a series of component tests are performed for selected critical plastic hinge locations, in which the recorded rotation histories are used to derive the tip displacement histories of component tests. The component specimen type described in Section 6.3.4 and nominally identical plastic hinge elements with the ones in the shaking table test frames are employed. The following three important plastic hinge locations of each test frame are tested: (1) the exterior first story column at the base of the test frame; (2) the exterior first floor beam; and (3) the third story column at the top.

The shaking table test rotation history over 1.5" length, as deduced from clip gage recording of a plastic hinge element, is created by connecting together the rotation histories from each testing phase of the Buffalo shaking table tests. Figure 6.37 shows the rotation history of the plastic hinge element of the first floor beam at the interior joint of test Frame #1 (location B1F1R), from elastic behavior up to collapse. In order to “translate” the input rotation history into a tip displacement history for the actuator, the elastic contributions of all the parts of the components that remain elastic need to be predicted (see parts 1-1 and 3-4 of Figure 6.38). Hence an estimate of the force (moment) at the plastic hinge element of interest is needed. For this reason a mathematical model that simulates hysteretic behavior based on the modified Ibarra-Krawinkler model is developed. Using the predicted stiffness and deterioration parameters from the pre-shaking table component tests summarized in Table 6.8 and the rotation as an input loading history, the moment needed to estimate elastic contributions is back-calculated analytically. Finally the input rotation history of the selected plastic hinge element is “translated” into a tip displacement history for the component test.

Figure 6.39 shows the experimentally obtained moment rotation diagram for the column base and first floor beam of test frame #1 together with the pre - test and post – test prediction using the modified Ibarra Krawinkler model. Figures 3.39(a) and 3.39(c) indicate that the pre-test predictions of the hysteretic response are close to the experimental data for both plastic hinge elements. Based on Figures 3.39(b) and 3.39(d) the only significant difference between the calibrated deterioration parameters of the same plastic hinge elements from post-test predictions is the post-capping rotation capacity, which in general is larger than the assumed pre-test values since during component experimentation (1) specimens used did not have final geometries (the dimensions were close to final) and (2) the monotonic curve for similar plastic hinge elements as the ones of the test frame (see Figure 6.35), was obtained after combining results based on single flange plate component tests subjected to tension and compression excluding location F2B1R; thus for this location

the calibrated θ_{pc} value (1.30 from Table 6.8) from pre-test component tests is similar to the calibrated θ_{pc} from post – test component tests (1.60 from Table 6.9).

Figure 3.39(e) shows the comparison between the clip gage histories recorded during the shaking table test at Buffalo and the histories recorded during the Stanford test for the same locations. The two rotation histories are almost identical indicating that the moment - rotation diagrams for the selected locations are reliable.

The pinching effect, which is observed in the component test prior to the Buffalo tests using symmetric cyclic loading histories, diminishes if we employ the loading histories from the Buffalo tests in which the test frame and plastic hinge elements are “drifting” in one direction. After significant plastic deformation the pinching effect would appear if the same specimen were pushed to the opposite direction. The latter can be seen from Figure 6.40(a), which shows the moment - rotation history at the top of the third story column. After the completion of the Buffalo loading history (point A in Figure 3.40(a)) the specimen is pushed in the opposite direction. As seen from the figure the pinching effect becomes evident because during the load reversal the top flange plate straightens out at a much reduced axial stiffness before picking up full tensile resistance. Figure 6.40(b) shows the calibrated moment - rotation diagram superimposed on the experimental data.

Table 6.9 summarizes the plastic hinge modeling parameters used for post–test collapse predictions of the tests conducted at the State University of New York at Buffalo and presented in Chapter 7. After comparing deterioration model parameters in Tables 6.9 and 6.10 it can be seen that the major difference between calibrated values for components tested prior to the shaking table test series and the post – test experimentation is the calibrated θ_{pc} values for the reasons stated earlier.

6.8 Summary and Observations

This chapter describes the testing program that was conducted in the laboratory of the John A. Blume Earthquake Engineering Center in order to investigate the hysteretic behavior of the components of the test frame used for shaking table tests. Two specimen types are investigated. Twelve specimens of type A and thirty eight specimens of type B are tested either monotonically or cyclically.

Specimens of type A fracture relatively early (at about 4% rotation) because of high curvatures induced by the additional moment due to eccentricity of the flange plates. The flange plate eccentricity also causes asymmetric hysteretic behavior. Another problem, using this type of specimens, is the undesirable slip between the aluminum beam and the solid aluminum block at the beam end.

Specimens of type B fracture at about the same plastic rotation as a W beam with RBS (at about 8% rotation). The fracture point is consistent for all the test specimens that were tested cyclically. For the symmetric cyclic loading history applied to the specimens the hysteretic behavior exhibits pinching characteristics. The pinching effect appears due to absence of the web in the model plastic hinge regions.

The stiffness of the specimens and of the model test frame is accurately predicted by means of relatively simple analytical models with concentrated plasticity springs that incorporate deterioration characteristics at the component ends.

The rates of cyclic deterioration are similar for all the specimens tested regardless of the width w of the flange plates. Based on experimental data extracted from the steel database described in Chapter 3 for similar connections used in the prototype 4- story structure the rate of cyclic deterioration for model and prototype connections is similar. However, the plastic rotation capacity and post capping rotation capacity are very different from the

target values of the prototype components. The effects of the differences in θ_p and θ_{pc} between the model and prototype components on the collapse capacity of the prototype frame are discussed in Chapter 8.

Three important plastic hinge regions of test Frame #1 are tested after conducting the shaking table collapse series presented in Chapter 7. The post-test evaluation is conducted in order to deduce the moment - rotation diagrams at the selected locations and improve on the calibration of modeling parameters for post-shaking table response predictions. Based on post- test component experimentation of selected plastic hinge regions, the pre-test calibrations of hysteretic response modeling parameters are comparable with the experimental data excluding the θ_{pc} values that differ due to the way that the monotonic moment rotation relationship was deduced.

The pinching effect that appears in the hysteretic response of plastic hinge elements in pre-shaking table component experimentation using symmetric loading histories diminishes. In the shaking table collapse test series both frames drift in one direction. Since no major reversal occurs in the loading histories of the plastic hinge elements, there was no significant pinching behavior in any of the plastic hinge elements of both test frames.

Table 6.1. Target modeling parameters of components of the 4–story EW frame of the prototype structure

Section	Type	(M_c/M_y)	κ	θ_p	$A = E_t/M_y$	θ_{pc}
W24x76	Column	1.05	0.40	0.025	1.50	0.35
W24x131	Column	1.05	0.40	0.025	1.50	0.30
W21x93	Beam	1.05	0.40	0.025	1.90	0.19
W27x102	Beam	1.05	0.40	0.020	1.50	0.16

Table 6.2. Material properties of steel material based on tensile coupon tests

Material	Stress Relief	Width (in)	Thickness (in)	Area (in ²)	F_y (ksi)	F_u (ksi)
A572Gr.50	Yes	0.505	0.243	0.12	47	65
A572Gr.50	No	0.505	0.241	0.12	47	66

Table 6.3. Summary table of test results of type A specimens

Type A Specimen	P_y (kips)	δ_y (in)	M_y (kips-in)	P_b (kips)	$\theta_{b,1.5''}$ (rad)	M_b (kips-in)	$\theta_{u,1.5''}$ (rad)	K_e (kips/in)	$K^R_{.1.5''}$ (kips-in/rad)
DB1-L/t=4-1-T ¹	0.56	0.39	10.9	na	na	na	0.068	1.42	7526
DB2-L/t=4-1-C ²	0.53	0.57	10.3	0.55	0.015	10.7	na	0.95	5035
DB5-L/t=4-2-Cyclic ³	1.1	0.32	21.3	1.24	0.0175	24.0	0.03 (during 2 nd Cycle)	3.47	15910

¹ DB1=L/t=4-1-T: specimen #1 with L/t=4; single flange plate (1); plate in tension (T)

² DB2=L/t=4-1-C: specimen #2 with L/t=4; single flange plate (1); plate in compression (C)

³ DB3=L/t=4-2-Cyclic: specimen #3 with L/t=4; two flange plates (2); cyclic test (Cyclic)

Table 6.4. Summary table of material properties obtained from tension tests of specimens of type B

Material	Stress Relief	L/t	F_y (ksi)	F_u (ksi)	ϵ_f
A572Gr.50	Yes	3	46	67	0.34
A572Gr.50	Yes	4	45	65	0.37

Table 6.5. Summary table of test results of specimens type B

Type B Specimens	P_y (kips)	δ_y (in)	M_y (kips-in)	P_b (kips)	$\theta_{b,1.5''}$ (rad)	M_b (kips- in)	$\theta_{u,1.5''}$ (rad)	K_e^* (kips/in)	$K^R_{,1.5''}$ (kips- in/rad)
DB: 33,34-L/t=6,8,8,2- Cyclic ¹	1.18	0.25	20.1	1.28	0.03	21.8	0.08 (during 1st cycle)	4.92	16997
DB: 35-L/t=6,8,8,1-C ²	0.64	0.23	10.9	0.78	0.04	13.3	na	2.74	5694
DB: 36-L/t=6,8,8,1-T ³	0.61	0.2	10.4	na	na	na	0.33	3	6029
DB: 37-L/t=6,8,8,1- Cyclic ⁴	0.61	0.24/ 0.19	10.03	0.61	0.02 (during 1st Cycle)	10.9	0.08 (during 1st cycle)	2.5/ 3.11	5700/ 6039
DB: 38-L/t=6,8,8,1-C	0.42	0.19	7.1	0.45	0.03	7.7	na	2.23	4286
DB: 39-L/t=6,8,8,1-T	0.39	0.15	6.6	na	na	na	0.31	2.52	4341
DB: 40-L/t=6,8,8,1- Cyclic	0.39	0.15/ 0.17	10.03	0.41	0.02 (during 1st Cycle)	10.9	0.08 (during 1st cycle)	2.61/ 2.26	6710/ 4363
DB: 41-L/t=6,8,8,1-C	0.85	0.24	14.5	1.11	0.04	18.9	na	3.57	10554
DB: 42-L/t=6,8,8,1- Cyclic	0.85	0.22/ 0.24	10.03	0.91	0.02 (during 1st Cycle)	10.9	0.08 (during 1st cycle)	3.80/ 3.57	11493/ 10554

¹ DB: 33, 34-L/t=6,8,8,2-Cyclic: specimen with flange plate #33, 34; with L/t=6; top spacer L/t=8; bottom spacer L/t=8; double flange plate (2); cyclic test (Cyclic)

² DB: 35-L/t=6,8,8,1-C: specimen with flange plate #35; with L/t=6; top spacer L/t=8; bottom spacer L/t=8; single flange plate (1); flange plate in compression (C)

³ DB: 36-L/t=6,8,8,1-T: specimen with flange plate #36; with L/t=6; top spacer L/t=8; bottom spacer L/t=8; single flange plate (1); flange plate in tension (T)

⁴ DB: 37-L/t=6,8,8,1-Cyclic: specimen with flange plate #37; with L/t=6; top spacer L/t=8; bottom spacer L/t=8; single flange plate (1); cyclic test (Cyclic)

* the two values of elastic stiffness for single flange plate specimens are the different stiffnesses in tension and compression because of the different elastic contribution to total deflection of the pin in the two loading directions.

Table 6.6. Predicted stiffness for exterior test frame subassemblages

Subassemblage at Floor	δ_b (in)	δ_{col} (in)	δ_{PZ} (in)	$K_{el,p}$ (kips/in)	$K_{el,target FEM}$ (kips/in)
3	0.247	0.017	0.008	3.68	3.50
2	0.143	0.017	0.008	5.95	6.04
1	0.137	0.025	0.008	5.87	5.91

Table 6.7. Experimental and analytical predictions of elastic stiffness for selected cantilever subassemblages

Specimen	δ_1 (in)	δ_2 (in)	δ_3 (in)	$K_{el,p}$ (kips/in)	$K_{el,exp}$ (kips/in)
DB:14,15-L/t=5,12,8,2-C	0.093	0.026	0.092	4.75	4.67
DB:25,26-L/t=7,12,12,2-M	0.093	0.032	0.092	4.61	4.54
DB:34,35-L/t=6,8,8,2-C	0.093	0.019	0.092	4.91	4.8

Table 6.8. Modeling parameters for pre – Buffalo collapse prediction

Location	K_e	F_c/F_y	θ_p	θ_{pc}	A	κ
C1S1B ¹	25883	1.09	0.050	1.3	1.35	0
C1S1T ²	20631	1.10	0.050	1.3	1.35	0
F2B1R ³	13000	1.10	0.050	1.3	1.35	0
C1S3T ⁴	11200	1.10	0.050	1.3	1.35	0

Table 6.9. Modeling parameters for post – Buffalo collapse prediction

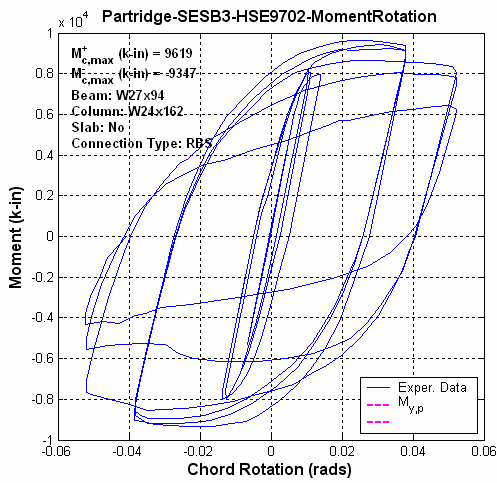
Location	K_e	F_c/F_y	θ_p	θ_{pc}	A	κ
C1S1B ¹	25700	1.10	0.050	2.0	1.30	0
C1S1T ²	20631	1.10	0.050	2.0	1.30	0
F2B1R ³	13000	1.10	0.050	1.6	1.80	0
C1S3T ⁴	11200	1.08	0.055	2.4	1.00	0

¹ C1S1B: Column 1 in Story 1 at Base

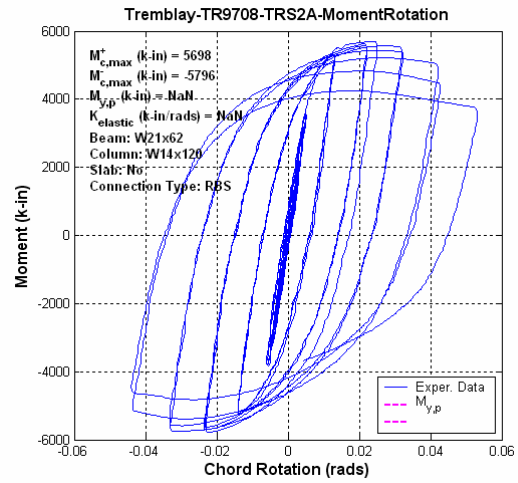
² C1S1T: Column 1 in Story 1 top location

³ F2B1R: Floor 2 Beam 1 right location

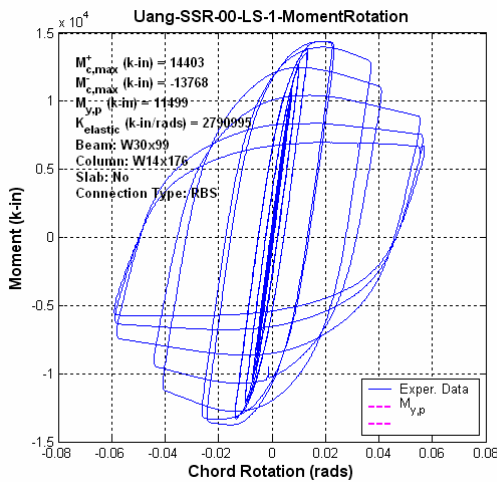
⁴ C1S3T: Column 1 in Story 3 at top



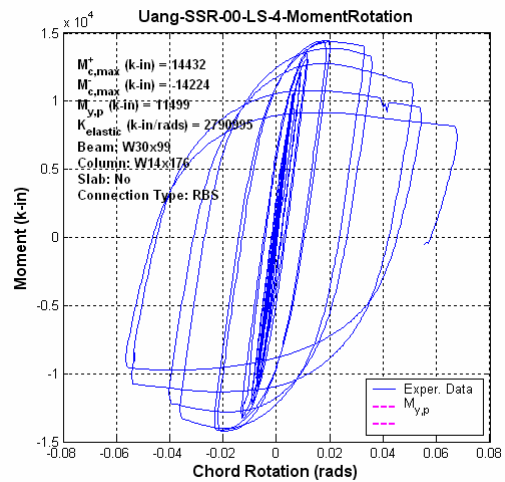
(a) W27x94



(b) W21x62



(c) W30x99 RBS



(d) W30x99 RBS and additional lateral support

Figure 6.1. Hysteretic behavior of basic structural components similar to ones used in the EW moment resisting frame of prototype structure (a) W27x94 beam (data from Partridge, 1997), (b) W21x62 beam (data from Tremblay et al. 1997) (c) W30x99 beam with RBS (data from Uang and Fan, 1999) and (d) W30x99 beam with RBS and additional lateral support near the RBS location (data from Uang and Fan, 1999)

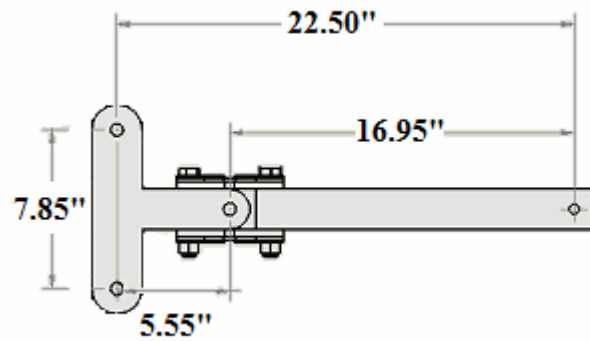
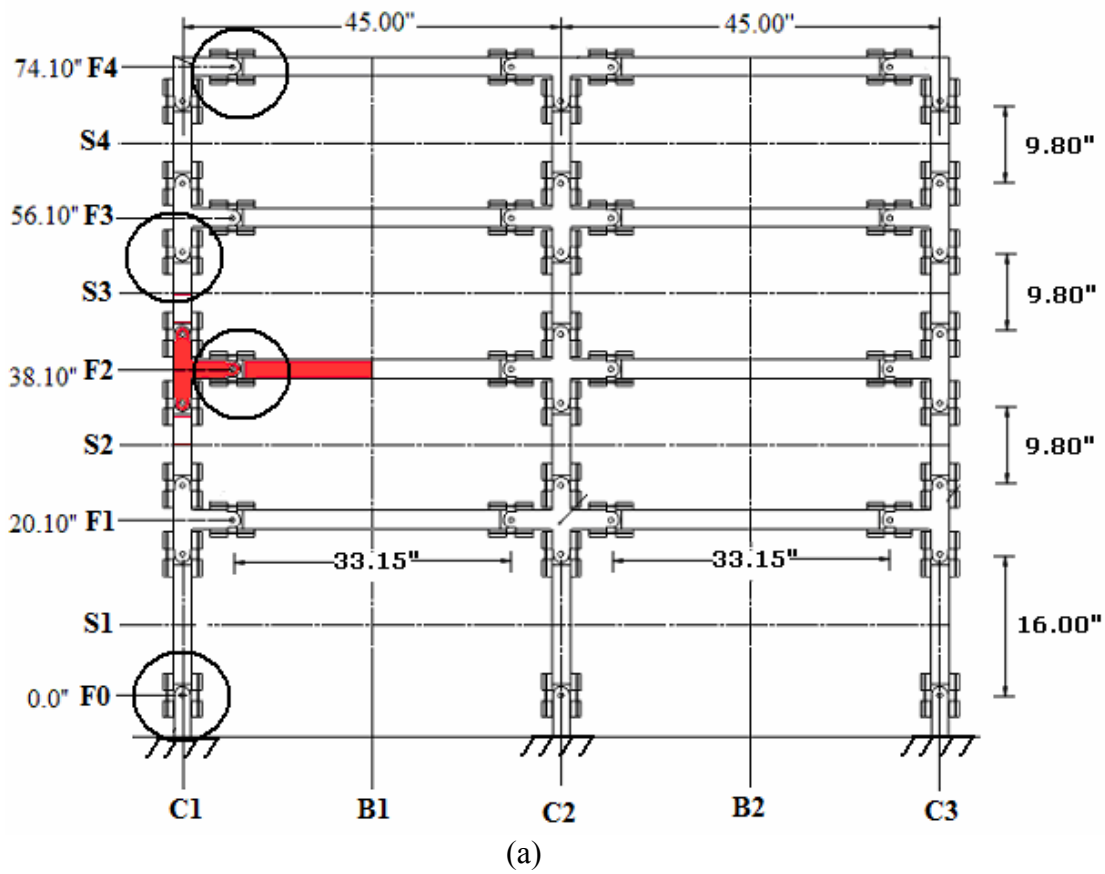


Figure 6.2. Exterior subassembly of test frame

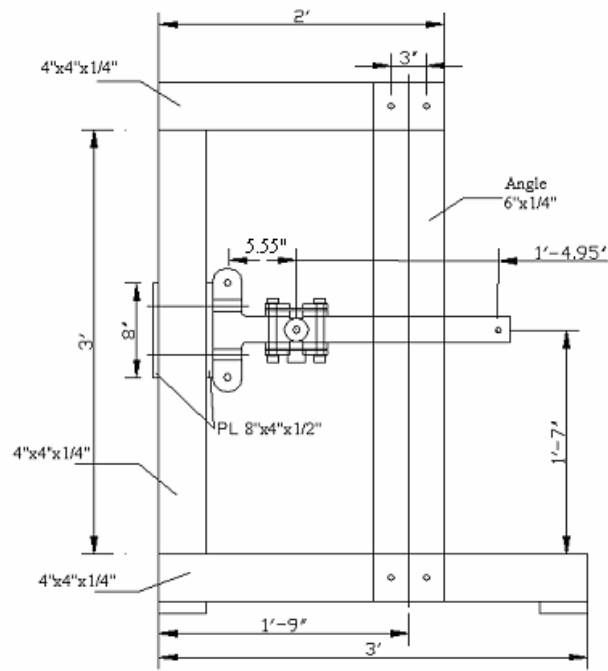


Figure 6.3. Test setup drawing

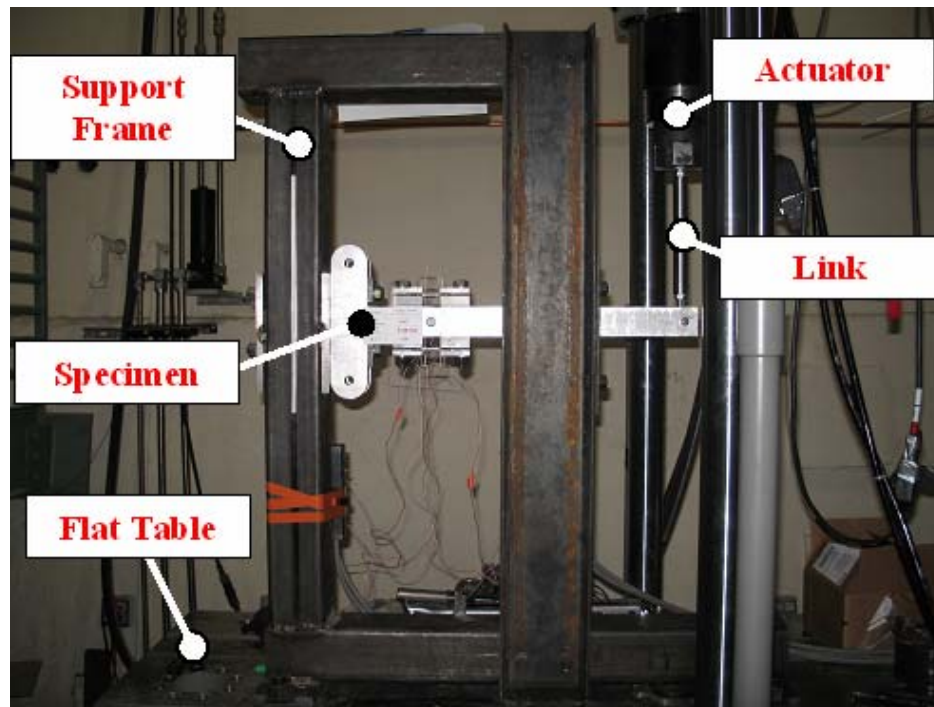


Figure 6.4. Component test setup at Stanford

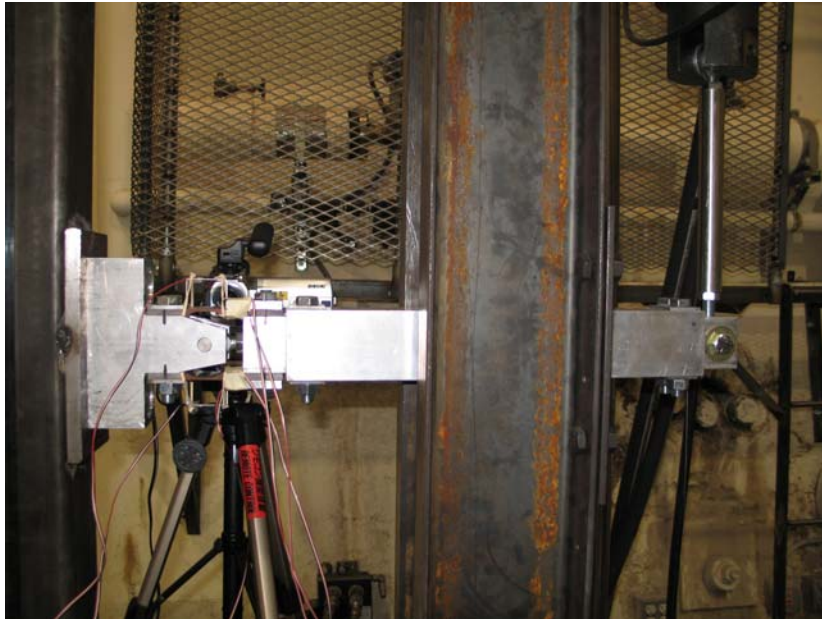


Figure 6.5. Cantilever subassembly after installation (Specimen type A)

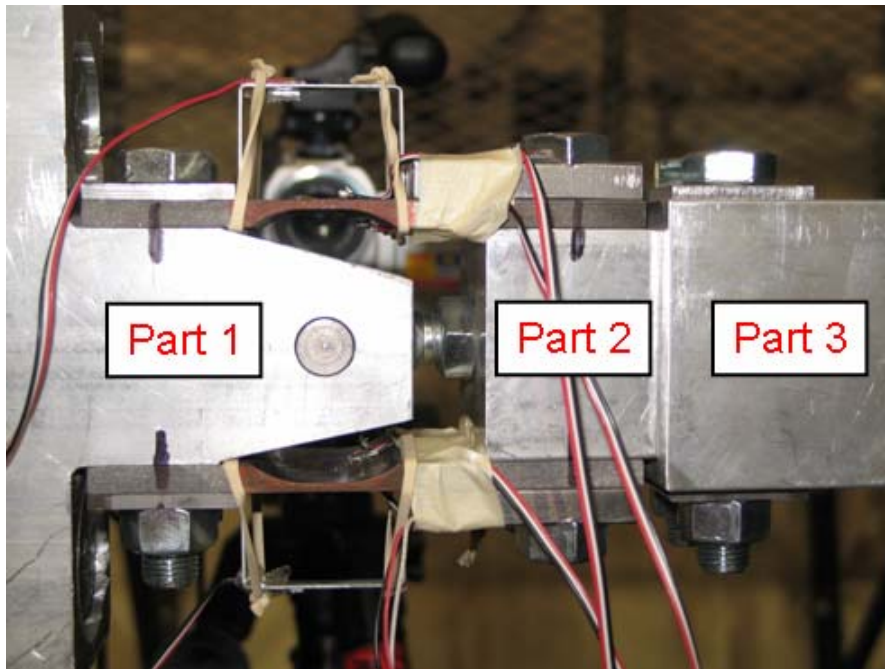


Figure 6.6. Component end of cantilever subassembly (plastic hinge region of specimen type A)

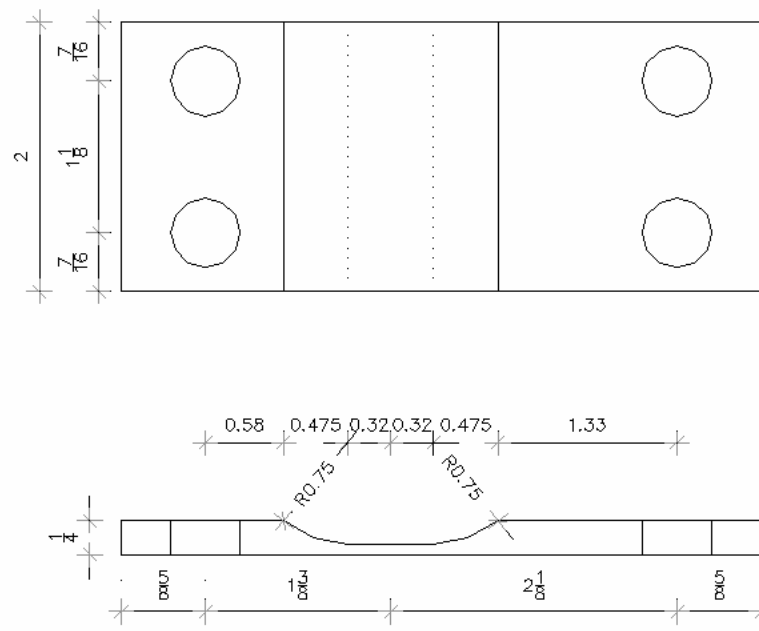


Figure 6.7. Typical flange plate with $L/t = 8.0$ (specimen type A)

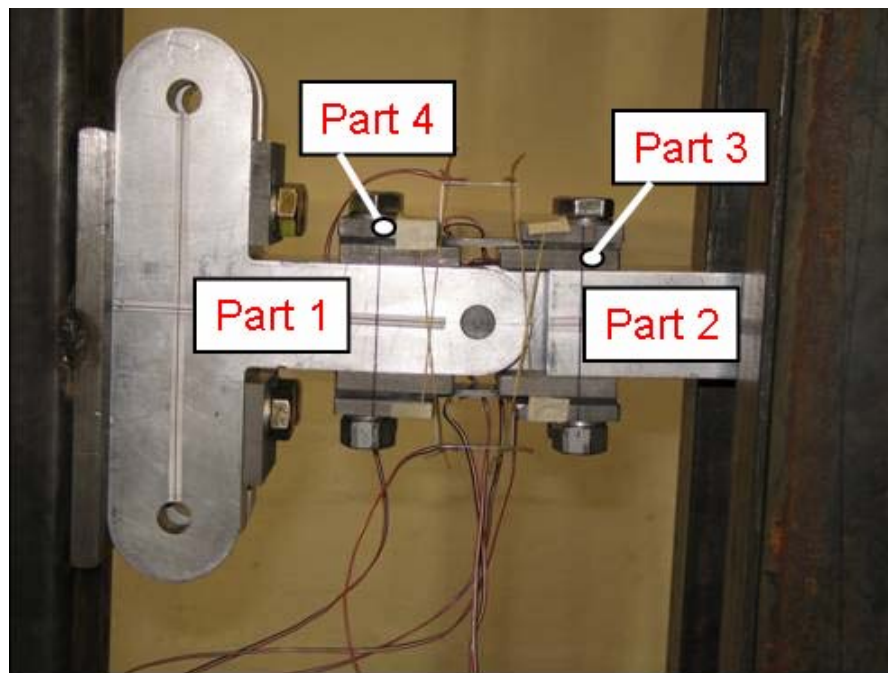
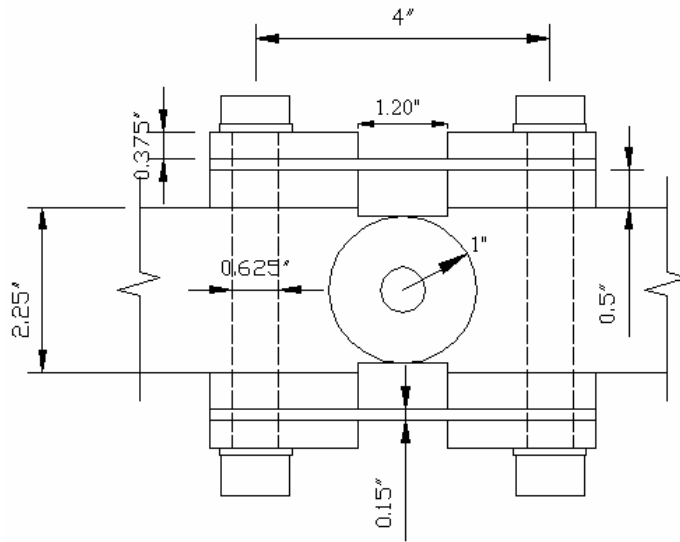
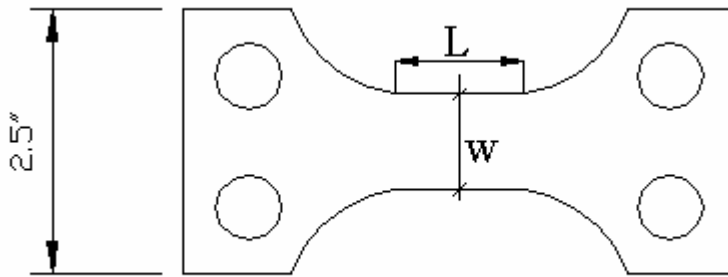


Figure 6.8. Main parts of component end of specimen type B (plastic hinge region)



(a) dimensions of plastic hinge element (specimen type B)



(b) control parameters of flange plates (specimen type B)

Figure 6.9. Plastic hinge element of specimen type B; (a) dimensions (b) control parameters of flange plates attached to the plastic hinge element

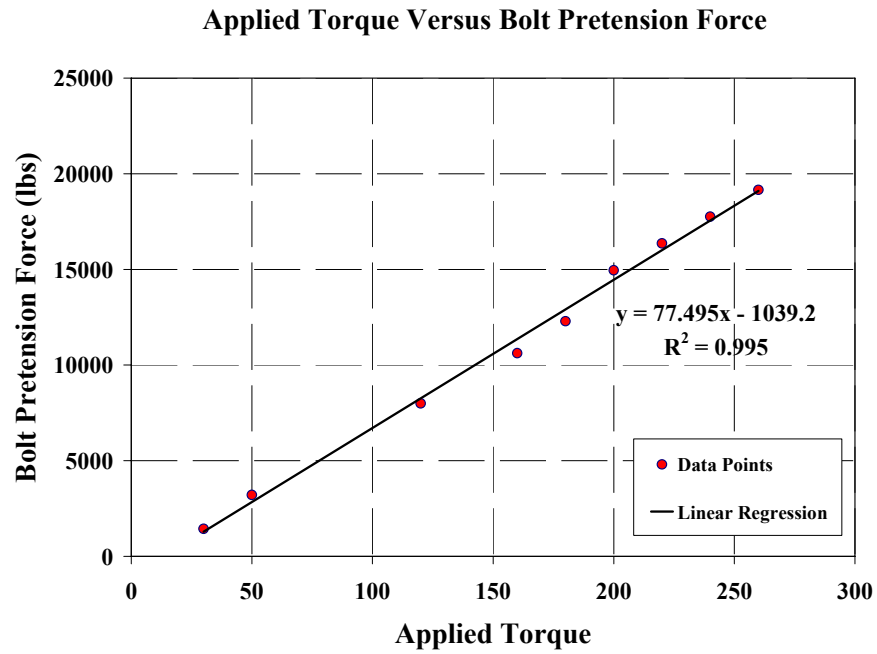


Figure 6.10. Relationship between bolt pretension force and applied torque

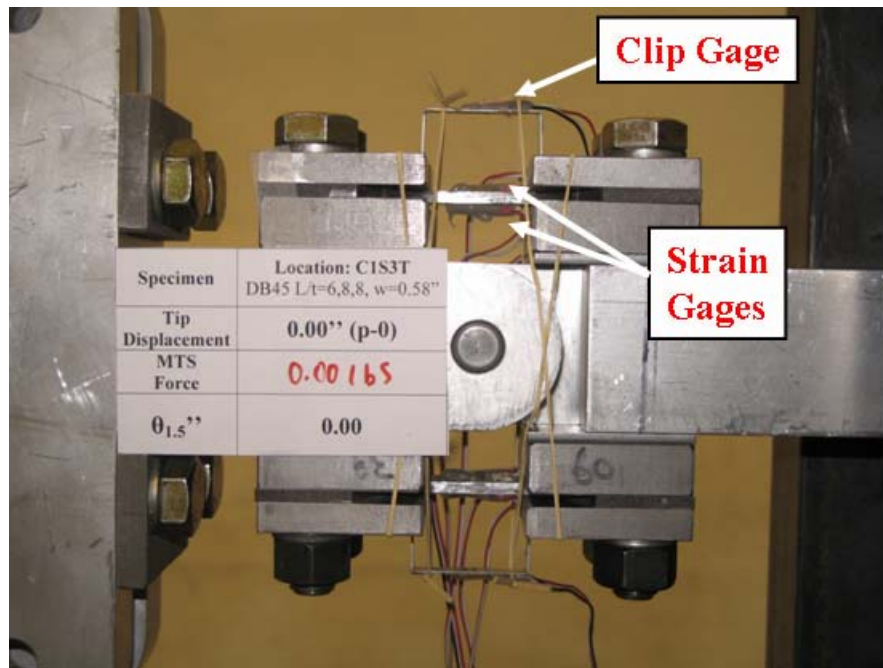


Figure 6.11. Strain gage and clip gage instrumentation

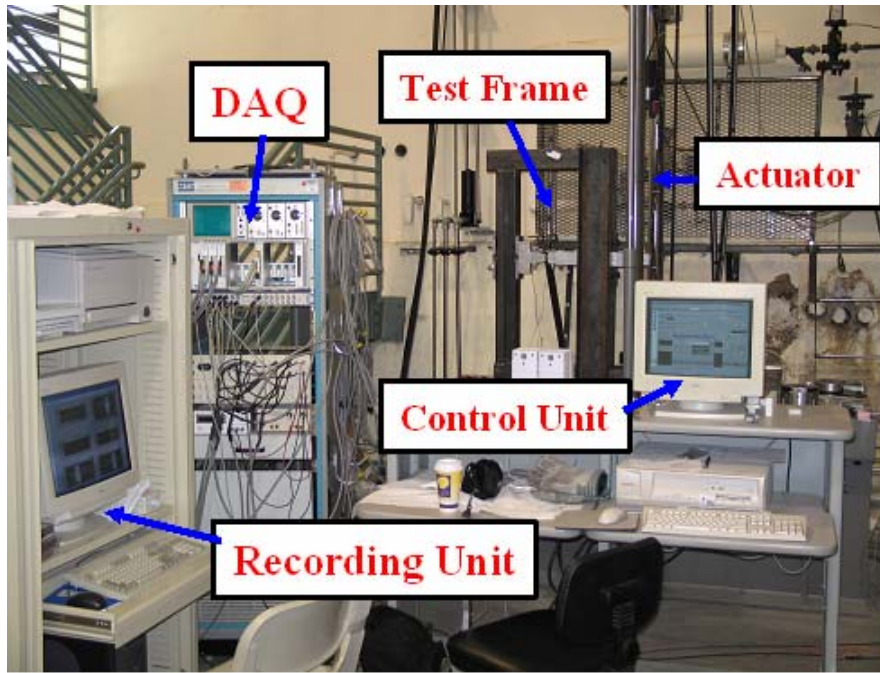


Figure 6.12. Experimental setup for component tests

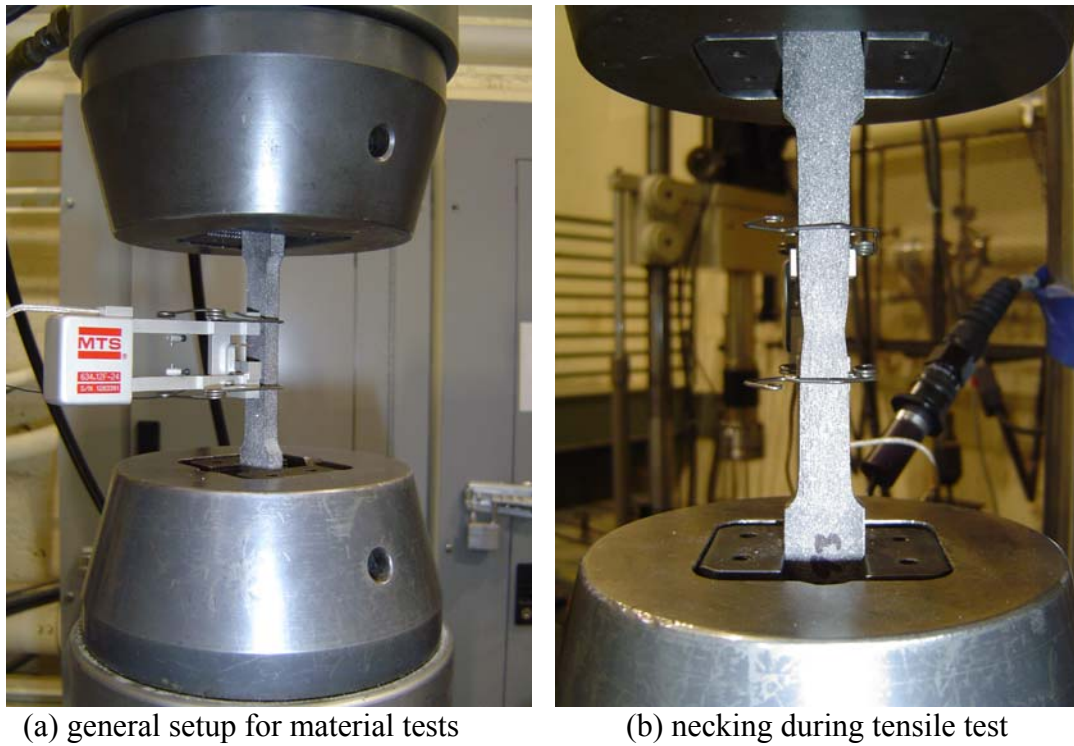


Figure 6.13. Material tests (a) general setup, (b) necking

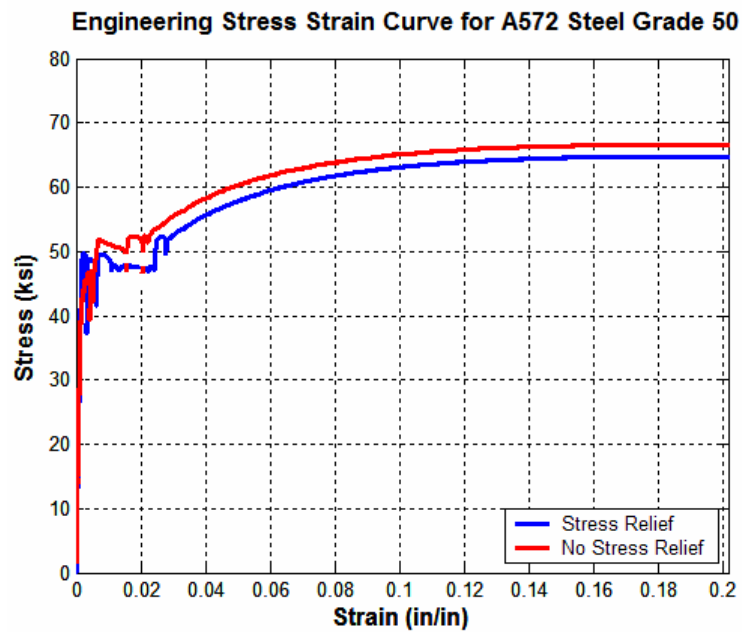


Figure 6.14. Engineering stress strain curve for A572 grade 50 steel plate used to machine flange plates

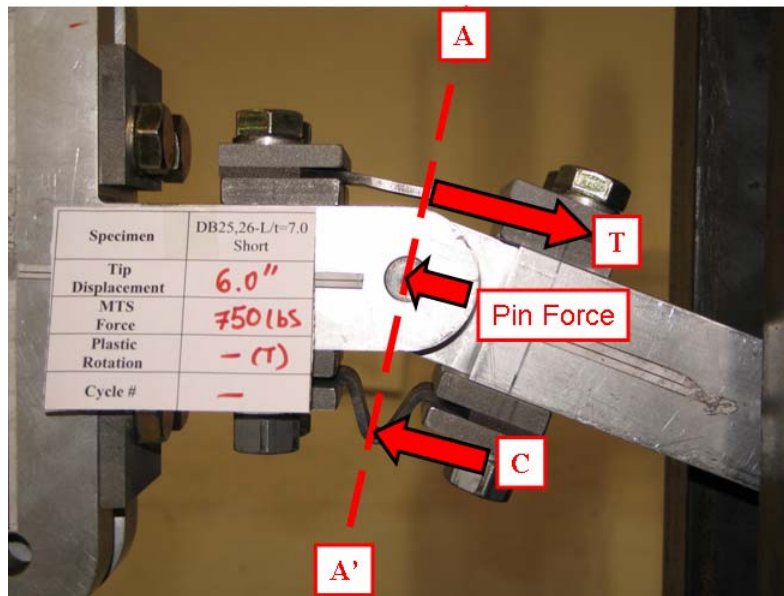


Figure 6.15. Force equilibrium of free body during inelastic action of the component

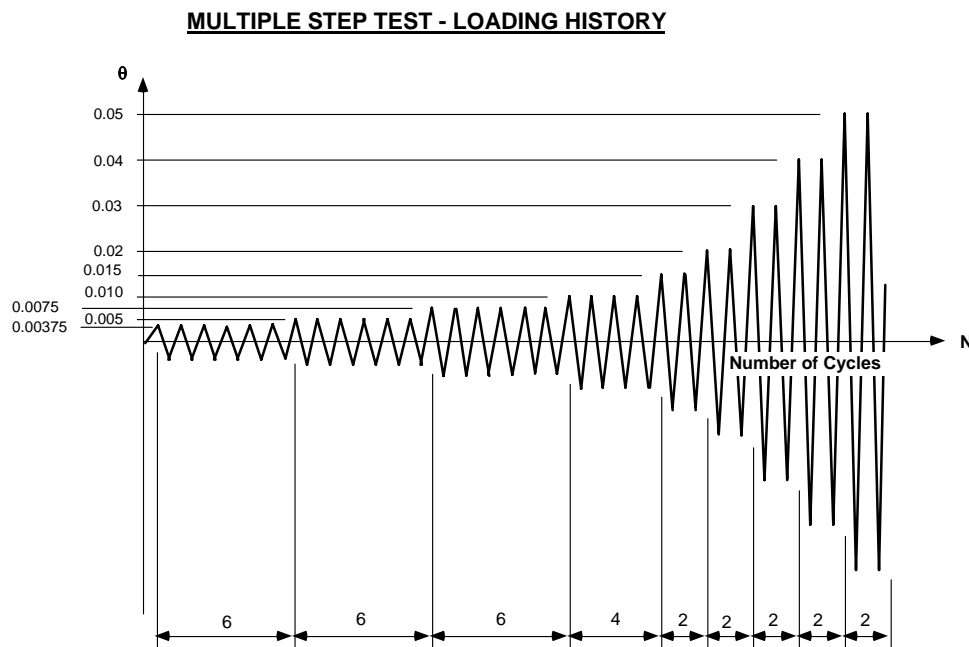
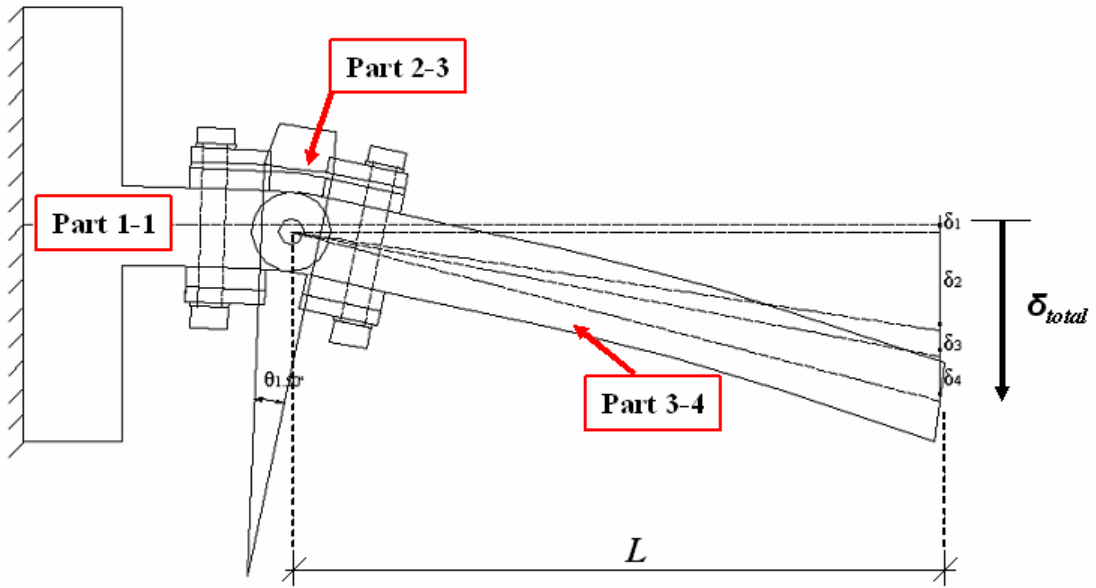
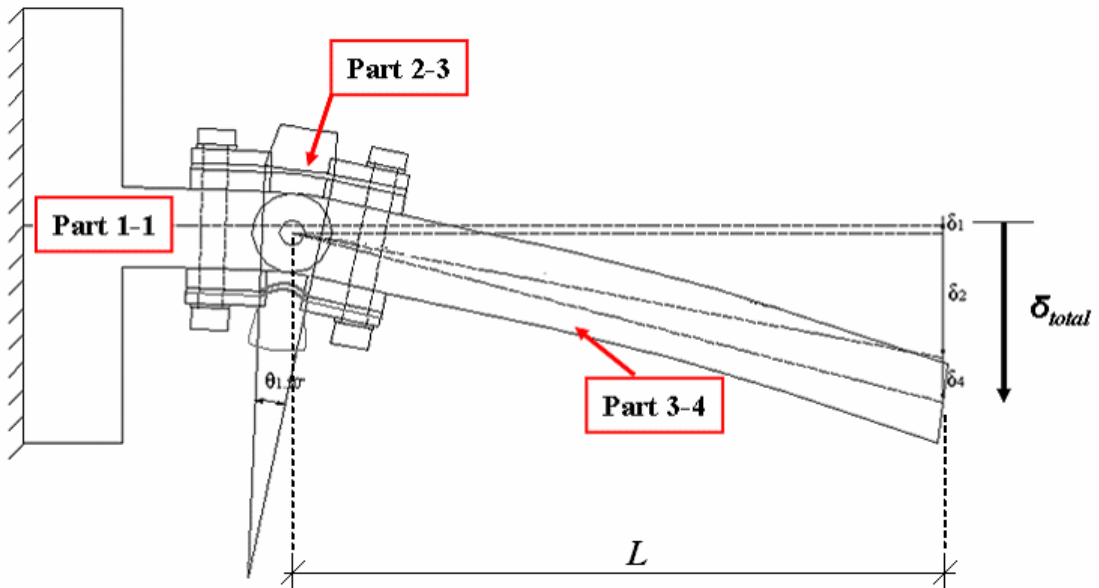


Figure 6.16. SAC loading protocol (Krawinkler et al. 2000), deformation parameter is interstory drift angle

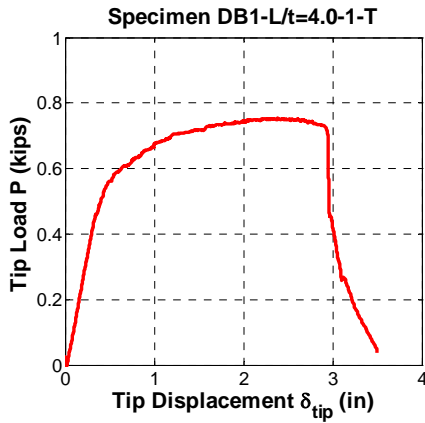


(a) specimen with single plate arrangement

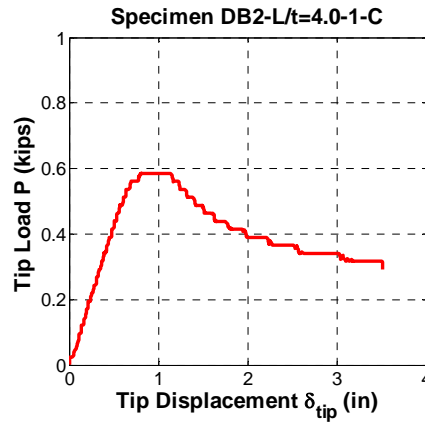


(b) specimen with double plate arrangement

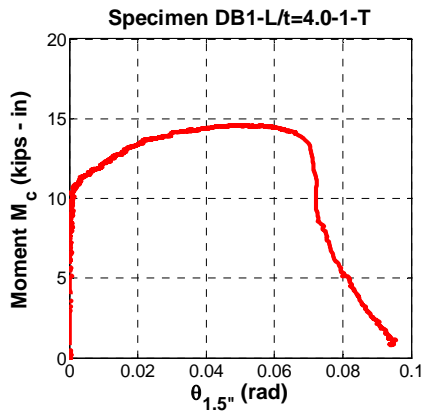
Figure 6.17. Deflection and rotation definitions for test specimens (specimen type B)



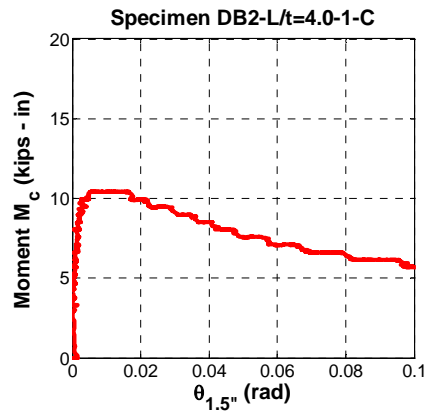
(a) Tip load – tip displacement (Tension)



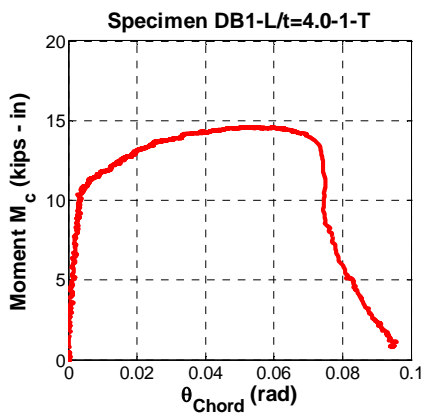
(d) Tip load – tip displacement (Compr.)*



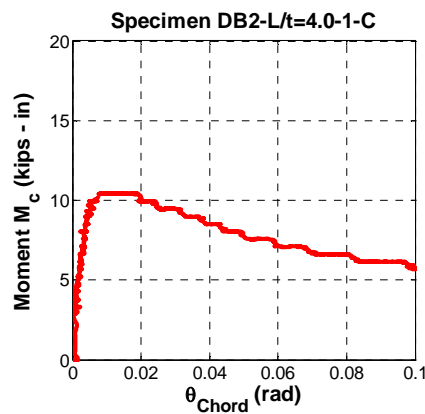
(b) $M - \theta_{1.5''}$ (tension)



(e) $M - \theta_{1.5''}$ (Compr.)



(c) $M - \theta_{Chord}$ (tension)



(f) $M - \theta_{Chord}$ (Compr.)

Figure 6.18. Monotonic tests of single plate specimens with $L/t = 4$ (Type A)

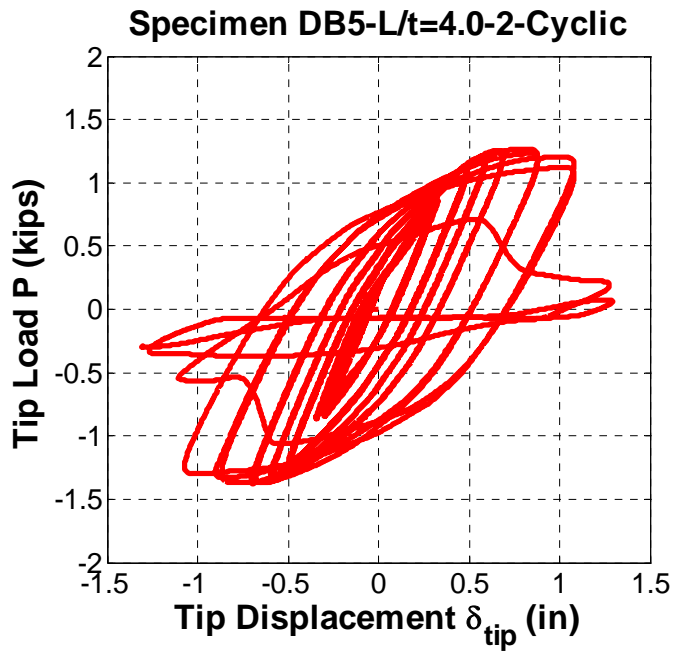


Figure 6.19. Tip load - tip displacement for specimen with two plates (specimen type A)

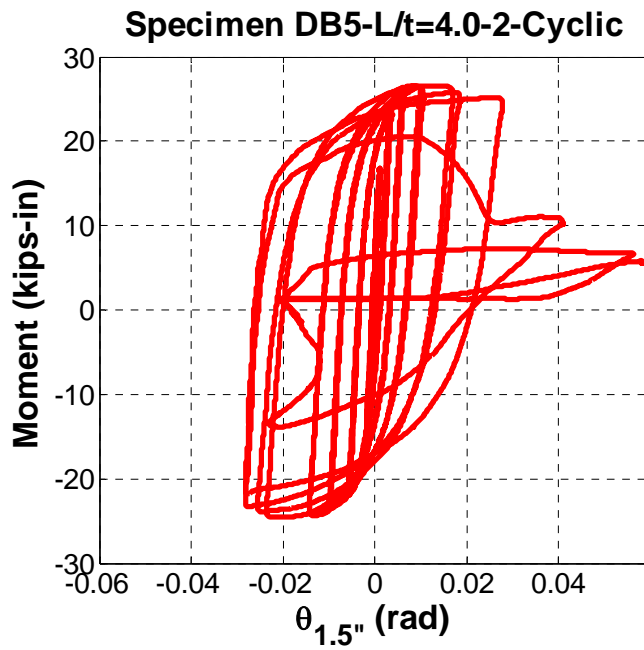
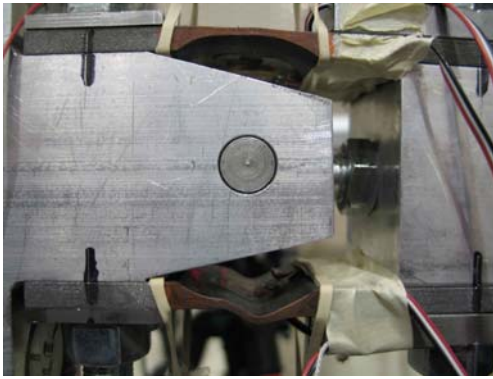
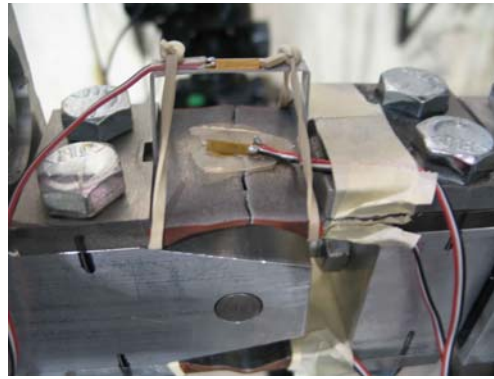


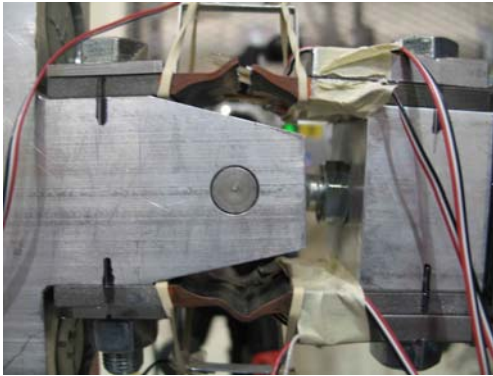
Figure 6.20. $M - \theta_{1.5''}$ rotation diagram for specimen with two plates (specimen type A)



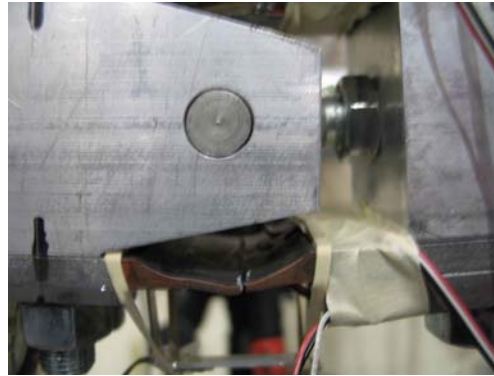
(a) Initiation of deterioration (point 1)



(b) crack propagation along the top steel plate (point 2)



(c) Fracture of top plate (point 3)



(d) fracture of bottom plate (point 4)

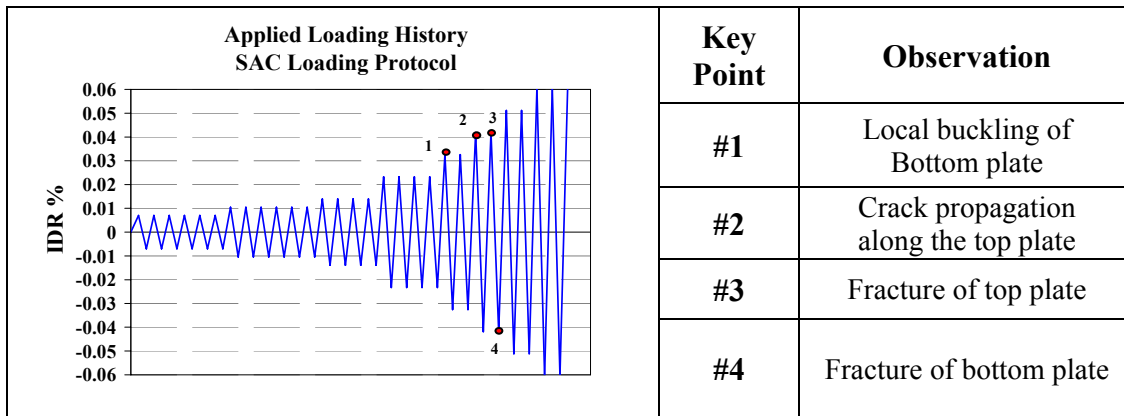
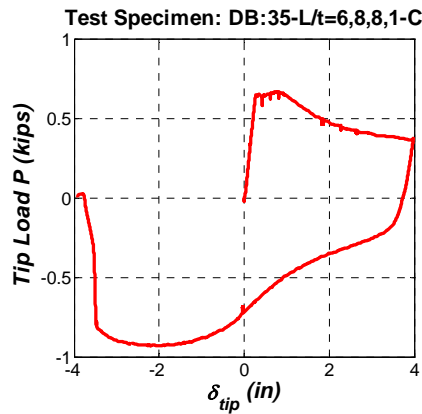
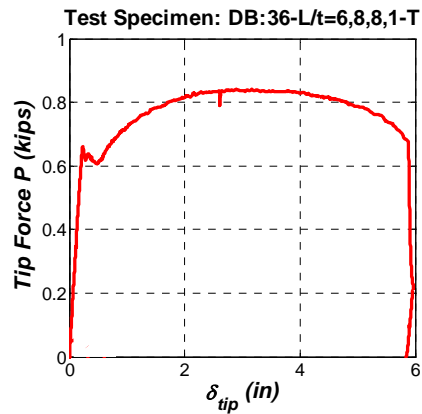


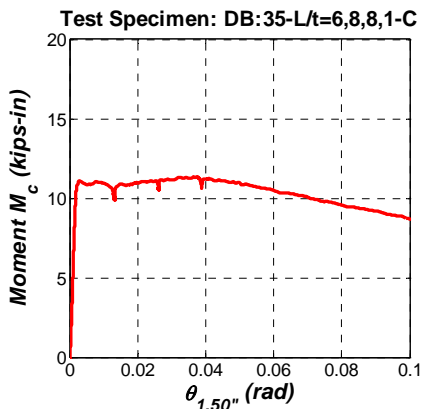
Figure 6.21. Summary of observations from cyclic static test for specimen DB4-L/t=4.0-2 (specimen type A)



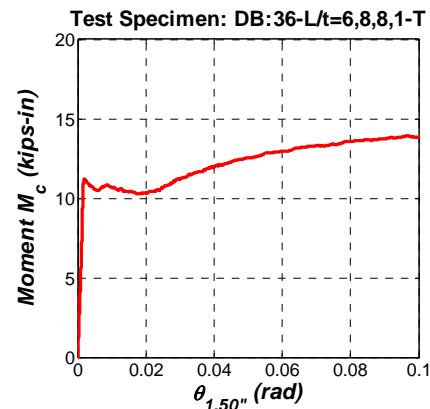
(a) Tip load – tip displacement (Compr.)



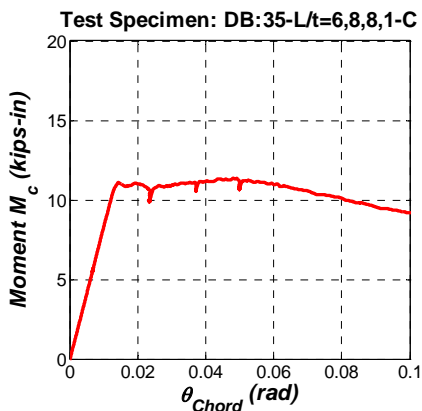
(d) Tip load – tip displacement (Tension)



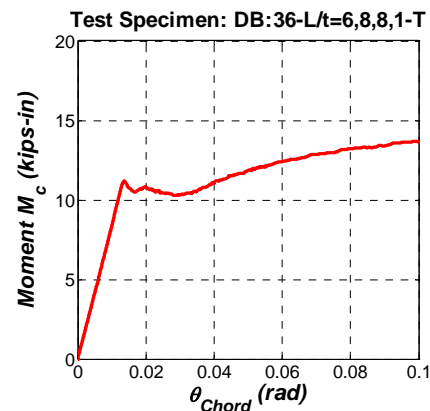
(b) $M - \theta_{1.5''}$ (Compr.)



(e) $M - \theta_{1.5''}$ (Tension)

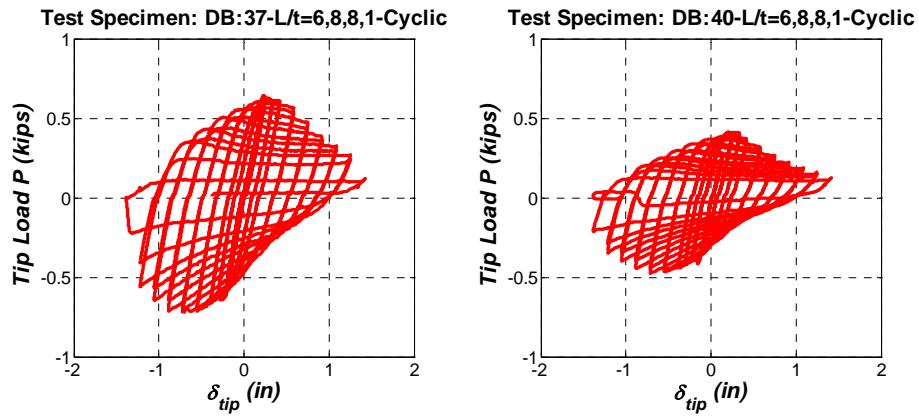


(c) $M - \theta_{Chord}$ (Compr.)

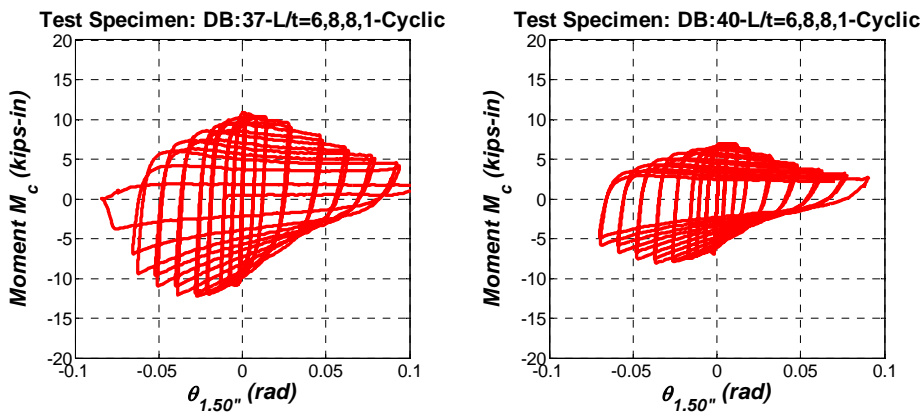


(f) $M - \theta_{Chord}$ (Tension)

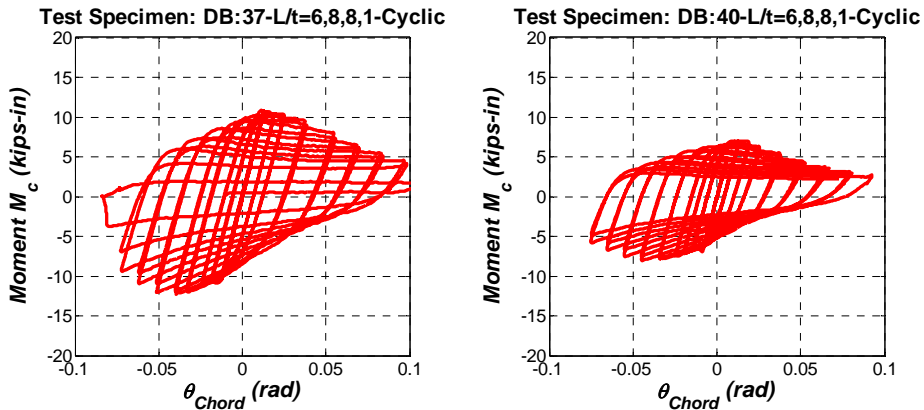
Figure 6.22. Monotonic (compression and tension) tests of single plate specimens with $L/t=6,8,8$ (Type B specimens)



(a) Tip load – tip displacement



(b) $M - \theta_{1.50}$ relationship



(c) $M - \theta_{Chord}$ relationship

Figure 6.23. Cyclic tests of single plate specimens with $L/t=6,8,8$ (Type B specimens)

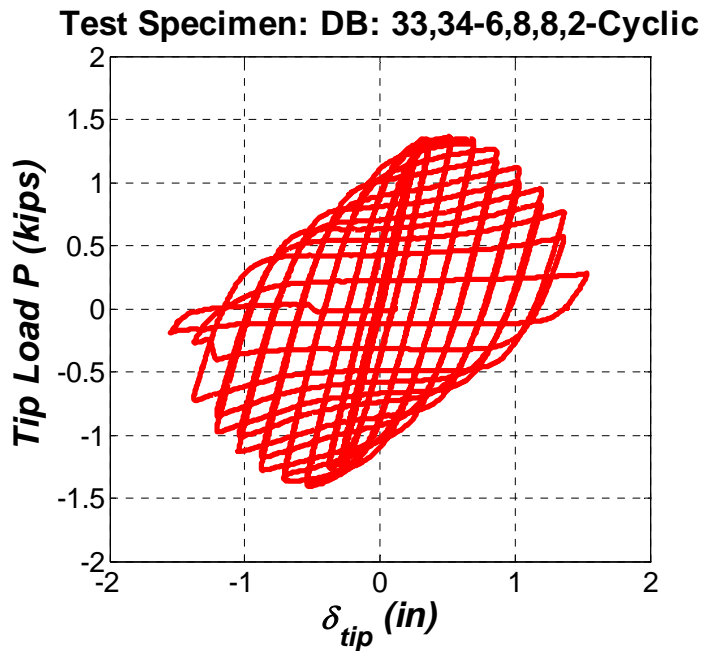


Figure 6.24. Tip load – tip displacement diagram of specimen “DB: 33,34-L/t=6,8,8,2–Cyclic” (Type B specimens)

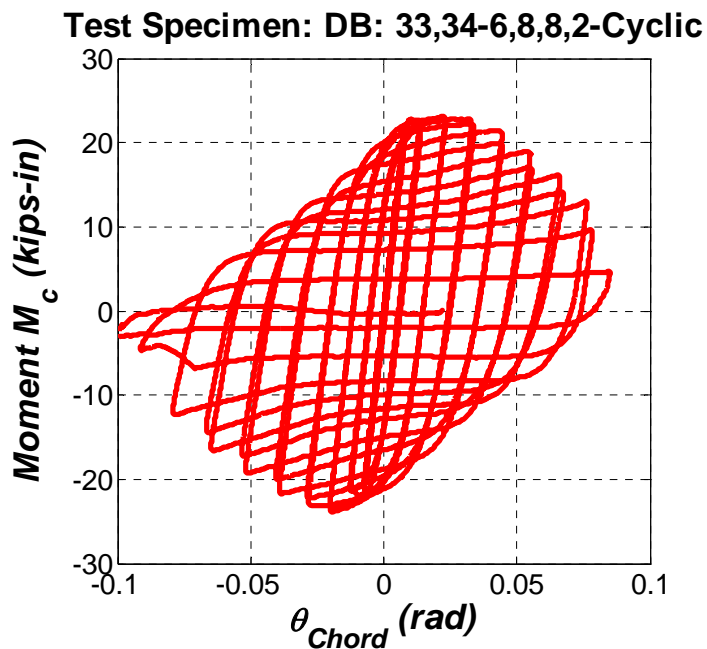
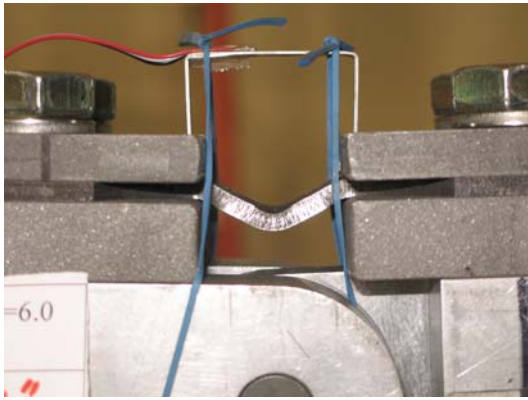
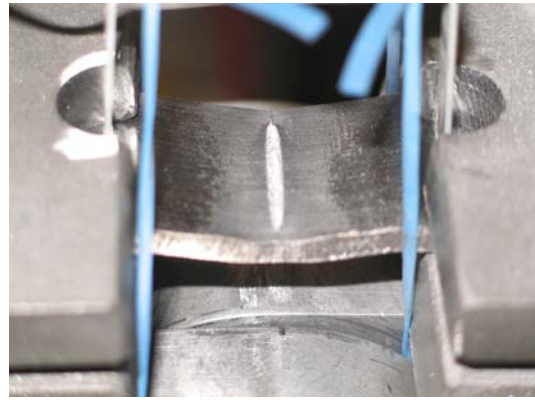


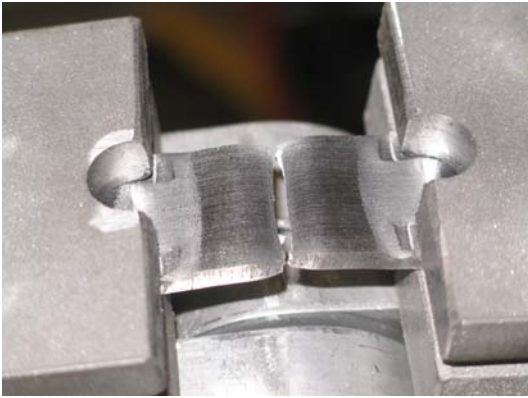
Figure 6.25. $M_c - \theta_{Chord}$ diagram of specimen “DB: 33,34-L/t=6,8,8,2-Cyclic” (Type B specimens)



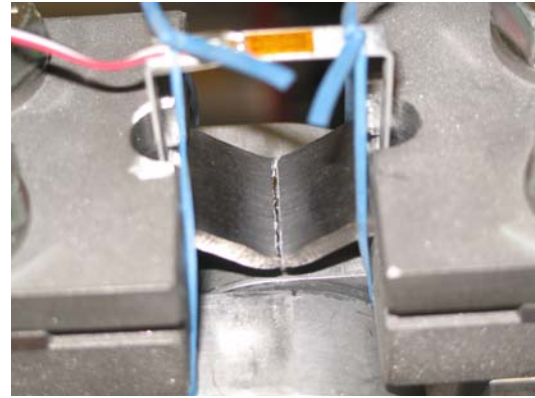
(a) Local buckling of top plate (point 1)



(b) Crack initiation of top plate (point 2)



(c) Fracture of bottom plate (point 3)



(d) Fracture of top plate (point 4)

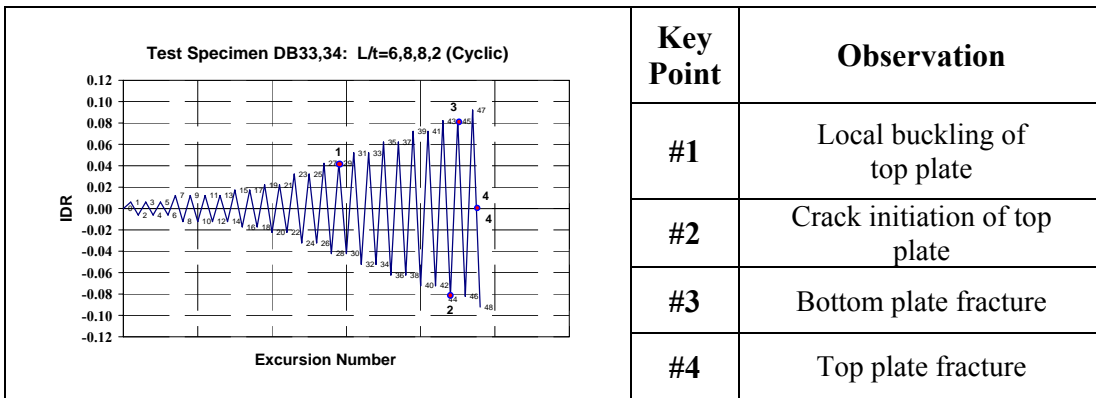
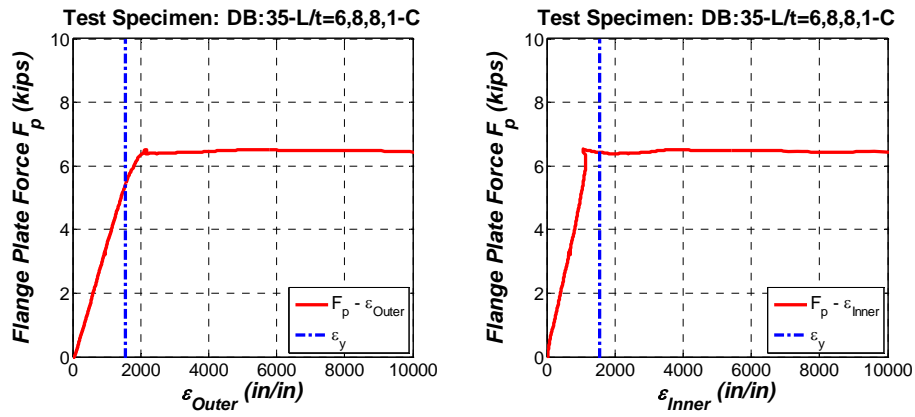
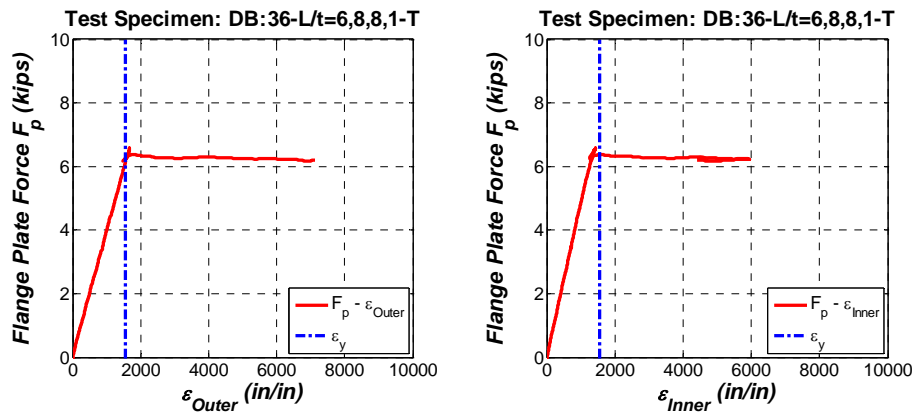


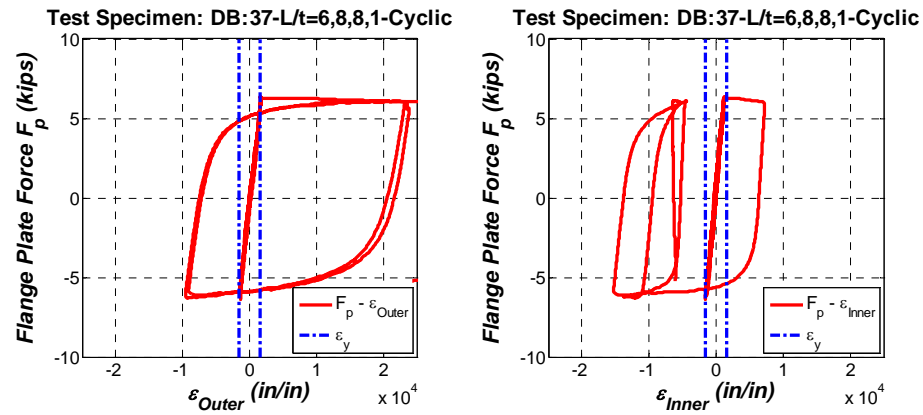
Figure 6.26. Summary of observations during the cyclic static test of specimen DB:33,34-
L/t=6,8,8,2–Cyclic (Type B specimens)



(a) Compression test



(b) tension test



(c) cyclic static test

Figure 6.27. Monotonic & cyclic flange plate force vs engineering strain relationships for outer & inner plate location of single plate specimens with $L/t=6,8,8$ (Type B specimens)

Test Specimen: DB:25,26-7,12,12,2-Monotoni

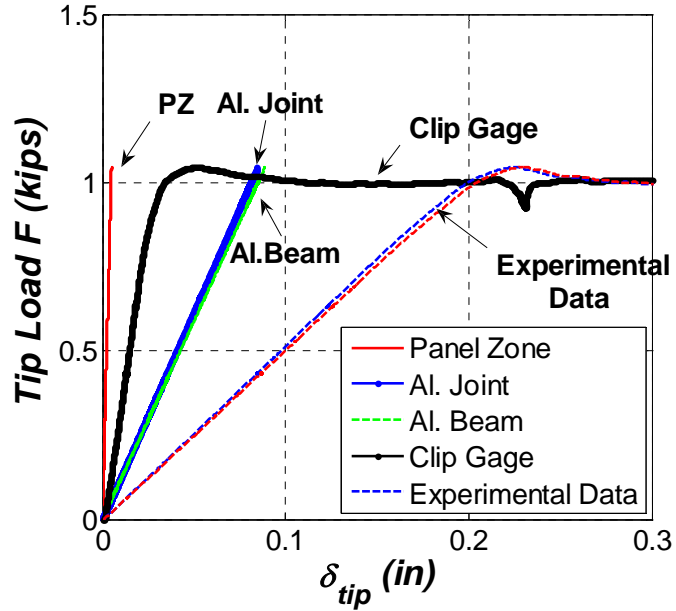


Figure 6.28. Components of elastic tip deflection

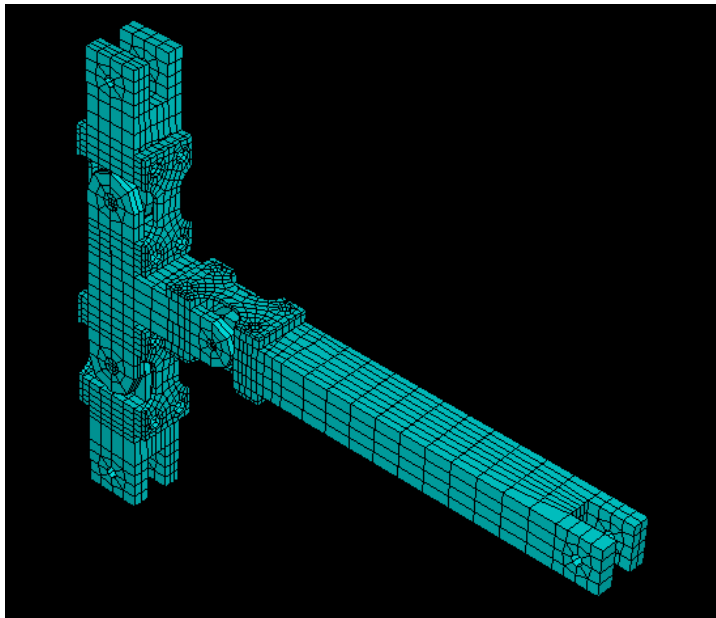


Figure 6.29. Detailed FEM model in ABAQUS

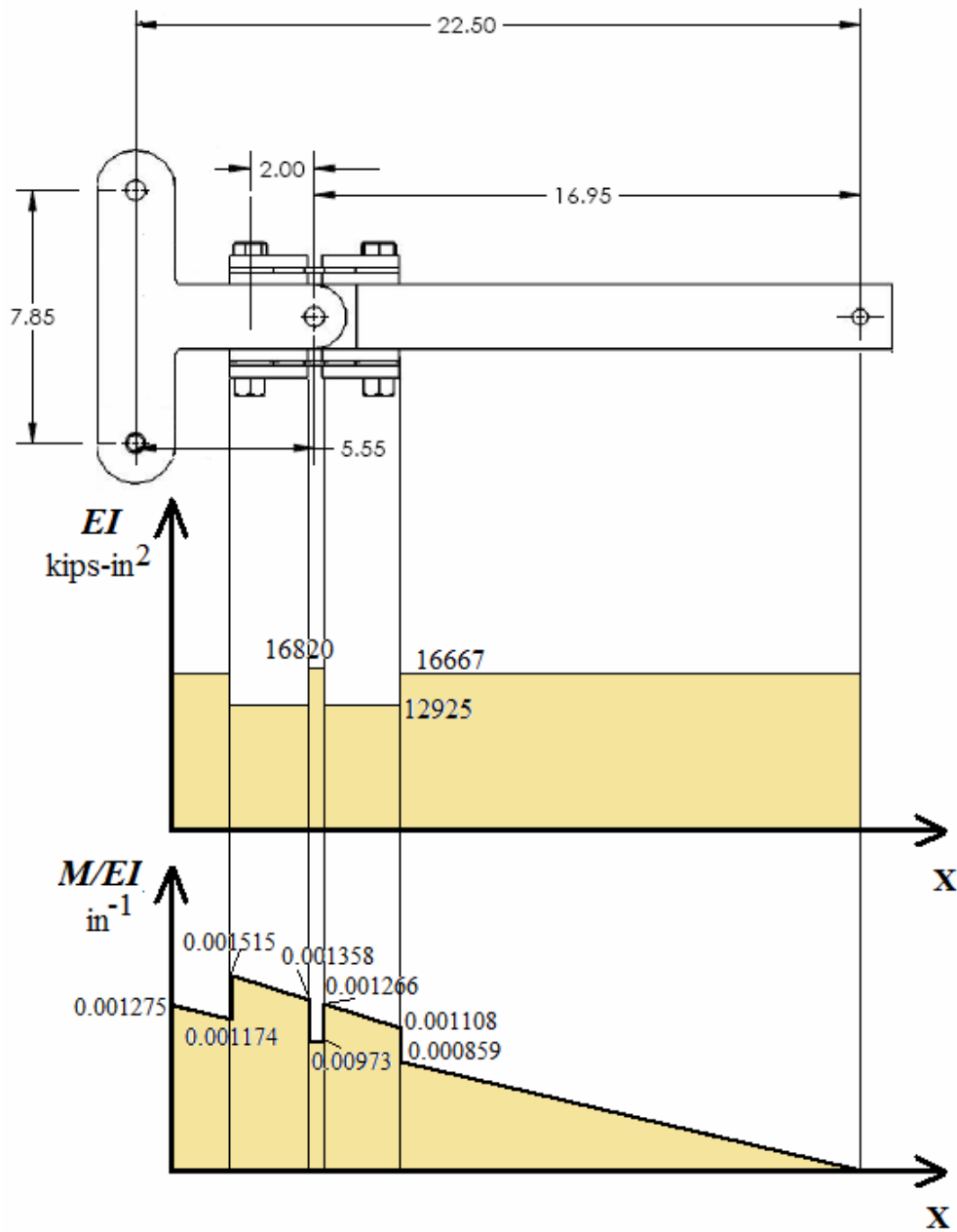


Figure 6.30. Variations of stiffness and curvature along the cantilever beam

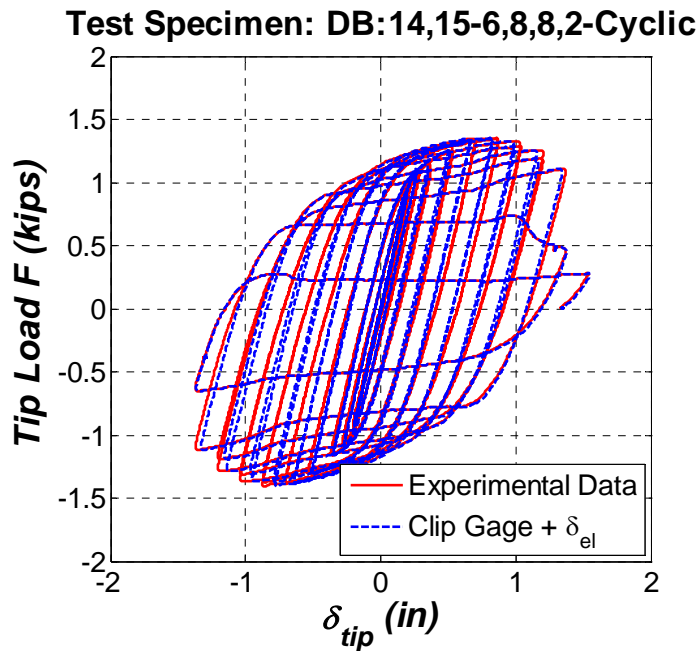


Figure 6.31. Comparison between experimental data and data deduced from clip gage measurement plus elastic components of deflection of all parts based on curvature calculations (Type B)

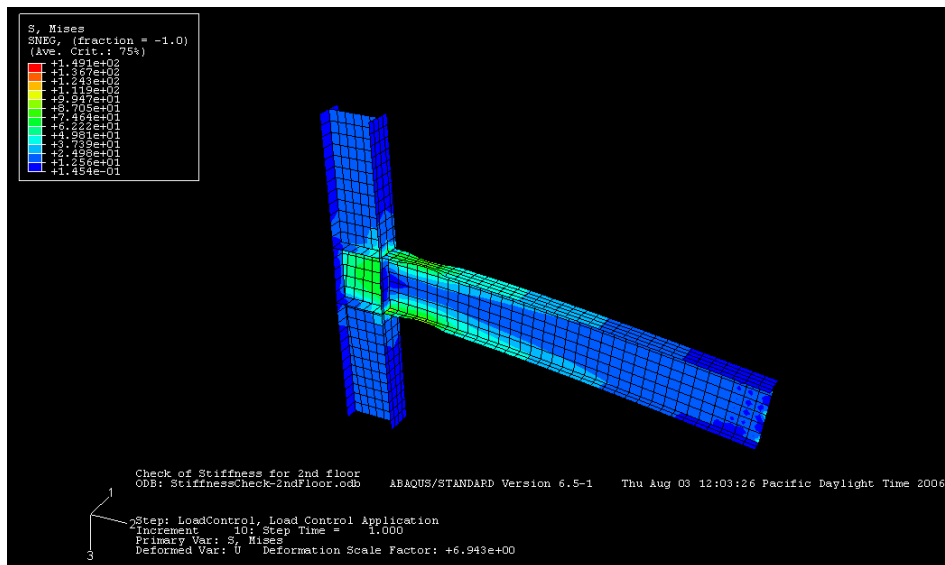


Figure 6.32. Exterior 1st story prototype subassembly modeled in ABAQUS

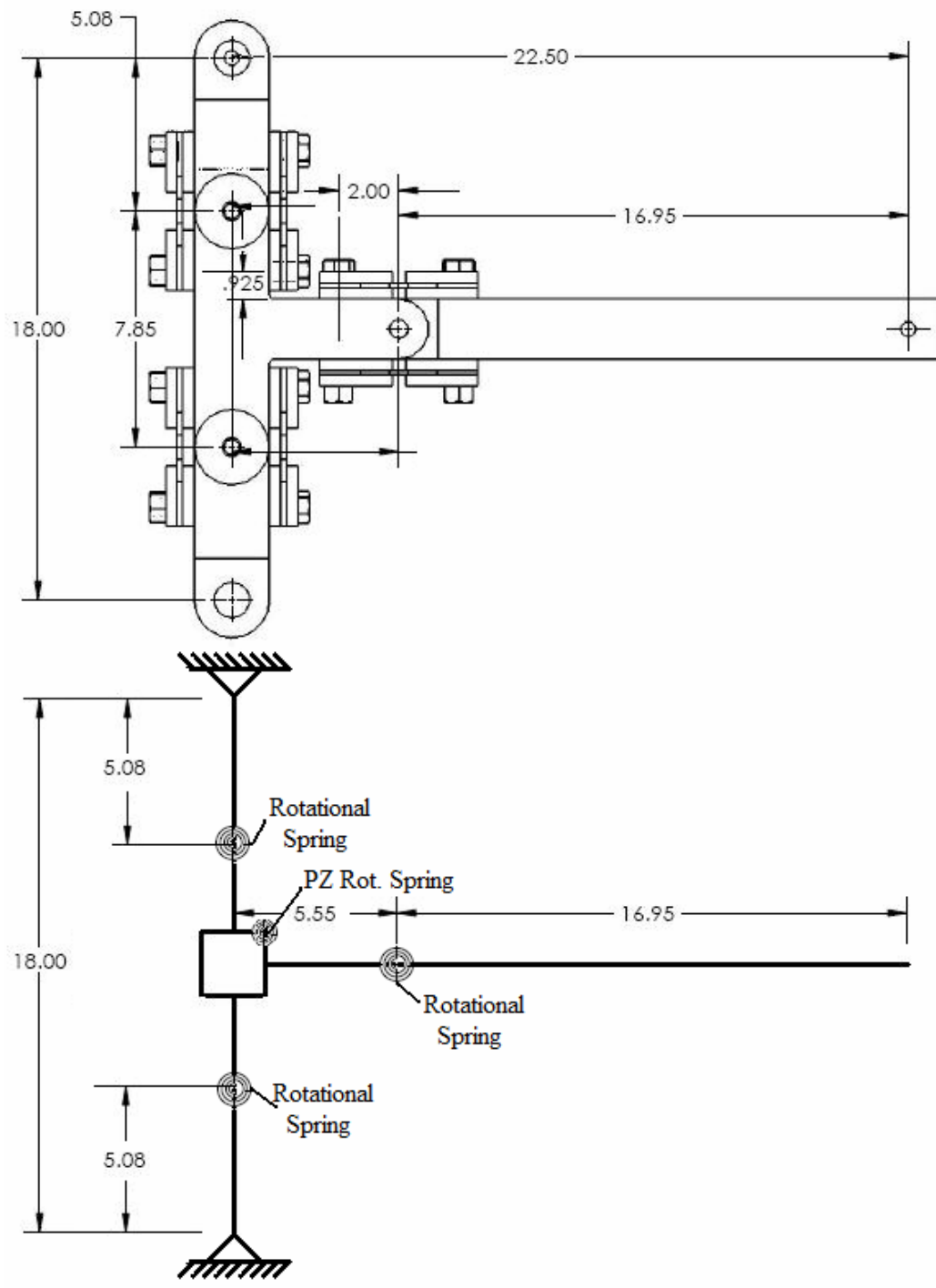
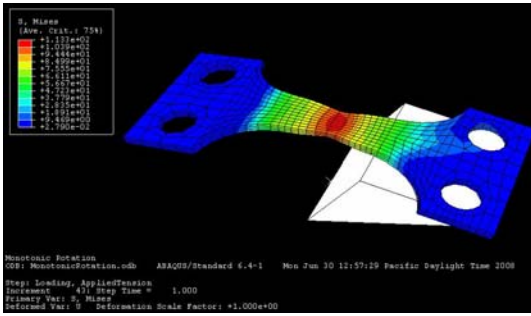
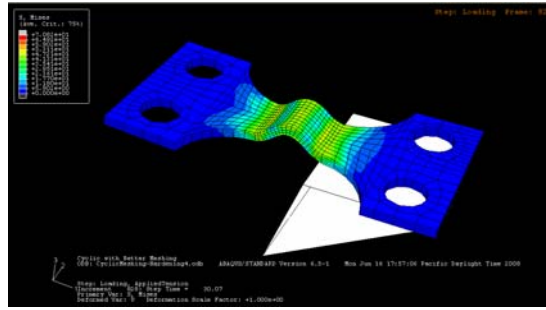


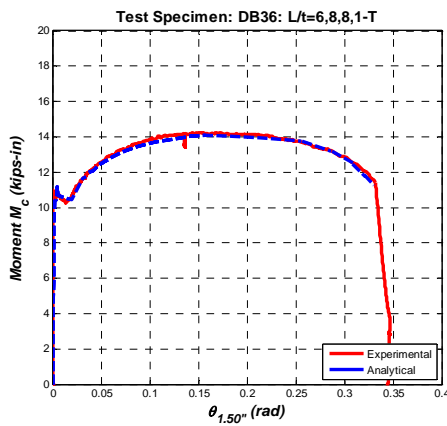
Figure 6.33. Simplified mathematical model used to simulate the behavior of model subassemblage



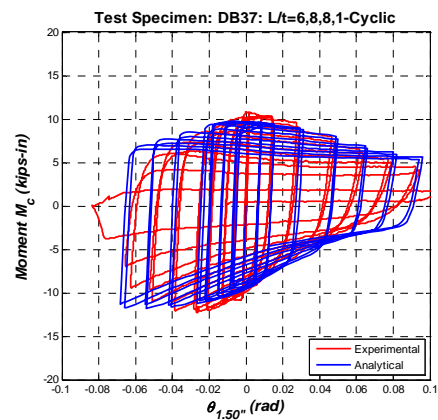
(a) Von Mises stresses (monotonic test)



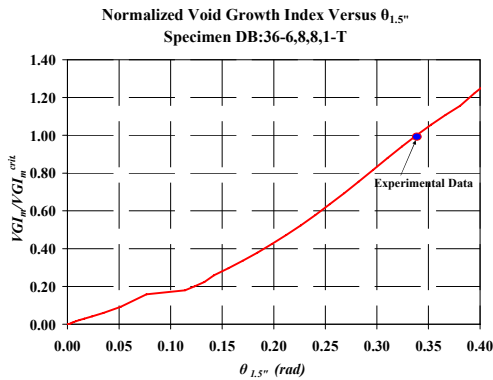
(d) Von Mises stresses (cyclic test)



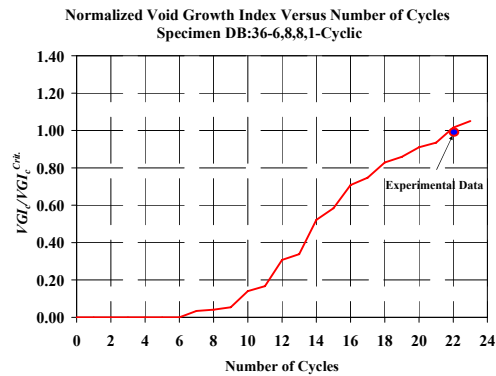
(b) $M_c - \theta_{1.5''}$ diagram (monotonic test)



(e) $M_c - \theta_{1.5''}$ diagram (cyclic test)



(c) Monotonic test



(f) Cyclic test

Figure 6.34. Comparison of FEM analytical predictions with ABAQUS versus experimental data of single plate specimens for monotonic and cyclic tests

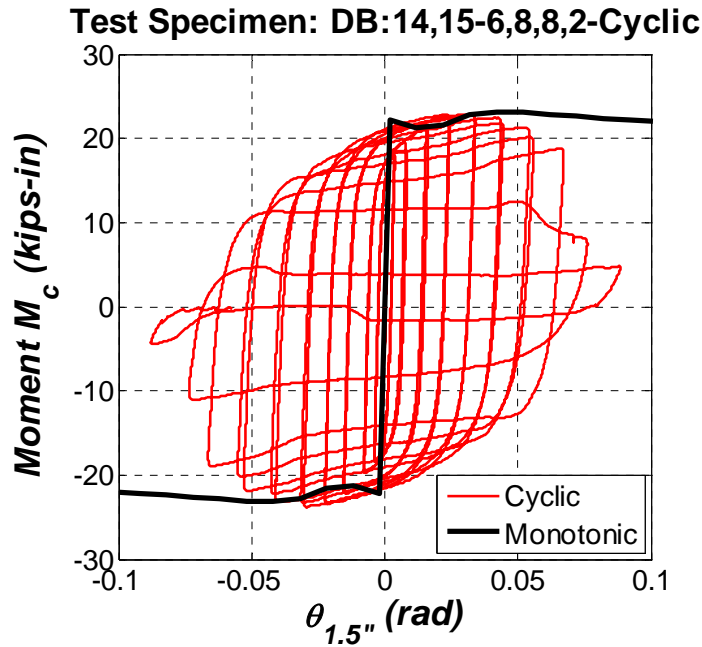
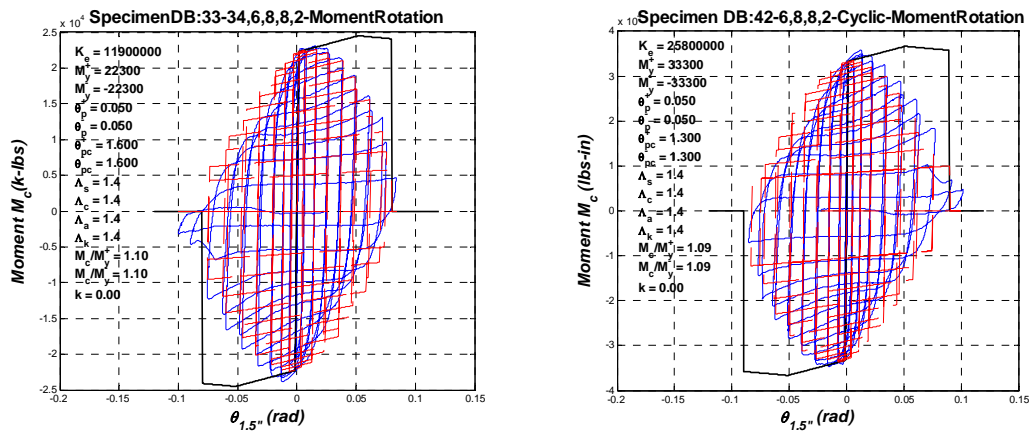


Figure 6.35. Monotonic and cyclic $M_c - \theta_{1.5''}$ diagram for typical plastic hinge location (Type B specimen)



(a) Exterior 1st floor beam

(b) Exterior 1st story column at the base

Figure 6.36. Calibrated $M_c - \theta_{1.5''}$ diagrams for typical plastic hinge locations

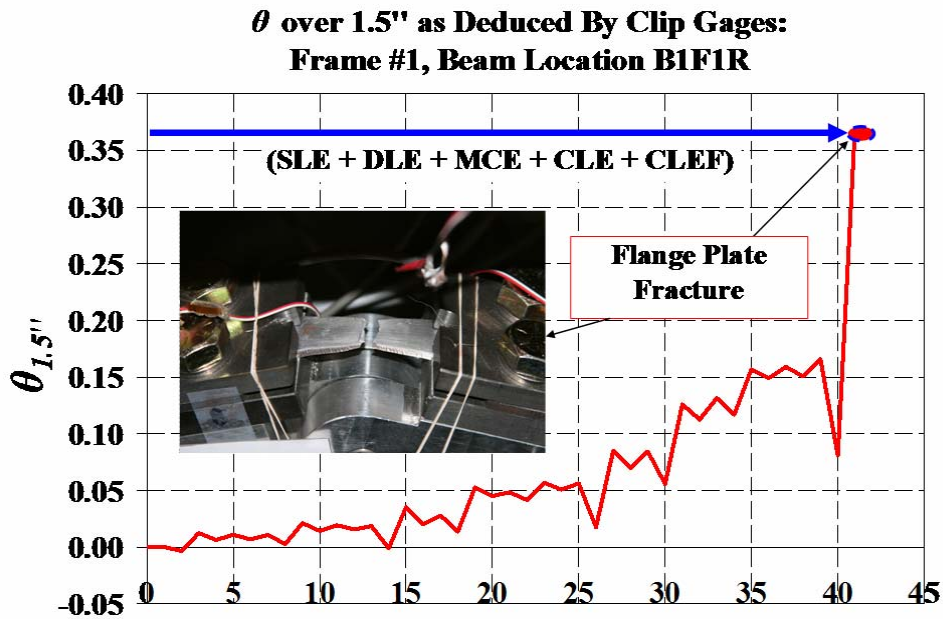


Figure 6.37. Rotation history over 1.5" length for first floor beam at interior joint based on clip gage histories for all 5 testing phases (Frame #1)

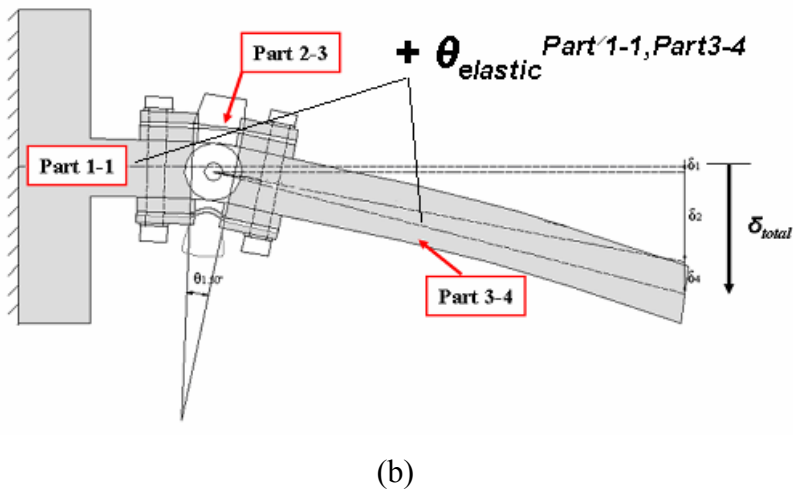
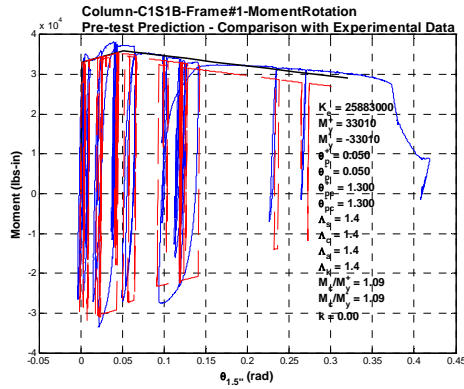
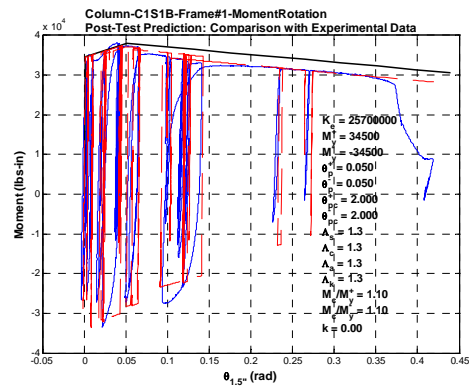


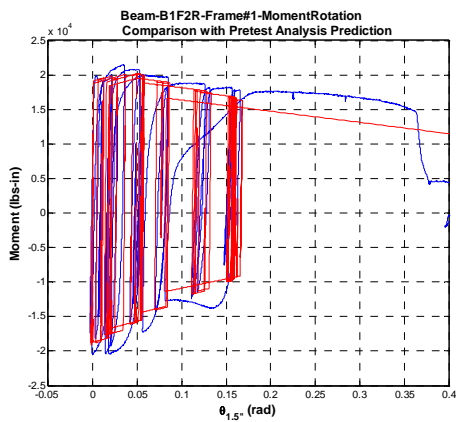
Figure 6.38. Contributions to elastic deflection of specimen subassembly for post-shaking table test evaluation



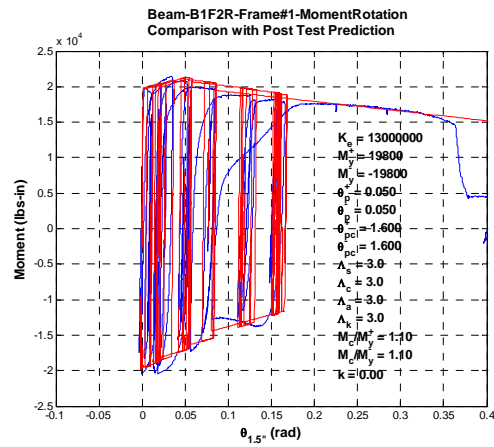
(a) pre-test prediction (column base)



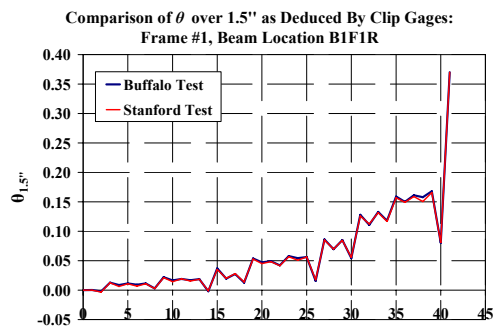
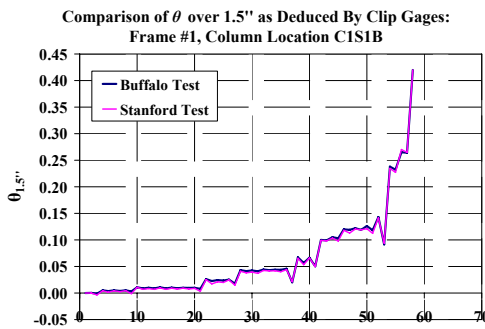
(b) post-test prediction (column base)



(c) pre-test prediction (1st floor beam)

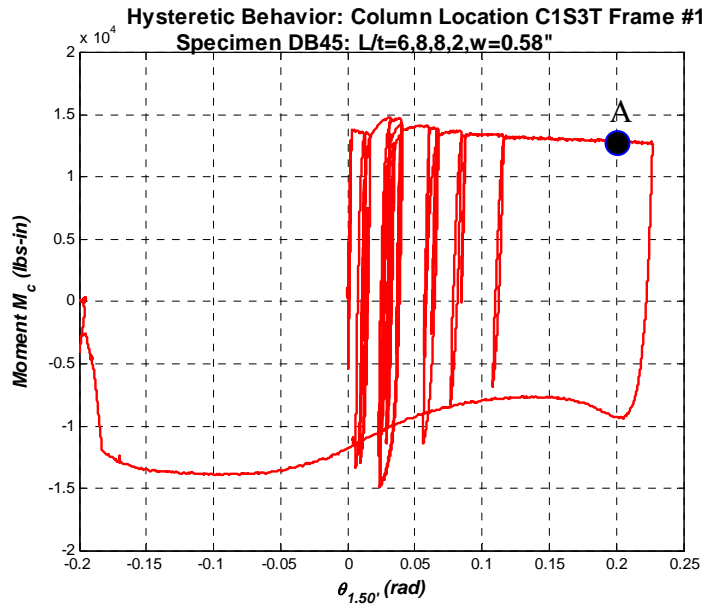


(d) post-test prediction (1st floor beam)

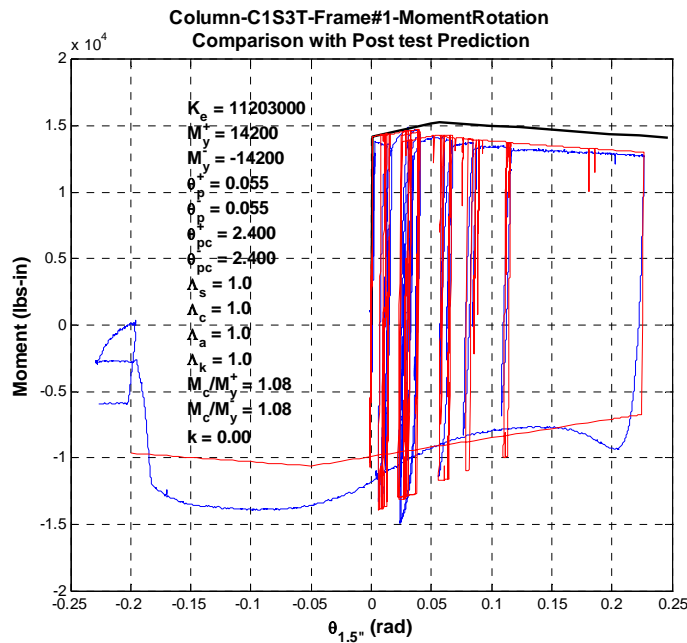


(e) comparison of rotation histories from Buffalo & Stanford tests; left=column base; right = 1st floor beam

Figure 6.39. Moment rotation ($M_c - \theta_{1.5''}$) diagrams for plastic hinge locations at column base and 1st floor beam obtained from component test using Buffalo rotation history as input (Frame # 1)



(a) moment rotation diagram (third story column, top location, Frame # 1)



(b) calibrated moment rotation diagram of third story column, top location (Frame # 1)

Figure 6.40. Moment rotation ($M_c - \theta_{1.50}$) diagram for plastic hinge location at top of third story column; Stanford component test with Buffalo rotation history followed by large displacement reversal

CHAPTER 7

SHAKING TABLE COLLAPSE TEST SERIES

7.1 Objective and Scope

The main objectives of the shaking table test series of the model frame discussed in Chapter 5 and presented in this chapter are: (1) quantification of engineering demand parameters from a physical experiment, including story forces and shears, story drifts, plastic rotations, and floor accelerations, in the elastic and inelastic range all the way to collapse; (2) demonstration that P- Δ induced sidesway collapse can occur under realistic structural and ground motion conditions and that P- Δ effect can be quantified up to collapse; (3) demonstration that collapse prediction is indeed feasible with reasonable accuracy using relatively simple models and (4) quantification of the effects of component deterioration on the collapse capacity of a frame structure.

Two scale models of the 4-story prototype moment resisting frame, which was discussed in Chapter 5, are tested on the shaking table of the NEES facility at the State University of New York at Buffalo. The behavior of both test frames are evaluated from elastic behavior up to collapse. In the subsequent discussion the frames are called Frame #1 and Frame #2. Due to the large amount of information collected during the shaking table collapse series only selected results are included in this chapter. A more comprehensive data is included in Appendix E and the complete data set is available through NEESCentral (<https://central.nees.org>).

7.2 Assembly of Test Frame and Installation on the Shaking Table

7.2.1 Assembly of Test Frame

Much effort was spent to assemble the test frame and guarantee that it is “perfectly” aligned in the plane of loading. The frame was firstly assembled horizontally on a flat 130" x 130" steel plate, as shown in Figure 7.1. Prior to the assembly of the test frame all the flange plates used at the plastic hinge elements were strain gauged. In order to tighten the bolt of the connections of the test frame the process described in Section 6.3.4 was employed, keeping the strain recordings for the flange plates at a relatively low level while pre-tensioning the bolts of each plastic hinge element.

7.2.2 Erection of Mass Simulator and Test Frame

After erecting the two individual bracing systems for out-of-plane support of the test setup the mass simulator was placed in the exact horizontal position on the shaking table. The ground level collapse impact prevention wood blocks, described in Section 5.3.3, were placed first on the shaking table in order to support the first story mass plate. The first story mass simulator plate was placed in its final horizontal position, resting on the wood blocks. The same process was continued until all mass plates were in exact horizontal position, resting on wood blocks as shown in Figure 7.2(a). In the vertical direction the top plate was 2 ½" lower than its final position because no gaps existed between the steel plates and the wood blocks. All gravity links (turn buckles), illustrated in Figure 7.2(b), were attached to the upper one of each pair of plates and the bolts connecting each gravity link to the mass plate were pretensioned. In order to vertically align the mass simulator plates we took advantage of the mass simulator’s own gravity. Four “lifting support plates” were tack-welded on top of the mass simulator bracing system, and with the help of lifting bolts threaded into the top mass plate the plates were raised one by one to the final position, connecting the bottom rod end of each gravity link to the lower one of the pair of plates

connected by the gravity link. By the time all gravity links were connected, all mass plates were hanging from the lifting support plates and the mass simulator self-aligned itself vertically by its own gravity. The weight per floor was equally distributed to the gravity links of each story by fine-adjustment of the gravity links that acted as turn buckles. The lowest links, once connected to bottom clevises, were just touching the base plates positioned on the shaking table.

After lowering the test frame in between its bracing system, as shown in Figure 7.3, and aligning the test frame in the transverse direction by attaching the horizontal bracing tubes (after greasing the sliding areas) the horizontal links were attached between the test frame and mass simulator (see Figure 7.4). The four links (one per floor), which served also as load cells, were fabricated as turn buckles for final adjustment in the horizontal direction. After fine adjustment to achieve zero force readings the bottom clevises of the test frame were field-welded to a support plate resting on the shaking table. The test frame was in final position and had in-plane resistance.

After field-welding the bottom clevises of the mass simulator gravity links to the base plate the four bolts of the mass simulator lifting mechanism were lowered until full weight was transferred to the gravity links. By fine-adjusting the horizontal links between test frame and mass simulator so that the force in all links was close to zero, minimum P- Δ effect was assured before beginning of the test series. Figure 7.5 shows the test frame and mass simulator after completion of erection process of the test setup on the shaking table.

This erection sequence made it possible to “swap” test frames with minimum effort, requiring only minute lifting of the mass simulator by means of bolts threaded into the top mass plate and supported on the “lifting support plates”, lowering the new test frame into position, and repeating the process described in the last two paragraphs. It should be mentioned that the new set of instrumented flange plates used for Frame # 2 were fabricated from a new steel plate with slightly different material properties than those of the steel plate

used to fabricate the flange plates of Frame #1. Thus the width w of the reduced section of the new set of flange plates was adjusted in order to achieve the same expected bending strength at every plastic hinge element as Frame #1 (for flange plate dimensions see Tables 5.8 and 5.9 in Section 5.3.1).

7.3 Instrumentation

A total of 314 channels were used for the instrumentation of Frame #1 and 247 channels were used for Frame #2. The number of strain gauged flange plates was smaller for Frame #2 than Frame#1 because of confidence in the selected instrumentation gained from the tests performed on Frame #1. This section discusses the main instruments used in the shaking table experimentation and their primary purpose. An instrumentation plan with locations of main instruments can be found in Appendix D. The complete instrumentation list for both frames can be downloaded through the NEESCentral repository (<https://central.nees.org>).

7.3.1 Load and Displacement Measurement Devices

The setup devised for the shaking table tests, in which lateral loads and P- Δ effects are transferred from the mass simulator to the essentially weightless frame through the instrumented horizontal links, provided the ability to measure directly the forces applied to the test frame at the individual floor levels (see Figure 7.4). All four links were strain gauged and calibrated in a tension machine in order to act as load cells. The links were designed to measure story forces in a range of +/- 20kips. Similarly, the gravity links of the first story of the mass simulator were instrumented in order to uniformly distribute the gravity load of the mass simulator to the individual vertical links.

To measure absolute displacements and derive relative displacements at each floor of the test frame and mass simulator, eight displacement transducers were used, one each per floor on the frame and mass simulator side. Three additional displacement transducers were used to measure the shaking table displacement in the direction of motion. The three displacement transducers were also used to trace any undesirable torsional motion of the shaking table.

7.3.2 *Accelerometers*

A set of ten accelerometers was used to measure absolute accelerations at floors of the test frame and mass simulator. Two accelerometers were installed on the shaking table to measure the achieved acceleration of the shaking table (“ground” acceleration). A set of two accelerometers was installed at each floor of the test frame and mass simulator. Acceleration measurements of the mass plates were used in order to compute the inertia story forces transferred to the test frame by multiplying the acceleration measurement at each floor with the individual story mass (see Table 5.10 for actual story weights).

7.3.3 *Strain and Deformation Measurements in Flange Plates*

Section 6.3.5 covered the details of strain and deformation measurements of the specimens tested in the laboratory of the John A. Blume Earthquake Engineering Center at Stanford University. The same arrangement of strain gages and clip gages was used for the flange plates of each plastic hinge element of both test frames. Due to limitations of available number of channels of the data acquisition system (DAQ), both sides of the flange plates were strain gauged for the interior and one of the exterior columns. In all other plastic hinge elements only the outer surface of each flange plate was strain gauged. Strain measurements in the flange plates were used to (1) locally trace the yield point of critical plastic hinge locations, (2) verify if the measured story forces from the horizontal links are reliable in the

elastic range, and (3) investigate how plastification of critical plastic hinge elements progresses based on the clip gage and strain gage measurements.

7.3.4 Krypton System

“State of the art” equipment used during the shaking table tests included a Krypton system (see Figure 7.6). The Krypton is a new generation of high performance dynamic mobile coordinate measurement machines. The system combines high accuracy, a large measurement volume and full freedom of space probe manipulation. This solid-state system is extremely reliable. The system is essentially a set of cameras (Krypton) that follow the 3-dimensional movement of a dot (LED) marked on the specimen.

Figure 7.7 shows the first floor interior joint of Frame #1 with all the aforementioned instruments installed, including nine LEDs (nine black dots). Forty LEDs in total were used during the shaking table test series. The arrangement of the LEDs was based on the analytically predicted collapse mechanism of the test frame for the ground motion sequence discussed later on in Section 7.4. The Krypton system was used also to measure rotations over a 4" length of selected plastic hinge elements in order to verify rotations as deduced by clip gages over 1.5" length. A detailed layout of all the LEDs can be found in the instrumentation plan of Appendix D. The sampling frequency of the Krypton DAQ was set to be 64Hz versus 128Hz of the Pacific DAQ in order to synchronize the two DAQs.

7.3.5 Cameras

A set of six digital local video cameras was used to monitor the behavior of selected critical plastic hinge elements. The monitored plastic hinge elements were selected based on the analytically predicted collapse mechanism of the test frame. Two more digital cameras were used in order to monitor the global behavior of the test frame and mass simulator. All eight digital cameras were synchronized with both DAQs. To monitor the global behavior

of the test frame and mass simulator from the north, south and south–west (for orientation see Figure 7.8) three high definition (HD) cameras were used. Telepresence equipment was also available, offering the opportunity to interested observers to watch remotely the erection process and shaking table experimentation. All the digital videos taken during the shaking table test series of both frames together with more than 3000 photos associated with the tests are available through NEESCentral (<https://central.nees.org>).

An illustration of the erection process and experimentation of Frames #1 and #2 is presented in Figures 7.9 and 7.10, showing the completion of erection of the mass simulator (see Figure 7.9(a)), the test setup of Frame #1 after completion of the collapse test (see Figure 7.9(b)), the removal of test Frame #1 from the shaking table(see Figure 7.9(c)) and assembly of test Frame #2 (see Figure 7.10(a)), test setup of the same frame after completion of the collapse test (see Figure 7.10(b)) and an exterior joint of the same frame in the final collapse configuration. (see Figure 7.10(c)).

7.4 Ground Motions and Testing Programs

7.4.1 Testing Program – Frame #1

In the shaking table test series of Frame #1 the Northridge 1994 Canoga Park station ground motion was used in order to evaluate performance of the frame from elastic behavior up to collapse. Figure 7.11(a) shows the acceleration time history of the unscaled record and Figure 7.11(b) shows a direct comparison between the design acceleration spectrum based on recent seismic provisions (IBC-2003) for soil type D and the acceleration response spectrum of the unscaled ground motion. In the range of periods of primary interest (1.32 sec and longer due to period elongation of the test frame) the Canoga Park spectrum matches well with the design spectrum; thus it was decided that the unscaled Canoga Park record is a good representation of a Design Level Earthquake (DLE).

A “physical” incremental dynamic analysis (IDA) was conducted since Frame #1 was subjected to five different levels of intensity of the same record, from elastic range all the way to collapse, recognizing that the initial conditions for each new test correspond to the deformed configuration of the frame after the previous test. The levels of intensity of the record were based on analytical simulations of the model frame prior to the shaking table experimentation summarized later on in Section 7.5.1.2.

The following test sequence was executed for Frame #1:

- Free and forced vibration tests for modal analysis (White noise (WN), sine-sweep (SS) and pulse type (PT) tests)
- Elastic ground motion test (Service Level Earthquake, SLE = 40% of unscaled record)
- Inelastic test at “design level earthquake” based on 10/50 hazard (DLE = 100% of unscaled record)
- Inelastic test at “Maximum Considered Earthquake” level based on 2/50 hazard (MCE= 150% of unscaled record)
- Inelastic test at “Collapse Level Earthquake” level (CLE = 190% of unscaled record)
- Inelastic test at “Final Collapse Level Earthquake” level (CLEF = 220% of unscaled record)

7.4.2 Testing Program – Frame #2

In the shaking table testing of Frame #2 a different ground motion sequence was used prior to collapse of the frame. One objective was to investigate the effect of cumulative damage on the collapse capacity of the test frame; thus in between the design level and collapse level earthquakes, 150% of the unscaled motion of the Chile 1985 Llole record was used,

intended to represent an MCE motion. Figures 7.12(a) and 7.12(b) show the acceleration time history and acceleration spectrum of the unscaled Llolleo record, respectively. In Figure 7.12(b) the design spectrum based on IBC-2003 is superimposed for comparison purposes. The shaking table did not succeed in reproducing the input table motion at the MCE level (see Section 7.5.2); thus it was decided to switch motions and subject Frame #2 to 220% of the unscaled Canoga Park record for the collapse level and final collapse level tests. Similarly to Frame #1 the levels of intensity of the ground motions were based on analytical simulations prior to collapse test of Frame #2. These simulations are summarized in Section 7.5.2.2.

The following test sequence was executed for Frame #2:

- Free and forced vibration tests for modal analysis (White noise (WN), sine-sweep (SS) and pulse type (PT) tests)
- Elastic ground motion test (Service Level Earthquake, SLE = 40% of unscaled Canoga Park record)
- Inelastic test at “design level earthquake” based on 10/50 hazard (DLE = 100% of Canoga Park unscaled record)
- Inelastic test at “Maximum Considered Earthquake” level based on 2/50 hazard (MCE= 150% of unscaled Llolleo record)
- Inelastic test at “Collapse Level Earthquake” level (CLE = 220% of unscaled Canoga Park record)
- Inelastic test at “Final Collapse Level Earthquake” level (CLEF = 220% of Canoga Park record unscaled record)

The reason why in both shaking table test series (Frames #1 and #2) a “Final Collapse Level Earthquake” test had to be performed was that in both cases collapse did not occur under the predicted “Collapse Level Earthquake” based on analytical simulations prior to the shaking table collapse tests.

7.5 Experimental Results

This section summarizes observations and selected results from the series of shaking table tests for both test frames. A total of 110 tests were carried out for both test frames. Most of the tests were used for identification of modal properties and in order to gain confidence in instrumentation based on the elastic response of both frames. All the tests conducted in the NEES facility at the U. of Buffalo are available through NEESCentral repository (<https://central.nees.org>).

7.5.1 Test Frame #1

7.5.1.1 Modal properties

A series of white noise (WN) and sine–sweep (SS) tests were conducted for identification of modal properties of Frame #1. This frame exhibited considerable friction damping attributed primarily to the spherical hinges of the mass simulator gravity links. Because of pre-tensioning of the bolts required to hold the links in place the ball joint at the ends of the links expanded due to Poisson’s effect. For all the WN and SS tests conducted it was not possible to identify more than the first mode of Frame #1 because of friction damping. In the tests on Frame #2 the first and second mode of the frame were reliably predicted because the amount of friction damping was reduced with the use of machine grease installed directly in the ball joint (See Section 7.5.2.1). The results discussed later demonstrate that the friction damping present in Frame #1 did not affect significantly the response at the DLE, MCE, and collapse levels.

Figure 7.13 shows the transfer function at the roof of Frame #1 after a WN test with amplitude at 0.1g. The scaled target first mode period of the test frame was 0.46sec. The first mode period obtained from WN and SS tests was 0.40sec.

Viscous damping identification was not possible because of the presence of friction damping. Based on pulse type tests the response of the frame decayed rapidly due to friction damping. From these tests an “equivalent” viscous damping of 15% was obtained based on a 0.60g amplitude pulse using the approach described in Bracci et al. (1992). This value is meaningless in terms of simulating viscous damping in Frame #1 but indicates how significant the effect of friction damping was on the elastic behavior of Frame #1. It was decided to use three percent Rayleigh damping at the first and second mode of the frame in all the analytical pre-test simulations.

7.5.1.2 Global Behavior

General description and observations

Figure 7.14 shows the roof drift response of Frame #1 during its main response phases at various intensities from elastic behavior up to collapse. The main response phases are separated with two solid lines. Figure 7.15 show the main story drift response phases. As seen from this figure, every story of Frame #1 “drifted” in the same direction as the ground motion intensity is increased until collapse occurred.

The response in the SLE test was elastic. In the DLE test Frame #1 exhibited a maximum IDR at the first story of about 0.016 rad. The inelastic action was concentrated at the column base, first and second floor beams, and third story columns at the top. Localized damage (i.e. local buckling of flange plates) was barely noticeable even though the residual first story drift after the end of DLE was about 0.01rad (for illustration see Figure 7.16(a), exterior column base after completion of DLE).

In the MCE test Frame #1 was severely damaged reaching a maximum IDR_1 of about 0.05 rad. Damage became evident in most of the plastic hinge elements that were part of the 3-story collapse mechanism. Figure 7.16(b) shows the exterior column base after completion

of MCE, having a residual plastic rotation of about 0.045 rad. The permanent deformation at this location is evident from local buckling of one of the flange plates.

Analytical pre-test predictions indicated that Frame #1 would collapse in the CLE test (see discussion in Section 7.6.5). The frame experienced a maximum IDR of about 0.13rad but did not fully lose its lateral resistance, i.e. it did not collapse. The 3-story mechanism, which started forming during DLE and progressed in the MCE test, was clearly noticeable. The columns at the top of the third story reached a maximum rotation of about 0.10rad, and the column base at the end of CLE had a permanent plastic rotation of about 0.12rad (see Figure 7.17(a)).

Frame #1 collapsed after the first reversal of the ground motion in the CLEF test. The fact that the frame collapsed very early in the test indicates that the analytical pre-test prediction of the CLE motion was fairly close to the collapse intensity. All the flange plates that were in tension at the column bases and in first and second floor beams did fracture. An example of a fractured flange plate is illustrated in Figure 7.17(b), which shows the exterior column base of Frame #1 after the end of CLEF.

Figure 7.18 shows the 3-story collapse mechanism of Frame #1 after completion of CLEF. The upper portion of the mechanism was formed by column plastic hinges at the top of the third story, even though the weak beam - strong column (WBSC) criterion was fulfilled in the design process (see Section 5.2).

As mentioned in Sections 5.3.3 and 5.3.4, a number of safety mechanisms was designed in order to protect the shaking table and laboratory equipment when the test frame lost its lateral resistance, i.e. collapse occurred. When one of the safety mechanisms “locks”, the recorded data after “locking” become meaningless. It is defined as Incipient Collapse Level (ICL) the point at which one or more safety mechanisms “catch” either the test frame or the mass simulator or both.

The first safety mechanism that engaged for Frame #1 was the transverse angle at the third floor level of the test frame lateral bracing system. Figure 7.19 illustrates the “catching” mechanism after the completion of CLEF. Based on the data evaluation the Incipient Collapse Level (ICL), i.e., the level when one of the safety mechanisms “locks”, was attained at 7.10 sec after the beginning of the test (2.10 sec after the beginning of the motion at CLEF). From this instance on the recorded data become meaningless.

Acceleration measurements

A comparison between peak accelerations from accelerometers attached to the beams of the test frame and peak average accelerations (average of two values) from accelerometers attached to the plates of the mass simulator is shown in Figure 7.20. As seen from this figure the peak accelerations of the test frame are consistently lower than the peak accelerations of the mass simulator. A possible reason is a high frequency component recorded with the accelerometers of the mass simulator. Based on a comparison of measurements recorded by instruments installed on the mass plates and on the shaking table it was concluded that there was no torsional motion in the mass plates. In subsequent presentations of results the mass simulator accelerations are utilized because the main purpose of the acceleration measurements is to quantify the inertia forces generated by the mass simulator.

Strain and clip gage measurements

In the elastic range of response the strain gage values that were calibrated against plastic hinge element bending moments in the component tests (see Section 6.5.4.2 and Table C1 of Appendix C) permit the derivation of all internal force quantities in the test frame. Figure 7.21 shows the moments at each joint of the test frame after extrapolating moments from the plastic hinge element locations that were deduced based on strain calibrations at 8.10 sec after the beginning of SLE. The sum of moments at each joint should be equal to zero,

which is reasonably well achieved with the exception of the right exterior joint at floor 3 where the sum of beam moments differs by 18% from the sum of column moments. The presented values provide an indication of the accuracy with which elastic moments can be predicted from strain measurements taken during the shaking table test.

The moments obtained from these strain measurements were used to derive column shear forces and story shear forces and to compare the latter to the story shear forces obtained from force measurements in the horizontal links. Figure 7.22 shows this comparison, with the story shear forces obtained from the horizontal links in parenthesis. The results are comparable but not identical, permitting further judgment on the accuracy of moment and shear force measurements from strain gage calibrations (based on extensive calibrations, full confidence is placed in the story shear force values obtained from the link measurements).

Strain measurements were also used to detect when and where the structure behaved inelastically for the first time. The first plastic hinge elements that reached the inelastic range were the first floor beams during DLE almost simultaneously with the column base. Figure 7.23 shows a time window of the strain histories of the top and bottom flange plates of the exterior first floor beam during DLE. The engineering yield strain as measured in the component tests is shown with horizontal lines in the figure. Based on this figure, local inelastic behavior occurred for the first time 6.66 sec after the beginning of DLE.

Peak interstory drift ratios and IDA curve

Peak interstory drift ratios (IDR) of Frame #1 at various levels of ground motion intensity are presented in Figure 7.24. For the CLEF test the peak IDR profile at the ICL are plotted. As seen from this figure, prior to CLEF the absolute maximum IDR of Frame #1 was in the second story. At the ICL the peak absolute IDR migrated to the first story. Interstory drift

ratios were deduced from the Krypton system since it was judged to be the most reliable instrument at large deformations (near ICL).

Figure 7.29 shows the residual drift ratios of Frame #1 at various ground motion intensities prior to ICL. Before the CLEF the test frame had a residual drift of about 13% in the second story. The existence of residual drifts in all stories at the DLE indicates that inelastic deformations were distributed over all four stories, including the top story that was not part of the final collapse mechanism of Frame #1 shown previously in Figure 7.18.

Ground motion intensity versus peak roof drift ratio of the “physical” IDA is shown in Figure 7.26. The basic difference between a typical IDA curve (Vamvatsikos and Cornell, 2002) and the one obtained experimentally in this testing program is that each time that the intensity of the ground motion is increased the initial conditions for the frame are determined by preceding loading histories. Thus, there is cumulative damage in the “physical” IDA that does not exist in a typical analytical IDA. In all the analytical simulations that were carried out the cumulative damage from previous tests was considered. Superimposed on the experimental IDA in Figure 7.26 is the IDA curve as obtained from the pre-test collapse predictions.

The analytical pre-test IDA curve shows that the last stable point of Frame #1 is at 190% of the unscaled Canoga Park record as illustrated in Figure 7.26. It was decided to “challenge” the pre-test analytical prediction and designate this level as the collapse level for the shaking table test. In the CLE test the frame experienced a large peak roof drift of about 11%, but it did not fully lose its lateral resistance. This necessitated the execution of an additional test, denoted as CLEF. Somewhat arbitrary, and in order to assure collapse, the CLEF level was chosen as 220% of the unscaled Canoga Park record. As noted before, Frame #1 collapsed very early in the CLEF test. Thus the final collapse level CLEF represents an experimental point only; but it is not part of the physical IDA curve shown Figure 7.26. The reason is that the test frame would have collapsed after the CLE even if a

motion with a relatively low ground motion intensity would have been used, as is discussed in Section 7.6.5.

Yield pattern and collapse mechanism

The yield patterns of Frame #1 are illustrated in Figures 7.27 and 7.28, in which the residual rotations over 1.50" length ($\theta'_{1.5''}$) of the plastic hinge element flange plates are presented, as deduced from the clip gages after completion of each applied ground motion. Figure 7.28(b) shows the actual rotations $\theta_{1.5''}$ of each plastic hinge element at the Incipient Collapse Level, ICL, since this was the last reading unaffected by interference from collapse prevention mechanisms. In case a clip gage measurement was not reliable (clip gage slipped with respect to its attachment point or the assigned channel was not recording properly), $\theta_{1.5''}$ was deduced from the Krypton system if measurements were available for the plastic hinge element of interest. In case no measurement was available, $\theta_{1.5''}$ is marked on the figure as not reported (NR). Since the yield rotation of each plastic hinge element is a "negligible portion of $\theta_{1.5''}$ " the latter was used as an approximation of the plastic rotation of each plastic hinge element that was damaged.

In summary, the shaking table tests provided an essentially complete set of experimental data from which all seismic force and deformation parameters of interest can be derived for the set of ground motions to which the test frame was subjected. Of primary interest is behavior close to collapse. The comparison of pre-test analytical collapse simulations of Frame #1 with the experimental data showed that even if the collapse point was not captured precisely the analytical prediction of the collapse capacity of Frame #1 for the Canoga Park record was within reasonable accuracy. Correlation between experimentally measured or derived parameters and corresponding analytical post-test predictions are discussed in Section 7.6.5.

7.5.2 Test Frame #2

7.5.2.1 Modal properties

In order to reduce the effect of friction damping on the dynamic response of Frame #2 all the gravity links used to support the mass plates were removed one by one and the interior surface of the ball joints of the spherical hinges was greased. After a sequence of WN and SS tests the properties of the first two mode shapes and periods of Frame #2 were reliably obtained. Figure 7.29 shows the transfer function at the roof level of Frame #2 after a 0.10g WN test. The first and second mode periods of Frame #2 were 0.457 sec and 0.158 sec. Both periods match well with the target scaled mode periods of the prototype frame ($T_{1,s} = 0.467$ sec and $T_{2,s} = 0.132$ sec). [An exact match should not be expected because of the simplifications made in the fabrication of the test frame.] Figure 7.30 shows the first two mode shapes of Frame #2 obtained based on the approach discussed in Bracci et al. (1992). Shown in the same figures are the first two mode shapes of Frame #2 as predicted from the mathematical model used for post-test collapse prediction (see Section 7.6). Even though the effect of friction damping on the elastic behavior of Frame #2 was smaller compared to Frame #1 (8% “equivalent” viscous damping based on a 0.6g PT test), it was not feasible to determine viscous damping properties from the conducted elastic tests. A detailed evaluation of friction damping is presented in Section 7.6.1.

7.5.2.2 Global Behavior

General description and observations

Figure 7.31 shows the roof drift response of Frame # 2 during its main response phases at various intensities of the Canoga Park record from elastic behavior up to collapse and also at the designated MCE level using the Llole record (from 9sec to 16sec). As seen from

this figure Frame #2 started drifting in the same direction as Frame #1 but it collapsed in the opposite direction.

Figure 7.32 shows the story drift history of Frame # 2 during its main response phases at various intensities. In the DLE test Frame #2 behaved almost identical to Frame #1 indicating that friction damping was not critical at this level of ground motion intensity and higher (see also Section 7.6.1). From the interstory drift ratio histories of the first three stories of the frame it can be seen that most of the inelastic action was concentrated in those three stories that were part of the final collapse mechanism.

In the MCE test (intended to reproduce 150% of Llolele motion) the applied ground motion did not cause an increase in residual drift, which was very puzzling until it was found out (long after all tests were completed) that the input ground motion was not reproduced successfully in the shaking table. Figure 7.33 shows the acceleration spectrum of the achieved table motion for 150% of the unscaled Llolele motion in comparison with the acceleration spectrum of the intended input in the model domain ($T_1=0.46\text{sec}$). The ordinates of the spectra differ by a factor of about two. Thus, the executed MCE level test was of about half the intended intensity, which changed the behavior radically compared to pre-test predictions.

The “MCE level” test did not change the residual drift in the individual stories by much and, if anything, it succeeded in straightening out the test frame (see later discussion related to IDR). In addition, significant out of plane movement was observed at the fourth floor beams due to the impact of those beams on the lateral bracing system of the test frame during the MCE test. The fourth floor beams were slightly distorted, as seen from Figure 7.34. After field welding a temporary local lateral support at the location of beam distortion (see Figure 7.34) it was decided to continue testing but to switch back to the Canoga Park record.

In the CLE test (220% of unscaled Canoga Park record) Frame #2 started to drift in the opposite direction of motion and did not exceed a maximum IDR of about 0.05 rad, as shown in Figure 7.32. The reason why Frame #2 drifted in the opposite direction is explained later in this section.

When repeating the 220% of Canoga Park record (CLEF) Frame # 2 collapsed 8.80sec after the scaled motion started, i.e., late in the test, which indicates that the actual collapse capacity of the frame was not much lower than the experimental point (see discussion in Section 7.6.5). The collapse mechanism shown in Figure 7.35 is identical to the collapse mechanism of Frame #1, except that Frame #2 collapsed in the opposite direction. The first safety mechanism that engaged in Frame #2 was the set of wooden blocks installed between the four stories of Frame #2. This occurred 8.80 sec after the beginning of CLEF. Figure 7.36 illustrates the “catching” mechanism after the completion of CLEF.

Acceleration measurements

Peak accelerations from accelerometers attached to the beams of the test frame and peak average accelerations (average of two values) from accelerometers attached to the plates of the mass simulator are compared in Figure 7.37 for various ground motion intensities, with similar observations as have been made for Frame #1. Comparing Figures 7.20 with 7.37 it is observed that the peak accelerations for Frame #1 and Frame #2 follow the same pattern for the same ground motion record and intensity. The fact that the peak floor accelerations in tests SLE and DLE are larger for Frame #2 than Frame #1 is attributed to the much reduced friction damping in Frame #2.

Strain and clip gage measurements

Since Frame #2 was not fully instrumented with strain gages (only interior column and beams), strain measurements (ϵ_{SG}) on the flange plates were correlated with the ones

measured from the clip gages (ϵ_{CG}) over 1.5" length in order to check the moment equilibrium per joint of Frame #2. Figure 7.38 shows a comparison of two strain histories at the exterior end of the first floor beam during SLE for top and bottom flange plates. The measurement denoted with a solid line was obtained directly from strain readings and the other (dashed line) was deduced from the clip gage. As seen, the two strain histories are almost identical with only a small deviation at the peaks, possibly because of the lower resolution of the clip gage readings.

Interstory drift ratios and IDA curve

Peak IDRs of Frame #2 are presented in Figure 7.39. Frame #2 performed very similarly to Frame #1 at the DLE level, indicating that friction damping was not a major issue at this or larger ground motion levels (see discussion in Section 7.6.1). As seen from the same figure, peak IDRs in the “MCE level” test (1.5 times the unscaled Llolleo record) did not exceed peak IDRs in the “DLE level”.

Even though the Llolleo record did not cause a significant increase in story drift in the MCE test, the residual story drifts along the height of Frame #2 after the MCE test were somewhat different compared to those after the DLE test of Frames #1 and #2. This can be seen in Figure 7.40, which shows residual drifts of Frame #2 at various ground motion intensities prior to CLEF. This relatively small difference in the residual drifts, together with the fact that in Frame #2 the subsequent test had an intensity of 2.2 times Canoga Park as compared to 1.5 times Canoga Park for Frame #1, are the reasons why Frame #2 started to drift in the opposite direction when the CLE motion was applied.

Figure 7.41 shows the experimental “IDA” curve of Frame #2. After DLE (CP) the “IDA” curve is dashed because the faulty Llolleo record was used at MCE (LL), which led to a decrease in the roof drift. The terms CP and LL are used to distinguish between the ground motions (Canoga Park and Llolleo) used. The CLEF (CP) point is not part of the “IDA”

curve because Frame #2 would have collapsed at a slightly lower intensity after CLE (CP) as discussed in Section 7.6.5. In the same figure the pre-test analytical predictions are superimposed. The analytical prediction indicated that Frame #2 would be close to collapse at the MCE level. However, the situation changed drastically because of the unsuccessful reproduction of the input ground motion in the MCE shaking table test. Using the recorded MCE table motion, the “pre-test” prediction for Frame #2, which was executed after completion of the test series, would have reproduced the test results rather well (see Figure 7.41 pre-test prediction #2).

Yield Pattern – Collapse mechanism

The yield pattern of Frame #2 is illustrated in Figures 7.42 and 7.43 in which the residual rotations over 1.50" length ($\theta_{1.5''}$) as deduced from clip gage readings are presented. Figure 7.43(b) shows $\theta_{1.5''}$ at the Incipient Collapse Level (ICL). As seen from Figure 7.42, at the DLE level the yield pattern of Frame #1 and #2 is the same. After the MCE test many of the residual rotations become smaller, and they clearly reverse direction after the CLE test.

In summary, the shaking table tests for Frame #2 provided another essentially complete set of experimental data from elastic behavior up to collapse. The major differences between Frames #1 and #2 were: (1) the amount of friction damping, which was much less in Frame #2, and (2) the effect of the poorly reproduced L1010 motion that changed the direction in which Frame #2 collapsed. The collapse mechanism was the same though for both frames.

Issues related to dynamic response of both frames from elastic behavior up to collapse are addressed in Section 7.6 and interpreted based on correlation between experimentally measured or derived parameters and corresponding post-test analytical predictions.

7.6 Test Evaluation

In this section the focus is on specific aspects of frame response derived from experimental data. Since Frames #1 and #2 were nominally identical (with minor deviations in flange plate strength of the plastic hinge elements) the test evaluation is presented together for both frames. The following issues are covered in this section: the effect of friction damping on global behavior of both frames, quantification of P- Δ effects from elastic behavior up to collapse, moment distribution at selected joints during plastification, and post-test collapse predictions of both frames. The mathematical model used to represent the model structure for the pre and post-test collapse predictions is based on concepts discussed in Sections 6.6 and 6.7.

7.6.1 Friction Damping

As discussed earlier in this chapter, the presence of Coulomb damping (friction damping) made it difficult to identify modal properties and viscous damping of both test frames since friction damping is amplitude dependent. Figure 7.44 shows a comparison of the roof displacement time histories during SLE and DLE for both frames. As seen from these figures the dynamic response of both frames is quite different in the SLE tests but becomes very similar in the DLE tests, which indicates that the effect of friction damping on the dynamic behavior of both frames was no longer important at DLE or higher levels of ground motion intensity.

In the pre-shaking table analysis predictions friction was not considered in the mathematical model of the test frame. Instead three percent viscous damping was assumed to approximately account for all sources of damping. For post-test analytical predictions of the response of the two frames a friction element was added per story, as shown in Figure 7.45(a). The friction element is a rotational spring with the moment rotation diagram shown in Figure 7.45(b), inserted at each end of the gravity links (P-Delta column) that were

modeled originally as rigid elements with hinged ends. The moment M_f is the moment at which friction is overcome and the individual story starts to move. Assuming that the friction forces at the hinges are proportional to gravity per floor, M_f is estimated based on the response of the two frames at SLE after calibrating the friction springs in order to match the analytically predicted elastic behavior of each one of the frames with the experimentally obtained SLE response. Figure 7.46 shows a comparison between analytically predicted response of Frame #1 and experimental data for roof displacement (Figure 7.46(a)) and first floor displacement (Figure 7.46(b)). After calibrating M_f at SLE an $M_f = 4\text{k-in}$ was obtained for the friction elements of the 4th story, i.e., 16k-in ($4M_f$) for the friction elements at the base. This result to a base shear force of about 1.3kips, which seems to be high but reflects the difficulties in quantifying all contributions to friction since the portion due to Poisson's effect from pre-tensioning the bolts of gravity links is not proportional to the gravity load in each story.

The same value for M_f was used in order to predict the response of Frame #1 at DLE. Figure 7.47 shows the comparison between analytical prediction and experimental data for the roof and first floor displacements. As seen from this figure the predicted response of Frame #1 (dashed line) is fairly close to the experimental data. A similar approach was used to calibrate the rotational spring for Frame #2. It was found that half of M_f of Frame #1 (2 k-in) should be used in order to match elastically the dynamic response of analytical model with the experimental data. Figure 7.48 shows the predicted and experimental response histories of Frame #2 at DLE using the calibrated rotational spring, and again the response is captured fairly well. The values of M_f of the calibrated friction elements indicate that the friction damping in Frame #2 was much smaller than in Frame #1.

7.6.2 Story Shear Distribution at Various Levels of Ground Motion

Story shear forces are usually defined as the sum of inertia force above a certain floor level. This definition implies that P-Delta effects, which amplify member forces and story drift,

are considered separately from inertia forces. In the shaking table tests performed in Buffalo the P-Delta effect is transferred through horizontal links from the gravity simulator to the test frame, which is fully equivalent to the use of a “leaning column” to simulate P-Delta effect in analytical models. Thus, in the evaluation of the tests we can distinguish between two types of story shear forces; those generated by inertia forces, and referred to here as inertia based story shear forces, and those generated by inertia forces plus P-Delta effects, referred to here as effective story shear forces. The former are measured as the sum of masses times accelerations of the mass simulator floor masses, and the latter are measured as the sum of the link forces transferred from the mass simulator to the essentially weightless test frame. The difference between the two shear force quantities is the effect of structure P-Delta.

Histories of inertia based story shear forces (denoted as V_i^a , in which i is the story number) of Frame #1 are presented in Figures 7.49(a) to 7.53(a) for a selected time window during SLE, DLE, MCE, and CLE tests. Each figure includes all four story shear force histories for comparison purposes. Superimposed in the same figure is the roof drift response (light grey dashed-dotted line) of the frame in order to map story shear forces with roof drift measurement. From these figures it can be seen that the inertia based story shear forces develop their maximum at roof displacements smaller than the maximum displacements because large displacements cause large P-Delta effects, which in turn reduce the inertia forces that can be resisted in the inelastic range.

The presented histories permit an assessment of the relative values of inertia based story shear forces over the height of the structure. The maxima of the shear forces in the individual stories are not well synchronized, which demonstrates that even in this first mode dominated structure the effects of higher modes on story shear force distribution are important. Moreover, there is little indication that a code based parabolic story shear force distribution is representative of actual behavior. A consistent observation is that the inertia based story shears become small as the story drifts become very large, which demonstrates

the importance of P-Delta effects. Story shear force histories based on force measurements in the four horizontal links which account for effect of P- Δ , are summarized in Appendix E.

Figures 7.49(b) to 7.53(b) show the distribution of maximum story shear forces along the height of the structure for at various ground motion intensities, for both inertia based shear forces (denoted as V_i^a) and effective shear forces based on link force measurements (denoted as V_i^L). The increasing difference with increasing ground motion intensity between the two measurements is fully attributed to P- Δ effects, as discussed later in Section 7.6.3. It is noteworthy that the difference between first and fourth story maximum shear force is small in the elastic range (SLE) but becomes larger as the intensity of the ground motion increases.

Peak overturning moments (OTM) at each floor level obtained from inertia based story shear forces (denoted as OTM_i^a) and effective shear forces (denoted as OTM_i^L) are illustrated in Figures 7.49(c) to 7.53(d) for various ground motion intensities. The difference between the two measurements is attributed to P- Δ effects. Overturning moment histories at the base of the frame based on horizontal link measurements are summarized in Appendix E for both frames.

7.6.3 Base Shear – 1st Story Drift and Quantification of P-Delta Effects

P-Delta becomes an increasingly important issue as drifts in the test frame become larger, and it becomes an overriding issue as the frame approaches collapse. The test setup, with the “weightless” test frame driven by a mass simulator that is connected to the test frame by a series of instrumented links, provides an excellent opportunity to measure and quantify P- Δ effects in an explicit manner. The floor forces measured by the horizontal links are the sum of the inertia forces plus P- Δ forces transferred from the mass simulator to the test frame. Summing these floor forces from top to bottom results in story shear force measurements that include both inertia forces and P- Δ effects. The inertia forces can be

quantified independently from the readings of the accelerometers attached to the floor plates multiplied by the masses of the floor plates. Summing these inertia forces from top to bottom results in story “shear” measurements that account for inertia force effects only. The difference between the two measurements is attributable to P- Δ effects. Strictly speaking the load cell measurements include also the forces due to friction in the mass simulator but these forces are negligible compared to forces due to P- Δ effects.

Figures 7.54 and 7.55 show measured base shear – first story drift relationships obtained from the link load cells (denoted as V_1^L) and from accelerometers, i.e., inertia forces (denoted as V_1^a), for the CLEF tests of Frames #1 and #2, respectively. The differences between the two diagrams are fully attributable to P- Δ effects. As can be seen, the differences are large and increase with the story drift (IDR₁). For Frame #1 (Figure 7.54) the inertia based shear force approaches zero at an IDR of 0.15, which means that the test setup (frame plus mass simulator) would collapse if the ground motion would stop at this instance, because the P- Δ effects fully offset the lateral resistance of the frame, i.e., the structure would continue to “rotate” about its base until a collapse prevention mechanism engages. The observed large increase in lateral resistance at drifts larger than 0.15 is due to table motion reversal that generates a wave traveling up the structure and recreates resistance that permits a large increase in inertia forces even though the structure continues to move towards collapse.

The actual resistance of the test frames is represented by the $V_1^L - IDR$ diagrams in Figures 7.54 and 7.55, and the difference between the $V_1^L - IDR$ and $V_1^a - IDR$ diagrams represents the P- Δ effect. For a given drift the P- Δ effect in the first story can be approximated by an equivalent story shear equal to $P\delta_l/h_l$, with P being the total weight of the plates of the mass simulator, h_l being the first story height, and δ_l being the first story drift. When this quantity is added to V_1^a , the shear forces shown dashed in Figures 7.54 and 7.55 are obtained. The observation that the dashed shear force - drift diagrams are close to the

measured V_I^L – drift diagrams confirms that all measurements are of adequate accuracy and that the P- Δ effect can indeed be represented reasonably by the simple term $P\delta/h$.

Superimposed on the shaking table results in Figures 7.54 and 7.55, and shown in heavy dashed-dotted lines, are static pushover curves with and without P- Δ obtained from post-test analytical predictions. A comparison of the pushover curves with envelopes of the dynamic test results provides insight into the value of a pushover analysis for response prediction close to collapse for a first mode controlled frame.

Of some interest, although not related to the P- Δ issue, are frequently observed dips followed by rapid shear force increases in the base shear – drift diagrams. Two examples are illustrated in Figure 7.56 in the CLE response of Frame #1 (point A followed by point B, and Point C followed by point D). In both cases the drift increases gradually from the first to the second point (see Figure 7.57) but the ground acceleration reverses rather rapidly at the first point (see Figures 7.58 and 7.60). This reversal creates a transient wave that causes a rapid change in the first story inertia force, as shown in Figures 7.59 and 7.61, which in turn is reflected in a rapid increase in the first story shear force.

The last observation made here may not be very important in the context of global response of the test frames, but it illustrates the value of the comprehensive set of data collected in these shaking table tests. The availability of experimental data that permits calculation of all relevant force and deformation quantities facilitates the study of phenomena that otherwise could be evaluated only from results of numerical investigations.

7.6.4 Moment Values During Plastification Based on Clip Gage Measurements

In Section 7.5 it was shown that in the range of elastic behavior the strain measurements of the flange plates at each hinge location of both frames can be correlated with the associated moments and that moment equilibrium is satisfied with reasonable accuracy. The post

shaking table component tests (see Section 6.7), in which the shaking table test “rotation” history experienced by several plastic hinge elements was simulated, permitted us to obtain loading history dependent calibrations of moments as a function of measured clip gage readings (see Section 6.6). Using these calibrations, moments at specific plastic hinge locations could be derived from clip gage readings obtained in the shaking table tests at very large inelastic deformations in which the structure approaches collapse. Locations for which these post shaking table test calibration tests were performed include plastic hinges at the base of the exterior column, first floor beam at the interior column line and third story column at the top.

Figure 7.62 shows moment values at the first floor exterior joint of Frame #1 at selected times during the ground motion intensities from DLE up to collapse. The moments are obtained from the aforementioned post shaking table calibration studies (column base and beam plastic hinge) and from previously discussed elastic calibrations for locations at which the response was elastic (top of first story column and bottom of second story column). For the CLEF level (see Figure 7.62(d)) the moment at the incipient collapse level (ICL) were computed. The moments at the base of the first story exterior column and the first floor beam are clearly smaller in the ICL case than the CLE case (Figure 7.62(c)) because of strength deterioration at these plastic hinge locations.

7.6.5 Post – Shaking Table Collapse Predictions

The first modification to the analytical model used to predict the dynamic behavior of Frames #1 and #2 from elastic range up to collapse was the incorporation of friction elements discussed in Section 7.6.1. Although this modification is not important for ground motion intensities larger than DLE it is appropriate to consider friction for the SLE and DLE.

The achieved table motions, as measured from the accelerometers installed on the shaking table, are used as the input motions for post-test analysis since they slightly differ (but not by much) compared to the original input motion for all the ground motion intensities except the MCE level motion used for Frame #2 in which the table did not successfully reproduce the input ground motion as discussed earlier.

There are differences in the deterioration parameters between the post-test and pre-test analytical model used to simulate component deterioration for critical plastic hinge locations. The new deterioration parameters used are based on the calibration of the three plastic hinge elements (column base, first floor beam and at the top of the third story column) discussed in Section 6.7. The calibrated deterioration parameters for the selected locations were summarized in Table 6.9. Comparing these values with pre-test calibrations (Table 6.8) it is seen that the plastic rotation capacity (θ_p) values are essentially identical. The rate of cyclic deterioration of the beams based on the post-shaking table test experimentation is slightly higher than the assumed values from tests prior to shaking table collapse series. Based on past studies by Ibarra and Krawinkler (2005) it was shown that variations in this parameter of the magnitude seen here do not have a significant effect on the collapse capacity of deteriorating structural systems.

The calibrated θ_{pc} values based on the post-shaking table component tests are almost 40% larger than the calibrated values obtained from pre-shaking table tests for reasons explained in Section 6.7. A smaller θ_{pc} value accelerates the P- Δ effect on the collapse capacity of a frame structure, i.e. the structure deflects more due to P- Δ and collapse occurs earlier.

Figures 7.63(a) and 7.63(b) show the “IDA” curves for both test frames, as obtained from the shaking table tests and as predicted analytically after the modifications discussed in the previous paragraphs. It is observed that the behavior of both frames can be predicted fairly well with the use of relatively simple analytical models. It is demonstrated that accurate representation of deterioration modeling parameters of both test frames near collapse is

important for predicting the collapse capacity of a deteriorating structural system with relatively small error.

The black dotted line that is superimposed in Figures 7.63(a) and 7.63(b) after the CLE level indicates that both frames would have collapsed at a lower level of intensity based on analytical simulations considering the deformed configuration of both frames after the CLE test. The fact that the dotted line is much steeper in Figure 7.63(a) compared to the one in Figure 7.63(b) is attributed to the larger permanent deformation of Frame #1 compared to Frame #2 after the completion of CLE.

Figure 7.64 show a time window of the story drift histories obtained from the CLE shaking table tests for Frames #1 and #2. In the same plots the responses from post -test analytical simulations are superimposed. As seen from these figures the fourth story drift histories are overestimated by the analytical model for both frames but in the first three stories, which are part of the collapse mechanism for both frames, the analytical prediction is not far from reality considering the simplifications of the mathematical model.

Figures 7.65 and 7.66 illustrate the base shear - first story IDR for Frames #1 and #2 based on experimental data and post-test analytical predictions including the effect of P- Δ , i.e., the base shear force is computed from measurements from the horizontal links. The overall response is captured fairly well, except that the analytical model seems not to be able to capture the sudden strength increases observed in Frame #1, particularly at drifts larger than 15%. This is an unresolved issue.

7.7 Summary and Conclusions

This chapter discusses shaking table test series of two 1:8 scale models of a two-bay steel frame with reduced beam section connections designed based on recent seismic provisions.

The steel frame serves as the lateral load resisting system of a 4-story office building as discussed in Chapter 5. The two scale models were subjected to a series of ground motions, using the shaking table of the NEES facility at the State University of New York at Buffalo. The shaking table tests produced a comprehensive set of well documented data that quantifies engineering demand parameters such as story forces and shears, story drifts, plastic rotations, and floor accelerations, in the elastic and inelastic ranges all the way to collapse. The data is available through (<http://central.nees.org>).

Frame #1 was subjected to five different intensities of the Northridge 1994 Canoga Park ground motion record in order to investigate the behavior of the frame from elastic behavior up to collapse. Frame #2 was subjected to a different ground motion sequence after the Design Level Earthquake in order to investigate the effect of cumulative damage prior to collapse. In the MCE test Frame #2 did not perform as predicted, but it was found out much later that the reason for the unexpected performance was the inability of the shaking table to reproduce the desired input motion. Hence, the MCE test was inconclusive, but it severely affected the initial conditions for the subsequent CLE test.

The test series performed on each model frame can be considered as IDAs, except that each subsequent test had different initial conditions that were created by cumulative damage caused in all preceding tests.

The collapse mechanism of both frames was a 3-story mechanism. In both frames plastic hinges formed at the top of the third story even though the prototype structure fulfilled the strong column weak beam criterion at these locations. The two frames collapsed in the opposite direction because of different ground motion sequence.

Friction damping was considered in the analytical model for post-shaking table collapse predictions with the use of a friction rotational element per story after matching the individual analytical responses of the two frames with the experimental data at SLE. It was

shown that friction damping had a negligible effect on the behavior of the two frames at the DLE level and larger intensities.

Using a combination of rotation measurements obtained from clip gage measurements in flange plates and calibrations from post-shaking table component tests of important regions of test Frame #1 (first floor beam and exterior column base) it was shown that moments in these regions can be deduced from clip gage measurements for the full range of behavior up to incipient collapse, including the range of strength deterioration.

In the shaking table collapse tests the instrumented links between the mass simulator and test frame offered an excellent opportunity to measure and quantify P- Δ effects in an explicit manner. It was demonstrated that from elastic response up to collapse the P- Δ effect in the first story is well represented by an equivalent story shear equal to $P\delta_1/h_1$, with P being the total weight of the plates of the mass simulator, h_1 being the first story height, and δ_1 being the first story drift. An observed large increase in lateral resistance at large drifts indicates that a collapse prevention mechanism engages due table motion reversal that generates a wave traveling up the structure and recreates resistance that permits a large increase in inertia forces even though the structure continues to move towards collapse.

The difference between overturning moments (OTMs) as deduced from inertia forces and OTMs as deduced from the horizontal links was again attributable to P- Δ effects. The reason why peak OTMs do not increase by much with an increase in ground motion intensity from DLE up to ICL is the strength deterioration observed at large drifts.

It was shown that relatively simple analytical models can be used to predict the behavior of both test frames up to collapse with a satisfactory level of accuracy – provided that the deterioration characteristics of critical components are adequately represented in the analytical models. It was shown that accurate representation of the post capping rotation capacity θ_{pc} is essential for prediction of the collapse capacity of a frame. After re-

calibrating the deterioration modeling parameters of critical plastic hinge elements based on component tests conducted at Stanford after the shaking table tests, it was feasible to accurately reproduce analytically the behavior of both frames near collapse. These post-shaking table component tests, and the collapse predictions based on these tests, did demonstrate that the response close to collapse is sensitive to the loading history every component experiences as part of the structure.

Both shaking table collapse test series demonstrated the value of the comprehensive set of data collected in these tests and facilitated the study of phenomena that otherwise could be evaluated only from results of numerical investigations. Both shaking table test series provided evidence that an accurate analytical model is capable of simulating dynamic behavior up to collapse.

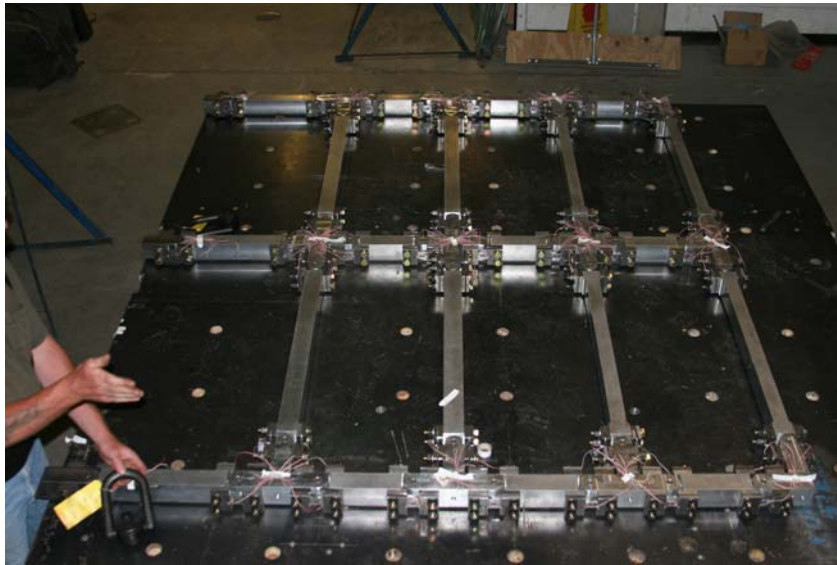


Figure 7.1. Test frame after completion of assembly on the flat steel plate



(a)



(b)

Figure 7.2. Mass simulator erection sequence; (a) installation of mass plates on the shaking table, (b) gravity links



Figure 7.3. Installation of test Frame #1 on the shaking table

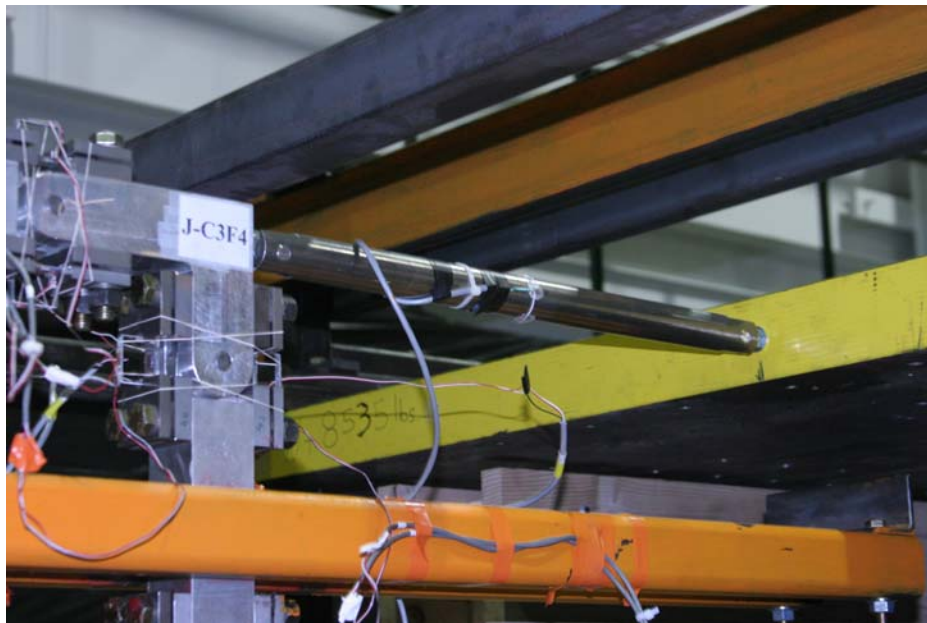


Figure 7.4. Horizontal link connecting the test frame and mass simulator



Figure 7.5. Test setup after completion of erection process on the shaking table (Frame #1)



Figure 7.6. Krypton system

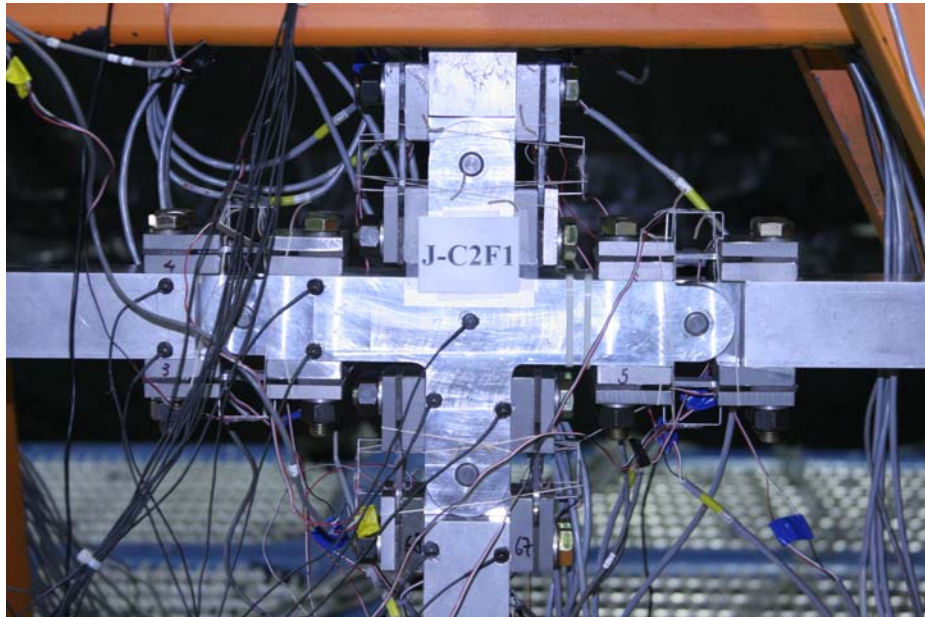


Figure 7.7. First floor interior joint after installation of all the local instruments (Frame #1)

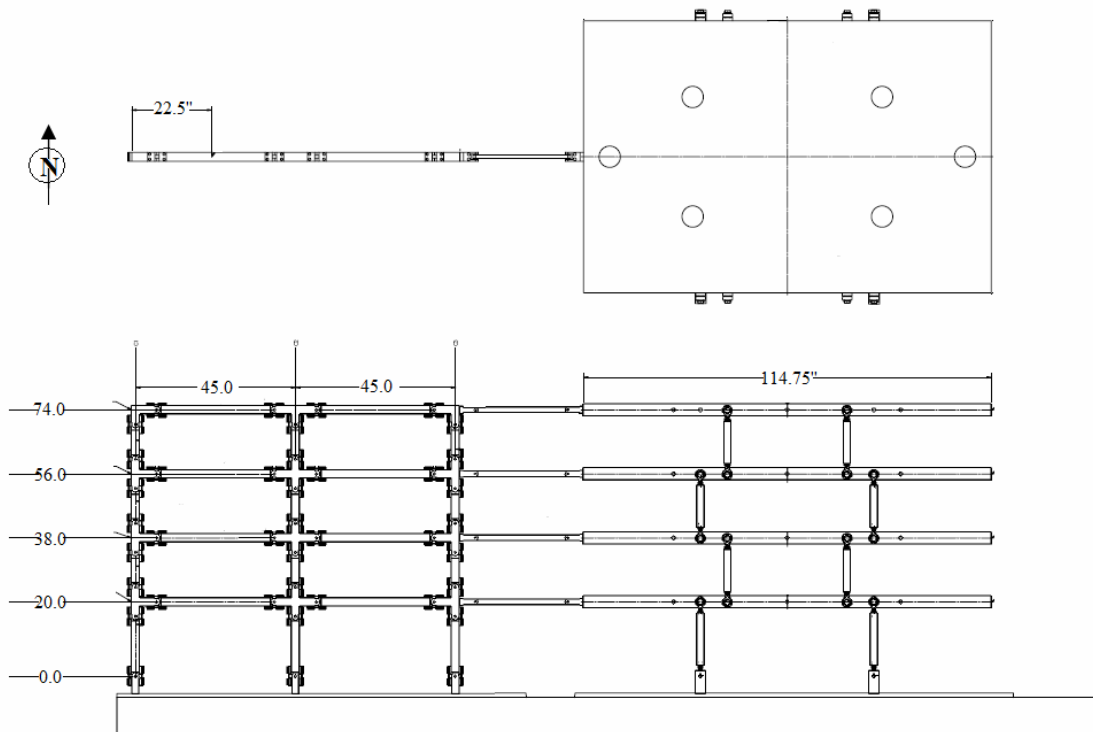


Figure 7.8. Plan view and elevation of the test frame and mass simulator



(a) completion of erection of mass simulator



(b) test setup at the end of collapse test (Frame #1)



(c) removal of test Frame #1 from the shaking table

Figure 7.9. Various snap shots during erection and experimentation (Frame #1)



(a) assembly of test Frame #2

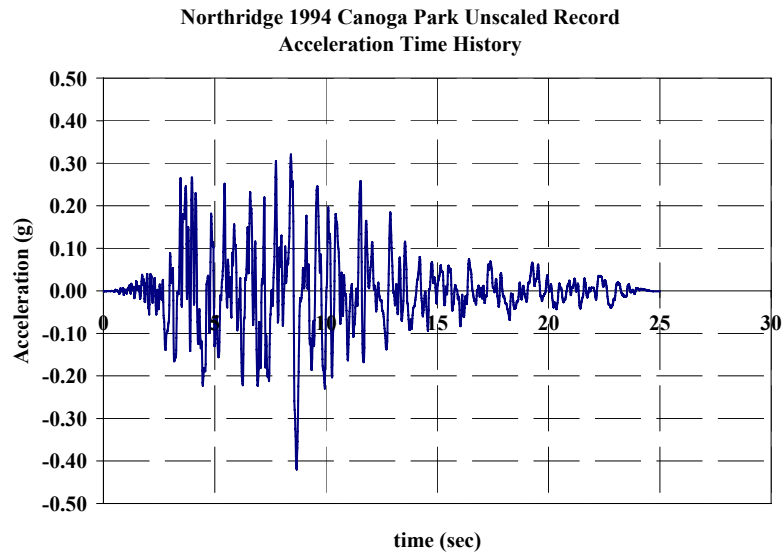


(b) test setup at the end of collapse test (Frame #2)

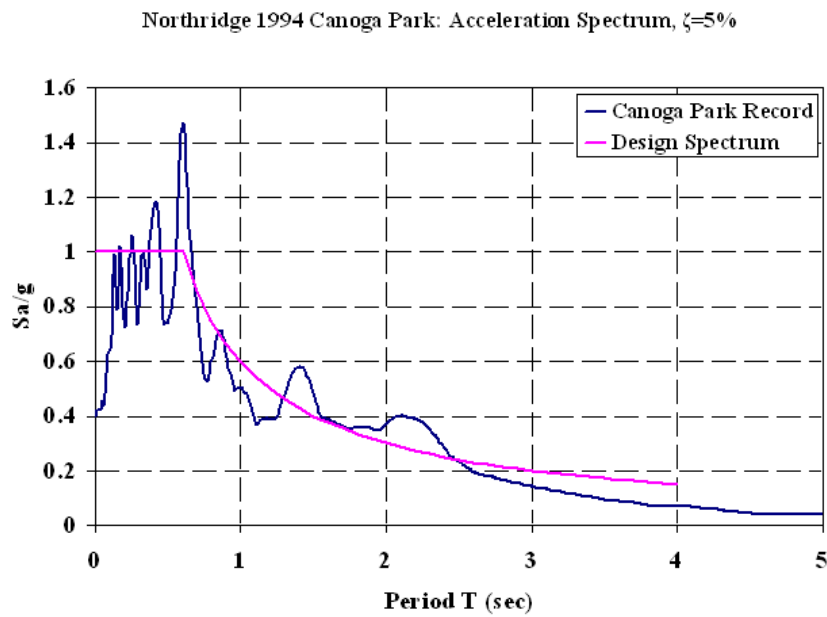


(c) exterior joint of test Frame #2 at the end of collapse test

Figure 7.10. Various snap shots during erection and experimentation (Frame #2)

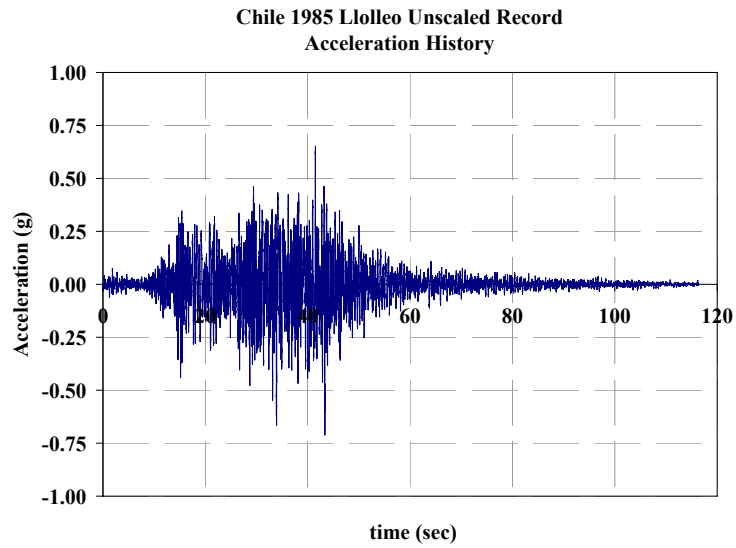


(a) Acceleration time history of Northridge 1994 Canoga Park record

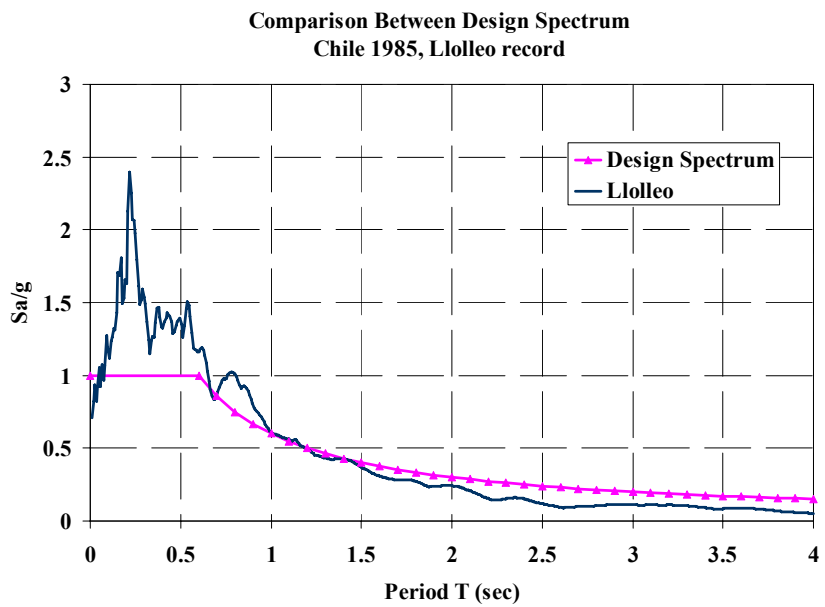


(b) Acceleration spectrum of Northridge 1994 Canoga Park record together with the design spectrum

Figure 7.11. Northridge 1994 Canoga Park unscaled record



(a) Acceleration time history of Chile 1985, Lolloe record



(b) Acceleration spectrum of Chile 1985 Lolloe record together with the design spectrum

Figure 7.12. Chile 1985 Lolloe unscaled record

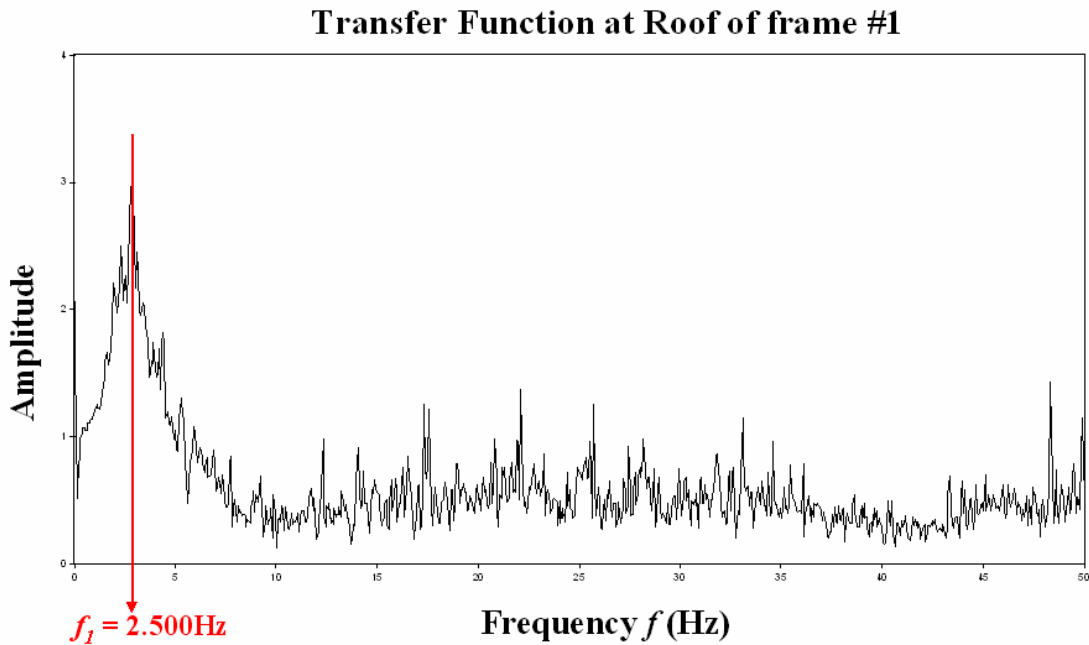


Figure 7.13. Transfer function at roof of Frame #1 based on a 0.1g WN test

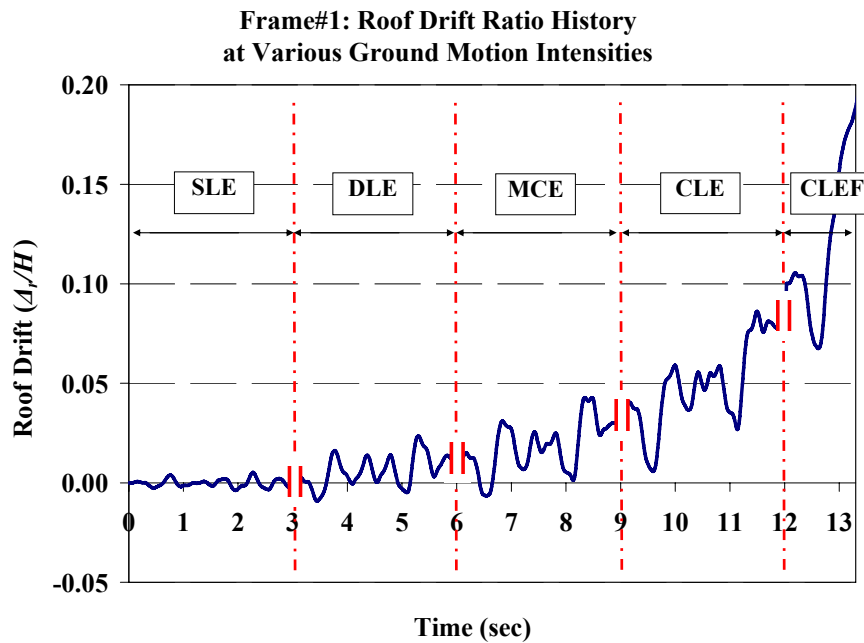
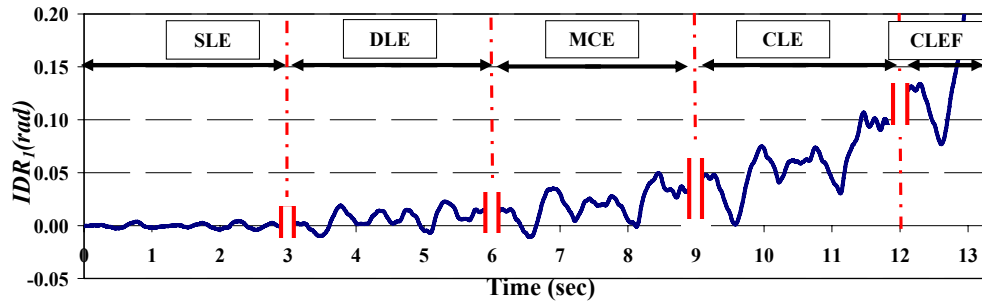
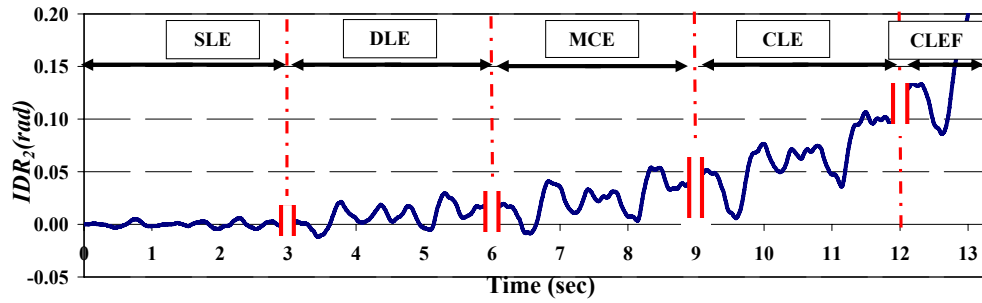


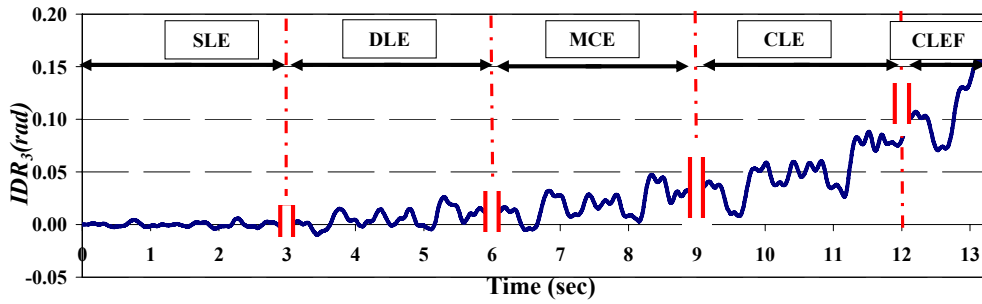
Figure 7.14. Roof drift ratio history for selected segments at various levels of intensity (Frame #1)



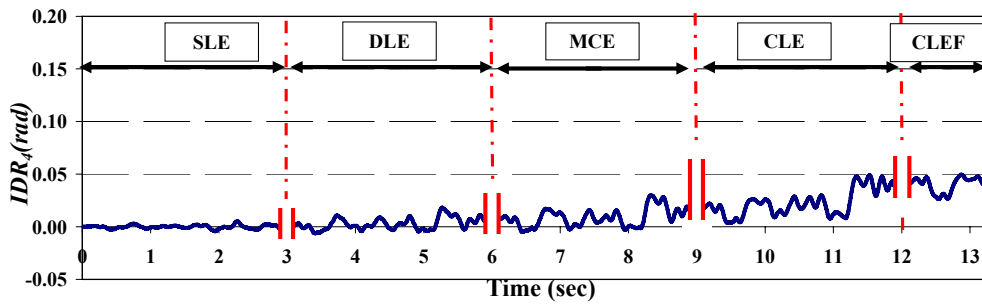
(a) IDR_1



(b) IDR_2

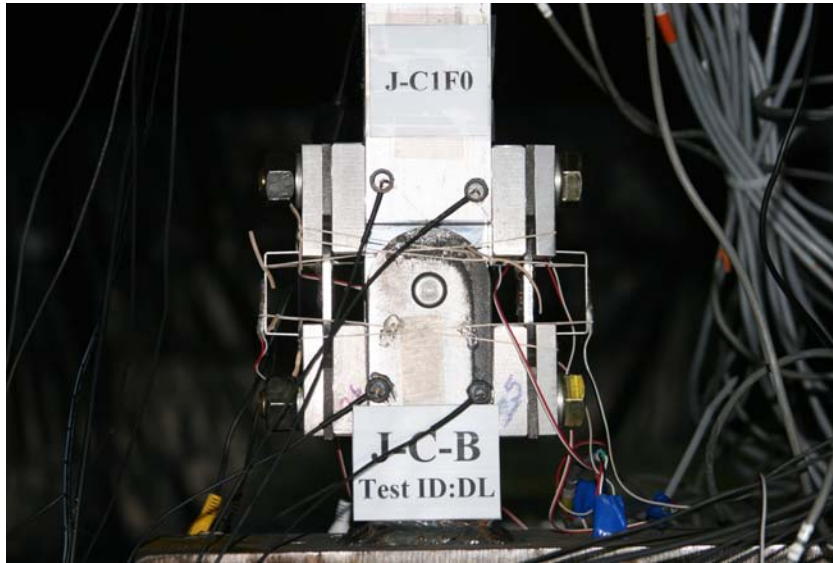


(c) IDR_3

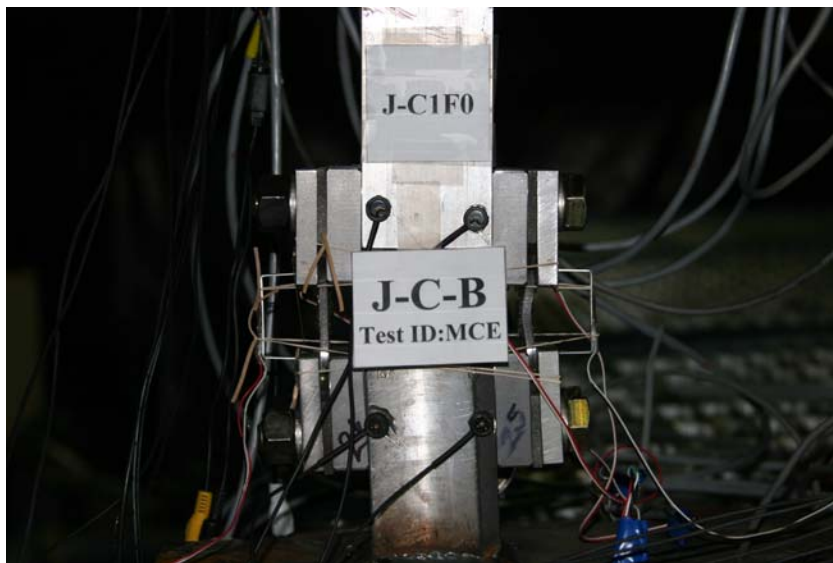


(d) IDR_4

Figure 7.15. Story drift history for selected segments at various levels of intensity (Frame #1)

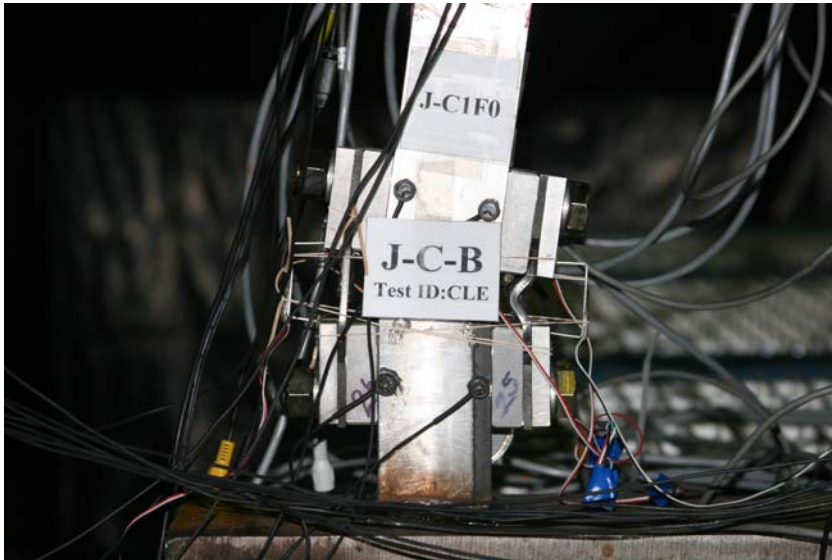


(a) after completion of DLE

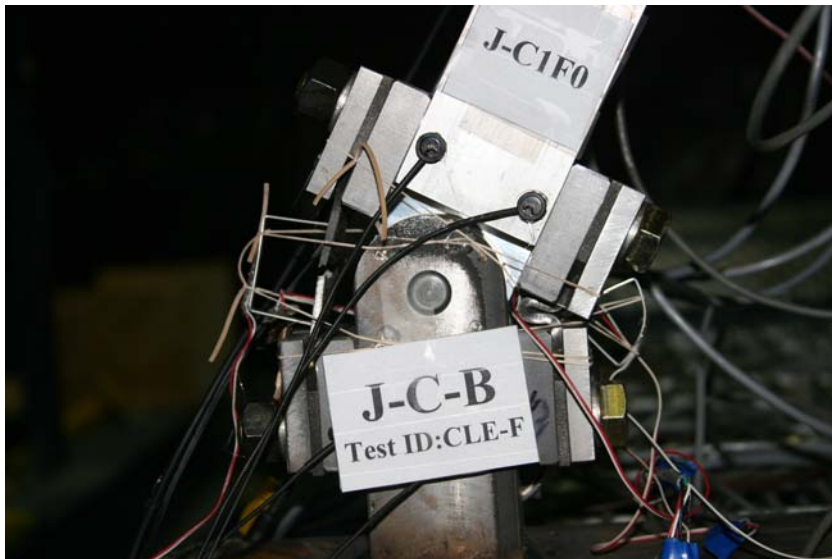


(b) after completion of MCE

Figure 7.16. Flange plate local buckling at exterior column base after DBE and MCE tests
(Frame #1)



(a) after completion of CLE



(b) after completion of CLEF

Figure 7.17. Flange plate local buckling at exterior column base after CLE and CLEF tests
(Frame #1)



Figure 7.18. Collapse mechanism of Frame #1 after completion of CLEF

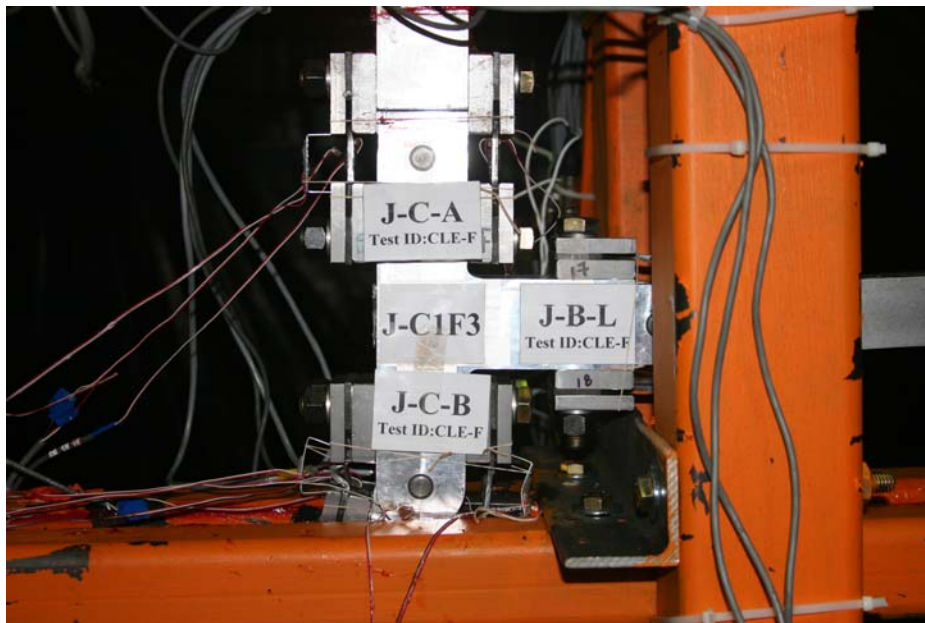


Figure 7.19. "Catching" mechanism of Frame #1 at the Incipient Collapse Level (ICL)

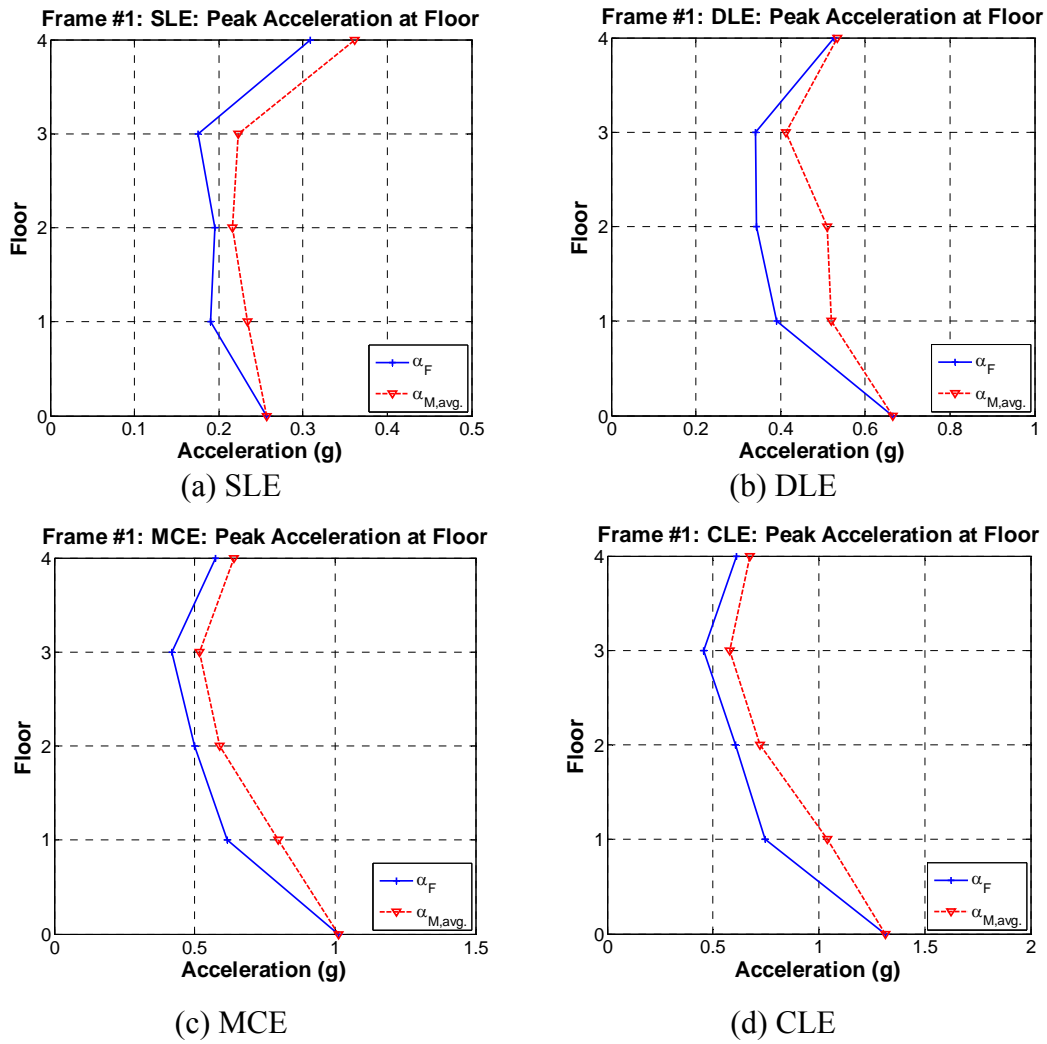


Figure 7.20. Peak absolute floor acceleration of Frame #1 and mass simulator at various ground motion intensities

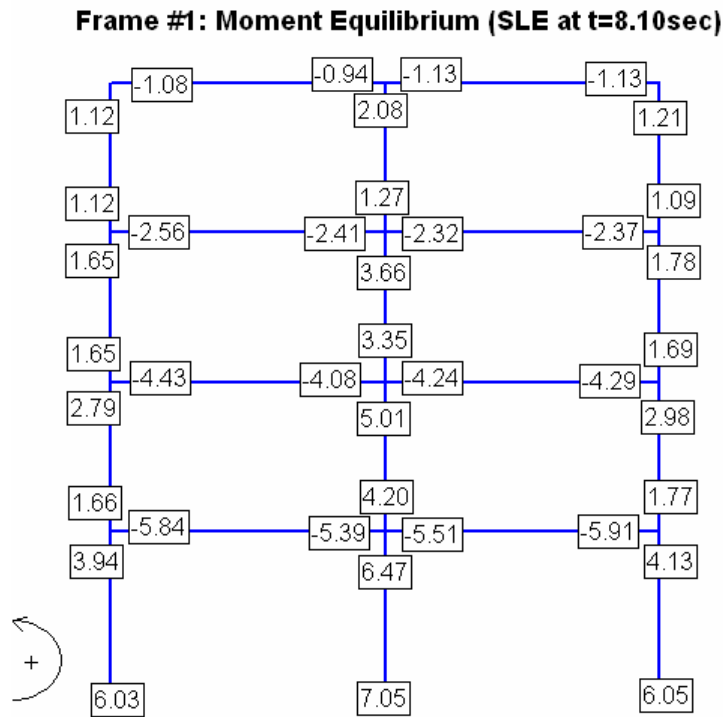


Figure 7.21. Moment equilibrium at joints of Frame #1 at t = 8.10sec, SLE

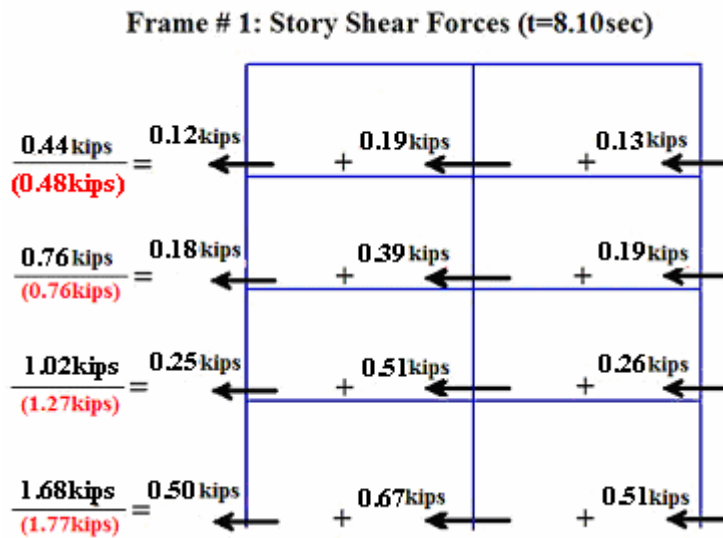


Figure 7.22. Story shear forces and distribution to story columns of Frame #1 (t = 8.10sec, SLE)

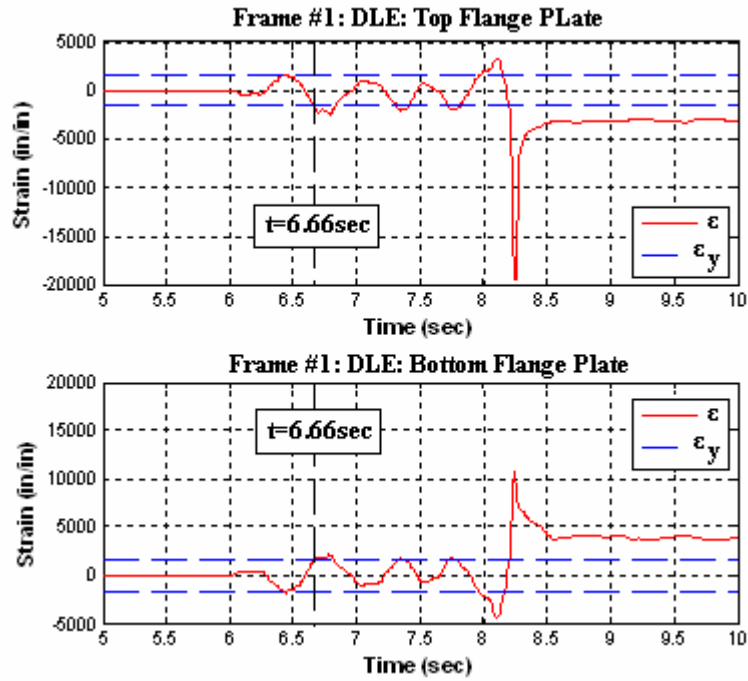


Figure 7.23. Strain history of flange plates of exterior first floor beam of Frame #1, DLE test

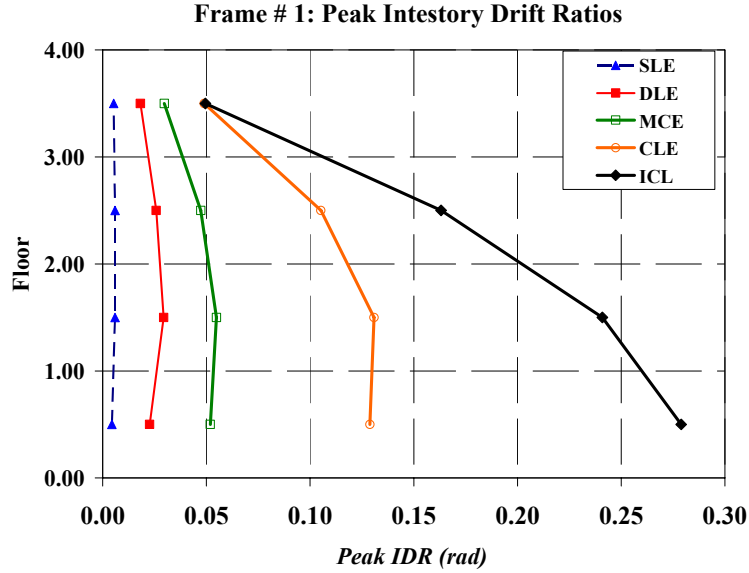


Figure 7.24. Peak interstory drift ratios at various ground motion intensities (Frame #1)

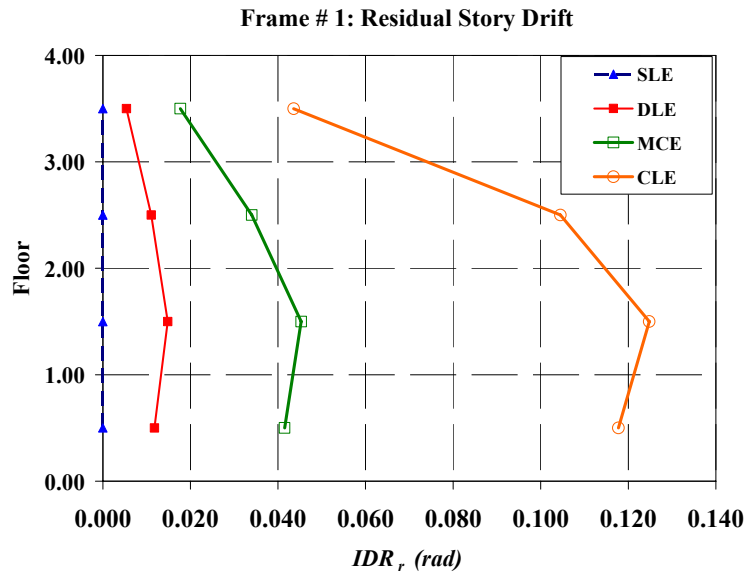


Figure 7.25. Residual story drift ratios of Frame #1 at various ground motion intensities

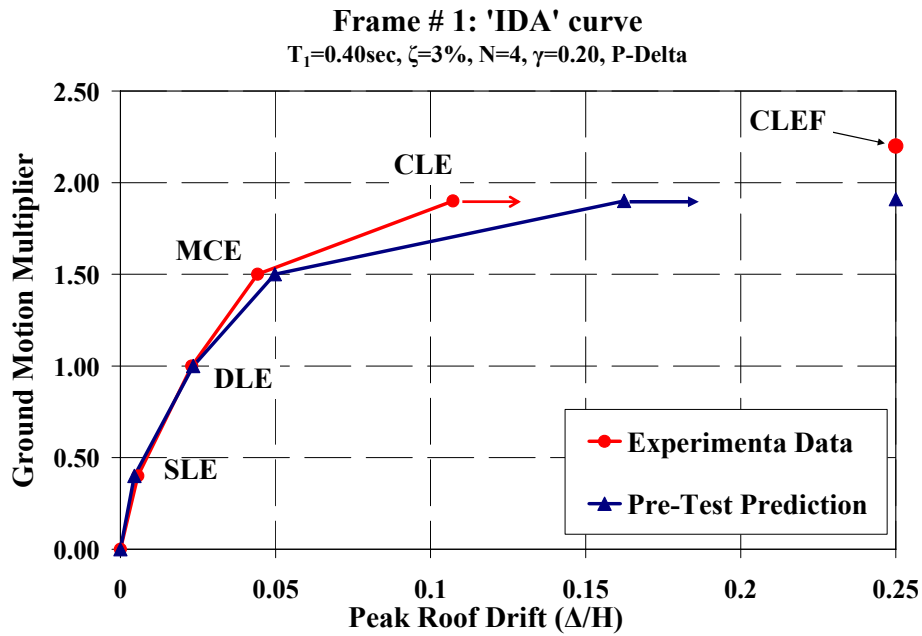
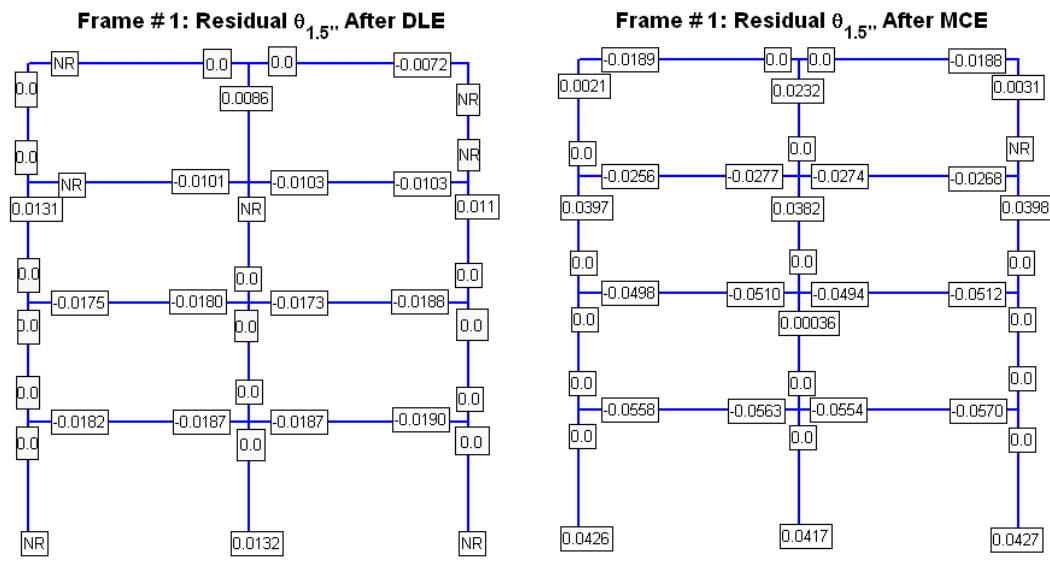


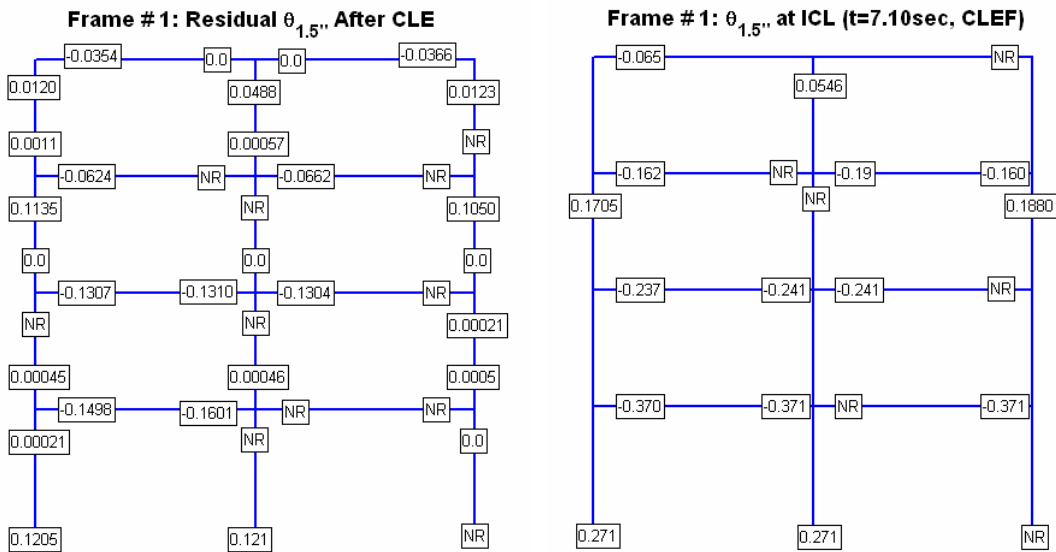
Figure 7.26. IDA curve for Frame #1 as obtained experimentally together with pre-test analytical prediction



(a) End of DLE

(b) End of MCE

Figure 7.27. Residual $\theta_{1.5''}$ at plastic hinge locations of Frame #1; (a) DLE, (b) MCE



(a) End of CLE

(b) ICL

Figure 7.28. Rotation $\theta_{1.5''}$ at plastic hinge locations of frame #1: (a) residual $\theta_{1.5''}$ after CLE, (b) $\theta_{1.5''}$ at ICL (positive direction is the same as used for moment equilibrium)

Transfer Function at Roof of Frame # 2

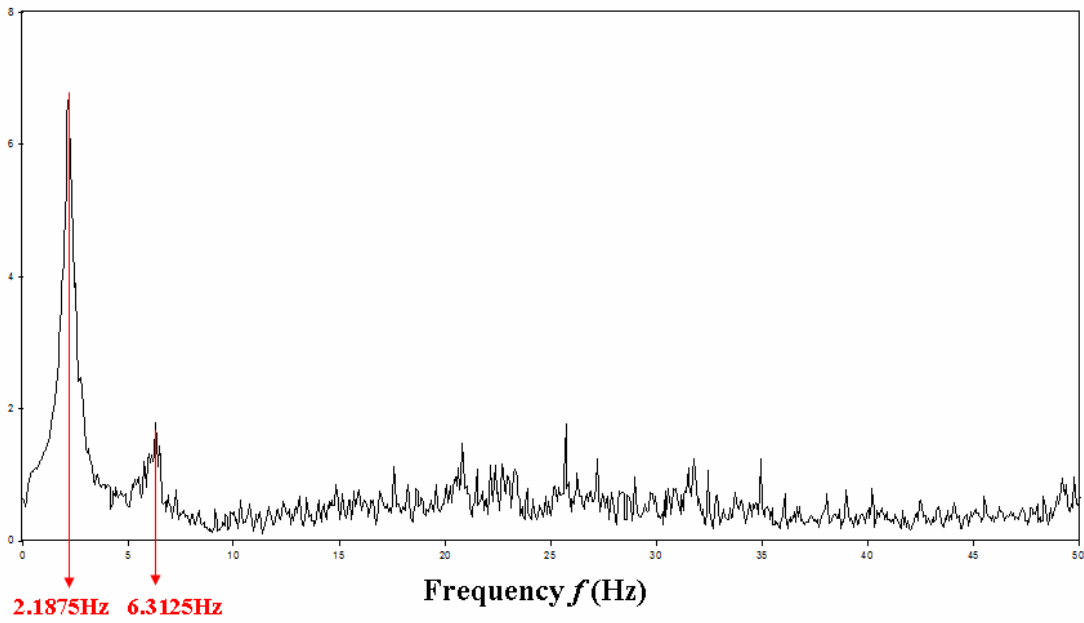
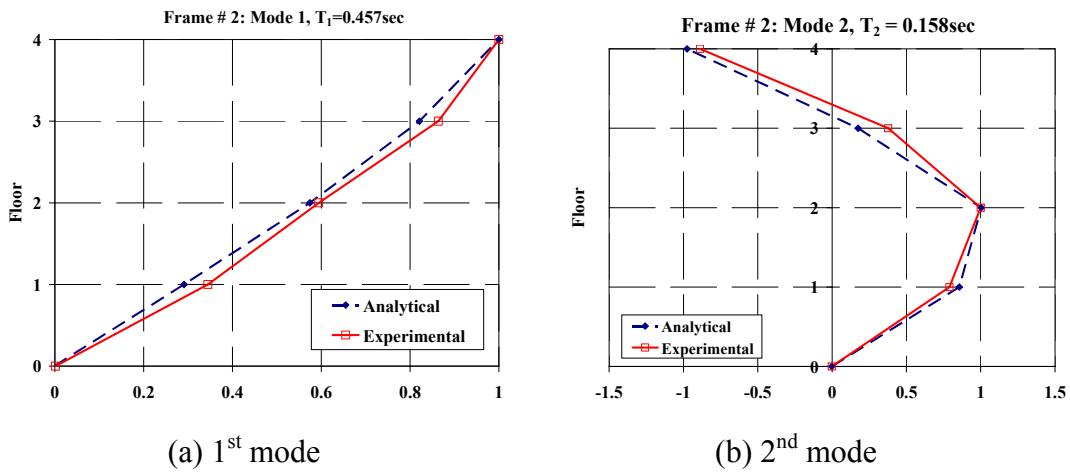


Figure 7.29. Transfer function at roof of Frame #2



(a) 1st mode

(b) 2nd mode

Figure 7.30. Mode shapes of Frame #2

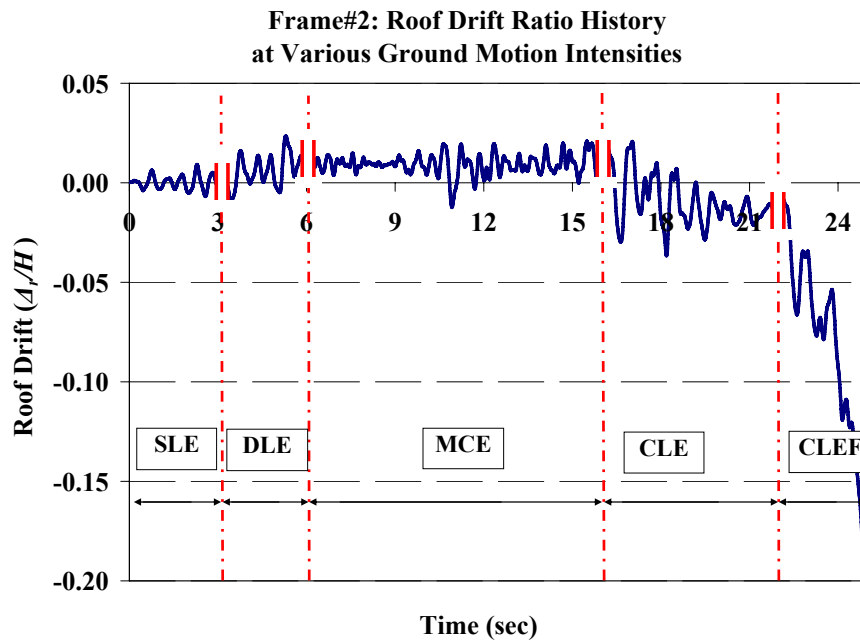
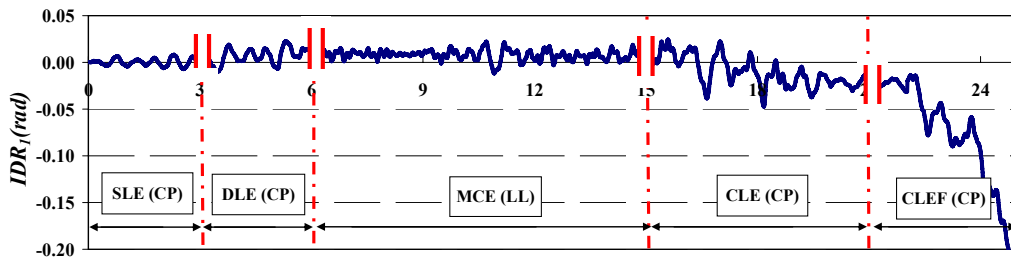
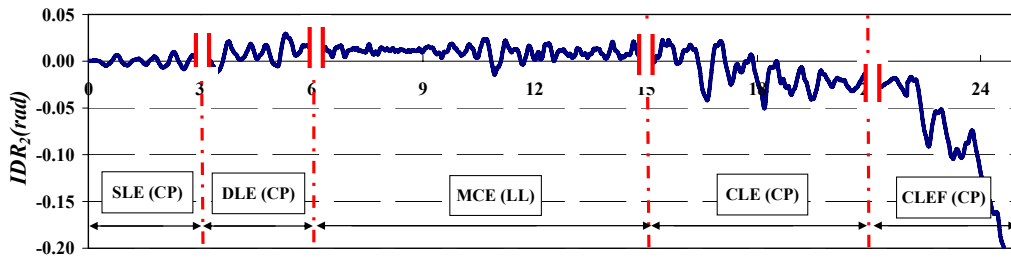


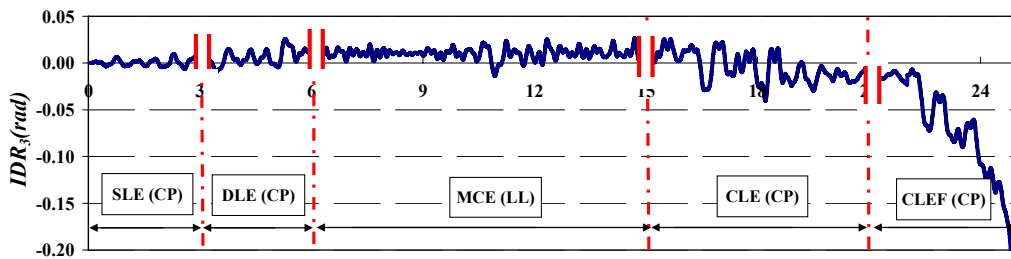
Figure 7.31. Roof drift history of Frame #2 for selected segments at various ground motion intensities



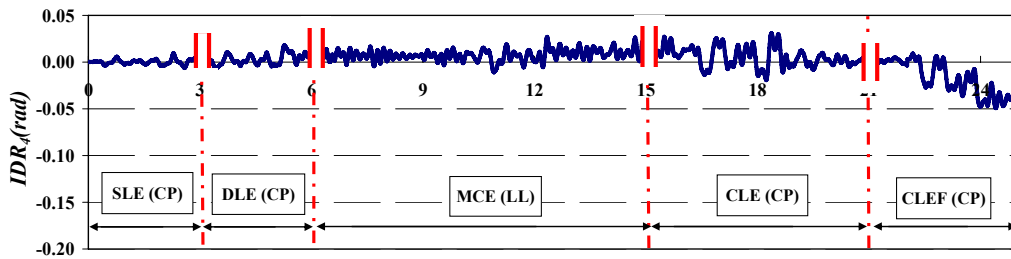
Time (sec)
(a) IDR_1



Time (sec)
(b) IDR_2



Time (sec)
(c) IDR_3



Time (sec)
(d) IDR_4

Figure 7.32. story drift history of Frame #2 for selected segments at various ground motion intensities

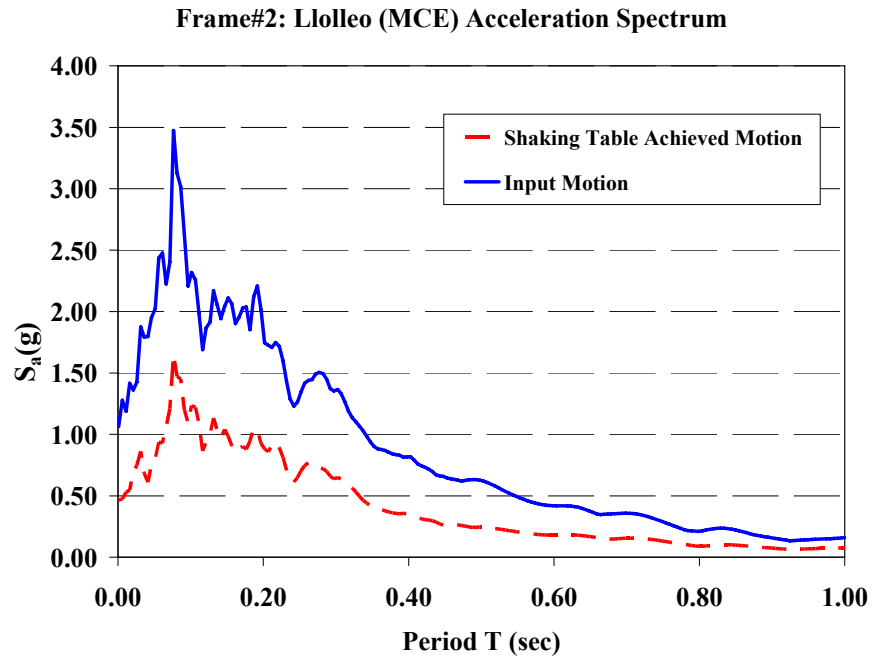


Figure 7.33. Comparison between input and achieved table motion of MCE test in model domain (Frame #2, $T_I=0.46\text{sec}$)

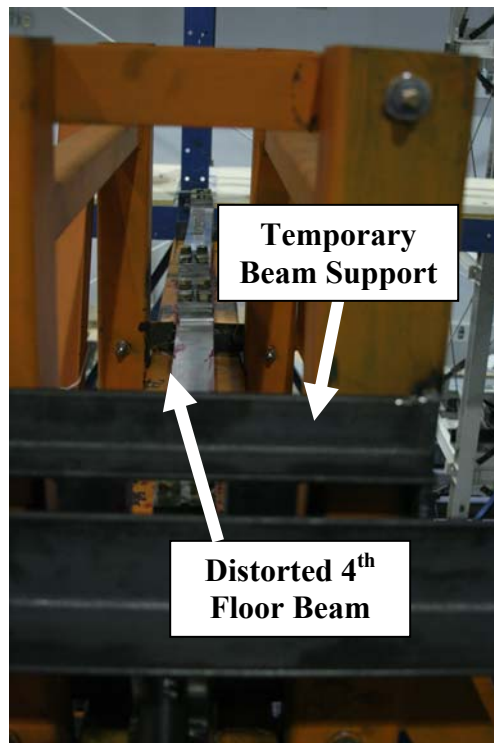


Figure 7.34. Distorted fourth floor beam after MCE due to out-of-plane motion



Figure 7.35. Collapse mechanism of Frame #2 after completion of CLEF

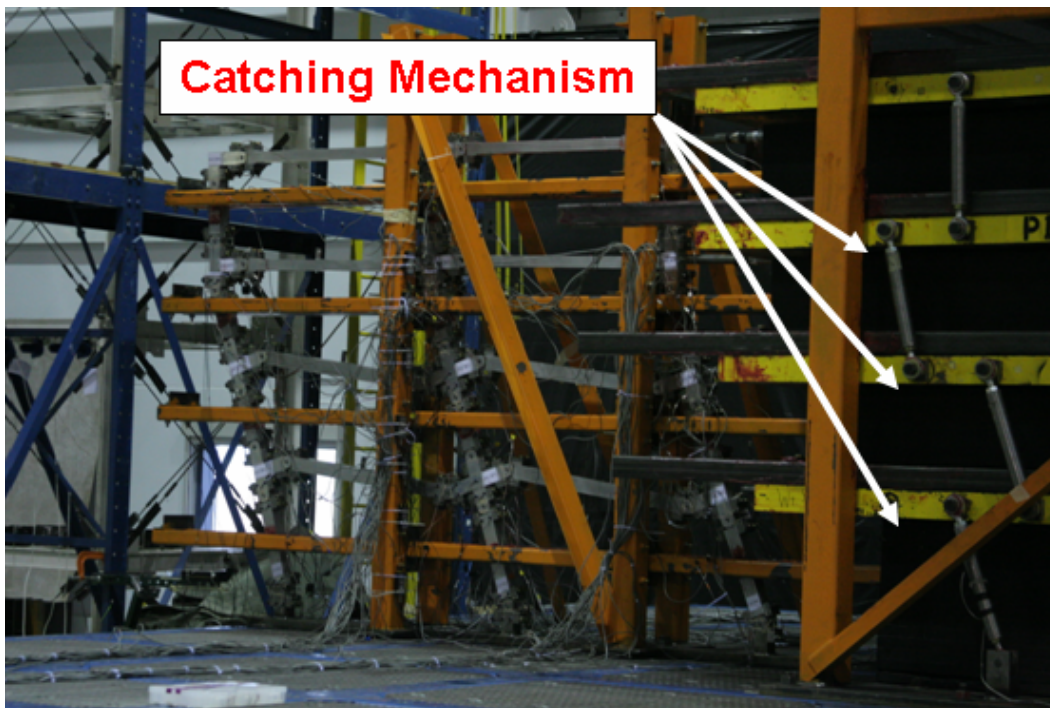


Figure 7.36. "Catching" mechanism of Frame #2 at the end of CLEF

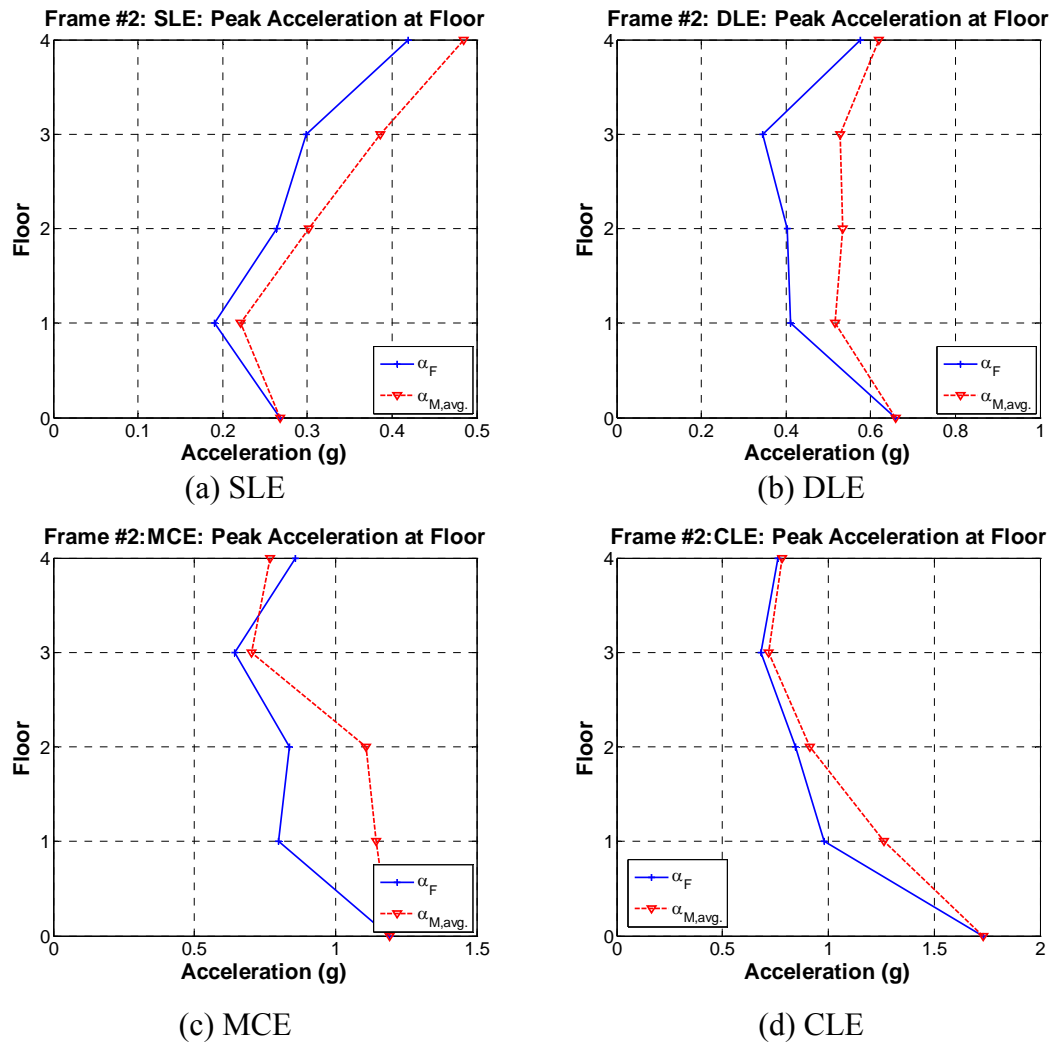


Figure 7.37. Peak absolute floor accelerations of Frame #2 and mass simulator at various ground motion intensities

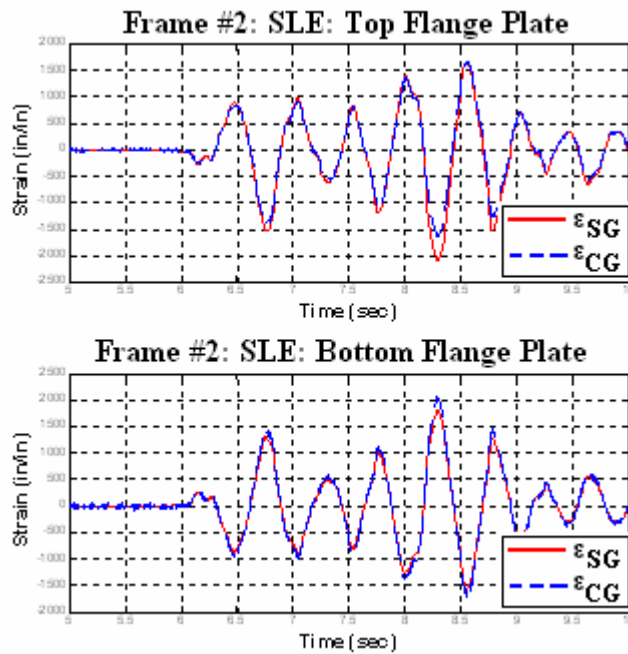


Figure 7.38. Correlation of strain history as measured from strain gages and clip gages over 1.5" length of flange plates of interior first floor beam of Frame #2

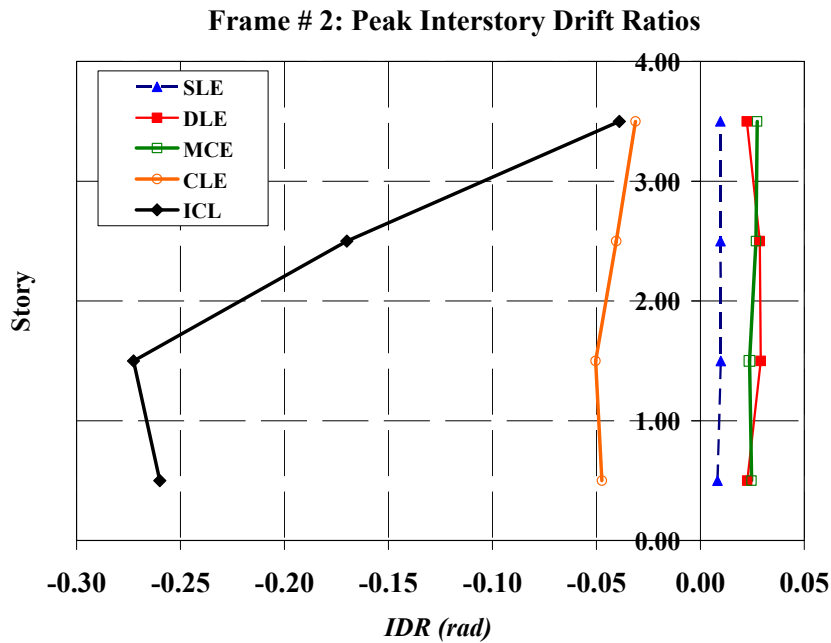


Figure 7.39. Peak interstory drift ratios of Frame #2 at various ground motion intensities

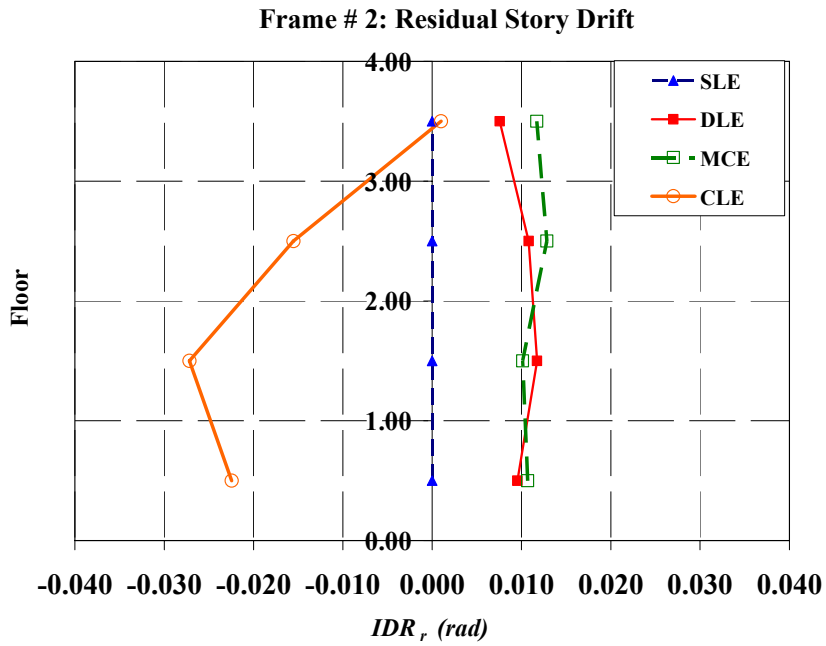


Figure 7.40. Residual interstory drift ratios of Frame #2

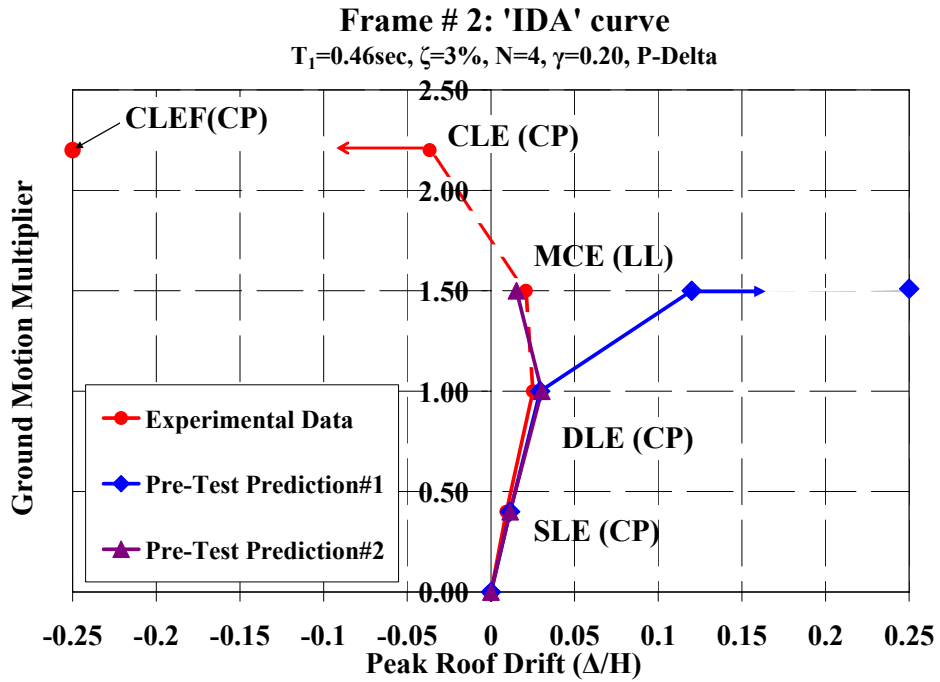


Figure 7.41. IDA curve for Frame #2 as obtained experimentally together with pre-test analytical prediction

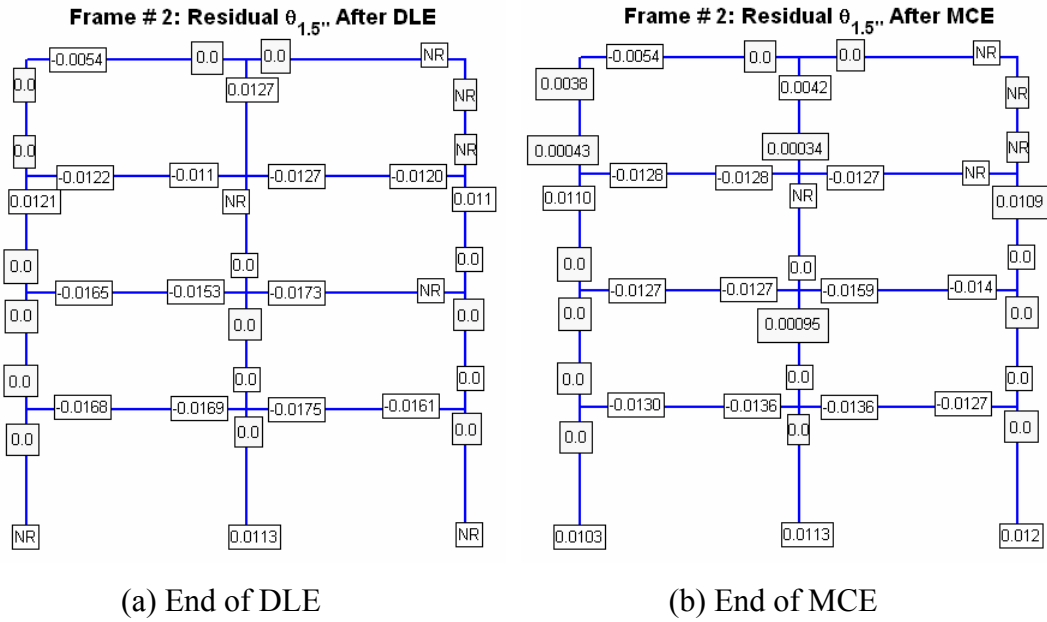


Figure 7.42. Residual $\theta_{1.5''}$ at plastic hinge locations of Frame #2; (a) DLE, (b) MCE

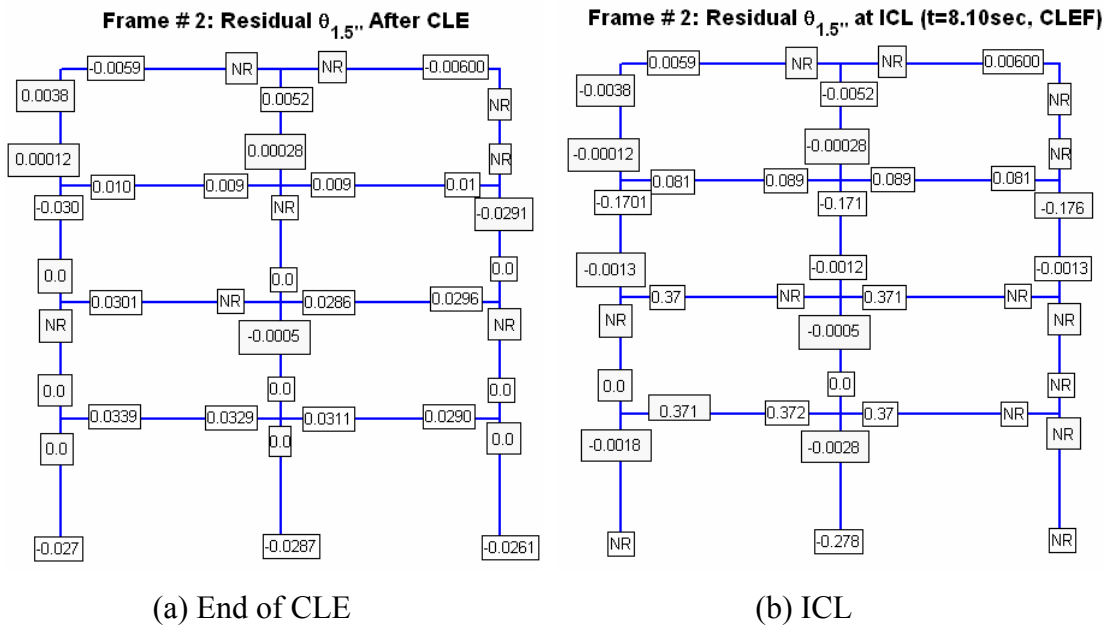
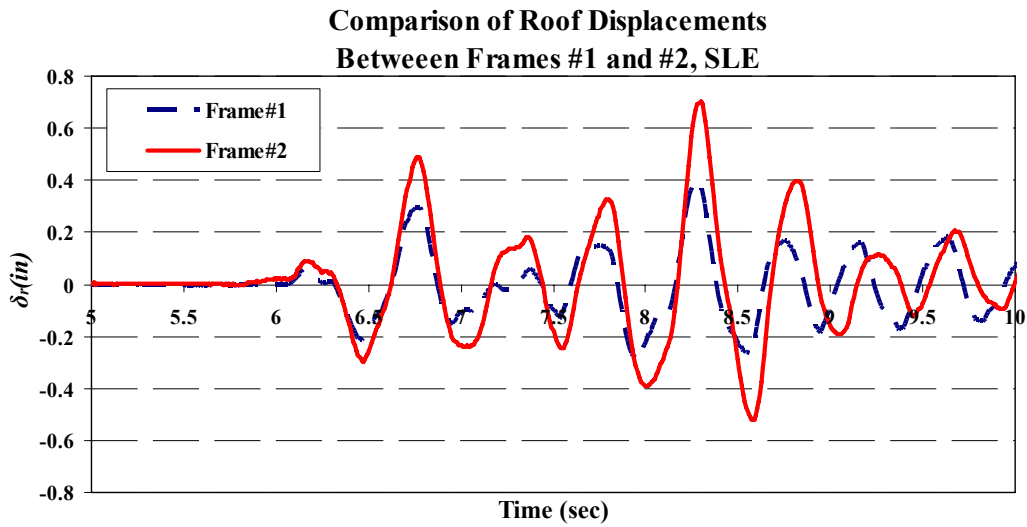
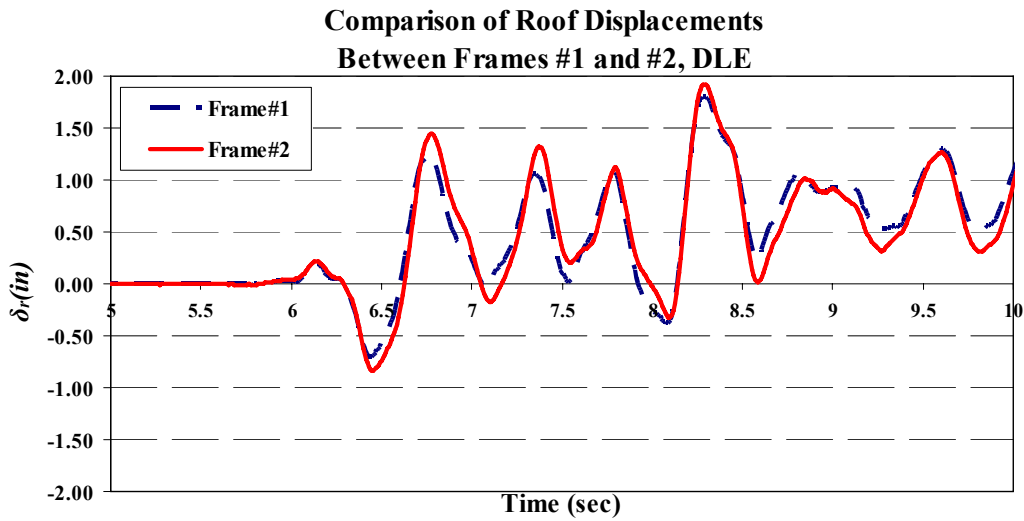


Figure 7.43. Residual $\theta_{1.5''}$ at plastic hinge locations of Frame #2; (a) CLE, (b) ICL

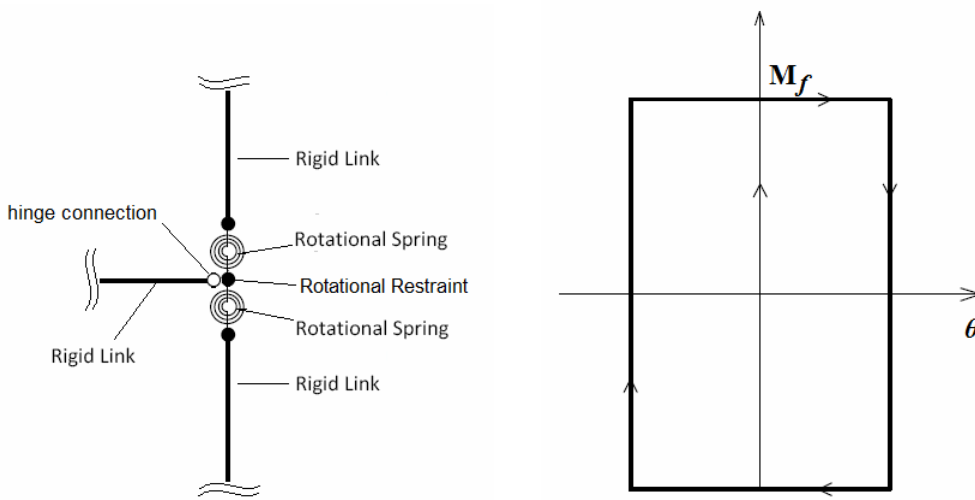


(a) SLE



(b) DLE

Figure 7.44. Comparison of roof displacement history between Frames #1 and #2; (a) SLE,
(b) DLE



(a) rotational springs representing friction (b) moment-rotation behavior of rotational springs

Figure 7.45. Friction element (a) mathematical model representation; (b) simplified behavior of friction element

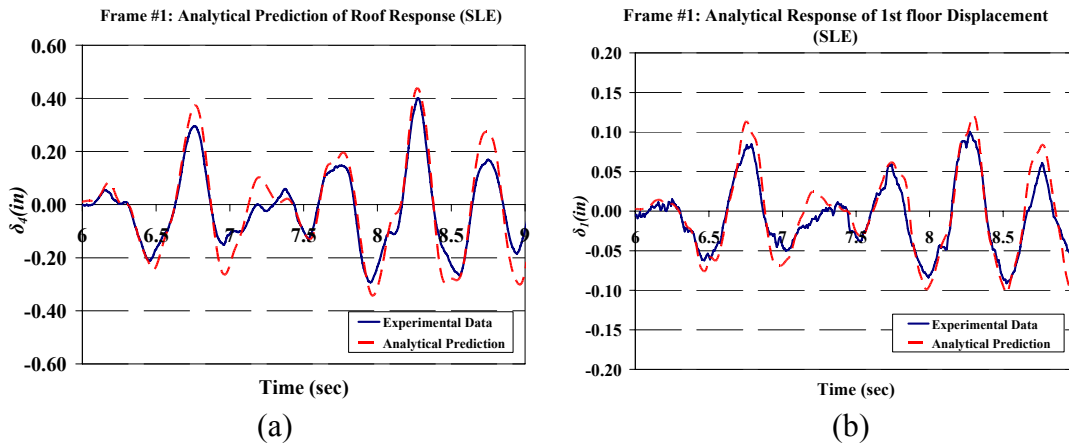


Figure 7.46. Response comparison between analytical predictions using the calibrated friction element and experimental data at SLE level, Frame #1; (a) roof displacement, (b) first story displacement

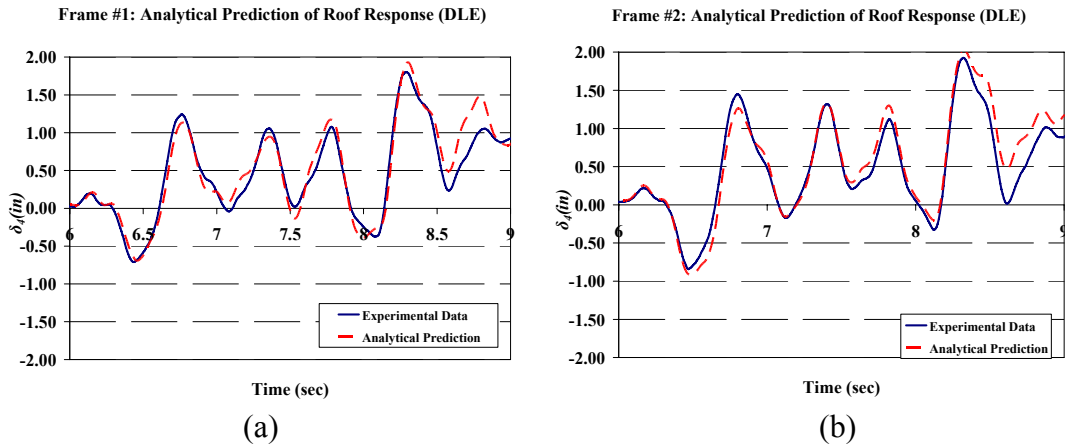


Figure 7.47. Response comparison between analytical predictions using the calibrated friction element and experimental data at DLE level, Frame #1; (a) roof displacement, (b) first story displacement

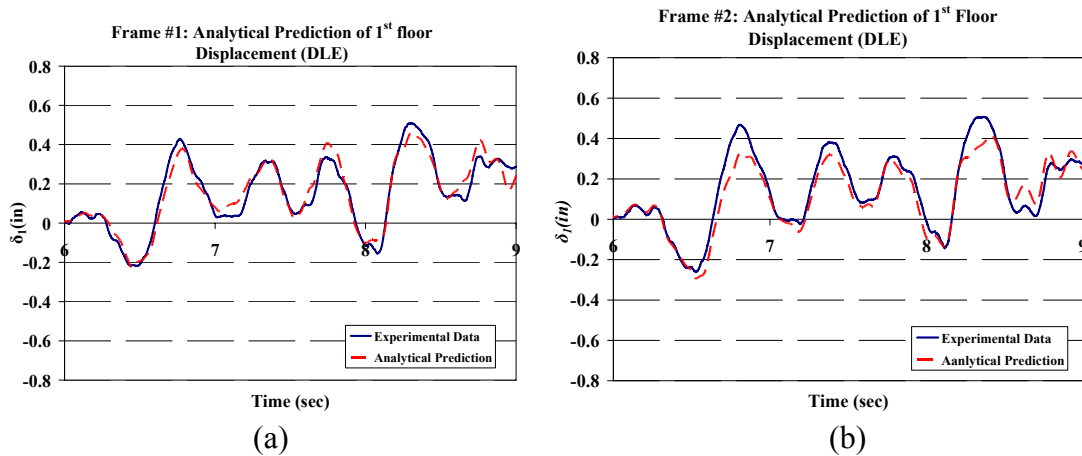
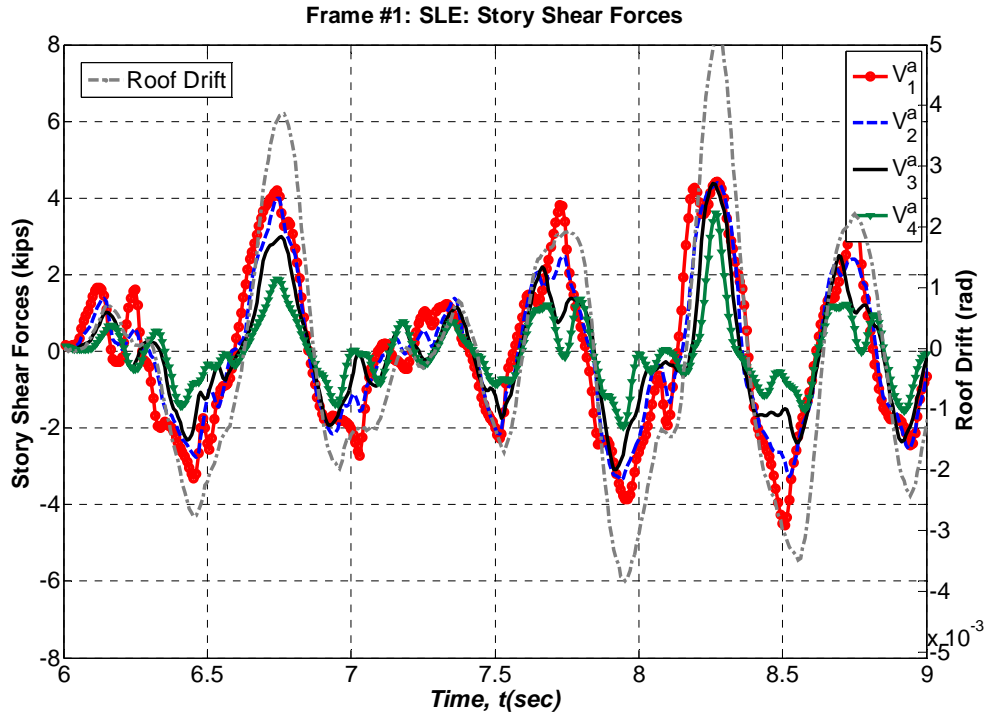
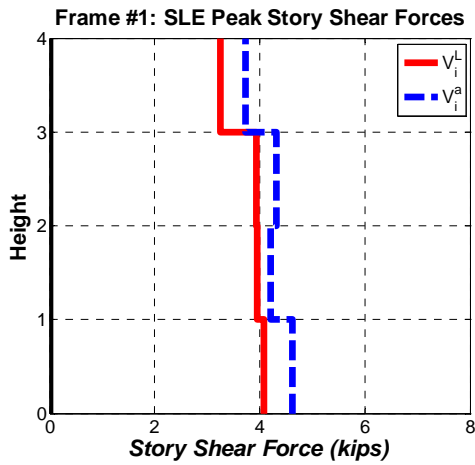


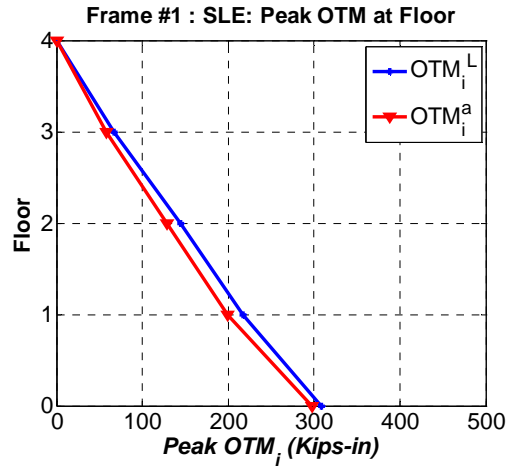
Figure 7.48. Response comparison between analytical predictions using the calibrated friction element and experimental data at DLE level, Frame #2; (a) roof displacement, (b) first story displacement



(a) Inertia based story shear force histories for Frame #1, SLE

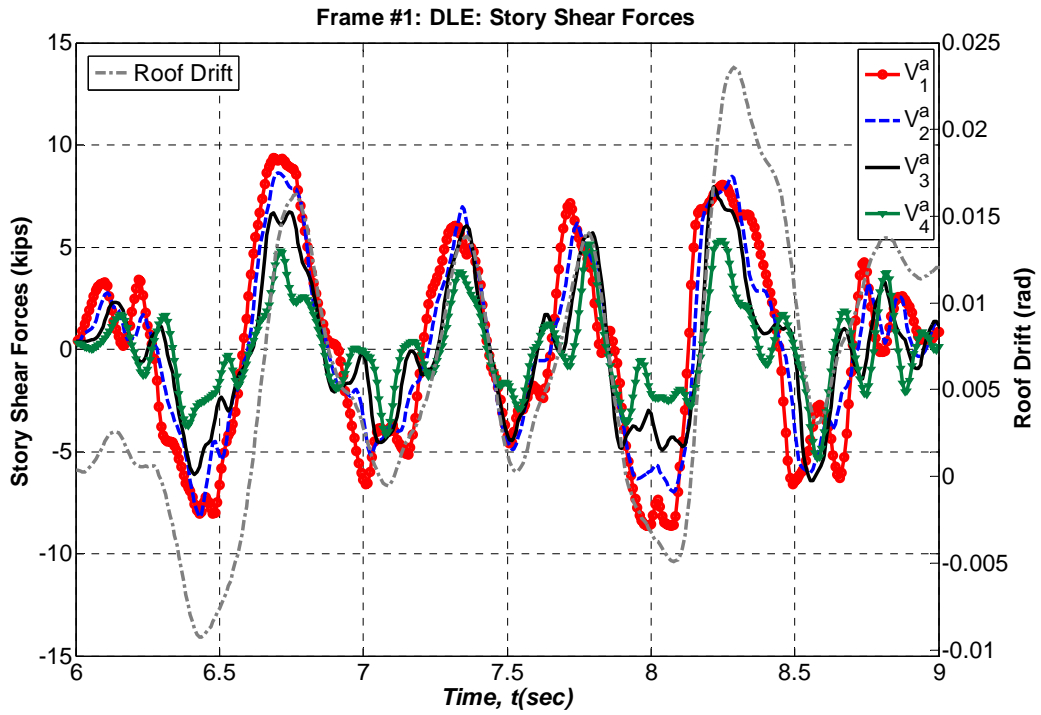


(b) peak story shear forces at SLE

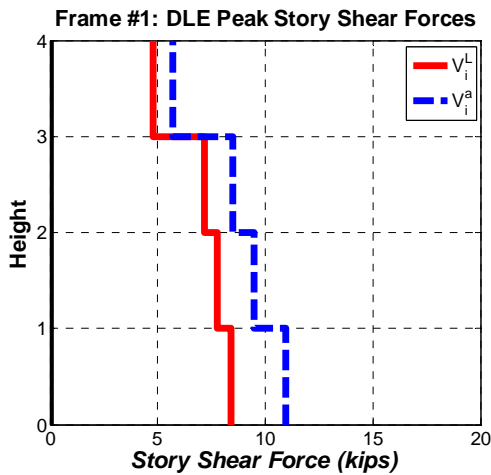


(c) peak OTM at floor levels, SLE

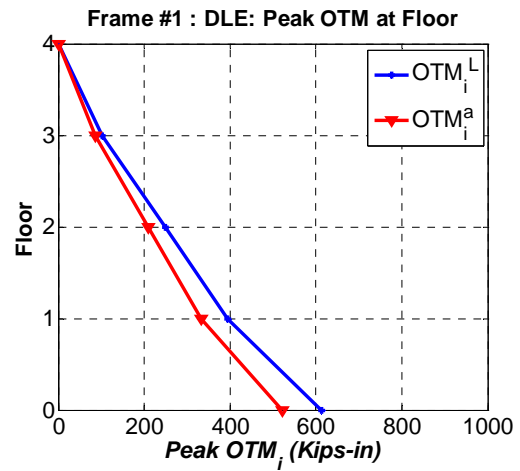
Figure 7.49. Story shear forces and peak OTMs of Frame #1 at SLE



(a) Inertia based story shear force histories for Frame #1, DLE

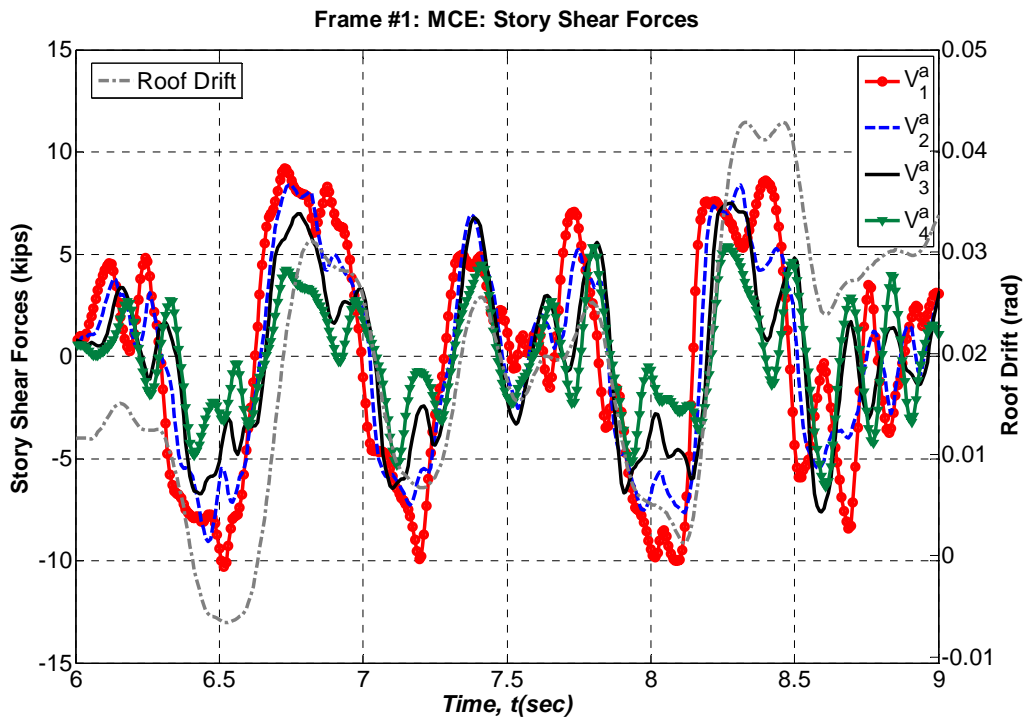


(b) peak story shear forces at DLE

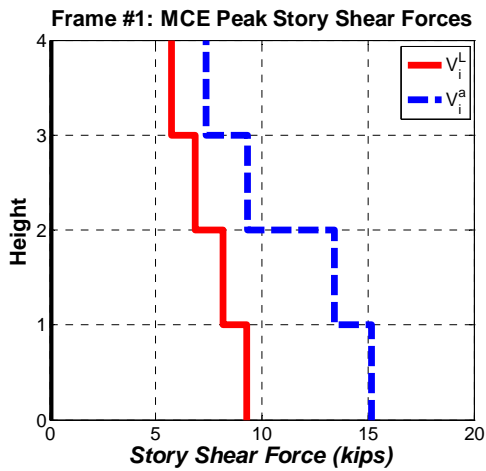


(c) peak OTM at floor levels, DLE

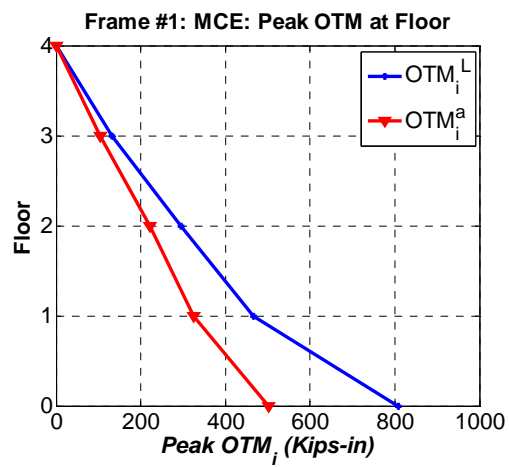
Figure 7.50. Story shear forces and peak OTMs of Frame #1 at DLE



(a) Inertia based story shear force histories for Frame #1, MCE

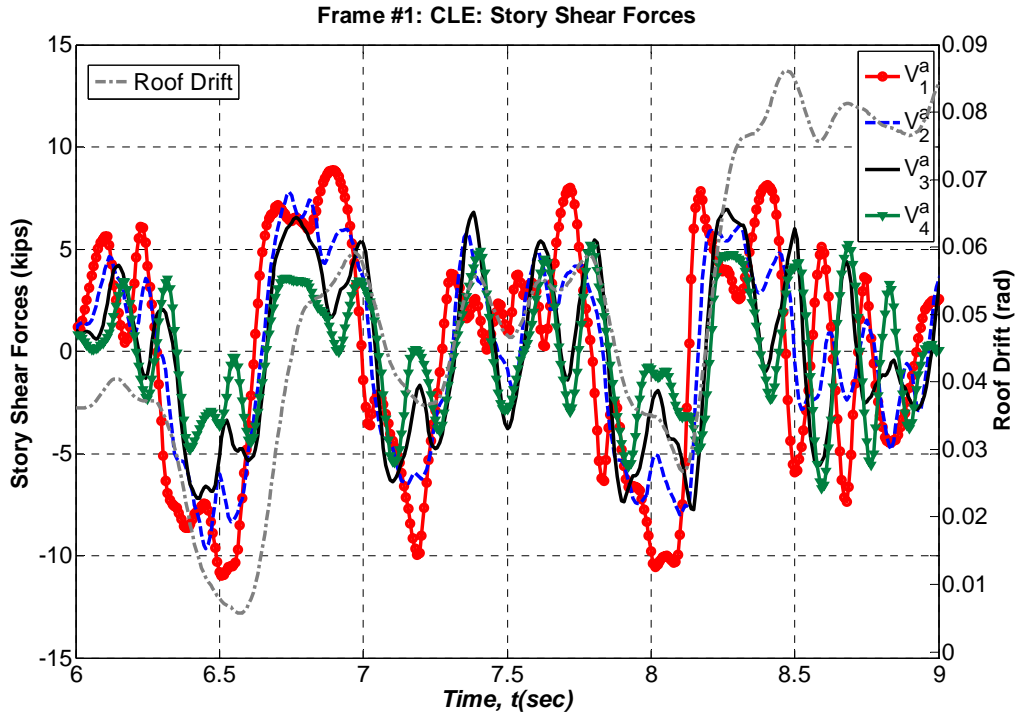


(b) peak story shear forces at MCE

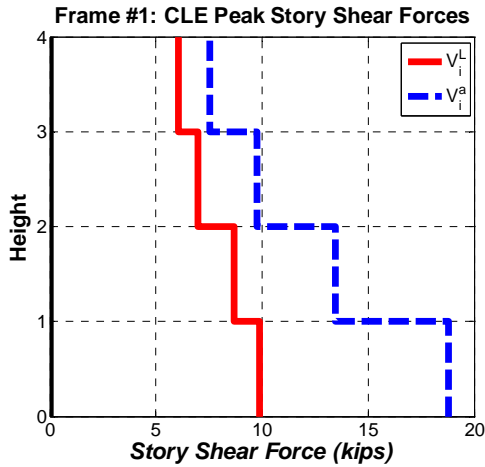


(c) peak OTM at floor levels, MCE

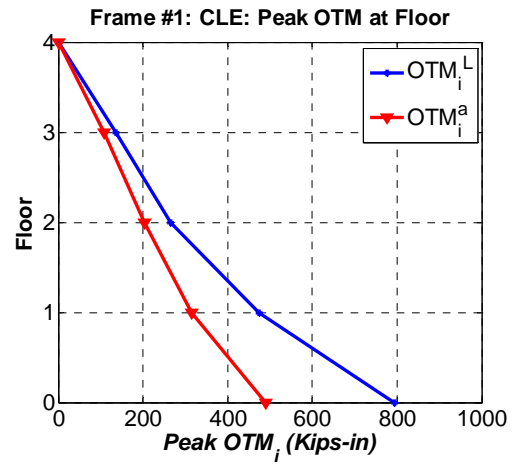
Figure 7.51. Story shear forces and peak OTMs of Frame #1 at MCE



(a) Inertia based story shear force histories for Frame #1, CLE

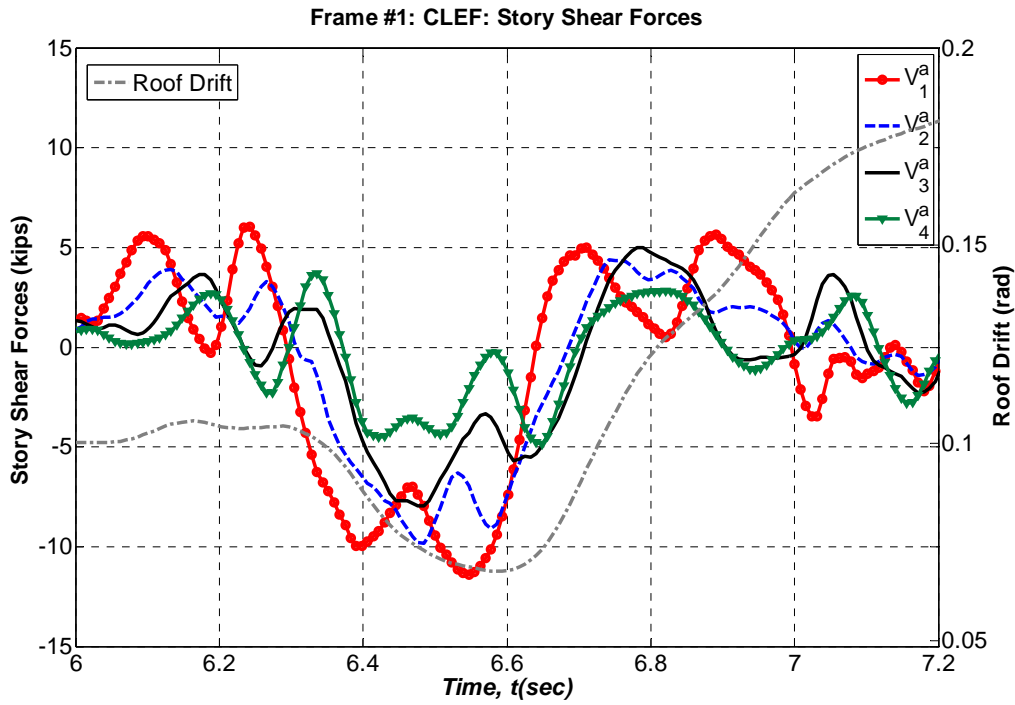


(b) peak story shear forces at CLE

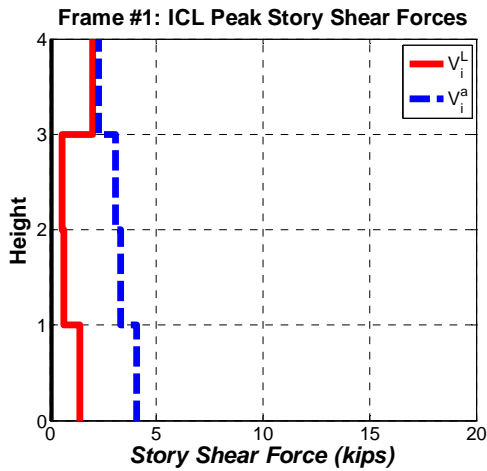


(c) peak OTM at floor levels, CLE

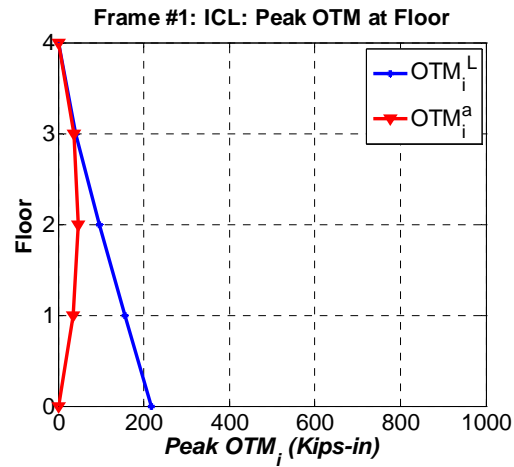
Figure 7.52. Story shear forces and peak OTMs of Frame #1 at CLE



(a) Inertia based story shear force histories for Frame #1, CLEF



(b) peak story shear forces at CLEF



(c) peak OTM at floor levels, CLEF

Figure 7.53. Story shear forces and peak OTMs of Frame #1 at CLEF

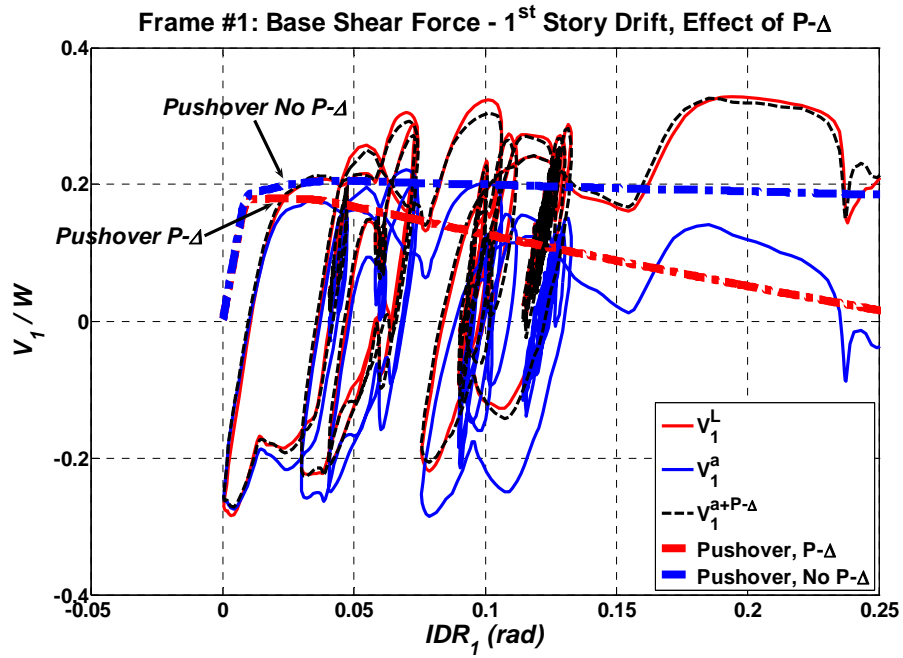


Figure 7.54. Inertia based and effective base shear force versus first story drift, Frame #1 (CLE, CLEF)

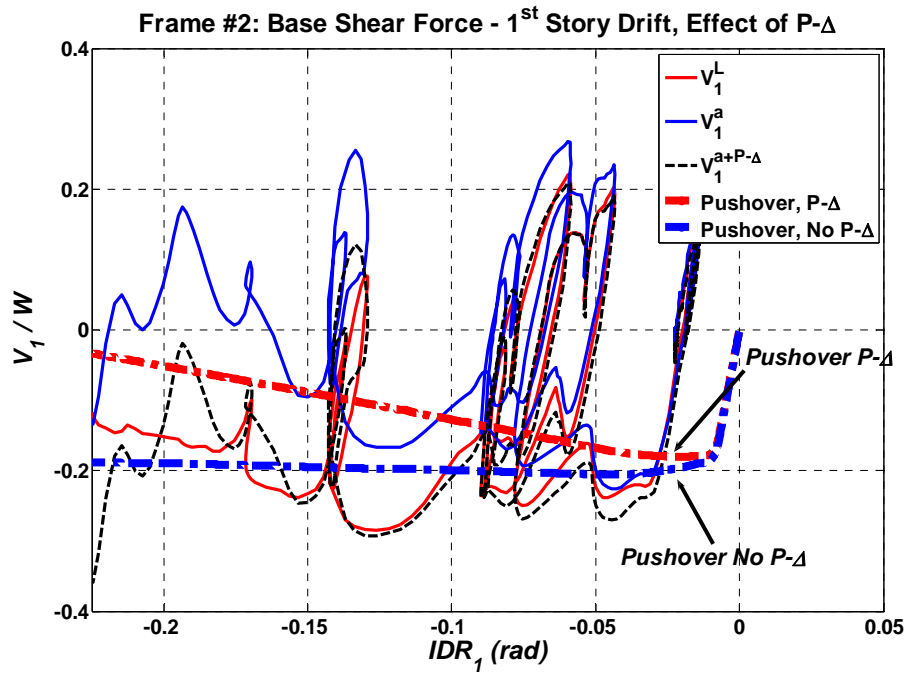


Figure 7.55. Inertia based and effective base shear force versus first story drift, Frame #2 (CLEF)

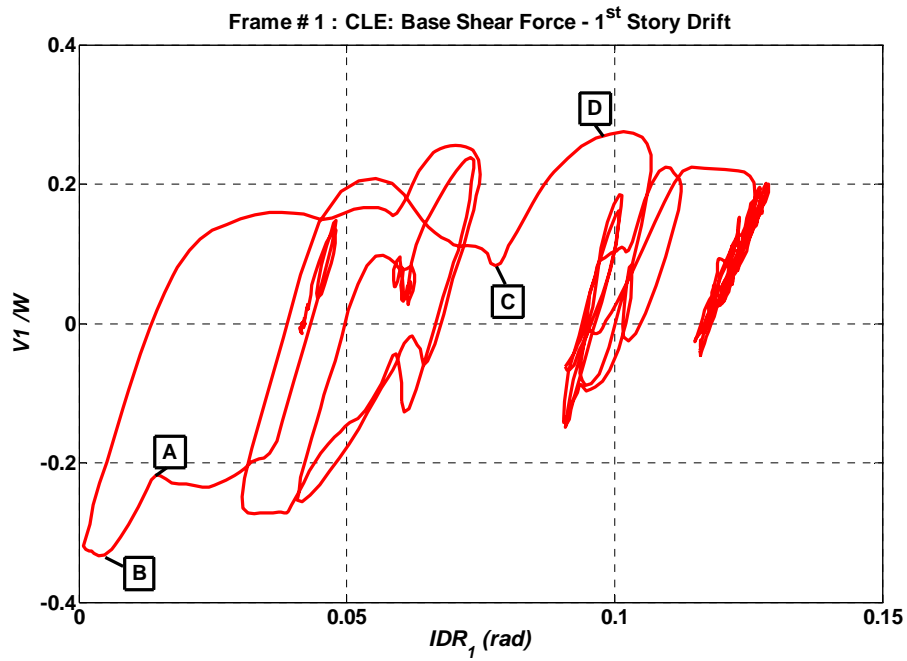


Figure 7.56. Effective base shear versus 1st story drift of Frame #1, CLE

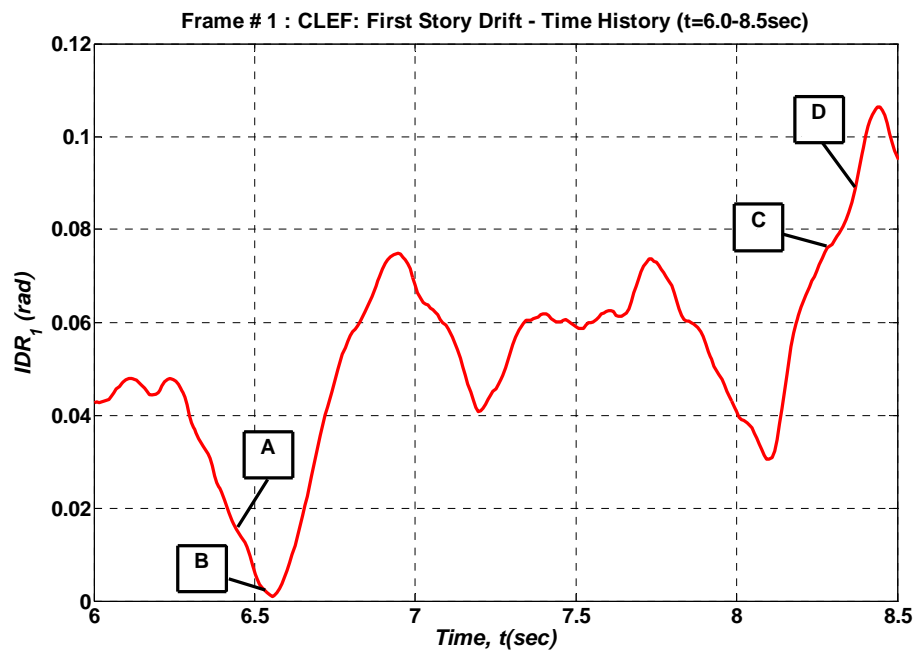


Figure 7.57. 1st story drift history of Frame #1 during CLE (t=6.0sec to 8.5sec)

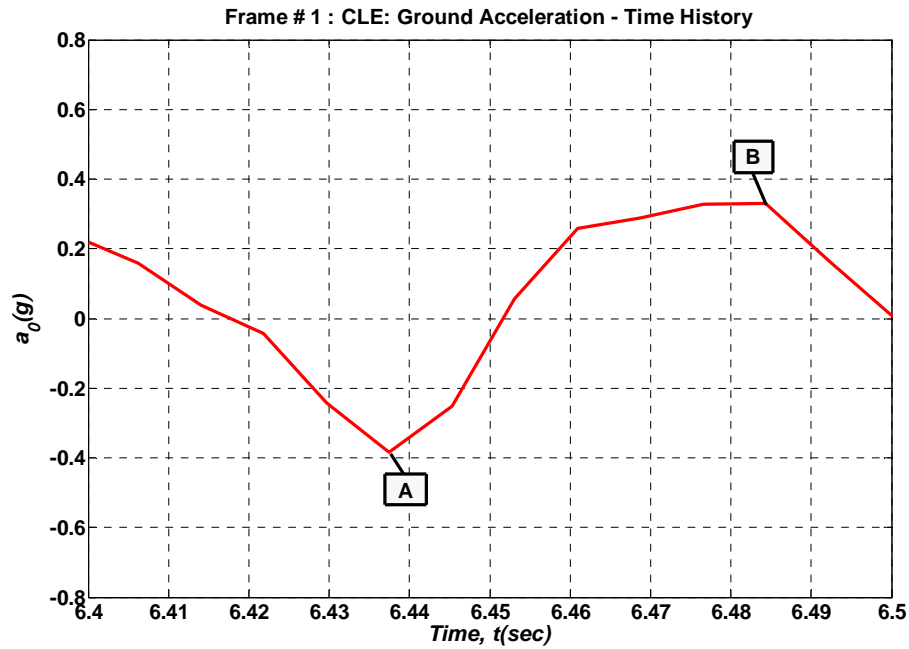


Figure 7.58. Ground acceleration history of Frame #1 during CLE (t=6.4sec to 6.5sec)

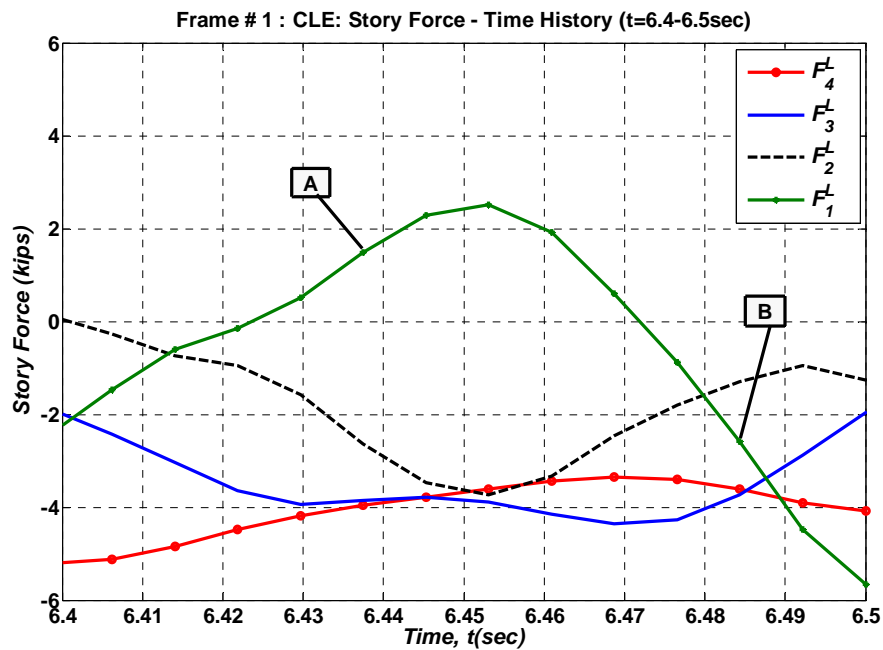


Figure 7.59. Story force histories of Frame #1 during CLE (t=6.4sec to 6.5sec)

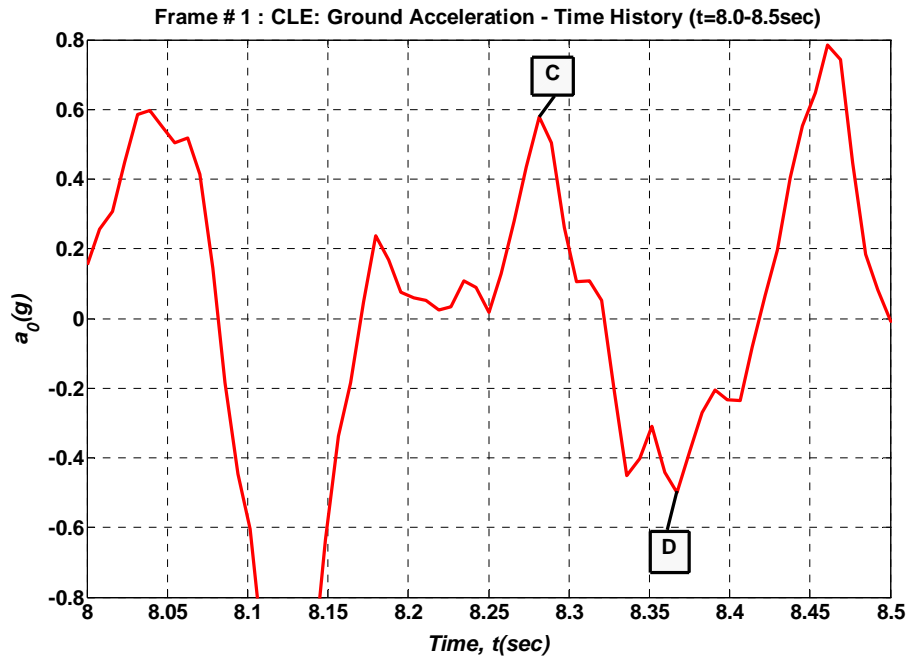


Figure 7.60. Ground acceleration history for Frame #1 during CLE (t=8.0sec to 8.5sec)

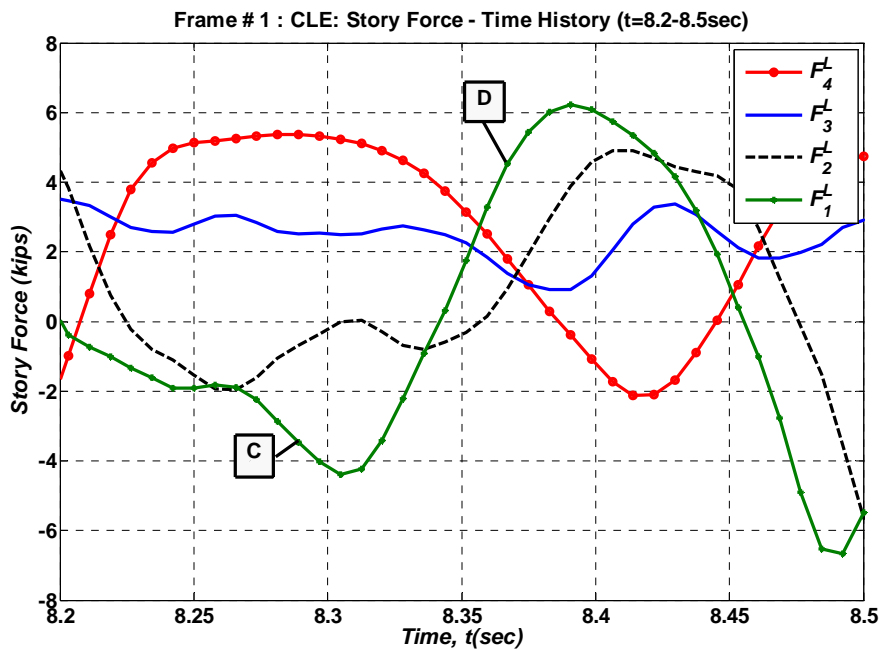


Figure 7.61. Story force histories of Frame #1 during CLE (t=8.2sec to 8.5sec)

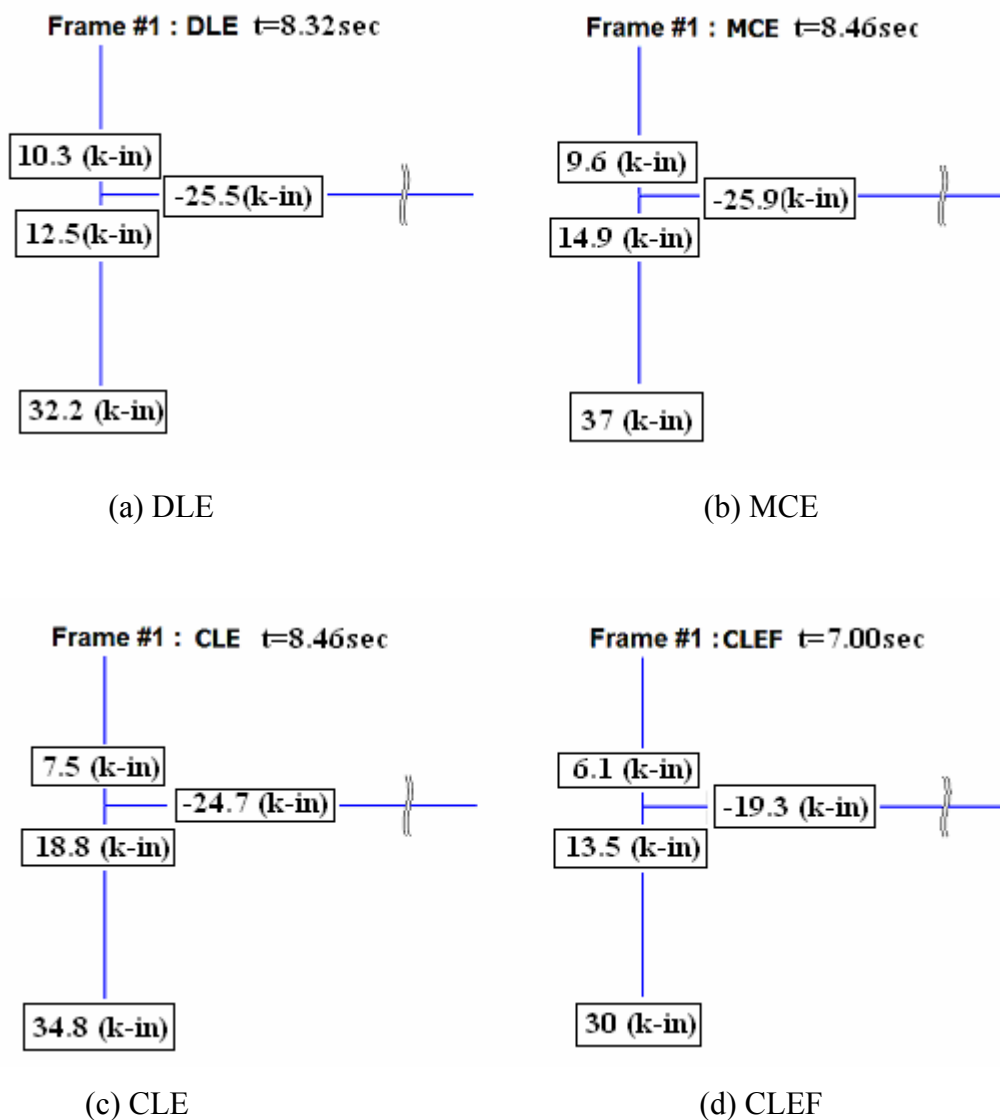
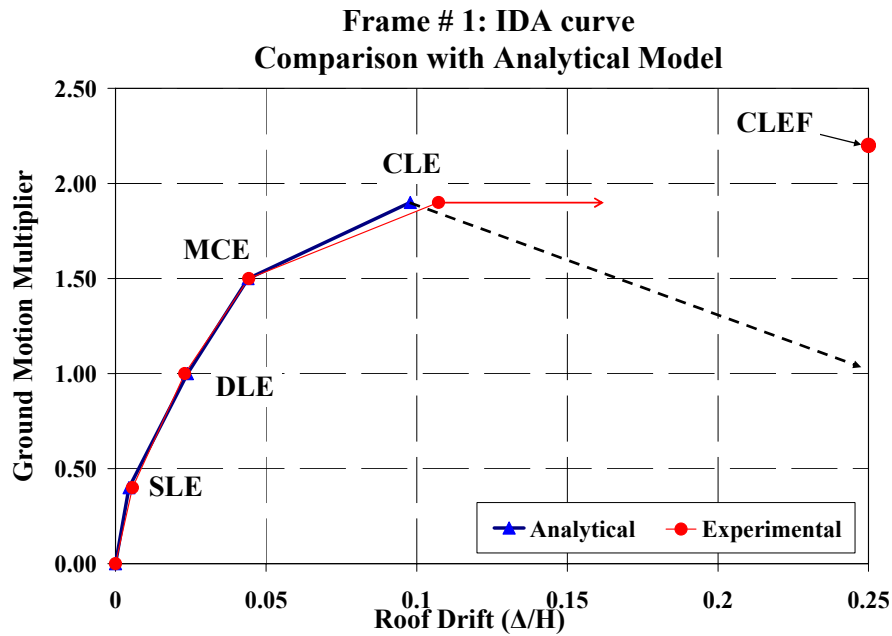
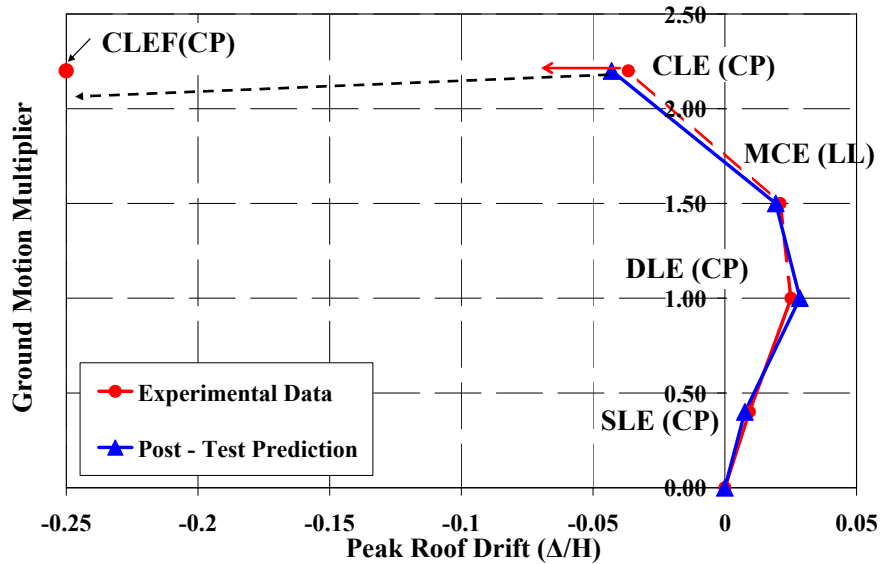


Figure 7.62. Moment equilibrium during plastification at exterior first floor joint of Frame #1 at four different “snap shots” at various ground motion intensities



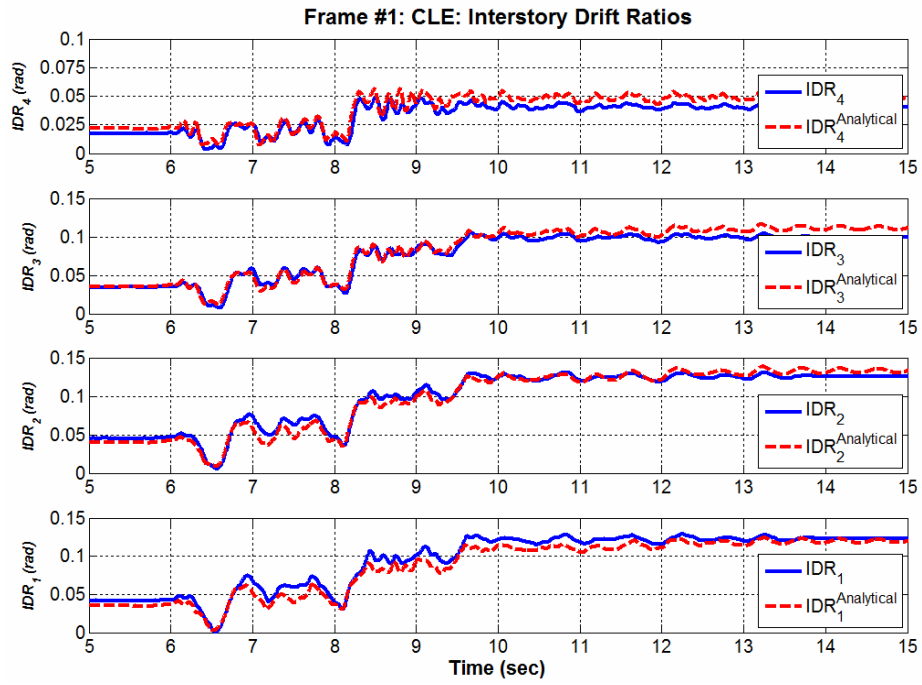
(a) 'IDA' curve for Frame #1

Frame #2: 'IDA' Curve Comparison with Post-Test Prediction
 $T_1=0.46\text{sec}$, $\zeta=1\%$, $N=4$, $\gamma=0.20$, P-Delta

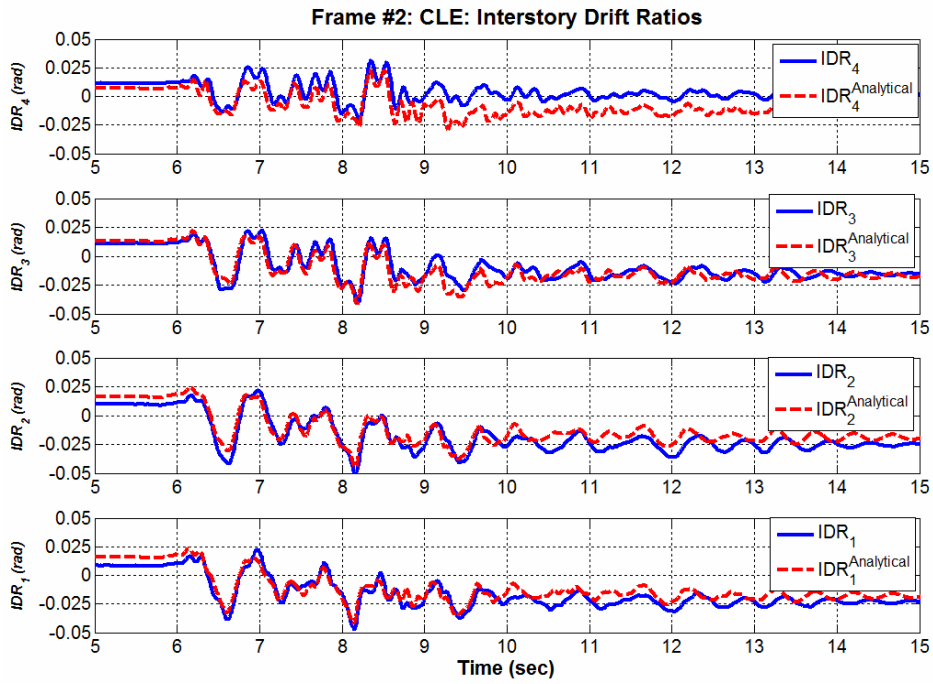


(b) 'IDA' curve for Frame #2

Figure 7.63. Experimental and post – test analytical 'IDA' curves; (a) Frame #1, (b) Frame #2



(a) Frame #1



(b) Frame #2

Figure 7.64. Interstory drift ratios of Frames #1 and #2 during CLE

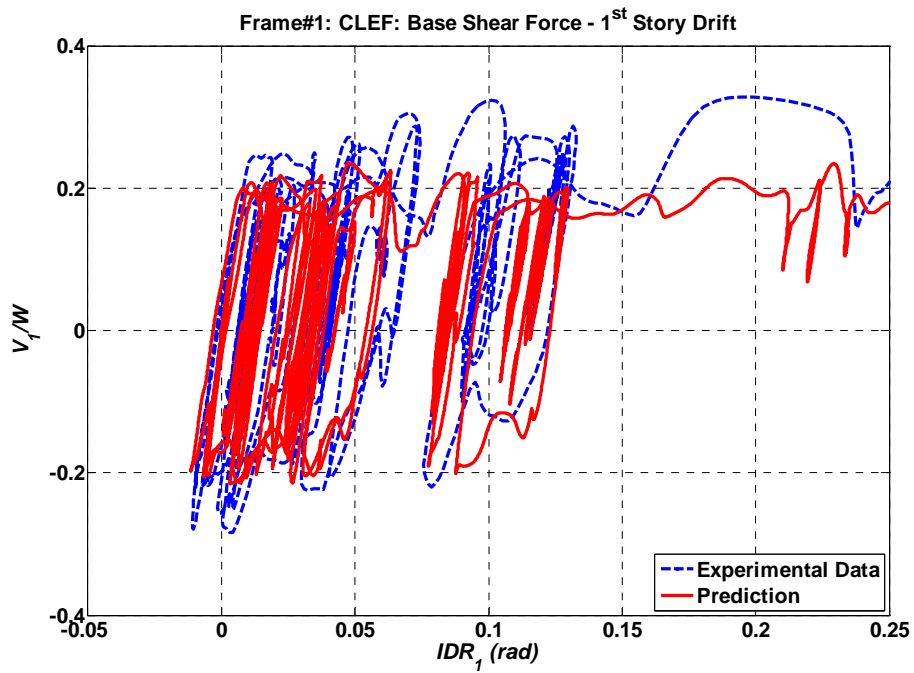


Figure 7.65. Base shear – 1st story IDR of Frame #1

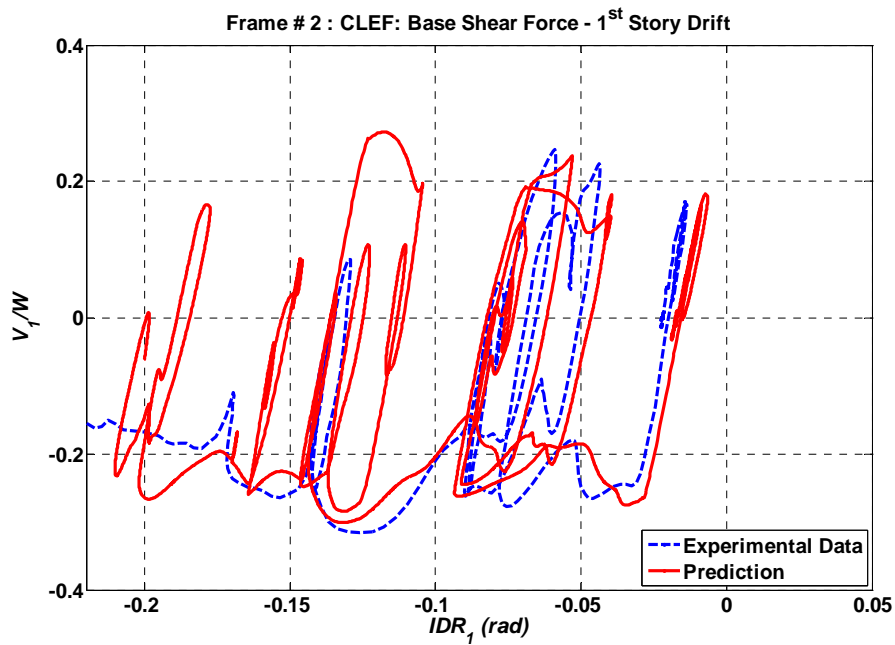


Figure 7.66. Base shear – 1st story IDR of Frame #2

CHAPTER 8

CASE STUDIES

8.1 Objective and scope

This chapter summarizes case studies performed in order to evaluate the capability to predict collapse of structural systems based on the knowledge gained from the previous chapters of this research. The case studies discussed in this chapter are: (1) analytical collapse predictions of the prototype structure presented in Chapter 5, (2) assessment of the importance of deterioration model parameters on collapse of this structure in view of the fact that there are significant differences between prototype and 1:8 scale model deterioration properties, (3) performance assessment of a 15-story building structure designed according to Japanese practice, with the design information provided by Kajima Corporation, (4) modeling and prediction effort for the Blind Analysis contest by E-Defense in advance of the shaking table test series performed on a 4-story steel frame building, (5) a parametric study evaluating the collapse capacity of non-ductile low-rise building structures based on evaluation of experimental data of infill walls, (6) collapse prediction of idealized models of Autoclaved Aerated Concrete (AAC) structures, and (7) collapse assessment of a residential adobe house reinforced with polymer mesh.

All analyses efforts are concerned with 2-dimensional (2-D) models because the emphasis is to “exercise” a collapse prediction methodology and to illustrate practical utilization of this methodology. The validity of results depends strongly on the availability of test data on which to base deterioration modeling. Most of the results available from experimental

studies are for 2-dimensional behavior except for the shaking table test conducted on the E-Defense facility.

For statistical evaluation of the collapse capacity a set of 40 “ordinary” ground motions recorded in California is used in several of the case studies. These ordinary ground motions were recorded on stiff soil (or soft rock) and do not exhibit pulse-type near-fault characteristics. In this set the source-to-site distances range from 13 to 40 km, and the moment magnitudes range from 6.5 to 6.9. A detailed description of the characteristics of the record set is provided in Medina and Krawinkler (2003). It is important to note that in California the long return period hazard may be controlled by near-fault ground motions with forward directivity (records exhibiting pulse-type characteristics), which have different frequency characteristics than the records contained in the set of 40 ordinary ground motions. However, the main purpose of the case studies is to illustrate collapse evaluation based on the knowledge gained from case specific experiments or the component databases discussed in Chapter 3, and for this reason the same set of ordinary ground motions is used at all hazard levels.

8.2 General Assumptions in 2-D Modeling of Frame Structures

Herein it is assumed that the objective of response prediction (analysis) is to compute demands for a performance evaluation of structures up to collapse, with an emphasis on forces and inelastic deformations around beam-column connections, forces in elements such as columns that need to be protected from excessive overloads, and deformations in walls that are dominated by flexural behavior.

In the case studies discussed in this section, beams and columns are modeled as elastic elements with plastic point hinges at the ends. Inelastic behavior in walls is represented either by flexural springs or by translational springs in SDOF systems. The point hinges are

represented by rotational springs whose properties are obtained from engineering mechanics principles supplemented by backbone curve and deterioration rules obtained from the databases and predictive equations of deterioration parameters of structural elements discussed in Chapter 3 and 4 and idealized by the modified Ibarra-Krawinkler model discussed in Section 2.3.

The tools used for analysis are a single degree of freedom program (SNAP) in which general hysteresis models and deterioration are incorporated and a modified version of the DRAIN-2DX computer program (Prakash et al. 1993). The original DRAIN-2DX version has been modified by Medina and Krawinkler (2003), Ibarra and Krawinkler (2005), Zareian (2006), and Lignos and Krawinkler (2008) and includes the deteriorating component models described in Sections 2.2 and 2.3 for various hysteresis behaviors (bilinear, peak-oriented, and pinching).

8.3 4-Story Prototype Building Used in this Study

This section summarizes the collapse evaluation of the east-west (EW) moment resisting frame with reduced beam sections (RBS) of the prototype 4-story office building, described in detail in Section 5.2. The calculated seismic weight per floor of the office building is summarized in Table 5.3 and the (EW) perimeter frame is shown in Figure 5.4.

Deterioration parameters for both columns and beams are extracted from the steel database described in Chapter 3. The deterioration parameters used in the analysis of the prototype EW frame have been summarized in Chapter 6 (see Table 6.1). Representative experimental data used to evaluate the behavior of reduced beam sections of the 4-story moment resisting frame have been presented in Figure 6.1.

8.3.1 Performance Evaluation – Nonlinear Static Analysis

Preliminary performance of the structure is evaluated from on a nonlinear static analysis, as illustrated in Figure 8.1. The design base shear is marked with a horizontal line. The main reasons for the observed overstrength (maximum strength versus design base shear) are (1) beam sections are stiffness controlled even though the flanges of the RBS moment connections were reduced close to the 50% maximum permitted by FEMA 350 (2000) provisions, and (2) implementation of the strong column – weak beam code criterion. In addition, seismic code provisions require seismic compactness checks for columns and beams in order to control local buckling. In the design of the 4-story structure compactness checks controlled the column sections (W24 sections were selected for column design).

The collapse mechanism at 8% roof drift is illustrated in Figure 8.2 based on static pushover analysis. As seen, on top of the third story plastic hinges develop in the columns even though the strong column - weak beam criterion in accordance with AISC (2005) seismic specifications is fulfilled. The collapse mechanism of both 4-story scale model frames during the shaking table collapse test series presented in Chapter 7 was identical with the one illustrated in Figure 8.8 (see Figures 7.18, 7.35).

8.3.2 Dynamic Analysis

For dynamic analysis of the 4-story moment resisting frame the set of 40 “ordinary” ground motions discussed in Section 8.1 is used. In order to determine the collapse capacity of the structure Incremental Dynamic Analysis (IDA) is employed. IDA plots for the set of 40 ground motions are presented in Figure 8.3 in which the spectral acceleration for 5% damping at the first mode period of the structure is plotted versus (1) the roof displacement normalized with respect to the total height of the building (see Figure 8.3(a)) and (2) the maximum story drift ratio (see Figure 8.3(b)). As seen from the figures the IDAs become horizontal, indicating that the collapse capacity has been reached, at roof drifts less than

8%. This agrees with general conclusions from other studies (ATC-63). The practical implication is that frame collapse is not overly sensitive to component behavior characteristics at drifts exceeding 6 to 8% (e.g., large ultimate deformation capacity θ_u and strength stabilization at a residual strength ratio values).

Collapse safety can be evaluated using fragility curves that describe the probability of collapse as a function of an intensity measure such as S_a/g (spectral acceleration at the first mode period of the structure (Ibarra and Krawinkler, 2005)). The counted collapse fragility function, as illustrated in Figure 8.4 for the prototype 4-story frame, is obtained by treating the collapse capacity data as a random sample, i.e., equally likely outcomes. A lognormal distribution is fitted to the counted fragility function in order to facilitate numerical and analytical calculations. Using the Boore et al. (1997) attenuation function the equal hazard spectrum for a 2% in 50 years probability of exceedence at the selected site is obtained. The steel frame has a first mode period of 1.32sec, for which the spectral acceleration from the equal hazard spectrum is 0.80g. The probability of collapse for this value of $S_a(T_1=1.32)$ is 0.07. Based on recent studies on collapse assessment of structures (ATC-63) a probability of collapse of 10% appears to be an acceptable value at the 2/50 hazard level, i.e., the case study frame structure exhibits adequate collapse performance.

8.3.3 Collapse Capacity of Prototype Frame Versus its 1:8 Scale Model

As discussed in Chapter 6 (see Sections 6.6 and 6.7) the component deterioration parameters of the 1:8 scale model of the E-W moment resisting frame used as the primary case study in this research are quite different based on the Tables 6.1 and 6.9, which summarize the target deterioration parameters of components of the EW prototype frame and the model deterioration parameters of test Frame #1 used for the shaking table experiments. Particularly the plastic rotation capacity θ_p and post capping rotation capacity θ_{pc} are much larger in the model than in the prototype. The consequence is that the prototype frame structure is expected to have a smaller collapse capacity, and the question

is how much smaller. Since it was demonstrated in Section 7.6.5 that the response of the physical model and its collapse capacity are very well simulated analytically, the analytical model of the prototype can be used with confidence to predict prototype behavior using the target deterioration parameters listed in Table 6.1.

In order to evaluate the effect of differences in component deterioration on the response and collapse capacity of the prototype frame structure, the analytical model of the prototype is subjected to the same ground motion sequence as test Frame #1 experienced in the shaking table tests. The achieved table motions from Testing Program #1 (see Section 7.4.1) are used for this purpose after scaling the time domain of the records by $\sqrt{8}$ in order to switch from model to prototype domain. The effect of cumulative damage from the sequential application of several ground motions is considered in the analysis. The following two cases are evaluated in the prototype domain:

- Case #1: Prototype frame with target deterioration parameters (see Table 6.1)
- Case #2: Prototype frame with model deterioration parameters (see Table 6.9)

Figure 8.5 presents the “IDA” curves of these two analysis cases together with the “IDA” curve of the shaking table test series (denoted as “Model Frame #1-Experimental Data”). Shown with a dashed line in the same figure is the collapse capacity of the Case #1 analysis model without considering the effect of cumulative damage. The following observations are made from comparing the “IDA” curves:

- The differences between the experimental response of the 1:8 scale physical model and the predicted response of the prototype with model deterioration parameters are noticeable but not large. These differences are attributed to (1) the plastic hinges in the model frame are not at exactly the same locations as in the prototype because of geometric constraints that were discussed in Section 5.3.1 and Section 6.3.4; (2) 2% Rayleigh damping has been assumed for the first and second period of the prototype

frame, and (3) the friction damping observed in the shaking table tests is not simulated in the prototype domain.

- The difference in the collapse capacities of Frame #1 and the prototype (Case #1) is fully attributed to differences in the deterioration parameters of the plastic hinge regions.
- The effect of cumulative damage decreases the collapse capacity of the prototype (Case #1) for the Canoga Park record from 1.65 to 1.45 (ground motion intensity multiplier).

This correlation between analytical simulations and experimental data from the collapse test series discussed in Chapter 7 emphasizes the importance of accurate simulation of deterioration characteristics of structural components for collapse assessment of deteriorating structural systems.

8.4 Kajima 15 story Building Model A

The collapse capacity of a 15-story moment resisting steel frame that is a lateral load resisting unit of a Kajima Corporation design of a 15-story building (Model A) is evaluated based on the knowledge gained from the material discussed in previous chapters. The dimensions of the frame are presented in Figure 8.6. Sections and seismic weights used in the analysis are presented in Tables 8.1 and 8.2, respectively. One basic difference between a Japanese steel moment resisting frame and a steel frame designed by US practice is the fact that many Japanese frames are constructed using tubular cross sections for the columns.

The mathematical model used for the performance evaluation of the building model A is a model that includes shear deformation of joint panel zones using the model described in

Gupta and Krawinkler (1999). The thickness of the joint panel zone is assumed to be equal to twice the thickness of the column tube section. In order to simulate P- Δ effects a leaning column is used similar to the one discussed in Chapter 5 for the 4-story prototype building. The first mode period of the structure is 1.99sec. For the dynamic analyses of the building 2% Rayleigh damping is assumed for the first and third mode ($T_3 = 0.387\text{sec}$) of the building, since the first 3 modes cover the 90% of the modal mass of the building.

8.4.1 Deterioration Modeling

Modeling of deterioration parameters for elements of the Japanese building is based on information provided by the two databases that were developed for steel beams and tubular steel sections. The deterioration parameters for beams and columns of Model A are obtained from data of the steel W-sections database (ignoring composite action) and the tubular hollow square column database discussed in Chapter 3. These parameters are summarized in Tables 8.3 and 8.4. In order to determine the deterioration parameters for tubular steel columns the effect of dynamic axial force on the exterior columns in addition to the gravity force was considered. This additional axial force was estimated by (1) calculating the overturning moment at the base from yield base shear times $2/3^{\text{rd}}$ of structure height (Bertero et al. 1984), (2) estimating the force in the first story exterior column from (maximum overturning moment)/(width of frame), and (3) reducing this force appropriately for the columns above the first story. This dynamic axial force is superimposed on the gravity force in the columns. The moment rotation behavior for all the elements of the frame was modeled with a bilinear hysteretic response.

8.4.2 Performance Evaluation

Preliminary performance evaluation of the structure was done based on a nonlinear static analysis, as illustrated in Figure 8.7. The structure attains zero lateral resistance at about 4.5% roof drift based on static pushover analysis. For dynamic analysis the set of ground

motions discussed in Section 8.1 is used. Incremental dynamic analysis, IDA (Vamvatsikos and Cornell 2002), is employed to determine the collapse capacity of the structure. IDA plots are presented in Figure 8.8 in which the spectral acceleration at the first mode period of the structure is plotted versus the roof displacement normalized with respect to the total height of the building. The collapse fragility curve for the set of 40 ground motions is illustrated in Figure 8.9. The median collapse capacity of the Japanese building is 1.30g.

To illustrate engineering demand parameters (*EDPs*), such as interstory drift ratios (*IDR*) and roof displacement, from elastic range up to collapse, we focus on results from dynamic analysis using the Northridge 1994 Canoga Park earthquake record. Figure 8.10 shows the IDA curve for the selected record versus peak roof drift of the building, indicating that the last stable point for the given record is 2.10g. Figure 8.11 shows the peak interstory drift ratios along the height for five different levels of intensity. Yielding is concentrated in the beams of the first 12 floors and column bases. There was no indication of yielding in any of the panel zones. As can be seen from Figure 8.11, the drift profile changes somewhat as the structure transitions from elastic to inelastic behavior, and changes drastically as the structure approaches collapse (from $S_a = 2.0g$ to $S_a = 2.1g$), i.e., when the drift amplifies greatly in the lower stories. At levels of intensity near collapse significant component deterioration is observed at the base columns and first three floor beams.

It is not possible to make a direct comparison with U.S design practice, since there is no equivalent U.S. design of the 15-story building. But it is noted that a U.S. steel moment resisting frame building probably will have a significantly longer period and a smaller effective yield strength coefficient V_y/W . The implication for collapse is not evident since many variables enter in such a comparison, such as the backbone curve and cyclic deterioration parameters of the components of the structural framing.

8.5 E-Defense 4-story Steel Frame Structure

A challenging test series conducted on the E-Defense shaking table in the Hyogo Earthquake Engineering Research Center in Japan was the collapse test of a full scale steel building (Kasai et al. (2007), Tada et al. (2007), Suita et al. (2007, 2008)) designed based on current Japanese seismic provisions. The 4-story building was two by one bays, with two moment frames in one direction and three in the other. Figures 8.12 to Figures 8.14 show the structural system in plan view and elevations in the north-south and east-west direction. A photo of the building on the E-Defense shaking table is shown in Figure 8.15. The information shown in Figures 8.12 to 8.15 was retrieved from the E-Defense website (https://www.blind-analysis.jp/index_e.html). Tables 8.5 and 8.6 summarize the section sizes of the building and its seismic weight per floor assumed for dynamic analysis, respectively.

In order to predict the collapse capacity of the building a two-dimensional (2-D) analytical model of the two-bay frame (see Figure 8.13) in the y-direction (see Figure 8.12 for orientation) is developed. Half of the gravity load of the structure is applied as concentrated loads to the columns of the moment resisting frame. Fixed end moments are applied to all beams of the moment resisting frame using a distributed load as determined from half of the weight of the structure. To identify the model dimensions the centerline of each floor beam is considered as floor level.

Based on elastic modal analysis the structure had a period of $T_1 = 0.86\text{sec.}$, ignoring stiffness contributions from the exterior cladding. To account somewhat for the effect of the Autoclaved Aerated Concrete (AAC) cladding 3% Rayleigh damping was assumed for the first and second mode of the frame.

8.5.1 Composite Action

The floor slab was considered for the estimation of stiffness and strength of the beams. Different equations are available in the literature for estimating the effective width of the floor slab (Brosnan and Uang. (1995), Plumier et al. (1998)) and for estimating the stiffness contribution from the slab under lateral loading. The effective width, B , of the exterior beam slab is estimated from

$$B = b_f + 0.1L \quad (8.1)$$

Where b_f is the flange width of the steel girder and L is the span of the girder. Using this definition for the effective width of the slab, the positive (slab in compression) and negative (slab in tension) effective moment of inertia is calculated using the approach proposed in Eurocode-8 (1998) assuming a cracked concrete section. For beams forming part of the perimeter moment resisting frames (exterior spans) the stiffness under compression is found to be about two times the stiffness of the bare steel beam. This ratio is very large compared to values reported by Gupta and Krawinkler (1999), but the factor of two in the stiffness is intentionally kept in order to account for the effect of exterior cladding on lateral stiffness of the structure. On the other hand beams are relatively shallow and the slab is thick relative to the beam depth. In the cases discussed by Gupta and Krawinkler the beams were deeper (primarily W24 to W36) in which case the slab has proportionally less effect on composite beam stiffness. The effective stiffness with the slab in tension was found to be very similar to the stiffness of the bare beam.

8.5.2 Deterioration Modeling

Modeling deterioration parameters for elements of the 2-bay frame was based on information provided by the two databases that were developed for steel beams and tubular HSS columns and on the component tests conducted in Japan with a symmetric loading

protocol prior to shaking table experimentation (see Figure 8.16 for a column tested under 45 degree loading). A bilinear hysteretic model was assumed to represent beam and column elements of the steel frame. Modified stiffness coefficients were used to account for the flexibility of the elastic beam-column elements as proposed by Zareian (2006). In order to determine the deterioration parameters for tubular steel sections the effect of dynamic axial load on the exterior columns was considered in addition to gravity load. The same assumption that was discussed in Section 8.4 for the 15-story Kajima structure Model A was used in order to obtain the dynamic axial load effect on the exterior columns.

The originally estimated θ_p and θ_{pc} values for tubular sections obtained from calibration of experimental results were reduced by 30% in order to account for the biaxial effect since a 2-D instead of three dimensional (3-D) analysis was conducted. The estimated deterioration parameters were fairly close to the ones calibrated from the E-Defense test conducted with a column configuration rotated by 45° (See Figure 8.16). Additional information regarding the deterioration parameters, hardening parameters, and effect of cyclic hardening on the element of the frame was extracted from the databases discussed in Chapter 3. Tables 8.7 and 8.8 summarize the assumed deterioration parameters for beams and columns for collapse assessment of the 4-story frame.

8.5.3 Ground Motion and Testing Phases

Time history analyses were conducted to evaluate response characteristics and their dependence on structural parameters. The north-south (NS) component of the Takatori record (FD Serial No. T065) was adopted for this purpose, since this one was used during the shaking table collapse series. The acceleration spectrum of the unscaled NS component is presented in Figure 8.17 for 2% damping. This ground motion was applied to the structure with the following sequence: (1) 40%, (2) 60% and (3) 100% intensity of Takatori unscaled motion. The deformed configuration of the frame was taken into consideration in the analytical modeling and dynamic analysis evaluation. Results of the post-test prediction

are summarized below using the achieved shaking table motions of the Takatori record provided by E-Defense (https://www.blind-analysis.jp/index_e.html).

8.5.4 Static Pushover Analysis

The 4-story frame was evaluated with the use of nonlinear static analysis. A triangular load pattern was applied to the frame. The frame collapsed at about 10% roof drift and the pushover analysis indicated that the collapse mechanism of the frame was a first story mechanism. The static pushover analysis of the 4-story frame is shown in Figure 8.18. Figure 8.19 shows the change in displacement profiles along the height of the frame normalized with respect to the height of the building at various roof drift levels based on pushover analysis. The figure indicates that the frame had a first story collapse mechanism.

8.5.5 Dynamic Analysis Results – Comparison with Experimental Data

8.5.5.1 Incipient Collapse Level (60% Takatori Record)

After applying 40% of the unscaled Takatori record the structure remained elastic. During the 60% of the unscaled Takatori record (called “Incipient Collapse Level” in the testing phases by E-Defense) the maximum story drift ratio was about 2% at the bottom story. Figure 8.20 illustrates the peak story drift ratio along the height of the building based on experimental results (E-Defense (2007)). In the same figure the analytically predicted peak IDR is superimposed. As seen from the comparison with the experimental data the analytical model slightly overestimates the peak story drift ratios from second story up but correlates well with the measured IDR of the first story.

A comparison between peak story shears and overturning moments (OTM) along the height of the 4-story structure as obtained analytically and experimentally is presented in Figures 8.21 and 8.22. Both demand parameters are overestimated by the analytical model by about

25% at the base. One reason for the difference may be the assumption regarding the effect of dynamic axial load on deterioration parameters of the exterior tubular HSS columns since the dynamic axial load was assumed to be constant during the entire history. Another reason for differences between the measured and calculated story shear forces and overturning moments may be that the component strength deterioration is larger in the analytical model than the actual component deterioration.

8.5.5.2 Collapse Level (100% Takatori Motion)

When the structure was subjected to the 100% of the Takatori unscaled motion it collapsed 6.24sec after the motion started (Suita et al. (2007, 2008)). The time based on the analytical prediction is 6.45sec. Based on test observations the structure had very little nonstructural damage prior to collapse. When the structure collapsed the ACC panels spalled significantly and failure was noted around the attachment. The motion was mostly in the NS direction and the biaxial effect was not significant. The structure collapsed with a first story mechanism that became clear late during the test. The collapse mechanism of the structure can be seen in Figure 8.23, which shows the structure resting on the impact frame support (“catching” mechanism) at about 20% first story drift. Plastic hinges formed at top and bottom of first story columns. Figure 8.24 illustrates severe buckling at the bottom of the exterior column at the base after the completion of the collapse test. Based on test observations local buckling was clearly visible around 2% story drift.

Analytical prediction of the first story drift are shown in Figure 8.25 and the predicted base shear versus first story drift angle response is presented in Figure 8.26 Unfortunately at this time there are no detailed data available on the experimental response during the 100% Takatori motion. Thus, no comparison can be made with the predictions shown in Figures 8.25 and 8.26.

8.6 Collapse Assessment of Low-rise Buildings with Low Ductility

This section is concerned with the quantification of the collapse potential of low-rise buildings constructed in highly seismic areas (e.g. Istanbul). Many of the vulnerable buildings have relatively poorly constructed concrete framing, which in part or fully is infilled with hollow clay or solid bricks. Configurations are often irregular, and the quality of construction is very variable. In many cases it is not clear how inertia forces find their way to the RC framing and how the wall forces and moments are transferred into the soil. These are additional complications, but the basic concept remains that in most practical cases the infilled frames are the primary lateral load resisting elements that have to transfer lateral loads into the soil.

A basic challenge is to assess the strength and deformation capacity of these walls and to assess the collapse potential of buildings, given that the cyclic response characteristics of the lateral load resisting system are known. The following discussion is a summary of information presented in Krawinkler and Lignos (2008).

8.6.1 Experimental Observations – Frames with Infill Walls

Many cyclic experiments have been reported in the literature on reinforced concrete frames with infill masonry, using either hollow clay brick or solid brick without and with retrofit techniques (reinforced concrete, solid or banded FRPs, and more recently sprayed on ECCs), e.g., (Mehrabi et al. 1994, 1996), (Karadogan 1998), (Wasti and Azcebe 2006), (Kyriakides and Billington 2008). Almost all tests are in-plane, with load applied directly to the RC floor beams by means of actuators, and with the framing fixed to a rigid foundation. For the time being it is assumed that such configurations represent actual buildings, i.e., the load-story drift responses of the test specimens do indeed represent the cyclic behavior of low-rise buildings.

An evaluation of the cyclic load–story drift (story displacement over story height) relationships of many of these experiments resulted in the following general observations:

- Frames with infill walls are not brittle (except if the surrounding frame fails early in a brittle mode), i.e., the frame provides good confinement for the infill (conditioned that out-of-plane action is not important)
- Yield strength and elastic stiffness are ambiguous quantities that can only be estimated with judgment
- Envelopes of the cyclic response curves indicate that “yielding” is followed by strain hardening, a subsequent drop in strength, and strength stabilization at some residual value.
- Unfortunately, most tests stopped way short of full loss of strength, which means that little information exists on the actual ultimate drift at which the strength drops to a negligible value. But a drop of strength to very small values is rarely observed at story drifts of less than about 2%.

Support for these observations can be found in Kyriakides and Billington (2008) and Mehrabi et al. (2004). Several calibrations were performed of the cyclic response of test specimen responses, utilizing the parameters of the modified Ibarra-Krawinkler model. A typical example is shown in Figure 8.27 using the peak-oriented hysteretic model. The information shown here, and data from many other in-plane experiments have been used to define a range of structural parameters that is believed to be representative of the response characteristics of infill wall structures.

8.6.2 Parameter Study Employing Deteriorating SDOF Systems

A parameter study was performed to assess the collapse potential of infill wall structural systems in order to provide preliminary information on the probability of collapse of infill wall systems and on the effectiveness of retrofit techniques in reducing this probability.

Only SDOF systems are used for this purpose; the assumption being that the primary concern is with low-rise construction in which higher mode effects are not very important and equivalent SDOF system can be used to represent dynamic behavior (this assumption eliminates structures with soft (weak) stories from consideration).

8.6.3 Parameters of Structural Models

Two central cases were created, a “low ductility” central case and a “high ductility” central case as shown in Figure 8.28. The central case parameters are circled and the variations around the central case values are partially illustrated in Fig. 8.28. The fundamental differences between “low” and “high” ductility are the rotation capacity at capping point θ_c ($\theta_c = \theta_y + \theta_p$) and θ_{pc} values, which are doubled from low to high ductility. A strength variation ($n_y = V_y/W$, in which V_y is the yield base shear and W is the total weight of the low rise structure) implies that the backbone curve is stretched in the vertical direction as illustrated in Figure 8.29 (dashed lines); it does not affect the deformation parameters. Somewhat arbitrary (because of the lack of information), but conceptually necessary, limits on the ultimate story drifts are set at 0.03 for the “low ductility” case and 0.04 for the “high ductility” case. In all cases the cyclic deterioration parameter λ was set at a constant value of 100 (based on calibrations of experimental results, and in order to eliminate one of the less important parameter variations based on Ibarra and Krawinkler (2005)). To assess the effect of residual strength, three cases were investigated; $\kappa = 0$ (no residual strength), $\kappa = 0.5$, and horizontal post-capping slope until θ_u is attained (i.e., $\theta_{pc} = \infty$).

8.6.4 Response – Examples

The importance of postulating an ultimate drift capacity, θ_u , is illustrated in Figure 8.30 for the “high ductility” central case with no post-capping stiffness deterioration. This case is an unlikely one, but it illustrates that the collapse capacity can be strongly affected by the existence of an ultimate drift capacity beyond which no reliance can be placed on the

resistance of the structural system. The figure shows IDA curves based on the assumption that no drift limit exists. Sooner or later (in the illustrated case around 7% drift) collapse will occur one way or another because of cyclic deterioration and P- Δ effect. But the ground motion intensity at which collapse occurs may depend strongly on the ultimate drift capacity, θ_u . If this capacity is only 3% (first vertical line), then the collapse capacity of the structural system is only about $2/3^{\text{rd}}$ of that without a drift limit.

8.6.5 Collapse Fragility Curves

The bases for collapse assessment are the fragility curves derived from the response history analyses using the set of 40 ground motions discussed in Section 8.1. Typical collapse fragility curves obtained from the parameter study are presented in Figure 8.31 for the low and high ductility central cases with 50% residual strength and the three values of base shear yield strength η_y . Given that the mathematical model is correct and deterministic (as has been assumed so far) and that the ground motion frequency characteristics are representative for the site conditions for which the evaluation is done, the probability of collapse, as a function of base shear yield strength, can be read directly from these curves for a given value of spectral acceleration.

Postulating that the design spectral acceleration (at a 10/50 hazard level) for short period structures is about 1.0g, it becomes evident that the collapse probability is high unless the base shear strength is very large. In concept this is not a surprise for short period structures since in the short period range the inelastic drift demand is known to be much larger than the elastic drift demand. But the quantification of this well known phenomenon in terms of the collapse probability is striking. For the low ductility central case the probability of collapse decreases from about 95% to about 8% by increasing the base shear yield strength from $0.15W$ to $0.45W$, and for the high ductility case it decreases from about 80% to 3%. From the same figures it is observed that a change of strength from $0.15W$ to $0.45W$ (factor of three) results in about the same change in median collapse capacity of the infill wall.

This shows that for short period structures the effect of yield strength is larger than the effect of ductility.

The intrinsic value of fragility curves is that they provide a perspective of the collapse probability for all values of spectral acceleration. Moreover, they can be utilized to assess the mean annual frequency (MAF) of collapse by integrating the fragility curve over the spectral acceleration hazard curve for a particular site. This exercise was performed using a typical short period hazard curve for the Los Angeles area, resulting in the following information:

For the high ductility cases the MAF of collapse is 0.0022, 0.00066, and 0.00014 for $n_y = 0.15, 0.30, \text{ and } 0.45$, respectively. For the low ductility cases the corresponding values are 0.0047, 0.00125, and 0.00027, i.e., about twice as large as for the high ductility cases. These numbers show that for these short period structures strength is a much more relevant parameter than ductility.

The hazard specific collapse probability and the MAF of collapse depend on aleatory and epistemic uncertainties. Most of the aleatory uncertainty comes from the record-to-record variability, which is accounted for in the fragility curves shown in Figure 8.31 and is expressed by the β value (standard deviation of the log of the data) shown in the two graphs. The general observation is that the β value for aleatory uncertainties is on the order of 0.40 for all the cases investigated.

8.6.6 Evaluation of Median (and 10-percentile) Collapse Capacity

The variations of collapse capacity of infill wall systems with various system parameters are illustrated in Figures 8.32 and 8.33. In these figures a dotted horizontal line is drawn at $S_a(T_1)/g = 1.0$ in order to provide a perspective with respect to design spectral acceleration

demands. From the presented graphs, and others not shown here, the following general observations can be made:

- Figure 8.32(a), which shows the effect of residual strength (κ) on median collapse capacity of low ductility systems for three different strength values, indicates that κ has some effect on the median collapse capacity but this effect is considerable only if the base shear yield strength (n_y) is large. The residual strength effect is not large because of the necessary assumption that the drift capacity is limited (to a value of $\theta_u = 0.03$ for low ductility systems). If future experiments will show that the drift capacity is larger, more benefit can be given to the residual strength effect. The data for $\kappa = 1.0$ are given for reference but cannot be considered as realistic because a horizontal post-capping slope in the backbone curve is only wishful thinking.
- Figure 8.32(b) shows the effect of yield strength (n_y) on median collapse capacities of low ductility wall systems for three different values of residual strength (κ). The figure indicates that yield strength has by far the largest effect on the median collapse capacity. Since a 50% probability of collapse at the design level should be unacceptable, the conclusion is that the provided base shear yield strength should be larger than $0.30W$, even if a 50% residual strength can be assured (the $\kappa = 1.0$ line is only for reference).
- Figures 8.33(a) and 8.33(b) present median and 10-percentile collapse capacities for low and high ductility systems, in a similar format as Figure 8.32. As seen from Figure 8.33(a), which shows the effect of residual strength on median collapse capacity of wall systems, it is concluded that κ does not affect by much the median collapse capacity (except for $\kappa = 1.0$), and does not vary by much between low and high ductility systems, as seen from the same figure.
- Figure 8.33(b) illustrates the dominant effect of base shear yield strength. The differences between low and high ductility are not very large, indicating that for these short period systems ductility considerations are not dominant (this does not imply that no attention needs to be placed to ductility, as some ductility is necessary in all cases). The figure also shows that an effective base shear yield strength of about $0.45W$ needs to

be provided (together with 50% residual strength) if the probability of collapse in a design event ($S_a = 1g$) is to be held below 10%.

8.7 Collapse Assessment of Autoclaved Aerated Concrete Block Masonry Units

AAC is a lightweight cementitious material with a closed cellular structure, made of cement, sand, lime, water, and possibly other materials such as fly ash. After initial curing, it is cured in an autoclave (Tanner, 2003). Compared to other (clay and concrete) masonry units, is of low density and low strength. It can be used to construct walls and floor systems, and possibly also for columns and beams. AAC is being used in many countries as a building material for single family and multi-unit residences and other buildings. Typical material properties for AAC can be found from Valera (2003). The following discussion is based on research by Krawinkler et al. (2005) as part of the ATC-63 project.

Two case study structures were developed in order to predict collapse fragility curves for representative AAC structures. The case study structures are based on an experimental program that was conducted at the University of Texas at Austin (Brightman, (2000), Tanner et al. (2005)). In this case study emphasis is on wall specimens 15a and 15b in terms of experimental data and on the 2-story assemblage specimen (see Figures 8.34(a) and 8.34(b)). These specimens were selected because they were described as having failed in a flexural mode. Most of the other specimens did fail in shear. Dimensions, reinforcement, and axial loads are summarized in Tanner, (2003). Based on the same study by Tanner the concrete strength of AAC is $f'_{AAC} = 1140$ psi, the modulus of elasticity $E = 462$ ksi and the yield strength of reinforcement $f_y = 75$ ksi. Properties of the two case studies are summarized in Table 8.9.

8.7.1 Calibration of Moment-Rotation Relationship for Specimens 15a and 15b (Case 1)

A comparison of measured and predicted (from the calibration) base shear– drift relationships for Specimens 15a and 15b is shown in Figure 8.35. It is noted that the test of Specimen 15a was terminated before severe deterioration was evident, and that the reliability of the largest cycle of the Specimen 15b test is of some debate since a large increase in displacement amplitude was used from cycle to cycle in the loading protocol, which typically is not the case in a standard symmetric loading protocol. For this reason two models were developed, one exhibiting very slow post-capping deterioration and called the optimist’s model in which $\theta_{pc} = 10\theta_p$ and the other exhibiting very rapid post-capping deterioration and called the pessimist’s model in which $\theta_{pc} = 0.5\theta_p$. Relevant calibration parameters are shown on the same graphs. It is important to point out that the same model parameters are used for both Specimens 15a and 15b, i.e., the objective was to find model parameters that fit both tests, which is always a compromise. Considering this constraint, it is noteworthy that the model fits both tests rather accurately, with the exception of the pessimist’s model for Specimen 15b.

The calibrations indicate a rather large ductility “capacity”, but this may not be very relevant because this perception is based on a very large elastic stiffness. The plastic rotation capacity at the plastic hinge location (base of structure) is only 0.0058.

In specimen 15b the last cycle (with amplitude of about 1.4”) is not reproduced in the model with rapid deterioration. First, it is not in line with expected behavior from specimen 15a, and second, it possibly is affected by the inability of the gravity load maintainers to maintain a constant axial force of 25 kips (see specimen 16 in Tanner, 2003). Thus, the model with rapid deterioration constitutes a model with low “toughness”. The model with slow post-capping deterioration can reproduce the large displacement cycle. It constitutes a model with high “toughness”. Based on experimental data from Tanner, (2003) the assumed

base shear for case 1 is 1.06, the natural periods for case study 1 are $T_1 = 0.135\text{sec}$ and $T_2 = 0.03\text{sec}$ and the mass participation factors are $M_1 = 0.83$ and $M_2 = 0.17$. The values are based on the calibrated values of stiffness from Figure 8.35a.

8.7.2 Calibration of Moment-Rotation Relationship for Assemblage Specimen (Case 2)

A comparison of measured and predicted (from the calibration) base shear– drift relationships for the Assemblage Specimen is shown in Figure 8.36. Also here two models are developed, the optimist’s model in which $\theta_{pc} = 10\theta_p$, and the pessimist’s model in which $\theta_{pc} = 0.5\theta_p$, even though in this case reality (the severe vertical cracking in wall flanges and web) clearly supports the pessimist’s perspective.

For this case, the data indicate no strain hardening and more rapid deterioration than in Case 1. The ductility “capacity” is even larger than in Case 1, and the plastic rotation capacity is somewhat larger than in Case 1 ($\theta_p = 0.0075$ versus 0.00584). In part, this plastic rotation capacity does not completely represent reality because the assemblage was modeled only by flexural elements, i.e., the large sliding at the base is included in the plastic hinge rotation. Using the calibrated values of elastic stiffness from Figure 8.36, the dynamic properties for case study 2 are $T_1 = 0.12\text{sec}$ and $T_2 = 0.026\text{sec}$ and the mass participation factors are $M_1 = 0.80$ and $M_2 = 0.20$. The assumed base shear coefficient for case study 2 is 1.12.

8.7.3 Ground Motions and its Scaling

The latest version of the ATC-63 set of 44 non-near fault ground motions (Set C) was used for this purpose. Two “scaling” methods for the set of ground motions are considered in the IDA analysis. One is the standard ATC-63 scaling method (scale factors by Haselton and Deierlein (2006)). The other scaling method focuses on the short period range and scales all records to a common S_a value at the period of 0.2 sec.

8.7.4 IDA Curves to Collapse

The results of the incremental dynamic analyses are shown in Figures 8.37 and 8.37 for both cases and for the optimist's and pessimist's model. In all four plots the intensity measure on vertical axis is the spectral acceleration at 0.2 sec., $S_a(0.2)$. This is merely a reference IM, which for each ground motion can easily be converted to other intensity measures (such as the ATC-63 spectral value at 1.0 sec.) by a simple transformation. It is noted that most IDA curves are close to bilinear, i.e., they show a long elastic range (relationship between roof drift and ground motion intensity is linear) and then bend over and approach dynamic instability rather rapidly. This is not uncommon for short period structural systems.

8.7.5 Collapse Fragility Curves for Base Cases

The collapse fragility curves obtained from the IDA curves are shown in Figures 8.39 and 8.40. Each one of the figures shows the collapse fragility curves for the optimist's and the pessimist's model and the base case structural properties as defined before ($\gamma = 1.06$ and 1.12 for cases 1 and 2, respectively). The first two figures use the $S_a(1.0)$ (ATC-63 scaling) as the intensity measure, and the last two figures use $S_a(0.2)$ as the intensity scale. The following observations are made from these figures given that yield base shear coefficient $\gamma = V_y/W$ is larger than 1.0 in all cases and the "code based" MCE level is 0.68.

- The optimist fares only slightly better than the pessimist, particularly in the lower portion of the fragility curves.
- The fragility curves for the two cases are rather similar even though they are based on two very different test specimens.
- For direct comparison of the fragility curves for ATC-63 scaling and $S_a(0.2)$ scaling the IM values of Figure 8.39 should be multiplied by about 2.2. Once this is done, it

becomes evident that the scaling method has relatively little effect on the median collapse intensity.

- The large median values give the perception that there is large collapse safety. But this may be misleading because both test cases have a yield base shear coefficient larger than 1.0 (1.06 and 1.12 for Cases 1 and 2, respectively).
- On the optimist's side it should be noted that the ratio of S_{as}/S_{a1} for the selected records is about 2.22, which is much larger than the design spectral ratio of 1.67. It can be argued that the values on the IM axis should be increased by the ratio $2.22/1.67 = 1.33$.
- The dispersion is on the order of 0.4 for the ATC-63 scaling and 0.25 for the Sa(0.2) scaling. The latter dispersion is rather small and is attributed to the common spectral acceleration scaling at 0.2 sec. period and the fact that the inelastic response of short period structures is not very sensitive to the value of $S_a(T_1)/(\gamma \cdot g)$ once the system has yielded.

8.8 Collapse Assessment of an Reinforced Adobe Wall with Polymer Mesh

This section is concerned with the quantification of probability of collapse of an adobe wall reinforced with polymer mesh, an emerging technique to improve the seismic behavior of simple adobe walls that historically behave very poorly in earthquakes. Poor masonry, low wall density, poor foundation or wall base, heavy roof are some of the reasons that lead to collapse of adobe structures based on previous studies by Torrealva, (2003) and Maheri, (2005) . The experimental data used in this case study are based on tests conducted in 2007 at the Pontificate Catholic University of Peru (PUCP). For more information regarding the experimental data see Hulburd, (2008)).

8.8.1 Seismic Characteristics of a Representative Adobe Dwelling

In order to estimate the lateral load resistance of a representative adobe house an idealized dwelling was created in which the shear wall was assigned the properties obtained from the tests of the reinforced wall specimen D1 (see Hulburd, 2008). Figure 8.41 shows the calibrated load-story drift response of specimen D1. A peak-oriented hysteretic response has been used and the modified Ibarra-Krawinkler model has been utilized.

Figure 8.42 shows an isometric view of the idealized adobe dwelling. All wall thicknesses are assumed to be 0.50m. The main concern is modeling the central transverse wall and its tributary area, because it is reasonably well represented by the wall specimen tested at PUCP. Assuming an adobe density of 1700 kg/m^3 and that the roof's weight comes mostly from a 0.30m thick mud covering, the total weight tributary to the central shear wall is about 320 kN. Based on experimental data the maximum shear stress is 47.6 kPa (6.9 psi) in the unreinforced wall and 95.8kPa (13.9 psi) in the reinforced wall. Using the wall dimensions shown in Figure 8.42 and the wall shear strength data the base shear “yield” coefficient of the reinforced and unreinforced cases is 0.70 and 0.37, respectively.

8.8.2 Collapse Fragility Curve for the Dwelling with Reinforced Walls

Figure 8.43 shows IDAs obtained by subjecting the analytical model of the reinforced case of the structure to the set of 40 ground motions discussed in Section 8.1. From this figure the median collapse capacity of the reinforced adobe wall is 2.9g.

Figure 8.44 shows the collapse fragility curve for the dwelling with reinforced walls assuming a log-normal cumulative distribution function fitted to the data points. To put the values of the fragility curve shown in Figure 8.44 into perspective with actual earthquake hazards, a value S_a of 1.5g is a good estimate for the maximum considered earthquake ground motion in California and Peru.

From the fragility curve presented in Figure 8.44 it can be seen that the probability of collapse at a ground motion intensity $S_a = 1.5g$ is only about 0.05. This is indeed a low probability of collapse, which is comparable to the tolerable probability of collapse for which modern buildings in California are designed. This demonstrates that reinforcement of adobe walls with polymer mesh is very effective in protecting adobe housing from collapse, provided that other collapse modes, such as out-of-plane failures and roof collapse are also prevented.

In contrast, if no wall reinforcement is provided, the representative adobe dwelling would have a base shear strength coefficient of 0.37 and very little, if any, inelastic deformation capacity. In such a case the probability of collapse at a spectral acceleration of 0.37g is very high (as compared to the low probability of collapse at $S_a = 1.5g$ for the reinforced dwelling). Unfortunately, a spectral acceleration of 0.37g can be expected in moderate earthquakes with a return period on the order of 100 years.

8.9 Summary and Conclusions

In this chapter an array of application studies were discussed in which the approach to collapse prediction that takes advantage of knowledge gained from previous chapters of this research was exercised. Three frame structures that were designed based on current US (prototype 4-story office building discussed in Chapter 5) and Japanese seismic provisions (15-story model A designed by Kajima corporations and E-Defense 4-story building) and a number of other case study structures related to dynamic behavior of infill walls and reinforced adobe walls were analyzed. A case study related to the collapse assessment of Autoclaved Aerated Concrete (AAC) block masonry units was also summarized.

Using the 4-story prototype moment resisting frame and experimental results from Chapters 6 and 7 concerned with a 1:8 scale model of the same prototype frame, the significance of deterioration parameters on collapse capacity of the prototype frame was demonstrated using the testing sequence from the shaking table collapse tests at Buffalo for Frame #1 discussed in Chapter 7. The effect of the differences between the deterioration model parameters for the test frame and the prototype structure was assessed and quantified. The conclusion is that the scale model frame is not the most accurate representation of the prototype frame, but the model served its intended purpose of providing a comprehensive set of data of a shaking table experiment that subsequently was used to validate analytical response predictions.

Based on the collapse assessment of the 15-story moment resisting frame designed by Kajima corporations and the 4-story prototype building that was described in Chapter 5 it was shown that global collapse of these frames is not overly sensitive to the ultimate deformation capacity θ_u and residual strength ratio values κ

The approach to collapse prediction was demonstrated on the recently conducted shaking table collapse experiment of a 4-story building at the E-Defense shaking table. Analytical simulations of a two dimensional model of one of the two moment resisting frames of the 4-story building and comparisons with experimental results showed that the predicted response in terms of maximum story shear forces and overturning moments is underestimated by about 25%, indicating that the assumed component strength and deterioration parameters do not accurately represent the actual ones particularly near collapse.

Based on a parametric study of the deterioration parameters of non-ductile structural systems consisting of frames with infill walls it was shown that the base shear strength (n_y) controls the collapse capacity of this type of short period structural systems, since an increase in n_y by a factor of three causes an equal increase in the median collapse capacity

regardless the assumed residual strength (κ). Doubling the ductility capacity of the infill wall does not increase the median collapse capacity by more than 25%. Residual strength increases the collapse capacity of infill walls somewhat (an increase of 20% of the median collapse capacity is attained with an increase of κ from 0.0 to 0.50) but it is not a dominant factor because second order effects and ultimate drift capacity will dominate once the drift demand exceeds the capping value.

Collapse assessment of a representative adobe dwelling with walls reinforced with polymer mesh based on available experimental data from cyclic tests indicated that such polymer mesh reinforcement can be very effective in reducing the collapse potential of adobe houses. If applied properly and if collapse modes related with out-of-plane failures and roof collapse are prevented, such reinforcement may reduce the probability of collapse of adobe houses to a level commensurate with that expected from designs performed according to modern codes.

Table 8.1. Beam and column sections (Model A, units are in mm)

Beam (SM490)			Column (SM490)		
Floor	G1	G2	Story	C1	C2
R	H-700x200x9x19	H-700x200x9x19	15	RHS-525x11	RHS-525x16
15	H-700x200x9x19	H-700x200x9x19	14	RHS-525x11	RHS-525x16
14	H-700x200x9x19	H-700x200x9x19	13	RHS-525x11	RHS-525x16
13	H-700x200x9x19	H-700x200x9x19	12	RHS-525x11	RHS-525x16
12	H-700x200x9x19	H-700x200x9x19	11	RHS-525x16	RHS-525x22
11	H-700x200x9x19	H-700x200x9x19	10	RHS-525x16	RHS-525x22
10	H-700x200x9x19	H-700x200x9x19	9	RHS-525x16	RHS-525x22
9	H-700x200x9x19	H-700x200x9x19	8	RHS-525x16	RHS-525x22
8	H-700x250x9x19	H-700x250x9x25	7	RHS-525x16	RHS-525x22
7	H-700x250x9x19	H-700x250x9x25	6	RHS-525x16	RHS-525x22
6	H-700x250x9x19	H-700x250x9x25	5	RHS-525x22	RHS-525x25
5	H-700x250x9x19	H-700x250x9x25	4	RHS-525x22	RHS-525x25
4	H-700x250x9x25	H-700x250x9x25	3	RHS-525x22	RHS-525x25
3	H-700x250x9x25	H-700x250x9x25	2	RHS-525x22	RHS-525x25
2	H-700x250x9x25	H-700x250x9x25	1	RHS-525x22	RHS-525x25

Table 8.2. Weights per floor for Model A

Floor	Total weight assigned per floor of the frame (kN)
R	1700
15	1135
14	1135
13	1135
12	1135
11	1135
10	1135
9	1135
8	1135
7	1135
6	1135
5	1135
4	1135
3	1135
2	1135

Table 8.3. Deterioration parameters for tubular sections of Model A including the effect of dynamic axial load in addition to gravity load

Column:	M_c/M_y	$\theta_{p,C1}$	$\theta_{p,C2}$	$\theta_{pc,B1}$	$\theta_{pc,B2}$	A_{C1}	A_{C2}	κ
15	1.1	0.011	0.016	0.148	0.208	0.21	0.54	0.3
14	1.1	0.011	0.015	0.132	0.185	0.19	0.49	0.3
13	1.1	0.012	0.015	0.118	0.165	0.17	0.44	0.3
12	1.1	0.011	0.014	0.105	0.147	0.15	0.4	0.3
11	1.1	0.015	0.02	0.156	0.215	0.42	0.92	0.3
10	1.1	0.014	0.02	0.143	0.198	0.39	0.85	0.3
9	1.1	0.014	0.019	0.132	0.182	0.36	0.79	0.3
8	1.1	0.014	0.019	0.121	0.167	0.33	0.73	0.3
7	1.1	0.013	0.018	0.111	0.154	0.31	0.67	0.3
6	1.1	0.013	0.018	0.102	0.141	0.28	0.62	0.3
5	1.1	0.018	0.02	0.146	0.164	0.64	0.82	0.3
4	1.1	0.014	0.019	0.082	0.152	0.34	0.76	0.3
3	1.1	0.013	0.019	0.064	0.141	0.25	0.7	0.3
2	1.1	0.011	0.013	0.048	0.054	0.17	0.22	0.3
1	1.1	0.009	0.011	0.036	0.04	0.11	0.14	0.3

Table 8.4. Deterioration parameters for steel beams of Model A

Beam at Floor	M_c/M_y	$\theta_{p,Beam}$	$\theta_{pc,Beam}$	A
15	1.05	0.023	0.125	0.62
14	1.05	0.023	0.125	0.62
13	1.05	0.023	0.125	0.62
12	1.05	0.023	0.125	0.62
11	1.05	0.023	0.125	0.62
10	1.05	0.023	0.125	0.62
9	1.05	0.023	0.125	0.62
8	1.05	0.023	0.125	0.62
7	1.05	0.023	0.129	0.64
6	1.05	0.023	0.129	0.64
5	1.05	0.023	0.129	0.64
4	1.05	0.023	0.129	0.64
3	1.05	0.023	0.129	0.64
2	1.05	0.023	0.129	0.64
1	1.05	0.023	0.129	0.64

Table 8.5. Section members for E-Defense 4-story structure (units in mm)

Beam (SN400B)				Column (BCR295)	
Floor	G1	G11	G12	Story	C1, C2
R	H-346x174x6x9	H-346x174x6x9	H-346x174x6x9	4	RHS-300x9
4	H-350x175x7x11	H-350x175x7x11	H-340x175x9x14	3	RHS-300x9
3	H-396x199x7x11	H-400x200x8x13	H-400x200x8x13	2	RHS-300x9
2	H-400x200x8x13	H-400x200x8x13	H-390x200x10x16	1	RHS-300x9

Table 8.6. Seismic weight per floor for E-Defense 4-story moment resisting frames

Floor	Total weight assigned per floor of the frame (kN)
R	339.75
4	262.25
3	260.50
2	262.75

Table 8.7. Deterioration properties for beams of E-Defense 4-story frame

Floor Beam Location	θ_p^+	θ_p^-	θ_{pc}	λ	κ
Roof interior joint	0.03	0.015	0.25	1.00	0.40
Roof exterior joint	0.03	0.03	0.25	1.00	0.00
4 interior joint	0.03	0.015	0.25	1.00	0.40
4 exterior joint	0.03	0.03	0.25	1.00	0.00
3 interior joint	0.03	0.015	0.25	1.00	0.40
3 exterior joint	0.03	0.03	0.25	1.00	0.00
2 interior joint	0.03	0.015	0.25	1.00	0.40
2 exterior joint	0.03	0.03	0.25	1.00	0.00

Table 8.8. Deterioration properties for columns using 45 degrees configurations

Story	θ_p^+	θ_p^-	θ_{pc}	λ	κ
4 exterior	0.0105	0.011	0.18	0.60	0.40
4 interior	0.0105	0.011	0.18	0.60	0.40
3 exterior	0.0105	0.011	0.18	0.60	0.40
3 interior	0.0070	0.007	0.18	0.40	0.40
2 exterior	0.0053	0.005	0.14	0.60	0.30
2 Interior	0.0035	0.004	0.12	0.40	0.40
1 exterior	0.0053	0.005	0.14	0.60	0.30
1 Interior	0.0035	0.004	0.12	0.40	0.40

Table 8.9. Basic parameters for cases 1 and 2 (AAC)

Case	Thickness t (in)	Length L (in)	Story height (in)	Gravity W (kips)	Base Shear V_y (kips)*	Base shear coeff. γ
1	10	112	92.4	12.5	26.5	1.06
2	10	250	96	60.4	136	1.12

*The gravity load is assumed to be lumped and are the same at both floor levels of structure

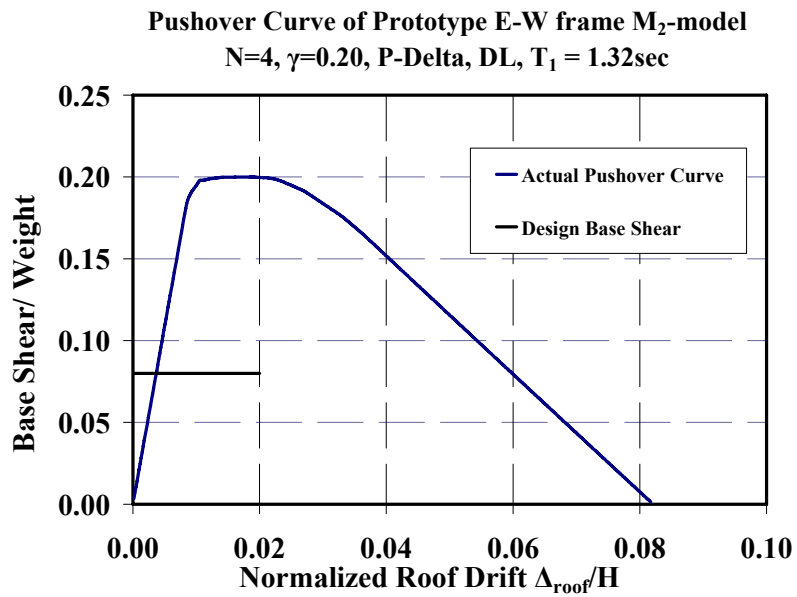


Figure 8.1. Pushover curve for EW perimeter 4-story moment resisting frame

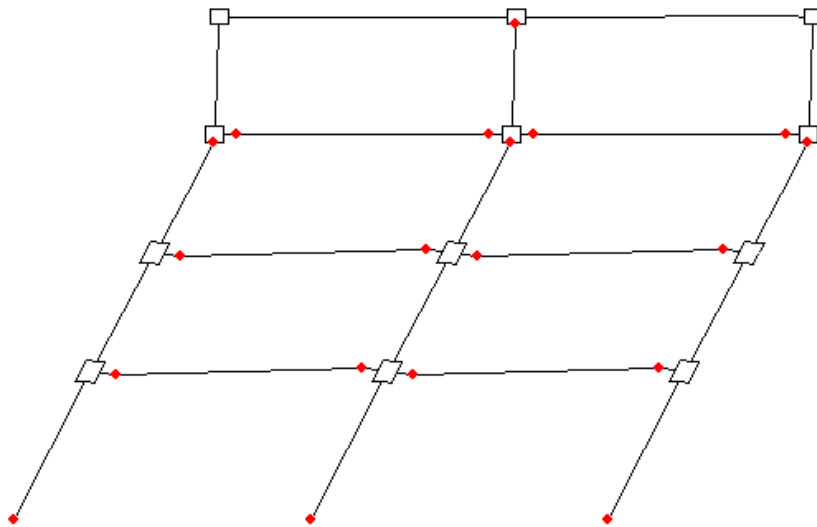


Figure 8.2. Collapse mechanism for EW perimeter 4-story moment resisting frame based on static pushover analysis at 8% roof drift

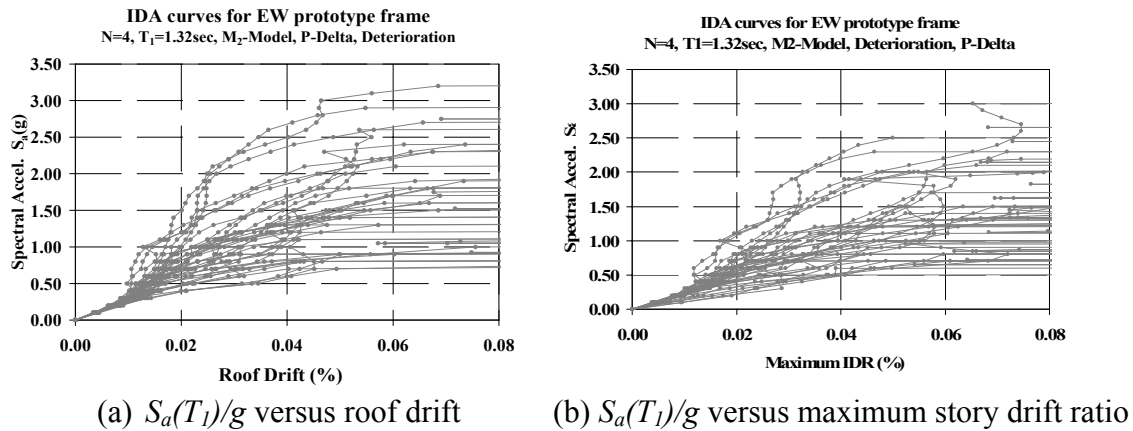


Figure 8.3. IDA plots for the EW 4-story moment resisting frame of the prototype building using a set of 40 ground motions

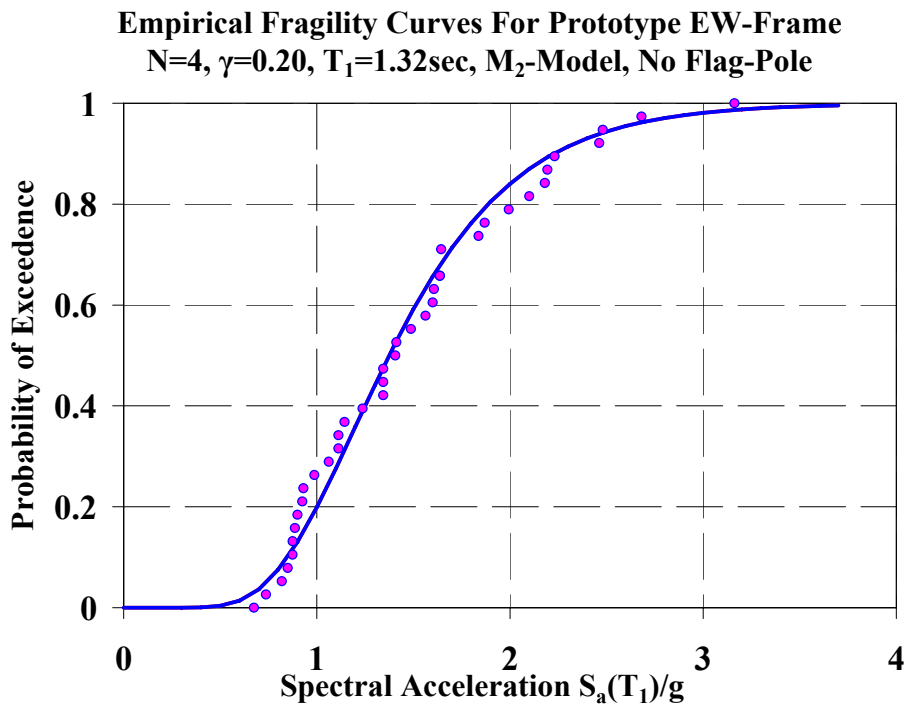


Figure 8.4. Fragility curve for the EW 4-story moment resisting frame of the prototype building using the set of 40 ground motions

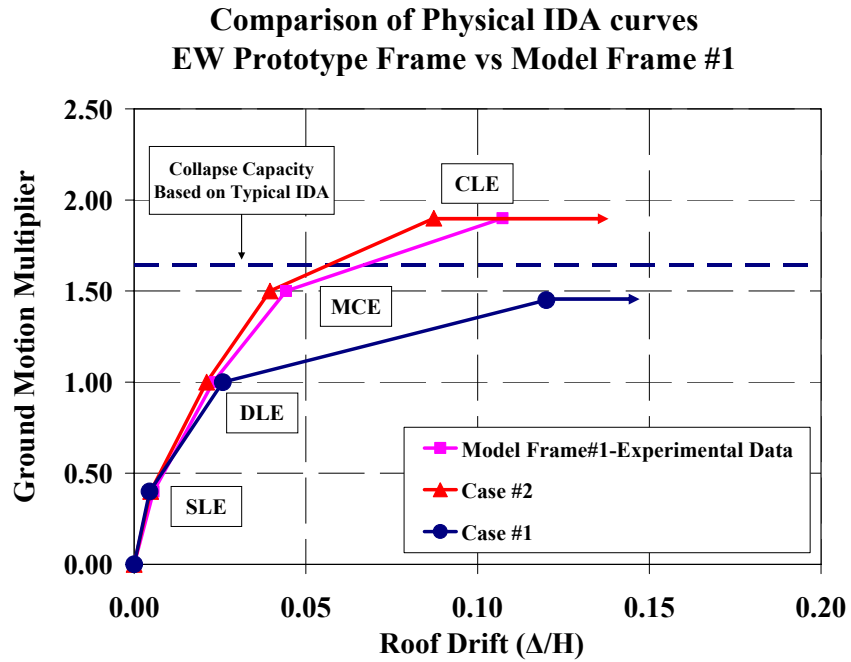


Figure 8.5. Comparison between “IDA” curves of EW 4-story moment resisting frame of the prototype building and model Frame #1 using the Canoga Park record

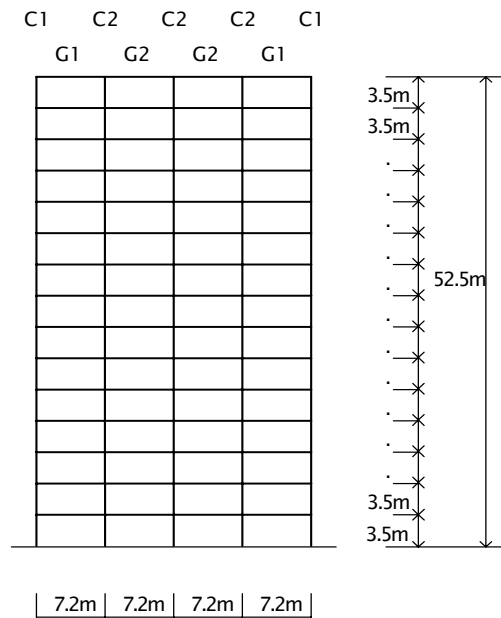


Figure 8.6. Kajima building Model A, basic dimensions

Model Building A: Pushover Curve
 $T_1=1.99\text{sec}$, $\zeta=2\%$, $N=15$, $\gamma=0.24$, P-Delta, M_2 -Model

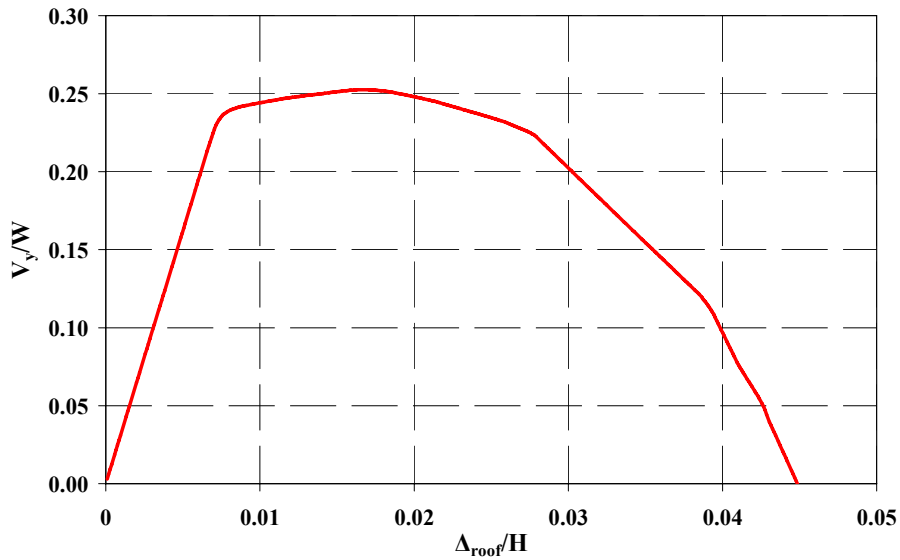


Figure 8.7. Pushover curve for 15- story Japanese building Model A

IDA curves for Japanese Building Model A
 $N=15$, $T_1=1.99\text{sec}$, M_2 -Model, P-Delta, Deterioration

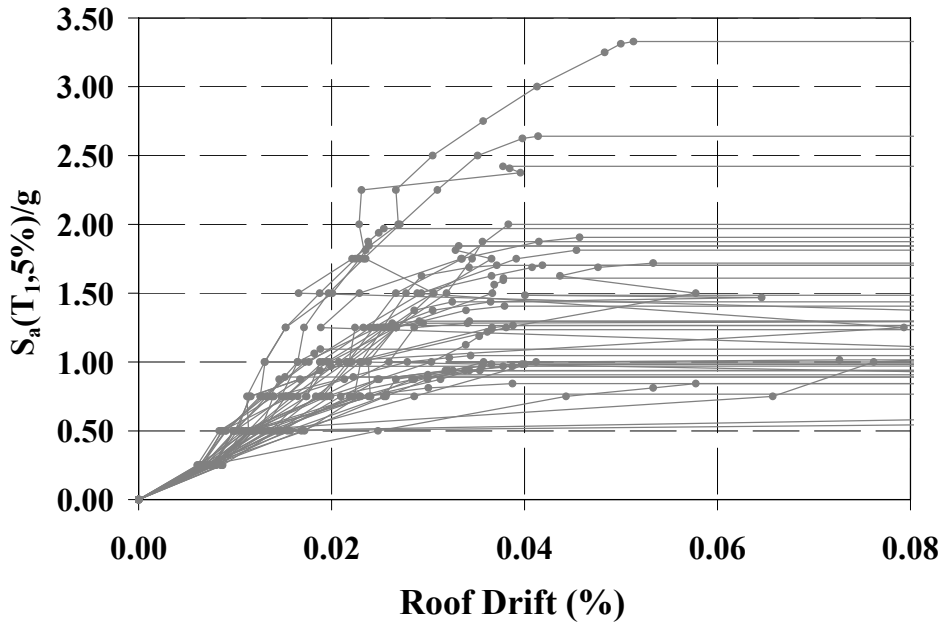


Figure 8.8. IDA plots for Model A for the set of 40 ground motions

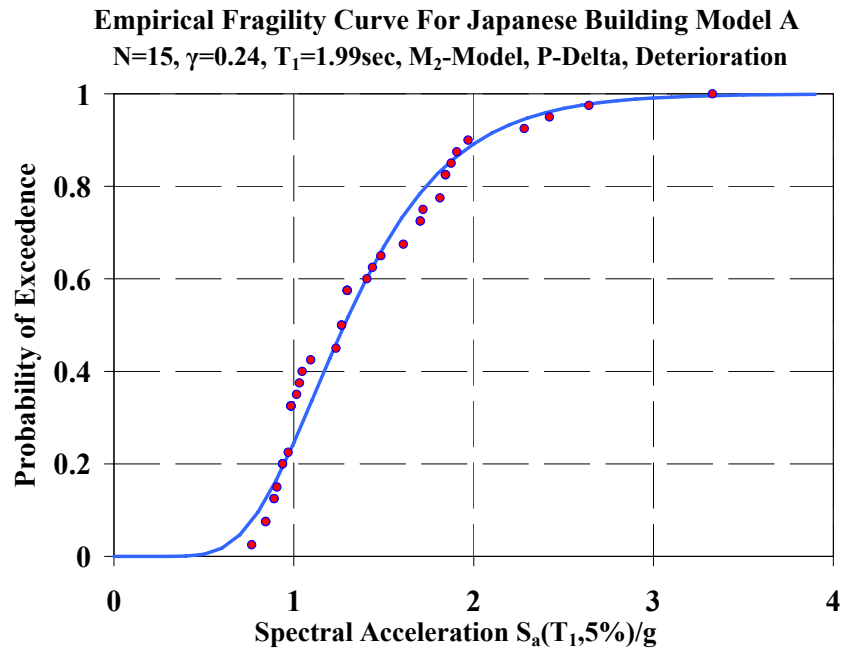


Figure 8.9. Collapse fragility function of Model A based on the set of 40 ground motions

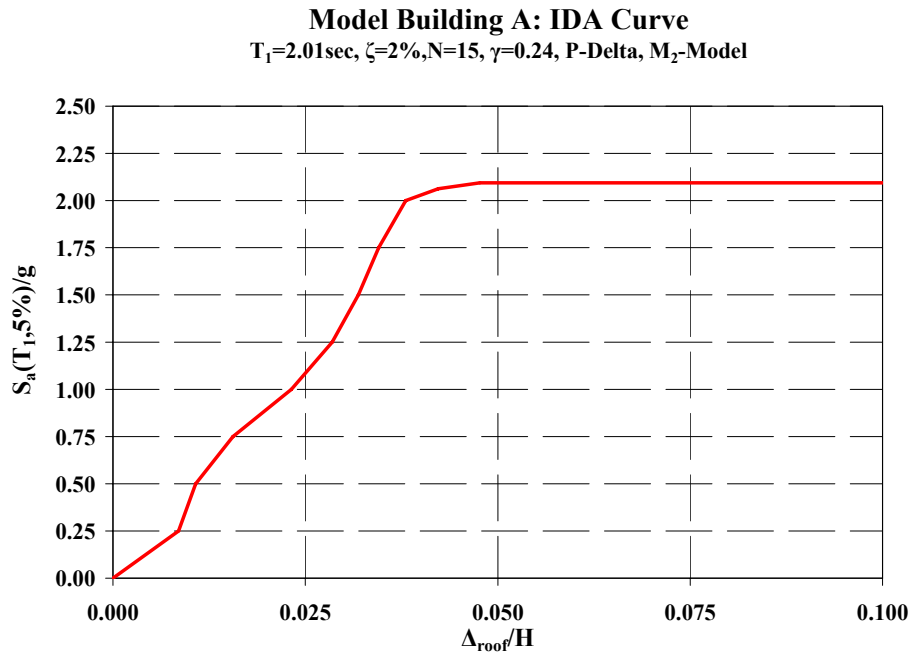


Figure 8.10. IDA plot for Model A using Canoga Park record

Model Building A: Interstory Drifts Over The Height

$T_1=1.99\text{sec}$, $\zeta=2\%$, $N=15$, $\gamma=0.24$, P-Delta, M_2 -Model

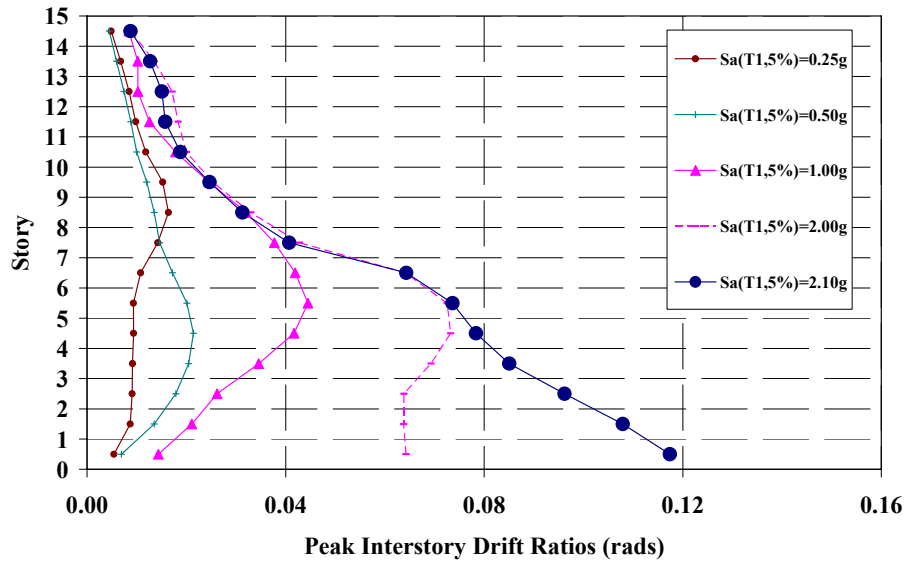


Figure 8.11. Peak IDR for Model A for various levels of intensity using Canoga Park record up to incipient collapse

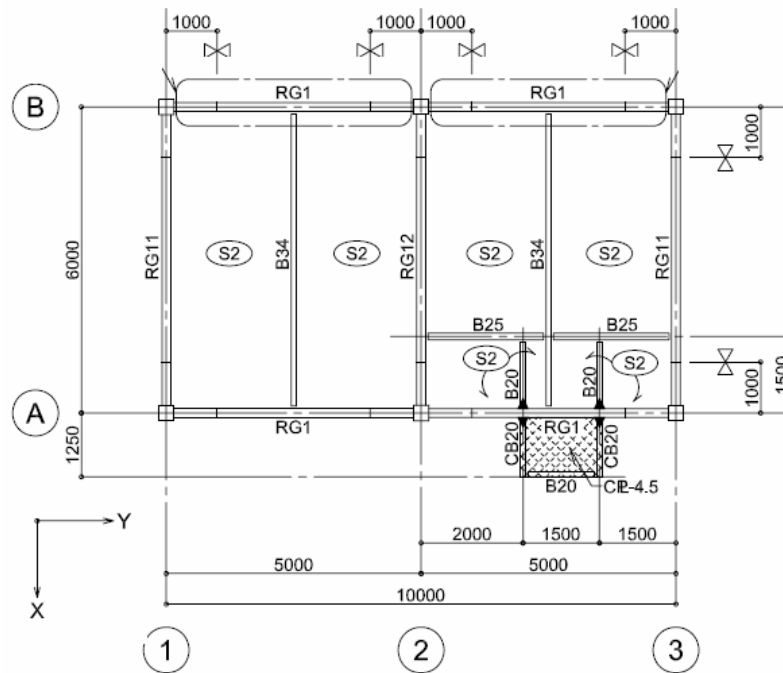


Figure 8.12. Plan view of 4-story building tested in the E-Defense facility (information from https://www.blind-analysis.jp/index_e.html)

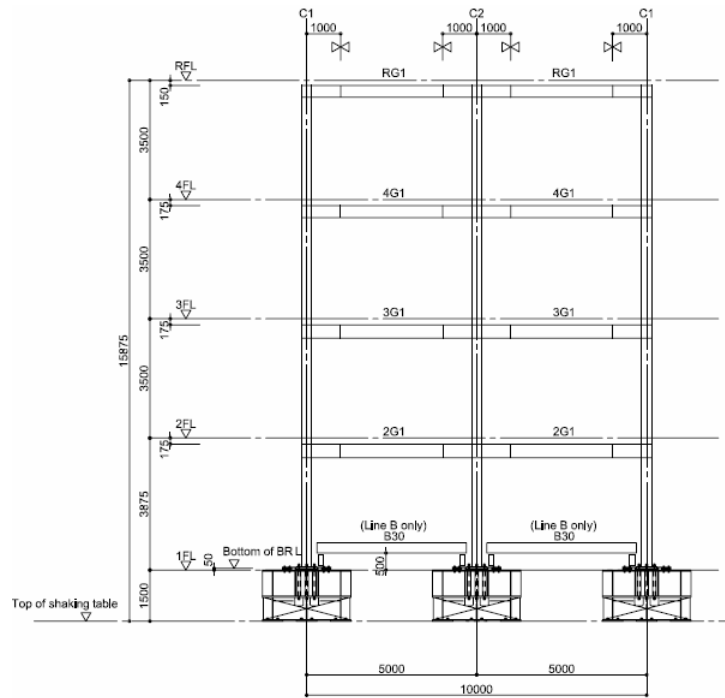


Figure 8.13. North-South elevation view of the 4-story building tested in the E-Defense facility (information from https://www.blind-analysis.jp/index_e.html)

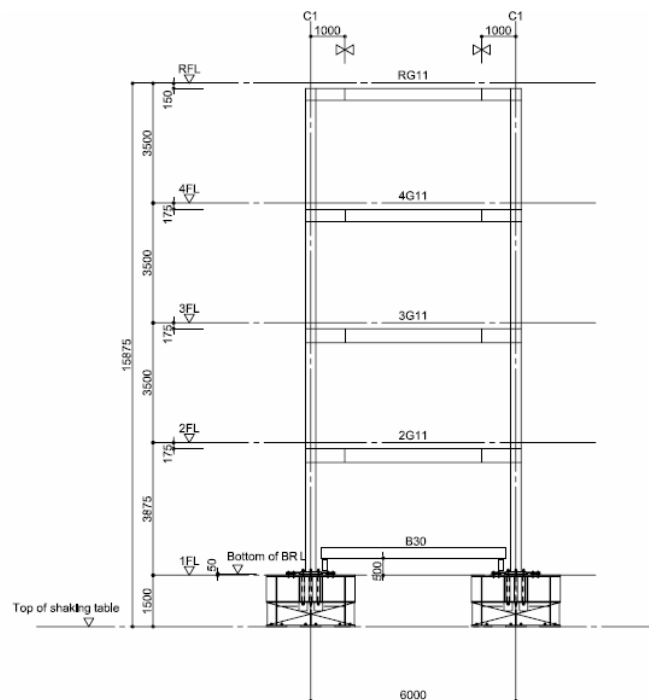


Figure 8.14. East-West elevation view of the 4 story building tested in the E-Defense facility (information from https://www.blind-analysis.jp/index_e.html)



Figure 8.15. E-Defence 4 story building after completion of construction on the shaking table (picture courtesy of Hyogo Earthquake Engineering Research Center)

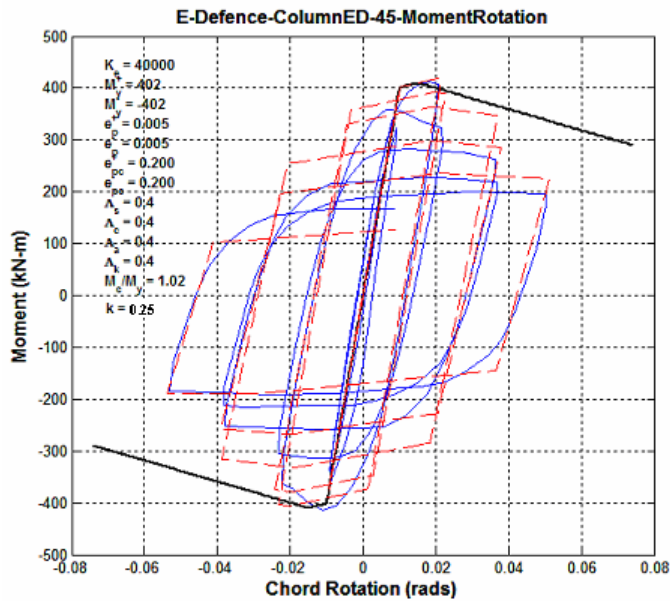


Figure 8.16. Calibration of moment rotation diagram for tubular column section at 45 degrees (data from E-Defence 2007, https://www.blind-analysis.jp/index_e.html)

Spectral Acceleration of Hyogoken-Nanbu Earthquake, Takatori NS for 2% damping

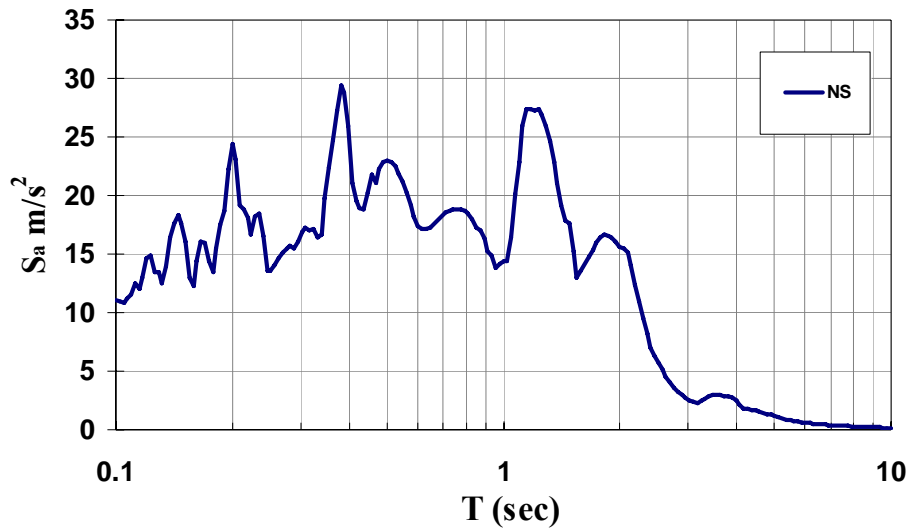


Figure 8.17. Spectral acceleration for 2% damping of Hyogoken – Nambu earthquake, Takatori NS component

E-Defense-4-Story Building: Pushover Curve
 $T_1=0.86\text{sec}, \zeta=3\%, N=4, \gamma=0.45, \text{P-Delta}, M_2\text{-Model}$

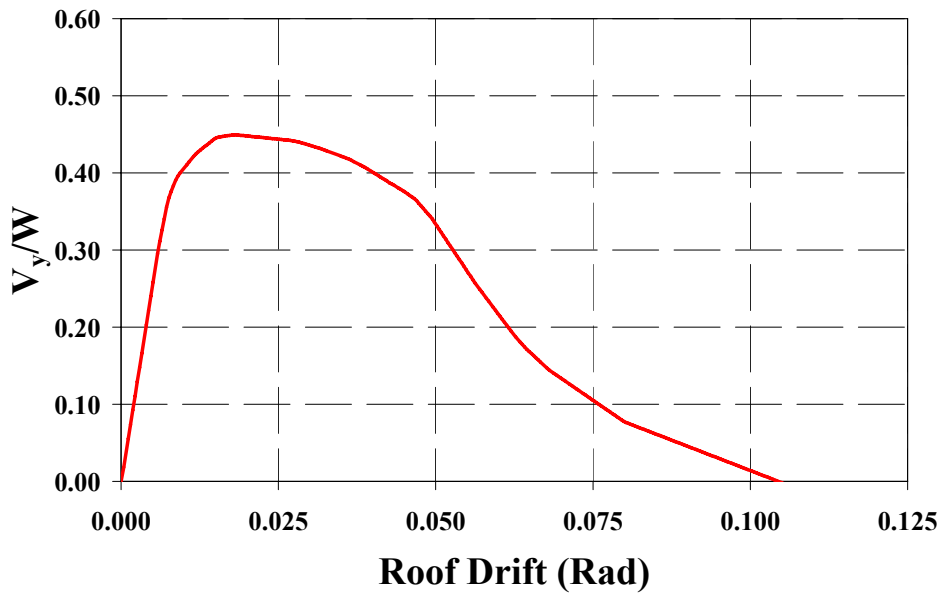


Figure 8.18. Pushover curve for E-Defense 4-story structure

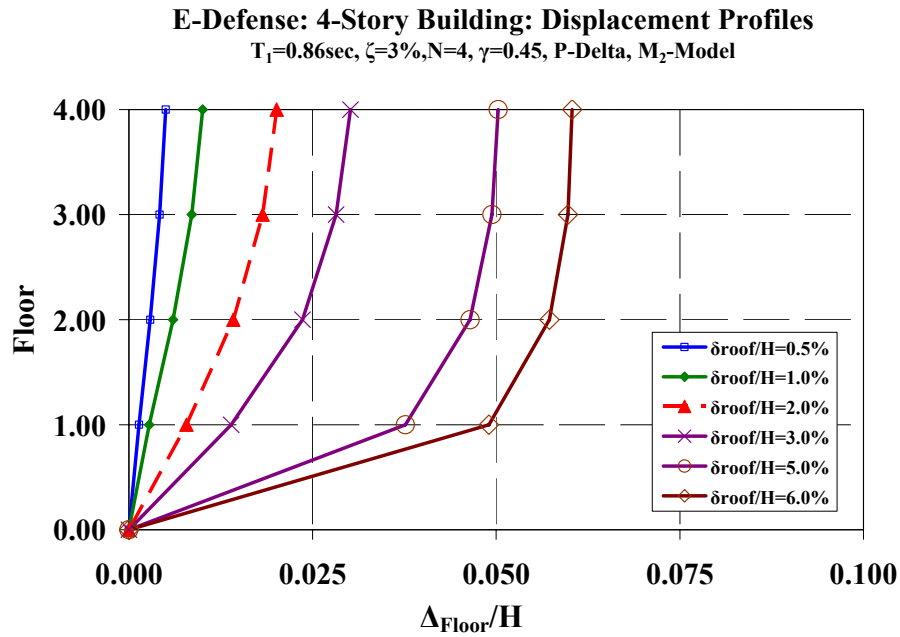


Figure 8.19. Displacement profiles of the E-Defense 4-story structure along the height based on pushover analysis

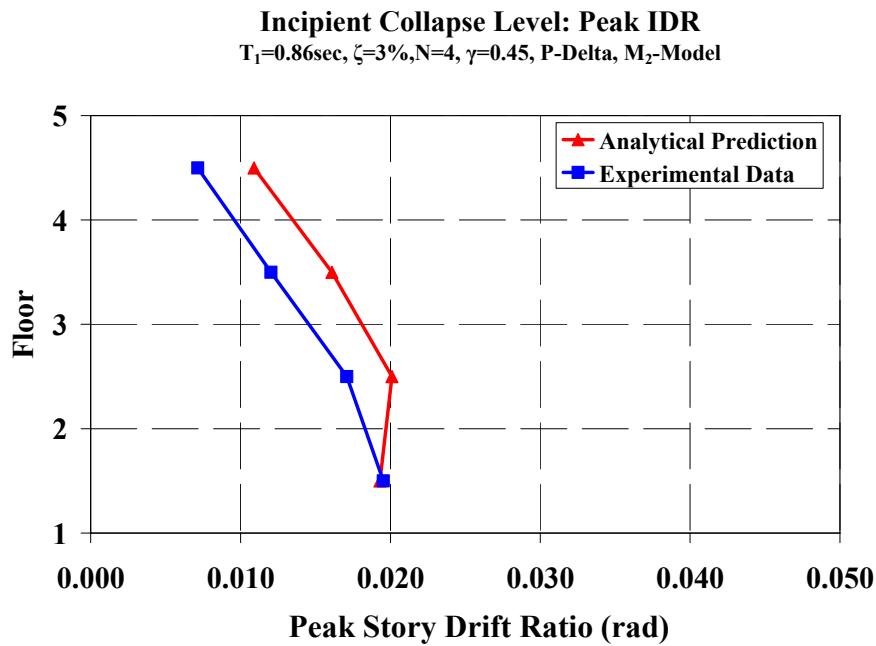


Figure 8.20. Comparison of peak story drifts along the height of the 4-story structure during 60% Takatori motion (Incipient Collapse Level)

E-Defense: 4-Story Building: Peak Story Shear Forces
 $T_1=0.86\text{sec}$, $\zeta=3\%$, $N=4$, $\gamma=0.45$, P-Delta, M_2 -Model
 Incipient-Collapse Level

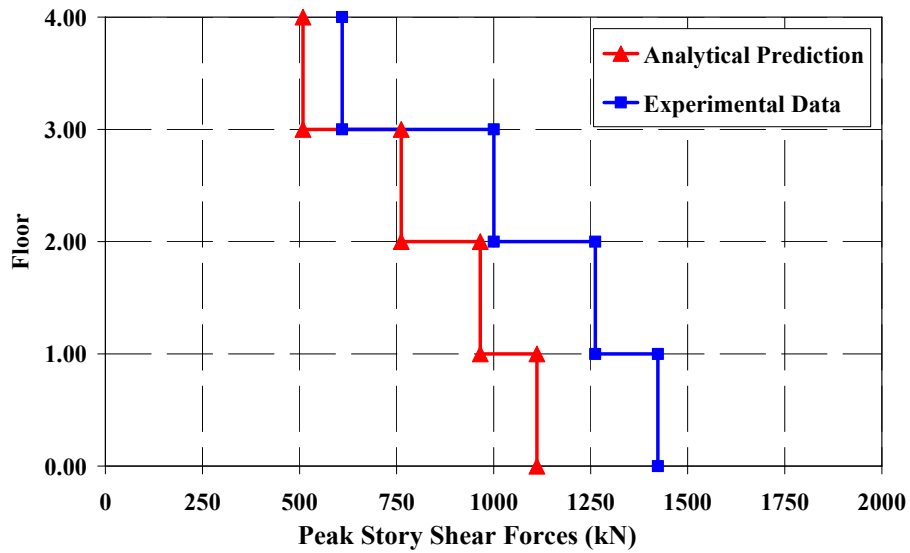


Figure 8.21. Comparison of peak story shears of the 4-story structure during 60% Takatori motion (Incipient Collapse Level)

E-Defense: 4-Story Building: Peak Overturning Moments
 $T_1=0.86\text{sec}$, $\zeta=3\%$, $N=4$, $\gamma=0.45$, P-Delta, M_2 -Model
 Incipient-Collapse Level

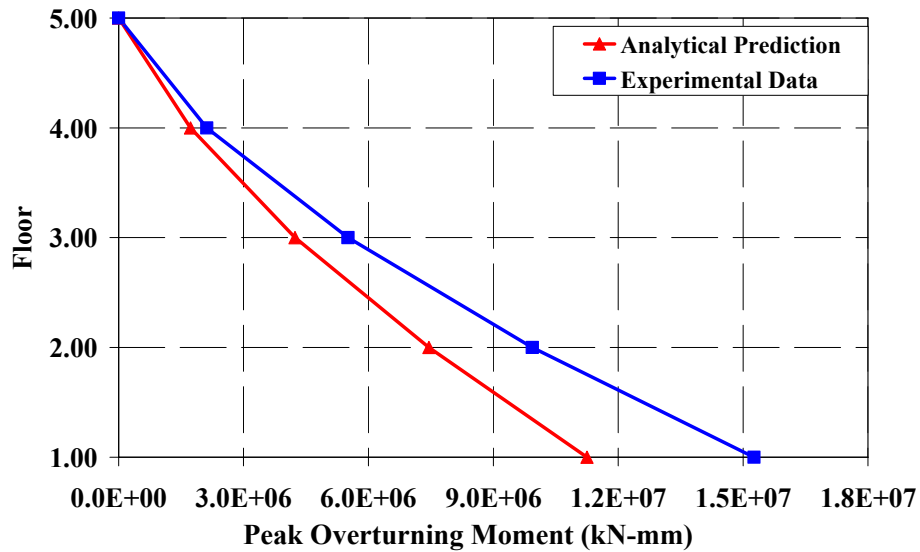


Figure 8.22. Comparison of peak overturning moments of the 4-story structure during 60% Takatori motion (Incipient Collapse Level)



Figure 8.23. First story collapse mechanism of the 4-story structure



Figure 8.24. Local buckling at the base exterior column after the end of the collapse test (100% Takatori motion)

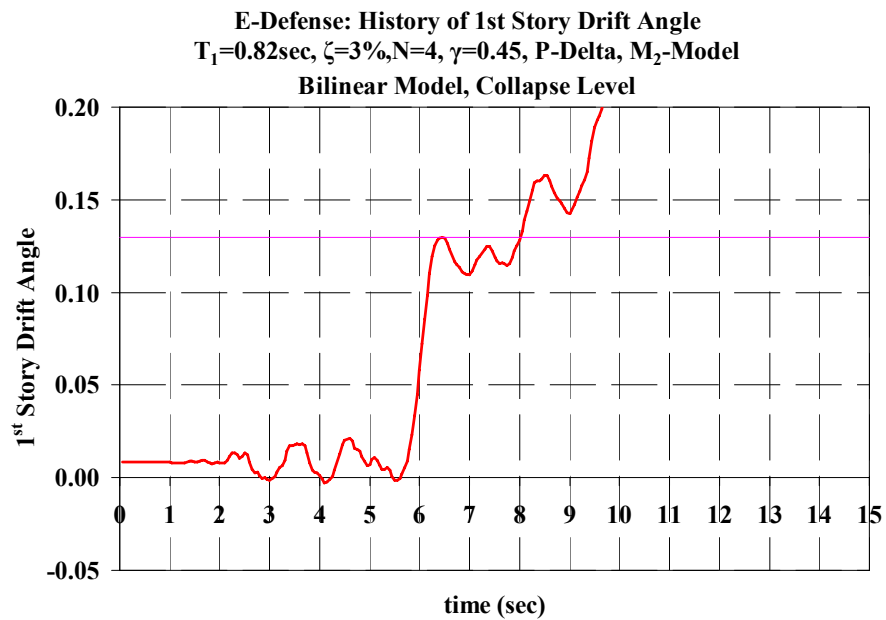


Figure 8.25. Analytical prediction of first story drift angle of the 4-story structure at 100% Takatori motion

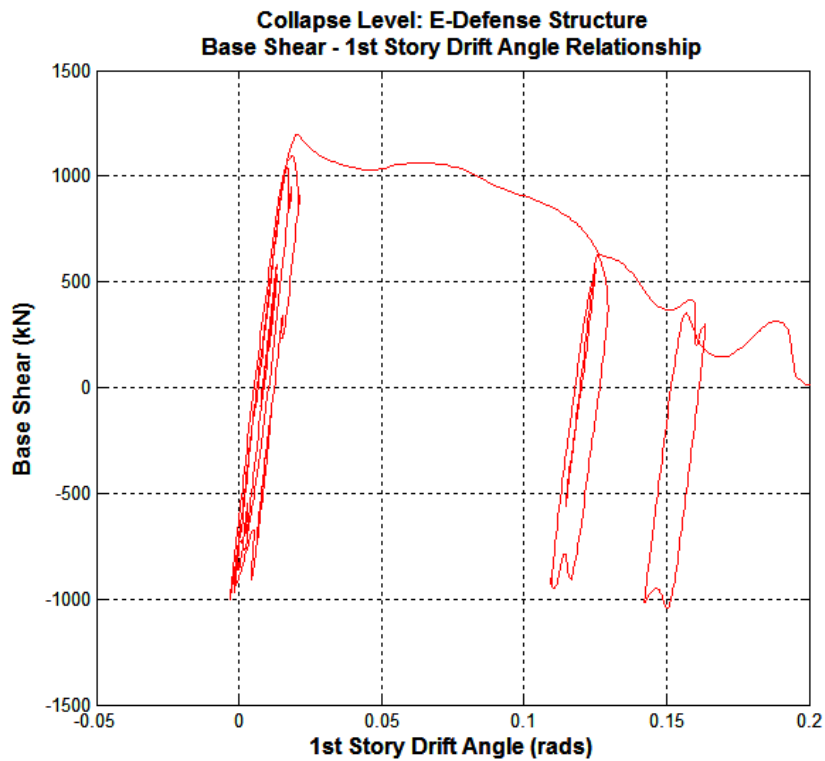


Figure 8.26. Analytical prediction of base shear – 1st story drift angle of the 4-story structure during 100% Takatori motion

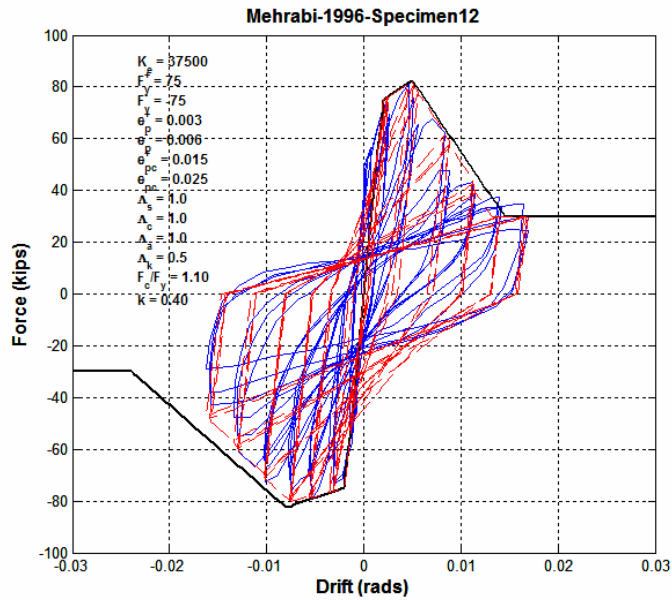


Figure 8.27. Matching a cyclic response with the Ibarra-Krawinkler deterioration model (data from Mehrabi, 1996)

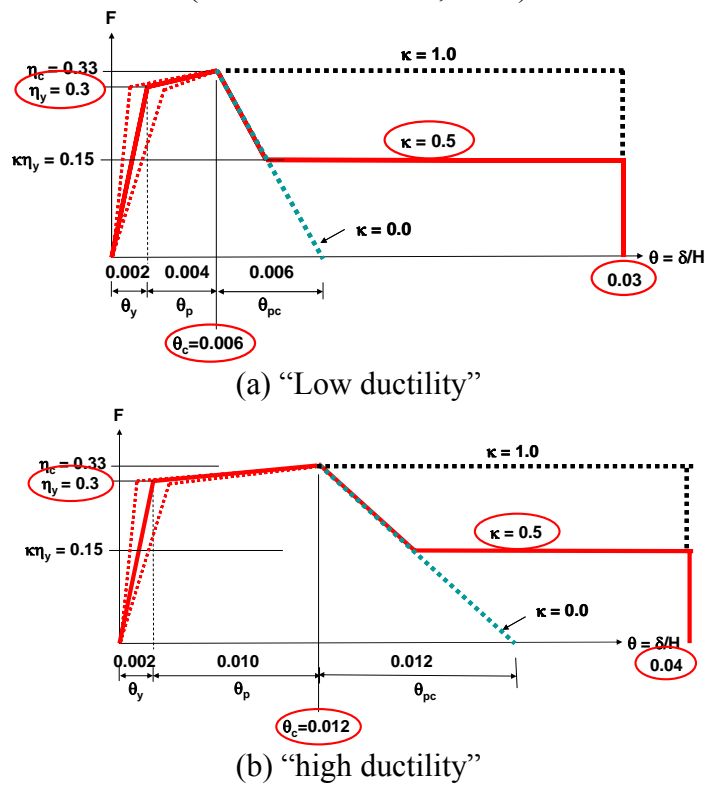


Figure 8.28. "Low ductility" and "high ductility" central cases with parameter variations

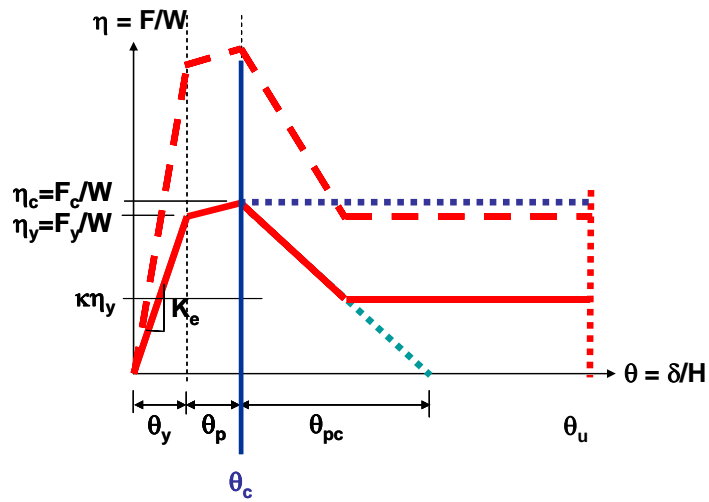


Figure 8.29. Generic backbone curve for infill wall systems, with parameter variations

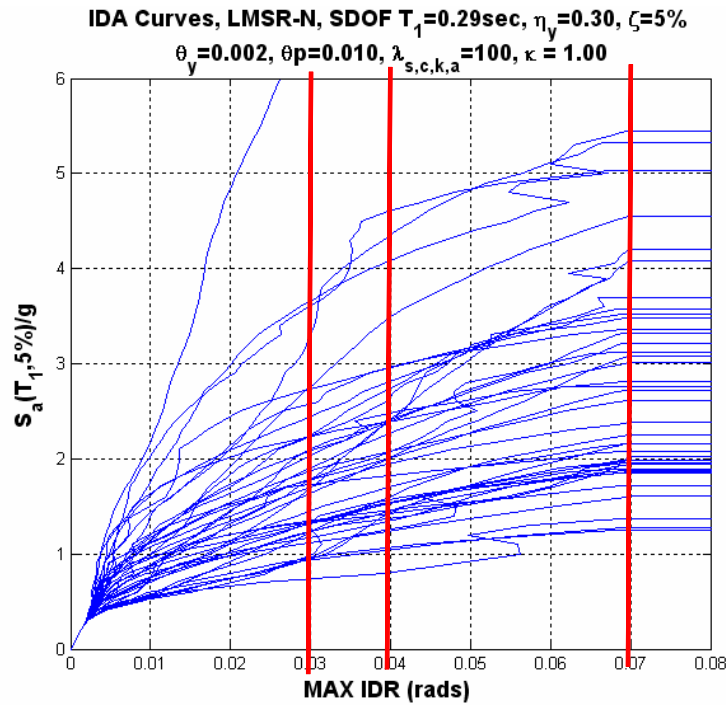


Figure 8.30. Effect of ultimate drift limit on collapse capacity, horizontal post-capping slope

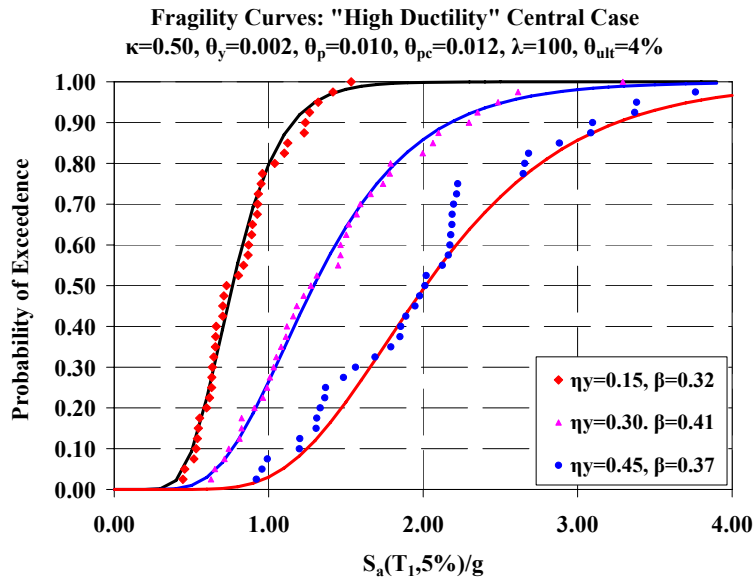
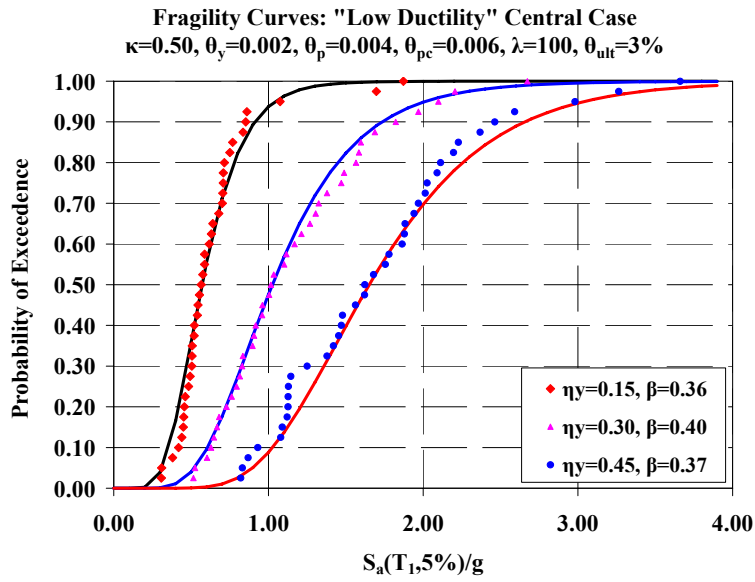
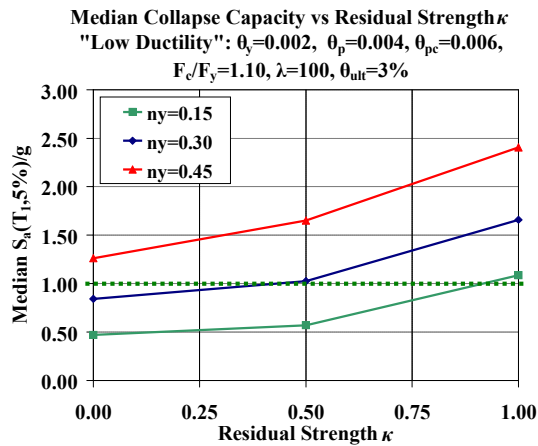
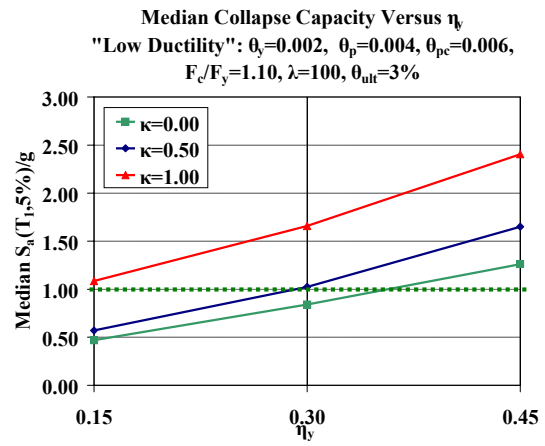


Figure 8.31. Collapse fragility curves for low and high ductility central cases with 50% residual strength; variation in base shear yield strength n_y

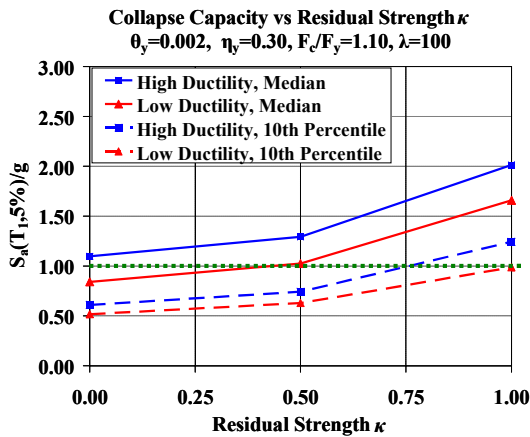


(a) Effect of residual strength (κ) on median collapse capacity, low ductility, $n_y = 0.15, 0.3, \text{ and } 0.45$

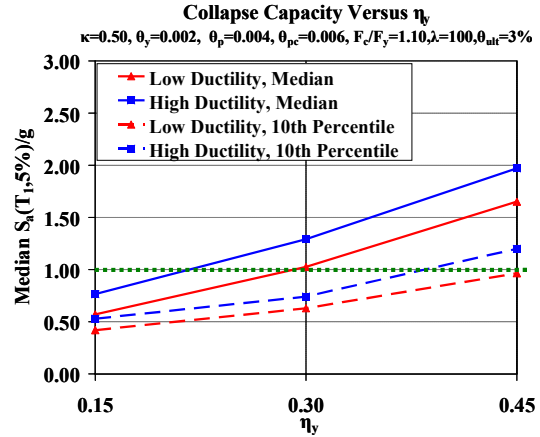


(b) Effect of yield strength (η_y) on median collapse capacity, low ductility, $\kappa = 0.0, 0.5, \text{ and } 1.0$

Figure 8.32. Effect of various parameters on median collapse capacity for low ductility cases

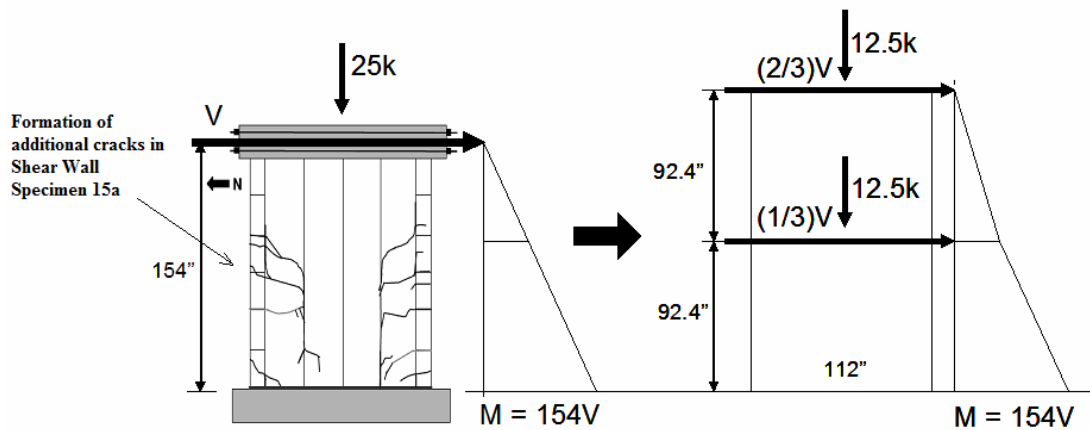


(a) Effect of residual strength (κ) on median and 10-percentile Collapse capacity low and high ductility, $n_y = 0.3$

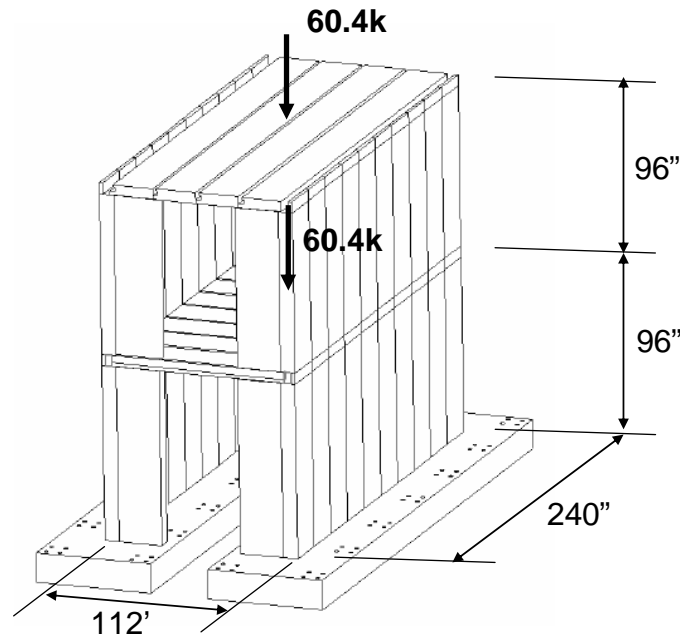


(b) Effect of yield strength (η_y) on median and 10-percentile collapse capacity, low and high ductility $\kappa = 0.5$

Figure 8.33. Effect of various parameters on median and 10-percentile collapse capacity for low and high ductility cases

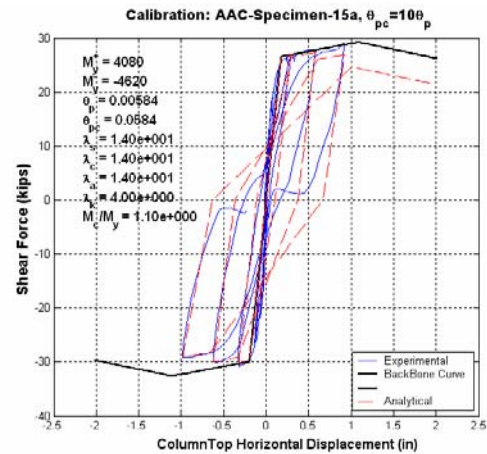
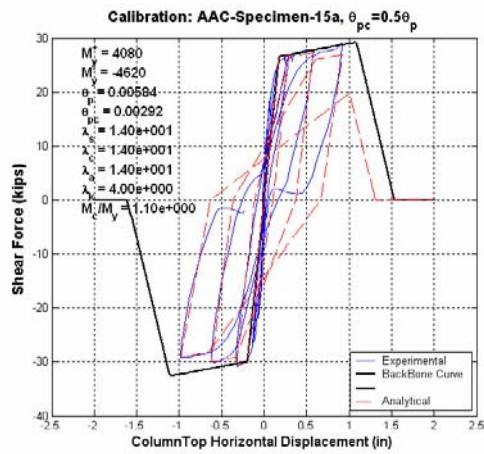


(a) Test Specimen 15(Tanner, 2003) and equivalent two-story building configuration for case 1

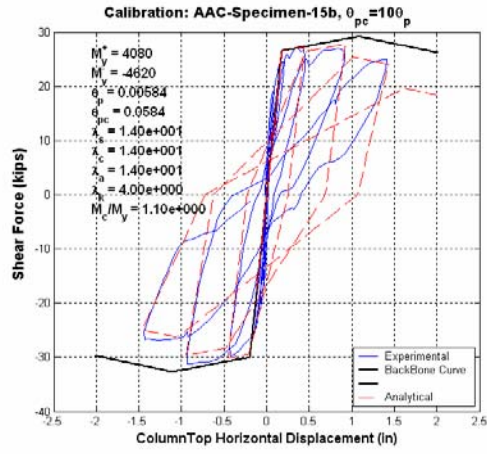
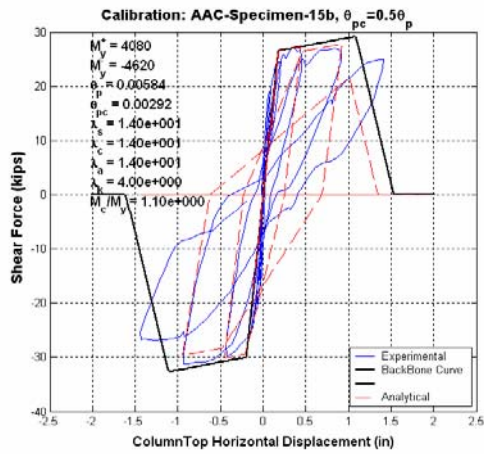


(b) Two-story building configuration represented by UT Austin Assemblage Specimen (Tanner, (2003))

Figure 8.34. Test configurations for AAC case studies used for collapse assessment



(a) specimen 15a



(b) specimen 15b

Figure 8.35. Comparison of measured and predicted responses, UTA Specimens 15a and 15b

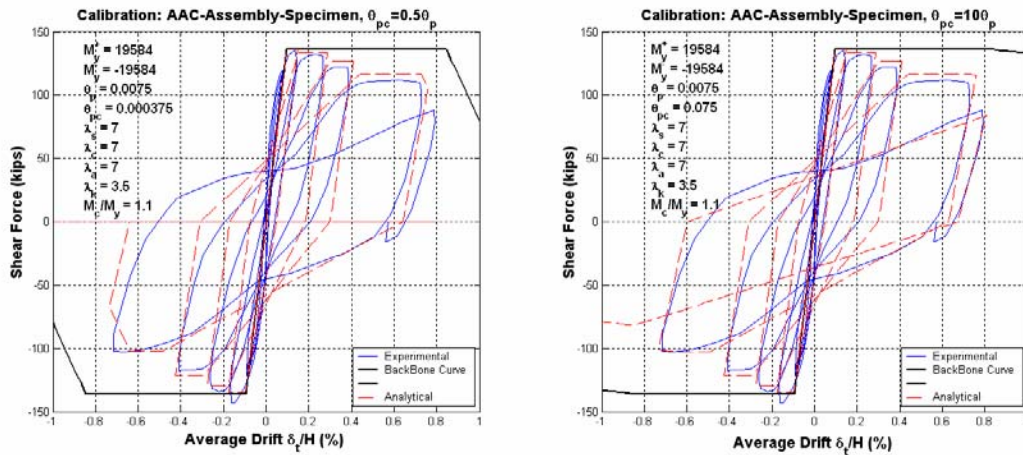


Figure 8.36. Comparison of measured and predicted responses, UTA Assemblage Specimen

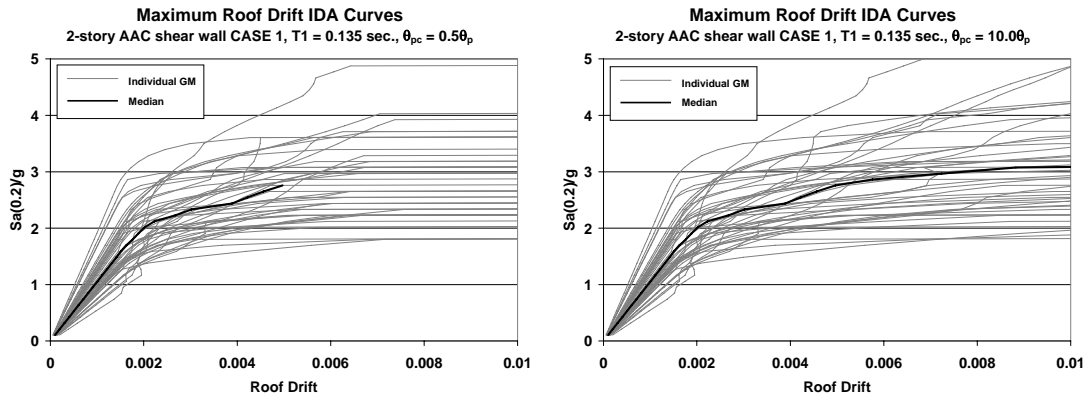


Figure 8.37. IDA curves to collapse, Case 1, (a) pessimist's model, (b) optimist's model

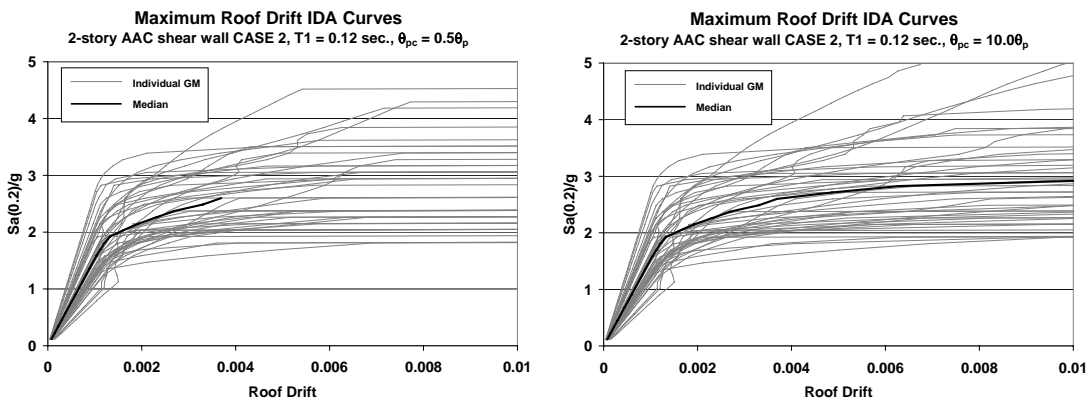


Figure 8.38. IDA curves to collapse, Case 2, (a) pessimist's model, (b) optimist's model

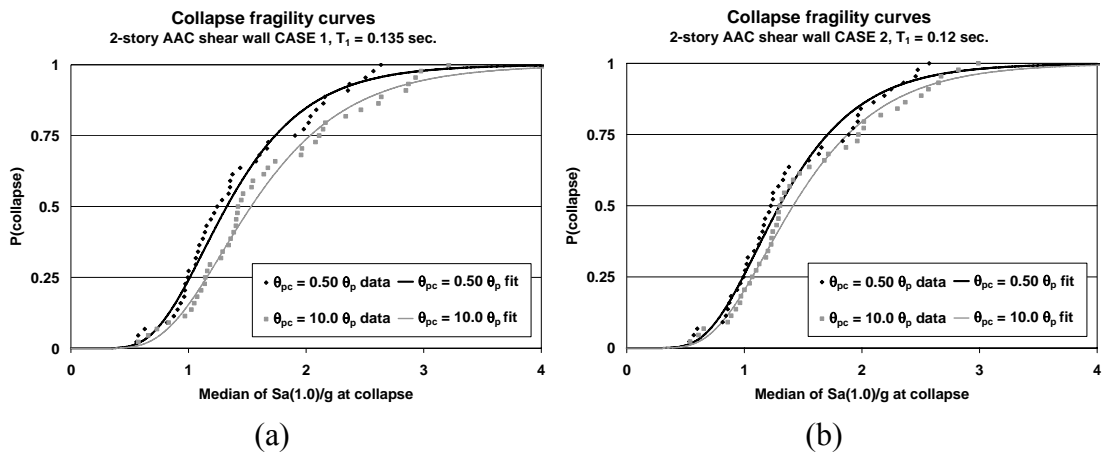


Figure 8.39. Collapse fragility curves, ATC-63 scaling of ground motions, optimist's and pessimist's model; (a) case study 1, (b) case study 2

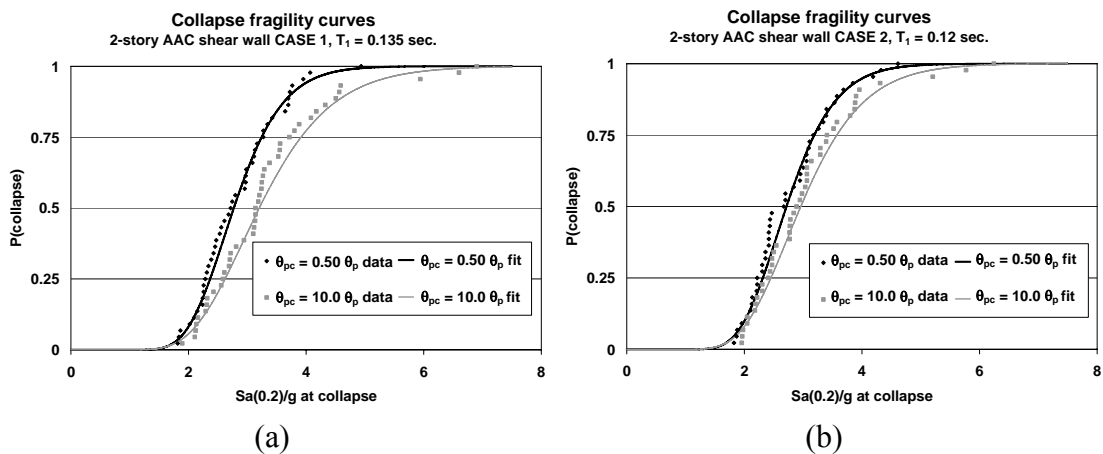


Figure 8.40. Collapse fragility curves, $S_a(0.2)$ scaling, optimist's and pessimist's model; (a) case study 1, (b) case study 2

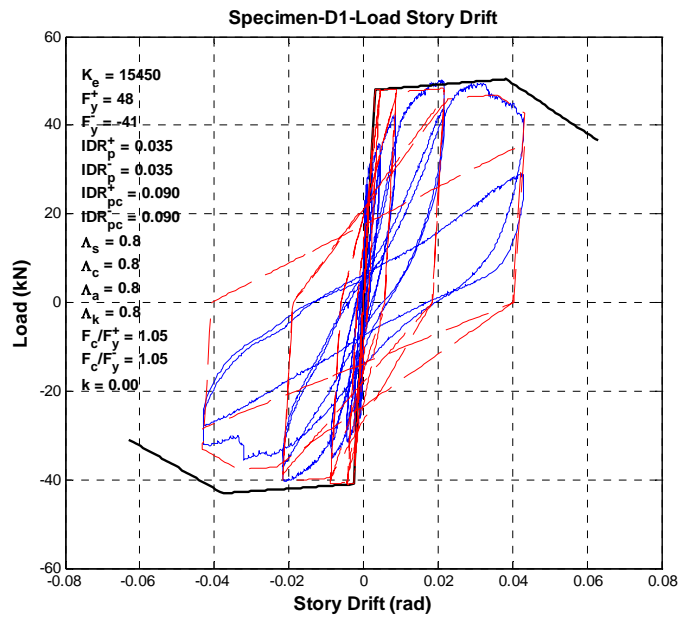


Figure 8.41. Calibration of load-story - drift response using the PUCP reinforced wall test

D1

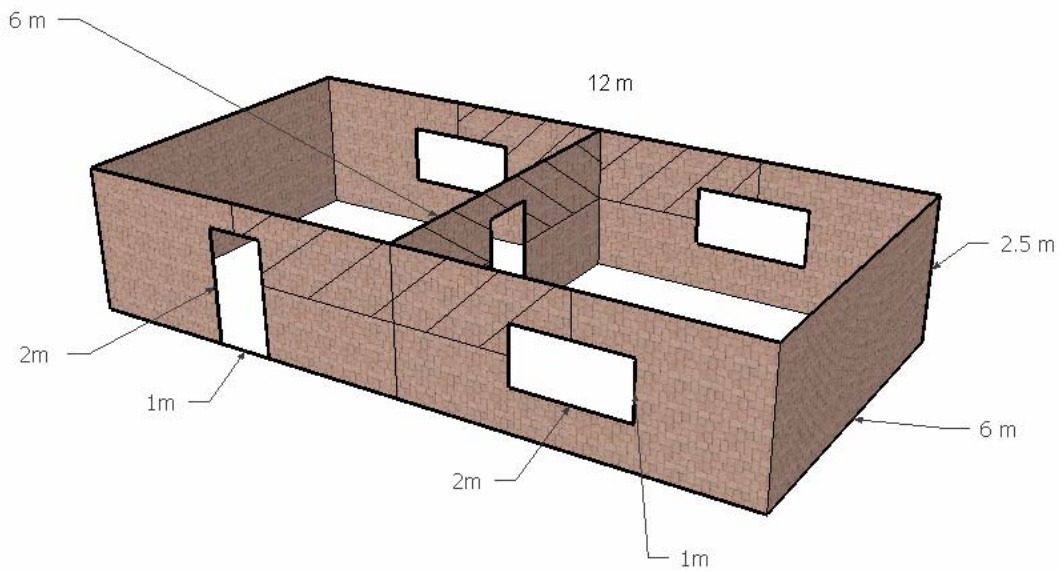


Figure 8.42. Isometric view of idealized adobe dwelling (figure by Hulburd, 2008)

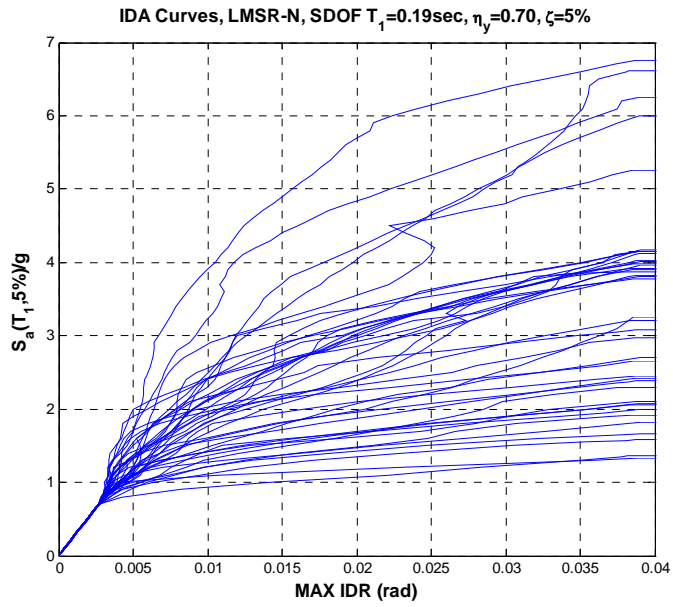


Figure 8.43. IDAs for the analytical model of the reinforced adobe dwelling

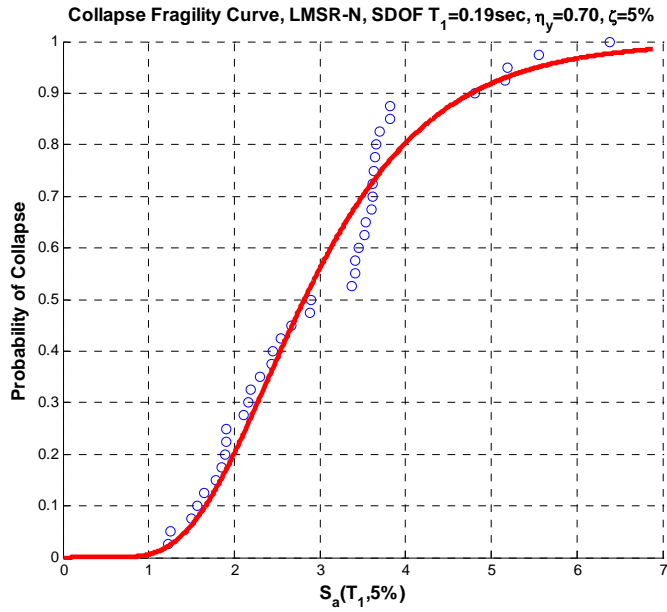


Figure 8.44. Collapse fragility curve for reinforced adobe dwelling

CHAPTER 9

SUMMARY AND CONCLUSIONS

The primary objective of this research is to advance, through analytical and experimental research, knowledge on collapse assessment of structural systems. The focus is on sidesway collapse of frame structures in which a specific story, or a series of stories, displaces sufficiently so that second order P-delta effects fully offset the first order shear resistance and dynamic instability occurs. The effect of component deterioration that accelerates sidesway collapse of structural systems is of primary interest in this research. Reliable prediction of collapse still has many hurdles to overcome, but the goal to improve the state of knowledge on how to predict the collapse capacity of deteriorating structural systems is achieved. In the subsequent sections the major results of this research are summarized.

9.1 Development of Databases of Structural Elements

In order to provide supporting information for modeling of structural component behavior under monotonic and cyclic loading, one of the goals of this research is to deliver an extensive collection of worldwide data on component experiments in a consistent format. For this purpose three databases for components made of steel and reinforced concrete are developed. The first database (steel W-sections database) includes data for more than 300 steel wide flange beams and a small number of wide flange columns. The second database includes 113 steel tubular sections with a wide range of applied axial load used primarily in Japanese construction. The third database includes 200 reinforced concrete beams and columns with low axial load that fail in a flexural mode. The goal of the databases

development effort is to model deterioration of structural components under different loading histories and evaluate analytical models and their capabilities for modeling all important modes of deterioration. An extensive calibration process of several hundreds of tests, discussed in Chapter 3, has resulted in the following:

- Statistical information (mean, standard deviation and correlation) on material properties and deterioration modeling parameters of structural elements
- Development of cumulative distributions functions (CDFs) of deterioration modeling parameters, such as plastic rotation capacity, post capping rotation capacity and rate of cyclic deterioration for beams with reduced beam section (RBS) and for beams other-than-RBS. The CDFs reveal statistical information but do not display dependencies of deterioration parameters on individual geometric and material properties of structural elements
- Identification of critical geometric parameters and their effect on deterioration characteristics of structural elements.
 - For steel W section beam specimens it is found that for all the connection types evaluated primary contributors to plastic rotation capacity θ_p are the beam web depth over thickness ratio h/t_w and the depth d primarily for beams with RBS due to flange reduction. Of some importance is the effect of flange width to thickness ratio $b_f/2t_f$.
 - For sections used commonly in steel moment frames ($d \geq 21"$) θ_p is weakly dependent on the span to depth ratio L/d . This implies that:
 - A description of beam deformation capacity in terms of a ductility capacity ratio θ_p/θ_y is misleading because θ_y increases linearly with L (for a given beam section) but θ_p does not.
 - The plastic rotation capacity is not very sensitive to the beam span (i.e., the length of the plastic hinge regions)
 - Closely spaced lateral bracing (small L_b/r_y ratio) increases the plastic rotation capacity, but not by a large amount (provided that the L_b/r_y ratio does not

exceed an upper limit on the order of 70). It is more important for post capping rotation capacity and rate of cyclic deterioration because lateral torsional buckling typically dominates the large cycles of a loading history.

9.2 Improved Component Hysteresis/ Deterioration Models

The information collected in the steel databases is used to evaluate whether a widely used deterioration model (Ibarra-Krawinkler deterioration model) is adequate to capture all important deterioration phenomena and to quantify the parameters of this model. One of the major benefits of the databases is that other analytical models can be validated and improved using actual experimental data.

Based on experimental evidence for steel components deteriorating in a local or lateral torsional buckling mode (brittle failures are not considered in this study) we identified that:

- The hysteretic response of steel components reaches stabilization at a considerable residual strength, which may be important for the collapse capacity of steel frame structures. The Ibarra-Krawinkler model was modified to account for hysteresis loop stabilization.
- At very large inelastic rotations, steel base material develops cracks at the apex of the most severe local buckle, and typically rapid crack propagation will occur followed by ductile tearing. A new branch has been added to the original backbone curve of the Ibarra-Krawinkler model that allows the simulation of ductile tearing as observed in many tests and in particular in steel components.
- Based on experimental evidence on composite slab action, the backbone curve and cyclic deterioration rates in the two loading directions of a component are different if a slab is present, i.e. the hysteretic response of a composite member is asymmetric in the two loading directions. Modeling of different backbone curves and rates of

deterioration in the two loading directions is incorporated in the modified version of the Ibarra-Krawinkler model presented in Chapter 2.

9.3 Development of Relationships for Modeling Deterioration of Plastic Hinge Regions

The missing aspect of modeling of deterioration characteristics of structural components is the availability of relationships that associate model parameters, such as plastic rotation capacity θ_p , post capping rotation capacity θ_{pc} , and rate of deterioration A , with geometric and material properties and detailing criteria that control deterioration of components. Based on statistical evaluation of the calibrated moment rotation diagrams from several hundreds of tests included in the steel databases, important contributors to deterioration model parameters were identified. With the use of multivariable regression analysis presented in Chapter 4 of this research empirical equations are proposed that predict deterioration modeling parameters for the following data sets:

- Beams other than RBS
- Beams with reduced beam section (RBS)
- Hollow square steel columns under a wide range of applied axial load.

The proposed equations provide satisfactory results in most cases but need improvements in some cases. Based on the regression equations it is concluded that an important aspect for reliable prediction of modeling parameters is to consider the interaction (correlation) of geometric and material properties of components.

9.4 Collapse Experiments and Predictions

Till recently there was no comprehensive physical experiment on steel structures that could be used to validate that prediction of collapse is indeed feasible. In the context of this research we designed, fabricated, and executed collapse tests of two scale model of a 4-story steel frame part of a prototype office building designed based on current seismic provisions. The integrated effort of shaking table collapse test series and associated pre- and post-test predictions led to:

- Measurement and documentation of comprehensive experimental data of a wide range of response parameters, including story shears and drifts, floor accelerations and displacements, and rotations at all important beam and column locations from elastic behavior up to collapse of the two test frames. The parameters are available to researchers to evaluate the effectiveness of analytical models for collapse prediction of steel frame structures through the Network for Earthquake Engineering Simulation (NEES)
- Demonstration on hand of analytical simulations of these experiments that P- Δ effect can be isolated and quantified from elastic behavior up to collapse
- Validation that relatively simple analytical models can be used to predict collapse capacity with a satisfactory level of accuracy – provided that the deterioration characteristics of critical components are adequately represented in the analytical models. In this research the deterioration characteristics were evaluated from pre-shaking-table and post-shaking-table component experiments. These component tests, and the collapse predictions based on these tests, did demonstrate that the response close to collapse is sensitive to the loading history every component experiences as part of the structure.
- The use of existing symmetric cyclic loading protocols provide insufficient information for component deterioration modeling as the structure approaches collapse, because the structure drifts to one side and the hysteresis loops become

very asymmetric with small deformation reversals. A test in which relatively small inelastic cycles are followed by unidirectional loading to extreme deformations would provide more relevant information for the purpose of collapse prediction.

The approach to collapse prediction of deteriorating structural systems is exercised and shown to provide valuable information in the case studies summarized in Chapter 8, in which advantage is taken of recently conducted shaking table experiments.

9.5 Concluding Remarks

Adequate safety against collapse is of fundamental concern in the design decision process. It is closely tied to life safety considerations and may be also an important factor in economic loss estimation. This research is a step towards a comprehensive quantification of the limit state of global or partial collapse in earthquakes. There are various modes of collapse and only the one associated with the sidesway mode is explicitly covered in this research.

The major aspects of this research on collapse assessment of structural systems are (a) the development of three extensive databases on steel and reinforced concrete beam elements that provide information on deterioration characteristics of structural components and serve as the basis for modeling recommendations for structural components, and (b) the design planning and execution of two shaking table tests of a 4-story frame that provides comprehensive information from elastic range up to collapse and demonstrates that sidesway collapse of frame structures can indeed be predicted analytically including the effects of component deterioration.

9.6 Suggestion for Future Work

Areas for future research on the evaluation of collapse potential of structures in earthquakes include the following:

- modeling deterioration characteristics of all important structural components
- improvement of the analytical tools to include all the deterioration effects and be able to model P-M-V interaction and local failure modes such as loss of gravity load resistance at beam-to-column and slab-to-column connections
- assessment of other collapse modes (local, story, global)
- incorporating all "intangible" contributions that delay collapse (e.g., cladding, structural and nonstructural partitions, floor systems, etc.)
- quantifying human error considerations

Other areas of future research, not necessarily related to collapse potential of structures during earthquakes, for which this study can provide useful information are:

- damage detection and localization based on damage detection algorithms with the use of information provided from the shaking table test series
- validation and improvement of models that predict low cyclic fatigue and ductile fracture taking advantage of the information from the testing program of component tests.

APPENDIX A

CALIBRATED VALUES OF DETERIORATION MODEL PARAMETERS AND EXPERIMENTAL DATA

This appendix includes experimental data used in Chapters 3 and 4 in order to identify trends of deterioration model parameters of the modified Ibarra-Krawinkler model versus geometric and material properties of steel and reinforced concrete structural components and develop empirical relationships in support to collapse assessment of deteriorating structural systems. The experimental data is included in the three databases developed as part of this research and is categorized per dataset used in Chapters 3.

Each table contains the basic deterioration model parameters after calibration of the moment rotation diagram of the individual components. Each component is distinguished from others based on the test identification that is used in the individual databases. In the individual tables a reference publication is also included. Connection type (if applicable), test configuration, and beam size is additional information provided in these tables.

A.1 Beams Other-than-RBS

Specimens that include beams other than RBS are summarized in Table A.1. The connection type and test configuration description of steel beams is summarized in Tables A.2 and A.3, respectively.

A.2 Beams with RBS

Specimens with beams with RBS are summarized in Table A.4. Similarly to beams other than RBS the description of connection type and test configuration is summarized in Tables A.2 and A.3, respectively.

A.3 Tubular Hollow Square Column Sections

Tubular hollow square column sections are summarized in Table A.5. The description of test configurations of the specimens is summarized in Table A.6.

A.4 Reinforced Concrete Beams

Reinforced concrete beams included in the data evaluation in Chapter 3 are summarized in Table A.7. As mentioned in Chapter 3, at this point only calibrated plastic rotation capacities and cyclic deterioration parameters are included in the table since the data for post capping rotation capacity is not complete. Descriptions of test configurations of the same specimens are summarized in Table A.8.

Table A.1. Beams other than RBS

Test ID	Reference	Con. Type	Test Conf.	Beam Size	K (kips-in/rad)	M_y (kips-in)	θ_p (rad)	θ_{pc} (rad)	A_s	A_κ	M_c/M_y	κ
1	Popov, E. P., Stephen, R. M., (1970)	WUF-B	N3SBNS	W24x76	900000	10684	0.049	na	0.00	0.00	1.17	0.00
2	Popov, E. P., Stephen, R. M., (1970)	WUF-B	N3SBNS	W18x50	450000	5446	0.048	0.460	0.00	0.00	1.12	0.00
3	Popov, E. P., Stephen, R. M., (1970)	WUF-B	N3SBNS	W24x76	1176470	8547	0.035	0.500	0.00	0.00	1.17	0.00
4	Engelhardt, M. D., Sabol, T. A., (1994)	WFP	SSBNS	W36x150	4500000	29182	0.017	0.100	1.00	1.00	1.10	0.60
5	Engelhardt, M. D., Sabol, T. A., (1994)	WFP	SSBNS	W36x150	4500000	28400	0.019	0.180	1.40	1.00	1.16	0.55
6	Engelhardt, M. D., Sabol, T. A., (1994)	WSEP	SSBNS	W36x150	4000000	26000	0.016	0.190	1.30	1.30	1.10	0.65
7	Engelhardt, M. D., Sabol, T. A., (1994)	WSEP	SSBNS	W36x150	4000000	30100	0.016	0.170	1.10	1.00	1.10	0.51
8	Engelhardt, M. D., Sabol, T. A., (1994)	WFP	SSBNS	W36x150	4000000	26000	0.017	0.170	1.50	1.30	1.10	0.52
9	Engelhardt, M. D., Sabol, T. A., (1994)	WFP	SSBNS	W36x150	4000000	26000	0.019	0.150	1.50	1.30	1.10	0.60
10	Engelhardt, M. D., Sabol, T. A., (1994)	WFP	SSBNS	W36x150	4000000	26100	0.018	0.150	1.50	1.30	1.10	0.60
11	Engelhardt, M. D., Sabol, T. A., (1994)	WFP	SSBNS	W36x150	4000000	26100	0.018	0.200	1.30	1.10	1.12	0.55
12	Engelhardt, M. D., Sabol, T. A., (1994)	WSPFF	SSBNS	W36x150	5500000	27273	0.018	0.200	0.80	0.60	1.21	0.00
13	Engelhardt, M. D., Sabol, T. A., (1994)	WSPFF	SSBNS	W36x150	6666667	26410	0.017	0.200	0.70	0.70	1.22	0.40
14	Taejin, K., et al. (2000)	WFP	SSBNS	W30x99	1600000	20500	0.016	0.100	0.65	0.65	1.06	0.41
15	Taejin, K., et al. (2000)	WFP	SSBNS	W30x99	1600000	20500	0.017	0.090	0.60	0.60	1.06	0.52
16	Taejin, K., et al. (2000)	WFP	SSBNS	W30x99	1600000	20700	0.018	0.105	0.60	0.60	1.06	0.39
17	Taejin, K., et al. (2000)	WFP	SSBNS	W30x99	1600000	20000	0.017	0.100	0.60	0.60	1.06	0.36
18	Taejin, K., et al. (2000)	WFP	SSBNS	W30x99	1600000	20000	0.018	0.120	0.80	0.80	1.06	0.34
19	Taejin, K., et al. (2000)	WFP	SSBNS	W30x99	1600000	20100	0.016	0.130	0.50	0.50	1.06	0.36
20	Taejin, K., et al. (2000)	WFP	SSBNS	W30x99	1600000	20300	0.019	0.120	0.60	0.60	1.07	0.36
21	Taejin, K., et al. (2000)	WFP	SSBNS	W30x99	1600000	20100	0.018	0.120	0.60	0.60	1.07	0.38
22	Taejin, K., et al. (2000)	WFP	SSBNS	W30x99	1600000	20200	0.028	0.300	0.90	0.90	1.11	0.38
23	Taejin, K., et al. (2000)	WFP	SSBNS	W30x99	1600000	23000	0.020	0.150	0.60	0.60	1.15	0.45
24	Seismic Structural Design Associates (2000)	SSDA	N3SBNS	W33x141	1886792	30000	0.032	0.160	1.00	1.00	1.11	0.00
25	Seismic Structural Design Associates (2000)	SSDA	N3SBNS	W27x94	814479.6	14400	0.028	0.120	1.00	1.00	1.12	0.37

Table A.1. Beams other than RBS (continue)

Test ID	Reference	Con. Type	Test Conf.	Beam Size	K (kips-in/rad)	M_y (kips-in)	θ_p (rad)	θ_{pc} (rad)	A_s	A_k	M_c/M_y	κ
26	Seismic Structural Design Associates (2000)	SSDA	N3SBNS	W36x300	4651163	80000	0.033	0.160	1.20	1.20	1.13	0.00
27	Tsai, K. C.; Popov, E. P. (1988)	WUF-B	N3SBNS	W18x40	630000	3590	0.026	0.300	0.00	0.00	1.17	0.00
28	Tsai, K. C.; Popov, E. P. (1988)	R-WUF-B	N3SBNS	W18x35	630000	3697	0.021	0.300	0.00	0.00	1.19	0.00
29	Tsai, K. C.; Popov, E. P. (1988)	WUF-B	N3SBNS	W21x44	640000	4579	0.009	0.150	0.00	0.00	1.07	0.00
30	Tsai, K. C.; Popov, E. P. (1988)	R-WUF-B	N3SBNS	W21x44	645000	5268	0.026	0.240	1.50	0.90	1.12	0.00
31	Tsai, K. C.; Popov, E. P. (1988)	BSEP	N3SBNS	W18x46	666667	4364	0.028	0.300	2.00	1.50	1.10	0.00
32	Tsai, K. C.; Popov, E. P. (1988)	BSEP	N3SBNS	W18x40	650000	4495	0.025	0.250	1.70	1.40	1.09	0.60
33	Tsai, K. C.; Popov, E. P. (1988)	BUEP	N3SBNS	W21x44	869565	4153	0.026	0.270	1.50	1.20	1.18	0.40
34	Tsai, K. C.; Popov, E. P. (1988)	BUEP	N3SBNS	W21x44	869565	4298	0.028	0.250	1.60	1.40	1.14	0.00
35	Choi, J., et al. (2000)	WUF-B	N3SBNS	W24x68	1176471	11000	0.015	0.140	0.80	0.80	1.07	0.44
36	Choi, J., et al. (2000)	WUF-B	N3SBNS	W30x99	3000000	18344	0.040	na	0.00	0.00	1.11	0.00
37	Choi, J., et al. (2000)	WUF-B	N3SBNS	W30x99	3000000	16909	0.017	0.110	0.80	0.80	1.07	0.44
38	Choi, J., et al. (2000)	WUF-B	N3SBNS	W30x124	5000000	24622	0.031	na	0.00	0.00	1.19	0.00
39	Choi, J., et al. (2000)	WUF-B	N3SBNS	W30x124	5000000	29000	0.029	0.210	0.00	0.00	1.11	0.00
40	Shuey, B., et al. (1996)	BH-WFP	SSBNS	W36x150	12500000	33000	0.014	0.220	0.80	0.80	1.11	0.00
41	Shuey, B., et al. (1996)	WUF-B	SSBNS	W36x150	5000000	22000	0.018	0.140	0.40	0.40	1.13	0.30
42	Shuey, B., et al. (1996)	H-WUF-B	SSBNS	W36x150	7692308	29495	0.018	0.200	0.90	0.50	1.07	0.76
43	Shuey, B., et al. (1996)	WFP	SSBNS	W36x150	5000000	27500	0.029	0.150	1.50	1.50	1.10	0.50
44	Uang, C.M., and Bondad, D., (1996)	BH-WUF-B	SSBNS	W30x99	1250000	15000	0.019	0.140	0.60	0.50	1.10	0.33
45	Uang, C.M., and Bondad, D., (1996)	BH-WUF-B	SSBNS	W30x99	1000000	15500	0.025	0.170	1.00	1.00	1.10	0.00
46	Anderson, J. C., Linderman, R. R. (1991)	WUF-B	N1SBNS	W16x26	666667	3120	0.013	0.200	0.80	0.80	1.10	0.00
47	Uang, C. M., Latham, C. T., (1995)	MNH-SMTFTM	SSBNS	W36x150	2759120	29000	0.02	0.22	0.80	0.70	1.10	0.33
48	Uang, C. M., Latham, C. T., (1995)	MNH-SMTFTM	SSBNS	W36x150	2761222	29500	0.02	0.215	1.40	1.10	1.10	0.60
49	Uang, C. M., Latham, C. T., (1995)	MNH-SMTFTM	SSBNS	W36x150	2719736	29500	0.019	0.2	1.10	0.90	1.10	0.45
50	Uang, C. M., et al. (1996)	MNH-SMTFTM	SSBNS	W36x170	3400152	36800	0.017	0.27	0.90	0.70	1.08	0.00
51	Suita, K., et al. (1998)	WUF-W	SSBNS	WF-500x200x10x16	714286	7568	0.036	0.250	1.40	1.40	1.11	0.52
52	Suita, K., et al. (1998)	WUF-W	SSBNS	WF-500x200x10x16	714286	7568	0.034	0.250	1.40	1.30	1.11	0.50
53	Suita, K., et al. (1998)	WUF-W	SSBNS	WF-500x200x10x16	714286	7636	0.037	0.250	1.50	1.40	1.10	0.53
54	Suita, K., et al. (1998)	WUF-W	SSBNS	WF-500x200x10x16	714286	7080	0.034	0.300	2.48	2.39	1.13	0.50
55	Suita, K., et al. (1998)	WUF-W	SSBNS	WF-500x200x10x16	714286	7043	0.035	0.300	2.51	2.42	1.15	0.50

Table A.1. Beams other than RBS (continue)

Test ID	Reference	Con. Type	Test Conf.	Beam Size	K (kips-in/rad)	M_y (kips-in)	θ_p (rad)	θ_{pc} (rad)	A_s	A_κ	M_c/M_y	κ
56	Suita, K., et al. (1998)	WUF-W	SSBNS	WF-500x200x10x16	714286	7043	0.041	0.300	2.00	1.90	1.15	0.44
57	Suita, K., et al. (1998)	WUF-W	SSBNS	WF-500x200x10x16	800000	8182	0.042	0.300	3.78	3.80	1.10	0.40
58	Ricles, J. M., et al. (2000)	WUF-B	N2SBNS	W36x150	4681400	40000	0.025	0.150	0.00	0.00	1.10	0.00
59	Ricles, J. M., et al. (2000)	WUF-B	N2SBNS	W36x150	4681400	41887	0.017	0.100	0.70	0.70	1.06	0.38
60	Ricles, J. M., et al. (2000)	WUF-B	N2SBNS	W36x150	4681400	45045	0.031	0.110	1.00	0.75	1.11	0.44
61	Ricles, J. M., et al. (2000)	WUF-B	N2SBNS	W36x150	4681400	36036	0.020	0.110	0.85	0.65	1.11	0.42
62	Ricles, J. M., et al. (2000)	WUF-B	N2SBNS	W36x150	4681400	36036	0.021	0.100	0.80	0.60	1.11	0.40
63	Ricles, J. M., et al. (2000)	WUF-B	N2SBNS	W36x150	4681400	39091	0.019	0.120	1.00	0.80	1.10	0.54
64	Ricles, J. M., et al. (2000)	WUF-B	N2SBNS	W36x150	4681400	38636	0.020	0.120	1.00	0.80	1.10	0.54
65	Ricles, J. M., et al. (2000)	WUF-B	N2SBNS	W36x150	4681400	41818	0.019	0.120	0.61	0.50	1.10	0.43
66	Ricles, J. M., et al. (2000)	WUF-B	N2SBNS	W36x150	4681400	37826	0.020	0.120	0.53	0.47	1.15	0.43
67	Ricles, J. M., et al. (2000)	WUF-B	N2SBNS	W36x150	4681400	45000	0.025	0.100	0.80	0.80	1.10	0.38
68	Ricles, J. M., et al. (2000)	WUF-B	N2SBNS	W36x150	4681400	37826	0.030	0.100	0.80	0.80	1.15	0.38
69	Ricles, J. M., et al. (2000)	WUF-B	N2SBNS	W36x150	4681400	42545	0.024	0.120	1.10	0.80	1.10	0.01
70	Ricles, J. M., et al. (2000)	WUF-B	N2SBNS	W36x150	4681400	39455	0.024	0.100	0.00	0.00	1.10	0.01
71	Krawinkler, H., et al. (1983)	WUF-W	N3SBNS	W4X13	20000	365	0.065	0.400	0.00	0.00	1.25	0.00
72	Krawinkler, H., et al. (1983)	WUF-W	N3SBNS	W6X9	33333	342	0.070	0.060	2.50	2.50	1.15	0.25
73	Krawinkler, H., et al. (1983)	WUF-W	N3SBNS	W6X9	33333	342	0.055	0.060	2.30	2.30	1.20	0.00
74	Nakashima, M., et al. (1998)	WUF-W	SSBNS	WF-600x250x12x25	1534263	18430	0.057	0.28	0.00	0.00	1.05	0.00
75	Kasai, K., and Hodgson, I., (1996)	H-BF-B	N2SBNS	W16X40	377653.4	4440	0.039	0.24	0.00	0.00	1.17	0.00
76	Kasai, K., and Hodgson, I., (1996)	BH-BF-B	N2SBNS	W16X40	406381	4750	0.044	0.22	2.00	2.00	1.20	0.48
77	Kasai, K., and Hodgson, I., (1996)	H-BF-B	N2SBNS	W36X150	8036164	30000	0.033	0.22	2.30	2.30	1.20	0.48
78	Kasai, K., and Hodgson, I., (1996)	BH-BF-B	N2SBNS	W36X150	8036164	28000	0.033	0.22	2.10	2.10	1.15	0.48
79	Kasai, K., and Hodgson, I., (1996)	H-BF-B	N2SBNS	W36X150	5943820	29900	0.022	0.28	2.00	2.00	1.10	0.75
80	Cheng, C. T., et al. (2007)	WUF-B-J	STBWS	H450X200X9X14	800000	8200	0.025	0.15	0.70	0.70	1.06	0.00

Table A.1. Beams other than RBS (continue)

Test ID	Reference	Con. Type	Test Conf.	Beam Size	K (kips-in/rad)	M_y (kips-in)	θ_p (rad)	θ_{pc} (rad)	A_s	A_k	M_c/M_y	κ
81	Cheng, C. T., et al. (2007)	WUF-B-J	STBWS	H450X200X9X14	800000	7800	0.025	0.15	0.70	0.70	1.06	0.00
82	Cheng, C. T., et al. (2007)	T-J (T @ E)	STBWS	H450X200X9X14	662702.7	9100	0.045	0.15	0.55	0.35	1.00	0.00
83	Cheng, C. T., et al. (2007)	T-J (T @ E)	STBWS	H450X200X9X14	662702.7	7000	0.045	0.15	0.55	0.35	1.00	0.00
84	Cheng, C. T., et al. (2007)	WUF-B-T-J	SSBWS	H450X200X9X14	600000	8800	0.06	0.12	1.00	1.00	1.20	0.36
85	Cheng, C. T., et al. (2007)	WUF-B-T-J	SSBWS	H450X200X9X14	600000	8800	0.06	0.16	1.30	1.10	1.25	0.36
86	Murray, T., and Sumner, E., (1999)	BUEP	N2TBWS	W24x68	1409800	13090	0.014	0.09	0.70	0.70	1.05	0.70
87	Murray, T., and Sumner, E., (1999)	BUEP	SSBNS	W24x68	859800	11300	0.014	0.09	0.80	0.80	1.05	0.70
88	Murray, T., and Sumner, E., (1999)	BUEP	SSBNS	W30x99	1597115	20500	0.013	0.15	0.60	0.60	1.05	0.70
89	Murray, T., and Sumner, E., (1999)	BSEP	SSBNS	W30x99	1674419	20000	0.011	0.085	0.60	0.60	1.05	0.70
90	Murray, T., and Sumner, E., (1999)	BSEP	SSBNS	W36x150	2803105	39000	0.016	0.1	0.60	0.60	1.05	0.60
91	Ricles, J. M., et al. (2004)	MT1	N2TBNS	W24X62	1200000	7900	0.04	0.14	2.00	2.00	1.15	0.45
92	Ricles, J. M., et al. (2004)	MDST	N2TBNS	W24X62	1200000	7000	0.037	0.18	3.00	3.00	1.20	0.45
93	Ricles, J. M., et al. (2004)	MDST-w/o S	N2TBNS	W24X62	1200000	7300	0.022	0.3	1.15	1.15	1.08	0.30
94	Ricles, J. M., et al. (2004)	TB	N2TBNS	W24X62	1200000	7300	0.021	0.27	1.30	1.30	1.08	0.35
95	Ricles, J. M., et al. (2004)	TB	N2TBNS	W24X62	1200000	7300	0.022	0.24	1.60	1.60	1.08	0.35
96	Shin, K.J., et al. (2008)	TS-W-K	SSBNS	H506X201X11X19	780000	8650	0.043	0.24	1.80	1.50	1.11	0.30
97	Shin, K.J., et al. (2008)	TS-W-K	SSBNS	H506X201X11X19	685056	7500	0.044	0.4	0.00	0.00	1.13	0.00
98	Shin, K.J., et al. (2008)	TS-W-K	SSBNS	H506X201X11X19	628246.6	8100	0.041	0.31	0.00	0.00	1.07	0.00
99	Allen, J., et al. (1996)	SSDA	SSBNS	W36x393	9989189	44550	0.029	0.24	0.00	0.00	1.08	0.00
100	Allen, J., et al. (1996)	SSDA	SSBNS	W36X280	10000000	45000	0.024	0.2	0.00	0.00	1.10	0.00
101	Allen, J., et al. (1996)	SSDA	SSBNS	W36X280	9458333	45000	0.025	0.25	0.00	0.00	1.08	0.00
102	Allen, J., et al. (1996)	SSDA	SSBNS	W36X150	12223667	24500	0.016	0.12	0.60	0.60	1.08	0.45
103	Allen, J., et al. (1996)	SSDA	SSBNS	W36X150	25000000	31000	0.018	0.17	0.53	0.53	1.08	0.42
104	Allen, J., et al. (1996)	SSDA	SSBNS	W33X141	12500000	26200	0.016	0.11	0.51	0.51	1.08	0.42
105	E-Defense (2007)	WUF-W-J	SSBWS	R-400X200X8X13	49360	550	0.024	0.17	1.10	1.00	1.05	0.00

Table A.2. Connection Type

Connection Type	Notation
Welded unreinforced flanges-Bolted Web	WUF-B
Welded unreinforced flanges-Welded Web	WUF-W
Free Flange	FF
Reduced Beam Section	RBS
Bolted Flange Plate	BFP
Bolted Unstiffened End Plate	BUEP
Bolted Stiffened End Plate	BSEP
Welded Flange Plate	WFP
Welded Flange Plate – Free Flange	WFPFF
Double Split Tee	DST
Slotted Web Connection	SSDA
Bolted Bracket connection	BB
Welded Stiffened End Plate	WSEP
Welded unreinforced flanges-Bolted Web, Welded Plate	WUF-BW
Ribs- Welded unreinforced flanges-Bolted Web	R-WUF-B
Bottom Haunch - Welded unreinforced flanges-Bolted Web	BH-WUF-B
Haunches - Welded unreinforced flanges-Bolted Web	H-WUF-B
Haunches – Bolted flanges-Bolted Web	H-BF-B
Haunches – Bolted flanges-Bolted Web, Bottom	BH-BF-B
Cover and Side Plate	MNH-SMTF
Japanese Welded unreinforced flanges-Welded Web	WUF-W-J
Japanese Welded – Bolted Web	WUF-B-J
Japanese Welded – Bolted Web – Tapered Flange	WUF – B – T - J
Korean – T – Stiffener – Welded	TS – W - K
Extended tee	T1
Extended tee with taper	MT1
Bolted split – tee with shear tab	MDST-ST
Bolted split – tee without shear tab	MDST
Tee-Bolted	TB

Table A.3. Test configuration description for steel beams

Notation	Test Configuration Description
SSBNS	Standard, single beam, no slab
STBNS	Standard, two beams, no slab
N1SBNS	Non Standard-1, column end fixed, single beam, no slab
N1TBNS	Non Standard-1, column end fixed, two beams, no slab
N2SBNS	Non standard 2, single beam, no slab
N2TBNS	Non standard 2, two beams, no slab
N3SBNS	Non standard 3, column stub, single beam no slab
DC	Double curvature assembly

Table A.4. Beams with RBS

Test ID	Reference	Con. Type	Test Conf.	Beam Size	$K(kips-in/rad)$	$M_y (kips-in)$	$\theta_p (rad)$	$\theta_{pc} (rad)$	A_s	A_x	M_c/M_y	κ
1	Uang et al. (2000a)	WUF-B-RBS	SSBNS	W30x99	2790995	15200	0.025	0.160	0.90	0.80	1.11	0.41
2	Uang et al. (2000a)	WUF-B-RBS	SSBNS	W30x99	2700000	15800	0.028	0.200	0.80	0.70	1.11	0.41
3	Uang et al. (2000a)	WUF-B-RBS	SSBNS	W30x99	2500000	14000	0.025	0.240	0.70	0.50	1.11	0.00
4	Uang et al. (2000a)	WUF-B-RBS	SSBNS	W30x99	2790995	15300	0.026	0.200	1.10	1.10	1.11	0.41
5	Uang et al. (2000b)	WUF-B-RBS	SSBNS	W36x150	7460000	30500	0.020	0.210	0.90	0.70	1.15	0.45
6	Uang et al. (2000b)	WUF-B-RBS	SSBNS	W24x62	1011000	7400	0.019	0.170	0.80	0.80	1.10	0.37
7	Uang et al. (2000b)	RBS	SSBNS	W36x150	7412000	30000	0.013	0.090	0.70	0.50	1.10	0.44
8	Uang et al. (2000b)	RBS	SSBNS	W36x150	7412000	30000	0.015	0.140	0.80	0.60	1.15	0.46
9	Engelhardt et al. (2000)	RBS	N2TBNS	W36x150	8890000	20000	0.025	0.320	1.20	1.20	1.10	0.40
10	Engelhardt et al. (2000)	RBS	N2TBNS	W36x150	8890000	20000	0.025	0.320	1.20	1.20	1.10	0.40
11	Tremblay et al. (1997)	RBS	SSBWS	W21x62	840000	5340	0.045	0.220	0.00	0.00	1.08	0.00
12	Tremblay et al. (1997)	RBS	SSBWS	W21x62	700000	5200	0.031	0.210	1.80	1.60	1.10	0.32
13	Herrick, Smith-Emery. (1996)	RBS	nr	W27x94	924000	9160	0.029	0.170	1.40	1.40	1.07	0.00
14	Ivankiw and Carter (1996)	RBS	nr	W30x99	550000	11500	0.031	0.130	0.80	0.70	1.10	0.35
15	Ivankiw and Carter (1996)	RBS	nr	W30x99	550000	11500	0.031	0.130	0.80	0.70	1.10	0.35
16	Herrick, Smith-Emery. (1996)	RBS	nr	W33x169	2200000	18100	0.023	0.240	2.00	1.50	1.10	0.00
17	Herrick, Smith-Emery. (1996)	RBS	nr	W36x135	1800000	17500	0.022	0.210	1.20	0.90	1.10	0.00
18	Herrick, Smith-Emery. (1996)	RBS	nr	W36x135	1800000	17000	0.018	0.170	1.20	0.90	1.10	0.00
19	Ivankiw and Carter (1996)	RBS	nr	W36x150	955000	21600	0.025	0.300	0.90	0.90	1.10	0.00
20	Engelhardt et al. (1996)	RBS	N3SBNS	W36x194	2250000	28500	0.025	0.310	1.80	1.80	1.10	0.00
21	Engelhardt et al. (1996)	RBS	N3SBNS	W36x170	2240000	29800	0.029	0.290	1.40	1.10	1.10	0.31
22	Engelhardt et al. (1996)	RBS	N3SBNS	W36x150	2240000	20200	0.020	0.260	1.40	1.10	1.08	0.31
23	Anderson and Duan (1998)	RBS	SSBNS	W21x68	700000	8900	0.021	0.230	0.00	0.00	1.12	0.00
24	Popov et al. (1998)	RBS	N1SBNS	W36x135	2450000	20000	0.019	0.150	0.90	0.70	1.10	0.38
25	Popov et al. (1997)	RBS	N3SBNS	W33x130	2220000	17400	0.018	0.170	1.00	0.80	1.08	0.46
26	Popov et al. (1997)	RBS	N3SBNS	W33x130	2220000	18000	0.020	0.170	1.00	0.80	1.09	0.43
27	Popov et al. (1997)	RBS	N3SBNS	W36x194	3510000	34500	0.024	0.300	2.20	2.00	1.06	0.38
28	Tsai and Chen (2000)	RBS	N3SBNS	H600X200 X11X17	837013	24900	0.033	0.35	2.20	2.00	1.07	0.00

Table A.4. Beams with RBS (continue)

Test ID	Reference	Con. Type	Test Conf.	Beam Size	$K(kips-in/rad)$	$M_y(kips-in)$	$\theta_p(rad)$	$\theta_{pc}(rad)$	A_s	A_κ	M_c/M_y	κ
29	Tsai and Chen (2000)	RBS	N3SBNS	H600X200 X11X17	837013	22900	0.035	0.35	0.00	0.00	1.07	0
30	Tsai and Chen (2000)	RBS	N3SBNS	H600X200 X11X17	837013	23100	0.034	0.25	0.00	0.00	1.1	0.55
31	Tsai and Chen (2000)	RBS	N3SBNS	H600X200 X11X17	837013	22900	0.036	0.24	1.70	1.70	1.1	0.45
32	Tsai and Chen (2000)	RBS	N3SBNS	H600X200 X11X17	837013	27500	0.038	0.24	2.00	1.80	1.10	0.38
33	Zekioglu et al. (1996)	RBS	SSBNS	W27x178	1800000	23200	0.035	0.260	2.00	2.00	1.08	0.00
34	Zekioglu et al. (1996)	RBS	SSBNS	W27x178	1800000	27500	0.035	0.350	2.00	1.80	1.06	0.00
35	Zekioglu et al. (1996)	RBS	SSBNS	W36x150	2000000	24500	0.022	0.230	0.90	0.70	1.06	0.00
36	Zekioglu et al. (1996)	RBS	SSBNS	W33x152	4000000	34000	0.021	0.240	0.90	0.70	1.06	0.38
37	Zekioglu et al. (1996)	RBS	SSBNS	W33x152	4000000	32500	0.021	0.230	0.90	0.70	1.06	0.34
38	Suita et al. (1998)	RBS	SSBNS	WF- 500x200x 10x16	750000	5800	0.042	0.380	1.80	1.80	1.08	0.45
39	Suita et al. (1998)	RBS	SSBNS	WF- 500x200x 10x16	750000	5600	0.041	0.320	1.30	1.30	1.08	0.47
40	Suita et al. (1998)	RBS	SSBNS	WF- 500x200x 10x16	750000	6200	0.038	0.360	1.40	1.00	1.08	0.52
41	Suita et al. (1998)	RBS	SSBNS	WF- 500x200x 10x16	900000	5900	0.039	0.280	1.50	1.00	1.08	0.50
42	Suita et al. (1998)	RBS	SSBNS	WF- 500x200x 10x16	900000	6250	0.040	0.320	1.71	1.65	1.08	0.55
43	Lee et al. (2005)	RBS	N3SBNS	H700x300 x13x24	2000000	18000	0.035	0.280	2.00	1.80	1.12	0.00
44	Lee et al. (2005)	RBS	N3SBNS	H700x300 x13x24	2000000	18000	0.031	na	0.00	0.00	1.12	0.00
45	Lee et al. (2005)	RBS	N3SBNS	H700x300 x13x24	2000000	13000	0.013	na	0.00	0.00	1.25	0.00
46	Lee et al. (2005)	RBS	N3SBNS	H700x300 x13x24	2000000	16000	0.015	na	0.00	0.00	1.11	0.00
47	Lee et al. (2005)	RBS	N3SBNS	H600x200 x11x17	807000	7900	0.028	0.180	1.30	1.30	1.10	0.00
48	Lee et al. (2005)	RBS	N3SBNS	H600x200 x11x17	780000	7900	0.024	0.165	1.00	0.80	1.10	0.30
49	Lee et al. (2005)	RBS	N3SBNS	H600x200 x11x17	950000	8100	0.025	0.260	1.00	0.90	1.11	0.35
50	Lee et al. (2005)	RBS	N3SBNS	H606x201 x12x20	1000000	9600	0.026	0.220	1.40	1.40	1.11	0.00
51	Shin et al. (2008)	TS-W-K	SSBNS	H506X201 X11X19	685056	7500	0.044	0.4	0.00	0.00	1.13	0
52	Shin et al. (2008)	TS-W-K	SSBNS	H506X201 X11X19	628247	8100	0.041	0.31	0.00	0.00	1.07	0

Table A.5. Tubular hollow square column sections

Test ID	Reference	Test Conf.	Column	K (kips-in/rad)	M_y (kips-in)	θ_p (rad)	θ_{pc} (rad)	A	M_c/M_y	κ
1	Tsuda and Matsui, (1998)	CF	HSS-100x100x4.5	10000	225	0.024	0.15	0.00	1.05	0.00
2	Tsuda and Matsui, (1998)	CF	HSS-100x100x4.5	12000	209	0.015	0.09	0.00	1.05	0.00
3	Tsuda and Matsui, (1998)	CF	HSS-100x100x4.5	12000	165	0.009	0.02	0.00	1.13	0.00
4	Tsuda and Matsui, (1998)	CF	HSS-150x150x5.8	45000	700	0.024	0.14	0.00	1.14	0.00
5	Tsuda and Matsui, (1998)	CF	HSS-150x150x5.8	45000	680	0.013	0.07	0.00	1.11	0.00
6	Tsuda and Matsui, (1998)	CF	HSS-150x150x5.8	45000	700	0.017	0.11	0.00	1.04	0.00
7	Tsuda and Matsui, (1998)	CF	HSS-100x100x3	10000	165	0.020	0.14	0.00	1.04	0.00
8	Tsuda and Matsui, (1998)	CF	HSS-100x100x3	10000	145	0.012	0.09	0.00	1.05	0.00
9	Tsuda and Matsui, (1998)	CF	HSS-150x150x4.3	38000	520	0.013	0.12	0.00	1.05	0.00
10	Tsuda and Matsui, (1998)	CF	HSS-150x150x4.3	38000	430	0.011	0.04	0.00	1.05	0.45
11	Tsuda and Matsui, (1998)	CF	HSS-150x150x4.3	40000	375	0.009	0.02	0.00	1.05	0.50
12	Tsuda and Matsui, (1998)	CF	HSS-150x150x3.2	27000	250	0.009	0.12	0.00	1.05	0.00
13	Tsuda and Matsui, (1998)	CF	HSS-150x150x3.2	27000	180	0.014	0.03	0.00	1.10	0.00
14	Tsuda and Matsui, (1998)	CF	HSS-150x150x3.2	28000	230	0.007	0.03	0.00	1.08	0.44
15	Tsuda and Matsui, (1998)	CF	HSS-150x150x3.2	28000	210	0.011	0.02	0.00	1.06	0.75
16	Tsuda and Matsui, (1998)	CF	HSS-150x150x3.2	28000	90	0.005	0.02	0.00	1.06	0.00
17	Tsuda and Matsui, (1998)	CF	HSS-150x150x3.2	30000	240	0.007	0.03	0.00	1.02	0.00
18	Tsuda and Matsui, (1998)	CF	HSS-150x150x3.2	30000	130	0.004	0.01	0.00	1.08	0.00
19	Tsuda and Matsui, (1998)	CF	HSS-150x150x3.2	25000	245	0.016	0.14	0.00	1.02	0.00
20	Tsuda and Matsui, (1998)	CF	HSS-150x150x3.2	25000	190	0.014	0.03	0.00	1.06	0.00
21	Tsuda and Matsui, (1998)	CF	HSS-150x150x2.5	20000	175	0.008	0.10	0.00	1.01	0.00
22	Tsuda and Matsui, (1998)	CF	HSS-150x150x2.5	25000	98	0.005	0.03	0.00	1.01	0.00
23	Tsuda and Matsui, (1998)	CF	HSS-150x150x2.0	20000	108	0.005	0.05	0.00	1.01	0.00
24	Tsuda and Matsui, (1998)	CF	HSS-150x150x2.0	15100	47	0.005	0.01	0.00	1.00	0.00
25	Tsuda and Matsui, (1998)	CF	HSS-150x150x1.6	20100	35	0.005	0.02	0.00	1.05	0.00

Table A.5. Tubular hollow square column sections (continue)

Test ID	Reference	Test Conf.	Column	K (kips-in/rad)	M_y (kips-in)	θ_p (rad)	θ_{pc} (rad)	A	M_c/M_y	κ
26	Tsuda and Matsui, (1998)	CF	HSS-150x150x3.2	30200	305	0.011	0.12	0.00	1.03	0.00
27	Tsuda and Matsui, (1998)	CF	HSS-150x150x3.2	30200	225	0.010	0.04	0.00	1.04	0.00
28	Tsuda and Matsui, (1998)	CF	HSS-150x150x2.7	25100	230	0.009	0.15	0.00	1.04	0.00
29	Tsuda and Matsui, (1998)	CF	HSS-150x150x2.7	20200	170	0.004	0.06	0.00	1.04	0.00
30	Sugiyama and Igarashi, (1986)	DC	HSS-100x100x3.2	13500	160	0.015	0.09	0.00	1.04	0.00
31	Sugiyama and Igarashi, (1986)	DC	HSS-100x100x3.2	17500	135	0.010	0.06	0.00	1.06	0.00
32	Sugiyama and Igarashi, (1986)	DC	HSS-100x100x4.5	18500	235	0.024	0.35	0.00	1.07	0.00
33	Sugiyama and Igarashi, (1986)	DC	HSS-100x100x4.5	20200	212	0.014	0.07	0.00	1.06	0.00
34	Sugiyama and Igarashi, (1986)	DC	HSS-100x100x3.2	10000	127	0.019	0.28	0.00	1.02	0.00
35	Sugiyama and Igarashi, (1986)	DC	HSS-100x100x3.2	8500	135	0.009	0.21	0.00	1.04	0.00
36	Sugiyama and Igarashi, (1986)	DC	HSS-100x100x3.2	8000	142	0.011	0.21	0.00	1.04	0.00
37	Sugiyama and Igarashi, (1986)	DC	HSS-100x100x4.5	13000	190	0.025	0.33	0.00	1.03	0.00
38	Sugiyama and Igarashi, (1986)	DC	HSS-100x100x4.5	10000	203	0.030	0.27	0.00	1.02	0.00
39	Kouichi and Yamada, (1984)	DC	HSS-125x125x3.2	35000	431	0.012	0.20	0.00	1.04	0.00
40	Kouichi and Yamada, (1984)	DC	HSS-125x125x3.2	35000	400	0.009	0.09	0.00	1.02	0.00
41	Kouichi and Yamada, (1984)	DC	HSS-125x125x3.2	38400	340	0.007	0.06	0.00	1.02	0.00
42	Kouichi and Yamada, (1984)	DC	HSS-125x125x4.5	29400	600	0.022	0.15	0.00	1.03	0.00
43	Kouichi and Yamada, (1984)	DC	HSS-125x125x4.5	37300	530	0.016	0.08	0.00	1.04	0.00
44	Kouichi and Yamada, (1984)	DC	HSS-125x125x4.5	31350	270	0.009	0.02	0.00	1.04	0.00
45	Tsuda and Matsui, (1998)	CF	HSS-150x150x5.8	50000	700	0.010	0.13	0.15	1.03	0.29
46	Tsuda and Matsui, (1998)	CF	HSS-150x150x4.3	35000	521	0.010	0.13	0.17	1.06	0.29
47	Tsuda and Matsui, (1998)	CF	HSS-150x150x4.3	35000	430	0.003	0.06	0.06	1.01	0.21
48	Tsuda and Matsui, (1998)	CF	HSS-150x150x4.3	35000	380	0.003	0.02	0.03	1.00	0.21
49	Tsuda and Matsui, (1998)	CF	HSS-150x150x3.2	30000	214	0.004	0.03	0.02	1.03	0.30
50	Tsuda and Matsui, (1998)	CF	HSS-100x100x3.2	10300	119	0.015	0.25	0.77	1.08	0.65

Table A.5. Tubular hollow square column sections (continue)

Test ID	Reference	Test Conf.	Column	K (kips-in/rad)	M_y (kips-in)	θ_p (rad)	θ_{pc} (rad)	A	M_c/M_y	κ
51	Tsuda and Matsui, (1998)	CF	HSS-100x100x4.5	15500	175	0.022	0.34	16.32	1.09	0.60
52	Yamanaka and Yamada, (1984)	CF	HSS-125x125x4.5	35000	500	0.008	0.10	0.30	1.05	0.25
53	Yamanaka and Yamada, (1984)	CF	HSS-125x125x4.5	35000	500	0.017	0.04	0.10	1.05	0.39
54	Tsuji and Nakatsura, (1986)	DC	HSS-100x100x3.5	20000	200	0.022	0.20	0.50	1.05	0.25
55	Tsuji and Nakatsura, (1986)	DC	HSS-100x100x4.5	30000	291	0.020	0.22	0.66	1.07	0.27
56	Kita and Tsuji, (1986)	DC	HSS-125x125x4.5	40000	370	0.010	0.08	0.20	1.05	0.20
57	Kita and Tsuji, (1986)	DC	HSS-125x125x4.5	40000	370	0.010	0.08	0.17	1.05	0.20
58	Kita and Tsuji, (1986)	DC	HSS-125x125x4.5	40000	370	0.010	0.12	0.32	1.05	0.30
59	Kita and Tsuji, (1986)	DC	HSS-125x125x4.5	40000	300	0.006	0.05	0.20	1.01	0.28
60	Kita and Tsuji, (1986)	DC	HSS-125x125x4.5	40000	340	0.006	0.05	0.10	1.03	0.28
61	Kita and Tsuji, (1986)	DC	HSS-125x125x4.5	40000	340	0.007	0.05	0.10	1.03	0.28
62	Tsuji, and Nakatsura, (1986)	DC	HSS-100x100x3.5	80000	640	0.015	0.22	0.60	1.03	0.20
63	Tsuji, and Nakatsura, (1986)	DC	HSS-100x100x3.5	80000	640	0.021	0.25	0.86	1.06	0.39
64	Tsuji, and Nakatsura, (1986)	DC	HSS-100x100x4.5	80000	640	0.019	0.24	0.60	1.06	0.26
65	Tsuji, and Nakatsura, (1986)	DC	HSS-100x100x4.5	80000	640	0.022	0.26	0.98	1.06	0.35
66	Kurata et al. (2005)	CF	HSS-200x200x6.0	100000	1000	0.011	0.20	0.60	1.03	0.23
67	Kurata et al. (2005)	CF	HSS-200x200x6.0	95000	900	0.007	0.08	0.10	1.03	0.17
68	Kurata et al. (2005)	CF	HSS-200x200x9.0	110000	1600	0.021	0.30	0.57	1.06	0.35
69	Kurata et al. (2005)	CF	HSS-200x200x9.0	110000	1600	0.013	0.09	0.35	1.06	0.12
70	Kurata et al. (2005)	CF	HSS-200x200x12	100000	1000	0.025	0.20	1.36	1.03	0.23
71	Kurata et al. (2005)	CF	HSS-200x200x12	100000	1000	0.011	0.15	0.60	1.03	0.23

Table A.6. Test configuration description for tubular hollow square column sections

Notation	Test Configuration Description
CF	Cantilever beam with column flexible with possible rotation
DC	Double Curvature assembly

Table A.7. Reinforced concrete beams

Test ID	Reference	Test Conf.	K (kips-in/rad)	M_y (kips-in)	θ_p (rad)	A_s	A_c	M_c/M_y
1	Popov et al. (1972)	CR	1314079	9100	0.029	1.00	0.60	1.11
2	Bertero and Popov, (1975)	CP	206897	1600	0.037	1.40	1.40	1.12
3	Ma et al. (1976)	CP	179394	1500	0.042	1.50	1.50	1.15
4	Ma et al. (1976)	CP	176970	1540	0.052	2.50	2.50	1.17
5	Ma et al. (1976)	CP	235294	2000	0.046	2.50	2.50	1.15
6	Liddell et al. (2000)	CP	390909	2150	0.043	1.50	0.70	1.17
7	Liddell et al. (2000)	CP	206000	2180	0.045	1.40	0.70	1.10
8	Liddell et al. (2000)	CP	206364	2180	0.040	1.35	0.60	1.10
9	Liddell et al. (2000)	CP	307500	2100	0.023	1.30	1.30	1.10
10	Liddell et al. (2000)	CP	336316	2130	0.080	0.00	0.00	1.10
11	Liddell et al. (2000)	CP	477372	2180	0.034	0.80	0.50	1.15
12	Liddell et al. (2000)	CP	352000	2250	0.086	0.00	0.80	1.14
13	Liddell et al. (2000)	CP	252000	2180	0.030	0.00	0.00	1.12
14	Liddell et al. (2000)	CP	200000	2200	0.039	0.00	0.00	1.12
15	Liddell et al. (2000)	CP	200000	2200	0.039	0.00	0.00	1.12
16	Liddell et al. (2000)	CP	219524	2300	0.045	0.40	0.40	1.12
17	Liddell et al. (2000)	CP	219524	2330	0.041	0.00	0.00	1.12
18	Scribner and Wight, (1978)	CF	65000	580	0.074	3.00	3.00	1.40
19	Scribner and Wight, (1978)	CF	56418	640	0.078	1.30	1.10	1.25
20	Scribner and Wight, (1978)	CF	28500	420	0.070	3.00	3.00	1.10
21	Scribner and Wight, (1978)	CF	60896	690	0.060	2.50	2.50	1.15
22	Scribner and Wight, (1978)	CF	143333	2200	0.080	2.00	2.00	1.15
23	Scribner and Wight, (1978)	CF	157317	2100	0.085	1.40	1.20	1.35
24	Lee and Wight, (1976)	CF	25648	280	0.043	1.00	1.00	1.15
25	Lee and Wight, (1976)	CF	41333	310	0.064	2.20	1.00	1.27

Table A.7. Reinforced concrete beams (continue)

Test ID	Reference	Test Conf.	K (kips-in/rad)	M_y (kips-in)	θ_p (rad)	A_s	A_k	M_c/M_y
26	Lee and Wight, (1976)	CF	36364	343	0.073	1.70	0.70	1.23
27	Lee and Wight, (1976)	CF	30910	343	0.072	1.70	0.80	1.20
28	Lee and Wight, (1976)	CF	37714	330	0.070	2.50	2.00	1.20
29	Lee and Wight, (1976)	CF	37714	330	0.071	2.00	2.00	1.20
30	Lee and Ko, (2005)	CF	15143	180	0.060	3.00	1.80	1.17
31	Lee and Ko, (2005)	CF	200000	2690	0.055	3.00	2.00	1.17
32	Lee and Ko, (2005)	CF	12727	155	0.060	2.00	2.00	1.17
33	Lee and Ko, (2005)	CF	11688	155	0.062	2.40	2.00	1.15
34	Lee and Ko, (2005)	CF	164835	2500	0.057	1.50	1.20	1.12
35	Nmai and Darwin, (1984)	CP	115385	1300	0.035	1.00	1.00	1.25
36	Nmai and Darwin, (1984)	CP	135000	1350	0.035	1.00	1.00	1.25
37	Nmai and Darwin, (1984)	CP	155556	910	0.029	1.40	1.20	1.25
38	Nmai and Darwin, (1984)	CP	245455	890	0.032	2.30	2.30	1.32
39	Nmai and Darwin, (1984)	CP	245455	890	0.032	2.80	2.00	1.32
40	Nmai and Darwin, (1984)	CP	225743	950	0.031	1.50	0.80	1.25
41	Nmai and Darwin, (1984)	CP	201429	950	0.030	1.20	0.60	1.25
42	Vintzileou et al. (2007)	DE	29667	445	0.042	1.00	0.70	1.03
43	Vintzileou et al. (2007)	DE	34286	410	0.054	0.60	0.60	1.11
44	Vintzileou et al. (2007)	DE	25263	405	0.047	0.50	0.50	1.06
45	Vintzileou et al. (2007)	DE	33333	500	0.072	0.90	0.90	1.02
46	Vintzileou et al. (2007)	DE	33750	450	0.035	0.80	0.80	1.00
47	Vintzileou et al. (2007)	DE	12000	180	0.048	0.70	0.60	1.00

Table A.7. Reinforced concrete beams (continue)

Test ID	Reference	Test Conf.	K (kips-in/rad)	M_y (kips-in)	θ_p (rad)	A_s	A_k	M_c/M_y
48	Vintzileou et al. (2007)	DE	40519	530	0.043	0.70	0.30	1.00
49	Vintzileou et al. (2007)	DE	32667	490	0.051	0.70	0.70	1.00
50	Vintzileou et al. (2007)	DE	32667	462	0.046	0.60	0.40	1.00
51	Vintzileou et al. (2007)	DE	33648	420	0.035	0.60	0.40	1.00
52	Vintzileou et al. (2007)	DE	29333	445	0.041	0.70	0.50	1.05
53	Vintzileou et al. (2007)	DE	29333	450	0.053	0.60	0.60	1.22
54	Vintzileou et al. (2007)	DE	31090	570	0.054	0.90	0.90	1.00
55	Vintzileou et al. (2007)	DE	33333	480	0.052	0.70	0.60	1.00
56	Vintzileou et al. (2007)	DE	13609	205	0.051	0.80	0.80	1.00
57	Vintzileou et al. (2007)	DE	26786	460	0.054	0.90	0.90	1.00
58	Vintzileou et al. (2007)	DE	30769	565	0.050	2.20	2.20	1.00
59	Vintzileou et al. (2007)	DE	30000	440	0.058	1.00	1.00	1.00
60	Vintzileou et al. (2007)	DE	22222	480	0.030	0.60	0.60	1.03
61	Vintzileou et al. (2007)	DE	29706	650	0.045	1.00	1.00	1.00
62	Vintzileou et al. (2007)	DE	26706	256	0.037	1.00	1.00	1.04
63	Vintzileou et al. (2007)	DE	43000	510	0.048	1.00	1.00	1.00
64	Ehsani and Wight (1985)	CF	200000	2100	0.060	1.20	1.20	1.07
65	Ehsani and Wight (1985)	CF	73810	1600	0.085	1.40	1.40	1.00
66	Ehsani and Wight (1985)	CF	700000	1500	0.070	1.80	1.80	1.03
67	Ozebe and Saatcioglu, (1987)	CF	136364	2100	0.067	1.00	1.00	1.10

Table A.7. Reinforced concrete beams (continue)

Test ID	Reference	Test Conf.	K (kips-in/rad)	M_y (kips-in)	θ_p (rad)	A_s	A_κ	M_c/M_y
68	Krawinkler and Haselton, (2003)	DE	12000	120	0.068	0.00	0.00	1.15
69	Krawinkler and Haselton, (2003)	DE	12000	130	0.072	0.00	0.00	1.15
70	Krawinkler and Haselton, (2003)	DE	13500	135	0.055	0.00	0.00	1.05
71	Biddah et al. (1997)	CR	375000	4500	0.070	1.00	1.00	1.00
72	Kwan, and Billington, (2001)	CR	100000	870	0.050	1.00	1.00	1.04
73	Kwan, and Billington, (2001)	CR	100000	1100	0.050	0.80	0.60	1.04
74	Nadim et al. (1996)	CR	400000	6000	0.075	1.00	1.00	1.12
75	Nadim et al. (1996)	CR	500000	6200	0.067	1.40	1.40	1.12
76	Kokusho et al. (1976)	DE	250000	1120	0.085	0.00	0.00	1.25
77	Kokusho et al. (1976)	DE	253600	1150	0.090	0.00	0.00	1.24
78	Chung et al. (1977)	DE	12000	130	0.051	0.00	0.00	1.09
79	Chung et al. (1977)	DE	8500	80	0.060	0.00	0.00	1.25
80	Chung et al. (1977)	DE	12000	120	0.050	0.00	0.00	1.25
81	Ohkubo et al. (1980)	BRI	16000	90	0.024	0.10	0.10	1.01
82	Ohkubo et al. (1980)	BRI	18000	115	0.030	0.70	0.70	1.08
83	Ohkubo et al. (1980)	BRI	18000	110	0.030	0.10	0.10	1.00
84	Ohkubo et al. (1980)	BRI	20000	129	0.040	0.10	0.10	1.00
85	Ohkubo et al. (1980)	BRI	25000	147	0.047	0.30	0.30	1.00
86	Korenaga et al. (1986)	OHNO	75000	780	0.055	0.00	0.00	1.08
87	Taga et al. (1988)	BRI	40000	700	0.080	1.80	1.80	1.15
88	Honda et al. (1989)	OHNO	870000	8800	0.049	1.50	0.80	1.12
89	Ichikawa et al. (1988)	CF	90000	2000	0.070	2.30	2.30	1.04
90	Ichikawa et al. (1988)	CF	100000	2450	0.042	0.70	0.70	1.04

Table A.7. Reinforced concrete beams (continue)

Test ID	Reference	Test Conf.	K (kips-in/rad)	M_y (kips-in)	θ_p (rad)	A_s	A_κ	M_c/M_y
91	Nakamura et al. (1992)	OHNO	400000	4900	0.032	0.10	0.10	1.04
92	Nakamura et al. (1992)	OHNO	400000	4850	0.045	0.50	0.50	1.06
93	Ishikawa et al. (1992)	OHNO	145450	800	0.055	0.30	0.30	1.03
94	Kamura et al. (1993)	OHNO	130000	1450	0.050	0.30	0.30	1.06
95	Kamura et al. (1993)	OHNO	100000	1270	0.030	0.50	0.50	1.00
96	Akira et al. (1984)	OHNO	125000	1200	0.025	0.65	0.60	1.00
97	Akira et al. (1984)	OHNO	200000	1750	0.055	1.50	1.40	1.03
98	Akira et al. (1984)	OHNO	180000	1700	0.055	1.20	0.50	1.15
99	Muguruma et al. (1988)	BRI	125000	700	0.040	0.80	0.50	1.10
100	Muguruma et al. (1988)	BRI	100000	710	0.060	1.20	1.20	1.06

Table A.8. Test configuration description of reinforced concrete beams

Notation	Test Configuration Description
CR	Cantilever beam with column rigidly attached to frame
CF	Cantilever beam with column flexible with possible rotation
CP	Cantilever beam with column pre-stressed
DE	Double ended with assembly simply supported
DC	Double Curvature assembly
S2	Simply supported beam with two point loads
S1	Simply supported beam with one point load
BRI	Japanese double curvature assembly
OHNO	Japanese double curvature assembly

APPENDIX B

DESIGN DRAWINGS OF TEST FRAME USED FOR SHAKING TABLE EXPERIMENTATION

This appendix includes all the drawings of the 1:8 scale model used for shaking table experimentation. The design of the test frame was discussed in Chapter 5. Test evaluation of the shaking table collapse test series of the test frame was discussed in Chapter 7. A complete set of drawings of the test frame, mass simulator and lateral bracing systems of both substructures is available through the NEESCentral (<https://central.nees.org/>) repository.

Figure B1 includes the assembly drawing of the test frame together with a material list. Figures B2 to B15 include detailed drawings of all the individual parts of the test frame. All the drawings were designed in SolidWorks, (2004).

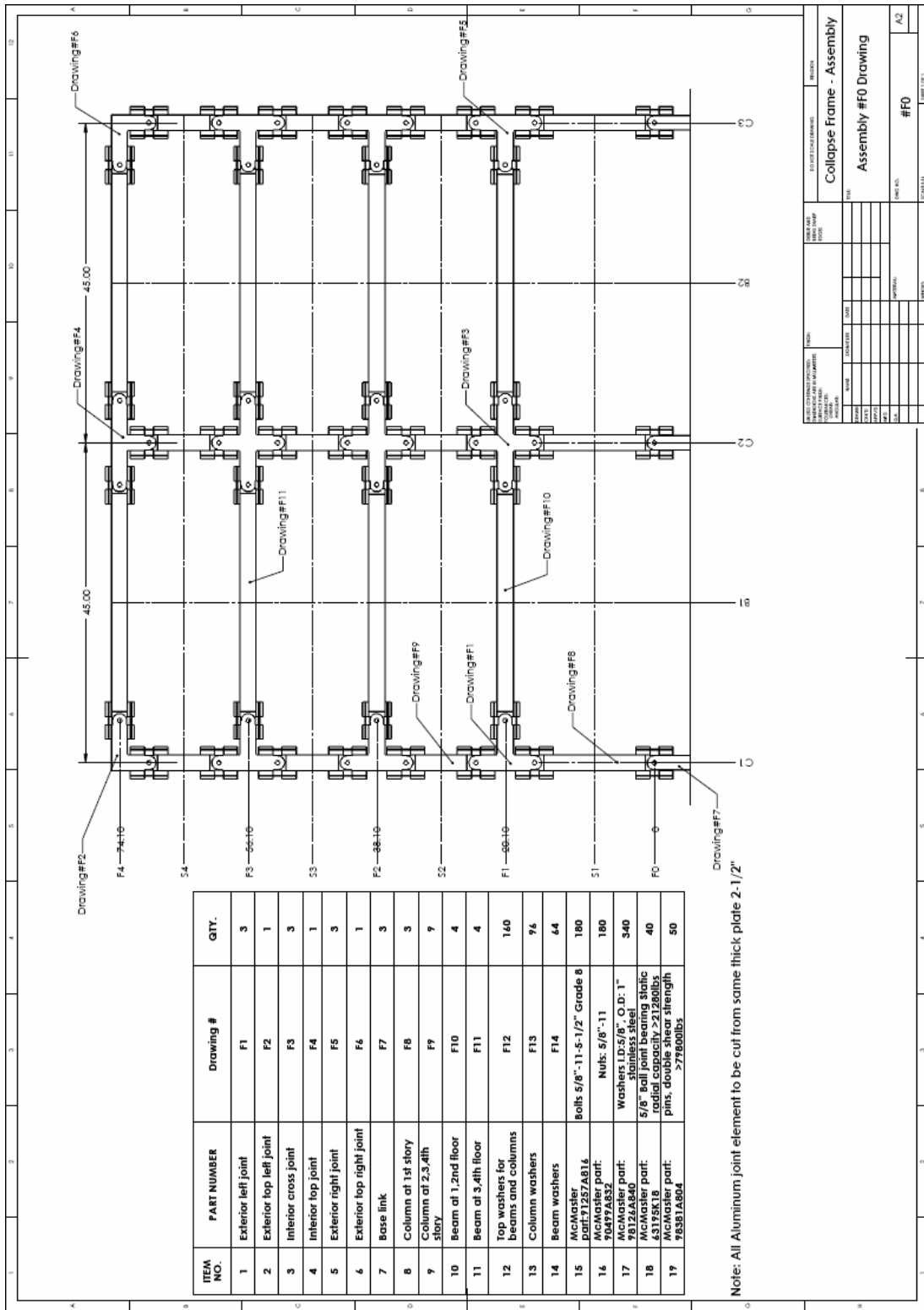


Figure B.1. Assembly drawing of test frame with material list

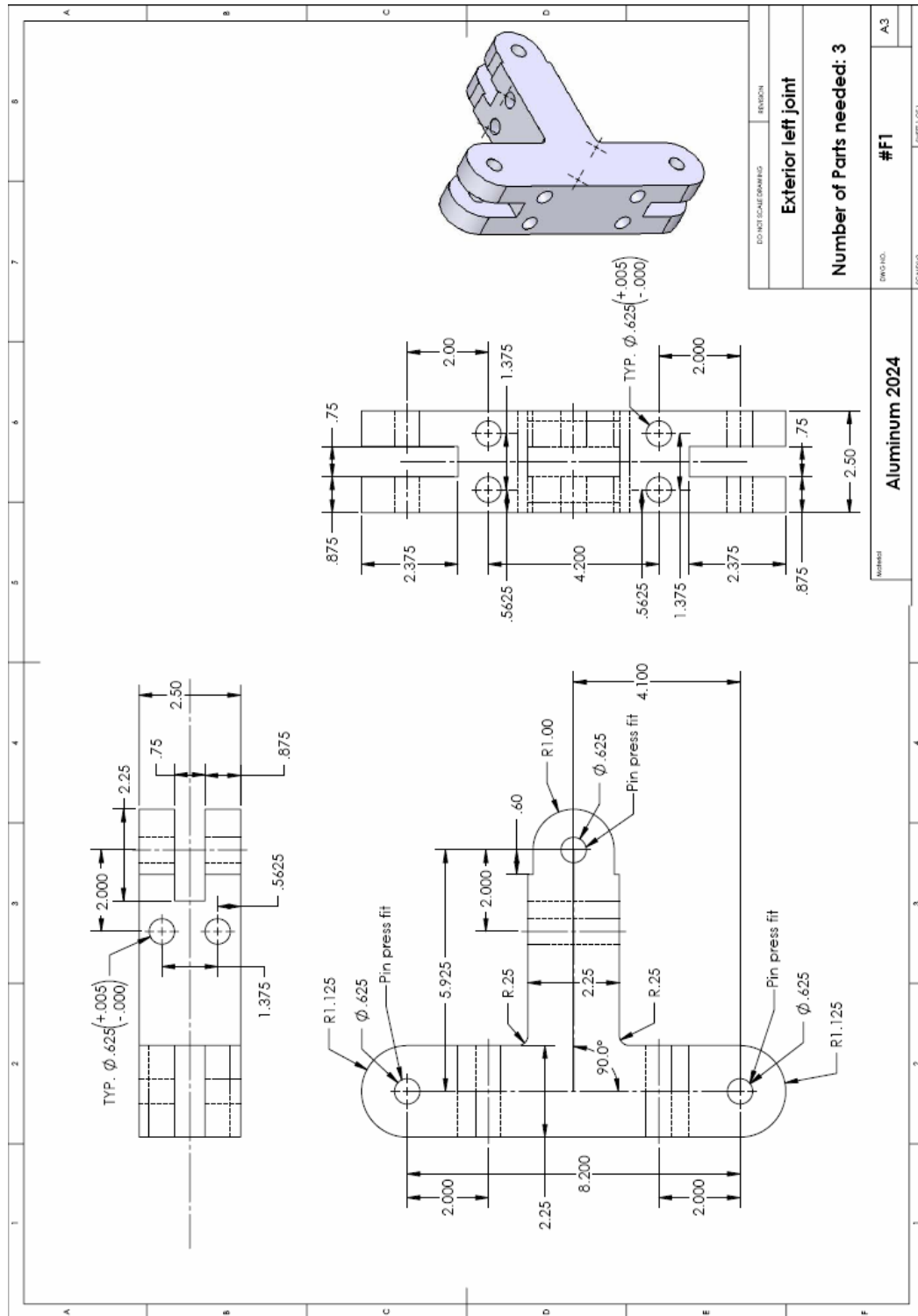


Figure B.2. Exterior left joint of test frame

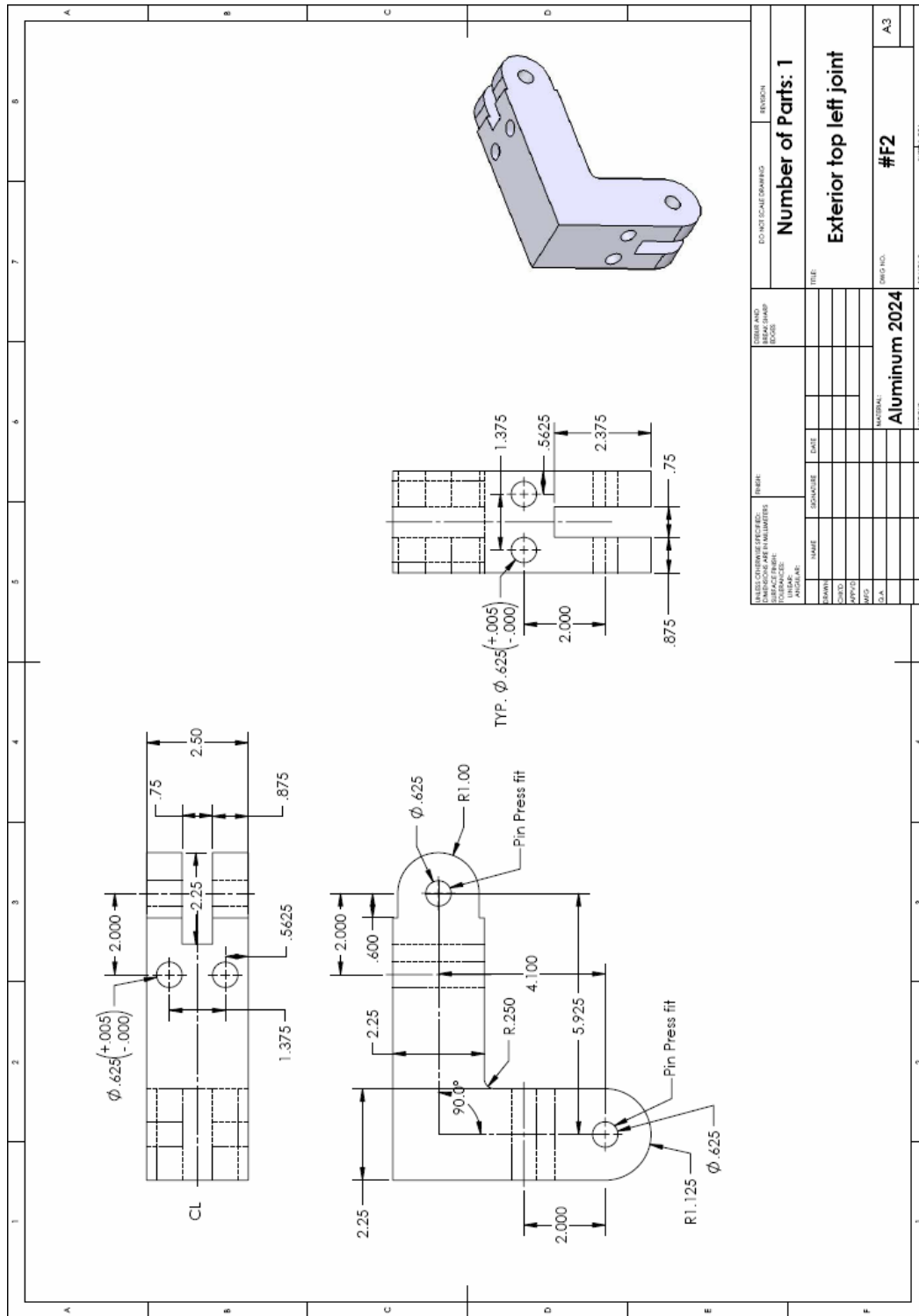


Figure B.3. Exterior top left joint of test frame

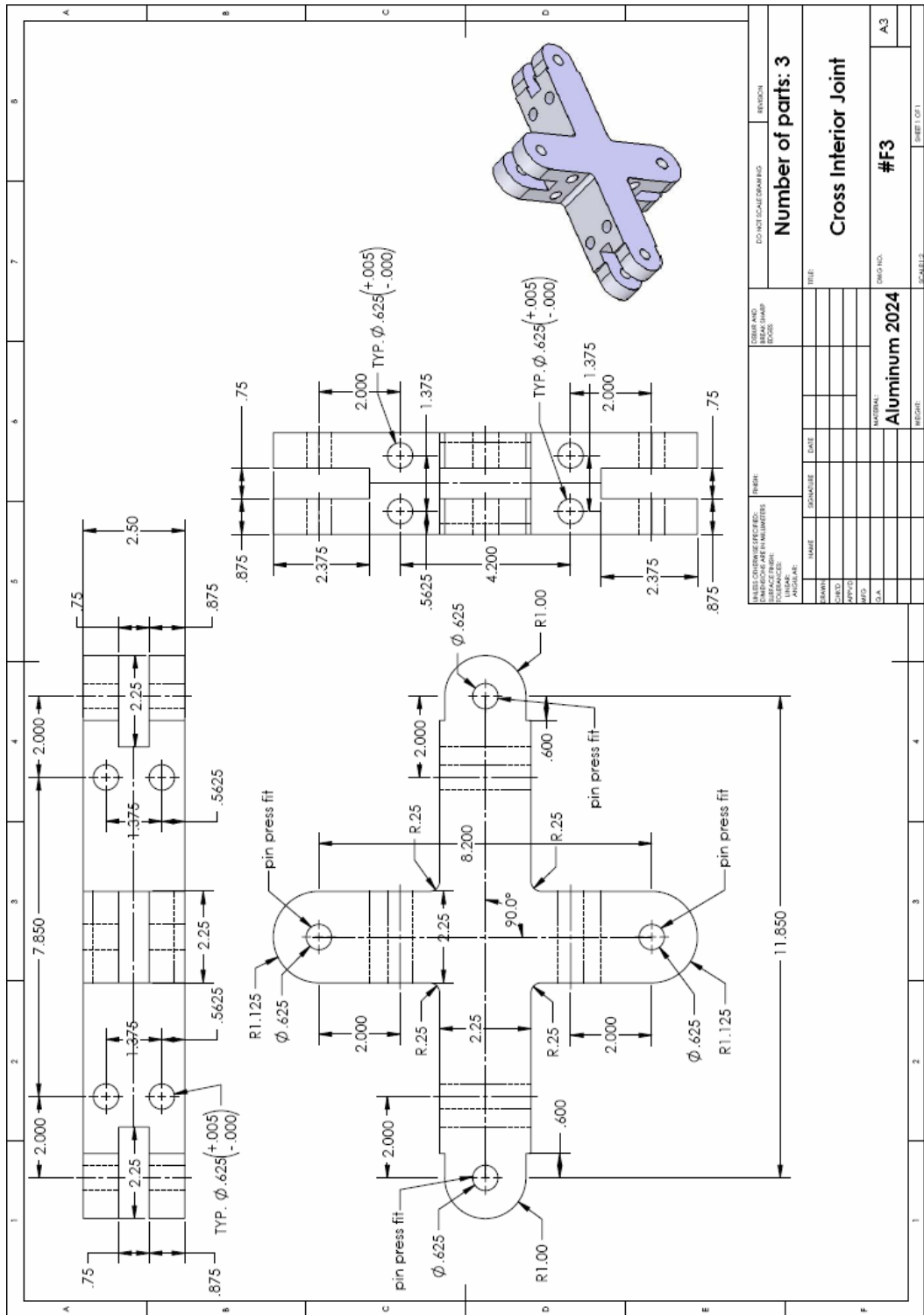


Figure B.4. Cross interior joint of test frame

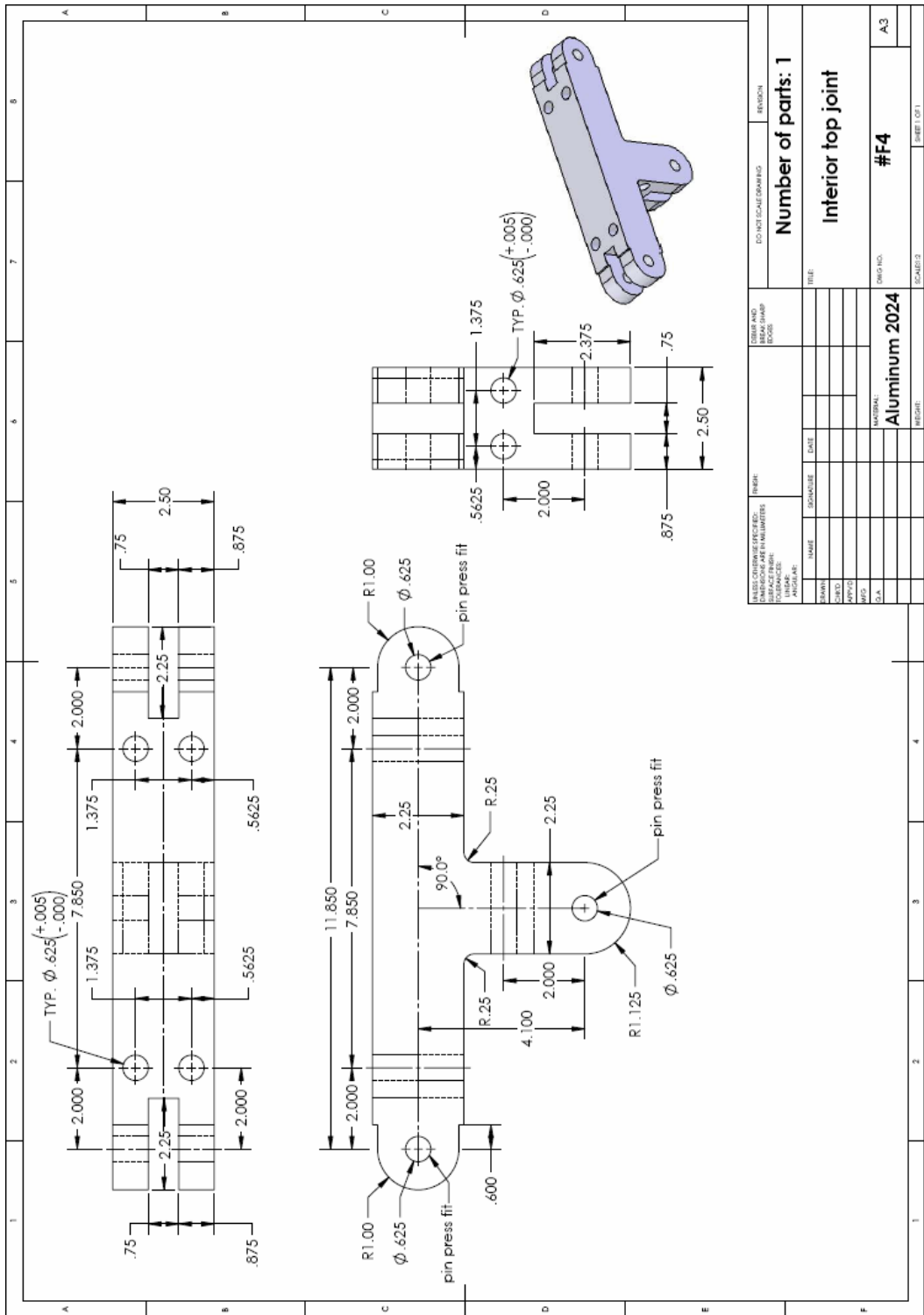


Figure B.5. Interior top joint of test frame

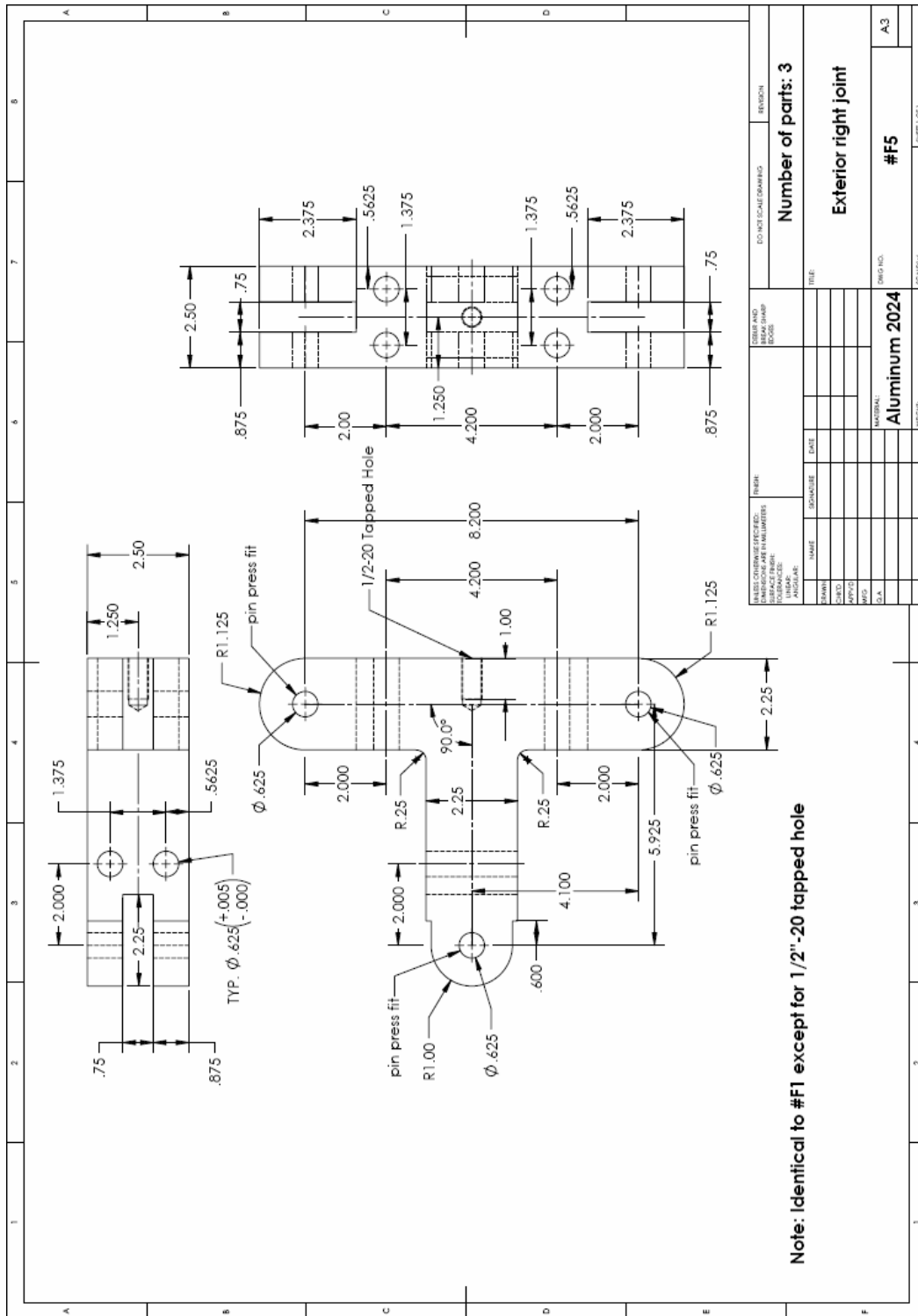


Figure B.6. Exterior right joint of test frame

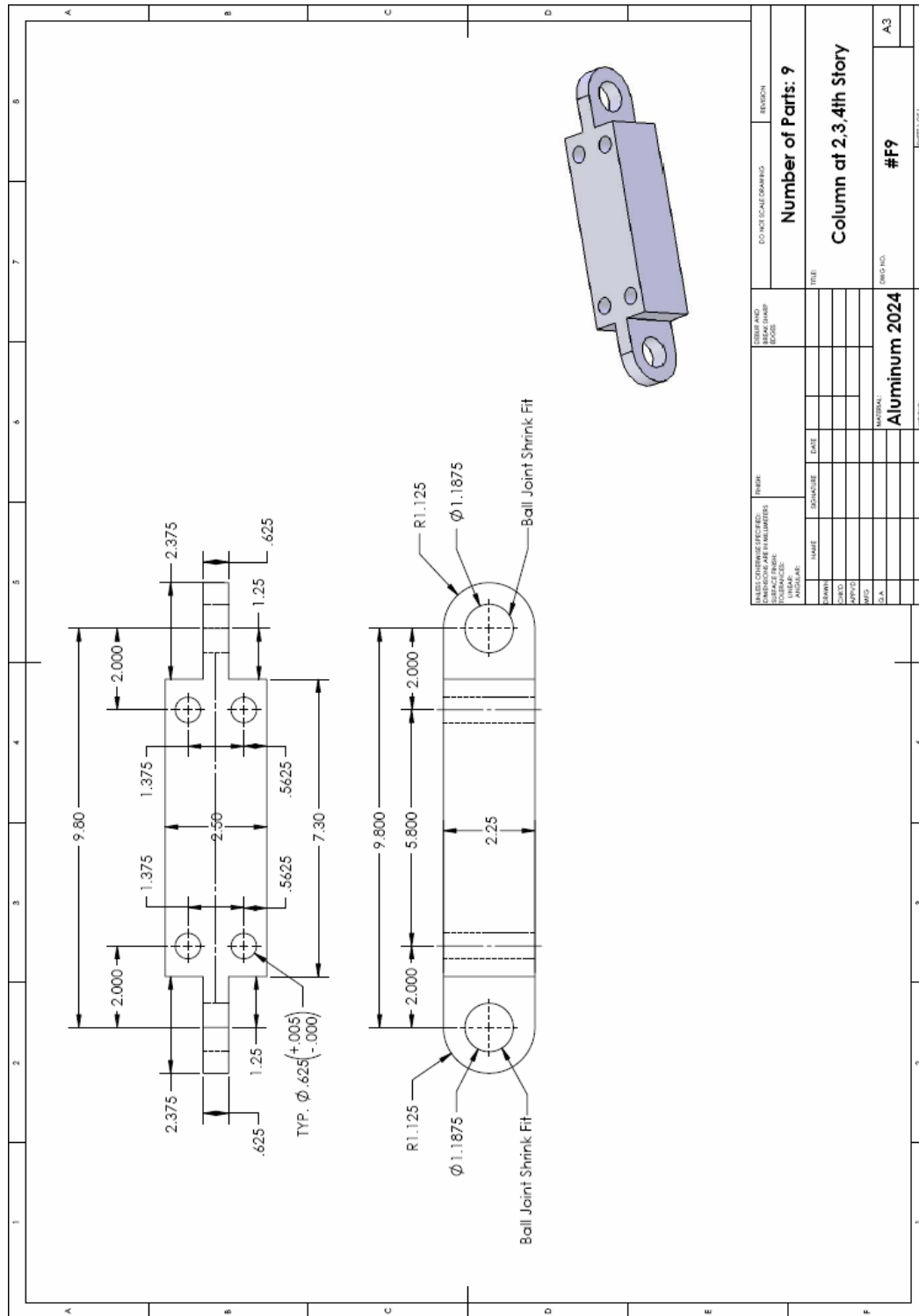


Figure B.10. Column of 2nd, 3rd and 4th story of test frame

DESIGN AND DRAWING NO.		REVISED	
DATE		BY	
DRAWN		CHECKED	
APPROVED		DATE	
SCALE		TITLE	
PROJECT		SHEET NO.	
MATERIAL		SHEET TOTAL	
Aluminum 2024		9	
PART NO.		#F9	
SHEET NO.		A3	

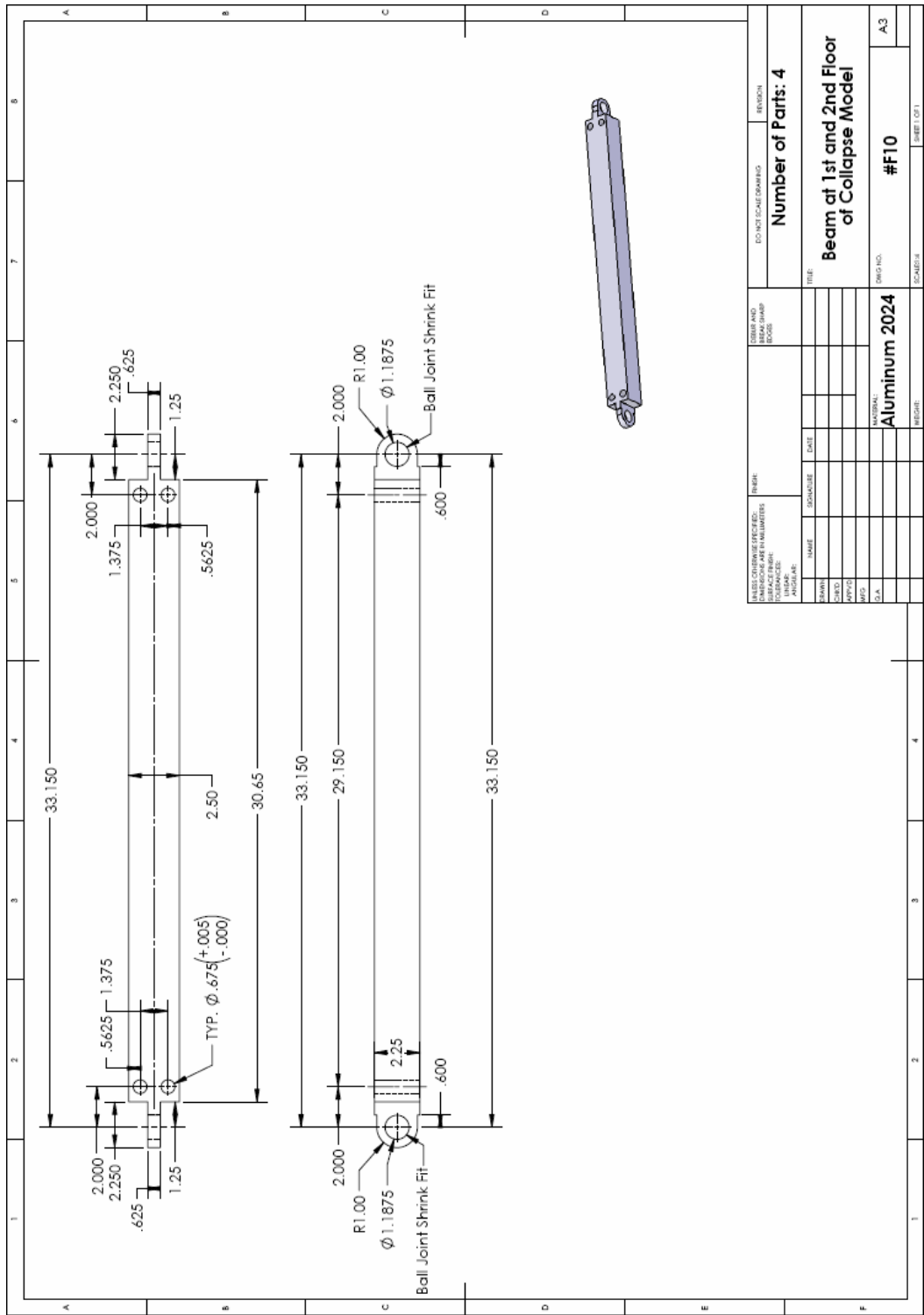


Figure B.11. Beam of 1st and 2nd floor of test frame

DESIGN AND CONSTRUCTION		DO NOT SCALE DRAWING		REVISION	
NUMBER OF PARTS		TITLE		SHEET NO.	
Number of Parts: 4		Beam of 1st and 2nd Floor of Collapse Model		#F10	
MATERIAL		DRAWING		A3	
Aluminum 2024					
DRAWN		CHECKED		DATE	
APPROVED		DATE		PROJECT	
SCALE		PROJECT		SHEET 1 OF 1	

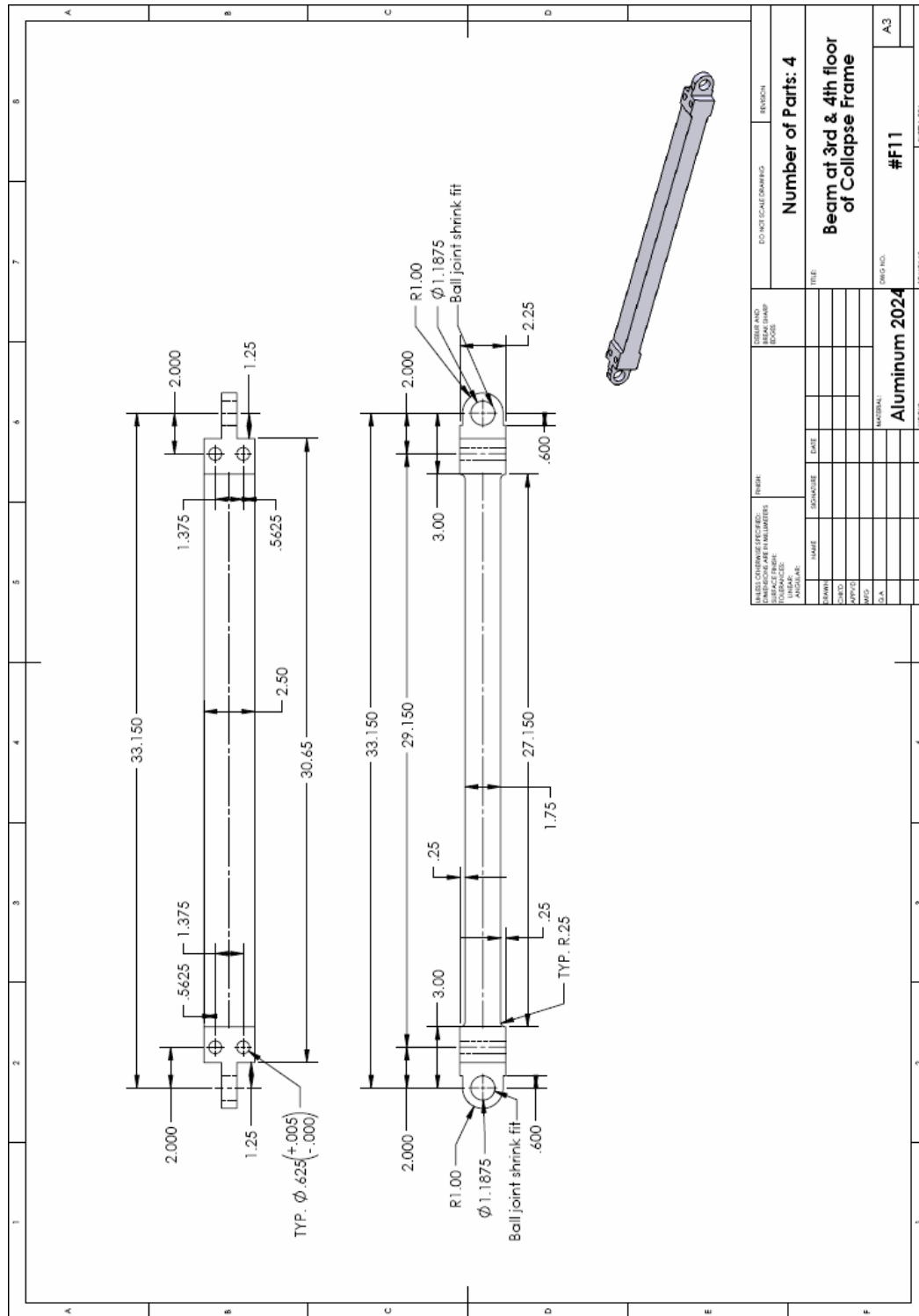


Figure B.12. Beam of 3rd and 4th floor of test frame

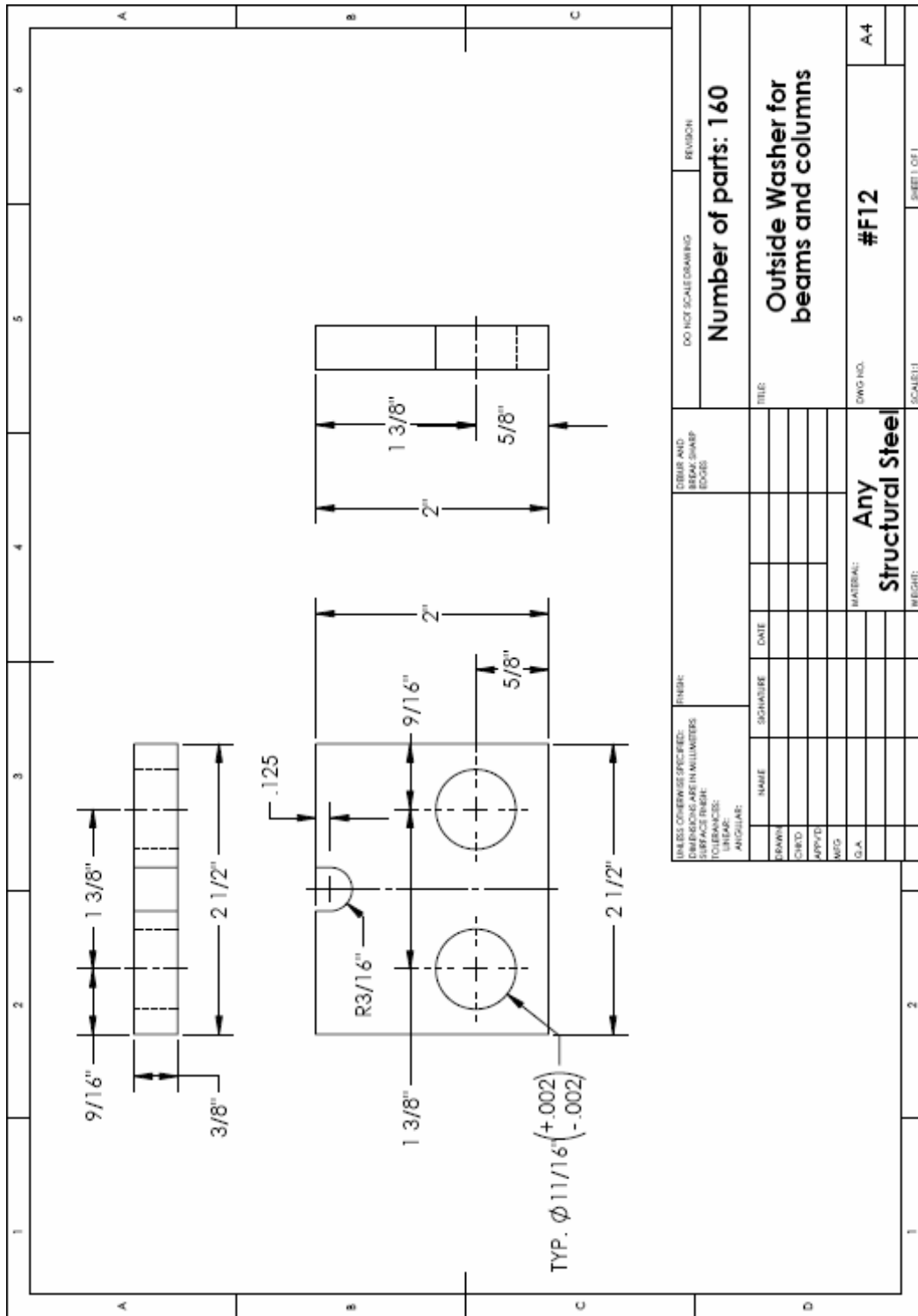


Figure B.13. Outside washer for beam and column plastic hinge elements of test frame

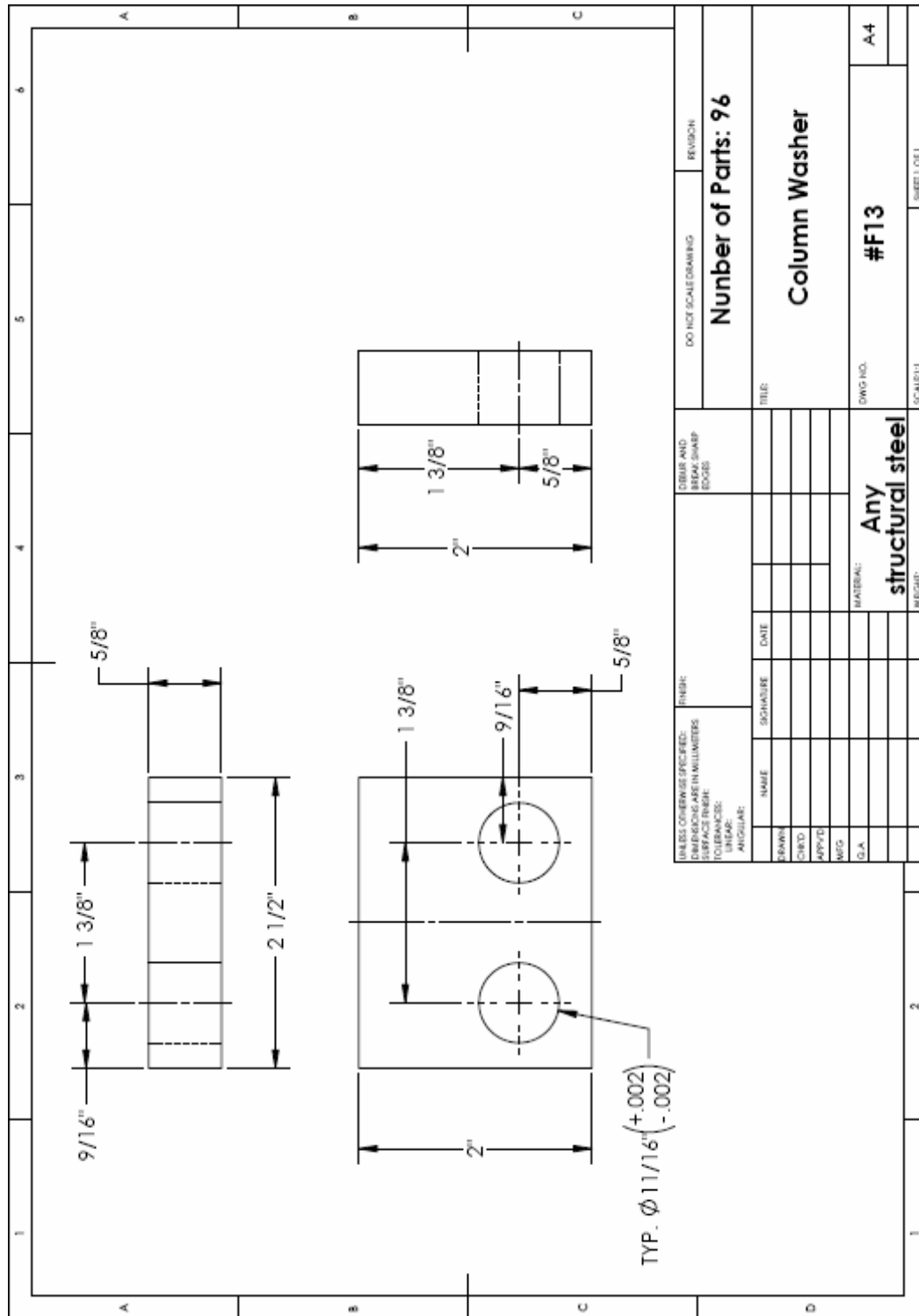


Figure B.14. Washer for column plastic hinge elements of test frame

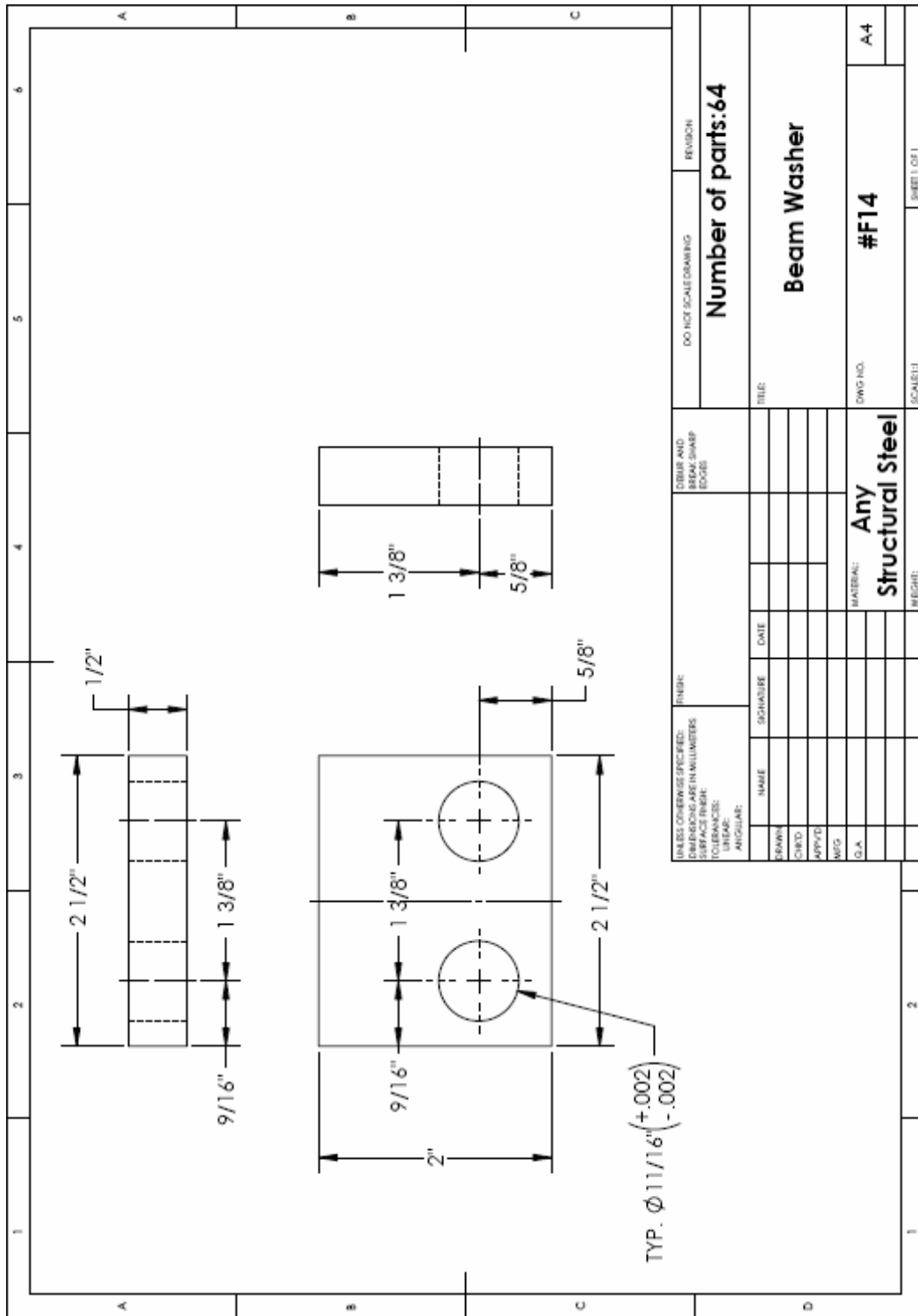


Figure B.15. Washer for beam plastic hinge elements of test frame

APPENDIX C

DEDUCED DATA FROM COMPONENT TESTS

This appendix includes selected monotonic and hysteretic plots of specimens that were tested as part of the testing program conducted at the laboratory of the John A. Blume Earthquake Engineering Center at Stanford University. The selected figures provide information related to Chapter 6 of this research that discusses about component tests of the model frame tested later on at the NEES facility at Buffalo. The hysteretic plots presented herein are categorized to:

1. tip load P versus tip displacement δ (P - δ_{tip}) used to obtain component elastic stiffness,
2. moment versus outer and inner strain (M_c - ε_{Outer} , M_c - ε_{Inner}) if available used to identify initiation of yielding and to correlate strain measurements with forces in the flange plates. The moment versus strain relationship for each plastic hinge served as a calibration for the shaking table collapse series in order to deduce flange plate forces, plastic hinge moments and beam and column shear forces, and
3. moment rotation over 1.5" length diagram (M_c - $\theta_{1.5''}$) of the plastic hinge element used to obtain the plastic hinge elastic rotational stiffness and the deterioration parameters for different plates and boundary conditions

C.1 Equivalent Modulus for Deduction of Flange Plate Forces

As mentioned in Chapter 7 it is not visible to measure directly forces and moments in components and connections during a shaking table test. In order to verify if (1) equilibrium

of moments was satisfied per joint of each test frame in the elastic range during shaking table experimentation and (2) validate story force measurements from the horizontal links that were acting as load cells, an equivalent modulus for deduction of flange plate forces was determined.

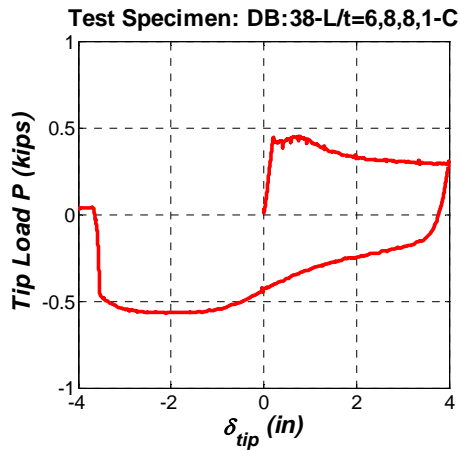
The equivalent modulus was obtained from the slope of the elastic range of the relationship between moment at centerline of the pin of the component tests versus outer and inner surface strain of flange plates for different flange plate widths w . Table C.1 summarizes the equivalent modulus for inner $E^{I-2}_{equiv.Inner}$ and outer $E^{I-2}_{equiv.Outer}$ surface of the flange plate for single and double flange plate configurations. The last three tests included in the same table are the three selected plastic hinge locations that were tested at Stanford after the completion of the shaking table collapse tests at Buffalo (see Section 6.7). As seen from the same table, specimens with single plates and approximately the same flange plate width with double plate specimens have an equivalent modulus approximately half compared to the one from double specimens. The small differences are attributed to the additional contribution to total deflection from the pin region for single plate specimens.

Selected moment–engineering strain ($M_c - \epsilon_{Inner}$, $M_c - \epsilon_{Outer}$) relationships for inner and outer flange plate surface of specimens with single and double flange plate configuration are presented in Figures C.1 to C.7 together with the tip load P versus tip displacement δ_{tip} , Moment – $\theta_{1.5''}$ and selected photos associated with critical points of the applied loading history.

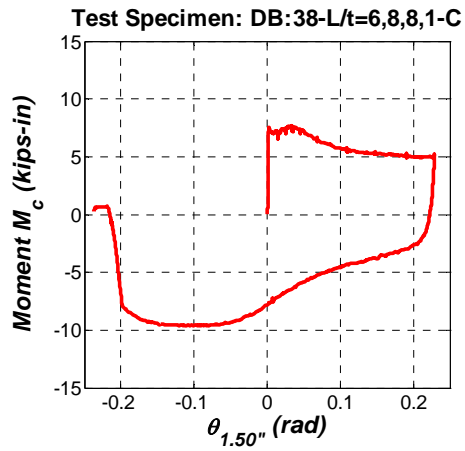
Table C.1. Equivalent modulus based on inner and outer strain of flange plates

Test ID	w (in)	E^{1-2} _{equiv.Inner} (kips-in)	E^{1-2} _{equiv.Outer} (kips-in)
DB: 35-L/t=6,8,8,1-C	0.92	0.0084	0.0064
DB: 36-L/t=6,8,8,1-T	0.92	0.0086	0.0066
DB: 37-L/t=6,8,8,1-Cyclic	0.92	0.0086	0.0064
DB: 38-L/t=6,8,8,1-C	0.56	0.0053	0.0040
DB: 39-L/t=6,8,8,1-T	0.56	0.0050	0.0042
DB: 40-L/t=6,8,8,1-Cyclic	0.56	0.0054	0.0040
DB: 41-L/t=6,8,8,1-C	1.38	0.0134	0.0098
DB: 42-L/t=6,8,8,1-Cyclic	1.38	0.0115	0.0094
DB: C1S1B-L/t=6,8,8,2-BUF*	1.38	0.0258	0.0230
DB: B1F1R-L/t=6,8,8,2-BUF*	0.83	0.0154	0.0131
DB: C1S3T-L/t=6,8,8,2-BUF*	0.58	0.0112	0.0099

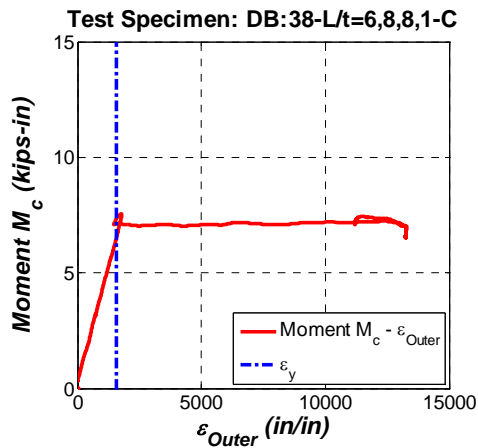
* The equivalent modulus of these specimens is obtained from the component tests that were conducted at the laboratory of the John A. Blume Earthquake Engineering Center using the histories from the shaking table collapse test of Frame #1 for the selected plastic hinge locations



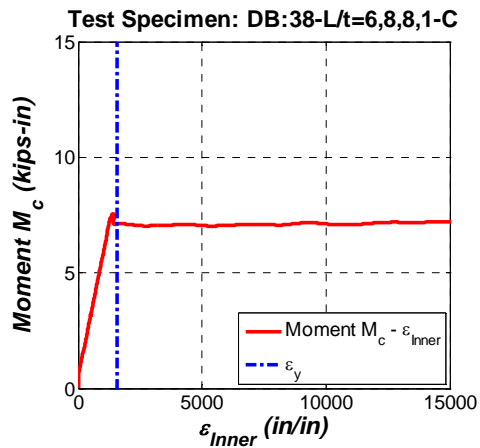
(a) Tip load P - δ_{tip}



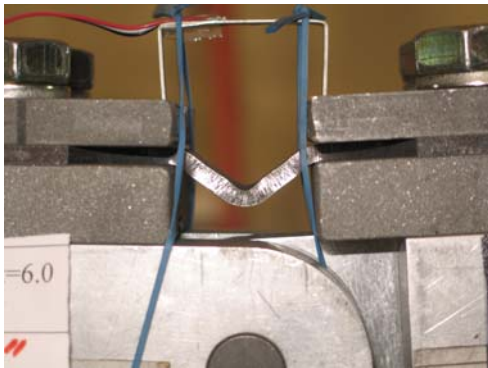
(b) M_c - $\theta_{1.5''}$



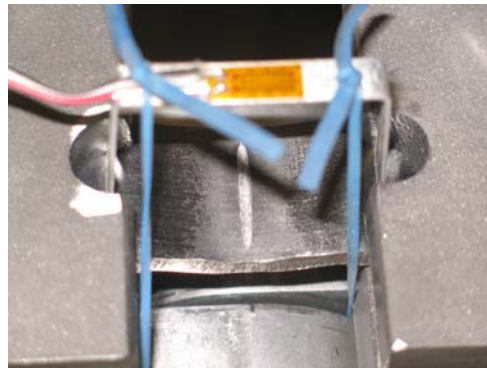
(c) M_c - ϵ_{Outer}



(d) M_c - ϵ_{Inner}

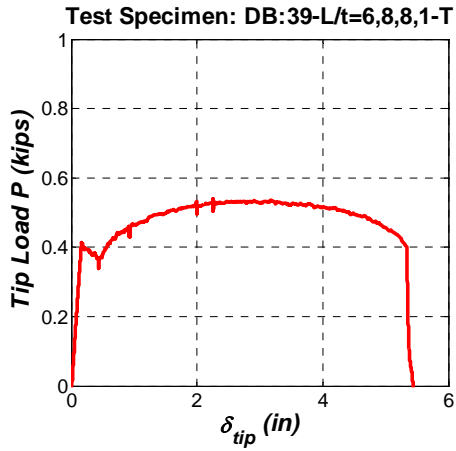


(e) local buckling at $\theta_{1.5''}=0.06\text{rad}$

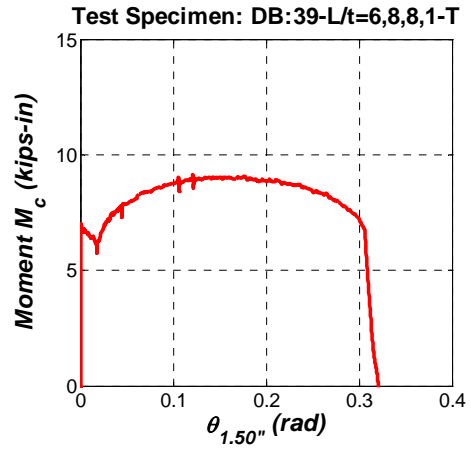


(f) crack initiation (-)

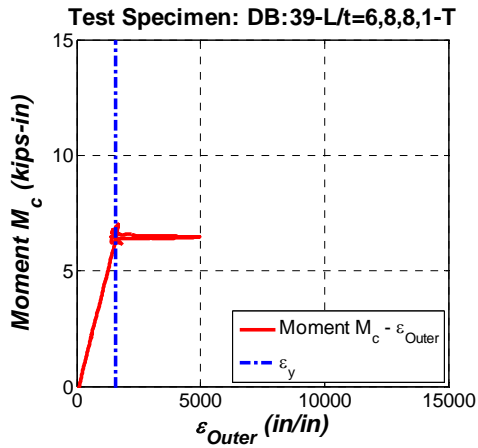
Figure C.1. Deduced data for specimen DB:38-L/t=6,8,8,1-C



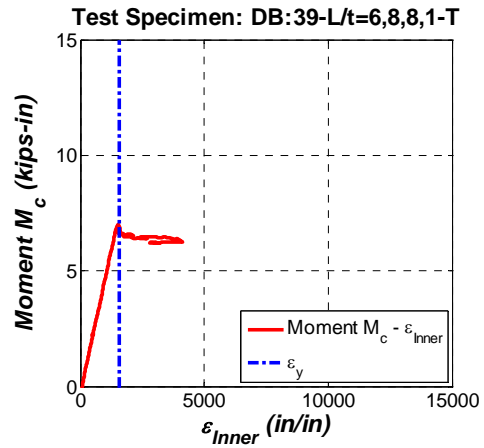
(a) Tip load $P-\delta_{tip}$



(b) $M_c - \theta_{1.50''}$

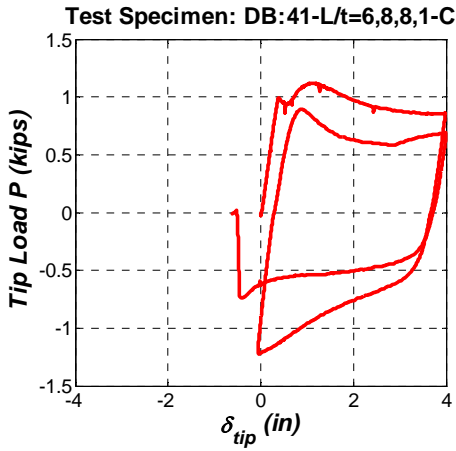


(c) $M_c - \epsilon_{Outer}$

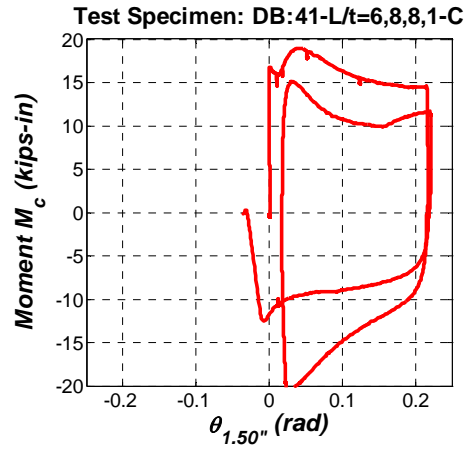


(d) $M_c - \epsilon_{Inner}$

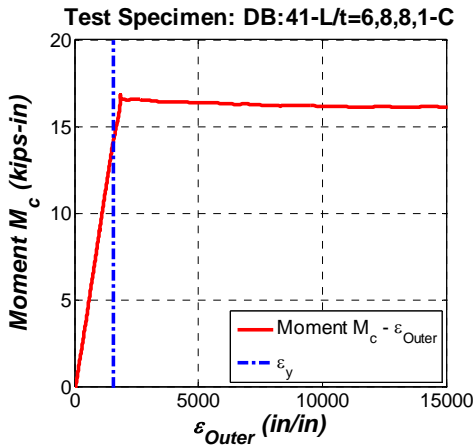
Figure C.2. Deduced data for specimen DB:39-L/t=6,8,8,1-T



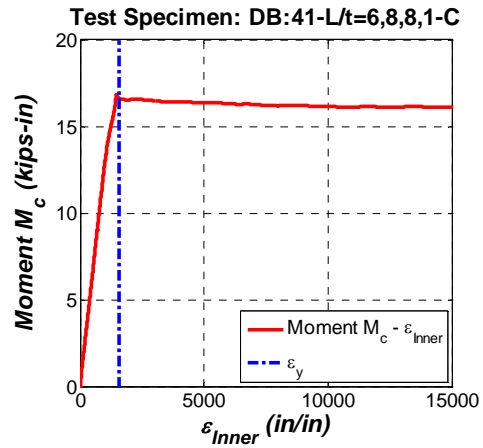
(a) Tip load P - δ_{tip}



(b) $M_c - \theta_{1.5''}$



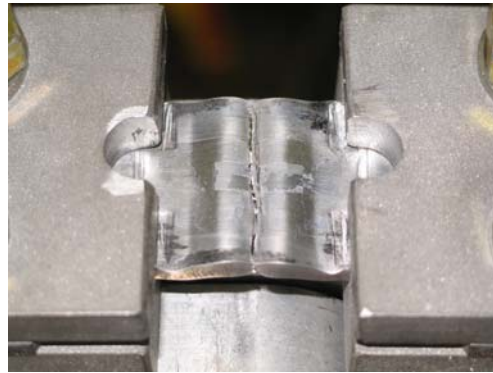
(c) $M_c - \epsilon_{Outer}$



(d) $M_c - \epsilon_{Inner}$

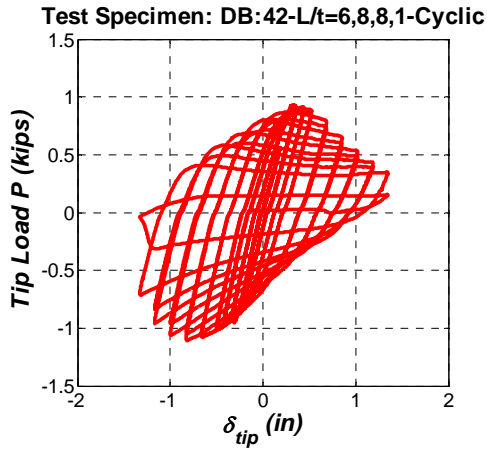


(e) local buckling at $\theta_{1.5''}=22.5\text{rad}$

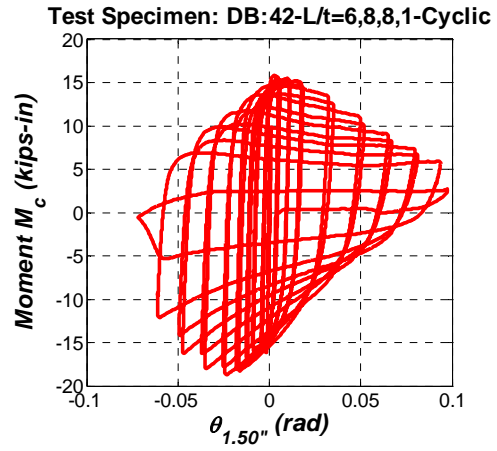


(f) crack propagation (-)

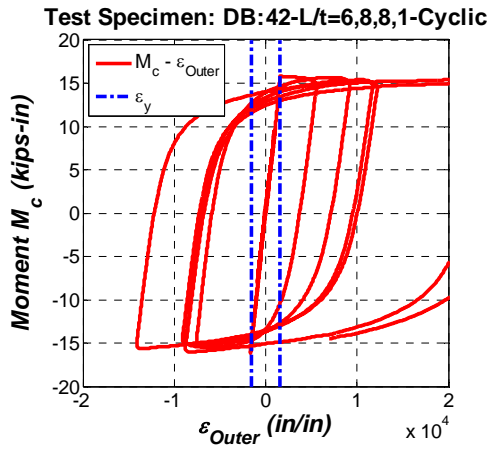
Figure C.3. Deduced data for specimen DB:41-L/t=6,8,8,1-C



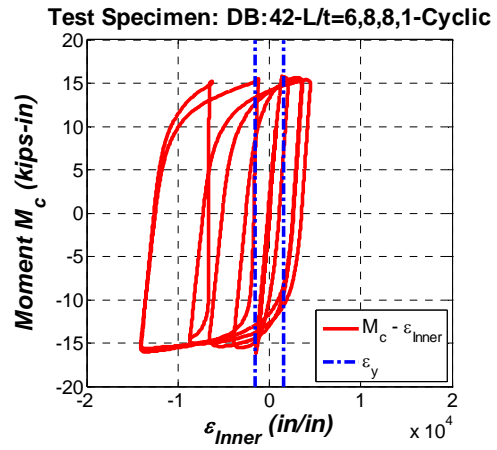
(a) Tip load $P-\delta_{tip}$



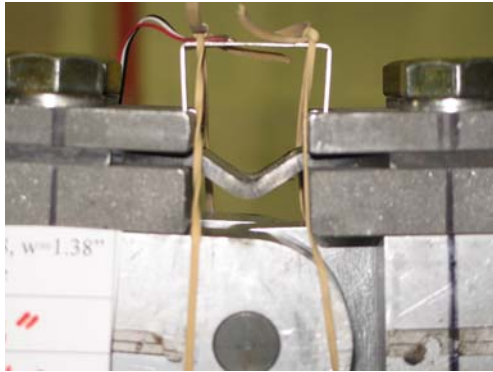
(b) $M_c - \theta_{1.5''}$



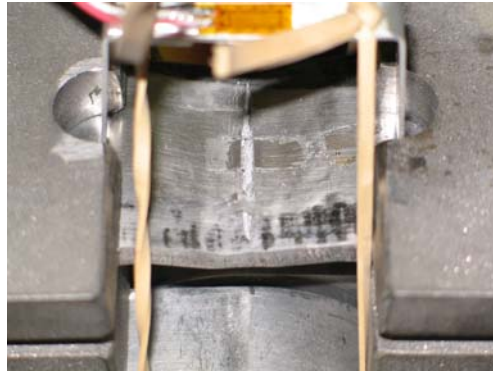
(c) $M_c - \epsilon_{Outer}$



(d) $M_c - \epsilon_{Inner}$

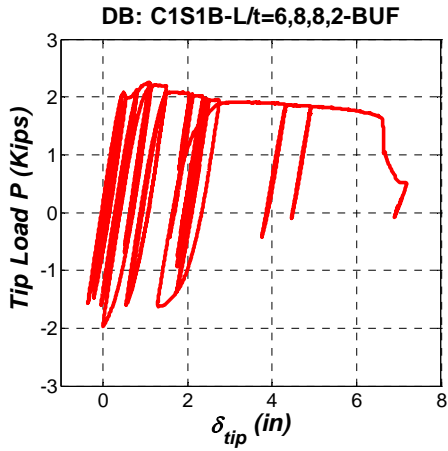


(e) local buckling at $\theta_{1.5''}=0.05\text{rad}$

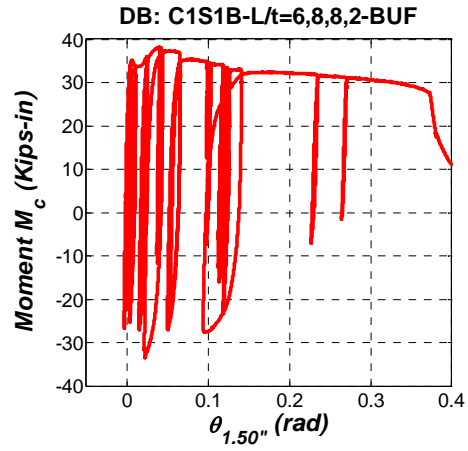


(f) crack initiation at $\theta_{1.5''}=0.05\text{rad}$ (-)

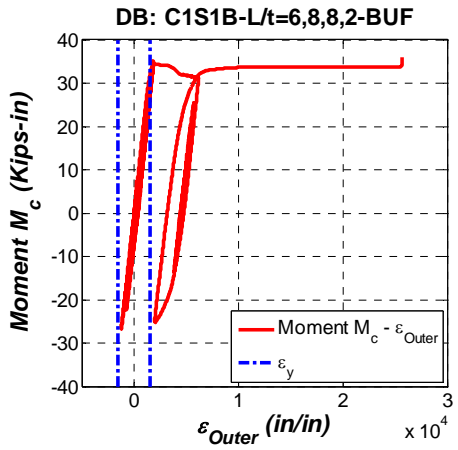
Figure C.4. Deduced data for specimen DB:42-L/t=6,8,8,1-Cyclic



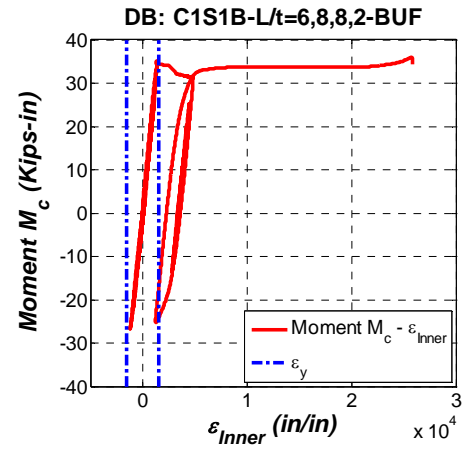
(a) Tip load P - δ_{tip}



(b) M_c - $\theta_{1.5}$



(c) M_c - ϵ_{Outer}



(d) M_c - ϵ_{Inner}

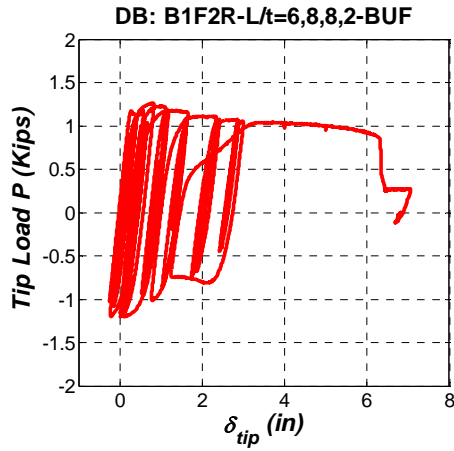


(e) plastic hinge element at $\theta_{1.5}=0.14$ rad

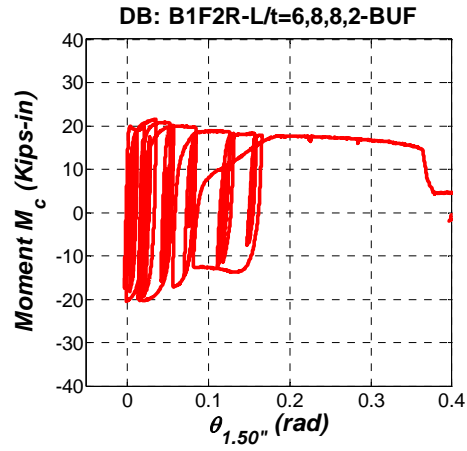


(f) fracture of top plate at $\theta_{1.5}=0.36$ rad

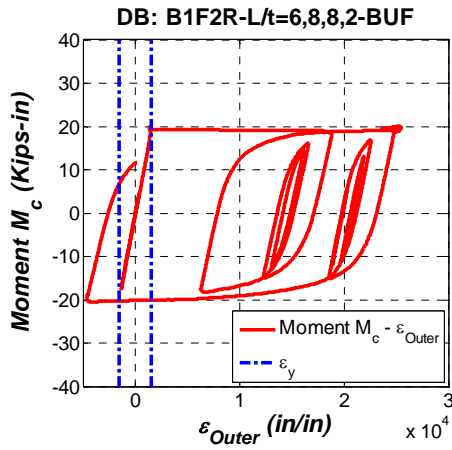
Figure C.5. Deduced data for specimen DB :C1S1B-L/t=6,8,8,2-BUF



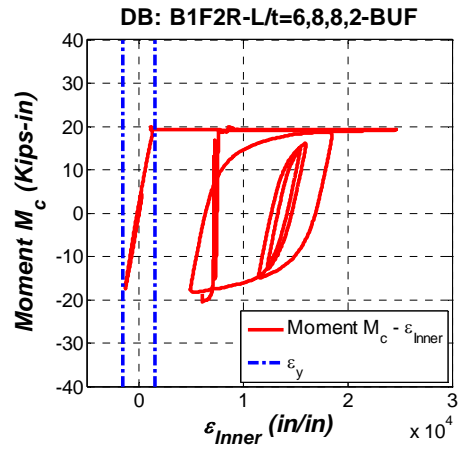
(a) Tip load $P-\delta_{tip}$



(b) $M_c - \theta_{1.5''}$



(c) $M_c - \epsilon_{Outer}$



(d) $M_c - \epsilon_{Inner}$

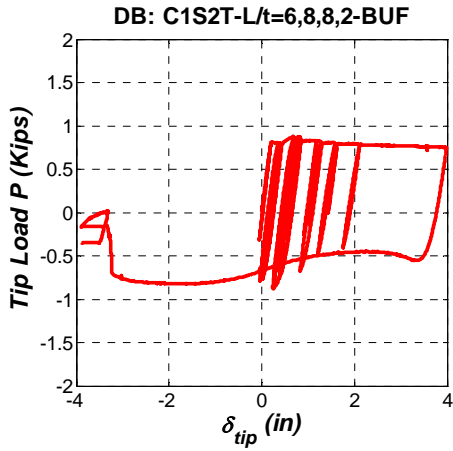


(e) plastic hinge element at $\theta_{1.5''}=0.25\text{rad}$

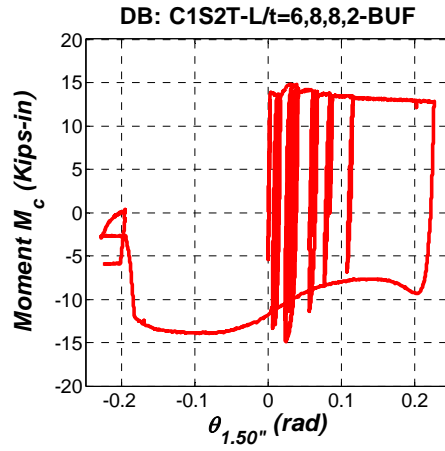


(f) Fracture of top plate at $\theta_{1.5''}=0.36\text{rad}$

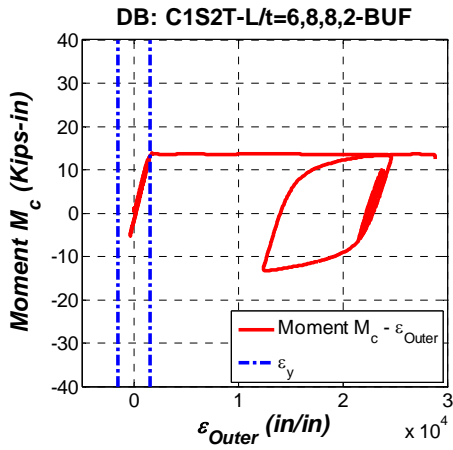
Figure C.6. Deduced data for specimen DB: B1F1R-L/t=6,8,8,2-BUF



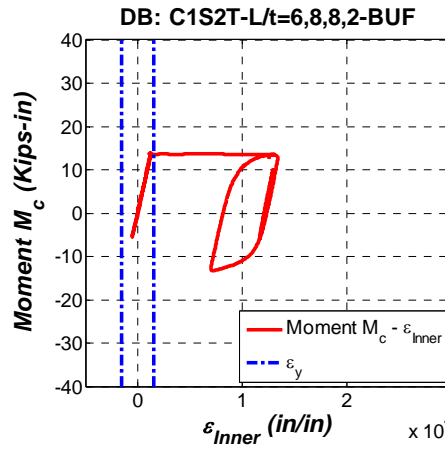
(a) Tip load P - δ_{tip}



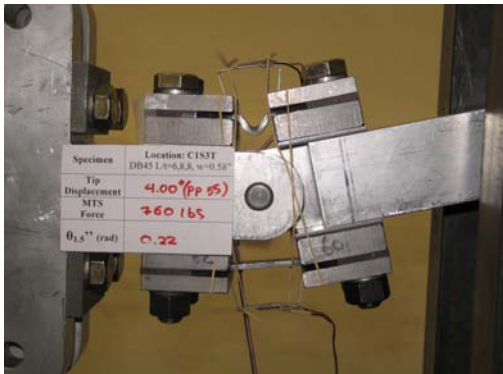
(b) $M_c - \theta_{1.5''}$



(c) $M_c - \epsilon_{Outer}$



(d) $M_c - \epsilon_{Inner}$



(e) plastic hinge element at $\theta_{1.5''}=0.22\text{rad}$ (f) fracture of top plate at $\theta_{1.5''}=0.19\text{rad}$ (-)

Figure C.7. Deduced data for specimen DB: C1S3T-L/t=6,8,8,2-BUF

APPENDIX D

INSTRUMENTATION PLAN FOR SHAKING TABLE COLLAPSE TEST SERIES

Appendix D includes basic instrumentation plan of test Frames #1 and #2 discussed in Chapter 7. Only general drawings that illustrate the instrument locations are presented here in. A complete instrumentation list together with the complete list of instruments can be downloaded through the NEESCentral repository (<https://central.nees.org/>) for both frames.

Table D.1 includes a notation of all the instruments used during shaking table experimentation. Figure D.1 includes all the load cells and accelerometers installed in both test setups. Figure D.2 shows a general drawing for clip and strain gauge locations and Figures D.3 and D.4 show typical locations of LEDs installed (as part of the Krypton system) on selected plastic hinge elements of the exterior and interior joints of the test frame.

Table D.1. Instrumentation list notation

Instrument	Notation
$ACCT_i$	Accelerometer i on the shaking table
$ACCB_jFi$	Accelerometer at beam j , at Floor i
$ACCiPjFk$	Accelerometer i at mass plate j , at Floor k
$DSPT_i$	Displacement Transducer i for the shaking table
$DSPFF_i$	Displacement Transducer at Frame at floor i
$DSPPF_i$	Displacement Transducer at Plate at floor i
LCF_i	Load cell at floor i
$SGCiSjBk$	Strain Gage at column i , Story j at bottom location k
$SGCiSjTk$	Strain Gage at column i , Story j at top location k
$SGBiFjLk$	Strain Gage at beam i , Floor j at left location k
$SGBiFjRk$	Strain Gage at beam i , Floor j at right location k
$CGCiSjBk$	Clip Gage at column i , Story j at bottom location k
$CGCiSjTk$	Clip Gage at column i , Story j at top location k
$CGBiFjLk$	Clip Gage at beam i , Floor j at left location k
$CGBiFjRk$	Clip Gage at beam i , Floor j at right location k
$KRYSiCjBk$	Krypton LED at story i , column j , bottom location k
$KRYSiCjTk$	Krypton LED at story i , column j , top location k
$KRYFiBjLk$	Krypton LED at floor i , beam j , left location k
$KRYFiBjRk$	Krypton LED at floor i , beam j , right location k
$KRYSi,Cj,Fk$	Krypton LED at story i , column j , floor k

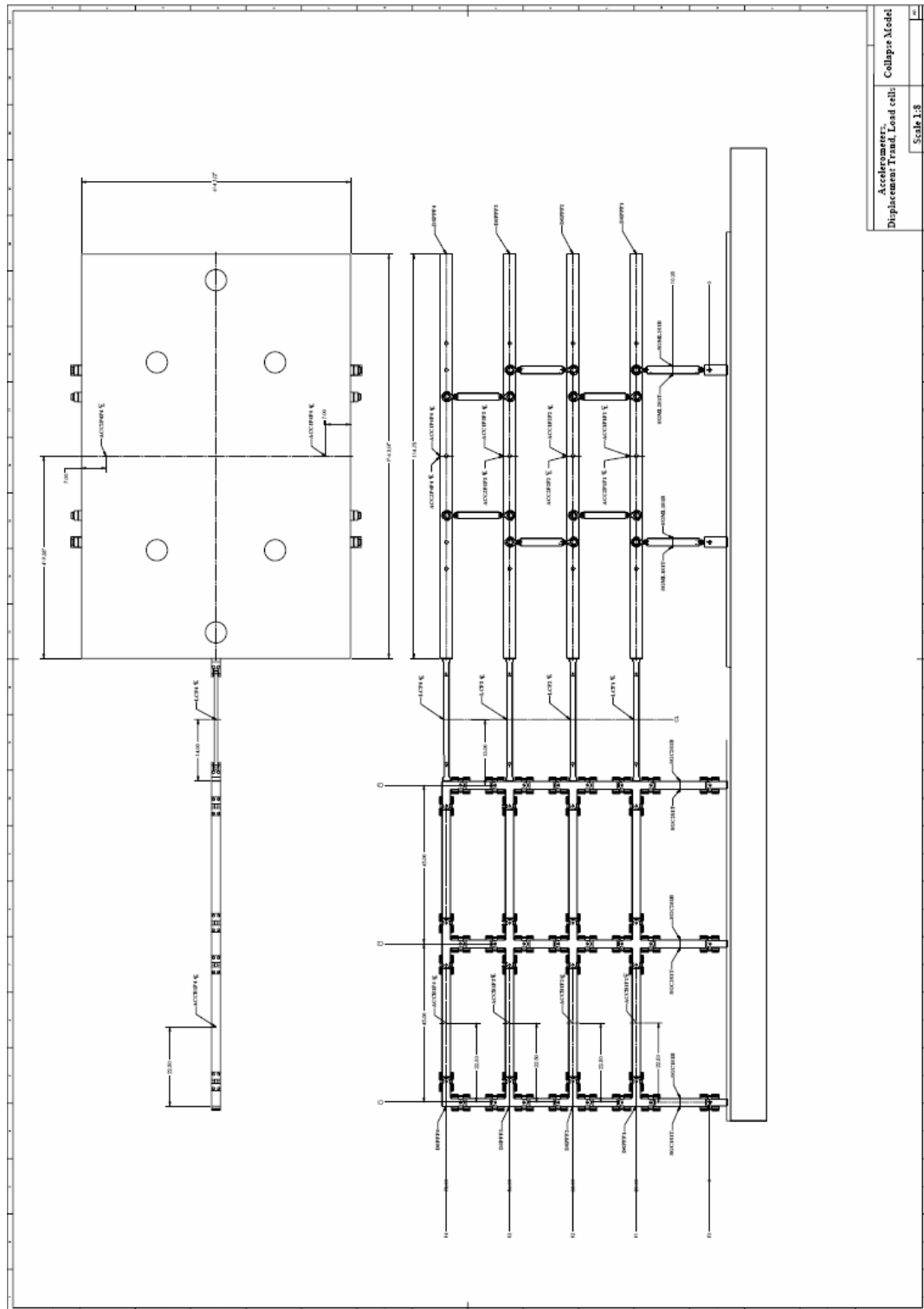


Figure D.1. Location of accelerometers and load cells installed in the test setup

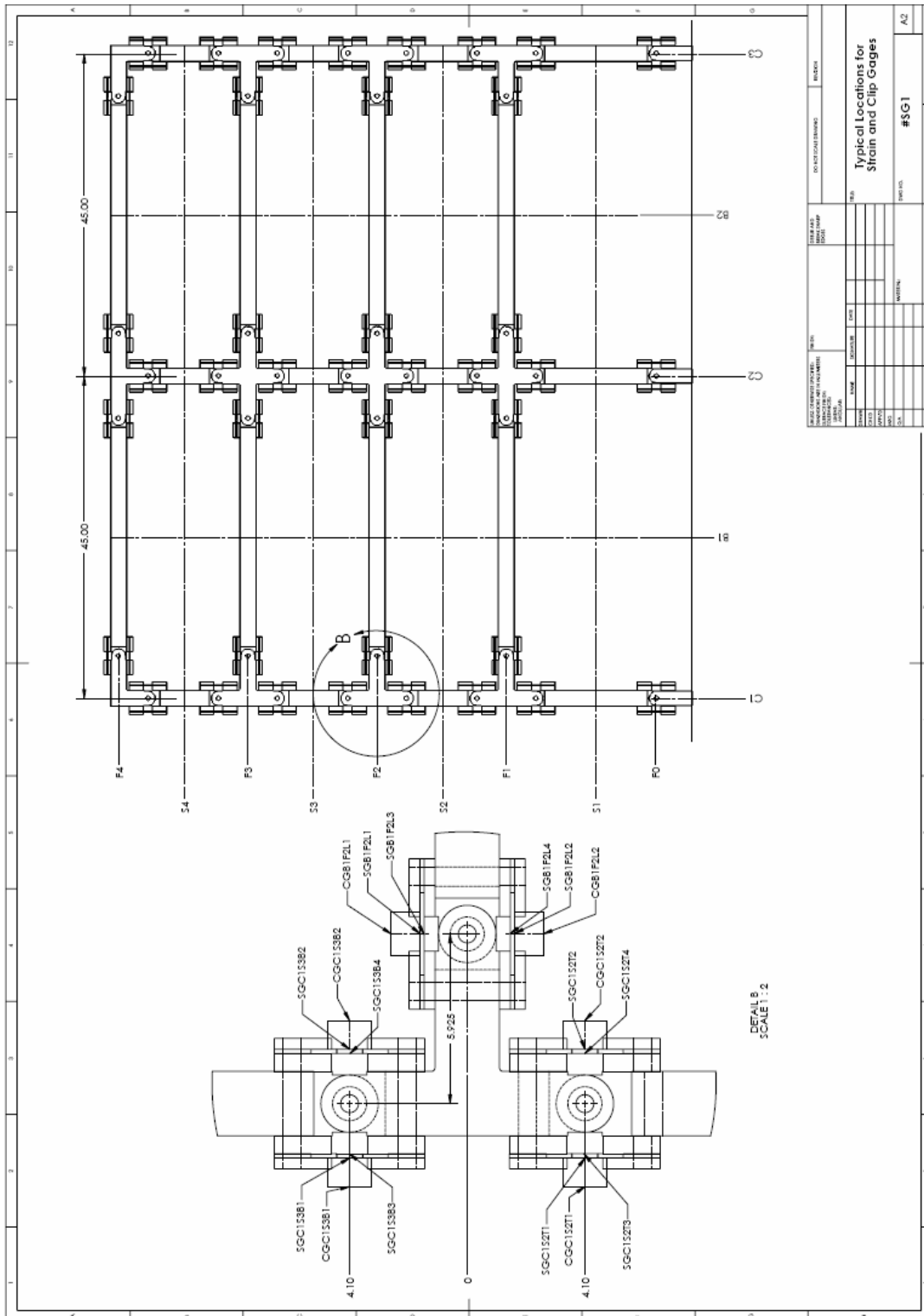


Figure D.2. Typical locations for clip and strain gauges installed on plastic hinge elements

APPENDIX E

SUMMARY OF RESULTS FROM SHAKING TABLE COLLAPSE TEST SERIES

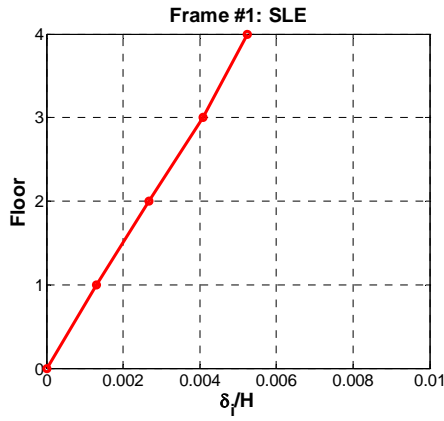
Basic results for the five tests utilizing increasing ground motion intensity for both frames tested in the NEES facility at the State University of New York at Buffalo (SUNY) are summarized in this appendix. A total of 110 tests were carried out for both test frames. Most of the tests were used for identification of modal properties and in order to gain confidence in instrumentation based on the elastic response of both frames. The complete data set for both frames can be downloaded from the NEESCentral repository (<https://central.nees.org/>).

E.1 Test Frame #1

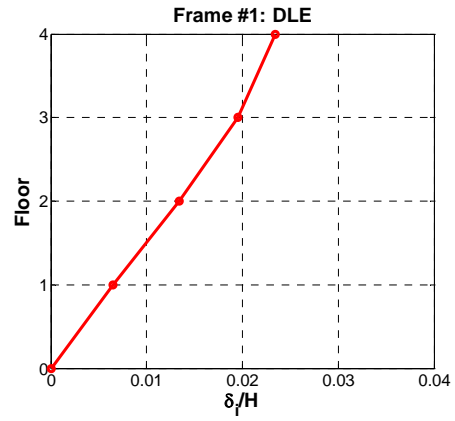
Figure E.1 includes the peak displacements along the height of test Frame #1, normalized with respect to the total height of the frame, at various ground motion intensities. Figures E.2 to E.11 include story shear force and OTM histories at the base of the frame during the main response time window of Frame #1 at various ground motion intensities as measured from the horizontal links. In the same plots the roof drift has been superimposed in a different scale. Peak and residual story drifts, plastic rotations have been reported in Chapter 7 during test evaluation of Frame #1.

E.2 Test Frame #2

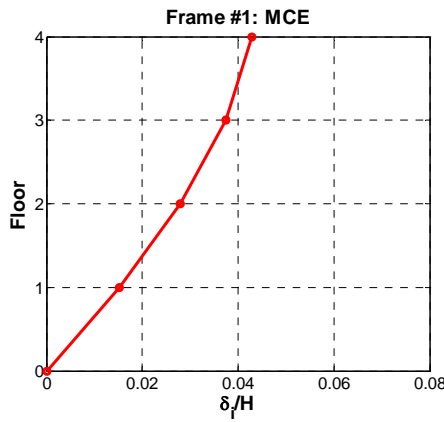
Peak displacement profiles along the height of test Frame #2, normalized with respect to the total height of the frame, at various ground motion intensities are summarized in Figure E.12. Figures E.13 to E.22 include Story shear force histories as measured from the horizontal links all superimposed in same graphs per ground motion intensity during the main response time window and OTM at the base for the same time window. In the same figures the roof drift at various ground motion intensities has been superimposed in different scale than the story shear forces and OTM.



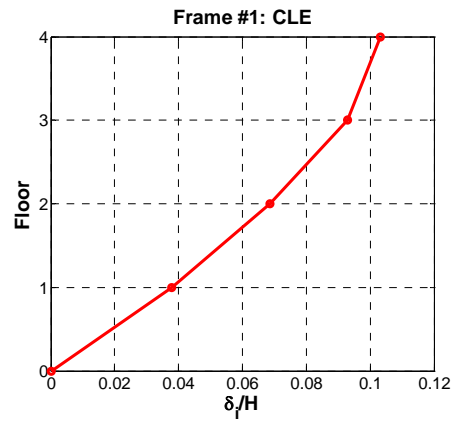
(a) SLE



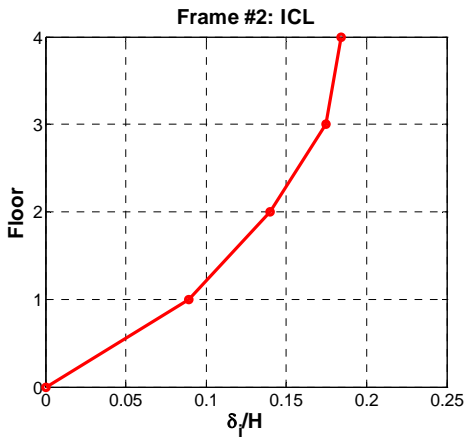
(b) DLE



(c) MCE



(d) CLE



(e) ICL

Figure E.1. Peak relative displacement profiles along the height of frame #1 normalized with respect to total height of the frame at various ground motion intensities

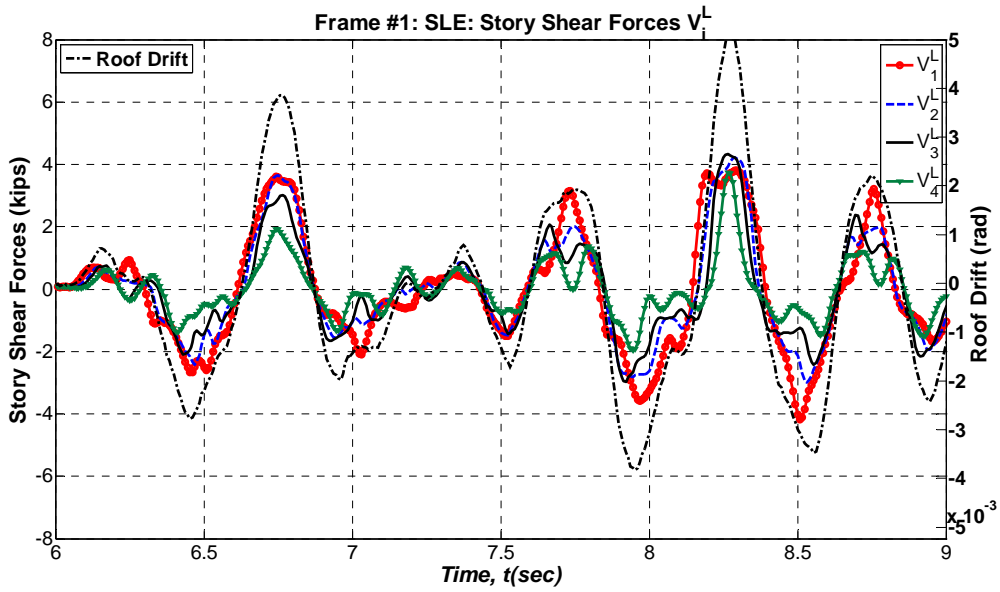


Figure E.2. Story shear histories for frame #1 during SLE as measured from horizontal links

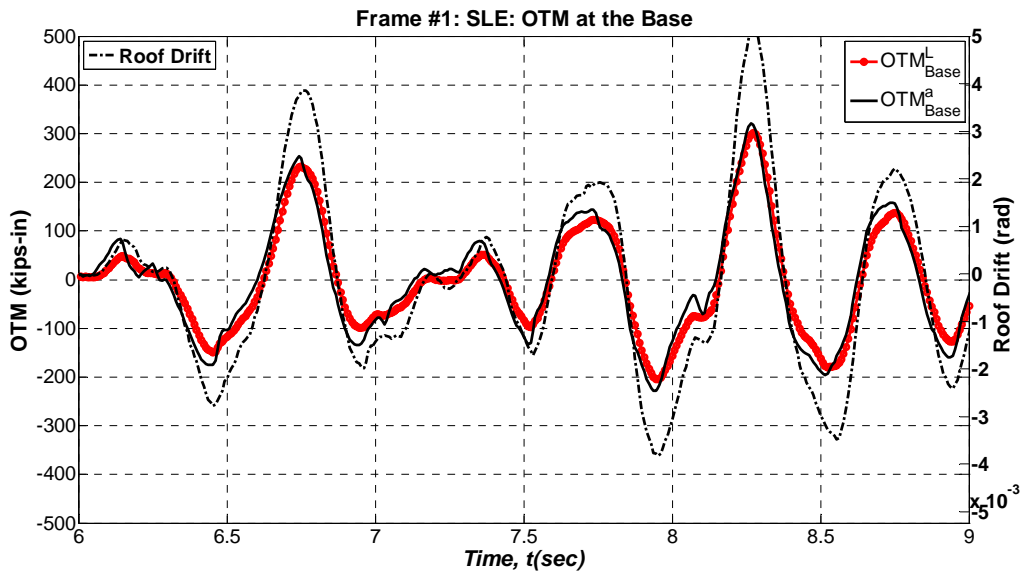


Figure E.3. Overturning moment at the base of frame #1 based on horizontal link and acceleration measurements during SLE

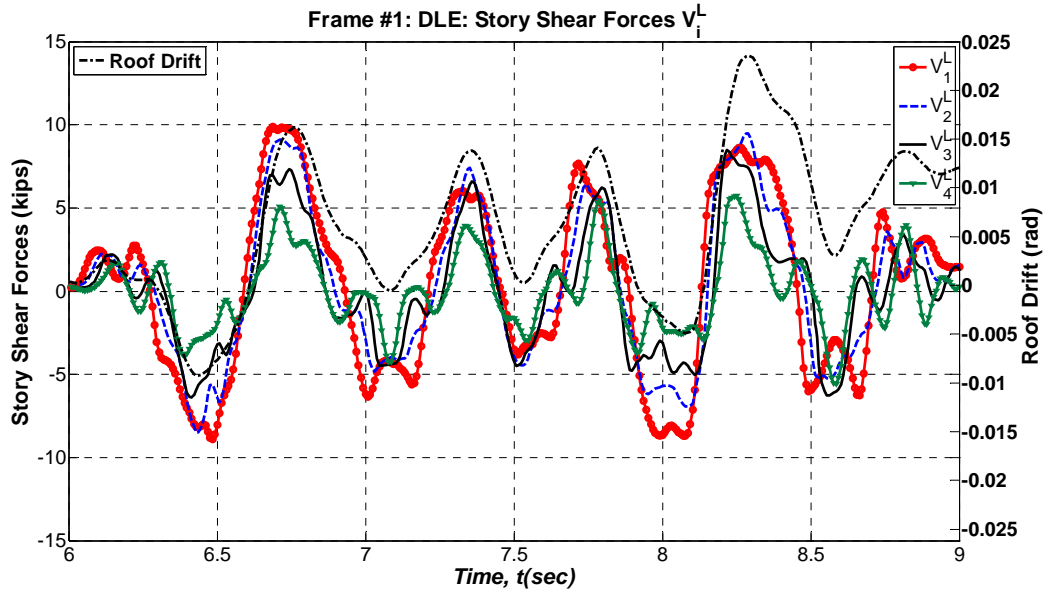


Figure E.4. Story shear histories for frame #1 during DLE as measured from horizontal links

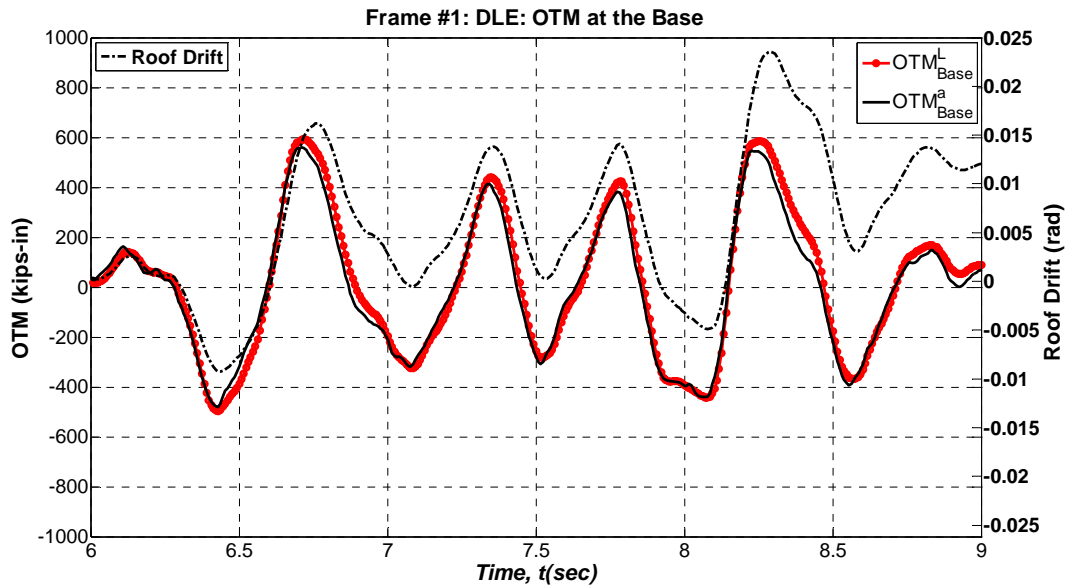


Figure E.5. Overturning moment at the base of frame #1 based on horizontal link and acceleration measurements during DLE

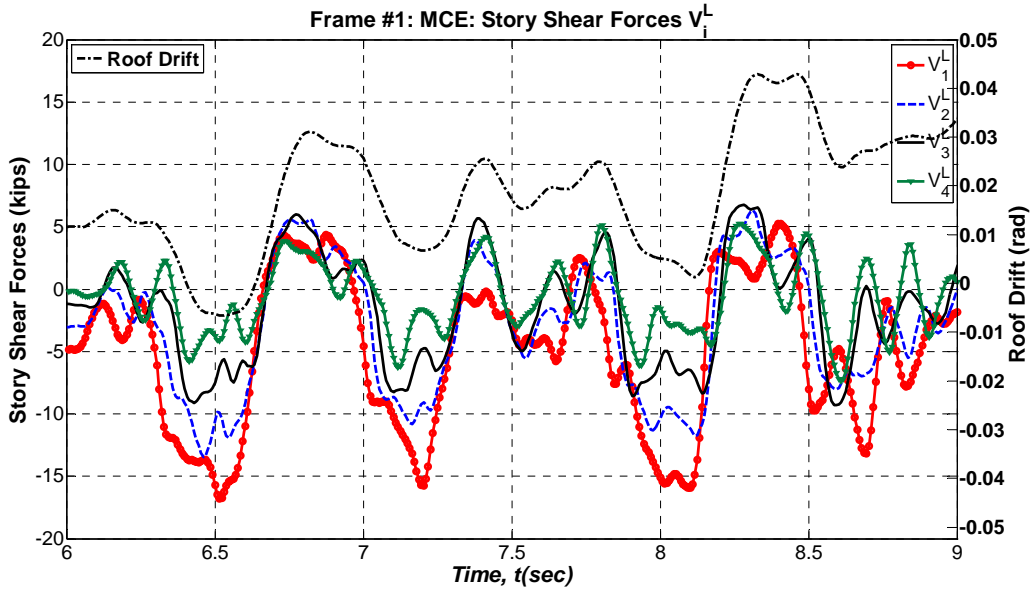


Figure E.6. Story shear histories for frame #1 during MCE as measured from horizontal links

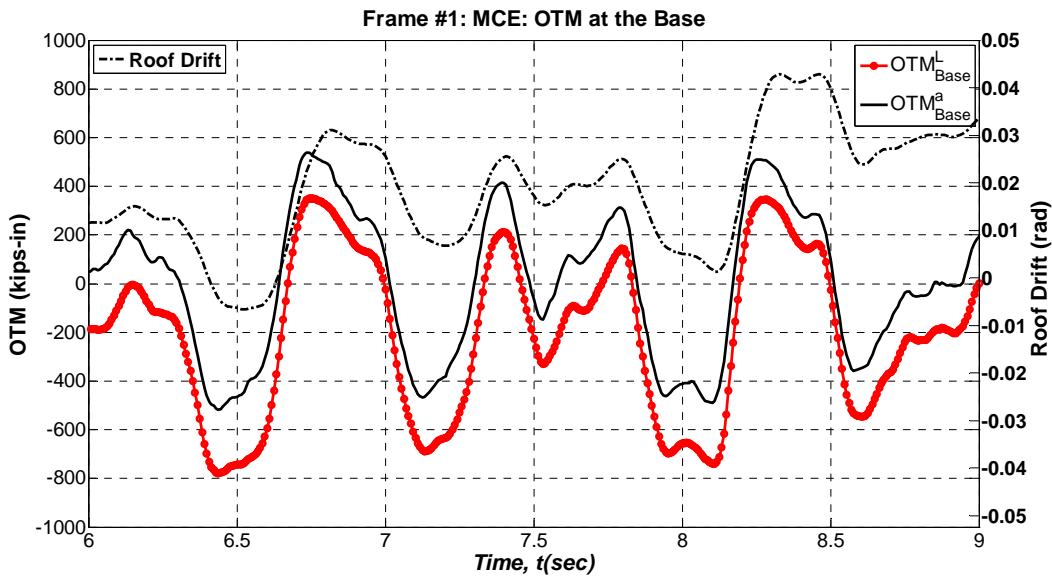


Figure E.7. Overturning moment at the base of frame #1 based on horizontal link and acceleration measurements during MCE

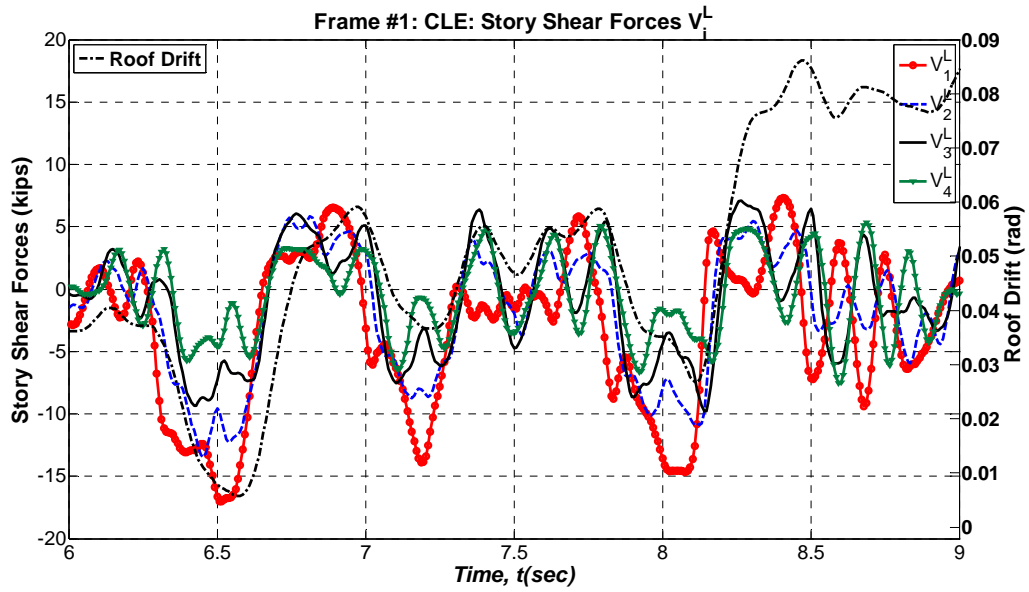


Figure E.8. Story shear histories for frame #1 during CLE as measured from horizontal links

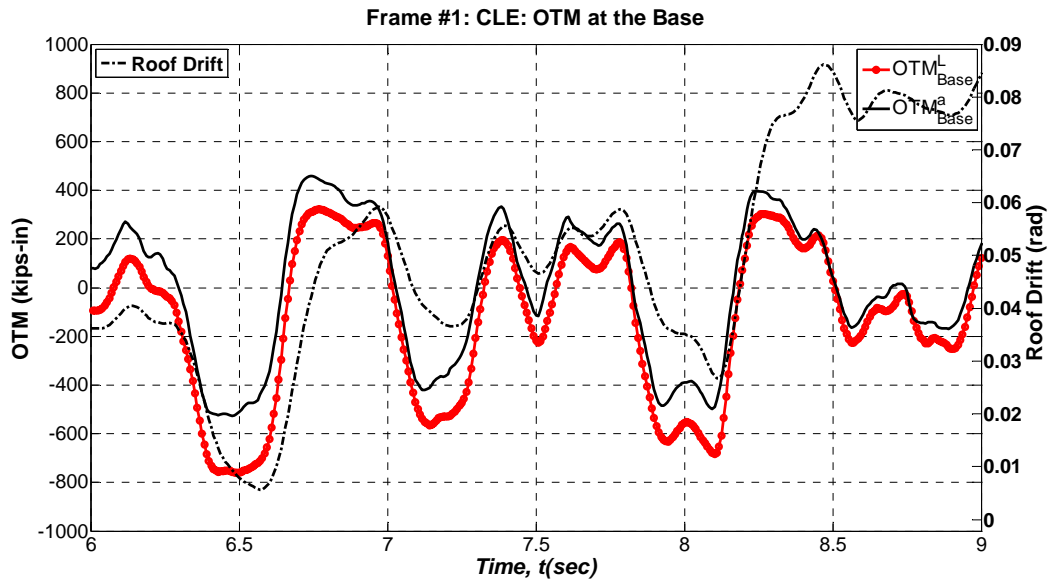


Figure E.9. Overturning moment at the base of frame #1 based on horizontal link and acceleration measurements during CLE

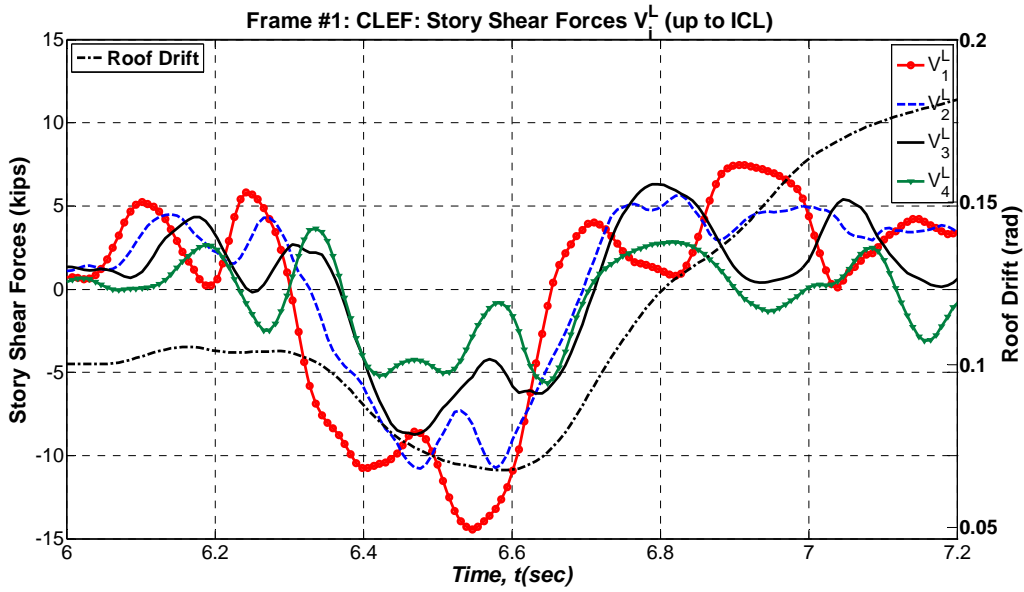


Figure E.10. Story shear histories for frame #1 during CLEF as measured from horizontal links

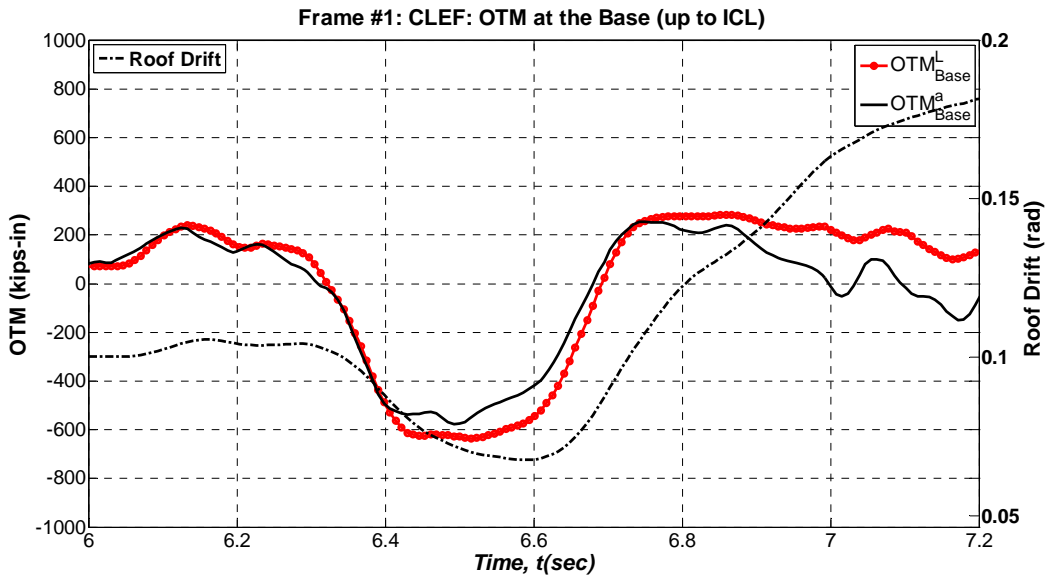


Figure E.11. Overturning moment at the base of frame #1 based on horizontal link and acceleration measurements during CLEF

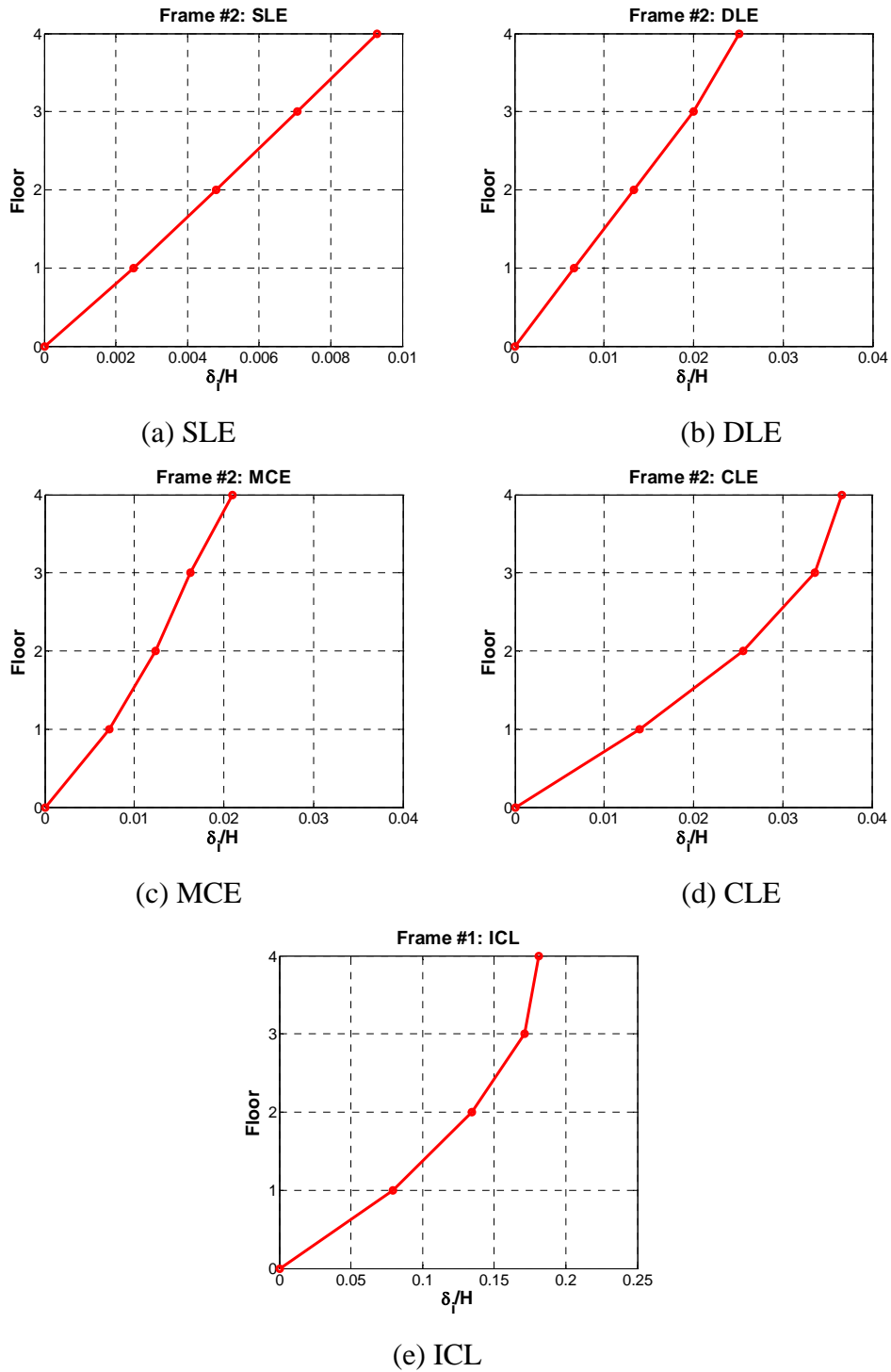


Figure E.12. Peak relative displacement profiles along the height of frame #1 normalized with respect to total height of the frame at various ground motion intensities

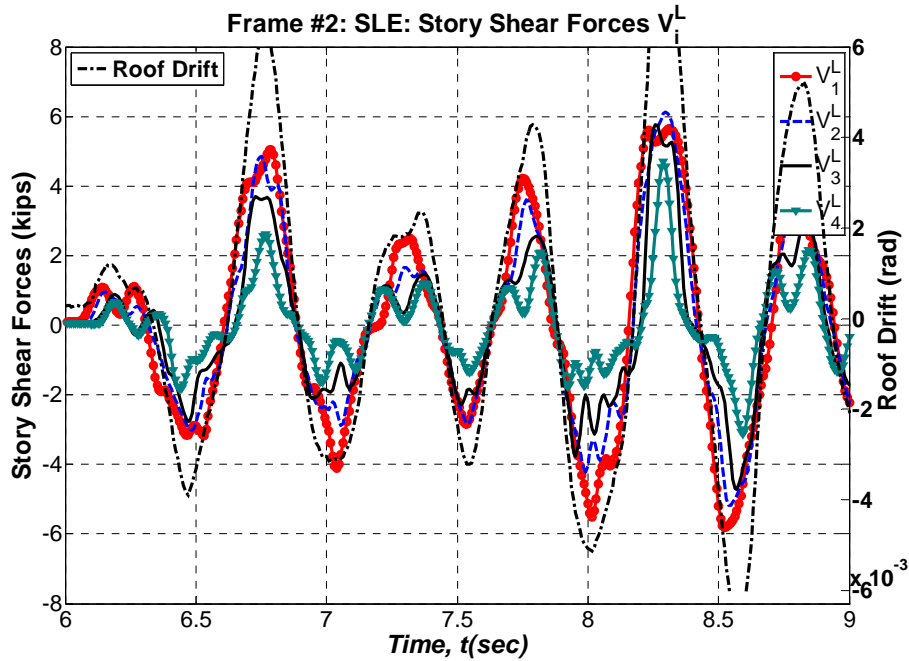


Figure E.13. Story shear histories for frame #2 during SLE as measured from horizontal links

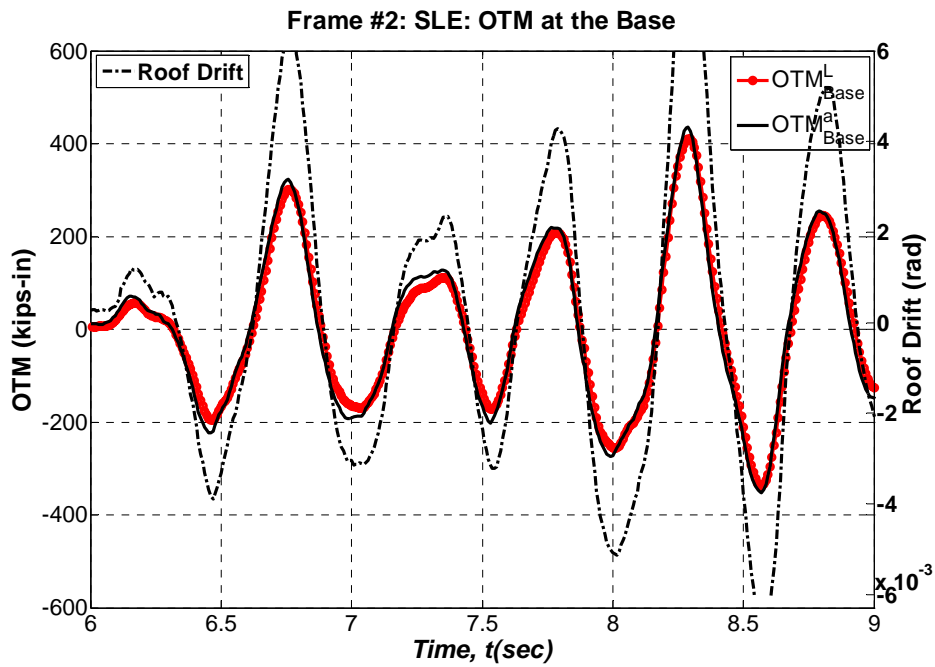


Figure E.14. Overturning moment at the base of frame #2 based on horizontal link and acceleration measurements during SLE

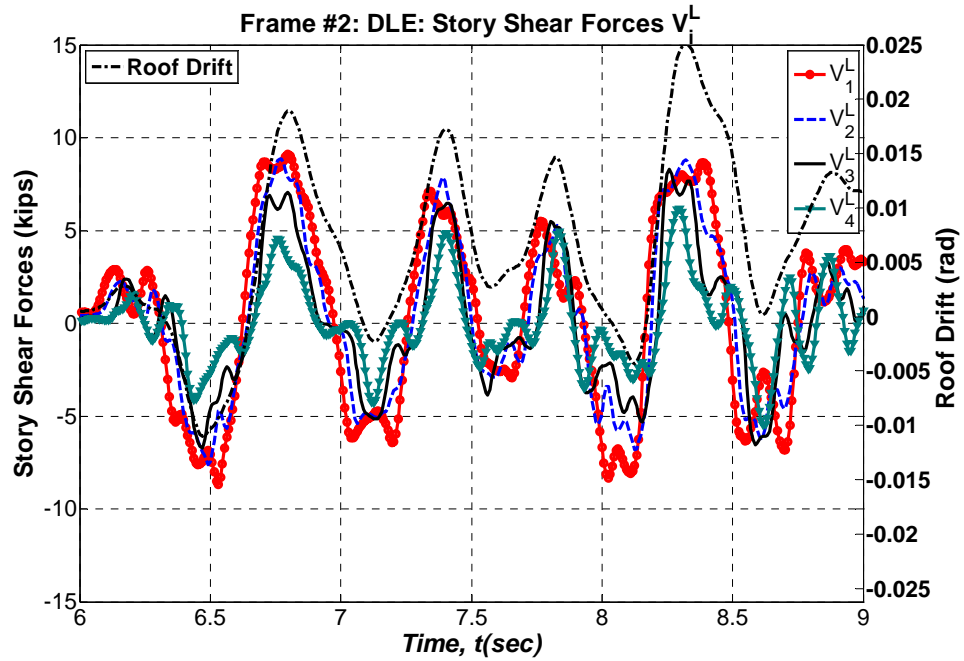


Figure E.15. Story shear histories for frame #2 during DLE as measured from horizontal links

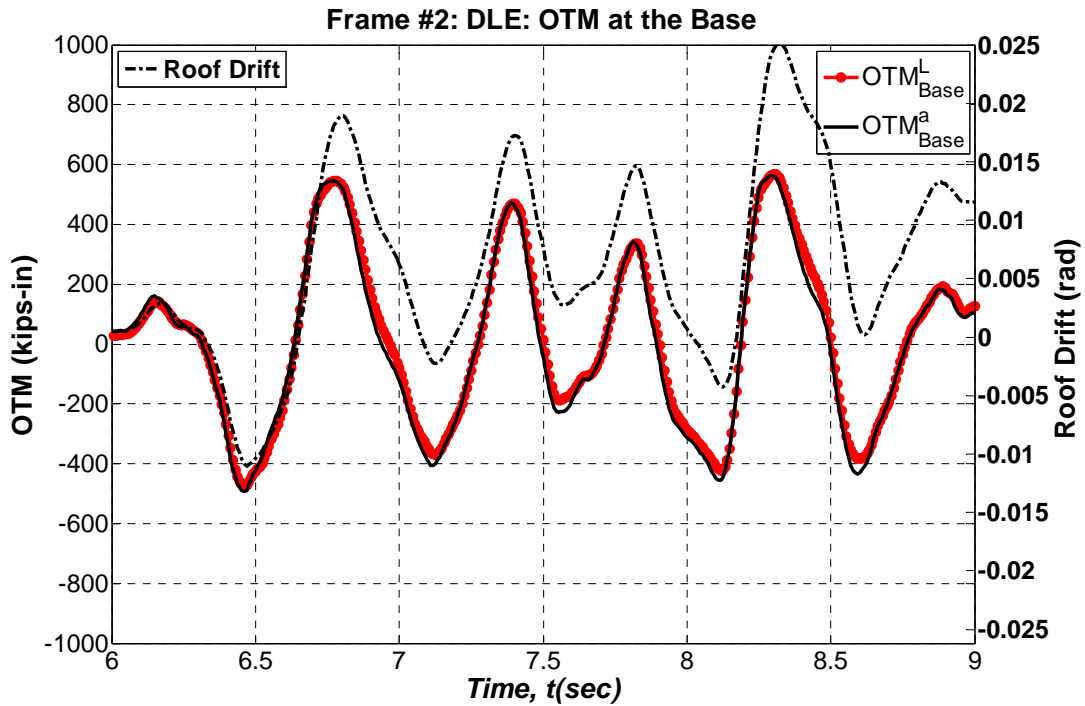


Figure E.16. Overturning moment at the base of frame #2 based on horizontal link and acceleration measurements during DLE

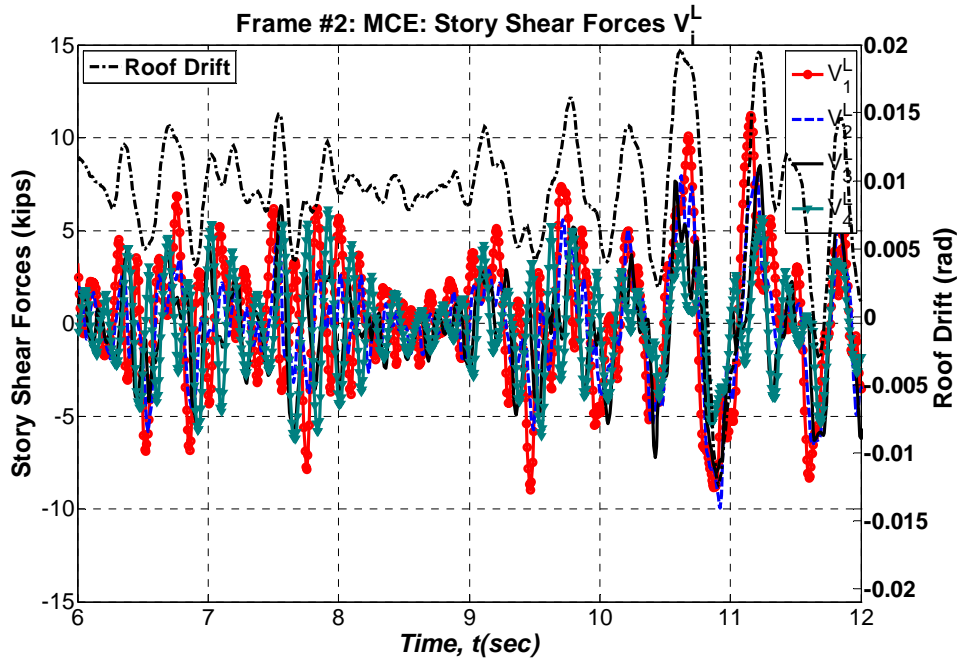


Figure E.17. Story shear histories for frame #2 during MCE as measured from horizontal links

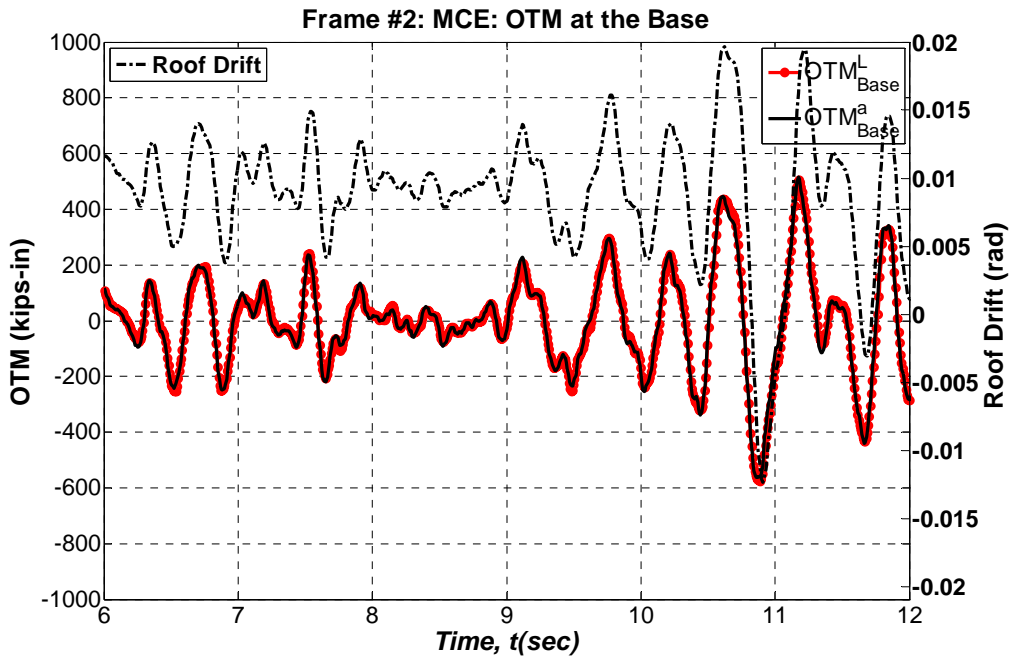


Figure E.18. Overturning moment at the base of frame #2 based on horizontal link and acceleration measurements during MCE

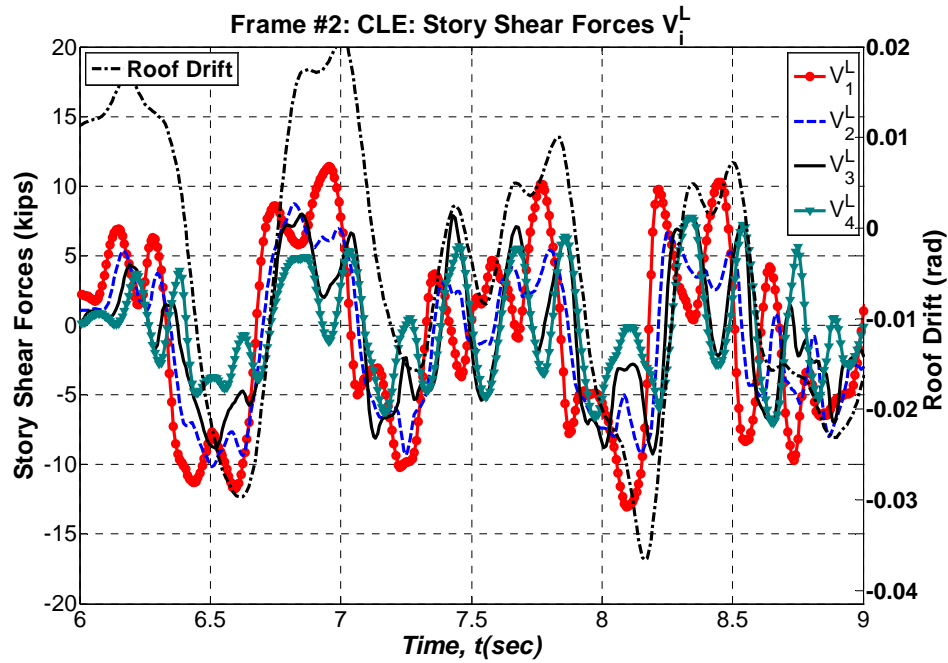


Figure E.19. Story shear histories for frame #2 during CLE as measured from horizontal links

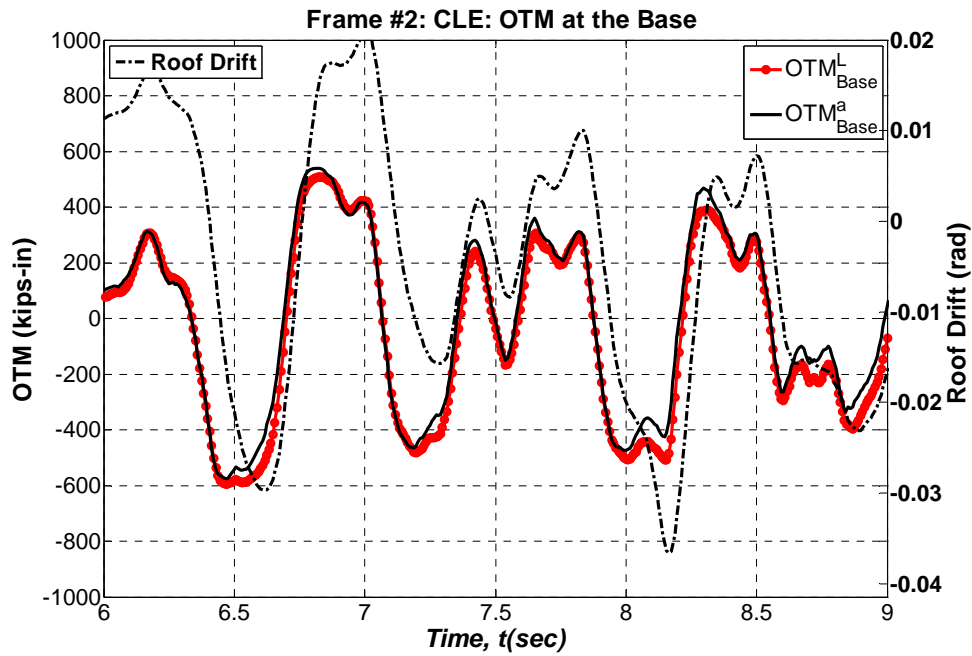


Figure E.20. Overturning moment at the base of frame #2 based on horizontal link and acceleration measurements during CLE

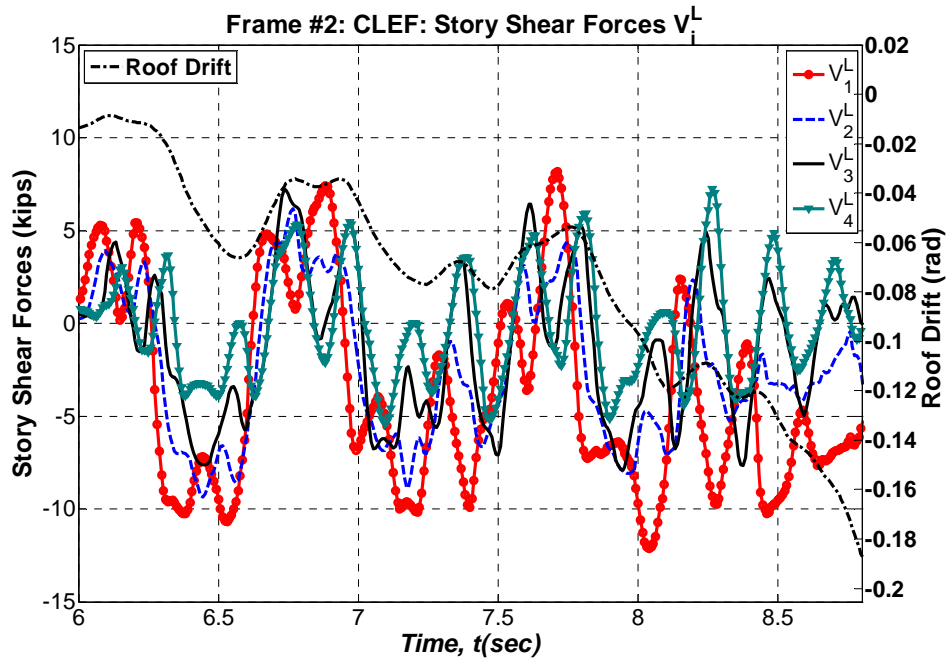


Figure E.21. Story shear histories for frame #2 during CLEF as measured from horizontal links

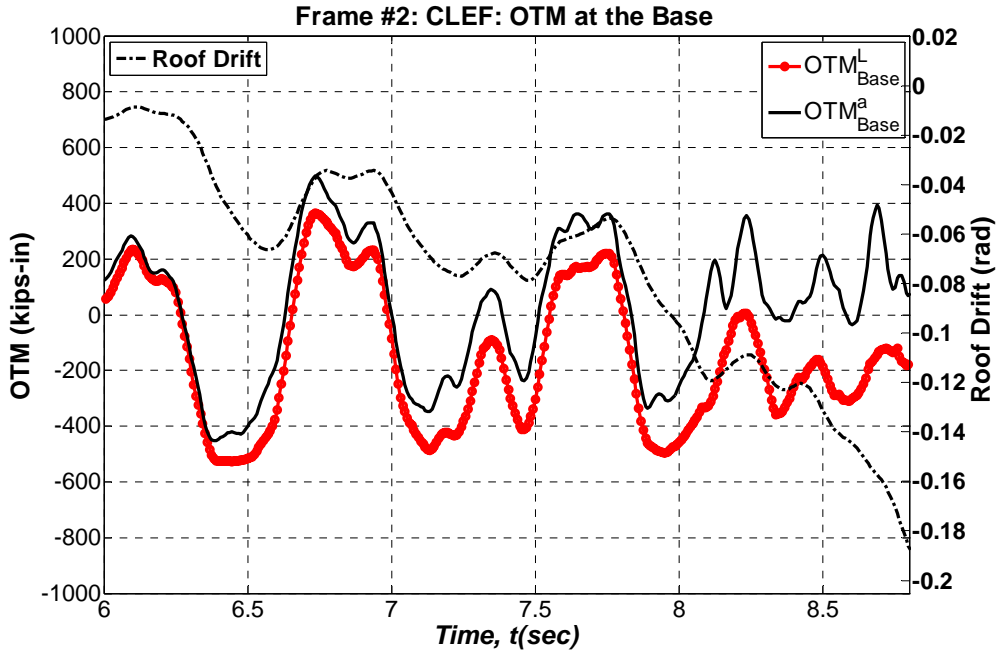


Figure E.22. Overturning moment at the base of frame #2 based on horizontal link and acceleration measurements during CLE

References

ABAQUS (2005), "Version 6.5 Theory manual and documentation"

Adam, C., Ibarra, L. F., and Krawinkler H. (2004), "Evaluation of P-delta effects in non-deteriorating MDOF structures from equivalent SDOF systems," *Proc., 13th World Conf. on Earthquake Engineering*, Vancouver, B.C., Canada, Paper No. 3407.

Allen, J. Partridge, J.-E. Richard, R.-M. (1996), "Stress distribution in welded/bolted beam to column moment connections," Internal report of Seismic Structural Design Association, Inc.

AISC (2005), "Seismic provisions for structural steel buildings, including supplement No. 1," American Institute of Steel Construction, Inc. Chicago, Illinois

American Concrete Institute, (2005), "Building code requirements for structural concrete (ACI 318-05) and commentary (ACI 318R-05)," Reported by ACI Committee 318.

Anastasiadis, A., Gioncu, V., Mazzolanni, F.M. (2000), "New trends in the evaluation of available ductility of steel members," In Behavior and Ductility of Steel Structures, SDSS 99, Timisoara, 0-11 September 1999, *Journal of Constructional Steel Research*, Vol. 55, No. 1-3, 211-227.

ASCE-7 (2002), "Minimum design loads for buildings and other structures," Structural Engineering Institute.

American Standards for Testing of Materials (1974), "Standard definitions of terms relating to constant – amplitude low-cycle fatigue testing," *ASTM Standard E466*.

ATC-63 (2007), "Recommended methodology for quantification of building system performance and response parameters; 75% Draft," *Applied Technology Council*, Redwood City (unpublished).

Axhag, F. (1995), "Plastic design of composite bridges allowing for local buckling," Technical Report, Lulea University of Technology, 09T

Baber, T., and Wen, Y.-K. (1981), "Random vibration of hysteretic degrading systems," *Journal of Engineering Mechanics*, ASCE, 107(EM6), pages 1069- 1089.

Baber, T., and Noori, M. N. (1985), "Random vibration of degrading, pinching systems," *Journal of Engineering Mechanics*, ASCE, 111(8), pages 1010-1026.

Baber, T., and Noori, M. N. (1986), "Modeling general hysteresis behavior and random vibration application," *Journal of Vibration, Acoustics, Stress and Reliability in Des.*, Vol. 108, 411-420.

- Benjamin, J. R. and Cornell, C. A. (1970), "*Probability, statistics, and decision for civil engineers*," McGraw Hill, Inc. New York
- Bernal, D. (1987), "Amplification factors for inelastic dynamic P-Delta effects in earthquake analysis," *Earthquake Engineering & Structural Dynamics*, 15, 5, July 1987, pages 635-651
- Bernal, D. (1992), "Instability of buildings subjected to earthquakes," *Journal of Structural Engineering*, 118, 8, Aug. 1992, pages 2239-2260
- Bernal, D. (1998), "Instability of buildings during seismic response," *Engineering Structures*, 20, 4-6, Apr.-June 1998, pages 496-502
- Bernal, D., Nasser, A., and Bulut, Y. (2006), "Instability inducing potential of near fault ground motions," *SMIP 06 Seminar Proceedings*, pages 41-62
- Berry, M., Parrish, M., and Eberhard, M. (2004), "PEER structural performance database user's manual," Pacific Engineering Research Center, University of California, Berkeley, California, 38 pp. Available at <http://nisee.berkeley.edu/spd/> and <http://maximus.ce.washington.edu/~peera1/>.
- Bouc, R. (1967), "Forced vibration of mechanical systems with hysteresis," *Abstract Proc., 4th Conference on Nonlinear Oscillation*.
- Boore, D. M., Joyner, W. B., Fumal, T. E. (1997), "Equations for estimating horizontal response spectra and peak acceleration from western north American earthquakes: A summary of recent work," *Seismological Research Letters*, Vol. 68, No. 1, 128-153.
- Bracci, J.M., Reinhorn, A.M., and Mander, J.B. (1992), "Seismic resistance of reinforced concrete frame structures designed only for gravity loads: Part III - Experimental performance and analytical study of a structural model," *Technical Report NCEER-92-0029*, National Center for Earthquake Engineering Research, University at Buffalo. December 1, 1992.
- Brightman, M. (2000), "AAC shear wall specimens: development of test setup and preliminary Results," *MS Thesis*, Department of Civil Engineering, The University of Texas at Austin.
- Brockenbrough, R.L. (2001), "MTR survey of plate material used in structural fabrication: Final report part A; Yield-Tensile properties," Report to American Institute of Steel Construction, R.L. Brockenbrough & Associates, Pittsburgh, PA
- Brosnan, D. P., Uang, C. M., (1995), "Effective width of composite L-beams in-buildings," *Engineering Journal*, Vol. 32, (2), pp.73-80.
- Carr, A. J. (2003), "Ruaumoko user manual," University of Canterbury, New Zealand.
- Casciati, F. (1989), "Stochastic dynamics of hysteretic media," *Structural Safety*, Amsterdam, 6, 259-269.

- Challa, V. R. M., and Hall, J. F. (1994), "Earthquake collapse analysis of steel frames," *Earthquake Engineering and Structural Dynamics*, 23 (11), pages 1199–1218.
- Chatterjee, S., Hadi, A.S., and Price, B. (2000), "*Regression Analysis by Example*," 3rd Edition, John Wiley and Sons Inc., New York.
- Choi, J., Goel, S. C., and Stojadinovic, B. (2000), "Development of free flange moment connection," *Research Report No. UMCEE 00-15*, Dept. of Civil and Environmental Eng., The University of Michigan, Ann Arbor, MI 48109-2125.
- Clarke, R., (2005), "Non-Bouc degrading hysteresis model for nonlinear dynamic procedure seismic design," *Journal of Structural Engineering* (ASCE), 2005, Vol. (131), 2, pages 287-291.
- Clough, R. W., and Johnston, S. B. (1966), "Effect of stiffness degradation on earthquake ductility requirements," Proceedings, Second Japan National Conference on Earthquake Engineering, 1966, pages 227-232.
- Conway, J., Watts, S. (2003), "A software engineering approach to LabView," Virtual instruments series, National Instruments, 2003.
- Dexter, R. J., Graeser, M., Saari, W. K., Parcoe, C., Gargner, C.A., and Galambos, T. V., (2000), "Structural shape material property survey," Technical Report for Structural Shape Producers Council, University of Minnesota, Mineapolis, MN.
- Dhokal, R.P. and Maekawa, K. (2002), "Modeling of post-yielding buckling of reinforcement," *Journal of Structural Engineering*, Vol. 128, No. 9, September 2002, pp. 1139-1147.
- DRAIN-2DX (1993), "DRAIN-2DX: Basic program description and user guide," Report No. UCB/SEMM-1993/17, by Prakash, V., Powell, G. H., and Campbell, S., University of California, Berkeley, CA, Nov. 1993, 97 pages
- Earls, C.J., Galambos, T. V. (1998), "Inelastic failure of high strength steel wide flange beams under moment gradient and constant moment loading," *SSRC Annual Technical Session*, Atlanta, 21-23 September 1998, pp. 131-153
- E-Defense Steel Building Project (2007), "Four-story steel building collapse analysis blind prediction," <http://www.blind-analysis.jp/eng/outline/outline.html>.
- Elwood, K. J. (2002), "Shake table tests and analytical studies on the gravity load collapse of reinforced concrete frames," *Ph.D. Dissertation*, Department of Civil and Environmental Engineering, University of California, Berkeley.
- Elwood, K.J., and Moehle, J.P. (2005), "Drift capacity of reinforced concrete columns with light transverse reinforcement," *Earthquake Spectra*, Earthquake Engineering Research Institute, vol. 21, no. 1, pages 71-89.

- Engelhardt, M. D., and Husain, A. S. (1993), "Cyclic - loading performance of welded flange-bolted web connections," *Journal of Structural Engineering*, (ASCE), 119(12), 3537-3550.
- Engelhardt, M. D., Sabol, T. A., (1994), "Testing of welded steel moment connections in response to the Northridge earthquake," Progress report to the AISC advisory subcommittee on special moment resisting frame research
- Engelhardt, M. D., Winneberger, T., Zekany, A. J., and Potyraj, T. J. (1996), "The dogbone connection: Part II," *Modern Steel Construction*., AISC, 36 (8), 46-55.
- Engelhardt, M. D., Fry, D. T., and Venti, M. J. (2000), "Behavior and design of radius cut reduced beam section connections," *Rep. No. SAC/BD-00/17*, SAC Joint Venture, Sacramento, Calif.
- Esteva, L. and Ruiz, S. (1989), "Seismic failure rates of multistory frames," *Journal of Structural Engineering*, 115, (2), Feb. 1989, pages 268-284
- Euler, G. D. (2002), "Structural analysis reference library: Bolt preload calculation," (<http://euler9.tripod.com/fasteners/preload.html>)
- Eurocode 8 (1998), "Design provisions for earthquake resistant structures."
- Fardis, M. N. and Biskinis, D. E. (2003), "Deformation capacity of RC members, as controlled by flexure or shear," *Otani Symposium*, pp. 511-530.
- Foliente, G. (1995). "Hysteresis modeling of wood joints and structural systems," *Journal of Structural Engineering*, ASCE, 121(6): pp. 1013-1022.
- Fry, G. T., Jones, S. L., and Holliday., S. D. (1997), "Protocol for fabrication, inspection, testing, and documentation of beam-column connection tests and other experimental specimens," *Rep. No. SAC/BD-97/02*, SAC Joint Venture, Sacramento, Calif.
- Fukada, Y., (1969), "Study on the restoring force characteristics of reinforced concrete buildings (in Japanese)," *Proceedings, Kanto Branch Symposium*, Architectural Institute of Japan, No. 40, 1969, pp.121-124.
- Ge, H., Usami, T. (1995), "Moment-thrust-curvature curves for locally buckled steel box columns," In *Stability of Steel Structures* (ed. M. Ivanyi), Budapest, 21-23 September 1995, Akademiai Kiado, Budapest, pp. 43-50
- Gioncu, V, Petcu D. (1995), "Numerical investigations on the rotation capacity of beams and columns," In *Stability of Steel Structures*, (ed. M. Ivayi), SSRC Colloquium, Budapest, 21-23 September 1995, Akademiai Kiado Budapest, Vol. 1, 163-174
- Gioncu, V, Petcu D. (1997), "Available rotation capacity of wide-flange beams and beam-columns: part 1. Theoretical approaches," *Journal of Construction Steel Research* (1997);43 (1-3): pp. 161–217.

- Gioncu, V., Mazzolani F.M. (2002), “Ductility of seismic resistant steel structures,” SPON press, London and New York
- Greschik, G., White, D. W., McGuire, W., Abel, J. F. (1990), “Toward the prediction of flexural ductility of wide-flange beams for seismic design,” In 4th US National Conference on Earthquake Engineering, Palm Springs, 20-24 May 1990, 107-113
- Gupta, A., and Krawinkler, H. (1999), “Prediction of seismic demands for SMRFs with ductile connections and elements,” *SAC Background Document, Report No. SAC/BD-99/06*.
- Haselton, C.B., and Deierlein G.G., (2006), “Assessing seismic collapse safety of modern reinforced concrete moment frame buildings,” *John A. Blume Earthquake Engineering Center Report No. TR 156*, Department of Civil Engineering, Stanford University.
- Hisada, T., Nakagawa, K., and Izumi, M., (1962), “Earthquake response of structures having various restoring force characteristics,” Proceedings, Japan National Conference on Earthquake Engineering, 1962, pages 63-68
- Hoshikuma, J., Kawashima, K., Nagaya, K., and Taylor, A.W., (1997), “Stress–strain model for confined concrete in bridge piers,” *Journal of Structural Engineering ASCE* (1997), Vol. **123** pp. 624–633
- Huang, P. Ch., Deierlein, G.G. (1996), “Investigation of beam rotation capacity using finite element analysis,” In 5th SSRC International Conference on Stability of Metal Structures. Future Direction in Stability Research and Design. Chicago, 15-18 April 1996, pp. 383-392
- Hubult, E., (2008), “Assessing potential of adobe walls reinforced with polymer mesh,” Undergraduate Honors Thesis, Department of Civil Engineering, Stanford University, Stanford CA.
- IBC (2003), “International building code *IBC* 2003,” *International Code Council*, Birmingham, AL.
- Ibarra, L., Medina, R., Krawinkler, H. (2002), “Collapse assessment of deteriorating SDOF systems,” *Proceedings of the 12th European Conference on Earthquake Engineering*, London, UK, Paper 665, Elsevier Science Ltd., September 9-13, 2002
- Ibarra, L. F., Krawinkler, H., (2005), “Global collapse of frame structures under seismic excitations,” *Report No. PEER 2005/06*, Pacific Earthquake Engineering Research Center, University of California at Berkeley, Berkeley, California.
- Ibarra L. F., Medina R. A., Krawinkler H., (2005), “Hysteretic models that incorporate strength and stiffness deterioration,” *Earthquake Engineering and Structural Dynamics*, **34**(12), pages. 1489-1511.
- Iwan, W. D. (1966). “A distributed-element model for hysteresis and its steady-state dynamic response,” *Journal of Applied Mechanics* 33(42), 893–900.
- Lubliner, J. (1990). *Plasticity theory*. Macmillan, New York.

Kabeyasawa, T. and Sanada, Y. (2002), "Shaking table test and analysis of a reinforced concrete wall-frame building with soft-first story," *Proceedings of Slovenia - Japan Workshops on Performance - Based Seismic Design Methodologies*; Ljubljana, Slovenia, 2-3 October 2000 and 1-2 October 2001. Fajfar, P and Otani, S, eds. University of Ljubljana, Slovenia, 2002, pages 51-60.

Kanvinde, A. M. (2003), "Methods to evaluate the dynamic stability of structures-shake table tests and nonlinear dynamic analyses," EERI Paper Competition 2003 Winner, *Proceedings of EERI Meeting*, Portland, Feb. 2003

Kanvinde A.M., and Deierlein, G.G., (2007), "A cyclic Void Growth model to assess ductile fracture in structural steels due to ultra low cycle fatigue," *Journal of Engineering Mechanics*, ASCE, 133(6),pp. 701-712.

Kanvinde A.M., and Deierlein, G.G., (2008), "Validation of cyclic Void Growth Model for fracture initiation in blunt notch and dogbone steel specimens," *Journal of Structural Engineering*, ASCE, September 2008 (scheduled for publication)

Kasai, K., Hodgson, I. (1996), "Repair of welded steel moment connections using bolted haunch brackets," *Report* submitted in the Department of Civil and Environmental Engineering, Lehigh University.

Kasai, K., Ooki, Y., Motoyui, S., Takeuchi, T. and Sato, E. (2007), "E-Defense tests on full-scale steel buildings: Part 1 – Experiments using dampers and isolators," *Proc. Structural Congress 2007*, ASCE, Long Beach, 247-17.

Karadogan, F., Editor (1998), "Repair and strengthening of existing buildings," *Proceedings of Second Japan-Turkey Workshop on Earthquake Engineering*, Istanbul, February 1998.

Kato, B., Akiyama, H., Suzuki, H., and Fukuzawa, Y. (1973), "Dynamic collapse tests of steel structural models," *Preprints, 5th World Conf. on Earthquake Engineering*, Rome.

Kato, B., Akiyama, H. (1981), "Ductility of members and frames subjected to buckling," ASCE Convention, 11-15 May 1981, New York, Preprint, pp. 81-100

Kato, B. (1989), "Rotation capacity of H section members as determined by local buckling," *Journal of Constructional Steel Research*, Vol. 13, pp. 95-109

Kawaguchi, J., and Morino, S. (2001), "Experimental Study on Post - Local Buckling Behavior of Beams-Columns Under Cyclic Loading," *Journal of Structural Construction Engineering.*, (AIJ), No. 540. 141-148.

Kawashima, K., Watanabe, G. and Hayakawa, R., (2003), "Seismic performance of RC bridge columns subjected to bilateral excitation," *Proc. 35th Joint Meeting, Panel on Wind and Seismic Effects, UJNR*, Public Works Research Institute, Tsukuba Science City, Japan, 193-207. (Database url Link:<http://seismic.cv.titech.ac.jp/ja/titdata/titdata.html>)

- Kecman, D. (1983), "Bending collapse of rectangular and square section tubes," *International Journal of Mechanical Science*, Vol. 25, No. 9-10, 623-636
- Kemp, A.R., Dekker, N. W. (1991), "Available rotation capacity in steel and composite beams," *The Structural Engineer*, Vol. 69, No. 5, 88-97
- Kollar, L., Dulacska, E. (1984), "Buckling of shells for engineers," Akademiai kiado Budapest
- Kouichi, Y., and Yamada. (1984). "Elasto - Plastics Deformation and Fracture Behavior of Steel Box Columns Subjected to Double Curvature Cyclic Bending Under Constant Axial Load," Proceedings of AIJ.
- Krawinkler, H., Zohrei, M., Irvani, B. L., Cofie, N., Tamjed, H. H., (1983), "Recommendations for experimental studies on the seismic behavior of steel components and materials", *John. A. Blume Earthquake Engineering Research Center Report No. 61*, September 1983.
- Krawinkler, H., Zohrei, M. (1983), "Cumulative damage in steel structures subjected to earthquake ground motions," *Computers and Structures*, Vol. 44, No. 2, pp. 229-251
- Krawinkler, H., Seneviratna, G. D. P. K. (1998), "Pros and cons of a pushover analysis of seismic performance evaluation," ASCE, *Journal of Engineering Structures*, Vol. (20), pp. 452-464.
- Krawinkler, H., Parisi, F., Ibarra, L., Ayoub, A. and Medina, R. (2000), "Development of a testing protocol for woodframe structures," *Consortium of Universities for Research in Earthquake Engineering (CUREE) Publication No. W-02*, 2000.
- Krawinkler, H., Medina, R., and Alavi, B. (2003), "Seismic drift and ductility demands and their dependence on ground motions," *Engineering Structures*, Vol. 25 (5): 637 – 643.
- Krawinkler, H., Miranda, E. (2004), "Performance-based earthquake engineering," *Earthquake Engineering: from engineering seismology to performance-based engineering. Chapter 9*, Bozorgnia Y, Bertero VV (eds); CRC Press: Boca Raton, 9-1 to 9-59.
- Krawinkler, H., Zareian, F., Haas, K., Lignos, D. G., (2006), "Issues affecting the R-factor determination AAC case study," Report submitted as part of the ATC-63 project.
- Krawinkler, H., Lignos, D. G., (2007), "How to predict and reduce the probability of collapse of non-ductile building structures," International Workshop On Measures for the Prevention of Total Collapse of Existing Low-Rise Structures, November 19-20, Istanbul Technical University, Istanbul, Turkey
- Kuhlmann, U. (1986), "Rotations kapazität biegebeanspruchter I-profile unter berücksichtigung des plastischen Beulens," Technical report, Bochum University, Mitteilung Nr. 86-5
- Kukreti, A.R., and Abolmaali, A.S. (1999), "Moment-rotation hysteresis behavior of top and seat angle steel frame connections," *Journal of Structural Engineering*, ASCE, Vol. 125(8), 810-820.

- Kunnath, S. K., Reinhorn, A.M., Park, Y.J. (1990), "Analytical modeling of inelastic response of R/C structures," *Journal of Structural Engineering*, 116, 4, Apr. 1990, pages 996-1027
- Kurata, M., Nakashima, M., and Suita, K. (2005). "Effect of column base behavior on the seismic response of steel moment frames," *Journal of Earthquake Engineering*, Vol. 9, Special Issue 2 (2005) 415-438, Imperial College Press.
- Kyriakides, M.A., Billington, S.L. (2008) "Experimental investigations of engineered cementitious composites as a seismic retrofit for masonry infill walls," *Proceedings of the 2008 IABSE Annual Meeting and Congress, Chicago*.
- Lay, M. G. and Galambos, T. V., (1966). "Bracing requirements for inelastic steel beams," *Journal of Structural Division*, Vol. 92, No. ST2, pp. 207-228, ASCE.
- Lay, M. G., (1965). "Flange local buckling in wide-flange shapes," *Journal of Structural Division*, Vol. 91, No. ST6, pp. 95-116, ASCE.
- Lee, K. and Stojadinovic, B. (2004), "Low-cycle fatigue limit on seismic rotation capacity for US Steel moment connections," *Proceedings, 13th World Conference on Earthquake Engineering*, August 2004, CD-ROM, Paper # 90.
- Liddell, D., Ingham J. M., Wight, J. K. (2000). "Influence of loading history on ultimate displacement of concrete structures," Report No. 597 University of Auckland,.
- Liel, A.B., Haselton, C.B., Deierlein, G.G., and Baker, J.W. (2007) "Incorporating modeling uncertainties in the assessment of seismic collapse risk of buildings," *Structural Safety* (accepted).
- Lignos, D. G., Krawinkler, H. (2007), "A database in support of modeling of component deterioration for collapse prediction of steel frame structures," ASCE Structures Congress, Long Beach CA, SEI institute.
- Lignos D. G., Krawinkler, H., and Whittaker, A. (2008), "Shake table collapse tests of a 4-story moment resisting steel frame," 14th World Conference on Earthquake Engineering, Beijing, China Oct. 12-17, 2008.
- Liu, J. (2003), "Examination of expected yield and tensile strength ratios," Report submitted to Americal Institute of Steel Construction, Inc., September, 2003
- Liu, J., Sabelli, R., Brockenbrough, R. L., Fraser, T. (2005), "Expected yield stress and tensile strength ratios for determination of expected member capacity in the 2005 AISC seismic provisions," *Engineering Journal*, 2005, First quarter: pp. 15-25
- Liu, X., DeVor, R.E., Kapoor, S.G., Ehmann, K.F., (2004), "The mechanics of machining at the microscale: Assessment of the current state of the science," *Journal of Manufacturing Science and Engineering*, Transactions of the ASME, Vol. 126(4), pp. 666-678

- Lukey, A. F., Adams, P.F. (1969), "Rotation capacity of beams under moment gradient," *Journal of the Structural Division*, Vol. 95, ST 6, pp. 1173-1188
- MacRae, G. A., (1994), "P- δ effects on single-degree-of-freedom structures in earthquakes," *Earthquake Spectra*, 10, 3, Aug. 1994, pp. 539-568
- Maheri, M. (2005), "Seismic performance of adobe construction during recent Iranian earthquakes," Sismo Adobe. 2005.
- Mahin, S. A., and Bertero, V.V., (1972), "Rate of loading effect on uncracked and repaired reinforced concrete members," EERC No. 73-6, Earthquake Engineering Research Center, University of California, Berkeley, 1972.
- Martin, S. C., and Villaverde, R. (1996), "Seismic collapse of steel frame structures," *Proc., 11th World Conf. on Earthquake Engineering*, Acapulco, Mexico, Paper No. 475.
- Mathworks (2005), "Matlab documentation," <http://www.mathworks.com/access/helpdesk/help/techdoc/matlab.shtml>.
- Mazzolani, F.M., and Piluso, V. (1992), "Evaluation of the rotation capacity of steel beams and beams-columns," in first State-of-the-Art workshop COST C1, Strasburg
- McDermott, J.F. (1969), "Local plastic buckling of A514 steel members," *Journal of the Structural Division*, Vol. 95, ST 9, pp. 1837-1850
- Medina, R. (2002), "Seismic demands for nondeteriorating frame structures and their dependence on ground motions," *PhD. Dissertation* submitted to the Department of Civil Engineering, Stanford University
- Medina, R., and Krawinkler, H. (2003), "Seismic demands for nondeteriorating frame structures and their dependence on ground motions," *John A. Blume Earthquake Engineering Center Report No. TR 144*, Department of Civil Engineering, Stanford University, and PEER Report 2003/15.
- Mehanny, S.S.F. and Deierlein, G.G. (2000), "Modeling of assessment of seismic performance of composite frames with reinforced concrete columns and steel beams," *John A. Blume Earthquake Engineering Research Center Report No. 135*, Department of Civil Engineering, Stanford University
- Mehanny, S. S. F., and Deierlein, G. G. (2001). "Seismic damage and collapse assessment of composite moment framesm" *Journal of Structural Engineering*, (ASCE) 127(9), 1045–1053.
- Mehrabi, A.B., Shing, P.B., Schuller, M.P., and Noland, J.L. (1994), "Performance of masonry-infilled R/C frames under in-plane lateral loads," *Report No. CU/SR-94-6*, Dept. of Civil, Environmental, and Architectural Engineering, University of Colorado, Boulder, CO.
- Mehrabi, A.B., Shing, P.B., Schuller, M.P., and Noland, J.L. (1996), "Experimental evaluation of masonry-infilled RC frames," *Journal of Structural Engineering*, (ASCE) 122(3), pp.228-237.

- Miranda, E., and Akkar, D. (2003), "Dynamic instability of simple structural systems." *Journal of Structural Engineering*, 129 (12), pages 1722–1726.
- Moehle, J.P., Elwood, K.J., and Sezen, H., (2002), "Gravity load collapse of building frames during earthquakes," *S. M. Uzumeri Symposium: Behavior and Design of Concrete Structures for Seismic Performance*, ACI Special Publication (SP-197), American Concrete Institute, pp. 215-238.
- Möller, M., Johansson, B., Collin, P. (1997), "A new analytical model of inelastic local flange buckling," *Journal of Constructional Steel Research*, Vol. (23) No. 1-3, pages 43-63.
- Moncarz, P.D., and Krawinkler, H., (1981), "Theory and application of experimental model analysis in earthquake engineering," *John A. Blume Earthquake Engineering Center, Report No. 50*, Department of Civil Engineering, Stanford University.
- Morrow, J., and Raske, D.T., (1969), "Mechanics of materials in low cycle fatigue testing," ASTM STP 465, American Society for Testing and Materials, pp. 67-86.
- Mostaghel, N. (1999). "Analytical description of pinching, degrading hysteretic systems." *J. Engrg. Mech.*, ASCE, 125(2), 216–224.
- Myers A.T., Kanvinde, A.M., Deierlein, G.G., and Fell, B.V. (2008), "Effect of weld details on the ductility of steel column Base plate Connections," *Journal of Constructional Steel Research*, Elsevier (in press).
- Nakashima, M., and Liu, D. (2005). "Instability and Complete Failure of Steel Columns Subjected to Cyclic Loading," *Journal of Engineering Mechanics*, Vol. 131, No. 6, June 1, 2005.
- Nakashima, M., Matsumiya, T., Suita, K., and Liu, D. (2006). "Test on full-scale three-story steel moment frame and assessment of ability of numerical simulation to trace cyclic inelastic behavior." *Earthquake Engineering and Structural Dynamics*, (35) 1, 3–19.
- Newell, J., and Uang, C. M. (2006), "Cyclic behavior of steel columns with combined high axial load and drift demand," *Final Report* to American Institute of Steel Construction, Inc, Report No. SSRP-06/22, Department of Structural Engineering University of California, San Diego.
- Nielsen, N.N., and Imbeault, F.A., (1971) "Validity of various hysteretic systems," *Proceedings*, Third Japan National Conference on Earthquake Engineering, 1971, pages. 707-714.
- OpenFresco (2008), "Open-source framework for experimental setup and control," (NEES, http://neesforge.nees.org/forum/forum.php?forum_id=200)
- Oppenheim, A. V., Schafer, R. W., Buck, J. R., (1999), "Discrete- time signal processing," 2nd edition, Prentice-Hall Signal Processing Series
- OpenSees (2007), "Open System for Earthquake Engineering Simulation," Pacific Earthquake Engineering Research Center (PEER), (<http://opensees.berkeley.edu>)

Otani, S., and M.A. Sozen, (1972), "Behavior of multistory reinforced concrete frames during earthquakes," *Structural Research Series No. 392*, Civil Engineering Studies, University of Illinois, Urbana, 1972.

Otani, S. (1974), "Inelastic analysis of R/C frame structures," *Journal of Structural Division, ASCE*, 100, ST7, July 1974, pages 1433-1449

Panagiotakos, T. B. and Fardis, M. N. (2001), "Deformations of reinforced concrete members at yielding and ultimate," *ACI Structural Journal*, 98, 2, March-April 2001

Piley, W. D., Peterson, J., Clark, K. (1997), "Peterson's stress concentration factors," Wiley John & Sons, Incorporated, April 1997

Pincheira, J. A., Dotiwala, F. S. and D'Souza, J. T. (1999), "Seismic analysis of older reinforced concrete columns", *Earthquake Spectra*, 15, 2, May 1999, pages 245-272

Plumier, A., Doneaux, C., Bouwkamp, J. G., Plumier, C., (1998), "Slab design in connection zone of composite frames," 11th European Conference on Earthquake Engineering, Balkema, Rotterdam

Popov, E. P., Stephen, R. M., (1970), "Cyclic loading of full-size steel connections," UCB/EERC-70/03.

Prakash, V., Powell, G. H., Campbell, S., (1993), "DRAIN-2DX: basic program description and user guide," *Report No. UCB/SEMM-93/17*. University of California at Berkeley, Berkeley, California.

Ramberg, W., and Osgood, W. R. (1943), "Description of stress-strain curves by three parameters," *Monograph No. 4*, Pubblicazione Italsider, Nuova Italsider, Genova.

Rahnama, M. and Krawinkler, H. (1993), "Effect of soft soils and hysteresis models on seismic design spectra," *John A. Blume Earthquake Engineering Research Center Report No. 108*, Department of Civil Engineering, Stanford University.

Reinhorn, A. M., Madan, A., Valles, R. E., Reichmann, Y., and Mander, J. B. (1995), "Modeling of masonry infill panels for structural analysis." *Tech. Rep. NCEER-95-0018*, State University of New York at Buffalo, Buffalo, N.Y.

Ricles, J. M., Mao, C., Lu, L.W., Fisher, J.W. (2000). "Development and evaluation of improved ductile welded unreinforced flange connections," *Report No. SAC/BD-00/24.*, SAC Joint Venture, Sacramento, CA.

Ricles, J.M., Zhang, X., Lu, L.W., and Fisher, J. (2004). "Development of seismic guidelines for deep-column steel moment connections," *Report No. 04-13*, Advanced Technology for Large Structural Systems.

- Roeder, C. W. (2002), "Connection performance for seismic design of steel moment frames," *Journal of Structural Engineering*, ASCE, April 2002, Vol. 128(4), pp. 517-525
- Rodgers, J. and Mahin, S. (2006), "Effects of Connection Fractures on Global Behavior of Steel Moment Frames Subjected to Earthquakes," *Journal of Structural Engineering*, (ASCE), January 2006, Vol. 132, No. 1, pages. 78-88
- SAC Joint Venture (1998) "Development of steel databases," (<http://www.sacsteel.org/connections/>)
- SAC Joint Venture. (2000a), "Recommended seismic design criteria for new steel moment frame buildings," *Rep. No. FEMA 350*, Federal Emergency Management Agency, Washington, D.C.
- SAC Joint Venture. (2000b), "Prestandard and commentary for the seismic rehabilitation of buildings," *Rep. No. FEMA 356*, Federal Emergency Management Agency, Washington, D.C.
- Schellenberg, A. and Mahin, S. (2006), "Integration of Hybrid Simulation Within the General-Purpose Computational Framework OpenSees," *Proceedings, 8th National Conference on Earthquake Engineering, EERI*, San Francisco, CA, April 2006, Paper 1378
- Shuey, B., Engelhardt, M. and Sabol, T. (1996), "Testing of repair concepts for damaged steel moment connections", in *Technical Report: Experimental Investigations of Beam-Column Subassemblages* (SAC 96-01, Part 2).
- Sivaselvan M., and Reinhorn, A.M. (2000). "Hysteretic models for deteriorating inelastic structures", *Journal of Engineering Mechanics*, ASCE, Vol. 126(6), 633-640.
- SolidWorks (2004), "Mechanical CAD software," SolidWorks Corporation, Concord, MA 01742.
- Song, J. and Pincheira, J. (2000), "Spectral displacement demands of stiffness and strength degrading systems," *Earthquake Spectra*, 16, 4, Nov. 2000, pages 817-851.
- Sucuoglu, H., and Erberik, A., (2004), "Energy-based hysteresis and damage models for deteriorating systems," *Earthquake engineering & structural dynamics*, 2004, vol. (33),(1),pages. 69-88
- Suita, K., Engelhardt, M. D., Inoue, K., Nakashima, M., (1998), "Plastic deformation capacity of cyclically loaded ductile moment connection, Comparison between post-Kobe and post-Northridge beam-to-column connection".
- Suita, K., Yamada, S., Tada, M. Kasai, K. Matsuoka, Y. and Sato, E. (2007), "E-Defense tests on full-scale steel buildings: Part 2 – Collapse experiments on moment frames," *Proc. Structures Congress 2007*, ASCE, Long Beach, 247-18.
- Suita, K., Yamada, S., Tada, M., Kasai, K., Matsuoka, Y. and Sato, E. (2008), "Results of recent E-Defense tests on full-scale steel buildings: Part 1 – Collapse experiment on 4-story moment frame," *Proc. Structures Congress 2008*, ASCE, Vancouver.

Sun Developer Network (2007), "Java 2 platform, standard edition (J2SE) performance," Java Performance Documentation.

Sugiyama S., and Igarashi (1986), "Experimental Investigation of Inelastic Behavior of Cold - Formed Rectangular Hollow Structural Sections under Bending and Constant Axial Force," *Journal of Structural Construction Engineering* (AIJ).

Tada, M., Ohsaki, M., Yamada, S., Motoyui, S. and Kasai, K. (2007), "E-Defense tests on full-scale steel buildings: Part 3 – Analytical simulation of collapse," *Proc. Structures Congress 2007*, ASCE, Long Beach, 247-19.

Taejin K., Whittaker, A. S. Gilani, A. S. Bertero, V. Takhirov, S., (2000), "Cover-plate and flange-plate steel moment-resisting connections." *Journal of Structural Engineering*, Vol. 128, No. 4, ASCE, Washington, D.C., pp 474-482

Takeda, T., Sozen, M., Nielsen, N. (1970), "Reinforced concrete response to simulated earthquakes," *Journal of the Structural Division*, 96, ST12, Dec.1970, pages 2557-2573

Takizawa, H. and Jennings, P. (1980), "Collapse of a model for ductile reinforced concrete frames under extreme earthquake motions," *Earthquake Engineering and Structural Dynamics*, 8, 1980, pages 117-144

Tanner, J. E. (2003), "Design provisions for autoclaved aerated concrete (AAC) structural systems," *Ph.D. dissertation*, Dept. of Civil Engineering, The University of Texas at Austin.

Tanner, J.E., Varela, J.L., Klingner, R.E., (2005), "Design and seismic testing of a two story full-scale Autoclaved Aerated Concrete (AAC) assemblage specimen," *Structures Journal*, American Concrete Institute, Farmington Hills, Michigan, vol. 102, no. 1, pp. 114-119.

Topper, T.H., and Sandor, B.I., (1970), "Effects of mean stress and pre-strain on fatigue – damage summation," ASTM STP 462, American Society for Testing and Materials, pp. 93-104.

Torrealva, D. (2003), "Caracterización de daños en construcciones de adobe," *Serie Cuadernos de Adobe*. Pontificate Catholic University of Peru. 2003

Totten. G. E., (2006), "Handbook of lubrication and Tribology," Raton, FL, USA, CRC Press

Tremblay, R., Tchegotarev, N., and Filiatrault, A. (1997), "Seismic performance of RBS connections for steel moment resisting frames: Influence of loading rate and floor slab," *Behavior of Steel Structures in Seismic Areas (Proceedings of the Second International Conference, STESSA '97)*, Kyoto, pp. 664-671.

Tsai, K.C., Chen, C.Y., (1996), "Performance of ductile steel beam-column moment connections," *Eleventh World Conference on Earthquake Engineering*, Acapulco, Paper No. 405.

Tsuda, K., and Matsui, C. (1998), "Strength of square steel tubular beam-columns under constant vertical and horizontal loads," *Journal of Structural Construction Engineering*, AIJ, No. 512. 149-156.

- Tsuji, B., Nakatsura, T. (1986), "Safety Criteria in Design of Tubular Structures," Proceedings of the International Meeting held in Tokyo, Japan on 11-12 July 1986.
- Uang, C. M., Bondad, D., Noel, S., (1996), "Cyclic testing of the MNH-SMTF™ dual strong axes moment connection with cruciform column", Final report to Myers, Nelson, Houghton, Inc. Costa Mesa, CA. Structural systems research project, Report No. TR-96/04.
- Uang, C.M., Fan, C. C., (1999), "Cyclic instability of steel moment connections with reduced beam sections", *Structural Steel Research Project Report No. SSRP-99/21*.
- Uang, C.M., Yu, K., and Gilton, C. (2000a). "Cyclic response of RBS moment connections: Loading Sequence and Lateral Bracing Effects," *Report No. SSRP-99/13*, 2000.
- Uang, C.M., Gilton, C., and Chi, B. (2000b). "Cyclic response of RBS moment connections: Weak-axis configuration and deep column effects," *Report No. SSRP-2000/03*, 2000.
- Varela, J. L. (2003). "Development of R and C_d factors for the seismic design of AAC structures," *Ph.D. dissertation*, Dept. of Civil Engineering, The University of Texas at Austin.
- Valles, R. E., Reinhorn, A.M., and Barrón, R. (1996), "Seismic evaluation of a low-rise RC building in the vicinity of the New Madrid seismic zone," *Technical Report NCEER-96-xxxx*, National Center for Earthquake Engineering Research, State University of New York at Buffalo (in press)
- Vamvatsikos, D. and Cornell, C. A. (2002), "Incremental Dynamic Analysis," *Earthquake Engineering and Structural Dynamics*, 31, 3, Mar. 2002, pages 491-514.
- Vayas, I., Psycharis, I. (1995), "Local cyclic behavior of steel members. In Behavior of Steel Structures in Seismic Areas, STESSA 94 (eds F.M Mazzolani and V. Gioncu) Timisoara, 26 June-1 July, 1994, E&FN Spon, London, 231-241
- Vian, D. and Bruneau, M. (2001), "Experimental investigation of P-Delta effects to collapse during earthquakes," *Technical Report MCEER-01-0001*, June 2001
- Vian D, Bruneau M. (2003), "Tests to structural collapse of single degree of freedom frames subjected to earthquake Excitations," *Journal of Structural Engineering (ASCE)* 2003; **129**, pages 1676–1685.
- Wasti, S.T. and Ozcebe, G., Editors (2006), "Advances in earthquake engineering for urban risk reduction," NATO Science Series IV: Earth and Environmental Sciences – Vol. 66, Kluwer Academic Publishers
- Wen, Y.-K. (1980), "Equivalent linearization for hysteretic systems under random excitation," *Journal of Applied Mechanics.*, Vol. 47, pages 150-154.
- White, D.W., Barth, K. E. (1998), "Strength and ductility of compact flange I-girders in negative bending," *Journal of Constructional Steel Research*, Vol. 45, No. 3, pp. 241-280

Williamson, E.B. (2003), "Evaluation of damage and P-D effects for systems under earthquake excitation," *Journal of Structural Engineering*, 129, 8, pages 1036-1046

Yamanaka, K., Yamada, (1984), "Elasto-plastic deformation and fracture behavior of steel box columns subjected to double curvature cyclic bending under constant axial load", *Journal of Structural Construction Engineering*, AIJ, Oct, 1984.

Yu, Q, S., Gilton, C., and Uang, C, M., (2000), "Cyclic response of RBS moment connections: loading sequence and lateral bracing effects," *Report No. SAC/BD-00/22*.

Zareian, F, (2006), "Simplified performance-based earthquake engineering", *Ph.D Dissertation*, Department of Civil and Environmental Engineering, Stanford University, Stanford California.

Zareian, F., and Krawinkler, H. (2007), "Assessment of probability of collapse and design for collapse safety," *Earthquake Engineering and Structural Dynamics*, **36**(13), 1901-1914.

Zohrei, M., Krawinkler, H. (1979), "Cyclic stress – strain behavior of A36 steel," *Engineering thesis*, J. A. Blume Earthquake Engineering Research Center.